

LECTURE NOTES IN GEOINFORMATION AND CARTOGRAPHY

LNG&C

Xiaojun Yang (Ed.)

**Remote Sensing and  
Geospatial Technologies  
for Coastal Ecosystem  
Assessment  
and Management**



Springer

# Lecture Notes in Geoinformation and Cartography

---

Series Editors: William Cartwright, Georg Gartner, Liqiu Meng,  
Michael P. Peterson

Xiaojun Yang (Ed.)

Remote Sensing  
and Geospatial Technologies  
for Coastal Ecosystem  
Assessment and Management

 Springer

*Editor*

Prof. Xiaojun Yang  
Florida State University  
Dept. of Geography  
Tallahassee FL 32306  
USA  
xyang@fsu.edu

ISBN: 978-3-540-88182-7

e-ISBN: 978-3-540-88183-4

DOI 10.1007/978-3-540-88183-4

Lecture Notes in Geoinformation and Cartography ISSN: 1863-2246

Library of Congress Control Number: 2008935905

© Springer-Verlag Berlin Heidelberg 2009

This work is subject to copyright. All rights are reserved, whether the whole or part of the material is concerned, specifically the rights of translation, reprinting, reuse of illustrations, recitation, broadcasting, reproduction on microfilm or in any other way, and storage in data banks. Duplication of this publication or parts thereof is permitted only under the provisions of the German Copyright Law of September 9, 1965, in its current version, and permission for use must always be obtained from Springer. Violations are liable to prosecution under the German Copyright Law.

The use of general descriptive names, registered names, trademarks, etc. in this publication does not imply, even in the absence of a specific statement, that such names are exempt from the relevant protective laws and regulations and therefore free for general use.

*Cover design:* deblik, Berlin

Printed on acid-free paper

9 8 7 6 5 4 3 2 1

springer.com

# Preface

Coastal areas, by virtue of their position at the interface between truly terrestrial ecosystems and aquatic systems, belong to the most dynamic and fascinating ecosystems on Earth. They are among the most productive ecosystems on our home planet, providing numerous ecological, economic, cultural, and aesthetic benefits and services. Meanwhile, they are also the foci of human settlement, industry, and tourism. Because of large population and intense development, global coastal ecosystems are under strain as never before and there is a strong need for environmental monitoring and assessment in order to manage and protect these sensitive areas more effectively. This in turn requires reliable information bases and capable analytical techniques. Conventional field-based survey and mapping methods are still vital but often logistically constrained. Because of cost-effectiveness and technological soundness, remote sensing and geospatial technologies have increasingly been used to develop useful sources of information that support decision making as related to many coastal applications. But coastal areas comprise complex, dynamic landscapes, thus challenging the applicability and robustness of these methods and technologies. Encouragingly, recent innovations in data, technologies, and theories in the wider arena of remote sensing and geospatial technologies have provided scientists with invaluable opportunities to advance the studies on the coastal environment.

Within the above context, a book on coastal ecosystems is timely. This book focuses on the development of remote sensing and related geospatial technologies for monitoring, synthesis and modeling in the coastal environment. The book is divided into three major parts. The first part examines several conceptual and technical issues of applying remote sensing and geospatial technologies in the coastal environment. The second part showcases some latest development in the use of remote sensing and geospatial technologies for coastal ecosystem assessment and management with emphasis on coastal waters, submerged aquatic vegetation, benthic habitats, shorelines, coastal wetlands and watersheds. The last part details a watershed-wide synthetic approach that links upstream stressors with downstream responses for integrated coastal ecosystem assessment and management.

This book is the result of an extensive research by interdisciplinary experts, and will appeal to students and professionals dealing with not only remote sensing, geospatial technologies and coastal science but also oceanography, ecology, environmental science, natural resources management, geography and hydrology in the academic, governmental and business sectors. The Editor is grateful to all the contributing authors and anonymous reviewers for their time, talents and energies and for keeping to a strict timeline and to staff at Springer-Verlag, especially Agata Oelschlaeger and Christian Witschel, for their encouragement, patience and support. Acknowledgements are due to Tingting Zhao and Libin Zhou for manuscript proofreading and to my wife Xiaode Deng and my son Le Yang for their patience and love. Lastly, the Editor would like to dedicate this book to the late Professor C. P. Lo who offered brilliant guidance and boundless encouragement over many years of my professional career.

Tallahassee, Florida

*Xiaojun Yang*

# Contents

<b>1</b>	<b>Remote Sensing, Geospatial Technologies and Coastal Ecosystems . . .</b>	<b>1</b>
	Xiaojun Yang	
<b>Part I Conceptual and Technical Issues</b>		
<b>2</b>	<b>Sensors and Techniques for Observing Coastal Ecosystems . . . . .</b>	<b>17</b>
	Victor V. Klemas	
<b>3</b>	<b>Geographic Information Systems and Spatial Analysis for Coastal Ecosystem Research and Management . . . . .</b>	<b>45</b>
	Jialing Wang, Libin Zhou and Xiaojun Yang	
<b>4</b>	<b>Fuzzy Approach for Integrated Coastal Zone Management . . . . .</b>	<b>67</b>
	Tao Cheng, Martien Molenaar and Alfred Stein	
<b>5</b>	<b>Spatial Data Infrastructures for Coastal Environments . . . . .</b>	<b>91</b>
	Dawn J. Wright	
<b>Part II Remote Sensing of Coastal Waters</b>		
<b>6</b>	<b>Airborne Remote Sensing of Chlorophyll in Chesapeake Bay, USA . .</b>	<b>115</b>
	Lawrence W. Harding, Jr. and W. David Miller	
<b>7</b>	<b>Bio-Optical Characteristics and Remote Sensing in the Mid Chesapeake Bay Through Integration of Observations and Radiative Transfer Closure . . . . .</b>	<b>139</b>
	Maria Tzortziou, Charles L. Gallegos, Patrick J. Neale, Ajit Subramaniam, Jay R. Herman and Lawrence W. Harding, Jr.	

**Part III Mapping Submerged Aquatic Vegetation and Benthic Habitats**

**8 High-Resolution Ocean Color Remote Sensing of Coral Reefs and Associated Benthic Habitats** . . . . . 171  
Deepak R. Mishra

**9 An Integrated Approach to Benthic Habitat Mapping Using Remote Sensing and GIS: An Example from the Hawaiian Islands** . . 211  
Ann E. Gibbs and Susan A. Cochran

**10 Assessment of the Abundance of Submersed Aquatic Vegetation (SAV) Communities in the Chesapeake Bay and its Use in SAV Management** . . . . . 233  
Kenneth A. Moore, Robert J. Orth and David J. Wilcox

**11 Distribution and Spatial Change of Hudson River Estuary Submerged Aquatic Vegetation: Implications for Coastal Management and Natural Resource Protection** . . . . . 259  
William C. Nieder, Susan Hoskins, Stephen D. Smith and Stuart E.G. Findlay

**12 Mapping Marine Macrophytes along the Atlantic Coast of Tierra Del Fuego (Argentina) by Remote Sensing** . . . . . 279  
Sandra E. Torrusio

**Part IV Shoreline Change, Coastal Wetland and Watershed Characterization**

**13 Shoreline Mapping and Coastal Change Studies Using Remote Sensing Imagery and LIDAR Data** . . . . . 297  
Hongxing Liu

**14 Remote Sensing of Coastal Mangrove Forest** . . . . . 323  
Le Wang and Wayne P. Sousa

**15 Remote Sensing Support for Tidal Wetland Vegetation Research and Management** . . . . . 341  
Maggi Kelly and Karin Tuxen

**16 Assessment of Coastal-Vegetation Habitats Using Airborne Laser Remote Sensing** . . . . . 365  
Amar Nayegandhi and John C. Brock

**17 Measuring Habitat Changes in Barrier Island Marshes: An Example from Southeastern North Carolina, USA** . . . . . 391  
Joanne N. Halls

**18 Mapping Fire Scars and Marsh Recovery with Remote Sensing Data** 415  
Elijah Ramsey III, Amina Rangoonwala, Frank Baarnes and Ruth Spell



**19 Response of Reed Mudflats in the Caspian Coastal Zone to Sea Level Fluctuations** ..... 439  
Valentina I. Kravtsova

**20 Integrating Satellite Imagery and Geospatial Technologies for Coastal Landscape Pattern Characterization** ..... 461  
Xiaojun Yang

**Part V Integrated Coastal Ecosystem Assessment**

**21 Remote Sensing and Spatial Analysis of Watershed and Estuarine Processes for Conservation Planning in Elkhorn Slough, Monterey County, California** ..... 495  
Kristin B. Byrd

**22 Runoff Water Quality, Landuse and Environmental Impacts on the Bellairs Fringing Reef, Barbados** ..... 521  
Marko Tomic, Robert B. Bonnell, Pierre Dutilleul and Hazel A. Oxenford

**Index** ..... 555

# Contributors

**Frank Baarnes** Department of Hydrology and Water Resources, University of Arizona, 1133 E. North Campus Drive, Tucson, AZ 85721, USA, fbarnes@hwr.arizona.edu

**Robert B. Bonnell** Department of Bioresource Engineering, McGill University, Macdonald Campus, 21,111 Lakeshore Road, Ste-Anne-de-Bellevue, QC, H9X 3V9, Canada, robert.bonnell@mcgill.ca

**John C. Brock** U.S. Geological Survey, Florida Integrated Science Center, 600 4<sup>th</sup> Street South, St. Petersburg, FL 33701, USA, jbrock@usgs.gov

**Kristin B. Byrd** California Academy of Sciences, 55 Concourse Drive, Golden Gate Park, San Francisco, CA 94118, USA, kbyrd@calacademy.org

**Tao Cheng** Department of Civil, Environmental and Geomatic Engineering, University College London, Gower Street, London, WC1E 6BT, UK, tao.cheng@ucl.ac.uk

**Susan A. Cochran** U.S. Geological Survey, Pacific Science Center, 400 Natural Bridges Drive, Santa Cruz, CA 95060, USA, scochran@usgs.gov

**Pierre Dutilleul** Department of Plant Science, McGill University at Macdonald, 21,111 Lakeshore Rd., Ste-Anne-de-Bellevue, QC, H9X 3V9, Canada, pierre.dutilleul@mcgill.ca

**Stuart E. G. Findlay** Institute of Ecosystem Studies, 65 Sharon Turnpike, P.O. Box AB, Millbrook, NY 12545, USA, findlays@ecostudies.org

**Charles L. Gallegos** Smithsonian Environmental Research Center, 647 Contees Wharf Road, P.O. Box 28, Edgewater, MD, 21037, USA, gallegosc@si.edu

**Ann E. Gibbs** U.S. Geological Survey, Pacific Science Center, 400 Natural Bridges Drive, Santa Cruz, CA 95060, USA, agibbs@usgs.gov

**Joanne N. Halls** Department of Geography and Geology, University of North Carolina Wilmington, 601 S. College Rd., Wilmington, NC 28403, USA, hallsj@uncw.edu

**Lawrence W. Harding, Jr.**, Horn Point Laboratory, University of Maryland Center for Environmental Science, Cambridge, MD 21613, USA, larry@hpl.umces.edu

**Jay R. Herman** National Aeronautics and Space Administration, Goddard Space Flight Center, 8800 Greenbelt Road, Greenbelt, MD 20771, USA, Jay.R.Herman@nasa.gov

**Susan Hoskins** Institute for Resource Information Sciences, Department of Crop and Soil Sciences, Cornell University, 302 Rice Hall, Ithaca, NY 14853, USA, sbh1@cornell.edu

**Maggi Kelly** Department of Environmental Sciences, Policy and Management, University of California at Berkeley, 145 Mulford Hall 3114, Berkeley, CA 94720, USA, mkelly@nature.berkeley.edu

**Victor V. Klemas** College of Marine and Earth Studies, University of Delaware, 110 Robinson Hall, Newark, DE 19716, USA, klemas@udel.edu

**Valentina I. Kravtsova** Department of Geography, Moscow State University, Moscow 119991, Russia, vik@lakm.geogr.msu.ru

**Hongxing Liu** Department of Geography, Texas A&M University, 814C O&M Building, College Station, TX 77843, USA, liu@geog.tamu.edu

**W. David Miller** Remote Sensing Division, Naval Research Laboratory, 4555 Overlook Ave, SW, Washington, DC 20375, USA, wdmiller13@gmail.com

**Deepak R. Mishra** Department of Earth and Environmental Sciences, University of New Orleans, 1039 Geology and Psychology, New Orleans, LA 70148, USA, dmishra@uno.edu

**Martien Molenaar** International Institute for Geo-Information Science and Earth Observation, 7500 AA Enschede, The Netherlands, molenaar@itc.nl

**Kenneth A. Moore** The Virginia Institute of Marine Science, School of Marine Science, College of William and Mary, 1208 Greate Road, Gloucester Point, VA 23062, USA, moore@vims.edu

**Amar Nayegandhi** U.S. Geological Survey, Florida Integrated Science Center, 600 4<sup>th</sup> Street South, St. Petersburg, FL 33701, USA, anayegandhi@usgs.gov

**Patrick J. Neale** Smithsonian Environmental Research Center, 647 Contees Wharf Road, Edgewater, MD 21037, USA, nealep@si.edu

**William C. Nieder** New York State Department of Environmental Conservation, 625 Broadway, Albany, NY 12233, USA, wcnieder@gw.dec.state.ny.us

**Robert J. Orth** The Virginia Institute of Marine Science, School of Marine Science, College of William and Mary, 1208 Grete Road, Gloucester Point, VA 23062, USA, jjorth@vims.edu

**Hazel A. Oxenford** Centre for Resource Management and Environmental Studies, University of the West Indies at Cave Hill, St Michael, Barbados, hazel.oxenford@cavehill.uwi.edu

**Elijah Ramsey III** U.S. Geological Survey, National Wetlands Research Center, 700 Cajundome Blvd, Lafayette, LA 70506, USA, elijah\_ramsey@usgs.gov

**Amina Rangoonwala** IAP World Services, Inc., 700 Cajundome Blvd, Lafayette, LA 70506, USA, amina\_rangoonwala@usgs.gov

**Stephen D. Smith** Institute for Resource Information Sciences, Department of Crop and Soil Sciences, Cornell University, 305 Rice Hall, Ithaca, NY 14853, USA, sds3@cornell.edu

**Wayne P. Sousa** Department of Integrative Biology, University of California at Berkeley, 3060 VLSB, Berkeley, CA 94720, USA, wpsousa@berkeley.edu

**Ruth Spell** Ducks Unlimited, Inc., 3074 Gold Canal Drive, Rancho Cordova, CA 95670, USA, rspell@ducks.org

**Alfred Stein** International Institute for Geo-Information Science and Earth Observation, 7500 AA, Enschede, The Netherlands, stein@itc.nl

**Ajit Subramaniam** Lamont Doherty Earth Observatory, Columbia University, 61 Route 9W, Palisades, NY 10964, USA, ajit@ldeo.columbia.edu

**Sandra E. Torrusio** Faculty of Natural Sciences and Museum, National University of La Plata, 122nd Street-corner 60th Street, La Plata (1900), Buenos Aires, Argentina, and National Commission of Space Activities (CONAE), 751 Paseo Colón street, Buenos Aires (1063), Argentina, torrusio@mail.retina.ar

**Marko Tusic** Department of Bioresource Engineering, McGill University at Macdonald, 21,111 Lakeshore Road, Ste-Anne-de-Bellevue, QC, H9X 3V9, Canada, marko.tusic@mail.mcgill.ca

**Karin Tuxen** Geospatial Imaging & Informatics Facility, University of California, Berkeley, CA 94720, USA, karintuxen@gmail.com

**Maria Tzortziou** Earth System Science Interdisciplinary Center, University of Maryland M-Square Research Park, 5825 University Research Court, Suite 4001, College Park, MD 20740, USA, Maria.A.Tzortziou@nasa.gov

**Jialing Wang** Department of Geography, Geology, and the Environment, Slippery Rock University of Pennsylvania, 331 Advanced Technology and Science Hall, Slippery Rock, PA 16057, USA, jialing.wang@sru.edu

**Le Wang** Department of Geography, State University of New York at Buffalo, 105 Wilkeson Quad, Buffalo, NY 14261, USA, lewang@buffalo.edu

**David J. Wilcox** The Virginia Institute of Marine Science, School of Marine Science, College of William and Mary, 1208 Greate Road, Gloucester Point, VA 23062, USA, dwilcox@vims.edu

**Dawn J. Wright** Department of Geosciences, Oregon State University, 104 Wilkinson Hall, Corvallis, OR 97331, USA, dawn@dusk.geo.orst.edu

**Xiaojun Yang** Department of Geography, Florida State University, 321 Bellamy Building, Tallahassee, FL 32306, USA, xyang@fsu.edu

**Libin Zhou** Department of Geography, Florida State University, 319 Bellamy Building, Tallahassee, FL 32306, USA, lz06c@fsu.edu

# Chapter 1

## Remote Sensing, Geospatial Technologies and Coastal Ecosystems

Xiaojun Yang

This introductory chapter defines the rationale and motivation leading to the development of remote sensing and related geospatial technologies for coastal ecosystem research and management. The chapter begins with a discussion on the motivation of this book project. It then reviews several major types of coastal ecosystems, followed by a discussion on the benefits and possible challenges of using remote sensing and geospatial technologies for coastal ecosystem research and management. Moreover, it provides an overview on the book structure with a chapter-by-chapter outline. Finally, the chapter highlights several areas that need further research.

### 1.1 Introduction

Coastal areas, by virtue of their position at the interface between truly terrestrial ecosystems and aquatic systems, belong to the most dynamic and productive ecosystems on Earth (Yang 2008). They are among the most important ecosystems, providing numerous ecological, economic, cultural, and aesthetic benefits and services. With only 20% of all land area, coastal areas are now the home of nearly half of the global population (Burke et al. 2001). Increased coastal population and intense development threaten and degrade global coastal ecosystems, placing an elevated burden on organizations responsible for the planning and management of these sensitive areas (Hobbie 2000, Hinrichsen 1998, National Research Council 1994, 2000, Small and Nicholls 2003, Selman et al. 2008).

Coastal ecosystem management involves the procedures of monitoring and modeling which require reliable information base and robust analytical technologies. Conventional field-based mapping methods can be still vital but often logistically constrained. Remote sensing and geospatial technologies, given their cost-effectiveness and technological soundness, are increasingly being used to develop useful sources of information supporting decision making for a wide array of coastal

---

X. Yang (✉)

Department of Geography, Florida State University, Tallahassee, FL 32306, USA  
e-mail: xyang@fsu.edu

applications (Yang et al. 1999, Yang 2005a,b). But the coastal environment, because of its complex and dynamic landscapes, challenges the applicability and robustness of remote sensing and geospatial technologies. Encouragingly, recent innovations in data, technologies, and theories in the wider arena of remote sensing and geospatial technologies have permitted scientists with invaluable opportunities to advance the studies on the coastal environment.

Within the above context, a book on coastal ecosystems is timely. Designed for both the academic and business sectors, this book is dedicated to the development of remote sensing and related geospatial technologies for monitoring, synthesis, and modeling in the coastal environment. Specifically, this book concentrates on the following aspects:

- Reviews the principles and methods of remote sensing and geospatial technologies as applied in the coastal environment;
- Examines some latest development in the use of remote sensing and geospatial technologies for coastal ecosystem assessment with emphasis on coastal waters, submerged aquatic vegetation, benthic habitats, shorelines, coastal wetlands and watersheds; and
- Highlights a watershed-wide synthetic approach that links upstream stressors with downstream responses for integrated coastal ecosystem assessment.

In addition to scientific research, the book has incorporated a management component that can be found in some major chapters. Cutting-edge research based on remote sensing and geospatial technologies helps improve our understanding of the status, trends and threats in coastal ecosystems; such knowledge is critical for formulating effective strategies in future management and sustainable coastal ecosystem planning.

Unlike most edited books that are largely based on paper presentations at a specific theme conference, this book features the research conducted by a selected group of interdisciplinary scholars:

- Researchers affiliated with the Estuarine and Great Lakes (EaGLE) research program (<http://es.epa.gov/ncer/centers/eagles/>) that was established by US Environmental Protection Agency (EPA) partnered with National Aeronautics & Space Administration (NASA);
- Researchers who present a scholarly paper in a special paper session on estuarine and coastal ecosystem analysis we organized at the Annual Meetings of Association of American Geographers (AAG) since 2003;
- Some active researchers largely identified from their presentations at several other premier conferences (e.g. annual meetings of American Geophysical Union-AGU or American Society for Photogrammetry and Remote Sensing-ASPRS) in recent years; and
- A small number of other world-level scholars in remote sensing, GIS, and coastal science.

A total of 44 authors from USA, Canada, UK, Holland, Russia, Argentina, and Barbados contribute to this book. Although most of the chapters are authored by US

scholars and with a clear focus on a study site in USA, the knowledge gained from this region can be applied to other coastal ecosystems globally.

## 1.2 Major Types of Coastal Ecosystems

There is no single definition on the coastal zone. Here we consider the coastal zone as a physical region extending from the edge of the continental shelf to the intertidal and near-shore terrestrial area. Globally, this physical region includes a wide array of near-shore terrestrial, intertidal, benthic and pelagic marine ecosystems (Burke et al. 2001). More comprehensive discussions on these ecosystem types are given elsewhere (e.g. Mann 2000, Beatley et al. 2002). Our current discussion limits to several coastal ecosystems including estuaries, coastal marshes, mangroves, sea-grass systems and benthic systems because they are among the major chapter subjects in this book. Note that these ecosystems are largely recognized according to the main primary producer with the exception of estuaries; as a rather large ecosystem, estuaries can include the other four as subsystems but the latter may also occur outside an estuary.

Estuaries are a partially enclosed body of coastal waters typically found where freshwater from rivers meet with saltwater from the ocean. As the tidal mouths of rivers, estuaries and the surrounding lands are places of transition from land to sea. They are often known as bays, lagoons, harbors, inlets, sounds, or fjord. Estuaries are important ecosystems, providing goods and services that are ecologically, economically, and culturally indispensable. Ecologically, estuaries are not only the 'nurseries of the sea,' providing habitats for many marine organisms, such as fish, mammals, birds, and other wildlife, but also serve as a natural buffer that filters out much of the sediments and pollutants carried in by terrestrial runoff, creating cleaner water that eventually benefits both human and marine life. Economically, estuaries support significant fisheries, tourism, and other commercial activities and the development of important public infrastructure, such as harbors and ports vital for shipping, transportation, and industry. Culturally, estuaries are often the focal points for recreation, commerce, scientific research and education, and aesthetic enjoyment. The major threats to estuaries are from human activities as more than two thirds of the global large cities are based on estuaries (Ross 1995). Stresses caused by excessive use of the natural resources and unchecked watershed land use practices have resulted in water quality degradation, harmful algal blooms, unproductive fisheries, loss of biodiversity, and many other human health and natural resource problems.

Coastal marshes are a sensitive, dynamic, and productive ecosystem. They are predominately grasslands that are periodically flooded by tides in the intertidal regions. The salinity from salt or brackish tidal waters creates a salt-stressed aquatic environment where halophytic plants thrive. Coastal marshes may be classified as salt marshes, brackish marshes and freshwater tidal marshes. They may be associated with estuaries, and are also along waterways between coastal barrier islands



and the inner coast. Coastal marshes are of great ecological values because they serve as the nursery grounds for fish, habitats for a wide variety of wildlife, and the buffer zones to protect water quality. The major disturbances and threats to coastal marshes largely come from human activities, such as draining, filling, ditching, and waste dumping, although natural processes like sea-level changes can also affect the areal distribution of coastal marshes.

The mangrove ecosystem is commonly found in tropical and subtropical tidelands throughout the world. The mangrove family of plants dominates this coastal wetland ecosystem due to their ability to thrive in the saline coastal environment. The three mangrove species grown in the United States are red, black, and white mangroves. The term *mangroves* can narrowly refer to these species but most commonly refers to the habitat and entire plant assemblages, for which the term *mangrove swamp* or *mangrove forest* is often used. Because mangroves are constantly replenished with nutrients, they sustain a huge population of organisms that in turn feed fish and shrimp, which support a variety of wildlife; their physical stability help prevent shoreline erosion, shielding inland areas from damage during severe storms and waves. The major threats to mangroves are mostly related to human impacts from dredging, filling and diking, oil spills, herbicide and urban waster runoff.

Seagrasses are aquatic flowering plants that live fully submerged in the saline coastal environment, and are also called 'submerged aquatic vegetation.' Seagrasses can form extensive beds or meadows, dominated by one or more species. They are distributed worldwide in soft sediments from mean low tide level to the depth limit determined by the penetration of light that permits seagrass plants to photosynthesize. Seagrass beds are a highly diverse and productive ecosystem, and they almost always support more invertebrates and fish than the adjacent areas lacking seagrasses (Mann 2000). Seagrass beds provide coastal zones with a number of ecosystem goods and services, such as fishing grounds, wave protection, oxygen production and protection against coastal erosion. Disturbances and threats to seagrasses include natural processes, such as grazing, storms, ice-scouring and desiccation; but human activities, such as eutrophication due to excessive nutrient inputs, mechanical destruction of habitat, and overfishing, are considered to be the major stressors.

The benthic system is the community of organisms living on the bottom of oceans in areas not colonized by macrophytes (Mann 2000). Benthic habitats are virtually bottom environments with distinct physical, chemical, and biological characteristics. They vary widely depending upon their location, depth, salinity, and sediment. Benthic habitats in areas with depth of larger than 200 m have been much less commonly observed and mapped. Estuarine and nearshore benthic habitats can be highly diverse, including submerged mudflats, rippled sandflats, rocky hard-bottom habitats, shellfish beds, and coral reefs. Note that seagrass beds can be described as a benthic system but they are treated separately (see the above paragraph). In terms of ecological functioning, the benthic system serves as the site of nutrient regeneration and the site of considerable secondary production that is utilized by important predators, such as bottom-feeding fish and crustaceans (Mann 2000). The major disturbances and threats to the benthic system are similar to those listed for seagrasses.

### 1.3 Remote Sensing and Geospatial Technologies

Remote sensing is the science and art of acquiring information by a recording device that is not in physical contact with the object under investigation. The technology of modern remote sensing began with the invention of camera more than 150 years ago, and by now many different remote sensing systems have been developed to detect and measure energy patterns from different portions of the electromagnetic spectrum. Remote sensing and related geospatial technologies can help improve our understanding of the coastal ecosystems in several ways, although the realistic potential for making these improvements are often challenged by the complexity in the coastal environment.

Remote sensing and related geospatial technologies (such as geographic information system and spatial analysis) provide at least five major benefits for coastal studies. Firstly, perhaps the largest benefit of remote sensing is its capability of acquiring photos or images that cover a large area, providing a synoptic view that allows us to identify objects, patterns, and human-land interactions. This unique perspective is highly relevant to the ecosystem approach we advocate to study the coastal environment in this book since many coastal processes are operating over a rather large area; failure in observing the entire mosaic of a coastal phenomenon may hinder our ability to understand the potential processes behind the observed patterns.

Secondly, remote sensing provides additional measures for coastal studies. Coastal researchers frequently use data collected from field surveys and measurements. This way of data collection is considered to be accurate but can introduce potential errors due to the bias in sampling design (Jensen 2007). Field measurements can become prohibitively expensive over a large area. Remote sensing can collect data in an unbiased and cost-effectiveness fashion. Moreover, remote sensors can measure energy at wavelengths which are beyond the range of human vision; remote sensor data collected from the ultra-violet, infrared, microwave portions of the electromagnetic spectrum can help obtain knowledge beyond our human visual perception. Data fusion from different sensors can improve coastal mapping and analysis.

Thirdly, remote sensing allows retrospective viewing of the Earth surface, and time-series of remote sensor data can be quite useful to develop a historical perspective of a coastal phenomenon or process, which can help examine significant human or natural processes that act over a long time period. Examples in this book include time-series data on chlorophyll (*chl-1*) and primary productivity that helped examine climate contribution in spatio-temporal dynamics of phytoplankton in Chesapeake Bay (Chap. 6); declining of submerged aquatic vegetation that was linked with increased nutrient and sediment discharges into Chesapeake Bay (Chap. 10); and marshland conversion into other habitat types driven by hydrological modifications and off-farm sedimentation (Chap. 21).

Fourthly, remote sensing can help make connections across levels of analysis for coastal studies. Coastal science disciplines and subdisciplines have their own preferred levels of analysis and normally do not communicate across these levels.

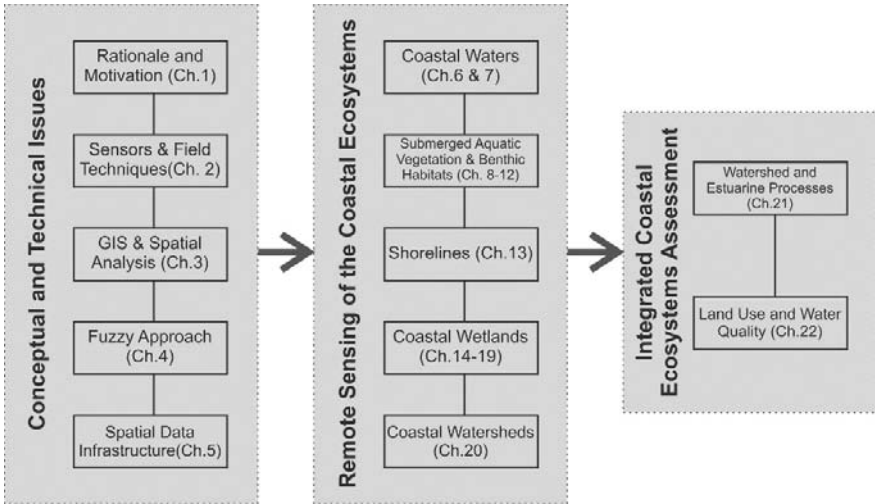
For example, coastal biologists tend to work with individual organisms and populations; oceanographers and coastal ecologists tend to work at higher levels defined by oceanographical features or ecological units; while geographers and coastal planners tend to work at community and ecosystem levels. On the other hand, the temporal scales used by these different coastal researchers vary greatly, from hourly, daily, weekly, monthly, seasonally, to annual or decadal basis. Remote sensing provides essentially global coverage of data with individual pixels ranging from sub-meters to a few kilometers and with varying temporal resolution; such data can be combined to allow work at any scales or levels of analysis, appropriate to the coastal process or phenomenon being examined (Millennium Ecosystem Assessment 2003). Therefore, remote sensing offers the potential for promoting coastal researchers to think across levels of analysis and to develop theories and models to link these levels.

Lastly, remote sensing integrated with other relevant geospatial technologies, such as geographic information systems, spatial analysis and modeling, offers an indispensable framework of monitoring, synthesis and modeling for the coastal environment. Such frameworks support the development of a spatio-temporal perspective of coastal processes or phenomena across different scales and the extension of historical and current observations into the future. They can also be used to relate different human and natural variables for developing an understanding of the indirect and direct drivers of changes in ecological services and the potential feedbacks of such changes on the drivers of changes in the coastal environment.

On the other hand, coastal environments are characterized by erratic climate conditions and complex ecosystem types, challenging the applicability and robustness of remote sensing and geospatial technologies. The high humidity in coastal areas makes difficult to obtain cloud-free images. The complex optical properties in coastal waters dilute the effectiveness of many algorithms for retrieving water quality parameters that were originally developed for open-ocean waters. The complex spectral signatures in coastal aquatic systems make difficult to map and classify benthic habitats. The presence of complex urban impervious materials and croplands, along with a variety of wetlands and vegetation cover, causes substantial inter-pixel and intra-pixel scenic changes, thus complicating the classification and characterization of coastal landscape types. Moreover, it is always difficult to organize field campaigns in coastal areas to acquire sufficient ground-truth data for model development and verification.

## **1.4 Overview of the Book**

With a total of 22 chapters, this book is divided into three major sections (Fig. 1.1). The first section includes the first five chapters that examine a set of core conceptual and technical issues. The second section consists of 15 chapters that showcase some latest development in remote sensing of the coastal ecosystems with emphasis on coastal waters, submerged aquatic vegetation populations, benthic habitats, shorelines, coastal wetlands and watersheds. The last major section comprises the



**Fig. 1.1** A graphical overview of the book structure

two remaining chapters highlighting a watershed-wide synthetic approach that links upstream stressors with downstream responses for integrated coastal ecosystem assessment and management.

In terms of the writing style and contents, this book contains at least three types of chapters. The first type is predominately an overview on one or more major conceptual or technical issues. There are three chapters falling into this category: a generic discussion on the rationale behind the development of remote sensing and related geospatial technologies for coastal ecosystem research and management (Chap. 1), a review on the advances in sensor design and related field observation techniques that are relevant to coastal studies (Chap. 2), and a review on the utilities of geographic information systems and spatial analysis as applied in the coastal environment (Chap. 3). The second type of chapters examines a significant coastal research topic, such as fuzzy approach for integrated coastal zone management (Chap. 4), coastal spatial data infrastructure (Chap. 5), airborne remote sensing of chlorophyll (*chl-a*) in Chesapeake Bay (Chap. 6), remote sensing of bio-optical properties of Chesapeake Bay waters (Chap. 7), remote sensing of submerged aquatic vegetation (SAV) populations in Chesapeake Bay (Chap. 10), shoreline mapping and change analysis (Chap. 13), remote sensing of tidal wetland vegetation (Chap. 15), LIDAR remote sensing of coastal-plant communities (Chap. 16), and remote sensing and spatial analysis of watershed and estuarine processes in Elkhorn Slough (Chap. 21). The last type of chapters discusses a specific research or application: coral reefs and associated benthic habitat mapping (Chap. 8), benthic habitat mapping (Chap. 9), submerged aquatic vegetation mapping and change analysis (Chap. 11), marine macrophyte mapping (Chap. 12), coastal mangrove species discrimination (Chap. 14), barrier island marshes mapping and change analysis (Chap. 17), reed mudflat characterization (Chap. 19),

coastal landscape pattern characterization (Chap. 20), and land use and water quality (Chap. 22). The following paragraphs provide a chapter-by-chapter overview.

As an introduction to the entire book, Chap. 1 discusses the rationale and motivation leading to the development of remote sensing and related geospatial technologies for coastal ecosystem assessment and management. It reviews the major types of global coastal ecosystems, discusses the major benefits and possible challenges of using remote sensing and geospatial technologies for coastal ecosystem research and management, and previews the book structure with a chapter-by-chapter outline. The chapter concludes by highlighting some areas that deserve further research.

Chapter 2 reviews the advances in remote sensor design and related field observation techniques that are appropriate for coastal ecosystem research and management. It covers a variety of remote sensors, such as multispectral and hyperspectral imagers, thermal infrared scanners, radar imagers, scatterometers, altimeters, and LIDAR. The discussion on the sensor development is closely tied with specific coastal and marine applications that characterize the physical and chemical properties of coastal waters, bathymetry or coastal land cover. It emphasizes not only the integration of data acquired from both satellite and airborne platforms to provide sufficient spatial, spectral, radiometric and temporal resolutions but also the incorporation of a reliable field data collection approach to acquire sufficient *in situ* measurements that are used to calibrate and validate the remotely sensed information.

Chapter 3 provides an overview on the utilities of geographic information systems (GIS) and spatial analysis techniques in the context of coastal and marine applications. It reviews several GIS data models that can be used to represent spatio-temporal information in digital environment and the four major groups of spatial analysis techniques, namely, basic spatial analysis, spatial pattern analysis, statistical spatial analysis and spatial modeling. These techniques are especially suitable for characterizing patterns, relationships, and trends in geographically referenced data that can help improve our understanding of the natural and social processes at work and make better decisions for coastal ecosystem planning and management. The chapter concludes by emphasizing technology integration that is needed to deal with the complex and dynamic coastal environment.

Uncertainties exist among almost all the activities in integrated coastal zone management (ICZM), from problem formulation, data collection, analysis and modeling, to decision making and implementation. Chapter 4 details a fuzzy approach to integrated coastal zone management by using the isle of Ameland in the Netherlands as a case study. It discusses the indeterminate nature of coastal landscape units and how they can be represented as fuzzy spatial objects in GIS. It further identifies the dynamic processes and investigates the changes of these fuzzy objects and uncertainties. It finally applies this fuzzy approach to characterize the dynamic changes of sediments along the Dutch coast.

Building a spatial data infrastructure (SDN) for coastal ecosystem assessment and management is critical yet quite challenging. Chapter 5 discusses use of the 'data portal' as the primary means for search, discovery and download of spatial data, one of the most important and intuitive aspects of an SDN. It discusses some of the most pressing challenges to effective implementation of portals within a broad

context of an SDI and explores the potential solutions by using two major case studies that demonstrate innovation, implementation, and practice. At the end, the chapter highlights the importance of partnerships behind the portals with a consideration of virtual communities as an emerging necessity.

Chapter 6 describes airborne remote sensing of phytoplankton dynamics in Chesapeake Bay, the largest estuary in the USA. The high-resolution data obtained in more than 400 flights are synthesized to document the strong role of climate in driving spatial and temporal variability of chlorophyll (*chl-a*) and primary productivity (PP) in the Bay. The climate-induced change is further separated from secular change due to nutrient overenrichment. The chapter further discusses the development of water quality ‘criteria’, including *chl-a* as an indicator of ecosystem responses to nutrient loading, which requires to consider climatic forcing of phytoplankton dynamics.

Remote sensing of water quality and biogeochemical processes largely depends on the accuracy and consistency of the in-situ data used in the calibration and validation of satellite signals and in algorithm development. Chapter 7 discusses how remote sensing of water quality in optically complex environments can be improved by integrating optical measurements and radiative-transfer model calculations. The approach is illustrated with recent findings on the bio-optical characteristics of Chesapeake Bay waters, including measurements of the magnitude and spectral characteristics of particulate backscattering. It then discusses progress on optical closure studies in coastal regions and proposes bio-optical relations for remote sensing retrieval of water quality indicators in the Chesapeake Bay ecosystem.

Remote sensing of benthic habitats is challenged by the confounding influence water column attenuation on substrate reflectance. Chapter 8 reports a research effort that aims to resolve this confounding influence. High-resolution multispectral satellite imagery and airborne hyperspectral imagery are used as inputs in semi-analytical models to derive water depth and water column optical parameters which are further used in various bio-optical algorithms to deduce bottom albedo and to map benthic habitats along the north shore of Roatan Island, Honduras. The hyperspectral data are found to consistently outperform the high spatial-resolution multispectral imagery in terms of classification accuracy but both show similar accuracies at the coarse classification level. This study suggests the need of data fusion from high spectral and spatial resolution sensors for accurate benthic habitat mapping.

Chapter 9 describes an effort to map benthic habitats within the Kaloko-Honokohau National Historic Park, Hawaii, USA, by combining color aerial photography, high-resolution bathymetrical data, and georeferenced underwater video and still photography. Individual habitat polygons are classified and several derivative data concerning seafloor morphology are also generated. It is found that benthic habitat and seafloor morphology vary greatly throughout the study area and the underlying geologic framework and morphology of the submerged volcanic flows provide the primary control on benthic habitats within the park. The habitat maps and associated data can be used as a stand-alone product or in a GIS to provide useful baseline information to coastal scientists and managers.

Chapter 10 reports airborne remote sensing of submerged aquatic vegetation (SAV) populations in Chesapeake Bay. The aerial mapping program began in 1978 and has continued on an annual basis since 1984; currently 173 flight lines are photographed and mapped for SAV each year. Aerial mosaics are produced and the SAV beds are delineated in a GIS environment. The SAV photo-interpretation results are further verified by using extensive ground survey data. A composite historical SAV coverage is also developed by using archival aerial photographs that date back to the 1930s. Comparisons of current SAV populations with historical restoration targets are used annually to provide important indexes of bay condition and trends that are further used to assess the effectiveness of nutrient and sediment reduction strategies for the Bay and its associated watershed.

Chapter 11 discusses the spatio-temporal change of SAV populations in the Hudson River estuary, New York, USA, by using remote sensing, GIS and statistical analysis. The SAV populations show obvious change but are always present in some areas; these persistent SAV beds serve as indicators of overall estuarine health and provide clues to the driving forces responsible for the observed changes in the Estuary. The tidal fresh and oligohaline zones support the greatest abundance of SAV per unit area while the mesohaline zone supports the least. Salinity, light availability, and turbidity are found to affect the SAV distribution. At the end, the chapter discusses how the SAV mapping and change detection information has been used to better protect SAV habitats in the Hudson River estuary.

In many coastal areas, rich marine macrophytes grow to form subaquatic 'forests' that are of great industrial values. Chapter 12 describes an effort aiming to map the marine macrophytes along the intertidal zones in the eastern coast of Tierra del Fuego, Argentina, by using satellite imagery from Landsat, SAC-C, Aster, Radarsat and QuickBird, as well as aerial photographs and maps. These data layers are co-registered before actual mapping the algae distribution. The final maps illustrate the algae distribution and temporal change, which can be useful for improving the management of coastal environment and resources in the study area.

Chapter 13 discusses algorithms and methods for shoreline extraction from remote sensor imagery and LIDAR elevation data. The shoreline extraction method from remote sensor data consists of preprocessing, segmentation and classification, and post-processing. Two methods are used for automated shoreline delineation from LIDAR data. The first method consists of contouring, line selection with a length threshold, and line smoothing and generalization; and the second one is based on LIDAR DEM segmentation. These methods are used to process multi-temporal digital orthorectified aerial photographs, Landsat imagery, and airborne LIDAR data in the upper Texas Gulf coast. The shorelines delineated from a time series of remote sensor images and LIDAR DEMs are further compared in GIS environment for coastal change analysis.

Mangroves are of great ecological and economic values and mangrove mapping can help derive vital information for developing a mangrove management plan. Chapter 14 discusses remote sensing based methods for mangrove species discrimination. Two IKONOS scenes acquired during dry and wet seasons are used to map mangrove species through a Clustering-Based Neural Network (CBNN) classifier.

CBNN is found to outperform two other conventional classifiers, namely, Back-Propagation Neural Networks classifier (BPNN) and Maximum Likelihood Classifier (MLC), when using textural information; rainy season is better than dry season for mangrove species classification. This chapter also examines the capability of hyperspectral data for distinguishing mangrove species.

Chapter 15 reviews the spatial and temporal patterns of tidal wetland vegetation and the ecosystem services these systems provide and examines how remote sensing has been used to map and monitor tidal wetlands. This is accompanied by examples from the authors' actual research and from the published literature. At the end, the chapter discusses some of the remaining technical challenges facing wetland managers and scientists who wish to study tidal marshes by remote sensing. The discussion is grounded in recent work in the San Francisco Bay area, but lessons learned can be applied to other estuarine systems globally.

Chapter 16 reviews airborne LIDAR technology and assesses the capabilities and limitations of LIDAR instruments available from research and commercial sources. The focus is on the extraction of canopy height of short shrubs, marsh, grass, and other vegetation found in the littoral zone. The accuracy in determining the height of low vegetation is considerably improved when using a small-footprint, waveform-resolving LIDAR system. The integration of spectral imagery and LIDAR has the potential of significantly improving the classification and structural mapping of coastal-plant communities. This chapter also identifies several technical challenges in LIDAR remote sensing. Overall, the chapter demonstrates that LIDAR remote sensing is a cost-effective and reliable tool for the quantitative assessment of vegetation habitats on barrier islands, wetlands, and other coastal-plant communities.

Chapter 17 reports a change analysis of back-barrier land cover types at Topsail Island in southeastern North Carolina, USA, by using historical aerial photography and GIS. Spatial analysis of land cover types indicates that when upland gains, it replaces marsh; when upland loses, marsh replaces it; when marsh gains, it replaces upland; when water loses, marsh replaces it; and there was no clear pattern for what transitions when marsh is lost. A series of tests are conducted to verify the accuracy of aerial photo rectification, digitizing and change detection. In addition, a fuzziness test is used to identify true changes in the marsh habitats versus positional changes (or sliver polygons). Results indicate that rectification, interpretation and digitizing of historical aerial photography can be done with reasonable accuracy that warrants meaningful change analysis of back-barrier land cover types.

Chapter 18 focuses on the development of remote sensing methods to detect, inventory and monitor burnt marshes. Two very different coastal marshes in terms of seasonal biomass turnover pattern are monitored with aerospace remote sensing and ground measurement of canopy structure and optical reflectance. The seasonal maidencane marsh produces a very different temporal response to burning than the non-seasonal black needlerush saline marsh does. A vegetation indicator derived from optical data is used to monitor the black needlerush marsh burn, and the use of SAR data further extends the time-since-burn to approximately 900 days. Multi-date TM data in combination with ground measurements are used to monitor the full burn



history of the maidencane marsh. This study indicates that it is possible to monitor marsh recovery history and predict burn history by using optical and radar data.

Chapter 19 examines the response of the Kalmykian coastal zone and the Ural River delta to sea level fluctuations by using a time series of optical and radar images. Photo-interpretation of optical data and digital analysis of radar images indicate that the reed mudflats have played a very important role in the coastal zone dynamics. When the Caspian Sea level rose, the shoreline began to change not from the front reed-belt bound but from the rear bound; when the sea level declined, the rear bound moved seaward faster than the front bound. The ecological niche for reed growth is further determined by constructing a series of profiles along the Ural River delta. Overall, this study shows the usefulness of satellite imagery for the study of coastal zone dynamics in the context of global changes.

Chapter 20 illustrates the utilities of integrating remote sensing and geospatial technologies for coastal landscape pattern characterization. Central to this study is the two satellite images that have been used to extract land cover information through hierarchic classification and spatial reclassification techniques. To suppress the information redundancy and improve the manageability, the initial landscape metrics derived from the land cover information are then reduced to a core set by using landscape ecology principles and multivariate statistical techniques, which are further used to examine the spatio-temporal pattern of landscape. This research demonstrates the integration of remote sensing and other geospatial technologies (such as GIS, landscape metrics and multivariate statistical analysis) has mutually reinforced their utilities effective for coastal landscape pattern characterization.

Chapter 21 discusses the roles of remote sensing and spatial analysis of watershed and estuarine processes for conservation planning in Elkhorn Slough, a coastal watershed in central California. The use of archival aerial photographs helps identify significant trends of marshland conversion to other habitat types, mainly due to hydrological modifications and off-farm sedimentation. Remote sensing research addressing nutrient and sediment runoff demonstrate the potential to correlate estuarine disturbance and response to watershed inputs or properties. Despite some challenges, remote sensing and spatial analysis, especially when applied for salt marsh vegetation change detection and bathymetric change detection, help identify areas for conservation; GIS-based watershed management continues to improve estuarine conditions, as restoration and erosion control are underway to reduce nutrient and sediment discharge.

Chapter 22 examines the impacts of land use upon surface water and seawater quality for a coastal watershed draining into the Hometown Lagoon, Barbados. Surface water quality was poorer in the sub-basin with the highest proportion of developed land; nutrient concentrations at the watershed outlet were quite high, suggesting overfertilization of agricultural lands and nutrient enrichment from urban impervious surfaces. Runoff discharge into the nearshore zone causes plumes with excessive turbidity and nutrients dispersing towards the Bellairs Reef, contributing to the chronic effects of eutrophication and sedimentation. It further recommends several remedy strategies, including improved farming practices for reducing the use of fertilizer quantities, enlargement of sewerage treatment facilities for

accommodating the Island's increasing local and tourism population and phasing out the use of soaps and detergents containing phosphates.

## 1.5 Conclusions

This chapter discusses the rationale and motivation behind the development of remote sensing and related geospatial technologies for coastal ecosystem research and management. It reviews several types of coastal ecosystems that are the major chapter subjects in this volume and discusses the major benefits and possible challenges of using remote sensing and related geospatial technologies for coastal studies. It also provides an overview on the book structure and a chapter-by-chapter preview.

While some significant progresses have been made in remote sensing of the coastal ecosystems, as discussed in this volume, there are several major areas that deserve further research. Firstly, the current ocean color scanners are basically designed for offshore waters, and they are of little use for optically complex near-shore waters. Further research is needed to help design future ocean color radiometers appropriate for shallow coastal waters. Secondly, most of the algorithms for retrieving water quality measures were originally designed for open-ocean waters, and a significant area for continuing research is the fundamental understanding of the functional linkage between water constituents and remote reflectance for coastal waters. Thirdly, more research is needed to advance the fundamental understanding of the relationship between the volumetric reflectance, the canopy density of submerged aquatic vegetation (SAV) populations, water depth, and bottom reflectance parameters. This will help develop more realistic volumetric reflectance models, thus increasing the likelihood of accurate SAV mapping. Fourthly, there is an increased research demand to develop improved methods and technologies for resolving the spectral confusion between different land cover classes from middle-resolution imagery (such as SPOT HRV and Landsat TM/ETM+ data) and for incorporating image spatial characteristics and ancillary data to improve land cover classification from high-resolution imagery. Fifthly, continuing research efforts are needed to help acquire good and sufficient *in situ* data for building comprehensive spectral libraries of different coastal plant species and for calibrating remote sensor signals and verifying information extraction algorithms for the coastal environment. Lastly, data integration plays a key role in coastal studies, and more research is needed to develop innovative data models used for representing dynamic processes and to identify improved methods and technologies that can be used to deal with data incompatibility in terms of parameter measuring and sampling schemes.

Finally, this volume promotes a watershed-wide synthetic approach for coastal ecosystem assessment and management that is based on the understanding of the entire ecosystem as a whole and the linkage between upstream stressors and downstream responses. The success of implementing this approach depends upon not only technological soundness in remote sensing but also intensive research collaboration from interdisciplinary experts and broad partnerships including virtual communities as well.

## References

- Beatley T, Brower DJ, Schwab AK (2002) *An Introduction to coastal zone management*, 2nd edn. Island Press, Washington, DC
- Burke LA, Kura Y, Kassem K, Revenga C, Spalding M, McAllister D (2001) *Pilot analysis of global ecosystems: coastal ecosystems*. World Resources Institute, Washington, DC
- Hinrichsen D (1998) *Coastal waters of the world: trends, threads, and strategies*. Island Press, Washington, DC
- Hobbie JE (ed) (2000) *Estuarine science: a synthetic approach to research and practice*. Island Press, Washington, DC
- Jensen JR (2007) *Remote sensing of the environment: an Earth resource perspective*. Prentice Hall, New Jersey
- Mann KH (2000) *Ecology of coastal waters with implications for management*, 2nd edn. Blackwell Science, Massachusetts
- Millennium Ecosystem Assessment (2003) *Ecosystems and human well-being: a Framework for assessment*. Island Press, Washington, DC
- National Research Council (1994) *Priorities for coastal ecosystem science*. National Academy Press, Washington, DC
- National Research Council (2000) *Clean coastal waters: understanding and reducing the effects of nutrient pollution*. National Academy Press, Washington, DC
- Ross DA (1995) *Introduction to oceanography*. Harper Collins College Publishers, New York
- Selman M, Sugg Z, Greenhalgh S, Diaz R (2008) *Eutrophication and hypoxia in coastal areas: a global assessment of the state of knowledge*. World Resources Institute, Washington, DC
- Small C, Nicholls RJ (2003). A global analysis of human settlement in coastal zones. *J Coastal Res* 18(3):584–599
- Yang X (2005a) Remote sensing and GIS applications for estuarine ecosystem analysis: an overview. *Int J Remote Sens* 26:5347–5356
- Yang X (2005b) Special issue: remote sensing and GIS for estuarine and coastal ecosystem analysis. *Int J Remote Sens* 26:5163–5356
- Yang X (2008) Theme issue: remote sensing of the coastal ecosystems. *ISPRS J Photogramm Remote Sens* 63(5):485–590
- Yang X, Damen MCJ, van Zuidam R (1999) Use of Thematic Mapper imagery and a geographic information system for geomorphologic mapping in a large deltaic lowland environment. *Int J Remote Sens* 20:568–591

**Part I**  
**Conceptual and Technical Issues**

# Chapter 2

## Sensors and Techniques for Observing Coastal Ecosystems

Victor V. Klemas

This chapter reviews the advances in sensor design and related field techniques that are particularly appropriate for coastal ecosystem research and management. Multi-spectral and hyperspectral imagers are available for mapping coastal land cover and concentrations of organic or inorganic suspended particles and dissolved substances in coastal waters. Thermal infrared scanners can map sea surface temperatures accurately and chart coastal currents, while microwave radiometers can measure ocean salinity, soil moisture and other hydrologic parameters. Radar imagers, scatterometers and altimeters provide information on ocean waves, ocean winds, sea surface height and coastal currents. Using airborne LIDAR one can produce bathymetric maps, even in moderately turbid coastal waters. Since coastal ecosystems have high spatial complexity and temporal variability, they frequently have to be observed from both, satellites and aircraft, in order to obtain the required spatial, spectral and temporal resolutions. A reliable field data collection approach using ships, buoys, and field instruments with a valid sampling scheme is required to calibrate and validate the remotely sensed information.

### 2.1 Introduction

To understand and manage ecosystems, one must monitor and study their biological/physical features and controlling processes. However, obtaining this information for coastal ecosystems is quite challenging since they exhibit extreme variations in spatial complexity and temporal variability. Also, the influence of coastal ecosystems extends well beyond the local scale, and the only realistic means of obtaining data over such large areas is by remote sensing. To accomplish such monitoring accurately and cost-effectively, the design of the monitoring approach must make integrated use of remote sensing and field techniques (Kerr and Ostrovsky 2003).

---

V.V. Klemas (✉)

College of Marine and Earth Studies, University of Delaware, Newark, DE 19716, USA  
e-mail: klemas@udel.edu

Advances in technology and decreases in cost are now making remote sensing (RS) and geographic information systems (GIS) practical and attractive for use in coastal ecosystem management. They are also allowing researchers and managers to take a broader view of ecological patterns and processes. Landscape-level environmental indicators that can be detected by remote sensors are available to provide quantitative estimates of coastal and estuarine habitat conditions and trends. Such indicators include watershed land cover, riparian buffers, wetland losses and fragmentation, marsh productivity, invasive species, beach erosion, water turbidity and chlorophyll concentrations, among others. New satellites, carrying sensors with fine spatial (1–4 m) and spectral (200 narrow bands) resolutions are being launched, providing a capability to more accurately detect changes in coastal habitat and wetland health. Advances in the application of GIS help incorporate ancillary data layers to improve the accuracy of satellite land-cover classification. When these techniques for generating, organizing, storing, and analyzing spatial information are combined with watershed and ecosystem models, coastal planners and managers have a means for assessing the impacts of alternative management practices.

In Sects. 2.2 and 2.3 of this chapter, the reader is introduced to those airborne and spaceborne remote sensors and techniques which are cost-effective for studying and monitoring coastal ecosystems. In Sects. 2.4 and 2.5, case studies are used to illustrate the application of selected remote sensors and techniques to monitor environmental indicators related to coastal wetland health and estuarine water quality. Section 2.6 describes the most important field techniques required for coastal remote sensing projects. Section 2.7 summarizes the main points followed by a list of carefully selected references.

## 2.2 Remote Sensors

Aerial photography started approximately in 1858 when the famous French photographer, Gaspard Tournachon, obtained the first aerial photographs from a balloon near Paris. Since then, aerial photography has advanced, primarily during war times, to include color infrared films (for camouflage detection) and sophisticated cameras. Aerial photography and other remote sensing techniques are now used successfully in agriculture, forestry, land use planning, fire detection, mapping wetlands and beach erosion, oceanography and many other applications. For instance, in agriculture they have been used for land-use inventories, soil surveys, crop condition estimates, yield forecasts, acreage estimates, crop insect/pest/disease detection, irrigation management, and more recently, precision agriculture (Jensen 2007).

A major advance in aerial remote sensing has been the development of digital aerial cameras (Al-Tahir et al. 2006). Digital photography is capable of delivering photogrammetric accuracy and coverage as well as multispectral data at any user-defined resolution down to 0.1 m ground sampling distance. It provides photogrammetric positional accuracy with multispectral capabilities for image analysis and interpretation. As no chemical film processing is needed, the direct digital

acquisition can provide image data in just a few hours compared to several weeks using the traditional film-based camera. Another advantage over the traditional film is the ability to assess the quality of data taken directly after the flight is completed. Two examples of digital mapping cameras, ADS40 by Leica Geosystems and DMC from Z/I Imaging, were first presented to the market in 2002 to address requirements for extensive coverage, high geometric and radiometric resolution and accuracy, multispectral imagery, and stereo capability (Leica 2002).

Since the 1960s, remote sensing has progressed to include new techniques of information collection that include aircraft and satellite platforms carrying electro-optical and antenna sensor systems (Campbell 2007). Up to that time, camera systems dominated image collection, and photographic media dominated the storage of the spatially varying visible (VIS) and near-infrared (NIR) radiation intensities reflected from the Earth. Beginning in the 1960s, electronic sensor systems were increasingly used for collection and storage of the Earth's reflected radiation, and satellites were developed as an alternative to aircraft platforms.

Advances in electronic sensors and satellite platforms were accompanied by an increased interest and use of electromagnetic radiant energy not only from the VIS and NIR wavelength regions, but also from the thermal infrared (TIR) and microwave regions. For instance, TIR is used for mapping sea surface temperature and microwaves (e.g. radar) are used for measuring sea surface height, currents, waves and winds on a global scale (Martin 2004).

While most geologists, geographers, and other earth scientists are familiar with aerial photography techniques (Sabins 1978, Avery and Berlin 1992), relatively few scientists have had the opportunity to use thermal infrared, radar, and LIDAR data. Since the TIR radiance depends on both the temperature and emissivity of the target, it is difficult to measure land surface temperatures, because the emissivity will vary as the land cover changes. On the other hand, over water the emissivity is known and nearly constant, 98%, approaching the behavior of a perfect blackbody radiator (Ikeda and Dobson 1995). Thus the TIR radiance measured over the oceans will vary primarily with the sea surface temperature (SST) and allow one to determine the SST accurately ( $\pm 0.5^{\circ}\text{C}$ ), with some atmospheric corrections (Martin 2004, Elachi and van Ziel 2006).

Radar images represent landscape and ocean surface features that differ significantly from those observed by aerial photography or multispectral scanners. A Side-looking Airborne Radar (SLAR) irradiates a swath along the aircraft flight direction by scanning the terrain with radar pulses at right angles to the flight path. Thus the radar image is created by pulse energy reflected from the terrain and represents primarily surface topography. Since radar images look quite different from visible photographs, they require specialized interpretation skills. Radar pulses penetrate only a few wavelengths into the soil, depending on soil moisture, salinity, surface roughness, etc. The range resolution of SLAR depends on the length of the radar pulse which can be made quite short with new electronic techniques. However, the azimuth resolution is limited by the antenna size and altitude, thus preventing SLAR systems to be used on satellites.

Synthetic Aperture Radar (SAR) was specifically developed to provide high resolution images from satellite altitudes. SAR employs the Doppler shift technique to narrow down the azimuth resolution even with a small antenna. Thus range and azimuth resolutions of the order of 10 m are obtainable with SAR mounted on satellite platforms (Radarsat, ERS-2). In oceanography, radar is used not only for imaging the sea surface but also as altimeters to map sea surface height; scatterometers to determine sea surface winds; etc. (Ikeda and Dobson 1995, Martin 2004). Radar can penetrate fog and clouds, making it particularly valuable for emergency applications and in areas where cloud cover persists. Passive microwave radiometers are becoming important for measuring sea surface salinity, soil moisture and a wide range of hydrology related parameters (Burrage et al. 2003, Parkinson 2003).

Airborne LIDAR (Light Detection and Ranging) has become quite useful for topographic and bathymetric mapping. Laser profilers are unique in that they confine the coherent light energy in a very narrow beam, providing pulses of very high peak intensity. This enables LIDARS to penetrate moderately turbid coastal waters for bathymetric measurements or gaps in forest canopies to provide topographic data for digital elevation models (Brock and Sallenger 2000). The water depth is derived by comparing the travel times of the LIDAR pulses reflected from the sea bottom and the water surface.

As shown in Table 2.1, remote sensors can be classified by application, wavelength or active/passive mode. Under applications we have imagers, which produce two-dimensional images and can be used for map-making. Radiometers measure the radiant energy in a few specific bands, while spectrometers provide the energy distribution across a spectral continuum or many spectral bands. Profilers, such as radar and LIDAR, measure the distance to features, allowing us to determine the topography or bathymetry of an area. Radar and LIDAR are primarily active devices, while most other sensors are passive. The passive sensors operate in three major wavelength regions, the visible, infrared and microwave (Fig. 2.1). In electro-optical multispectral sensors, the visible region is divided into many bands, whereas aerial photography uses blue, green and red bands, plus one reflected band in the near-infrared. Figure 2.2 illustrates different types of visible and infrared imaging

**Table 2.1** Classification of remote sensors

Application	Wavelength	Mode
Imagers (Mappers)	Visible	
Photographic (Film)	Near infrared (Reflected)	Active
Multispectral (Array)	Thermal Infrared (Emitted)	Lidar
Radar (SAR & SLAR)	Microwave	Radar
Side-scanning sonar*	Sound Waves*	Sonar*
Radiometers	Seismic Waves*	
Spectrometers		
Profilers (Rangers)		Passive
Lidar		Visible
Radar (Altimeter)		Infrared
Echo Sounder*		Microwave

\*Not electromagnetic (EM) waves.



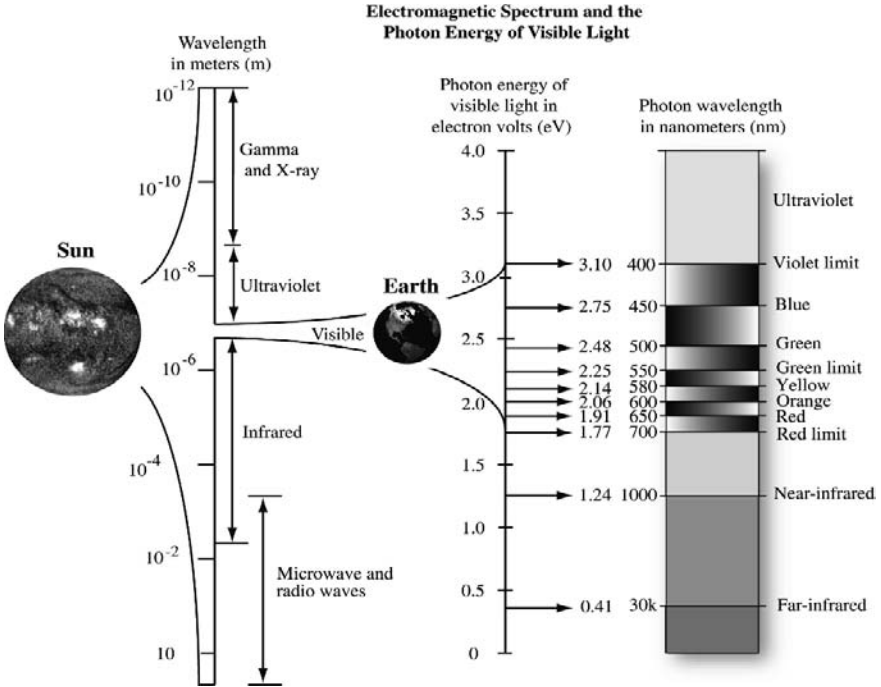
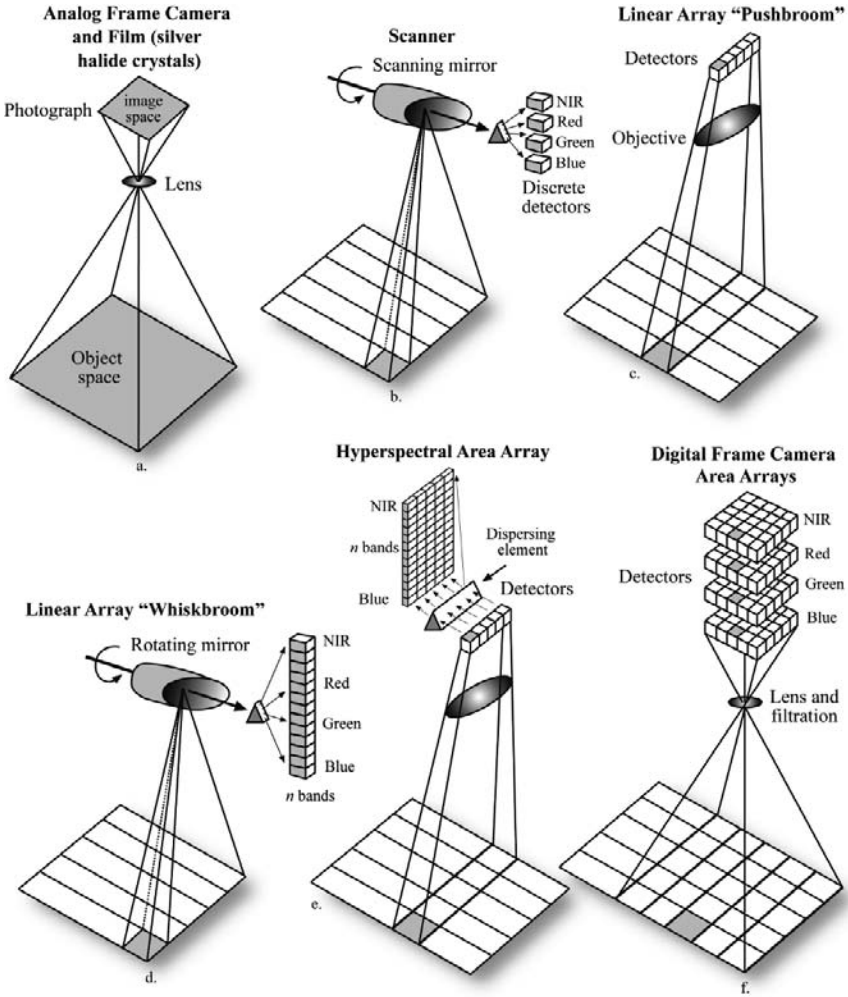


Fig. 2.1 Electromagnetic spectrum (Jensen 2007)

sensors, including a framing camera; two types of multispectral scanners, the cross-track or whisk-broom and the along-track or push-broom type; a hyperspectral area array; and a digital framing camera. After being focused by a mirror system, in a typical multispectral imager the radiation from each imaged pixel is broken down into spectral bands with one image being produced in each spectral band. The thermal infrared uses primarily the 10 $\mu$ m atmospheric window. The microwave region contains active radar and passive microwave radiometers (see Fig. 2.1).

### 2.3 Airborne and Satellite Systems

Which remote sensing platform and sensor data are used depends on the mission requirements. These can be broken down into spatial, spectral, radiometric and temporal. Spatial requirements include the ground resolution (minimum mapping unit) and coverage (swath-width). Spectral requirements include the location, width and number of the spectral bands. For radiometry we must choose the suitable dynamic range and the number of quantization (grey) levels. There are usually between 256 (8-bit) and 4096 (12-bit) quantization levels. The temporal resolution is determined by the required frequency of coverage (i.e. hourly, daily, seasonal), cloud cover, sun



**Fig. 2.2** Remote sensing systems used to collect multispectral and hyperspectral imagery (Jensen 2007)

angle and tidal conditions. The general requirements for open ocean, coastal and upland remote sensing are summarized in Table 2.2. As shown, the spatial, spectral, radiometric and temporal resolution requirements are quite different for each of these applications and depend on the specific problem to be solved (Bissett et al. 2004, Jensen 2007).

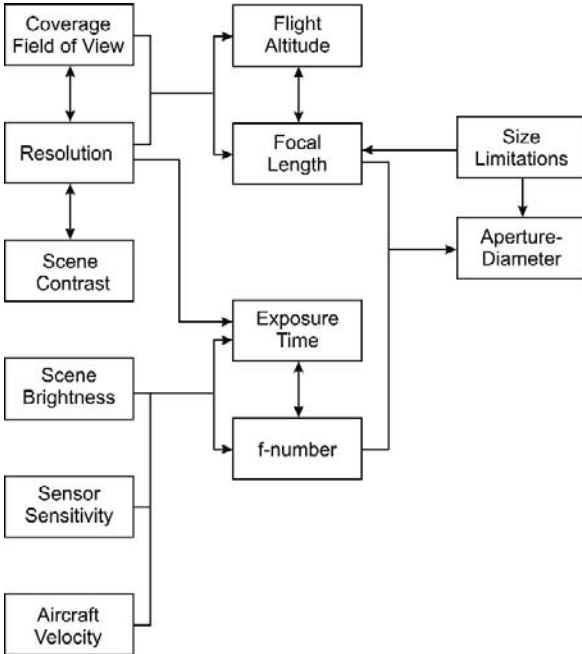
Remote sensing aircraft are usually flown at high, medium, or low altitudes, depending on the resolution and coverage requirements. High altitude flights covering large regions are normally performed by government agencies, whereas medium altitude flights are often provided by private companies. Low altitude flights may involve small aircraft, sometimes used to supplement field data collection. The trade-offs one must make in selecting flight altitudes and imaging systems are outlined in

**Table 2.2** Remote sensing requirements

	Open ocean	Estuaries	Land
Spatial Resolution	1–10 km	20–200 m	1–30 m
Coverage Area	2000 × 2000 km	200 × 200 km	200 × 200 km
Frequency of Coverage	1–6 days	0.5–6 h	0.5–5 years
Dynamic Range	Narrow	Wide	Wide
Radiometric Resolution	10–12 bits	10–12 bits	8–10 bits
Spectral Resolution	Multispectral	Hyperspectral	Multispectral (Hyperspectral)

Fig. 2.3. For instance, spatial resolution can be traded off for coverage (swath width) by varying the flight altitude or the focal length of the camera’s lens system.

There are about 29 civil land imaging satellites in orbit and 34 more are planned. Among these are 18 high-resolution (0.5–1.8 m) and 44 mid-resolution (2–36 m) systems. A list of the more relevant satellites is shown in Table 2.3. Most of these satellites are in polar, sun-synchronous orbits. As the Earth rotates beneath the polar orbiting satellite, its sensors eventually are able to observe and map every part of the globe. The satellite’s orbit can also be adjusted to be sun-synchronous, repeating its passes over a site during the same time of day (or same solar illumination angle). Geostationary orbit satellites are stationed above a fixed point on the equator, having the same angular velocity as the Earth, and thus continuously observe the same one third of the Earth’s surface. Geostationary satellites provide less spatial resolution



**Fig. 2.3** Aerial photography trade-offs

**Table 2.3** Coastal zone related sensors on satellite platforms

Satellite	Sensor	Spectral band ( $\mu\text{m}$ )	Resolution (m)	Cycle (days)	Swath width (km)		
Landsat 1, 2, 3	MSS	4	0.5–0.6	80	18	180	
		5	0.6–0.7				
		6	0.7–0.8				
		7	0.8–1.1				
Landsat 4, 5	TM	1	0.45–0.52	30 band 1–6	16	180	
		2	0.52–0.60				120 band 7
		3	0.63–0.69				
		4	0.76–0.90				
		5	1.55–1.75				
		6	2.08–2.35				
		7	10.40–12.50				
Landsat 7	TM	1	0.450–0.514	30 band 1–7	16	180	
		2	0.525–0.605				60 band 6
		3	0.630–0.690	15 band 8			
		4	0.750–0.900				
		5	1.55–1.75				
		6	10.40–12.50				
		7	2.08–2.35				
		8	(Pan) 0.52–0.90				
SPOT	HRV	1	0.50–0.59	20 band 1–3	26 (daily if camera tilted)	60	
		2	0.61–0.68				10 band 4
		3	0.79–0.89				
		4	0.51–0.73				
IKONOS		1	0.45–0.52	4 band 1–4	< 3 days	11	
		2	0.52–0.60				1 band 5
		3	0.63–0.69				
		4	0.76–0.90				
		5	(Pan) 0.45–0.90				
NOAA	AVHRR	1	0.58–0.68	1,100	2/day	2,400	
		2	0.725–1.1				
		3	3.55–3.93				
		4	10.5–11.3				
		5	11.5–12.5				
Orbview 2	SeaWiFS	1	404–422	1,100	Daily	2,800	
		2	433–453				
		3	480–500				
		4	500–520				
		5	545–565				
		6	660–680				
		7	745–785				
		8	845–885				

(4–8 km), but have the short repeat cycles needed for tracking storms and weather fronts (every 15–30 min) (Lillesand and Kiefer 1994, Jensen 2007).

Two of the more common medium-resolution satellites for mapping coastal land cover on a regional scale have been the U.S. Landsat and French SPOT (Le Systeme pour l'Observation de la Terre). As shown in Table 2.3, the satellites have multispectral scanners which provide spatial resolutions of 10–30 m and cover swaths from 60 km to 180 km wide. Their repeat cycle, even without cloud cover, is only every 16–26 days. SPOT has the ability to tilt its camera, resulting in a daily repeat cycle and stereo mapping capability.

The medium resolution data from the Landsat and SPOT systems provide information for local or regional studies, but are not quite suitable for investigations at global scales, because of cloud cover and differences in sun angle which prevent convenient comparisons and mosaicking of many scenes into a seamless data set covering a large area.

For global land cover mapping, the NOAA-AVHRR sensors seem to be more efficient, having 2,400 km swath widths and 1.1 km spatial resolutions. Vegetation indices derived from the NOAA-AVHRR sensor have been employed for both qualitative and quantitative studies of forest, desert and other ecosystems, including the contraction and expansion of the Sahara desert, Sellers and Schimel (1993), the calculation of biophysical parameters for climate models, etc. An overview of these studies is given by Prince and Justice (1991), Tucker et al. (1991), and Kogan (2001).

In the late nineties, private satellite companies started collecting high-resolution remote sensing data. The satellites from Space Imaging (IKONOS), Digital Globe (QuickBird) and Orbimage (Orbview-3) are already in orbit capturing imagery at down to 0.6 m resolution. Table 2.4 lists specific information about these satellite systems, including ground resolution, swath width and spectral coverage (Al-Tahir et al. 2006).

**Table 2.4** Satellite parameters and spectral bands (Space Imaging 2003, Digital Globe 2003, Orbimage 2003)

		Ikonos	QuickBird	OrbView-3
Sponsor		Space Imaging	Digital Globe	Orbimage
Launched		Sept. 1999	Oct. 2001	June 2003
Spatial Resolution (m)	Panchromatic	1.0	0.61	1.0
	Multi-Spectral	4.0	2.44	4.0
Spectral Range (nm)	Panchromatic	525–928	450–900	450–900
	Blue	450–520	450–520	450–520
	Green	510–600	520–600	520–600
	Red	630–690	630–690	625–695
	Near Infrared	760–850	760–890	760–900
Swath width (km)		11.3	16.5	8
Off nadir pointing		±26°	±30°	±45°
Revisit time (days)		2.3–3.4	1–3.5	1.5–3
Orbital Altitude (km)		681	450	470

As shown in Table 2.4, these systems share several common specifications with respect to spectral and spatial resolution as well as orbital details. (Space Imaging 2003, Digital Globe 2003, Orbimage 2003) Their 11-bit dynamic range allows greater detail to be extracted from scenes that are very dark (e.g. shadows) or very washed out due to excessive sun reflectance. Also, one-meter color imagery can be created using a pan-sharpening process that combines the high spatial resolution of the panchromatic image with the spectral information of the multispectral bands (Read et al. 2003, Souza and Roberts 2005).

In the early 1990s NASA developed a program to acquire the environmental data needed to address specific questions posed by concerns over global environmental change, called Earth Science Enterprise. This initiated a long-term effort to study the total Earth system and the effects of natural and anthropogenic changes on the global environment. One program component is an integrated system of satellites, the Earth Observing System (EOS), designed to provide a continuous stream of data with instruments tailored to answer specific questions for a better understanding of the nature, rates, and consequences of global environmental change (Campbell 2007).

The EOS plan has included over 30 instruments designed to monitor physical and biological components of the Earth. One example of such a satellite mission is Aqua, a satellite launched in 2002. This satellite carried six distinct Earth-observing instruments to measure numerous aspects of the Earth's atmosphere, land, oceans, biosphere, and cryosphere, with a focus on water in the Earth system. The six instruments include the Atmospheric Infrared Sounder (AIRS), the Advanced Microwave Sounding Unit (AMSU-A), the Humidity Sounder for Brazil (HSB), the Advanced Microwave Scanning Radiometer for EOS (AMSR-E), the Moderate-Resolution Imaging Spectroradiometer (MODIS), and the Cloud's and Earth's Radiant Energy System (CERES). Each instrument has unique characteristics and capabilities, and all six serve together to form a powerful package for Earth observations. (Parkinson 2003). The first satellite in the EOS series, Terra, was launched by NASA in 1999 to analyze the dynamic processes of Earth's land, sea and atmosphere. Several of Terra's key sensors, such as the MODIS, are described in Table 2.5.

## 2.4 Remote Sensing of Coastal Wetlands and Land Cover

Most coastal watershed models require land cover or land use as an input. Knowing how the land cover/use is changing, these models, together with a few other inputs like slope and precipitation, can predict the amount and type of run-off into rivers, bays, and estuaries (Donato and Klemas 2001, Jensen 2007). The Landsat Thematic Mapper (TM) has been a reliable source for land cover data. Its 30 m resolution and spectral bands have proven adequate for observing land cover changes in large coastal watersheds (e.g. Chesapeake Bay). Other similar satellites with medium resolution imagers can also be used, as shown in Table 2.5. The classification schemes used, usually employ the Anderson USGS land cover classification

**Table 2.5** Characteristics of some current and scheduled satellite remote sensing systems (From Donato and Klemas 2001)

Satellite/Sensor	Spectral range	Bands	GSD	Revisit time	Swath width	Application
AVHRR NOAA 15/16	580–12500 nm	6	1.1 km	–12h	2400 km	SST, Turbidity, Circulation
SeaWiFS	402–885 nm	8	1.1 km	daily	2800 km	Ocean Color, Red Products
MODIS Terra/Aqua	620–14385 nm	16VNIR 4SWIR 16TIR	250 m – 1 km	daily –12h	2330 km	SST, Turbidity, Circulation, Ocean Color
MISR Terra (9 Camera angles)	425–886 nm	4	275 m	9d	360 km	Ocean Color, Circulation
ASTER Terra	520–11650 nm	3VNIR 6SWIR 5TIR	15 m 30 m 90 m	16d	60 km	Bathymetry, Vegetation, Land Use, Change Detection, Circulation, Geomorphology
LANDSAT-7	450–2080 nm 10420 nm	6VNIR 1TIR 1 Pan	30 m 60 m 15 m	16d	180 km	
SPOT 1-2-4-5	500–890 nm	3MS 1 Pan	20 m 10 m	26d daily	60 m	
IKONOS	450–750 nm	4MS 1 Pan	4 m 1 m	1–3d	13 km	Bathymetry, Vegetation, Littoral Processes, Digital Elevation models
Quick Bird 2	450–900 nm	4MS 1 Pan	4 m 1 m	< 3d	22 km	
Orbview 3	450–900 m	4MS 1 Pan	4 m 1 m	< 3d	8 km	
Orbview 4	450–2500 nm 450–900 nm	200HS 4MS 1 Pan	8 m 4 m 1 m	< 3d	5 km	

**Table 2.5** (continued)

Satellite/Sensor	Spectral range	Bands	GSD	Revisit time	Swath width	Application
ALIEO-1	400–2400 nm	9MS 1 Pan	30 m 10 m	19d	37 km	Bathymetry, Vegetation, Land Use, Change Detection, Circulation, Geomorphology
Hyperion EO-1	400–2400 nm	220	30 m	16d	8 km	Bathymetry, Vegetation, Littoral Processes
NEMO/COIS	400–2500 nm	210	30 m			
MERIS ENVISAT-1	290–1040	15	300 m	< 3d	1150 km	Ocean Color, Circulation
ASAR ENVISAT-1	C-band 4 pol	2	30 m	< 3d	50–100 km	Circulation, Waves
AMI ERS-2(SAR)	C-band V pol	1	25 m	28d	100 km	
RADARSAT-1 (SAR)	C-band H pol	1	6–100 m	1–4	20–500 km	
RADARSAT-2 (SAR)	C-band HV pol	1	3–100 m		20–500 km	



system (Anderson et al. 1976) for the top level, and develop their own classification for the more detailed levels, such as the C-CAP Classification System (Klemas et al. 1993, Dobson et al. 1995). A very detailed wetlands classification system is the one developed by Cowardin et al. (1979). However, this classification system proved to be too complex for satellite remote sensing. Some of the ecosystem health indicators that can be observed by remote sensors include percent of impervious areas, natural vegetation cover, buffer degradation, wetland loss and fragmentation, wetland biomass change, invasive species, etc. (Odum 1993, Lathrop et al. 2000, Klemas 2005).

There are numerous approaches to computer-aided image classification (Jensen 1996). A typical digital image analysis approach for classifying coastal wetlands or land cover is shown in Fig. 2.4. Before analysis, the multispectral imagery must be radiometrically and geometrically corrected. The radiometric correction reduces the influence of haze and other atmospheric scattering particles and any sensor anomalies. The geometric correction reorients the image to compensate for the Earth's rotation and for variations in the position and attitude of the satellite. Image segmentation simplifies the analysis by first dividing the image into ecologically distinct areas. Then training sites are identified for supervised classification and interpreted via field visits or other reference data, such as aerial photographs. Next, an

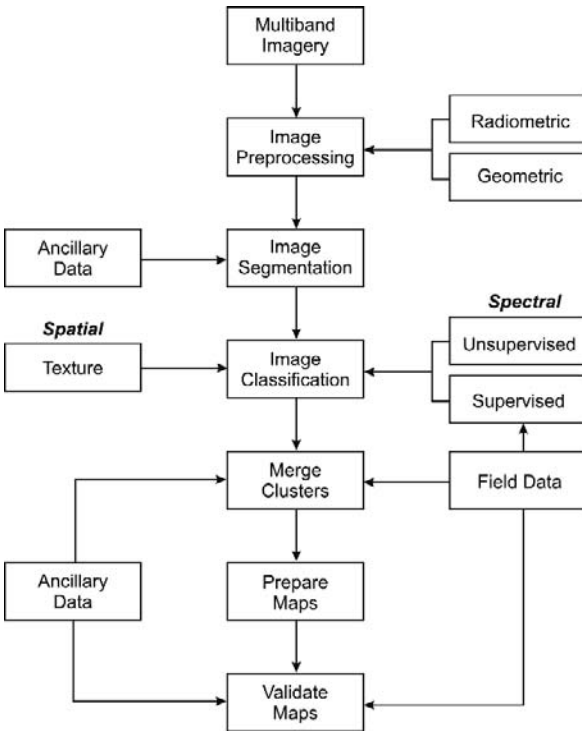


Fig. 2.4 Typical image analysis procedure

unsupervised classification is performed to identify variations in the image not contained in the training sites. Training site spectral clusters and unsupervised spectral classes are then analyzed using cluster analysis to develop an optimum set of spectral signatures. Final image classification is then performed to match the classified themes with the project requirements. (Lachowski et al. 1995, Jensen 1996). Texture analysis is quite useful, but more difficult to automate and is best performed visually (Sabins 1978, Purkis 2005). Note that throughout the process, ancillary data is used, whenever available (e.g. aerial photos, maps, field data, etc.).

When studying critical wetland sites or small watersheds one can use aircraft or high resolution satellite systems. Airborne digital cameras, providing color and color infrared digital imagery are particularly suitable for mapping or validating satellite data. Such digital imagery can be integrated with GPS information and used as georeferenced layers in a GIS for a wide range of modeling applications (Lyon and McCarthy 1995). Small aircraft flown at low altitudes (e.g. 500 m) can be used to supplement field data. High resolution imagery (0.6–4 m) can also be obtained from satellites, such as IKONOS and QuickBird (see Table 2.4). The cost becomes excessive if the site is larger than a few hundred square kilometers. Wetland species identification is difficult; however, some progress is being made using hyperspectral imagers (Schmidt et al. 2004, Porter 2006).

For looking at coastal land cover changes or beach erosion over long time periods, it is important to review historical airphotos, held by local, state and federal agencies. The U.S. Geological Survey and the USDA Soil Conservation Service have useable aerial photos of the coast dating back to the 1930s. They also have various maps, including planimetric, topographic, quadrangle, thematic, orthophoto, satellite and digital maps (Rasher and Weaver 1990, Lachowski et al. 1995). For instance, to map long-term changes of the shoreline due to beach erosion, time series of aerial photographs are used. The shoreline is divided into segments which are uniformly eroding or accreting. Then the change in the distance of the waterline is measured in reference to some stable feature like a coastal highway (Jensen 2007).

The actual beach profile can be obtained with low altitude LIDAR flights. Optical water clarity is the most limiting factor for LIDAR depth detection. Therefore, it is important to conduct the LIDAR overflights during tidal and current conditions that minimize the water turbidity due to sediment resuspension and river inflow. The LIDAR system must have a  $kd$  factor large enough to accommodate the water depth and water turbidity at the study site ( $k$  = attenuation coefficient;  $d$  = water depth). For instance, if a given LIDAR system has a  $kd = 3$  and the turbid water has an attenuation coefficient of  $k = 1$ , the system will be effective only to depths of about 3 m. Beyond that depth, one may have to use acoustic echo-sounding techniques (Brock and Sallenger 2000).

Mapping submerged aquatic vegetation (SAV) and coral reefs requires high resolution (1–4 m) imagery (Mumby and Edwards 2002, Purkis 2005). Coral reef ecosystems usually exist in clear water and can be classified to show different forms of coral reef, dead coral, coral rubble, algal cover, sand lagoons, different densities of seagrasses, etc. SAV may grow in more turbid waters and thus is more difficult to map. High resolution (e.g. IKONOS) multispectral imagers have been used in the

past to map SAV and coral reefs; however, hyperspectral imagers should improve the results significantly (Maeder et al. 2002, Mishra et al. 2006).

Digital change detection using satellite imagery can be performed effectively by employing one of several techniques, including post-classification comparison and temporal image differencing (Dobson et al. 1995, Jensen 1996, Lunetta and Elvidge 1998). Post-classification comparison change detection requires rectification and classification of the remotely sensed images from both dates. These two maps are then compared on a pixel-by-pixel basis. One disadvantage is that every error in the individual date classification maps will also be present in the final change detection map.

Temporal image differencing minimizes this problem by performing the traditional classification of only one of the two time-separated images. One band from both dates of imagery is then analyzed to find differences. Pixel intensity difference values exceeding a selected threshold are considered as changed. A change/no change binary mask is overlaid onto the second date image and only the pixels classified as having changed are classified in the second date imagery. This method usually reduces change detection errors and provides detailed from-to change class information (Jensen 1996). As shown in Fig. 2.5, change analysis results can be further improved by including probability filtering, allowing only certain changes and forbidding others (e.g. urban to forest).

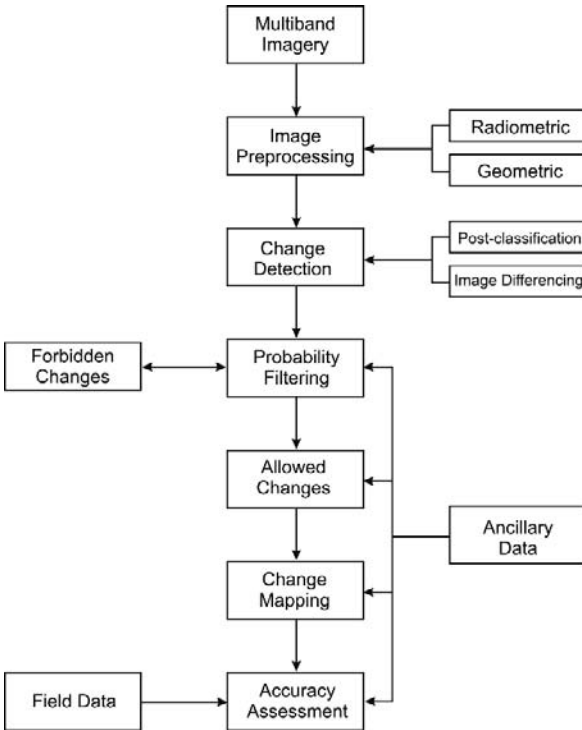


Fig. 2.5 Change detection using probabilities

Biomass and vegetation indices have long been used in remote sensing for monitoring the health and temporal changes associated with wetland or other vegetation (Goward et al. 1991, Lyon and McCarthy 1995). The spectral bands used for biomass mapping are primarily the red band, which is absorbed by the chlorophyll in the upper leaf layers, and a near-infrared band, which is reflected from the inner leaf structure, yet still penetrates several leaf layers and thus provides information on the canopy thickness and density. These spectral bands are combined in the Normalized Difference Vegetation Index (NDVI) to provide an estimate of above-ground wetland plant biomass in grams dry weight per square meter. The NDVI consists of the difference of the near-infrared and red band radiances (digital numbers) divided by their sum (Hardisky et al. 1984, Gross et al. 1987).

A particularly effective method for remotely sensing wetland changes uses biomass as an indicator. To detect biomass changes the Modified Soil Adjusted Vegetation Index (MSAVI) is used with red and near-infrared reflectances derived from Landsat/TM images (Qi et al. 1994). This biomass algorithm is applied to a time series of Landsat/TM images and used with selected thresholds to detect wetland changes. To minimize natural variations between images in the time series (e.g. atmospheric, annual, seasonal, etc.) it is assumed that the relative distribution of biomass in each sub-basin will remain essentially constant over time. Wetland pixels whose MSAVI deviation from the sub-basin mean changes from its previous deviation by more than a selected threshold value are considered as having changed. Threshold selection determines whether many small changes or only the more significant ones are detected. To minimize data costs, only changed sites “flagged” by Landsat/TM are studied in more detail with high-resolution systems, such as IKONOS or airborne scanners (Porter 2006, Klemas 2007).

## 2.5 Remote Sensing of Coastal and Estuarine Waters

In the open ocean, biological productivity can be estimated by measuring the chlorophyll-a concentration. It is the primary substance determining the color of so-called Case 1 waters, i.e. waters whose color is determined primarily by the chlorophyll concentration, shifting from blue towards green as that concentration increases. Several satellites with multispectral imagers, such as the Coastal Zone Color Scanner (CZCS) and NASA’s Sea-viewing Wide Field-of-view Sensor (SeaWiFS), were specifically designed to map ocean color and sea temperatures on a global scale (Martin 2004, McClain et al. 2006). With the help of calibration data from buoys and ships, these satellites have been able to determine chlorophyll concentrations in the open ocean. Typical ocean color products provided by these and more recent satellites and sensors, such as MODIS, MERIS and AQUA, are shown in Table 2.6 (Arnone and Parsons 2004, Bissett et al. 2004).

The purpose of NASA’s Sea-viewing Wide Field-of-view Sensor (SeaWiFS) is to provide quantitative data on global ocean bio-optical properties to biological and physical oceanographers. Subtle changes in ocean color signify various types and

**Table 2.6** Ocean color products (Arnone and Parsons 2004)

Chlorophyll concentration	Biological processes such as algal (harmful and non-harmful) blooms and decay
Spectral backscattering coefficient $bb(\gamma)$	90–180° particle scattering linked to concentration, composition, index of refraction of organic (marine) and inorganic (terrigenous) particles, resuspension
Spectral absorption coefficient $a(\lambda)$	Total absorption, changes in water quality
Spectral absorption colored dissolved organic matter $a(CDOM\lambda)$	Conservative tracer of river plumes, linked with coastal salinity, photo-oxidation processes
Spectral particle absorption coefficient $a(p\lambda)$	Particle composition, (organic and inorganic particles)
Spectral phytoplankton absorption coefficient $a(\phi\lambda)$	Absorption linked to differences in chlorophyll packaging within phytoplankton cells
Remote sensing reflectance $RRS(\lambda)$	Spectral absolute water color and water signature
Diffuse attenuation coefficient (k532, k490)	Light penetration depth, light availability at depth
Aerosol concentration – Epsilon	Type and distribution, affects visibility, Atmospheric correction methods
Beam attenuation coefficient – $c(\lambda)$	Total light attenuation using a collimated beam
Diver visibility	Horizontal visibility, average target size, target contrast, solar overhead illumination
Laser penetration depth	Underwater performance of lasers (imaging or bathymetry systems)

quantities of marine phytoplankton, the knowledge of which has many scientific and practical applications. The ability to map the color of the world's oceans has been used to estimate global ocean productivity (Longhurst et al. 1995, Behrenfeld and Falkowski 1997), aid in delineating oceanic biotic provinces (Longhurst 1998), and study regional shelf break frontal processes (Ryan et al. 1999, Schofield et al. 2004). As shown in Table 2.5, SeaWiFS has eight spectral bands which are optimized for ocean chlorophyll detection and the necessary atmospheric corrections. The spatial resolution is 1.1 km and the swath width 2,800 km. Due to the wide swath width, the revisit time is once per day. Data in the form of analyzed sea surface temperature and chlorophyll charts are provided daily to the fisheries and shipping industries over Marine Radio Networks. Because certain species of commercial and game fish are indigenous to waters of a specific temperature, fishermen can cut fuel costs and time by being able to locate areas of higher catch potential (Cracknell and Hayes 2007).

Wind-induced upwelling in coastal regions brings nutrients to the surface, creating zones of high biological productivity, accompanied by high concentrations of chlorophyll and phytoplankton, which can be detected by color sensors on satellites. The waters off Peru and California are good examples, where long term upwelling events influence the abundance of fish over periods of months. When wind patterns over the Pacific Ocean change, warm waters from the Western Pacific shift to the

Eastern Pacific and the upwelling of nutrient-rich cold water off the Peruvian coast is suppressed, resulting in well-recognized “El Nino” conditions (Yan et al. 1993). Such upwelling areas and their condition can be observed by satellites with thermal infrared imagers, such as NOAA’s AVHRR, or ocean color sensors, such as SeaWiFS (Schofield et al. 2004, Martin 2004).

As one approaches the coast and enters the bays and estuaries, the water becomes quite turbid and contains suspended sediment, dissolved organics and other substances, in addition to chlorophyll. To identify each substance in this complex mixture of Case 2 waters requires hyperspectral sensors and more sophisticated algorithms than the empirical regression models (Sydor 2006, Cannizzaro and Carder 2006) used in Case 1 waters in the open ocean (Ikeda and Dobson 1995, Bukata 2005). Neural network approaches have been used to map chlorophyll and suspended sediment concentrations in Delaware Bay and other estuaries (Keiner and Brown 1999, Dzwonkowski and Yan 2005a). Neural networks, however, require extensive calibration with coincident ship and satellite observations of radiance, and shipboard measurements of chlorophyll and sediment concentrations.

There are many other coastal and estuarine pollutants and ecosystem health indicators that can be sensed by remote sensors. However, to fully understand the behavior and environmental impact of water pollutants such as oil spills or chemical dumps, one usually needs to measure the following parameters:

- source (point, distributed, surface, subsurface)
- location (within permit zone)
- movement (currents, wind, waves, etc.)
- dispersion (density, thermocline, currents, waves, wind, etc.)
- identity (spectral signature)
- condition (weathering, decomposition, etc.)
- concentration (ambient, source, surface, subsurface, etc.)
- environmental impact (animals, plants, beaches, water quality, etc.)

Most of these pollution characteristics can be sensed remotely, especially if hyperspectral imagers having adequate spatial resolution are employed.

High concentrations of nutrients exported from agriculture or urban sprawl in coastal watersheds, or produced by coastal upwelling, are causing harmful algal blooms in many estuaries and coastal waters. Algal blooms are harmful in that they cause eutrophic conditions, depleting oxygen levels needed by organic life and limiting aquatic plant growth by reducing water transparency. Most algal blooms can be observed from satellites, due to their distinct color, location or repetitive seasonal appearance (Ruddick 2001). Furthermore, hyperspectral sensors with spectral bands fine-tuned for specific pigment analysis allow detection and analysis of algal taxonomy. This can be accomplished because the species-specific algal accessory pigments produce unique spectral signatures. Remote sensing data can complement the monitoring networks existing in many parts of the world to get data on nutrient loading and algal growth to provide better insights into overall water quality, distribution of toxin-producing algae, and aquatic biogeochemical cycling (Gitelson 1993).

**Table 2.7** Water quality levels

<b>Water quality</b>	<b>Chl-a concentration</b>
Oligotrophic	< 8 µg/L
Mesotrophic	8–25 µg/L
Eutrophic	> 25 µg/L
<b>Water quality</b>	<b>Total Suspended Sediment (TSS)</b>
Clear	0–10 mg/L
Moderately turbid	10–50 mg/L
Highly turbid	> 50 mg/L
<b>Examples</b>	Delaware Bay is mesotrophic and moderately to highly turbid Chesapeake Bay is mesotrophic to eutrophic and moderately turbid

Concentrations of chlorophyll-a (chl-a) and total suspended sediments (TSS) can be sensed remotely and used as indicators of the severity of eutrophication and turbidity, respectively. If such general criteria, as shown in Table 2.7, are used to compare estuarine water quality, it is possible to get satisfactory results with sensors having fewer spectral bands and lower signal to noise ratios than the hyperspectral imagers needed for measuring precise concentration levels (Chipman et al. 2004).

Most riverine and estuarine plumes and some ocean-dumped waste plumes can be detected remotely due to their strong surface signatures caused by high turbidity. The drift and dispersion of coastal plumes and ocean dumped waste have been tracked with satellite imagery. (Klemas and Philpot 1981, Dzwonkowski and Yan 2005b, Thomas and Weatherbee 2006). To study the dynamics of such plumes one can use a small number of multispectral bands. However, to detect the composition and concentration of their content is difficult, even with hyperspectral images.

Some studies of coastal ecosystems require physical data as well as biological information. As shown in Table 2.8, radar and thermal infrared sensors are available on aircraft and satellites for measuring and mapping the physical properties of coastal and estuarine waters. Surface and internal wave fields as well as oil slicks can be mapped with radar imagers, such as the Synthetic Aperture Radar (SAR) mounted on satellites. Radar altimeters provide accurate sea surface height as well

**Table 2.8** Space-borne ocean-sensing techniques

Sensing technique	Environmental parameters
Color Scanner –	Ocean Color (chlorophyll concentration, suspended sediment, attenuation coefficient)
Infrared Radiometer –	Sea surface temperature (surface temperature, current patterns)
Synthetic Aperture Radar –	Short surface waves (swell, internal waves, oil slicks, etc.)
Altimeter –	Topography and roughness of sea surface (sea level, currents, wave height)
Scatterometer –	Amplitude of short surface waves (surface wind velocity, roughness)
Microwave Radiometer –	Microwave brightness temperature (salinity, surface temp., water vapor, soil moisture)

as wave amplitude information. Radar scatterometer data can be analyzed to extract sea surface winds. (Martin 2004, Elachi and van Ziel 2006). The two passive devices, microwave radiometers and thermal infrared scanners can sense sea surface salinity and temperature, respectively. Microwave radiometers can also measure a wide range of climate related parameters, such as soil moisture (Parkinson 2003, Burrage et al. 2003).

Oil spills are best detected by imaging radars, such as SAR on satellites, because oil slicks dampen small surface wavelets, which otherwise backscatter a strong radar return signal. Small aircraft can be used to verify oil spill drift and dispersion models by tracking the movement and spreading of oil slicks in coastal waters and their interactions with fronts. A typical estuarine front may be caused by flooding higher density ocean water gliding under the lower density, lower salinity river water and thus causing a strong convergence zone, which may be marked by a foam line and color line. Estuarine fronts are narrow features, quite dynamic and have high convergence velocities (Sarabun 1993). Coastal and estuarine fronts can concentrate nutrients, pollutants and capture oil slicks causing their paths to deviate from drift and dispersion model predictions (Klemas 1980). To study frontal dynamics and track oil slicks one needs spatial and temporal resolutions of 10–50 m and 0.5–3 h, respectively.

Currents and breaking waves strongly affect coastal ecosystems, especially in the nearshore, which is an extremely dynamic environment. Currents influence the drift and dispersion of various pollutants, and together with breaking waves mobilize and transport sediments, resulting in erosion and morphological evolution of natural beaches. Changes in the underlying bathymetry in turn affect the wave and current patterns, resulting in a feedback mechanism between the hydrodynamics and morphology. The ability to monitor these processes is necessary in order to understand and predict the changes that occur in the nearshore region. Arrays of current meters, acoustic Doppler velocimeters, and pressure sensors are not very effective for determining surface currents and waves over large coastal regions, since these sensors measure currents at a point and are expensive, when large numbers of sensors have to be deployed.

Shore-based high frequency (HF) and microwave Doppler radar systems are used to map currents and determine swell-wave parameters in coastal waters with considerable accuracy. (Paduan and Graber 1997, Graber et al. 1997, Bathgate et al. 2006). The surface current measurements use the concept of Bragg scattering from a slightly rough sea surface, modulated by Doppler velocities of the surface currents. Extraction of swell direction, height and period from HF radar data is based on the modulation imposed on the short Bragg wavelets by the longer faster moving swell. HF radars can determine coastal currents and wave conditions over a range of up to 200 km. (Cracknell and Hayes 2007). While HF radar provides accurate maps of surface currents and wave information for large coastal areas, their spatial resolution, which is about 1 km, is more suitable for measuring mesoscale features than small scale currents. On the other hand, shore-based microwave X-band and S-band radars have resolutions of the order of 10 m, yet have a range of only a few kilometers.



Estimates of currents over large coastal areas, such as the continental shelf, can also be obtained by tracking the movement of drogues, dyes or natural surface features which differ detectably in color or temperature from the background waters (Davis 1985, Breaker et al. 1994). Examples of such features include sediment or chlorophyll plumes, patches of different water temperature, surface slicks, coastal fronts, etc.

Large ocean internal waves on continental shelves strongly influence acoustic wave propagation; submarine navigation; mixing nutrients to euphotic zone; sediment resuspension; cross-shore pollutant transport; and coastal engineering and oil exploration. Internal waves move along pycnoclines, which are surfaces that separate water masses of different densities. The water column is frequently not homogeneous, but stratified, containing thermoclines and pycnoclines that mark boundaries between water masses. The periods of internal waves are measured in minutes, rather than in seconds, and their wavelengths in kilometers rather than in tens of meters. Furthermore, the larger internal waves can attain heights of 100 m (Alford 2003). The period of the internal wave packets approximates the period of the tides, suggesting a cause-and-effect relationship. Internal waves can be detected visually and by radar since they cause local currents which modulate surface wavelets and slicks (Zhao et al. 2004).

Oil tankers, cargo ships, pleasure craft and military vessels navigating in bays such as Delaware Bay or Chesapeake Bay and further north, require information on the extent and type of ice cover during winter months. Types of ice cover may include fast ice, pack ice, large drift ice, small drift ice, etc. Radar and multispectral visible bands can provide such information.

The devastating effects of Atlantic hurricanes and tsunamis in the Indian Ocean bring out the need for timely monitoring of coastal flooding. There are many other storm events, such as Nor'easters, that impact the Atlantic coast more frequently than hurricanes. A good example of a major coastal flooding event is the Nor'easter storm of 1962 (Mather et al. 1967). The waves and storm surge broke through the dune line, flooded the entire coastal zone and damaged boardwalks and homes in settlements along the mid-Atlantic coast. The extensive damage and flooding along the coast was captured in aerial photographs after the storm.

Obtaining images before and after the landfall of hurricane Katrina in New Orleans in 2005, Landsat TM effectively showed the wetland losses and inundation over the entire region at 30 m resolution, while high resolution satellites, like IKONOS and QuickBird, documented the details, including actual breaks in the levees protecting the city. However, more frequent repeat cycles would have been useful for emergency operations. Only SAR could penetrate the clouds to observe coastal inundation conditions during the time of the hurricane's landfall. Radar can detect flooded coastal marshes because they usually provide a weaker radar return than non-flooded ones. The marsh grasses may calm the water surface accentuating specular reflection (Ramsey 1995). The radar return from flooded forests is usually enhanced compared to returns from nonflooded forests. The enhancement is due to the double bounce mechanism where the signal penetrating the canopy is reflected off the water surface and subsequently reflected back toward the sensor by a second reflection off a tree trunk (Hess et al. 1990).

## 2.6 Field Data

Field or ship data need to be collected for developing a spectral “signature library” for supervised classification of land cover, calibrating remotely sensed data or training neural networks. Field checks may also have to be conducted in order to guide the interpreters during the image classification stage. Finally, field data is gathered at the end of a project to validate the remotely sensed products (e.g. wetland maps) and assess their accuracy.

Training sites for supervised classification of coastal land cover must meet well-defined criteria. They should be homogeneous with regard to vegetation/land cover and in accessible areas. They should be large enough so they can be located on satellite images, but small enough to minimize within-site variation (10–25 pixels in size). Multiple training sites for each category of the classification scheme are required. (e.g. 10 sites).

To determine the reflectance characteristics of a land surface, a goniometer can be used to measure the Bidirectional Reflectance Distribution Function (BRDF). This is a tedious procedure, requiring that the irradiance and radiance be measured at all sensor positions and all solar angles. A more practical way is to compare the site’s reflectance with that of a Lambertian white panel (diffuse reflector) made of special materials, such as Halon, having controlled reflectivities from 95% to 99% (McCoy 2005, Jensen 2007). To convert ground reflectances to at-satellite-reflectances, one can use large white canvas sheets or natural targets large enough to be identifiable in the satellite imagery and having reflectances covering the entire range of the reflectances of the land cover sites to be mapped. (e.g. a corn field, a large lawn, a field of dry soil, etc.). By measuring the reflectances of these targets on the ground and at the satellite, and comparing them with the Lambertian white (Halon) panels, one can calibrate the satellite sensor so it could measure the reflectances of all the pixels in the scene (Gross et al. 1987).

To validate the remote sensing results and determine their accuracy, a statistically valid sampling scheme should be selected. For instance, for land cover maps a systematic unaligned sampling pattern is frequently used. On the other hand, some situations may require a clustered or stratified random sampling pattern. Tests by various researchers have shown the simple random and stratified random patterns both give satisfactory results. However, the stratified random approach requires some advance knowledge of where the land cover boundaries are located (McCoy 2005).

The accuracy of completed map products can be expressed in terms of an error matrix for land cover mapping applications and as percentage error for water quality studies. Furthermore, a Kappa coefficient can be calculated to show how much better the map results are than a totally random labeling of the pixels in the image (Jensen 1996, Campbell 2007).

Instrumented ships, buoys, and ocean gliders are used to calibrate and validate chlorophyll-a and total suspended sediment maps obtained with multispectral ocean color sensors. Some typical ship or buoy measurements are shown in Table 2.9. In coastal and estuarine waters this data must frequently be obtained very close to the

**Table 2.9** Remote sensing related ship measurements**Direct measurements**

Temperature, Salinity, Secchi Depth, pH, Attenuation Coefficient, Spectral Reflectance  
(Radiance and Irradiance)

**Water sample analysis**

Chl-a, TSS, Nitrogen, Phosphorus

**Ship data acquisition**

Water samples obtained from upper 0.5 m of water column; Ship data obtained within 20 min of satellite overpass; GPS used for sample site location

satellite overpass time and be statistically representative of prevailing conditions. The water samples are usually taken from the upper half meter of the water column. Sites for calibrating remotely sensed data, such as chlorophyll concentrations in coastal waters, must be located at well-known points representing the entire range of variables to be measured.

## 2.7 Summary and Conclusions

Since the early 1970s, civilian remote sensing satellites have made major contributions to our understanding of the Earth's ecosystems and warned us of critical natural and man-made changes taking place, such as deforestation, desertification and shrinking glaciers in Greenland and the Antarctic. In the open ocean, satellites have tracked storms and major oil spills. They have also monitored fisheries-related chlorophyll concentrations, algal blooms and sea surface temperatures. However, obtaining this information for coastal and estuarine ecosystems is more challenging, since they exhibit extreme variations in spatial complexity and temporal variability. After several decades of improvements, it now appears that remote sensing needs, cost and technology are converging in a way that will prove practical and cost-effective for coastal managers and ecosystem researchers. A few specific conclusions and recommendations are outlined below:

- As shown in Table 2.2, remote sensing of coastal ecosystems requires high spatial, spectral, and temporal resolution.
- Aerial photography of coastal ecosystems is usually performed at medium altitudes with color film, color infrared film and digital cameras at scales of 1:1,200–1:24,000. Large coastal regions can be mapped from high altitudes (scale 1:100,000), while low altitude flights (scale 1:600) can be used in support of field data collection (Jensen 2007, Campbell 2007).
- Georeferenced orthophotos, topographic maps and land cover maps represent good base maps for creating a multi-layer GIS database. Digital camera images are especially suited for use with GIS databases and for interpreting land cover maps derived from satellite imagery (Porter 2006).

- To keep costs reasonable, large coastal watersheds should be studied with medium resolution satellite sensors (e.g. 30 m Landsat TM) and only small areas and critical sites mapped with airborne or high resolution satellite sensors (e.g. 1–4 m IKONOS).
- For detecting changes of coastal land cover, including tidal marshes, in a time-series of images, post-classification comparison, image differencing and biomass change techniques can be used. To determine man-made changes, the images must be corrected for natural variations such as atmospheric, inter-annual, seasonal, and tidal differences (Lunetta and Elvidge 1998).
- On land, field data are often collected along transects using systematic random sampling. The sampling scheme should be optimized for each type of image classification approach, e.g. supervised, unsupervised, etc. (McCoy 2005, Jensen 1996).
- Mapping wetlands, coral reefs and submerged aquatic vegetation requires high resolution (1–4 m) imagery. Wetland species identification is possible only with hyperspectral sensors and large amounts of field data (Klemas 2005, Mumby and Edwards 2002, Schmidt et al. 2004).
- Airborne LIDAR is effective for near-shore bathymetry, but in turbid waters when the  $kd$  product exceeds the vendor specified value, acoustic echo sounding techniques must be used ( $k$  = attenuation coefficient;  $d$  = depth) (Brock and Sallenger 2000).
- Coastal and estuarine waters contain a complex mixture of chlorophyll, suspended sediments, dissolved organics, and other substances. Therefore, hyperspectral imagers, calibrated ship data and advanced algorithms or neural network methods are required to map the concentrations of these substances (Ikeda and Dobson 1995).
- Approximate concentrations of chl-*a* and total suspended sediments can be obtained with multispectral scanners and a small number of ship samples.
- Ship samples and water reflectances must be gathered very close to satellite overpass times. Spotter planes can be used to guide the research vessels to water features of interest.
- Thermal infrared radiometers or imagers, such as the AVHRR on NOAA satellites, can map sea surface temperature to within 0.5°C accuracy.
- Radar altimeters, scatterometers and SAR imagers can be used for mapping sea level height, sea surface winds, waves and currents (Ikeda and Dobson 1995, Martin 2004).

## References

- Alford MH (2003) Redistribution of energy available for ocean mixing by long-range propagation of internal waves. *Nature* 423:159–162
- Al-Tahir A, Baban SMJ, Ramlal B (2006) Utilizing emerging geo-imaging technologies for the management of tropical coastal environments. *West Indian J Eng* 29:11–22

- Anderson JR, Hardy EE, Roach JT, Witmer RE (1976) A land use and land cover classification system for use with remote sensor data. US Geological Survey Professional Paper 964, Washington, DC, 28p
- Arnone RA, Parsons AR (2004) Real-time use of ocean color remote sensing for coastal monitoring. In: Miller RL, Del Castillo CE, McKee BA (eds) Remote sensing of the coastal environment. Springer Publishing, Kluwer Academic, New York
- Avery TE, Berlin GL (1992) Fundamentals of remote sensing and airphoto interpretation. Macmillan, New York
- Bathgate J, Heron M, Prytz A (2006) A method of swell parameter extraction from HF ocean surface radar spectra. *IEEE J Oceanic Eng* 31:812–818
- Behrenfeld MJ, Falkowski PG (1997) Photosynthetic rates derived from satellite-based chlorophyll concentration. *Limnol Oceanogr* 42:1–20
- Bissett WP, Arnone R, Davis CO, Dye D, Kohler DDR, Gould R (2004) From meters to kilometers—a look at ocean color scales of variability, spatial coherence, and the need for fine scale remote sensing in coastal ocean optics. *Oceanography* 17:32–43
- Breaker LC, Krasnopolski VM, Rao DB, Yan X-H (1994) The feasibility of estimating ocean surface currents on an operational basis using satellite feature tracking methods. *Bull Am Meteor Soc* 75:2085–2095
- Brock J, Sallenger A (2000) Airborne topographic LIDAR mapping for coastal science. U.S. Geological Survey, Open-File Report 01–46
- Bukata R (2005) Satellite monitoring of inland and coastal water quality: retrospection, introspection, future directions. Taylor & Francis, London
- Burrage DM, Heron ML, Hacker JM, Miller JL, Stieglitz TC, Steinberg CR, Prytz A (2003) Structure and influence of tropical river plumes in the Great Barrier reef: Application and performance of an airborne sea surface salinity mapping system. *Remote Sens Environ* 85:204–220
- Campbell JB (2007) Introduction to remote sensing. The Guilford Press, New York
- Cannizzaro JP, Carder KL (2006) Estimating chlorophyll-a concentrations from remote sensing reflectance in optically shallow waters. *Remote Sens Environ* 101:13–24
- Chipman JW, Lillesand TM, Schmaltz JE, Leale JE, Nordheim MJ (2004). Mapping lake water clarity with Landsat images in Wisconsin, USA. *Can J Remote Sens* 30:1–7
- Cowardin L, Carter V, Golet F, LaRoe E (1979) Classification of wetlands and deep water habitats of the United States. US Department of the Interior, Fish and Wildlife Service, Office of Biological Services, FWS/OBS-79/31. Washington, DC, 131p
- Cracknell AP, Hayes L (2007) Introduction to remote sensing. CRC Press, New York
- Davis RE (1985) Drifter observations of coastal surface currents during CODE: the method and descriptive view. *J Geophys Res* 90:4741–4755
- Digital Globe (2003) Quickbird imagery products and product guide (revision 4). Digital Globe, Inc., Colorado, USA
- Dobson JE, Bright EA, Ferguson RL, Field DW, Wood LL, Haddad KD, Iredale H, Jensen JR, Klemas V, Orth RJ, Thomas JP (1995) NOAA Coastal Change Analysis Program (C-CAP): Guidance for regional implementation, NOAA Technical Report NMFS 123, U.S. Department of Commerce, Washington, DC
- Donato T, Klemas V (2001) Remote sensing and modeling applications for coastal resource management. *Geocarto Int* 16:23–29
- Dzwonkowski B, Yan X-H (2005a) Development and application of a neural network based ocean color algorithm in coastal water. *Int J Remote Sens* 26:1175–1200
- Dzwonkowski B, Yan X-H (2005b) Tracking of a Chesapeake Bay estuarine outflow plume with satellite-based ocean color data. *Continental Shelf Res* 25:1942–1958
- Elachi C, van Ziel J (2006) Introduction to the physics and techniques of remote sensing. John Wiley & Sons, New Jersey
- Gitelson A (1993) Quantitative remote sensing methods for real-time monitoring of inland water quality. *Int J Remote Sens* 14:1269–1295
- Goward SN, Markham B, Dye DG, Dulaney W, Yang J (1991) Normalized Difference Vegetation Index measurements from the Advanced Very High Resolution Radiometer. *Remote Sens Environ* 35:257–277

- Graber H, Haus B, Chapman R, Shay L (1997) HF radar comparisons with moored estimates of current speed and direction: expected differences and implications. *J Geophys Res* 102:18, 749–18, 766
- Gross MF, Hardisky MA, Klemas V, Wolf PL (1987) Quantification of biomass of the marsh grass *Spartina Alterniflora* Loisel using Landsat Thematic Mapper imagery. *Photogramm Eng Remote Sens* 53:1577–1583
- Hardisky MA, Daiber FC, Roman CT, Klemas V (1984) Remote sensing of biomass and annual net aerial productivity of a salt marsh. *Remote Sens Environ* 16:91–106
- Hess L, Melack J, Simonett D (1990) Radar detection of flooding beneath the forest canopy: a review. *Int J Remote Sens* 11:1313–1325
- Ikeda M, Dobson FW (1995) Oceanographic applications of remote sensing. CRC Press, New York
- Jensen JR (1996) Introductory digital image processing: a remote sensing perspective. Prentice-Hall, New Jersey
- Jensen JR (2007) Remote sensing of the environment: an Earth resource perspective. Prentice Hall, New Jersey
- Keiner LE, Brown CW (1999) Estimating oceanic chlorophyll concentrations with neural networks. *Int J Remote Sens* 20:189–194
- Kerr JT, Ostrovsky M (2003) From space to species: ecological applications of remote sensing. *Trends Ecol Evol* 18:299–305
- Klemas V (1980) Remote sensing of coastal fronts and their effects on oil dispersion. *Int J Remote Sens* 1:11–28
- Klemas V (2005) Remote sensing: Wetlands classification. In: Schwartz ML (ed) *Encyclopedia of coastal science*. Springer, Dordrecht, The Netherlands, pp 804–807
- Klemas V (2007) Remote sensing of coastal wetlands and estuaries. *Proc of Coastal Zone 07*. NOAA Coastal Services Center, Charleston, South Carolina
- Klemas V, Dobson JE, Ferguson RL, Haddad KD (1993) A coastal land cover classification system for the NOAA Coastwatch Change Analysis Project. *J Coast Res* 9:862–872
- Klemas V, Philpot W (1981) Drift and dispersion studies of ocean-dumped waste using Landsat imagery and current drogues. *Photogram Eng Remote Sens* 47:533–542
- Kogan FN (2001) Operational space technology for global vegetation assessment. *Bull Amer Meteor Soc* 82:1949–1964
- Lachowski H, Maus P, Golden M, Johnson J, Landrum V, Powell J, Varner V, Wirth T, Gonzales J, Bain S (1995) Guidelines for the use of digital imagery for vegetation mapping. U.S. Department of Agriculture, Forest Service EM-7140-25, Washington, DC
- Lathrop RG, Cole MB, Showalter RD (2000) Quantifying the habitat structure and spatial pattern of New Jersey (USA) salt marshes under different management regimes. *Wetl Ecol Manag* 8:163–172
- Leica (2002) ADS40 Airborne digital sensor. Leica Geosystems, GIS and Mapping, LLC, Atlanta, Georgia, USA
- Lillesand TM, Kiefer RW (1994) Remote sensing and image interpretation. John Wiley & Sons, New Jersey
- Longhurst A (1998) *Ecological Geography of the Sea*. Academic Press, London
- Longhurst A, Sathyendranath S, Platt T, Caverhill C (1995) An estimate of global primary production in the ocean from satellite data. *J Plank Res* 17:1245–1271
- Lunetta RS, Elvidge CD (1998) Remote sensing change detection: environmental monitoring methods and applications. Ann Arbor Press, Michigan
- Lyon JG, McCarthy J (1995) Wetland and environmental applications of GIS. Lewis Publishers, New York
- Maeder J, Narumalani S, Rundquist D, Perk R, Schalles J, Hutchins K, Keck J (2002) Classifying and mapping general coral reef structure using Ikonos data. *Photogram Eng Remote Sens* 68:1297–1305
- Martin S (2004) *An introduction to remote sensing*. Cambridge University Press, Cambridge
- Mather JR, Field RT, Yoshioka GA (1967) Storm damage hazard along the East Coast of the United States. *J Appl Meteor* 6:20–30

- McClain C, Hooker S, Feldman G, Bontempi P (2006) Satellite data for ocean biology, biogeochemistry, and climate research. *Eos, Transactions, Amer Geophys Union* 87:337–343
- McCoy R (2005) *Field methods in remote sensing*. Guilford Press, New York
- Mishra D, Narumalani S, Rundquist D, Lawson M (2006) Benthic habitat mapping in tropical marine environments using QuickBird multispectral data. *Photogram Eng Remote Sens* 72:1037–1048
- Mumby PJ, Edwards AJ (2002) Mapping marine environments with Ikonos imagery: enhanced spatial resolution can deliver greater thematic accuracy. *Remote Sens Environ* 82:248–257
- Odum EP (1993) *Ecology and Our Endangered Life-Support Systems*, 2nd edn. Sinauer Associates, Inc., Sunderland, MA
- Orbimage (2003) *OrbView-3 Satellite and ground systems specifications*. Orbimage Inc., Virginia, USA
- Paduan JD, Graber HC (1997) Introduction to high-frequency radar: Reality and myth. *Oceanography* 10:36–39
- Parkinson CL (2003) Aqua: An earth-observing satellite mission to examine water and other climate variables. *IEEE T Geosci and Remote* 41:173–183
- Porter DE (2006) RESAAP/Final Report, NOAA/NERRS Remote sensing applications assessment project. University of South Carolina
- Prince SD, Justice CO (1991) Coarse resolution remote sensing of the Sahelian environment. *Int J Remote Sens* 12:1133–1421
- Purkis SJ (2005) A reef-up approach to classifying coral habitats from IKONOS imagery. *IEEE T Geosci Remote* 43:1375–1390
- Qi J, Chehbouni A, Huete AR, Kerr YH, Sorooshian S (1994) A modified soil adjusted vegetation index. *Remote Sens Environ* 48:119–126
- Ramsey E (1995) Monitoring flooding in coastal wetlands by using radar imagery and ground-based measurements. *Int J Remote Sens* 16:2495–2502
- Rasher ME, Weaver W (1990) *Basic photo interpretation: a comprehensive approach to interpretation of vertical aerial photography for natural resource applications*. U.S. Department of Agriculture, Washington, DC
- Read JM, Clark DB, Venticinque EM, Moreira MP (2003) Application of merged 1-m and 4-m resolution satellite data to research and management in tropical forests. *J Appl Ecol* 40:592–600
- Ruddick KG (2001) Optical remote sensing of chlorophyll-a in case 2 waters by use of an adaptive two-band algorithm with optimal error properties. *Appl Optics* 40:3575–3585
- Ryan JP, Yoder JA, Cornillon PC, Barth JA (1999) Chlorophyll enhancement and mixing associated with meanders of the shelf break front in the Mid-Atlantic Bight. *J Geophys Res* 104:23, 479–23, 493
- Sabins FF (1978) *Remote sensing: principles and interpretation*, 2nd edn. Freeman & Co, New York
- Sarabun CC (1993) Observations of a Chesapeake Bay tidal front. *Estuaries* 16:68–73
- Schmidt KS, Skidmore AK, Kloosterman EH, Van Oosten H, Kumar L, Janssen JAM (2004) Mapping coastal vegetation using an expert system and hyperspectral imagery. *Photogram Eng Remote Sens* 70:703–716
- Schofield O, Arnone RA, Bissett WP, Dickey TD, Davis CO, Finkel Z, Oliver M, Moline MA (2004) Watercolors in the Coastal Zone: What can we see? *Oceanography* 17:25–31
- Sellers PJ, Schimel D (1993) Remote sensing of the land biosphere and biochemistry in the EOS era: science priorities, methods of implementation – EOS biosphere and biochemical panels. *Global Planet Change* 7:279–297
- Souza CM, Roberts DA (2005) Mapping forest degradation in the Amazon region with Ikonos images. *Int J Remote Sens* 26:425–429
- Space Imaging (2003) *IKONOS Imagery products and product guide (version 1.3)*. Space Imaging LLC., Colorado, USA
- Sydor M (2006) Use of hyperspectral remote sensing reflectance in extracting the spectral volume absorption coefficient for phytoplankton in coastal water: remote sensing relationships for the inherent optical properties of coastal water. *J Coastal Res* 22:587–594

- Thomas AC, Weatherbee RA (2006) Satellite-measured temporal variability of the Columbia River plume. *Remote Sens Environ* 100:167–178
- Tucker CJ, Dregne HE, Newcomb WW (1991) Expansion and contraction of the Saharan desert from 1980 to 1990. *Science* 253:299–301
- Yan X-H, Ho C, Zheng Q, Klemas V (1993) Using satellite IR in studies of the variabilities of the Western Pacific Warm Pool. *Science* 262:440–441
- Zhao X, Klemas V, Zheng Q, Li X, Yan X-H (2004) Estimating parameters of a two-layer stratified ocean from polarity conversion of internal solar waves observed in satellite SAR images. *Remote Sens Environ* 94:276–287



# Chapter 3

## Geographic Information Systems and Spatial Analysis for Coastal Ecosystem Research and Management

Jialing Wang, Libin Zhou and Xiaojun Yang

This chapter is designed to review the utilities of geographic information systems (GIS) and spatial analysis techniques that are particularly relevant for coastal ecosystem research and management. While remote sensing provides a primary source of data for mapping physical and cultural attributes (see Chap. 2), GIS provides a platform for data integration, synthesis, and modeling to support decision making, essential in many coastal applications. This chapter first reviews GIS data models that can be used to represent spatial or temporal information in digital environment. It then examines a variety of spatial analysis techniques suitable for the study of patterns, relationships, and trends in geographically referenced data that help understand the natural and human-dimensional processes at work, make better decisions for planning and management of the coastal ecosystems. It is concluded that most of the coastal applications need to combine several techniques and no single technique could handle all the problems in such a complex environment.

### 3.1 Introduction

Coastal areas are by location across two distinct systems, land and ocean. The land-ocean interaction creates unique ecosystems supporting many different habitat types, such as freshwater and salt marshes, sandy beaches, rocky shores, mangrove forests, river deltas, tidal pools, and forest swamps. These habitats provide home to a great diversity and abundance of plant and wildlife species. Coastal areas are also the foci of human settlement, development, and tourism, and thus under constant pressure from human-induced as well as natural stressors. To manage the impacts of development and other activities, it is necessary to monitor and characterize every aspect in coastal ecosystems.

Coastal studies address many different aspects, such as mapping of the distribution of plant and wildlife species (Garibaldi and Caddy 1998); change detection

---

J. Wang (✉)

Department of Geography, Geology and the Environment,  
Slippery Rock University of Pennsylvania, Slippery Rock, PA 16057, USA  
e-mail: jialing.wang@sru.edu

of land use/cover, landscape, or ecosystems (Wilcock and Cooper 1993, Kastler and Wiberg 1996, Yang and Liu 2005a,b); monitoring of water distribution, quality, and pollution (Hedger and Malthus 2001); monitoring of the distribution of sediments and suspended particulates in coastal water (Brown et al. 2006); monitoring of coastal hazards (Pérez-Maqueo et al. 2007); and examining of coastal morphological change, shoreline erosion, or dune field evolution (Siddiqui and Maajid 2004). These specific applications require the integration and synthesis of a variety of information concerning biophysical and socio-economic characteristics, which further justify the use of geographic information systems (GIS) and spatial analysis techniques.

The purpose of this chapter is not to offer a comprehensive review on GIS and spatial analysis since readers can easily find such information from any premier GIS textbooks, such as Lo and Yeung (2007) and Chang (2008). Instead, this chapter focuses on the utilities of GIS and spatial analysis that are particularly relevant for coastal ecosystem research and management. It begins with the GIS data models that can be used to represent spatio-temporal information in digital environment. The chapter then moves to the four groups of spatial analysis techniques: basic spatial analysis (e.g. buffering, neighborhood functions, overlay, and distance modeling), spatial pattern analysis (e.g. spatial autocorrelation, quadrat analysis, nearest-neighbor analysis, landscape metrics, and spatial interpolation), statistical spatial analysis (e.g. descriptive statistics, regression, clustering analysis, principal component analysis, artificial neural networks, and fuzzy logic systems), and spatial modeling (e.g. statistical models, cellular automata models, and agent-based models) (Table 3.1).

## **3.2 Digital Representations of Spatio-Temporal Data**

Building a digital database to represent spatial and temporal information is a prerequisite to GIS-based spatial analysis. This section briefly reviews several popular GIS data models that can be used to represent environmental and social information concerning the coastal environment.

### ***3.2.1 Spatial Data Models***

Field-based and feature-based models are two fundamental models used to represent spatial data in digital environment. Field-based models depict the real world phenomena as continuous surfaces, while feature-based ones represent the real world phenomena as discrete objects. Both are useful for the coastal environment and thus have been incorporated into ESRI's Arc Marine Data Model (Wright et al. 2007).

Raster data model is a very important field-based data model. It uses a regular grid of cells to represent the entire study area. Each cell has a single value of a

**Table 3.1** List of selected spatial analysis techniques appropriate for coastal ecosystem research

Major Techniques	Sample Applications	Examples
<b>Basic Spatial Analysis</b>		
Buffering	Water distribution, quality, and pollution	Basnyat et al. 1999, McLaughlin et al. 2003
Neighborhood Function Map Overlay	Coastal geomorphology Landscape change	Marfai and King 2008 Ayad 2005, Basnyat et al. 1999
Distance Modelling	Distribution of plant and wildlife species	Berberoglu et al. 2004, Karthik et al. 2005
	Habitat change Landscape change, habitat change	Green and Ray 2002 Ayad 2005, Lirman and Fong 2007
<b>Spatial Pattern Analysis</b>		
Spatial Autocorrelation	Distribution of sediments and suspended particulates in water Landscape, land use, ecosystem, or habitat change	Raaphorst et al. 1998 Kitsiou et al. 2001
Quadrat Analysis	Distribution of plant and wildlife species	Laiker et al. 2005 Fonseca et al. 2008
Nearest-Neighbor Analysis	Distribution of plant and wildlife species	Desmet and Cowling 1999
Landscape Metrics	Distribution of plant and wildlife species	Jackson et al. 2006
Spatial Interpolation	Distribution of sediments and suspended particulates in water	Raaphorst et al. 1998
<b>Statistical Spatial Analysis</b>		
Basic Statistical Analysis	Water distribution, quality, and pollution	Hedger and Malthus 2001
	Coastal geomorphology and hydrology	Ari et al. 2007, Li et al. 2007
Regression Analysis	Natural hazards	Pérez-Maqueo et al. 2007
	Landscape, land use, ecosystem, or habitat change	Koneff and Royle 2004
Clustering Analysis	Landscape, land use, ecosystem, or habitat change	Isacch et al. 2006, Li et al. 2007
	Distribution of plant and wildlife species	Fuller et al. 2005
Principal Component Analysis	Distribution of plant and wildlife species	Soletchnik et al. 2007
Artificial Neural Networks	Water distribution, quality, and pollution	Schiller and Doerffer 1999
Fuzzy Logic System	Water distribution, quality, and pollution	Ghayoumian et al. 2007
<b>Spatial Modeling</b>		
Statistical Models	Habitat suitability analysis	Hamer et al. 2008
Cellular Automata Models	Distribution of plant and wildlife species	Huang et al. 2008
Agent-Based Models	Landscape, land use, ecosystem, or habitat change	Sperb et al. 2006

given attribute. Cell size defines the data spatial resolution. Remotely sensed imagery and digital elevation model (DEM) are often represented into rasters. The former typically includes aerial photography and satellite imagery. Orthophotos are orthorectified aerial photographs that combine the image characteristics of a photograph with the geometric characteristics of a map; they can be used as base images onto which other maps may be overlaid. Satellite imagery with different resolutions can be used to support various coastal applications. For example, high spatial-resolution (e.g. Quickbird) or spectral-resolution (e.g. Hyperion) satellite data have been used to map mangroves (Saleh 2007) and other types of coastal wetlands (Pengra et al. 2007). Low and medium resolution data (e.g. Landsat MSS, TM, and ETM+) have been used to detect coastal landform changes (Siddiqui and Maajid 2004), monitoring tidal wetlands (Nayak et al. 1989), mapping coastal water pollution (Ahn et al. 2006), modeling rates of coastal ecosystem recovery (Viedma et al. 1997), and analyzing coastal forest dynamics (Baskent and Kadiogullari 2007). A digital elevation model (DEM) is a raster representation of landscape topography. DEM data are widely used in 3D visualization of coastal landscape (Brown 2006), determining coastal area erosion (Euán-Avila et al. 2004), evaluating morphometric change (Austin and Rehfishch 2003), assessing debris-flow runout paths (Miller and Burnett 2008), modeling coastal floodplain inundation (Benavente et al. 2006), predicting precipitation (Marquinez et al. 2003), mapping coastal soil types (Carre and Girard 2002), and measuring basin depths (Johansson et al. 2001).

In addition to square, other shapes, such as hexagon, triangles, and octagons, can be used in field-based models to represent the real world. An example is a triangular irregular network (TIN) model that uses a set of irregular triangles covering an entire landscape; the size of these triangles can be adjusted according to sampling density to reflect the complex elevations. Makiaho (2007) estimated the ancient and future shoreline positions using DEM and TIN models respectively, and found that the TIN-based technique provided more detailed information about the shoreline features.

A typical example of the feature-based data model is the vector data model, which represents each feature as a row in a table and define feature shapes by x,y locations in space; features can be discrete locations or events, lines, or polygons. Topology defines the spatial relationships between features. The use of vector data models is very important because many data for coastal studies are vector data, such as plant information recorded for small plots as point features, rivers as line features, and forest cover as area features.

Recently, object-oriented data models are receiving more attention. An object-oriented data model comprises geographic objects and relationships among the objects. Different from raster and vector data models that organize data on the base of geometric shapes, an object-oriented data model organizes data by geographic objects each of which consists of geometry, properties, and methods. Geographic objects of the same type are grouped into object classes. Each object class is stored in GIS as a database table with rows corresponding to an object and columns to its properties. The geometric shape is treated as an attribute of an object. Within

the same object class, every object has some type of relationship to other objects. A good example of object-oriented data model is ESRI's geodatabase data model (Zeiler 1999).

### 3.2.2 *Spatio-Temporal Data Models*

Temporal dimension is an essential property of the coastal environment due to its high dynamics by nature. Conventional GIS limits to static representation of reality and is difficult to investigate dynamic processes. In recent years, many efforts have been made to develop spatio-temporal data models to represent the temporal dimension in GIS, which shed light on modeling and visualizing coastal dynamics. Based on data organizational bases, spatio-temporal data models can be classified into four approaches: location-based, entity-based, time-based, and combined approaches (Peuquet 1999).

A location-based approach organizes data by documenting changes for a given location at given time points. An example of this approach is a snapshot model that uses different timestamped layers to represent changes through time (Armstrong 1988, Langran and Chrisman 1988). The snapshot model is the simplest spatio-temporal data model. However, it suffers from data redundancy and inexplicit temporal relationships of changes (Yuan 1996, Peuquet 1999, Pelekis et al. 2004). To overcome the above drawbacks, the raster-based snapshot model was modified to store only the changes related to specific locations (Langran 1993, Peuquet 1999).

An entity-based approach records changes of specific geographical entities at given time points. For example, the space-time composite model (STCM) suggested by Langran and Chrisman (1988) records changes through time as new attributes in the database. If spatial changes of geographical entities are involved, the geometrical and topological relationships among the original geographical entities need to be regenerated and the database needs to be reconstructed accordingly with new attributes. Another attempt based on entity is a spatio-temporal object model (STOM) (Worboys 1994). In this model, the real world is considered as a set of discrete objects consisting of spatio-temporal atoms that are the largest homogeneous units holding specific properties in space and time (Yuan 1996). Different from a STCM, a STOM does not need to reconstruct databases. However, both models only represent sudden changes instead of gradual changes.

Time-based approaches use time as the organizational base to facility time-based queries. Peuquet and Duan (1995) applied such an approach to an event-based spatio-temporal data model (ESTDM). An ESTDM is a raster based approach that groups timestamped layers to show observations of a single event in a temporal sequence (Pelekis et al. 2004). This model includes a header file containing information about its thematic domain, a pointer to a base map describing the initial state of a geographic area, and pointers to the first and last event lists consisting of event components to indicate changes in space and time. The ESTDM overcomes the redundancy of snapshot models by only storing changes from previous state.

Combined approaches consider two or more organizational bases in a single model framework. An attempt in this approach is the domain oriented spatiotemporal data model (Yuan 1994, 1996). This three-domain model includes three separate domains, semantics, space, and time. Locational-centered, entity-centered, and time-centered perspectives are used to dynamically link objects of the three domains. This model outperforms many existing models in that it is able to handle changes and movements as well (Pelekis et al. 2004). Claramunt and Thériault (1995) provided an alternative three-domain model that focuses on spatio-temporal events. In addition to spatial and temporal domains, this model also includes a thematic domain to describe the state of a spatio-temporal object. Due to its first successful attempt to record individual descriptive characteristics of dynamic objects, this model is considered as a revolution in the development of spatio-temporal database (Pelekis et al. 2004).

### **3.3 Basic Spatial Analysis**

While GIS offers a rich pool of tools for basic spatial analysis to support many different applications (see Lo and Yeung 2007, Chang 2008), some tools are quite relevant to address a range of coastal research questions. This section focuses on the four major techniques, namely buffering, neighborhood functions, map overlay, and distance modeling.

#### **3.3.1 Buffering**

A very important objective of coastal ecosystem assessment and management is to consider the possible influence areas of specific human activities, which can be identified by using buffering analysis. Buffering analysis is to identify areas within a specified distance of an existing geographic feature. It is one of the most useful GIS functions and is usually associated with proximity analysis. Buffering can be used to depict zones of influence or to define zones of protection. To describe zones of influence is to identify nearby places that are more impacted by a given phenomenon than other places; while to define zones of protection is to find out areas that are protected from the impact of a given phenomenon. Buffering can be employed in both raster and vector data models. In vector data model, buffer operation results in a new feature or features that are within a user-defined distance of the original feature (point, line, or area); in raster data model, buffer can be thought of as spreading a feature by a given distance. It reclassifies cells into three groups: cells of original feature, cells inside the buffer, and cells outside the original feature and buffer.

Buffering analysis is very useful for coastal studies. For example, Basnyat et al. (1999) defined buffer areas around each questioned stream to examine the relationships between water characteristics and nonpoint source pollution inputs to coastal estuaries. McLaughlin et al. (2003) used a 1.5-degree buffer around the central point

of the high runoff coastal cells to study the relation between occurrence of coral reefs and runoff effects. Green and Ray (2002) used buffering analysis to select suitable artificial reef siting. Bourcier (2001) created buffer zones around routeways adjacent to the Natural Reserve of the Seine Estuary to evaluate the impacts of traffic noise on bird lives.

### ***3.3.2 Neighborhood Functions***

One of the important dynamic properties in coastal areas is the tidal and wave movement, which can cause inundation. Neighborhood functions can be used to simulate tidal and wave dynamics and subsequent coastal flood spreading. These operations generate a new value for each cell based on the original values of the cell and its neighborhood. The operation requires users to define a neighborhood and a statistic used to calculate new values. Neighborhood shapes could be rectangle, circle, annulus, and wedge. Statistics mainly include majority, maximum, mean, median, minimum, minority, range, standard deviation, sum, and variety. Neighborhood functions mainly includes overlapping neighborhoods or non-overlapping neighborhoods. For overlapping neighborhood, a moving window is used for every grid cell to get the new value based on the values in the window; while for non-overlapping neighborhood, a specified block is used to calculate the new value for all the cells in the block. An example of applying neighborhood functions was presented by Marfai and King (2008). In their studies, a model to simulate the coastal inundation area was established based on elevation using overlapping neighborhood operation and iterative calculation.

### ***3.3.3 Map Overlay***

Coastal studies and management often require the analysis of many different factors, which is greatly benefited from GIS overlay analysis. Overlay enables users to integrate spatial data and attributes from different sources to produce a composite map and to analyze how these attributes relate to each other. Overlay can be applied on both vector data and raster data. Data layers to be overlaid must be spatially registered to the same coordinate system. Vector overlay uses the geometry and attributes of input layer and overlay layer to create an output layer with new geometry and combined attributes, while raster overlay uses arithmetic or Boolean operators to combine grid cell values in all input layers to produce a new value in the output composite map. Note that raster overlay also allows zonal statistics and weighted overlay.

There are many examples of applying GIS overlay for coastal studies. For instance, Basnyat et al. (1999) used vector overlay to derive the area of each land use/cover category within each nutrient and nonpoint pollutant contributing zone of each stream. Ayad (2005) overlaid the raster layers of the degree of naturalness, land cover diversity, topographic variety, and shoreline proximity to calculate

a composite visual index for each grid cell, which was used to assess the visual changes in a rapidly developing coastal landscape of Egypt. Berberoglu et al. (2004) overlaid a land cover map with plant and bird survey maps to study the linkage between plant and bird diversity and different wetland and terrestrial habitats. Karthik et al. (2005) used weighted overlay method to delineate the potential areas of shrimp farming in Maharashtra, India.

### ***3.3.4 Distance Modeling***

Distance modeling is to determine the distance between two locations on the earth's surface. In general, distance modeling includes measuring Euclidean distance, Manhattan distance or network distance (Wang 2006). Euclidean distance is the straight-line distance between two points. Manhattan distance is the sum of the changes in the horizontal direction and in the vertical direction between two locations. Network distance is the distance between two locations along actual travel routes (road network). The consideration of other factors, such as travel-time, cost, or energy, in distance modeling will result in weighted distance.

A very common application of distance modeling in coastal areas is proximity analysis. For example, Ayad (2005) selected proximity to the shoreline as one of the visual attributes to indicate the attraction of different locations in the study area. The straight-line distances between the grid cells and the shoreline were calculated and coded into five categories from 5 being the closest to 1 being the furthest. Lirman and Fong (2007) investigated the relationship between proximity to land-based sources of coral stressors and risks to coral reefs by measuring the straight-line distances to shore and tidal creeks. Their study concluded that proximity to potential sources of stressors might not necessarily lead to potential risks to reef health.

## **3.4 Spatial Pattern Analysis**

An important aspect of coastal studies is to uncover spatial patterns of specific phenomena and to link patterns to possible processes. This section reviews five commonly used techniques for spatial pattern analysis, namely spatial autocorrelation analysis, quadrat analysis, nearest-neighbor analysis, landscape metrics, and spatial interpolation.

### ***3.4.1 Spatial Autocorrelation Analysis***

Spatial autocorrelation is the formal property that measures the degree to which near and distant things are related. In other words, it is a term referring to the



degree of dependency among observations in a geo-space. It can be measured by using semivariogram, Geary's index ( $C$ ), Moran's index ( $I$ ), or general G-statistics. Semivariogram analysis uses a visual plot of structure function to describe the relationship between measured points and distance. Raaphorst et al. (1998) used semivariogram to study spatial distribution of suspended particulate matter (SPM) in the North Sea. They created several semivariograms using SPM concentrations over different periods. The scattered semivariograms indicated that the SPM concentrations were poorly correlated ever at short distance over short periods of observation time. But when using long-term data, the results indicated a strong correlation for stations less than 50 km from each other. Another application was reported by Kitsiou et al. (2001) who used semivariogram to assess and select optimal sampling sites in a coastal area.

Both Moran's  $I$  index and Geary's  $C$  index are quantitative approach to measure spatial autocorrelation. They are similar to a non-spatial correlation coefficient except that these two consider spatial context. Moran's  $I$  compares the value at any one location with the values at all other locations. Geary's  $C$  index uses the deviations in intensities of each observation with one another. It is more sensitive to differences in small neighborhoods. Although these two indices were originally developed for area objects, they can also be applied to analyze the spatial pattern of points, lines, and raster objects (Lo and Yeung 2007). Moran's  $I$  and Geary's  $C$  have been applied to study the spatial distribution of marine species and their genetic structures (Laiker et al. 2005).

A problem associated with Moran's  $I$  and Geary's  $C$  is that both indices are global indices without considering location-specific spatial patterns. To address this issue, several local indicators of spatial association (LISA) have been developed, such as local Moran's  $I$ , local Geary's  $C$ , and G-statistics ( $G_i$  and  $G_i^*$ ). Local Moran's and local Geary's  $C$  are created by disaggregating global Moran's  $I$  and global Geary's  $C$  to produce a LISA measure. G-statistics is another way to measure local pattern. Different from local Moran's  $I$  and local Geary's  $C$ , G-statistics,  $G_i$  and  $G_i^*$ , were developed to describe the local relationship between particular observations and their neighbors (Getis and Ord 1996).  $G_i$  does not include the target observation  $i$  itself and  $G_i^*$  includes the target observation  $i$  in the sum. A cluster of observations with high  $G_i^*$  values indicates positive location spatial autocorrelation, and vice versa.

### 3.4.2 *Quadrat Analysis*

Many phenomena can be perceived as point features. Point patterns are usually classified as random, uniform, or clustered. Quadrat analysis can be used to quantify spatial point pattern. A quadrat is a well defined area in a region of interest. The shape of a quadrat can be circular, rectangular, square, hexagon, or any other defined shape. The number of points (events) in each quadrat, or sometimes the percent of area covered or the biomass, is counted or measured and is used to generate

a variance. The variance compares the number of points in each quadrat with the average number of points over all the quadrats. The variance is then compared with a random distribution variance. If the two variances are the same, it indicates that the interest point features have a random distribution. Otherwise, it is a non-random distribution. Further analysis may be needed to identify the potential processes leading to the non-random distribution. An example of applying quadrat analysis to study the spatial organization of seagrasses is reported by Fonseca et al. (2008).

Quadrat analysis has two major limitations. First, it can be affected by the quadrat size. To address this issue, some rules have been developed to determine an appropriate quadrat size. For example, ecologists consider the size to be twice of the mean area per point, while some geographers suggest the size as the mean area per point. Also, it is suggested to test different quadrat sizes in order to determine the effects of sizes on results. The other problem is that quadrat analysis is actually the measure of dispersion rather than pattern because it is based on the density of points in quadrats without considering the spatial arrangement of points in relation to one another.

### ***3.4.3 Nearest-Neighbor Analysis***

Nearest-neighbor analysis is another well-known method to study point spatial pattern. To avoid the problems of quadrat analysis, nearest-neighbor analysis uses distance between sample points and their nearest neighboring points as the measurement basis. The mean distance observed is then compared with the expected distance that would occur if the distribution is random. If the two distances are the same, it indicates a random distribution in the interest phenomenon. Otherwise, it indicates a non-random distribution of the interest point phenomenon. Desmet and Cowling (1999) examined the relationship between the occurrence of plants and burrow mounds by measuring the nearest-neighbor distances between all burrow entrances and their nearest plant neighbors for each of the nine  $5 \times 5$  quadrats. The cumulative distribution of these nearest-neighbor distances was compared to that of point-plant distances in each quadrat. A Kolmogorov-Smirnov test was then used to test whether the cumulative frequency distribution of the above two were significantly different.

A problem associated with nearest-neighbor analysis is the edge effect of study area. Boundaries have to be decided to measure the mean nearest-neighbor distance within the study area. Some points may be very close to the boundaries and their nearest neighbors may be located outside of the boundaries. If only those nearest neighbors within the study area are considered, the nearest-neighbor distance measured may be greater than the actual distance for points located near the boundaries. Some methods are used to overcome this weakness. For example, a buffer area is constructed inside the boundaries of the study area. Points located within the buffer area will not be considered in the distance measurement. Another method is to assume that the study area is a torus. The bottom edge is connected to the top edge and the right edge is joined to the left edge.

### ***3.4.4 Landscape Metrics***

Landscape metrics are algorithms to quantify spatial patterns based on categorical maps (McGarigal et al. 2002). Numerous landscape metrics have been developed in the last two decades. They are used to quantify the composition and configuration of a landscape. Landscape composition refers to features associated with the variety and abundance of patch types within the landscape, but without considering the spatial attributes (Gustafson 1998). Landscape configuration refers to the spatial characteristics of individual patches and the spatial relationships among multiple patches within the class or landscape (McGarigal et al. 2002). Landscape metrics can measure landscape patterns at three levels: patch level, class level and landscape level. A problem associated with landscape metrics analysis is that this method based on categorical maps cannot consider the transitional areas between adjacent habitats. Many computer algorithms have been developed to calculate landscape metrics. Some of these programs are directly combined with GIS software or image processing software, while others are separately applied. Landscape metrics analysis has been used to measure spatial patterns of coastal landscapes (Yang and Liu 2005b). Jackson et al. (2006) selected several landscape metrics to quantify the configuration and habitat characteristics of eight seagrass beds. Their study concluded that more fragmented seagrass beds supported lower numbers of fish species than more homogenous seagrass landscapes did.

### ***3.4.5 Spatial Interpolation***

A direct implementation of Tobler's First Law of Geography, spatial interpolation is a procedure of estimating the attribute values at the unsampled, missing, or obscured locations, given a set of measured values at some sites. It can be used to create a continuous surface from the measured points, lines, or polygons, which is useful for data exploration, spatial analysis, and environmental modeling (Yang and Hodler 2000). The measured point dataset can be either site-specific data or the aggregate data over basic spatial units. Contour map is an example of the measured polyline dataset. DEM data can be derived from contour maps or scattered point samples by using spatial interpolation. Many different algorithms have been developed for spatial interpolation (Bailey and Gatrell 1995), and some commonly used interpolators include inverse distance weighting, kriging, Thiessen polygons, radial basis functions, polynomial regression, triangulation, among others (Yang and Hodler 2000). Spatial interpolation has been quite effective but it has some limitations. It can not effectively model a sudden interruption in the value of properties. Furthermore, most interpolators attempt to underestimate the variability in the properties. Thus, we must objectively estimate the reliability of the results and use them with caution.

An example of applying spatial interpolation in the coastal environment is given by Raaphorst et al. (1998). They developed three models to predict the

concentrations of suspended particulate matter in the North Sea by interpolating the *in situ* data. The first model used a distance-weighted interpolation algorithm with the *in situ* data as the input data; the second model interpolated the ratios between the *in situ* data and reflectance in the NOAA/AVHRR imagery; and the third model used a distance-weighted algorithm with an addition weight factor indicating local difference of the reflectance. The results show that the last two models that incorporated satellite signals performed better.

### 3.5 Statistical Spatial Analysis

Statistical spatial analysis employs statistical methods to interrogate spatial data to determine whether the data are ‘typical’ or ‘unusual’ relative to a statistical model (O’Sullivan and Unwin 2002). This section specifically examines six commonly used methods for statistical spatial analysis, namely basic statistical analysis, regression analysis, clustering analysis, principal component analysis, artificial neural networks, and fuzzy logic system.

#### 3.5.1 Basic Statistical Analysis

Basic statistical analysis is a basic procedure of data analysis, which includes descriptive statistics for the distribution of one variable, statistics for the relationship between two variables, hypothesis testing, and visualization. Descriptive statistics adopt a series of indicators to describe the general properties of one variable. For example, the central tendency of the data can be measured using mean, median, and mode. The dispersion of data values can be quantified using range, percentiles, standard deviation, and variance. The relationship between two variables can be measured by some conventional statistical parameters, such as coefficient of correlation (CC) and Chi-square. These parameters indicate whether the development of one phenomenon depends on the other phenomenon. Statistical hypothesis testing is an important way to lead to a conclusion from an uncertain hypothesis through its observable consequences.

Basic statistical analysis has been widely used to describe the distribution and level of variables in the coastal environment. For instance, the basic statistical analysis of the long-term wind direction and speed and wave height has been used to determine the level and reasons of the longshore sediment transport (Ari et al. 2007). Li et al. (2007) examined chemical properties of soil samples across each management zone by using variance analysis to investigate the statistical differences in each defined management zone in a coastal saline land. Basic statistical analysis can also be used to compare two features based upon a large amount of samples, such as a comparative analysis of lakes and basins regarding object size, goodness of elliptic fit, shape complexity, shape asymmetry, and orientation of the major axis (Hinkel

et al. 2005). Also, the cross-correlations between the same size areas in two temporal images can be used to measure the surface water velocity fields in an estuary (Hedger and Malthus 2001).

### ***3.5.2 Regression Analysis***

Regression analysis is a technique used to model and analyze numerical data comprising values of a dependent variable and of one or more independent variables. By using regression analysis, the dependent variable is modeled as a function of the independent variables, corresponding constants, and an error term. The constants are normally estimated using the least squares or other robust methods; the error term represents unexplained variation in the dependent variable. Many efforts have been made to expand the capability of regression analysis from modeling linear relationships to non-linear relationships through the use of higher orders of variables or log-transformed variables instead of original variables.

Regression analysis can be used to identify relationships among various coastal phenomena or to predict the occurrence or development of a particular phenomenon. For example, Pérez-Maqueo et al. (2007) used a stepwise linear regression model to predict the mortality rate caused by hurricanes, with the use of such explanatory (independent) variables as hurricane frequency, natural ecosystems, semi-altered ecosystems, croplands, urban lands, life expectancy, adult literacy, GDP (Gross Domestic Product), liberty, press freedom, and equality. All variables were transformed to a natural logarithm scale to standardize the data before actual statistical modeling. They found that the mortality rate was significantly affected by hurricane frequency, percentage of area covered by semi-altered ecosystems, GDP, and liberty. Basnyat et al. (1999) adopted a multivariate regression analysis to model the effects of the spatial pattern of land use/cover on water quality in an estuarine area.

### ***3.5.3 Clustering Analysis***

Clustering analysis allows to statistically group the observations through the measurement of their similarities using distance measurement algorithms or similarity coefficients. This can be implemented by using either a hierarchical or a non-hierarchical strategy. The hierarchical strategy conducts the grouping process by either merging from bottom to top or dividing from top to bottom. This strategy has several limitations. It is quite sensitive to data noise; the item allocation done at an early stage can not be adjusted later; and the actual computation process can be quite time consuming since the similarities of each individual item need to be dealt with. The non-hierarchical clustering strategy uses the seed points or the randomly partitioned groups as the initial clusters, and then add or remove the observations from the clusters by measuring the similarities changes (Johnson and Wichern 2002). It

does not need to compute the similarities of each individual item, and therefore can be used for working with large datasets.

Many coast-related studies involve the use of clustering analysis. For example, Isacch et al. (2006) grouped three distinct salt marsh habitats by using a Euclidean distance algorithm. Li et al. (2007) delineated the management zones based on a series of concerned factors using fuzzy clustering analysis. Moreover, the application of clustering analysis has been extended into the measurement of statistically significant relationships among two or more phenomena. For example, Fuller et al. (2005) used multivariate K-means clustering method to link the field-observed bird species and the remote sensing derived coastal habitats.

### ***3.5.4 Principal Component Analysis***

Principle component analysis (PCA) orthogonally transforms the original data to a new coordinate system such that the greatest variance by any projection of the data comes to lie on the first coordinate (namely the first principal component), the second greatest variance on the second coordinate, and so on. PCA can be useful to reduce data redundancy, suppress data noise, or enhance some particular patterns. It is important to note that the proportions of variability explained by principal components only reflect their statistical importance. In some cases, subject-matter knowledge may also be required to justify the important components. Furthermore, the results of PCA are affected by many factors, such as the quality of original data, the standardization of samples, and data scales. It is better to apply PCA on different data samples to test the consistency of the results, or to compare the solutions obtained by different methods.

PCA is a well-known tool for data exploration and usually serves as the preliminary step of data analysis. The transformed components can be used as inputs for further statistical analysis, such as clustering analysis and multivariate regression modeling. It can be very useful for coastal applications. For example, Yang and Liu (2005b) used PCA to help select a small set of core landscape metrics from a large number of initial metrics, which were further used to quantify the spatio-temporal patterns of the landscape in a coastal watershed. In a project examining oyster mortality patterns along the coasts of France, Soletchnik et al. (2007) used PCA to identify environmental factors that had significantly affected oyster mortality, and then investigated the oyster mortality patterns by using these factors.

### ***3.5.5 Artificial Neural Networks***

Artificial neural networks (ANNs) are a mathematical model of theorized mind and brain activity, attempting to parallel and simulate the powerful capabilities for knowledge acquisition, recall, synthesis, and problem solving of the human brain. Theoretically, ANNs are highly robust in data distribution and can handle

incomplete, noisy and ambiguous data. They are well suited for modeling complex, nonlinear phenomena. Among the types of neural networks available, the multi-layer-perceptron (MLP) neural networks are most popular largely due to their easiness to understand and implement. A typical MLP neural network is a layered structure with interconnected, weighted neurons. These neurons are very simple processing elements that individually handle pieces of a big problem. A training procedure is normally used to determine the weights. ANNs can be superior to conventional statistical methods only through careful parameterization (Yang 2008).

ANNs have been used to address a number of problems concerning the coastal environment. For example, Schiller and Doerffer (1999) parameterized a MLP feed-forward neural network model with two hidden layers to predict the concentrations of water constituents from remotely sensed data. ANNs are also useful for measuring the coastal bathymetry (Sandidge and Holyer 1998), submarine and subaerial sandy substrate (Conger et al. 2005), wave predictions (Makarynskiy et al. 2004), wind and wave parameters derivation (Kalra et al. 2005, Kalra and Deo 2007), estuarine ecological variable (Miller and Burnett 2008), among others.

### 3.5.6 *Fuzzy Logic System*

Many algorithms tend to ignore or simplify the problem of uncertainty and vagueness that occur in reality more often than the crisp phenomena. Fuzzy logic system offers an effective way to represent environmental phenomena that cannot be properly described using conventional hard algorithms (e.g. Boolean logic). Mathematically, fuzzy logic system defines the membership of a fuzzy set ranging from 0 to 1 to describe the support for the potential classes by using a set of fuzzy rules. Defining fuzzy rules normally involves the use of human expert knowledge or other advanced techniques, such as ANNs. With the rules, the membership of the fuzzy set for each unit can be measured.

Fuzzy logic system can be used to represent environmental variables. For example, Ghayoumian et al. (2007) used the membership of a fuzzy logic set to measure the potential of the geomorphologic factors in certain unit areas for artificial groundwater recharge in a coastal aquifer. They further adopted the fuzzy algebraic product to synthesize the overall suitability that can be compared to justify the optimal discharge area. Fuzzy logic system has been also used in such applications as land cover classification (Filippi and Jensen 2006) and coastal hazard management (Liu and Wirtz 2007).

Furthermore, fuzzy logic system has been often integrated with other techniques, such as clustering and ANNs. For instance, Li et al. (2007) combined fuzzy logic with clustering techniques to help delineate site-specific management zones in a coastal area. Several other coastal applications involved the use of a neuro-fuzzy system that integrated the advantages of ANNs and fuzzy logic system (Mas 2004, Kazeminezhad et al. 2005, Filippi and Jensen 2006).

## 3.6 Spatial Modeling

A group of important activities in coastal studies is to understand coastal dynamics and to predict future consequences of physical processes and human activities. This section briefly reviews several spatial modeling techniques that can be used for the above purposes. They include statistic modeling, cellular automata modeling, and agent-based modeling.

### 3.6.1 *Statistical Models*

Statistics models are empirical models by nature and include both linear and logistic regression models that relate a dependent variable to one or more independent variables, which can be further used for prediction and simulation. Linear regression model is used when both dependent and independent variables are numerical (see Sect. 3.5.2). Logistic regression should be used when the dependent variable is categorical and independent variables are numerical, categorical, or both. Although having the identical form as linear regression, logistic regression uses the natural logarithm of the odds as the dependent variable. Logistic regression does not require linear relationships between the dependent and the independents, but does assume a linear relationship between the logit of  $y$  and the independents. In this sense, logistic regression is still intrinsically linear (Yang 2008).

Statistical regression models have been developed to support coastal ecosystem research and management. For example, Kovacs et al. (2001) built a logistic regression model to assess the hurricane-induced damage to the mangrove forests of the Teacapan-Agua Brava Lagoon System of Mexico. Specifically, the logistic model was used to examine the predicted outcome, vegetation condition by species, main stem condition and diameter at breast height. They found that the probability of a mangrove being found in a dead condition as compared to a well-vegetated one is significantly influenced by the diameter and main stem condition but not by the species. Gibson et al. (2004) developed a logistic regression model for predicting rufous bristlebird habitat in order to identify critical areas requiring preservation, such as corridors for dispersal. Hamer et al. (2008) created a logistic regression model for predicting occupancy of a forest patch by marbled murrelets (a small Pacific seabird) by using a suite of forest structural characteristics. They found that the use of predictive models could help identify the forest area with higher probability of use as murrelet nesting habitat.

### 3.6.2 *Cellular Automata Models*

A cellular automaton (CA) is a discrete model that can be used to model and predict many environmental and social processes. It generally comprises a fixed grid of cells, cell states, cell neighborhood, and transition rules. Cell states correspond to



the potential values of the interested geographic variable, such as land cover classes. Each cell is initialized with one of the cell states. The development of the variable can be simulated by using transition rules that dictate the state of a cell based on the states of its neighborhood. As time goes on, spatial patterns emerge as cells change states; this alters the conditions for future time periods. CA models have the strong ability to replicate real-world spatial form, especially fractal structures. They can be used to model some complex behaviors, such as self-organization, emergence, multiple interactions, spatio-temporal dynamics, and feedbacks.

CA models have been applied to study the ecological problems in coastal areas. For example, Huang et al. (2008) developed a CA model, coupling with remote sensing, to simulate and predict the biological invasion at the Yangtze River estuary, China. In their study site, biological invasion has been characterized by the spatial interactions between exotic species and native plants. Local spatial process plays a significant role in the expanding of invasive species. The authors derived salt marsh vegetation information from remotely sensed images, including non-native species and native species. They used this information to initialize a CA model and further assess the simulation accuracy. They also predicted the distribution of salt marshes in a future year by using the CA model. By visualizing the CA model outputs, they demonstrated the progressive process of biological invasion in their study area.

### ***3.6.3 Agent-Based Models***

An agent-based model (ABM) comprises a collection of autonomous decision-making agents, a network through which agents can react, interact and modify their environment while seeking their goals, and rules governing the actions of the agent. Unlike the cells in cellular automata, agents can be mobile with respect to space. The agents make choices based on their limited knowledge about the environment and feedbacks obtained by them (Parker et al. 2003). An example of applying the agent-based modeling approach is reported by Sperb et al. (2006). They used an agent-based model, coupling with fuzzy logic, to simulate the interactions between land cover change and people's spatial perception and behavior in a coastal area. Their study demonstrates the capability of the agent-based model for predicting land occupation in the coastal environment.

Cellular automata and agent-based modeling are divergent yet complimentary modeling strategies; they can be integrated into a common geographic automata system where some agents are fixed while others are mobile.

## **3.7 Summary and Conclusion**

The geographical location determines the uniqueness of coastal ecosystems that are affected by both land and sea, and by human and nature as well. Coastal ecosystem research and management requires the integration of many different datasets. GIS

offers a platform for data integration, synthesis, and modeling to support decision making, which is critical in many coastal applications.

This chapter discusses the utilities of GIS and spatial analysis in the context of coastal applications. It has begun with the GIS data models for representing spatial and temporal information in digital environment, including field-based and feature-based models for representing spatial information; time-based, location-based, entity-based, and combined approaches for representing the temporal dimension in GIS. These spatio-temporal data models, although still at the stage of development, will soon find their way to apply in the coastal environment. The discussion has expanded to review the four groups of spatial analysis techniques that are particularly relevant to coastal studies. Techniques used in basic spatial analysis include buffering, map overlay, neighborhood function, and distance modeling. Techniques suitable for spatial pattern analysis include spatial autocorrelation analysis, quadrat analysis, nearest-neighbor analysis, landscape metrics, and spatial interpolation. Techniques used in statistical spatial analysis involve basic statistical analysis, regression, clustering analysis, principal component analysis, artificial neural networks, and fuzzy logic system. Spatial modeling techniques include statistical models, cellular automata models, and agent-based models.

It is worth to point out that coastal studies often involve the use of more than one spatial analysis technique and none of the methods discussed in this chapter would be sufficient to handle all the problems encountered. Each method has its advantages and disadvantages. This chapter provides a brief review only on the techniques commonly used in the coastal environment. Besides these major methods, there are some other techniques that may have been adopted or developed to support coastal applications. Because of the space limit, this chapter does not include some other technical issues, such as data quality and error propagation, which can also be critical for coastal studies; in any case, readers can always refer to some premier GIS textbooks (Lo and Yeung 2007). Finally, with the advanced development of computational facilities and the growth of human knowledge about the world, more techniques and methods are expected to be available to monitoring and modeling the coastal environment in the near future.

## References

- Ahn Y, Shanmugam P, Lee J, Kang YQ (2006) Application of satellite infrared data for mapping of thermal plume contamination in coastal ecosystem of Korea. *Mar Environ Res* 61:186–201
- Ari HA, Yuksel Y, Cevik EO, Guler I, Yalciner AC, Bayram B (2007) Determination and control of longshore sediment transport: A case study. *Ocean Eng* 34:219–233
- Armstrong MP (1988) Temporality in spatial databases. *Proc GIS/LIS'88* 2:880–889
- Austin GE, Rehfish MM (2003) The likely impact of sea level rise on waders (Charadrii) wintering on estuaries. *J Nat Con* 11:43–58
- Ayad YM (2005) Remote sensing and GIS in modeling visual landscape change: a case study of the northwestern arid coast of Egypt. *Landscape Urban Plan* 73:307–325
- Bailey TC, Gatrell AC (1995) *Interactive spatial data analysis*. Addison Wesley Longmans, Cambridge

- Baskent EZ, Kadiogullari AI (2007) Spatial and temporal dynamics of land use pattern in Turkey: A case study in Inegol. *Landscape Urban Plan* 81:316–327
- Basnyat P, Teeter LD, Flynn KM, Lockaby BG (1999) Relationships between landscape characteristics and nonpoint source pollution inputs to coastal estuaries. *Environ Manage* 23:539–549
- Benavente J, Del Rio L, Gracia FJ, Martínez-del-Pozo JA (2006) Coastal flooding hazard related to storms and coastal evolution in Valdelagrana spit (Cadiz Bay Natural Park, SW Spain). *Cont Shelf Res* 26:1061–1076
- Berberoglu S, Tuluhan Yilmaz K, Ozkan C (2004) Mapping and monitoring of coastal wetlands of Cukurova Delta in the Eastern Mediterranean region. *Biodivers and Conserv* 13:615–633
- Bourcier JC (2001) A Territorial Information System (TIS) for the Management of the Seine Estuary – Environmental and Management Applications. In: Bartlett D, Smith J (eds) *GIS for coastal zone management*. CRC Press, Boca Raton, pp 257–267
- Brown I (2006) Modeling future landscape change on coastal floodplains using a rule-based GIS. *Environ Modell Softw* 21:1479–1490
- Brown I, Jude S, Koukoulas S, Nicholls R, Dickson M, Walkden M (2006) Dynamic simulation and visualisation of coastal erosion. *Comput Environ Urban Sys* 30:840–860
- Carre F, Girard MC (2002) Quantitative mapping of soil types based on regression kriging of taxonomic distances with landform and land cover attributes. *Geoderma* 110:241–263
- Chang KT (2008). *An introduction to geographic information systems*, 4th edn. McGraw Hill, Boston
- Claramunt B, Thériault M (1995) Managing time in GIS: an event oriented approach. In: Clifford J, Atuzhilin A (eds) *Recent advances on temporal databases*. Springer, Berlin, pp 23–42
- Conger CL, Fletcher CH, Barbee M (2005) Artificial neural network classification of sand in all visible submarine and subaerial regions of a digital image. *J Coastal Res* 21:1173–1177
- Desmet PG, Cowling RM (1999) Patch creation by fossorial rodents: a key process in the revegetation of phytotoxic arid soils. *J Arid Environ* 43:35–45
- Euán-Avila JI, Liceaga-Correa MA, Rodríguez-Sánchez H (2004) GIS for assessing land-based activities that pollute coastal environments. In: Bartlett D, Smith J (eds) *GIS for coastal zone management*. CRC Press, Boca Raton, pp 229–238
- Filippi AM, Jensen JR (2006) Fuzzy learning vector quantization for hyperspectral coastal vegetation classification. *Remote Sens Environ* 100:512–530
- Fonseca MS, Kenworthy WJ, Griffith E, Hall MO, Finkbeiner M, Bell SS (2008) Factors influencing landscape pattern of the seagrass *Halophila decipiens* in an oceanic setting. *Estuar Coast Shelf S* 76:163–174
- Fuller RM, Devereux BJ, Gillings S, Amable GS, Hill RA (2005) Indices of bird-habitat preference from field surveys of birds and remote sensing of land cover: a study of south-eastern England with wider implications for conservation and biodiversity assessment. *Global Ecol Biogeogr* 14:223–239
- Garibaldi L, Caddy JF (1998) Biogeographic characterization of Mediterranean and Black Seas faunal provinces using GIS procedures. *Ocean Coast Manage* 39:211–227
- Getis A, Ord JK (1996) Local spatial statistics: an overview. In: Longley P, Batty M (eds) *Spatial analysis: modeling in a GIS environment*. John Wiley, New York, pp 261–277
- Ghayoumian J, Saravi MM, Feiznia S, Nouri B, Malekian A (2007) Application of GIS techniques to determine areas most suitable for artificial groundwater recharge in a coastal aquifer in southern Iran. *J Asian Earth Sci* 30:364–374
- Gibson LA, Wilson BA, Cahill DM, Hill J (2004) Spatial prediction of rufous bristlebird habitat in a coastal heathland: a GIS-based approach. *J Appl Ecol* 41:213–223
- Green DR, Ray ST (2002) Using GIS for siting artificial reefs—data issues, problems, and solutions: ‘Real World’ to ‘Real World’. *J Coastal Cons* 8:7–16
- Gustafson EJ (1998) Quantifying landscape spatial pattern: what is the state of the art? *Ecosystems* 1:143–156
- Hamer TE, Varland DE, McDonald TL, Meekins D (2008) Predictive model of habitat suitability for the marbled murrelet in western Washington. *J Wildl Manage* 72:983–993

- Hedger RD, Malthus TJ (2001) Estimation of velocity fields at the estuary—coastal interface through statistical analysis of successive airborne remotely sensed images. *Int J Remote Sens* 22:3901–3906
- Hinkel KM, Frohn, RC, Nelson FE, Eisner WR, Beck RA (2005) Morphometric and spatial analysis of thaw lakes and drained thaw lake basins in the western Arctic Coastal Plain, Alaska. *Permafrost Periglac* 16:327–341
- Huang H, Zhang L, Guan Y, Wang D (2008) A cellular automata model for population expansion of *Spartina alterniflora* at Jiuduansha Shoals, Shanghai, China. *Estuar Coast Shelf S* 77:47–55
- Isacch JP, Costa CSB, Rodriguez-Gallego L, Conde D, Escapa M, Gagliardini DA, Iribarne OO (2006) Distribution of saltmarsh plant communities associated with environmental factors along a latitudinal gradient on the south-west Atlantic coast. *J Biogeogr* 33:888–900
- Jackson EL, Attrill MJ, Rowden AA, Jones BM (2006) Seagrass complexity hierarchies: Influence on fish groups around the coast of Jersey (English Channel). *J Exp Mar Biol Ecol* 330:38–54
- Johansson M, Migon P, Olvmo M (2001) Development of joint-controlled rock basins in Bohus granite, SW Sweden. *Geomorphology* 40:145–161
- Johnson RA, Wichern DW (2002) Applied multivariate statistical analysis, 5th edn. Prentice Hall, New Jersey
- Kalra R, Deo MC (2007) Derivation of coastal wind and wave parameters from offshore measurements of TOPEX satellite using ANN. *Coast Eng* 54:187–196
- Kalra R, Deo MC, Kumar R, Agarwal VK (2005) Artificial neural network to translate offshore satellite wave data to coastal locations. *Ocean Eng* 32:1917–1932
- Karthik M, Suri J, Saharan N, Biradar RS (2005) Brackish water aquaculture site selection in Palghar Taluk, Thane district of Maharashtra, India, using the techniques of remote sensing and geographical information system. *Aquacult Eng* 32:285–302
- Kastler JA, Wiberg PL (1996) Sedimentation and Boundary Changes of Virginia Salt Marshes. *Estuar Coast Shelf S* 42:683–700
- Kazeminezhad MH, Etemad-Shahidi A, Mousavi SJ (2005) Application of fuzzy inference system in the prediction of wave parameters. *Ocean Eng* 32:1709–1725
- Kitsioudis D, Tsirtsis G, Karydis M (2001) Developing an optimal sampling design—A case study in a coastal marine ecosystem. *Environ Monit Assess* 71:1–12
- Koneff MD, Royle JA (2004) Modeling wetland change along the United States Atlantic Coast. *Ecol Model* 177:41–59
- Kovacs JM, Blanco-Correa M, Flores-Verdugo F (2001) A logistic regression model of hurricane impacts in a mangrove forest of the Mexican Pacific. *J Coastal Res* 17:30–37
- Laiker L, Müller LM, Palme A, Palm, S, Kapuscinski AR, Thoresson G, Ryman N (2005) Spatial genetic structure of northern pike (*Esox lucius*) in the Baltic Sea. *Mol Ecol* 14:1995–1964
- Langran G (1993) Time in geographic information systems. Taylor & Francis, London
- Langran G, Chrisman NR (1988) A framework for temporal geographic information systems. *Cartographica* 25:1–14
- Li Y, Shi Z, Li F, Li H (2007) Delineation of sit-specific management zones using fuzzy clustering analysis in a coastal saline land. *Comput Electro Agri* 56:174–186
- Lirman D, Fong P (2007) Is proximity to land-based sources of coral stressors an appropriate measure of risk to coral reefs? An example from the Florida Reef Tract. *Mar Pollut Bull* 54:779–791
- Liu X, Wirtz KW (2007) Consensus building in oil spill response planning using a fuzzy comprehensive evaluation. *Coast Manage* 35:195–210
- Lo CP, Yeung AKW (2007) Concepts and techniques of geographic information systems, 2nd edn. Pearson Prentice Hall, New Jersey
- Makarynsky O, Pires-Silva AA, Makarynska D, Ventura-Soares C (2004) Artificial neural networks in wave predictions at the west coast of Portugal. *Compute Geosci* 31:415–424
- Makiaho JP (2007) Estimation of ancient and future shoreline positions in the vicinity of Olkiluoto, an island on the western coast of Finland: The difference between Grid and TIN based GIS approaches. *Palaeogeogr Palaeoclimatol* 252:514–529
- Marfaei MA, King L (2008) Potential vulnerability implications of coastal inundation due to sea level rise for the coastal zone of Semarang city, Indonesia. *Environ Geol* 54:1235–1245

- Marquinez J, Lastra J, Garcia P (2003) Estimation models for precipitation in mountainous regions: the use of GIS and multivariate analysis. *J Hydrol* 270:1–11
- Mas JF (2004) Mapping land use/cover in a tropical coastal area using satellite sensor data, GIS and artificial neural networks. *Estuar Coast Shelf S* 59:219–230
- McGarigal K, Cushman SA, Neel MC, Ene E (2002) FRAGSTATS: Spatial Pattern Analysis Program for Categorical Maps. Computer software program produced by the authors at the University of Massachusetts, Amherst, URL: <http://www.umass.edu/landeco/research/fragstats/fragstats.html> (Last access on 20 July 2007)
- McLaughlin CJ, Smith CA, Buddemeier RW, Bartley JD, Maxwell BA (2003) Rivers, runoff, and reefs. *J Global Planet Change* 39:191–199
- Miller DJ, Burnett KM (2008) A probabilistic model of debris-flow delivery to stream channels, demonstrated for the Coast Range of Oregon, USA. *Geomorphology* 94:184–205
- Nayak S, Pamdeya A, Gupta MC, Trivedi CR, Prasad KN, Kadri SA (1989) Application of satellite data for monitoring degradation of tidal wetlands of the Gulf of Kachchh, Western India. *Acta Astronaut* 20:171–178
- O'Sullivan D, Unwin DJ (2002) Geographic information analysis. Wiley, New Jersey
- Parker DC, Manson SM, Janssen, MA, Hoffmann MJ, Deadman P (2003) Multi-agent systems for the simulation of land-use and land-cover change: a review. *Annals Assn of Amer Geog* 93:314–337
- Pelekis N, Theodoulidis B, Kopanakis I, Theodoridis Y (2004) Literature review of spatio-temporal database models. *Knowl Eng Rev* 19:235–274
- Pengra BW, Johnston CA, Loveland TR (2007) Mapping an invasive plant, *Phragmites australis*, in coastal wetlands using the EO-1 Hyperion hyperspectral sensor. *Remote Sens Environ* 108:74–81
- Pérez-Maqueo O, Intralawan A, Martínez ML (2007) Coastal disasters from the perspective of ecological economics. *Ecol Econ* 63:273–284
- Peuquet DJ (1999) Time in GIS and geographical databases. In: Longley PA, Goodchild MF, Maguire DJ, Rhind DW (eds) *Geographical information systems- principles and technical issues*, vol 1. Wiley, New York, pp 91–103
- Peuquet DJ, Duan N (1995) An event-based spatio-temporal data model (ESTDM) for temporal analysis of geographic data. *Int J Geogr Inf Syst* 9:2–24
- Raaphorst WV, Philippart CJM, Smit JPC, Dijkstra FJ, Malschaert JFP (1998) Distribution of suspended particulate matter in the North Sea as inferred from NOAA/AVHRR reflectance images. *J Sea Res* 39:197–215
- Saleh MA (2007) Assessment of mangrove vegetation on Abu Minqar Island of the Red Sea. *J Arid Environ* 68:331–336
- Sandidge JC, Holyer RJ (1998) Coastal Bathymetry from hyperspectral observations of water radiance. *Remote Sens Environ* 65:341–352
- Schiller H, Doerffer R (1999) Neural network for emulation of an inverse model—operational derivation of Case II water properties from MERIS data. *Int J Remote Sens* 20:1735–1746
- Siddiqui MN, Maajid S (2004) Monitoring of geomorphological changes for planning reclamation work in coastal area of Karachi, Pakistan. *Adv Space Res* 33:1200–1205
- Soletchnik P, Ropert M, Mazurie J, Fleury PG, Le Coz F (2007) Relationships between oyster mortality patterns and environmental data from monitoring databases along the coasts of France. *Aquaculture* 271:384–400
- Sperb RM, Cabral RB, Bughi CH (2006) Fuzzy agents: a hybrid tool for exploring coastal zone spatial processes. *J Coastal Res* 3:1510–1514
- Viedma O, Melia J, Segarra D, Garcia-Haro J (1997) Modeling rates of ecosystem recovery after fires by using Landsat TM data. *Remote Sens Environ* 61:383–398
- Wang F (2006) *Quantitative Methods and Applications in GIS*. CRC Press, Boca Raton
- Wilcock D, Cooper A (1993) Monitoring Losses of Semi-natural Vegetation to Agricultural Grassland from Satellite Imagery in the Antrim Coast and Glens AONB, Northern Ireland. *J Environ Manage* 38:157–169
- Worboys MF (1994) A unified model for spatial and temporal information. *Comput J* 37:26–34

- Wright DJ, Blongewicz MJ, Halpin PN, Breman J (2007) *Arc Marine: GIS for a blue planet*. ESRI Press, Redlands
- Yang X (2008) Artificial neural networks for urban modeling. In: Madden M (ed) *Manual of geographic information systems*, American Society for Photogrammetry and Remote Sensing (in press)
- Yang X, Hodler T (2000) Visual and statistical comparisons of surface modeling techniques for point-based environmental data. *Cartogr Geog Inf Sci* 17:165–175
- Yang X, Liu Z (2005a) Using satellite imagery and GIS to characterize land use and land cover changes for integrated estuarine watershed assessment. *Int J Remote Sens* 26:5275–5296
- Yang X, Liu Z (2005b) Quantifying landscape pattern and its change in an estuarine watershed using satellite imagery and landscape metrics. *Int J Remote Sens* 26:5297–5323
- Yuan M (1994) Wildfire conceptual modeling for building GIS space-time models. *Proceedings of GIS/LIS 94*, Phoenix, Arizona, pp 860–869
- Yuan M (1996) *Temporal GIS and spatio-temporal modeling*. National center for Geographical Information and Analysis, SANTA\_FE\_CD-ROM
- Zeiler M (1999) *Modeling our world: the ESRI guide to geodatabase design*. ESRI Press, Redlands

## Chapter 4

# Fuzzy Approach for Integrated Coastal Zone Management

Tao Cheng, Martien Molenaar and Alfred Stein

Integrated Coastal Zone Management (ICZM) is “a dynamic, multi-disciplinary and iterative process to promote sustainable management of coastal zones” (ICZM 2008). It covers the full cycle of information collection, planning, decision making, management and monitoring of the implementation. Uncertainties, however, exist in almost all the activities in this cycle. This chapter presents the isle of Ameland as the case study area where uncertainties in ICZM can be identified, which provides a direct impression of the problems to be solved. The indeterminate nature of coastal zones and landscape units and associated uncertainties are discussed. This is followed by a discussion of formal fuzzy spatial object models, serving as the basis for representing fuzzy coastal landscape units. It then discusses the dynamic processes and their interactions of these landscape units that can be derived from the temporal series data. A further discussion on the change in area and volume of beach is given. The final Section concludes with the major findings and suggestions for further research.

### 4.1 Introduction

Coastal zones are the primary interface for the exchange of natural and man-made materials between territorial and coastal ecosystems. Such areas are important for living, fishery, agriculture, and tourism, etc. The growing concentration of population and socio-economic activities puts increasing pressure on coastal ecological systems, which at same time are threatened by inundation, coastal erosion, increased flooding, and loss of freshwater reserves and arable land, particular due to rising sea-levels. To sustain development and to minimize loss from possible natural disasters

---

T. Cheng (✉)

Department of Civil, Environmental and Geomatic Engineering, University College London,  
Gower Street, London, WC1E 6BT UK  
e-mail: tao.cheng@ucl.ac.uk

in these areas, ongoing developments and their consequences have to be guided and monitored.

Integrated Coastal Zone Management (ICZM) is “a dynamic, multi-disciplinary and iterative process to promote sustainable management of coastal zones” (ICZM 2008). ICZM aims to balance between economic development, coastal area prevention, and public access. It covers the full cycle of information collection, planning, decision making, management and monitoring of the implementation. Uncertainties, however, exist in almost all the activities in this cycle. During information collection, sampling and measurement usually contain errors, whereas during planning and decision making, the definition of objects and criteria are usually uncertain. The concept of “beach”, for example, commonly refers to the sandy area that separates the sea from the land. Definition of the boundary of a beach is difficult, because of tidal changes, ambiguous transition zones and different concepts in using it.

In this study we distinguish two types of uncertainty in the ICZM: data uncertainty and uncertainty in object/criteria definition. Data uncertainty means that the true value of a measurement is unknown. We are unsure of what exactly we are observing or measuring. It usually includes sampling and measurement errors. Because of its random nature, probability theory can be applied to handle this type of uncertainty. Uncertainty in the object and criteria definition refers to unsure knowledge such as how to define beach precisely. Mathematically, probability density function and membership functions are in the essence of “probability” and “fuzziness,” respectively (Chang 2005). Applications have emerged in environmental risk analyses based on probability theory and fuzzy sets theory, respectively (Chang 2005). Combination of the two would exhibit a synergistic effect in systems analysis, e.g. for illustrating interactive sources of uncertainty (Cheng et al. 1997).

Since Zadeh (1965) proposed fuzzy sets theory, its applications have flourished, varying from solving the inherent problem of uncertainty in natural resources assessment to accommodating vagueness and complexities of modeling environmental systems (see also Robinson 2003). This chapter discusses uncertainties of fuzziness involved in integrated coastal zone management. The fuzzy approach is still immature, especially for coastal zone studies, although data uncertainties have been extensively studied.

The chapter is organized into seven sections. After the introduction, we present the isle of Ameland as the case study area where uncertainties in ICZM can be identified. This provides a direct impression of the problems to be solved. The indeterminate nature of coastal zones and landscape units and associated uncertainties are discussed in Sect. 4.3. This is followed by a discussion of formal fuzzy spatial object models in Sect. 4.4, serving as the basis for representing fuzzy coastal landscape units. Section 4.5 discusses the dynamic processes and their interactions that can be derived from the temporal series data. A further discussion on the change in area and volume of beach is given in Sect. 4.6. The final Section concludes with the major findings and with suggestions for further research.



## 4.2 The Case – Changing Beach of Ameland

### 4.2.1 General Description of the Case Study Area

Ameland, one of the six Dutch barrier islands, is situated north of the coast of the Netherlands (Fig. 4.1). Length in the East–West direction is approximately 24 km, and varies in the North–South from 1.5 to 4 km. It consists of three dune complexes: the Hollum-Ballum complex in the west, the Nes-Buren complex in the center, and the Oerderduinen complex in the east. These three dune complexes were originally separated from by tidal inlets, but they are connected today by sand dikes, as such forming one island (Van Zuidam et al. 1994, 1998). The test area is the right window in Fig. 4.1 and it occupies  $54 \times 60$  grids in the 60-m DEM.

Processes influencing landscape units of Ameland can be divided into two types: erosion in the middle and southern parts of the western end due to shifting inlets by marine current and sedimentation in the northwest. To predict future development, we have to understand the various processes, their interaction and their effect on the development of the island. The results of the geomorphological processes can be measured qualitatively and quantitatively. Qualitative results can be identified by the erosion or accumulation of the landscapes, whereas quantitative results emerge from estimating (or calculating) volume changes. Such information is important for optimizing costly coastal defense works, e.g. beach nourishment or replantation of vegetation. This study mainly focuses on sediment transport at the land–sea interface as a result of erosion and sedimentation. To do so, the morphodynamically most active area in the northwest section of the island (the area in the small rectangle in the northwest) was selected as the test site.

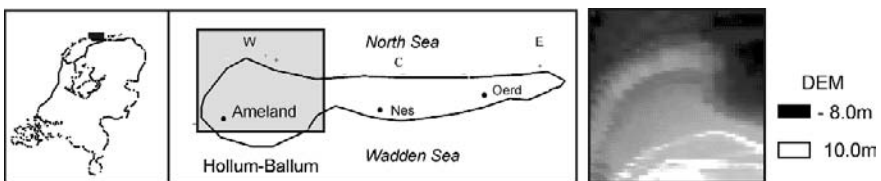


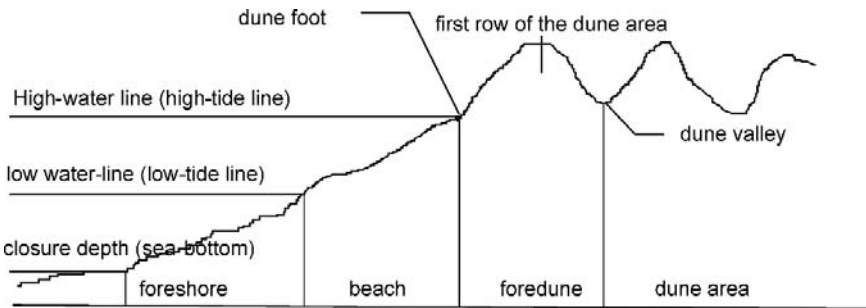
Fig. 4.1 Test site – Ameland, The Netherlands (after Cheng and Molenaar 1999b)

### 4.2.2 Definition of the Geomorphological Landscape Units

Traditionally, the effect of erosion and accretion is estimated using annual measurements in the form of coastal profile. Erosion and accumulation are identified by comparing the same profile for two different time horizons. Changes in volume of sand sediments are calculated. From these calculations, inferences of the changes in profiles over the years can be obtained. Some geomorphologists, however, try to

analyze the development trend of the landscape units. To do so, the geomorphologic processes, particularly the erosion and accumulation of sediments, should be distinguished through interpretation of changes in the landscape units, i.e. the foreshore, beach and foredune areas. Therefore, to monitor these geomorphologic processes it is necessary to identify these landscape units and trace their changes by field observations.

The landscape units – foreshore, beach and foredune – have specific characteristics in terms of altitude, slope, roughness, size, material, composition of mineral elements, compaction, humidity, and vegetation/land cover, etc. The definitions of these landscape units usually differ from surveyor to surveyor, from case to case and from time to time. Among other ways, the landscape units may be defined based upon altitude of terrain surface according to different water lines. Van Heuvel and Hillen (1994) considered that the area beneath the high-tide line (HT) and above the low-tide line (LT) is foreshore; the area beneath the very high-tide (VHT) and above the HT is beach, and the area above the VHT and below the foot of dune is foredune. Others, however, consider that the foreshore is the area above the closure depth (Ruessink and Kroon 1994) and beneath the low-water line (De Graaff 1977), that beach is the area above the low-water line and beneath dune foot (Reineck and Singh 1980), and that the foredune is the first row of dunes inland from dune foot. Furthermore, the values for these water lines are not fixed. Ruessink and Kroon (1994) used  $-6\text{m}$  to represent the closure depth in the years 1965–1984 and in year 1989, and used  $-8\text{m}$  to represent the closure depth in the years 1985–1988 and 1990–1993. De Ruig and Louisse (1991) used  $-6\text{m}$  to represent it in all these years. Therefore, there is no invariable and fixed definition of the landscape units. Figure 4.2 illustrates one set of definitions of the landscape units.



**Fig. 4.2** Landscape units are defined by the closure depth, low water line and dune foot (Cheng and Molenaar 1999b)

### 4.2.3 Data

Since the mid – 1800s, the location of the foot of dune, the high-water line and low-water line along the Dutch coast have been measured each year. These

measurements are carried out along defined sections, each demarcated by beach posts. These posts are encountered on the beach along the entire North Sea coast, with distances of 200–250 m between each of them. Since 1963, the coastal profile has been measured every year in each section. This includes that the heights/depths are determined up to a distance of about 800 m to seaward of the posts, and up to some 200 m landwards of the first line of dunes. Once every three years the profiles are extended up to 2–3 km to seaward (Van Heuvel and Hillen 1994). The inaccuracy of the height/depth measurements is between 0.1 m and 0.2 m and the inaccuracy in the horizontal position is up to 10 m.

The annual coastal measurements are interpolated along the profile with 10–20 m intervals. They are further interpolated into a height raster of (60 m × 60 m) grids to obtain a complete coverage of the test site (as shown in Fig. 4.1). The accuracy of the height on grid is 0.2 m (Van Heuvel and Hillen 1994).

#### **4.2.4 Summary**

To summarize, there are several issues in the study of the change of coastal landscape units in Ameland: (i) the definition of the landscape units are highly subjective; (ii) the definition of the landscape units changes with time; and (iii) the measurements of the profiles of coastal zones contains errors, so does the DEM derived from them.

The first and second points are the uncertainties associated with the definitions of landscape units, we will discuss in detail in the following sections. The third point, however, is the uncertainty associated with the data (observation), which we will not discuss further. The reason is that research on uncertainties has been well documented in this aspect (Fisher 2003, Zhang and Goodchild, 2002). Data uncertainties, however, affect the classification accuracy when the data are applied for further analysis (Cheng et al. 1997). A vast body of research is included in this heading, looking at both positional and thematic accuracy and the consequences of error (Leung et al. 2004, Heuvelink et al. 2006a,b) based upon probability theories. Such research is usually under the assumption that the spatial objects can be defined precisely and identified crisply.

### **4.3 Indeterminate Nature and Associated Uncertainties of Coastal Landscape Units**

Definitions of coastal landscape units are variant. This inherently results from the indeterminate nature of natural objects. These natural phenomena are distributed continuously in space, leading to a transitional boundary between these objects. When we delineate them from remotely sensed images, the boundary may even be

drawn in a subjective way, i.e. different from one person to another (Lowell et al. 2000). Also spatial objects as such may be heterogeneous or may be mixed with each other. The mixture of trees and grass or of several types of trees is common in forests (Brown 1998, Foody 1999). Further, most geographical entities are dynamic and change with time. It is hard to measure them accurately since they change after the measurement. With geographical entities, taking more observations in the boundary zone does not necessarily resolve the “boundary” but reveals new details of variation in that zone (Burrough 1996). Therefore the “boundary” of dynamic entities is not fixed such as the coastline. Furthermore, definition of geographical entities is also scale- and context-dependent. Increasing the level of resolution often results in identification of new areas or classes, particularly in the border areas of the higher aggregation level (Burrough 1996). The measured lengths of coasts and frontiers depend on the scales at which they are measured (Mandelbrot 1983). What is a beach, and what are the boundaries of the beach, are both scale- and context-dependent.

The *continuity*, *heterogeneity*, *dynamics* and *scale-dependence* cause uncertainties when we model and represent natural phenomena as spatial objects (Fisher 2000, Cheng 2002).

Due to the continuity and heterogeneity of natural phenomena, the central or core concept of classes of a phenomenon of study (vegetation and vegetation class) can be clearly and explicitly described and defined in categorical terms, but the boundary conditions between one core class and another are problematic (Fisher 2003, Robinson 2003). This is vagueness in class definition.

Ambiguity is usually resulted from the scale issues in geographical analysis. It arises when we have very well defined conceptualizations of categories in which we are interested, but categorization process has multiple equally valid correct outcomes at different scales which are, however, contradictory.

Discord is when one investigator uses one classification scheme, and a second uses a non-overlapping classification. For example, Ahlqvist et al. (2000, 2003) examined contradictory classifications of vegetation of the same area resulted from remote sensing imagery and from wetness of soils. Furthermore, the core concept of spatial objects might change with time; dynamics of reality will also cause discord.

Therefore, when we model coastal landscapes, these units are intuitively uncertain. There are vagueness, ambiguity and discord in the definition. Many ways of handling uncertain spatial data due to indeterminate categories have been proposed. For examples, fuzzy set theory has been applied to handle the vagueness in class definition; rough set theory has been adopted to model the ambiguity due to scale change and the discord in classification. Each of these theories has been largely developed independently of the others, but with the same goal of addressing the problems inherent in uncertainty. Among others, fuzzy set theory is far more popular and successful. In the next section, we will apply fuzzy approach to model the coastal landscape units.

## 4.4 Fuzzy Modeling and Representation of Coastal Landscape Units

### 4.4.1 Fuzzy Landscape Classification/Definition

Following Sect. 4.2.2 landscape units should be clearly identified, in order to understand the erosion and accumulation of geomorphological process. Due to their indeterminate nature, however, it is difficult to have a crisp definition to classify the foreshore, beach and foredune areas. Hereby we adopt a fuzzy approach to define them.

Fuzzy sets are sets or classes that for various reasons cannot, or do not, have sharply defined boundaries (Zadeh 1965), e.g. the “class of all real numbers which are much greater than 1”, or “the class of beautiful women”, or “the class of tall men”. If  $Z$  denotes a space of objects, then the fuzzy set  $A$  in  $Z$  is the set of ordered pairs

$$A = \{z, MF_A(z)\} \quad z \in Z$$

where the membership function  $MF_A(z)$  represents the “grade of membership of  $z$  in  $A$ ” and  $z \in Z$  means that  $z$  is contained in  $Z$ . Usually  $MF_A(z)$  is a number in the range  $[0, 1]$ , with 0 representing non-membership and 1 representing full membership of the set.

Usually there are two ways to define the fuzzy membership function, either on the basis of expert knowledge or by using methods of numerical taxonomy. The semantic import model (*SIM*) is used when users have a more or less clear idea to group the data in a qualitative way, i.e. the central concept of the class is clear, but for various reasons the exact boundary can only be approximated. The fuzzy membership function is defined by adapting a crisp classification, e.g. extending the crisp boundaries into a transition zone. Therefore, fuzzy sets can be characterized by the boundaries ( $b_1$  and  $b_2$ ) plus the transition zones ( $d_1$  and  $d_2$ ). For mathematical description, the fuzzy membership function can be a linear, a curved, or an S-shaped function (Robinson 2003). For example, Burrough (1989) used this approach for soil evaluation. A symmetric membership function was chosen to distinguish “deep” soil from “shallow” and from “very deep” soils. Other application of *SIM* in GISs can be widely found in literature, such as the definition of sharpness of boundaries in Wang and Hall (1996), an air pollution danger zone around a city in Usery (1996).

Opposite to the subjective approach of *SIM*, the fuzzy c-means (*FCM*) approach tends to be an objective approach. It is analogous to cluster analysis and numerical taxonomy in that the value of the membership function is computed from a set of attribute data. In such a way, an individual sample may have memberships of multi-classes. *FCM* is usually used in image classification (Bezdek et al. 1984, Chi and Yan 1995). Furthermore, other objective methods are applied to derive fuzzy membership values, such as self-organizing maps (Chi et al. 1995), fuzzy supervised classification (Mannan et al. 1998) and neural network (Sun and Jang 1993).

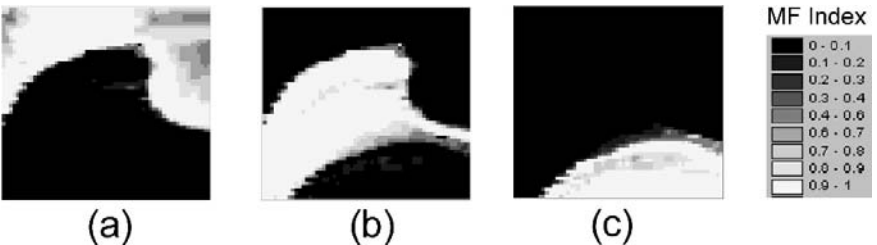
**Table 4.1** Fuzzy definition for coastal landscape units (after Cheng and Molenaar 1999b)

ClassId	Landscape Unit	$b_1$ (m)	$b_2$ (m)	$d_1$ (m)	$d_2$ (m)
1	Foreshore	-6.0	-1.1	2.0	0.5
2	Beach	-1.1	2.0	0.5	0.5
3	Foredune	2.0	25.0	0.5	3.0

Note:  $b_1$  and  $b_2$  represent the boundaries of the landscape units;  $d_1$  and  $d_2$  represent the half width of the transition zone.

Here we took the *SIM* approach and defined the coastal landscape units by modifying the crisp definition in Fig. 4.2. The transition zones between these landscape units are defined as in Table 4.1.  $b_1$  and  $b_2$  represent the boundaries of the landscape units;  $d_1$  and  $d_2$  represent the half width of the transition zones. For example, if a region belongs to the foreshore then the height value of the region should be between  $-6.0\text{m}$  and  $-1.1\text{m}$ . As most experts take  $-6\text{m}$  to be the closure depth, we could consider  $-6\text{m}$  to be the boundary between foreshore and deep sea, but sometimes others take  $-8\text{m}$  to be the closure depth. We use  $-8\text{m}$  to be the outmost boundary of the foreshore. Thus the transition zone between foreshore and deep sea has a height range of about  $4\text{m}$  and  $d_1$  has a value of  $2\text{m}$  (half width). The height range of transition zone from foreshore to beach is  $0.5\text{m}$ , from beach to dune  $0.5\text{m}$ , and from foredune to dune  $3\text{m}$ . In order to reveal the vagueness of definitions for the landscape units, we adopt a trapezoidal membership function to represent the fuzzy semantics.

We classify the grid cells of the case study area (Fig. 4.1) into classes of landscape units. As shown in Fig. 4.3(a) (b) and (c), each pixel has three membership values to three classes of landscape units.



**Fig. 4.3** Fuzzy classification results of Ameland (Cheng 1999): (a) Membership value of belonging to foreshore; (b) Membership value of belong to beach; and (c) Membership value of belonging to foredune (*darker* means lower membership)

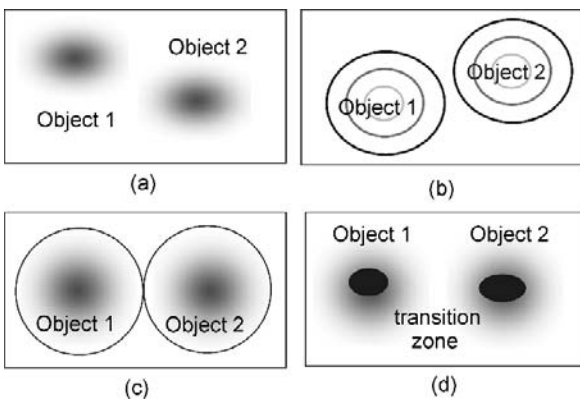
### 4.4.2 Fuzzy Spatial Representation of Coastal Landscape Units

Figure 4.3 shows that the uncertainties in the specification of the spatial extent of objects are in this case due to fuzzy thematic classification of the raster cells. Although

the uncertain classification is primarily considered to be thematic, it will lead to the geometry vagueness. For example, during image classification the certainty that a pixel belongs to a thematic class might be expressed through a likelihood function, which is evaluated in the classification process (Lillesand and Kiefer 1994). Image segments can then be formed of contiguous sets of pixels falling under the same class. If these segments represent the spatial extent of objects then the uncertainty of the geometry of these objects is due to the fact that the value of the likelihood function varies per pixel (Canter 1997, Wickham et al. 1997). Therefore, the thematic uncertainty is transferred to geometric uncertainty after segmentation (Molenaar 1998, Cheng and Molenaar 1999a). This section discusses how to represent coastal landscape units as fuzzy spatial objects.

The estimation of the spatial extent of objects from these fuzzy classifications is related to the interpretation of fuzziness of the objects and their topological relationship, as is their representation. In general, four views are applied to represent the fuzzy objects (Cheng 2002):

- **Fuzzy – fuzzy area:** This representation is intuitively coming from the fuzzy classification result. Spatial objects can be extracted from these classification results with image segments consisting of contiguous sets of pixels, or grid cells, belonging to one class. The objects of one class can then be represented as a layer of the raster, so that layers of objects will be formed, each consisting of fuzzy regions (Molenaar 1998). If each region represents the spatial extent of an object, the object is called a fuzzy-fuzzy object (*FF-Object*), where the first “fuzzy” means that its spatial extent is fuzzy and the second “fuzzy” means that its thematic interior is fuzzy, because it contains cells that have been assigned to the thematic class of the region with a certainty less than 1 (see Fig. 4.4a). The representation of *FF-objects* is apparently similar to the fully-fuzzy area concept proposed by Foody (1999). The fully-fuzzy area is, however, still a direct representation of the fuzzy classification result. This means that thematic data is represented per cell (or pixel). The information has not been aggregated to an



**Fig. 4.4** Four ways to represent fuzzy objects (Cheng 2002): (a) Fuzzy-fuzzy areas; (b)  $\alpha$ -cut boundaries; (c) Conditional boundaries; and (d) Core-transition zones

object level so that the uncertainty of the spatial extent of objects does not play a role in the analysis.

- **$\alpha$ -cut boundary:** If we define a threshold value  $\alpha$ , for the classification for each layer of the fuzzy-fuzzy areas, an  $\alpha$ -cut boundary will be formed (Fig. 4.4b). In this case, the segments of each layer will have  $\alpha$ -cut boundaries.
- **Conditional boundary:** In other applications, area objects are defined as being spatially disjoint in space (in single context), i.e. they do not overlap such that each grid cell belongs in principle to one object. If the objects form a spatial partition then each cell should belong to exactly one object, as in the case study of coastal zone, where foreshore, beach and foredune are considered to be spatially disjoint objects. Although the boundary between beach and foredune cannot be located very crisply, the conceptual model suggests that a specific location should either belong to beach or foredune, but not to both. In this case it is necessary to combine the objects of different layers into one layer and to form a complete spatial partition of the area, which can be further differentiated into two classes of objects. One case is that a boundary has to be set to define explicitly the spatial extent of any object by assigning each grid cell to exactly one object. In such cases criteria (conditions) have to be applied to assign a cell to a specific class. After segmentation, the spatial extents of objects are identified and the boundaries between them are apparent automatically (Fig. 4.4c). These boundaries are called conditional-boundaries since they are based upon conditions (or criteria, Cheng et al. 2001).
- **Core-transition zone:** Another case is that a clear boundary cannot be defined, but that there are transition zones between the objects. In the transition zones, no decision is made about which object the grid cells might belong to. Similarly, certain criteria are applied to assign the cell to the core of the objects or to the transition zones (Fig. 4.4d).

To differentiate between the last two situations, we call objects with conditional boundaries as crisp-fuzzy objects (CF-Object, see Fig. 4.4c), which means that the conditional boundaries between objects are crisp but the interiors of the objects are fuzzy. We call objects with core-transition zones as fuzzy-crisp objects (FC-Object, see Fig. 4.4d), where fuzzy means that their spatial extents (transition zones) are fuzzy and crisp means that their interiors (cores) are certain. Therefore, we call the objects based upon fuzzy-fuzzy areas and  $\alpha$ -cut boundaries as FF-objects and  $\alpha$ F-objects, respectively. The conventional objects with crisp boundary and crisp interiors are called CC-objects (see also Table 4.2).

**Table 4.2** Different views of objects and their characteristics (Cheng 2002)

Type*	Boundary	Interior	Transition
CC	Crisp	Crisp	/
FF	Fuzzy	Fuzzy	Fuzzy
$\alpha$ F	Crisp( $\alpha$ )	Fuzzy	Fuzzy
CF	Crisp(c)	Fuzzy	/
FC	/	Crisp(c)	Fuzzy

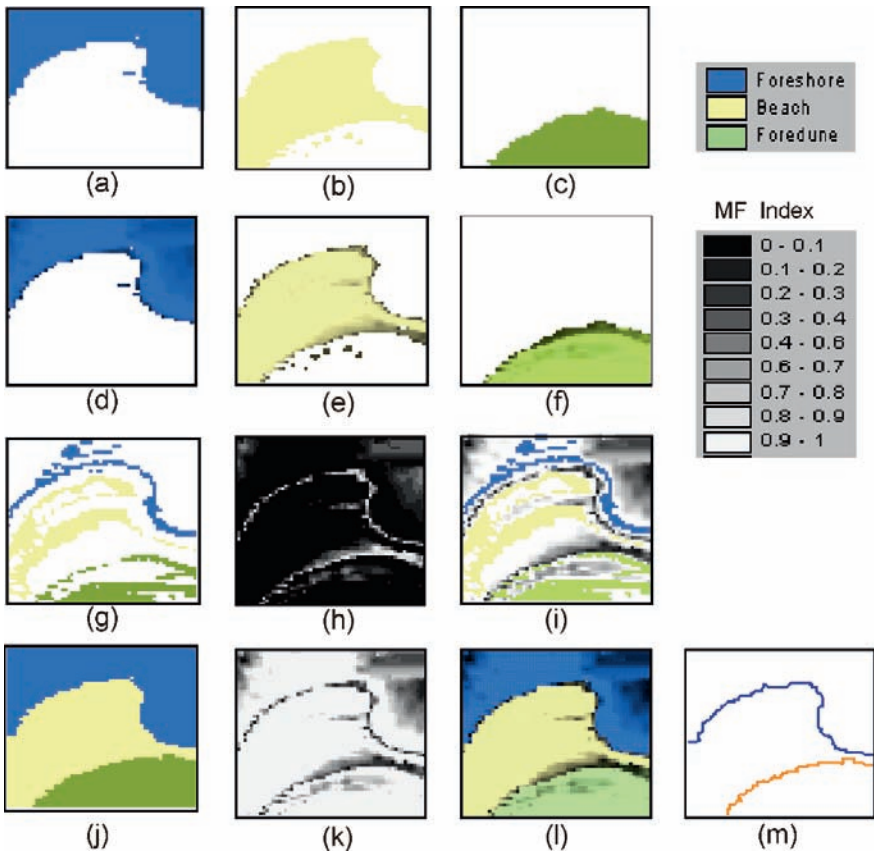
\*Refer to Fig. 4.4 for the definition of each type of fuzzy object representation.



How to derive the fuzzy spatial objects from fuzzy classification please refer to Cheng et al. (2001) for details. The next subsection shows the results of Ameland case under different fuzzy spatial object models.

#### 4.4.3 Modeling Results of Ameland

Here we present the spatial representation of the landscape units under four fuzzy object models:



**Fig. 4.5** Fuzzy modeling results of Ameland (Cheng 1999). Results from the FF-objected modeling are represented by (a): FF-objects belong to foreshore\*; (b): FF-objects belong to beach\*; (c): FF-objects belong to foredune\*; (d): (a) FF-objects belong to foreshore with fuzziness; (e): FF-objects belong to beach with fuzziness; and (f): FF-objects belong to foredune with fuzziness. Results from the FC-object modeling are represented by (g): Cores of FC-objects; (h): Transition zones of FC-objects; and (i) FC-objects with fuzziness. Results from the CF-Object modeling are shown in (j): CF-object model; (k): Certainty of cells belonging to objects; (l): Objects with uncertainty; and (m): Conditional boundaries between regions. Note that the threshold value (\*) used was 0.2 and darker means greater uncertainty

- **Modeling by fuzzy-fuzzy object model:** The modeling results by FF-object model are shown in Fig. 4.5(a–f). The edges of the outmost grid cells of each object are the conditional boundaries, with a threshold of 0.2. Figure 4.5(a–c) each represents a layer with objects of one type. When these layers are overlaid, it is clear that these regions overlap. The fuzzy spatial extent of the objects is shown in Fig. 4.5(d–f).
- **Modeling by fuzzy-crisp object model:** Figure 4.5(g–i) represents the core of the FC-objects. Figure 4.5g represents the cells with values approximately equal to 1, which represent transition zones among FC-objects. By combining Fig. 4.5(g,h), FC-objects are shown in Fig. 4.5i.
- **Modeling by crisp-fuzzy object model:** The modeling results of the CF-object model are shown in Fig. 4.5(j–m). Figure 4.5j shows the spatial extent of CF-objects. Figure 4.5k represents the uncertainty of cells belonging to the objects. The transition boundaries among objects (belonging to three classes) are shown in Fig. 4.5l.

## 4.5 Dynamic Process of Fuzzy Coastal Landscape Units

When fuzzy regions are extracted from field observation data, a further step is needed to identify the objects that are represented by these regions. Conventionally, this step is based on interpretation by domain experts or by a field check. Afterwards, changes in objects are detected by comparing their states at different epochs. The experts then analyze the processes the objects have undergone by linking the lifeline the regions at different epochs to form lifelines of the objects (Cheng 1999). This section, however, proposes a method for analyzing the relationships of regions and for identifying objects and their processes automatically.

This can be realized based on the assumption that natural phenomena are changing gradually, especially the change of coastal zone can be regarded as a gradual continuous process (Galton 1997), so the objects are considered to be rather stable. This implies that if two regions are the spatial extents at two subsequent epochs of one and the same object, their overlap should be larger than their overlaps with the region of any other object. Under this assumption we can find the successor of a region at epoch  $t_n$  by calculating its spatial overlaps with all the regions that appeared at epoch  $t_{n+1}$ . The one that has maximum overlap will be identified as the successor (Cheng and Molenaar 1999b).

### 4.5.1 Linkage Between Epochs

Let  $\mu_s$  denote the membership of a grid cell belonging to the region S, and  $\mu_{s'}$  the membership to the region  $S'$ . Then  $\mu_{S \cap S'} = \text{Min}(\mu_s, \mu_{s'})$  denotes the membership to the overlap between S and  $S'$ .

Assuming that  $Size(P(i, j)) = 1$ , then  $\mu_s(i, j) \cdot Size(P(i, j)) = \mu_s(i, j)$ . Further, let  $Size(S) = \sum_{(i,j)} \mu_s(i, j)$  be the integral of the membership function associated to the region  $S$ , over the spatial domain. Then  $Size(S \cap S') = \sum_{(i,j)} \mu_{s \cap s'}(i, j)$  is the integral of the membership function associated to the overlap between  $S$  and  $S'$ .

Based upon the spatial overlap between regions, we can match the regions that are spatially related. Let  $R_1$  be the set of regions at epoch  $T_i$  and  $R_2$  the set of regions at epoch  $T_{i+1}$ . Further, let  $S \in R_1$  and  $S' \in R_2$ . The following indicators can be used to evaluate the types of relationship between regions at two epochs.

The relative fuzzy overlap between two regions can be defined as (Molenaar 1998)

$$ROverl(S'|S) = \frac{Size(S \cap S')}{Size(S)} \quad (4.1)$$

$$ROverl(S|S') = \frac{Size(S \cap S')}{Size(S')} \quad (4.2)$$

where  $ROverl(S|S')$  represents the ratio of the overlap to the size of  $S$  (relative fuzzy overlap to  $S$ );  $ROverl(S'|S)$  is the ratio of the overlap to the size of  $S'$  (relative fuzzy overlap to  $S'$ ).

The similarity of two fuzzy regions can be defined as (Cheng and Molenaar 1999b)

$$Similarity(S, S') = \frac{Size(S \cap S')}{\sqrt{Size(S) \cdot Size(S')}} \quad (4.3)$$

### 4.5.2 State Transitions

Using these indicators, object state transitions can be identified between two epochs. Seven fundamental cases are shown in Table 4.3. The combinations of indicator functions behave differently for these seven cases. State transitions can be identified by the following process:











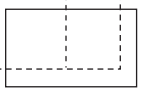







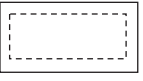



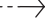


```

For all  $S' \in R_2$  compute  $Size(S')$ 
For all  $S \in R_1$  do
  >compute  $Size(S)$ 
  For all  $S' \in R_2$ 
    >compute  $Size(S \cap S')$ 
    >compute  $ROverl(S'|S)$ ,  $ROverl(S|S)$ ,  $Similarity(S'|S)$ 
    >evaluate  $shift(S; S')$ ,  $expand(S; S')$ ,  $shrink(S; S')$ 
  >evaluate  $split(S; \dots S', \dots)$ ,  $appear(S')$ 
>evaluate  $merge(\dots, S, \dots, S')$ ,  $disappear(S)$ 

```

Evaluation is done by identifying the type of state transition between  $S$  and  $S'$  based upon the indicators according to the situations indicated in Table 4.1. For

**Table 4.3** Identification and presentation of state transition (Cheng1999)

Regions at $T_1$	Regions at $T_2$	Overlay	Indicators			State Transition	Symbol
			Rovelap( $S_b S_a$ ) Similarity Rovelap( $S_c S_a$ )	Rovelap( $S_a S_b$ ) /Rovelap( $S_c S_a$ )	Rovelap( $S_a S_b$ )		
			Large -	Large -	High -	shift( $S_a;S_b$ )	
			Small Small	Large Large	Low Low	split( $S_a;S_b,S_c$ )	
			Small Small	Large Large	Low Low	merge( $S_b,S_c; S_a$ )	
			Large -	Small -	Low -	expand( $S_a;S_b$ )	
			Small -	Large -	Low -	shrink( $S_a;S_b$ )	
		-	- -	- -	- -	appear( $S_b$ )	
	-	-	- -	- -	- -	disappear( $S_a$ )	

example, the split process implies that one region  $S \in R_1$  splits in two or more regions  $S' \in R_2$  and the merge process implies that two or more regions  $S \in R_1$  merge into one region  $S' \in R_2$ . Here we illustrate how the indicators could be used to detect the state transitions. Threshold vales have been chosen intuitively based on expert knowledge. Further research is required to establish threshold values for these indicators.

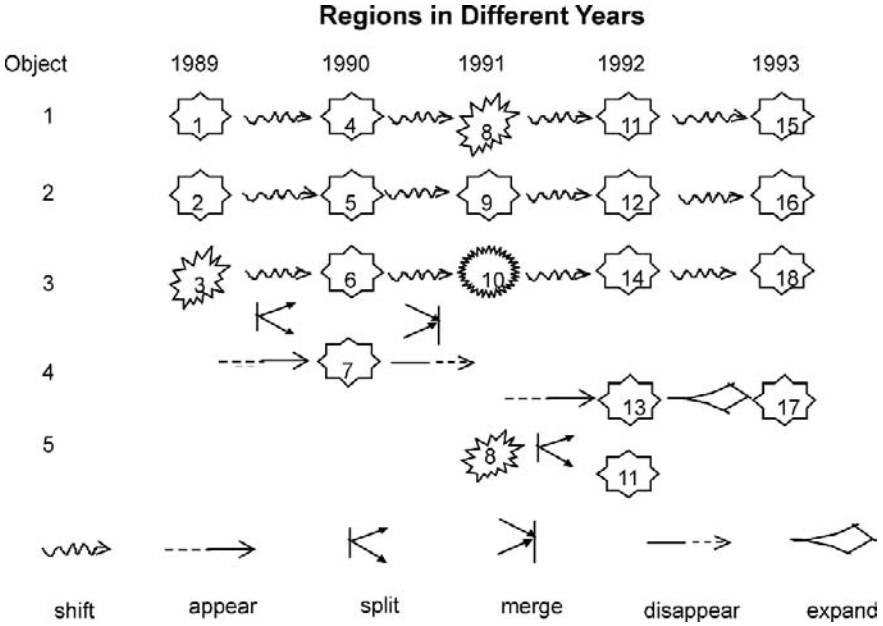
The fuzzy sizes of these regions and the fuzzy overlap of regions of successive years are shown in Table 4.4. The indicators of Sect. 4.5.1 can now be evaluated; with these we can link the regions (as shown in Table 4.4) which indicate that the linked regions are most likely the representations of the spatial extent of an object in successive years. For example, region 1 has been linked with 4, 4 with 8, 8 with 11; region 3 has been linked with region 6, 6 with 10, 10 with 14. We also found that there is a new region in 1990 (Region 7). By checking the overlap of this region with the regions at 1989 and 1991, we found it has overlap with region 3 and 10; these regions are linked by a line too.

**Table 4.4** Fuzzy overlaps and links between fuzzy regions (Cheng and Molenaar 1999b)

Year	Region	Area	Overlap with regions in next year				Class Type	
			4	5	6	7		
1989/1990	1	1108.1	937.5	81.8	0.0	0.0	Foreshore	
	2	1246.8	106.3	1104.8	9.2	0.0	Beach	
	3	644.3	0.0	12.7	572.5	27.5	Foredune	
1990/1991			8	9	10			
	4	1138.7	975.0	76.0	0.0		Foreshore	
	5	1229.7	76.0	1129.5	2.6		Beach	
	6	586.8	0.0	0.0	64.3		Foredune	
1991/1992	7	28.0	0.0	0.0	26.3		Beach	
			11	12	13	14		
	8	1101.3	862.7	116.9	6.4	0.0	Foreshore	
	9	1260.1	87.3	1146.6	0.0	0.5	Beach	
1992/1993	10	609.8	0.0	3.3	0.0	605.7	Foredune	
			15	16	17	18		
	11	1004.9	751.5	6.8	0.0	0.0	Foreshore	
	12	1288.7	119.3	1101.1	38.9	2.8	Beach	
		13						
		14	625.7	0.0	2.7	0.0	604.4	Foredune

### 4.5.3 Lifelines of Dynamic Objects

The procedure of the previous section identified possible dynamic relationships between regions at two different epochs. Regions thus related can be linked to form lifelines of objects that may have “shifted”, “expanded” or “shrunk” between two



**Fig. 4.6** Identified fuzzy objects and processes (Cheng 1999)

successive epochs. The regions that appeared at a specific moment represent a new object, and regions that disappeared at some moment represent disappearing objects. Furthermore, “merging” and “splitting” objects can be identified (See Fig. 4.6). The objects are finally identified and are represented in Fig. 4.7a.

Recently Guilbert and Lin (2007) used snake algorithm to detect the change of cloud for weather forecasting, which is quite similar to the method proposed here. It implies that the method proposed is also applicable for crisp objects.

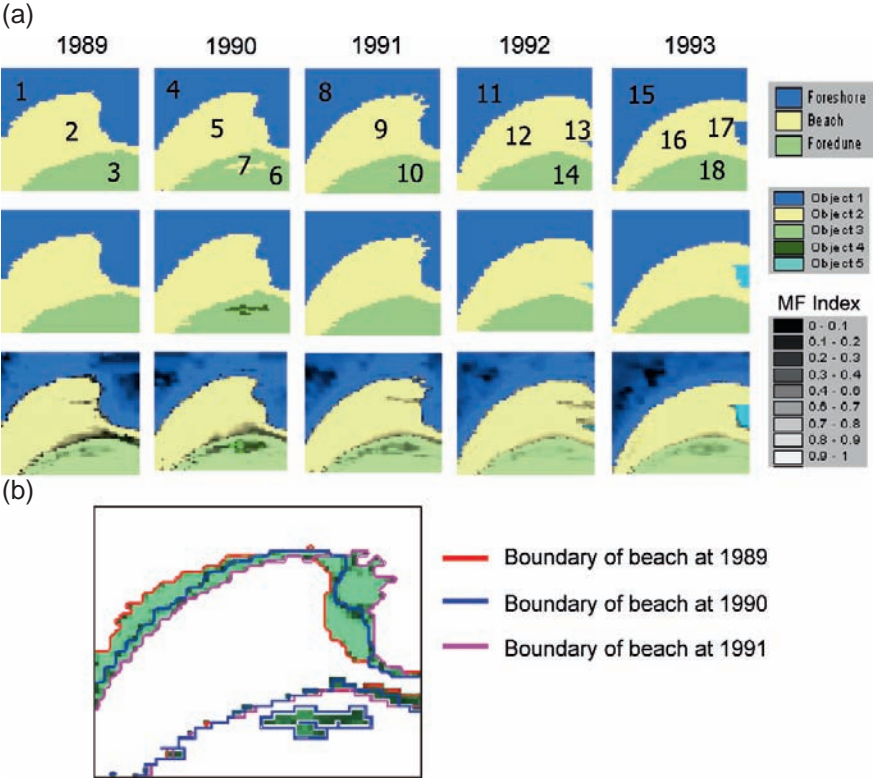
## 4.6 Change in Area and Volume of Beach

### 4.6.1 Change of Shape and its Uncertainty

By comparing the spatial extents of an object in two successive years we can derive the change of shape. This can be done through a simple spatial overlay operation. The uncertainty of change can be derived from the classic intersection of the uncertainty of the grid cells belonging to the object’s extent for each year (Molenaar 1998, Cheng 2002)

$$\mu_{S_a;S_b}^p = \text{MIN}(\mu(P,S_a)_{t_1}, \mu(P,S_b)_{t_2}) \quad (a \neq b) \tag{4.4}$$

where  $\mu_{S_a;S_b}^p$  is the uncertainty of the change of a grid cell  $P$  which belongs to Object  $O_a$  at  $t_1$  and Object  $O_b$  at  $t_2$ ;  $S_a$  is the spatial extent of  $O_a$  at  $t_1$ ,  $S_b$  is the



**Fig. 4.7** (a) Dynamics of fuzzy objects (after Cheng 1999) (the top three rows): the top row for identified fuzzy-crisp regions, the second row for fuzzy objects without showing uncertainties, and the third row for fuzzy objects showing uncertainties; (b) Change of beach during 1989–1991 (Cheng 2002) (the bottom row)

spatial extent of Object  $O_b$  at  $t_2$ ;  $\mu(P, S_a)_{t_1}$  represents the uncertainty of  $P$  belonging to  $S_a$  at time  $t_1$ ;  $\mu(P, S_a)_{t_2}$  represents the uncertainty of  $P$  belonging to  $S_b$  at time  $t_2$ .

For example, a grid cell belonged to foreshore (Object  $O_a$ ) in year 1989 with certainty value  $\mu(P, S_a)_{t_1} = 0.65$ . It belonged to beach (Object  $O_b$ ) in year 1990 with certainty value  $\mu(P, S_b)_{t_2} = 0.78$ . Therefore, the uncertainty of change of this cell according to Eq. (4.4) is then,

$$\mu^P_{S_a:S_b} = \text{MIN}(0.65, 0.78) = 0.65.$$

The changes of extent of these landscape units of 1989–1990 and 1990–1991 are presented in Fig. 4.7b. It can be seen that the foreshore and beach were very active, but the fore dune was quite stable. The changes of the foreshore and the beach were normally opposite to each other. It was also found that the certainties of change of the cells close to the center of the changed area were higher than those close to the edge of the changed area. This is due to the fact that the cells closer to the edge of

the changed area are closer to one of the edges of the two objects, which are less certain than the cells closer to the centers of the objects.

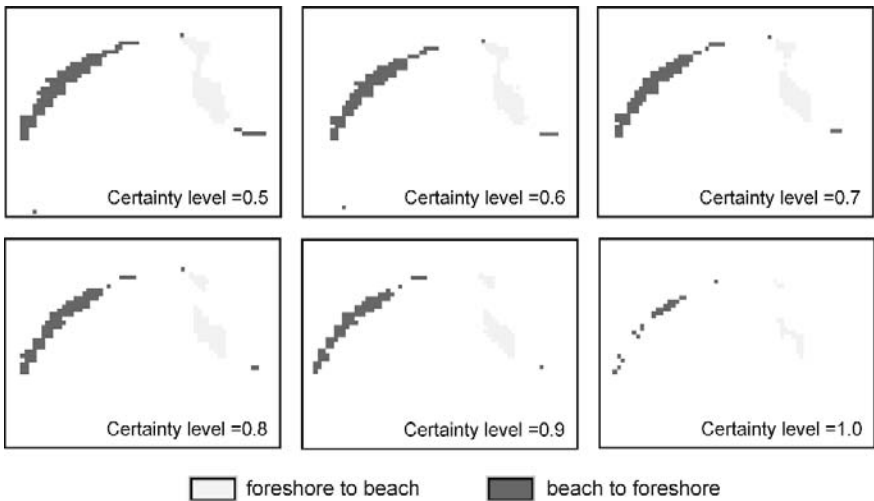
Based upon this analysis, the developing trends of these landscape units can be analyzed qualitatively. Moreover, based upon this result, the changes of the landscape units can be calculated at different certainty levels. The changes of foreshore and beach (1989–1990) at different certainty levels are reported in Table 4.5. The number of cells falls with the increasing level of certainty. It implies that only definite changes from foreshore to beach (accumulation) fare in 25 pixels and beach to foreshore (erosion) are in a different 25 cells.

Based upon the change map of Fig. 4.7b, a series of change maps for different  $\alpha$ -cuts (certainty levels) was derived in Fig. 4.8.

**Table 4.5** Changes between foreshore and beach at different certainty levels (Cheng 2002)

Certainty level $\geq$	1.0	0.9	0.8	0.7	0.6	0.5
Foreshore to beach*	25	58	67	75	87	94
Beach to foreshore*	25	77	92	102	110	121

\*Number of grid cells.



**Fig. 4.8** Change between foreshore and beach at different certainty level (1989–1990) (Cheng 2002)

### 4.6.2 Changes of Area and Volume

In the crisp object model, the area of an object  $O$  is

$$Area(O) = \sum_{P \in O} Size(P) \tag{4.5}$$



The area of a fuzzy object  $O$  is then defined as (Molenaar 1998)

$$FArea(O) = \sum_{P \in S} \mu(P, S) * Size(P) \tag{4.6}$$

where  $S$  is the fuzzy spatial extent of  $O$ ,  $\mu(P, S)$  is the uncertainty that grid cell  $P$  belongs to  $S$ , and in our case  $Size(P) = 60 \times 60 \text{ (m}^2\text{)}$ .

Calculating the volume of a fuzzy object is similar to calculating its area. In both case uncertainties of the grid cells belonging to the objects have to be taken into account.

$$FVolume(S) = \sum_{P \in S} \mu(P, S) * Size(P) * h_P \tag{4.7}$$

where  $h_p$  is the height of the grid cell with respect to a reference level and it is  $-20\text{ m}$  in our case, since some points on the test area are lower than sea level, e.g.,  $-16\text{ m}$ . Other symbols refer to Eq. (4.4).

The area and volume of the landscape units are presented in Fig. 4.9, which shows that the fuzzy area of the whole region is not constant. This is because the certainties of the spatial extents of the landscape units varied from year to year. The total volume of sediment in the test field is decreasing which indicates general erosion. This information can be used to guide the coastal defense works such as beach nourishment that needs high investments.

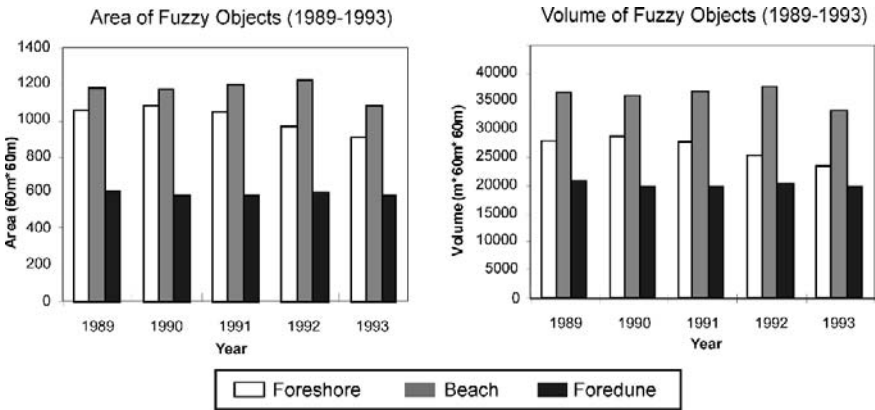


Fig. 4.9 Dynamic changes of area and volume of fuzzy objects (after Cheng 2002)

### 4.6.3 Discussion

#### 4.6.3.1 Two Ways of Calculating Change of Beach

Two ways were proposed to calculate the change of beach area. In the first approach the changes are based upon the areas of beach in the consecutive years. The cells of

the whole area of beach, including the unchanged part, are considered for the calculation. Therefore, in this case, the calculation is related to cells in the changed areas and to their certainties of belonging to the areas. It is also related to the change of certainty in the unchanged area (Cheng 2002). In the second approach, only cells in the changed area are considered for the calculation. In this case study, the calculation is related to the certainties of the cells in the changed areas, which are related to both the certainties the cells belonging to foreshore, beach and foredune in two years.

The first approach has been based on the changes of the certainties of cells belonging to beach in two consecutive years, while the second approach has been based only on the areas of the change. Which method should be chosen for fuzzy objects depends on the specific case. It is important to understand and analyze the uncertainty behind the calculations in order to provide accurate information to decision makers. In the first case the area is predefined, the uncertainty is related to the whole area. The change of area also considers the uncertainty of the whole area. In the second case, uncertainty is considered only for the changed area which implies a specification of the type of change. Therefore, when we want to measure the change related to a landscape unit, the first approach should be taken. When we want to measure the change as an interaction between two landscape units, the second approach should be taken. Generally Fig. 4.7b provides a more accurate and efficient way of representing the change, since the maps in Fig. 4.8 could be derived from it (Cheng 2002).

#### 4.6.3.2 Fuzzy and Crisp Approaches

In order to estimate the consequence of the uncertainties in object definition and field observation data, we derive crisp objects by using crisp object definition and without considering the uncertainty of object identification. The spatial extents of crisp objects are similar to fuzzy objects. However, the area and volume of crisp objects are different, they are larger (please refer to Cheng (2002) for details). The differences between these imply the influences of uncertainties. The foreshore area has the most obvious difference because its fuzzy definition has a wider transition zones (2.0 m) than beach (0.5 m) and foredune (0.5 m). The change of beach derived from crisp approach is similar to the result derived from fuzzy approach 1 since they apply similar approach i.e. consider the whole area of beach for calculation (Cheng 2002).

#### 4.6.3.3 Prediction of Changes

To model and predict changes of coastal landscape units, we analyzed the stationarity of change over a period of 7 years (1989–1995) by both crisp and fuzzy approaches. This study extends previous work on fuzzy Markov chains by Dilo (2006, Chap. 7). For the fuzzy approach, the changes of objects under the *CF* model have been discussed above (as shown in Fig. 4.9). We also analyzed the interactive changes between Foreshore, Beach, Foredune and undecisive areas for the  $\alpha F$  model (Table 4.2) with  $\alpha$  at 0.25, 0.5, 0.75 and 1, respectively.

1. The results of the CF model are similar to those for  $\alpha$  is at 0.25 or 0.5, but they are quite different from the results for  $\alpha$  is at 0.75 or 1. These results clearly confirm the fuzzy nature of these coastal landscape units and that a crisp or a slightly fuzzified approach does not give very realistic results.
2. We further see that the average interactive changes for  $\alpha$  at 0.25, 0.5 are the same as those for the CF model:
  - the average percentages of the beach area changing into respectively foreshore, foredune, undecisive areas are 9.8%, 1.2%, 0%, and
  - the average percentages of respectively foreshore, foredune and undecisive areas changing into beach are 4.8%, 2.8% and 0%.

This indicates the whole case study area has been eroded over this period of seven years since there is a dominant change from beach to foreshore and from foredune to beach. This is also shown in our results, only 89% of the beach area remains beach in the consecutive years.

3. In most years, at almost all levels of  $\alpha$ , undecisive areas change into foreshore, whereas only a small part changes to beach for  $\alpha > 0.5$ . This implies that the foreshore area is fuzzy indeed, with low membership values. Those areas might have height  $< -6.0\text{m}$ , indicating erosion in the area, which is mainly changing into foreshore. That also indicates a general erosion of this coastal area, with a dominant change from beach to foreshore.

#### 4.6.3.4 Other Approaches

Fuzzy area estimation is also discussed in Woodcock and Gopal (2000), but their analysis is based upon fuzzy classes, not fuzzy objects. Although they also intended to estimate the area of a class as a function of levels of fuzzy membership, they calculated the area of a class meeting certain criteria, i.e. membership levels. The class proportions have to be calculated for each class at different membership levels. In our case, the membership function per cell belonging to an object (the spatial extent) is considered in the calculation of the area of the fuzzy object. We cannot tell which method is better, but the method proposed here is quite simple and straightforward. However, the author agrees with Woodcock and Gopal (2000, p. 171) to that to determine areas meeting various conditions, questions of the sum equaling unity are irrelevant. Since the problem of area estimate is viewed from fuzzy set theory, this assumption of unity for the sums of the areas of map categories also becomes irrelevant. It also applies to the fuzzy areas that change with time.

## 4.7 Conclusion

This chapter presents a systematic discussion of fuzzy approach for integrated coastal zone management. It discussed the indeterminate nature of coastal landscape units and how they are represented as fuzzy spatial objects in GIS. Furthermore, the

identification of dynamic process and the change of these fuzzy objects and uncertainties are investigated. An example of the dynamic changes of sediments along the Dutch coast is applied to illustrate the methodology. The method is also applicable in monitoring geographical entities such as natural vegetation units or land use areas.

By comparing the results mapped by the crisp object model and the fuzzy object model, it was revealed that uncertainties in object definition and in field measurements have obvious influences on change detection of geometric attributes of geographical entities. It is important to study these influences to provide accurate information to decision makers. The changes of uncertainty for an object imply its potential change in future. Exploring these changes is essential for the prediction of the potential development of geographical entities; this will be the future direction of this research. Moreover, this chapter only discussed the situation that fuzzy classification is due to multiple criteria of object definition and errors in the measurement. How to handle other situations, such as the definition of objects changing with time, will be another topic for future research (Van de Vlag and Stein 2006). Furthermore, the uncertainties resulted from multi-scale definitions needs further investigation and further reading can be found at (Cheng et al. 2004, Fisher et al. 2007).

**Acknowledgements** The first author would like to thank the International Institute for Aerospace Survey and Earth Sciences (ITC) for funding her PhD (1995–1999) which contributes most part of the research. She appreciates the grants received from the Chinese University of Hong Kong (CUHK 4334/98E and CUHK 4132/99H), the University of Leicester and the Hong Kong Polytechnical University (no. G-YW92), which also supported the research. The Survey Department of the Directorate-General for Public Works and Water Management of the Dutch Ministry of Transport, Public Works and Water Management kindly made the data for the Ameland case available.

## References

- Ahlqvist O, Keukelaar J, Oukbir K (2000) Rough classification and accuracy assessment. *Int J Geogr Inf Sci* 14:475–496
- Ahlqvist O, Keukelaar J, Oukbir K (2003) Rough and fuzzy geographical data integration. *Int J Geogr Inf Sci* 17:223–234
- Bezdek JC, Ehrlich R, Full W (1984) FCM: the fuzzy C-mean clustering algorithm. *Comput Geosci* 10:191–203
- Brown DG (1998) Classification and boundary vagueness in mapping presettlement forest types. *Int J Geogr Inf Sci* 12:105–129
- Burrough PA (1989) Fuzzy mathematical methods for soil survey and land evaluation. *J Soil Sci* 40:477–492
- Burrough PA (1996) Natural objects with indeterminate boundaries. In: Burrough PA, Frank AU (eds) *Geographic objects with indeterminate boundaries*. Taylor & Francis, London, pp 3–28
- Canter F (1997) Evaluation the uncertainty of area estimates derived from fuzzy land-cover classification. *Photogramm Eng Rem S* 63:403–414
- Chang N (2005) Sustainable water resources management under uncertainty. *Stoch Env Res Risk A* 19:97–98
- Cheng T (1999) A process-oriented data model for fuzzy spatial objects. PhD thesis, Wageningen Agriculture University/ITC, Enschede, The Netherlands

- Cheng T (2002) Fuzzy spatial objects, their change and uncertainties. *Photogramm Eng Rem S* 68:41–49
- Cheng T, Fisher P, Li Z (2004) Double vagueness: effect of scale on the modeling of fuzzy spatial objects. In: Fisher PF (ed) *Developments in spatial data handling, proceedings of the 11th International Symposium on spatial data handling (SDH2004)*, pp 299–313
- Cheng T, Molenaar M (1999a) Objects with fuzzy spatial extent. *Photogramm Eng Rem S* 65:797–801
- Cheng T, Molenaar M (1999b) Diachronic analysis of fuzzy objects. *GeoInformatica* 3:337–356
- Cheng T, Molenaar M, Bouloucos T (1997) Identification of fuzzy objects from field observation data. In: Hirtle SC, Frank AU (eds) *Spatial information theory: a theoretical basis for GIS, lecture notes in Computer Sciences*, vol 1329. Springer-Verlag, Berlin, pp 241–259
- Cheng T, Molenaar M, Lin H (2001) Formalization and application of fuzzy objects. *Int J Geogr Inf Sci* 15:27–42
- Chi Z, Wu J, Yan H (1995) Handwritten numeral recognition using self-organizing maps and fuzzy rules. *Pattern Recogn* 28:59–66
- Chi Z, Yan H (1995) Image Segmentation using fuzzy rules derived from K-means clusters. *J Electron Imaging* 4:199–206
- De Graaff LWS (1977) *Het Strand: De Relatie Tussen Processen, Materialen en Vormen. en Een Proeve van Terminologie-Gebruik*. Koninklijk Nederlands Aardrijkskundig Genootschap Geografisch Tijdschrift, Nieuwreeks XI, Nr. 1, pp 47–67
- De Ruig JHM, Louisse CJ (1991) Sand budget trends and changes along the Holland coast. *J Coastal Res* 7:1013–1026
- Dilo A (2006) Representation of and reasoning with vagueness in spatial information - a system for handling vague objects. PhD thesis, Wageningen Agriculture University/ITC, Enschede, The Netherlands
- Fisher P (2000) Sorites paradox and vague geographies. *Fuzzy Set Syst* 113:7–18
- Fisher P (2003) Data quality and uncertainty: ships passing the night! In: Shi W, Goodchild M, Fisher P (eds) *Proceedings of the 2nd International Symposium on spatial data quality*, pp 17–22
- Fisher P, Wood J, Cheng T (2007) Higher order vagueness in a dynamic landscape: multi-resolution morphometric analysis of a coastal dunefield. *J Env Inform* 9:56–70
- Foody GM (1999) The continuum of classification fuzziness in thematic mapping. *Photogramm Eng Rem S* 65:443–451
- Galton A (1997) Continuous change in spatial regions. In: Hirtle SC, Frank AU (eds) *Spatial information theory: a theoretical basis for GIS, lecture notes in computer sciences*, vol 1329. Springer-Verlag, Berlin, pp 1–13
- Guilbert E, Lin H (2007) A new model for cloud tracking and analysis on satellite images. *GeoInformatica* 11:287–309
- Heuvelink GBM, Burrough PA, Stein A (2006a) Developments in analysis of spatial uncertainty since 1989. In: Fisher PF (ed) *Classics from IJGIS: 20 years of the international journal of geographical information science and systems*. CRC, Boca Raton, pp 91–95
- Heuvelink GBM, Burrough PA, Stein A (2006b) Propagation of errors in spatial modelling with GIS. In: Fisher PF (ed) *Classics from IJGIS: 20 years of the international journal of geographical information science and systems*. CRC, Boca Raton, pp 67–89
- ICZM (2007) [http://www.ikzm-oder.de/en/was\\_ist\\_ikzm.html](http://www.ikzm-oder.de/en/was_ist_ikzm.html) (Last access on 10 June 2008)
- Leung Y, Ma JH, Goodchild MF (2004) A general framework for error analysis in measurement-based GIS Part 1: the basic measurement-error model and related concepts. *J Geogr Syst* 6:325–354
- Lillesand TM, Kiefer RW (1994) *Remote sensing and image interpretation*, 3rd edn. John Wiley, Chichester
- Lowell K, Groeve TD, Thierry B (2000) Combining map geometry and polygon attributes to estimating spatial uncertainty from multiple realizations. In: Forer P, Yeh AGO, He J (eds) *Proceedings of the 9th international symposium on spatial data handling-SDH2000*. Beijing, 10–12 August, pp 5a.32–43
- Mandelbrot B (1983) *The fractal geometry of nature*. W.H. Freeman, New York

- Mannan B, Roy J, Ray AK (1998) Fuzzy ARTMAP supervised classification of multi-spectral remotely-sensed images. *Int J Remote Sens* 19:767–774
- Molenaar M (1998) An introduction to the theory of spatial object modelling for GIS. Taylor & Francis, London
- Reineck HE, Singh IB (1980) Depositional sedimentary environments, 2nd edn. Springer Verlag, Berlin
- Robinson VB (2003) Fuzzy sets in geographical information systems. *T in GIS* 7:3–30
- Ruessink BG, Kroon A (1994) The behaviour of a multiple bar system in the nearshore zone of Terschelling, The Netherlands: 1965–1993. *Inl J Marine Geology, Geochemistry and Geophysics* 121:187–197
- Sun CT, Jang JS (1993) A neuro-fuzzy classifier and its applications. *Proceedings of the 2nd IEEE international conference on fuzzy systems*. San Francisco, USA, pp 94–98
- Usery EL (1996) A conceptual framework and fuzzy set implementation for geographic feature. *In: Burrough PA, Frank AU (eds) Geographic objects with indeterminate boundaries*. Taylor & Francis, London, pp 71–85
- Van de Vlag DE, Stein A (2006) Modeling dynamic beach objects using spatio-temporal ontologies. *J Environ Informatics* 8:22–33
- Van Heuvel T, Hillen R (1994) Coastline management, internal publication of Directorate-Generala for public works and water management, the Dutch Ministry of Transport, Public Works and Water Management
- Van Zuidam RA, Farifteh J, Eleveld M, Cheng T (1998) Research in remote sensing, dynamic models and GIS applications for integrated coastal zone management. *J Coastal Cons* 4:191–202
- Van Zuidam RA, van Ploh C, van Genderen JL (1994) Synergy of remotely sensed data for coastal environmental studies: the Ameland-Waddensea example, northern Netherlands. *Proceedings of the 2nd thematic conferences on remote sensing for marine and coastal environments*. New Orleans, Louisiana, USA, pp I-323–334
- Wang F, Hall G (1996) Fuzzy representation of geographical boundaries in GIS. *Int J Geogr Inf Syst* 10:573–590
- Wickham JD, O’Neil RV, Ritters KH, Wade TG, Jones KB (1997) Sensitivity of selected landscape pattern metrics to land-cover misclassification and differences in land-cover composition. *Photogramm Eng Rem S* 63:397–402
- Woodcock C, Gopal S (2000) Fuzzy set theory and thematic maps: accuracy assessment and area estimation. *Int J Geogr Inf Syst* 14:153–172
- Zadeh LA (1965) Fuzzy sets. *Inform Control* 8:338–353
- Zang JX, Goodchild MF (2002) *Uncertainty in Geographical Information*, Taylor and Francis, New York

# Chapter 5

## Spatial Data Infrastructures for Coastal Environments

Dawn J. Wright

Central to this chapter is a review and discussion of the “data portal” as the primary means for search, discovery and download of spatial data. Discussed are some of the most pressing challenges to effective implementation of portals within the broader context of a spatial data infrastructure or SDI. Potential solutions are featured via two major case studies of interest to practitioners in coastal ecosystem assessment and management. While there are numerous projects that can be pointed to as successful case studies to emulate, the projects highlighted, along with related efforts and initiatives, are significant demonstrations of innovation, implementation, and practice, from which lessons can be learned. And finally, as critical as a data portal may be to successful SDI implementation, so too are the partnerships behind the portals, which are discussed at chapter’s end with a consideration of virtual communities as an emerging necessity.

### 5.1 Introduction: The Continuing Challenge of Data

This chapter is about the effective sharing of digital data sets for practitioners in coastal and estuarine ecosystem assessment and management. Digital data sets continue to grow exponentially worldwide, especially with recent launches of high-resolution satellite systems (e.g., Carlson and Patel 1997, Uça et al. 2006, Zibordi et al. 2006) and the increasing ease with which digital imagery, video, and sound are delivered over the Internet. Digital libraries have largely achieved the initial vision of enabling 24-h access to digital papers, journals, books, and data (Buttenfield and Goodchild 1996, Buttenfield 1998, Beard 2007). And with the steady rise in the adoption and use of remote sensing and geographic information systems (GIS), there continues to be a proliferation of digital geospatial data available, along with a considerable increase in the number of users and producers of these data, making access and effective integration a very difficult challenge (e.g., Nedovic-Budic 2002).

---

D.J. Wright (✉)

Department of Geosciences, Oregon State University, Corvallis, OR 97331, USA  
e-mail: dawn@dusk.geo.orst.edu

Indeed, our entire society has changed from being data-poor to data-rich, but our ability to derive knowledge and management decisions from all of these data in an analytical context remains poor. This is especially problematic in the dynamic zones of coasts and estuaries where it can be difficult to capture features accurately in both space and time or to adequately monitor and manage resources (Kracker 1998, Cimino et al. 2000, Wright and Bartlett 2000, Valavanis 2002, Paul et al. 2003). Government agencies, businesses, academic institutions, and even non-profit organizations all have a tremendous stake in the development and management of geospatial data resources, especially in the coastal zone where, worldwide, 20% of humanity lives less than 25 km away from the coast, and 39%, or 2.2 billion people, live within 100 km of the coast (World Resources Institute 2000). Any problems that remain in finding data are now compounded by the additional challenge of effectively filtering through large volumes of them in order to find meaningful knowledge. From an organizational perspective, although geospatial data sets are legion, there has been a general inability and often unwillingness to exchange data across boundaries, exacerbated by low levels of coordination (Mapping Science Committee 2001, Nedovic-Budic 2002, de Man 2007).

Several nationwide partnerships have been launched in order to build a spatial data infrastructure or SDI, defined in U.S. Presidential Executive Order 12906 as, “the technologies, policies, and people necessary to promote sharing of geospatial data throughout all levels of government, the private and non-profit sectors, and the academic community” ([www.archives.gov/federal-register/executive-orders/pdf/12906.pdf](http://www.archives.gov/federal-register/executive-orders/pdf/12906.pdf)). A similar definition may be found in Masser (2007) or Craglia and Annoni (2007) on behalf of the Infrastructure for Spatial Information in Europe (INSPIRE): “both technical and non-technical issues, ranging from technical standards and protocols, organizational issues, data policy issues including data access policy and the creation and maintenance of geographical information for a wide range of themes”; or in Nebert (2000) on behalf of the Global Spatial Data Infrastructure (GSDI): “the relevant base collection of technologies, policies and institutional arrangements that facilitate the availability of and access to spatial data” ([www.gsdi.org/pubs/cookbook/](http://www.gsdi.org/pubs/cookbook/)).

In the U.S., federal and state governments, commercial entities, universities, and non-governmental organizations have all worked to create searchable metadata catalogs that enable users to search descriptions of geospatial datasets as contained in web-based clearinghouses. Notable efforts in the U.S. include the Federal Geographic Data Committee (FGDC, [www.fgdc.gov](http://www.fgdc.gov)), the Geospatial One-Stop (GOS) Initiative ([gos2.geodata.gov](http://gos2.geodata.gov)), and The National Map ([nationalmap.gov](http://nationalmap.gov)), all of which share the goal of building the U.S. National Spatial Data Infrastructure (NSDI) (Mapping Science Committee 2001, Nedovic-Budic 2002, DeMulder et al. 2004, Crompvoets and Bregt 2007). Other large initiatives include the National Biological Information Infrastructure (NBII, [nbii.gov](http://nbii.gov)), a coastal NSDI coordinated largely by the NOAA Coastal Services Center ([www.csc.noaa.gov/shoreline/cnsdi.html](http://www.csc.noaa.gov/shoreline/cnsdi.html)), and the Geography Network of the Environmental Systems Research Institute (ESRI, [geographynetwork.com](http://geographynetwork.com)). In Canada, there is a Canadian Geospatial Data Infrastructure (CGDI, [cgdi.gc.ca](http://cgdi.gc.ca)), and in Europe past notable efforts include CORINE



(Coordination of Information on the Environment), NATURA 2000 (in support of natural habitat conservation) (see more descriptions in Masser 1998). The European Commission of the European Union has recently established the ambitious INSPIRE ([eu-geoportal.jrc.it](http://eu-geoportal.jrc.it)). And further international cooperation is now being facilitated by the GSDI ([gsdi.org](http://gsdi.org)), particularly where the developing world is concerned. Both INSPIRE and the GSDI will be revisited near the end of the chapter.

Coastal and marine data have many unique requirements that warrant special consideration within an SDI (e.g., the dynamic complexity of this geography as an interface between land and ocean, the multiple jurisdictional issues, the cultural nuance of coastal space, etc.). The reader is referred to the very complete reviews by Lockwood and Fowler (2000), Bartlett et al. (2004) and Canessa et al. (2007), which define and discuss all the essential components of coastal SDIs for the U.S., Europe, and Canada respectively (e.g., framework and specialized datasets of coasts and estuaries, metadata, clearinghouses, standards, policies, partnerships at all levels, cultural issues, etc.). This chapter does not attempt to revisit the excellent background already covered by these works, but rather focuses on one of the most important and intuitive aspects of an SDI: the search, discovery and download of spatial data via a clearinghouse (also known as and hereafter referred to as “data portal”). Here I define a data portal as an Internet environment (large web site or content management system) that features some kind of metadata catalogue with descriptions of available data sets and imagery. The portal may be rich in content itself, but more often than not serves as a focal point linking many networked servers distributed over a large geographic area (these being invisible to the user if need be). In addition to spatial data, content available to the user also includes documents, web sites addresses, and even software applications. In addition, registered map services allow users to build online maps using data within the portal. Another critical ingredient is Internet map service technology allow users to visually browse and query individual or multiple data sets in order to determine whether a download is necessary. Once downloaded, the data may then be viewed in other software or analyzed using a GIS or image processing package. Canessa et al. (2007) describes the evolution of coastal and marine infrastructure in Canada as a progression from hardcopy atlases in the 1970s and 1980s to information systems in the 1980s, to integrated, distributed networks and portals that emerged in the 1990s. A modern, present-day data portal may encompass digital versions of all of these.

### ***5.1.1 Limitations of Past Approaches***

The national efforts mentioned in the previous section, including a National Academy of Science study (Mayer et al. 2004), have all called for or involved the development of data portals (often with the inclusion of an Internet map service) in order to connect the variety of spatial data producers with their users. Again, this has normally involved government at all levels, the private sector, and academic institutions. However, as reported by Sarkar (2003), despite the expense and energy devoted to information sharing initiatives, governments at all three levels (local, state,

and federal) are left to wonder if it really knows how to implement them successfully. The pieces are out there, but they still haven't been applied well to large-scale efforts (e.g., nationwide scale). Communication about the availability or the need for data is also lacking (caused usually by the lack of proper metadata in order to properly assess geographic coverage, quality, accuracy, point of contact for access, etc.), and thus the duplication of data sets is still a huge problem.

In the state of Oregon for example, even experienced users of geospatial data with some GIS sophistication working in state agencies and local governments continue to have a serious problem finding natural resources data. They can locate bits and pieces here and there via portals but, over time as they locate a data type (e.g., a digital elevation model for a landslide susceptibility study along the Oregon coast or stream data for evaluating sediment load delivered to estuaries from surrounding watersheds), they end up finding several different versions of the same in varying degrees of completeness or update, and some or most of which may be poorly documented. If they do find a completed data set, how do they know it is the best or most up-to-date data set available? Are there any policy restrictions or proprietary holds that would prevent access? What if they decide to create a data set and then later find out that another agency has already created such a data set? And as a related issue, what if they find an ecosystem assessment tool developed by a university scientist to work with the data but it only runs with software X and their agency uses software Y? How easy will it be to integrate these newly obtained data with existing data? Workers in different agencies and regions around the state experience these problems, where different data sets are obtained in order to solve the same natural resource problems, but integration or analyses may yield different answers.

## 5.2 Successful Partnerships and Portals

Fortunately, there are efforts underway that are addressing problems with sharing and finding geospatial data and are thus contributing greatly to the development of coastal SDIs (important background discussions can be found in Katz et al. 1991, Masser 1998, Lockwood and Fowler 2000, Gärtner et al. 2001, Miller and Han 2001, Bartlett et al. 2004, Canessa et al. 2007). Toward this end, there has been a steady advancement over the last decade in the design and effective implementation of data portals specifically for coastal data. The key to this success has been comprehensive partnerships that ascribe to the vision and principles of an SDI. Without these partnerships, the proliferation of data portals can become as problematic as the duplication of individual data sets (i.e., the duplication of portals adding to the confusion – which portal to use and why). Regional partnerships that seek to guide and/or influence coastal resource planning and management for example, have been identified as critical not only for data solutions but for enabling creative solutions to broader environmental and socio-economic problems, for economic development, community service, and even emergency and disaster response (Nedovic-Budic 2002, Eleveld et al. 2003, Sietzen 2003, Asante et al. 2007). While

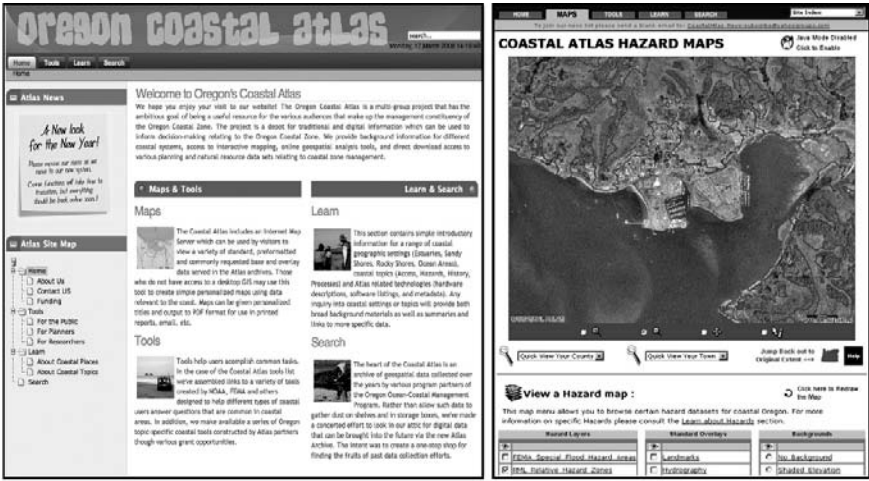
there are numerous projects that can be pointed to as successful case studies to emulate, three projects are highlighted here as significant demonstrations of innovation, implementation, and practice. These are projects that are within the realm of the author's experience and participation.

### ***5.2.1 The Oregon Coastal Atlas***

In coastal and estuarine ecosystem assessment and management, computer applications are often developed expressly for the benefit of decision-makers, at all levels of government and in various non-governmental organizations. As alluded to already, there are still many challenges faced by these practitioners, including gaps in data, effective data integration, data presentation, how to turn existing data products and information management tools into useful information products, and how to use or create appropriate indicators of varying types (e.g., hazard, health, suitability, etc.). In Oregon, effective coastal management relies largely on the outcome of resource decisions made at the local level, by local officials and ordinary citizens (e.g., Smith 2002, Wood and Good 2004).

Resource decisions are problematic, however, because they implicitly require that accurate and appropriate resource status information be available in a usable form and manner that are timely to the decision process. In the absence of such information, the possibility exists that resource decisions may not adequately or efficiently protect systems of value to the community. In answer to these needs, a partnership was formed between the Oregon Coastal Management Program (OCMP, state government), the Davey Jones Locker Seafloor Mapping/Marine GIS Laboratory at Oregon State University (OSU, academic), and Ecotrust (one of the largest non-profit environmental conservation organizations in the Pacific Northwest and headquartered in Portland, Oregon). These organizations came together in order to allocate resources, conduct individual work programs, and share the effort needed to design, build, test and deploy a new portal to support data sharing, spatial analysis for statewide coastal management, and resource decision making.

A primary driver for the portal effort was the need to integrate the data distribution efforts of the OCMP with complementary data emerging from federal agencies, academic research institutions, and local government/volunteer organizations. The OCMP is a state-networked program whose data products are distributed free of charge to the public and local governments. The primary user group for OCMP data products are agency program partners (e.g., the Oregon Division of State Lands, Oregon Department of Fish and Wildlife, Oregon Department of Environmental Quality, Oregon Department of Geology and Mineral Industries), academic partners (e.g., OSU Geosciences, OSU College of Oceanic and Atmospheric Science, Oregon Sea Grant, the University of Oregon's Institute of Marine Biology), and coastal county and city planners. The intent is that easy access to up-to-date information about coastal resources will lead to improved resource management decisions in the coastal zone.



(a)

(b)

**Fig. 5.1** (a) Opening page of the Oregon Coastal Atlas (OCA), with tabbed navigation at the top (circled in red) guiding users to the four main sections of the atlas, “Maps”, geospatial “Tools”, “Learn”, and “Search” (for GIS data and remotely-sensed images archived in the atlas). There is also a wealth of background information on the project, and related links; (b) Hazard mapping portion of the OCA, resulting from a user navigating to the “Hazards” coastal topic within the “Learn” section of the atlas, and then choosing a coastal site and hazards data layers from that section to map out in the Maps section

The portal itself is called the Oregon Coastal Atlas (OCA; www.coastalatlant.net; Fig. 5.1a). Powered by the open source Minnesota MapServer (mapserver.gis.umn.edu) and hypertext processor (PHP) scripting, it provides background information on different coastal systems, access to interactive mapping, online geospatial analysis tools, and direct download access to an array of natural resource data sets with associated metadata related to Oregon coastal zone management. The Oregon coastal zone is loosely defined as extending from the crest of the Oregon Coast Range to its territorial sea boundary 3 nautical miles offshore. Embedded in the OCA is the Oregon Coast Geospatial Clearinghouse, a node of the NSDI that aids in advertising OCA metadata well beyond Oregon by way of the Geospatial One-Stop. A typical session within the OCA includes (Fig. 5.1b):

- selecting a region of interest from a map of the Oregon coastal zone;
- enlarging the selected region and specifying an environment such as rocky or sandy shore;
- exercising an option to display one or more layers (e.g., swash zones, land use zones, recreational areas, watershed boundaries, rivers, etc.);
- viewing and printing more detailed data related to specific layers;
- linking to an OCA metadata table, glossary definition, scientific document, or additional resources located elsewhere on the web; and
- downloading simple, generic spatial tools based on the user’s selections and/or criteria, in order to solve a coastal management or scientific problem.

The OCA is indeed somewhat unique in that it couples up-to-date, interdisciplinary resource data along with several online tools for coastal decision-making. These include a coastal erosion suite that calculates dune overtopping, dune undercutting or bluff recession based on the foredune erosion models of Marra (1998) and Ruggiero et al. (2001), as well as traditional ground survey beach elevation data (Haddad et al. 2005). A watershed assessment tool provides the necessary GIS data, instructions, and an Internet map service to facilitate watershed assessment and mitigation according to the Oregon Watershed Enhancement Board (OWEB) assessment manual (Haddad et al. 2005). A coastal inundation tool uses an Internet map services to help users visualize near real-time coastal storm flooding near Tillamook, Oregon and project potential wave inundation for that region. Emergency response agencies and coastal planners can then establish appropriate setback distances along the coast in order to protect the built environment.

The OCA has grown to a catalogue of over 3380 data layers, having served over 3 million hits in the last 2 years to over 35,000 unique visitors (it “went public” in December 2002). In the last year, average daily visits have grown from ~100 to ~200. January 2005 was the all-time highest traffic volume month ever, attributable (based on items downloaded) to users seeking maps and information about the potential effects of a tsunami on coastal communities, after hearing about the December 2004 Sumatra earthquake. It has received considerable interest and advocacy by the Oregon Ocean Policy Advisory Council (an advisory board appointed by the Governor of Oregon), the Oregon Department of Geology and Mineral Industries, the Oregon Geospatial Enterprise Office, the Oregon Coastal Program Network of Local Planners, the Oregon Shores Conservation Coalition, and the Oregon Land Conservation & Development Commission, as well as feature coverage in Oregon’s top newspaper, *The Oregonian*. Beyond Oregon, it has received advocacy from the NOAA Coastal Services Center (South Carolina), the NOAA Pacific Services Center (Hawaii), and the Federal Geographic Data Committee.

### **5.2.1.1 Next Stage: Improving the Search for Data**

The OCA is established, well used, and decision-makers and general citizenry are accessing the data and metadata. It is now at the stage where the coordinating partners seek to better understand how decision makers use its data. In order to do that, the partners seek to improve the use of the metadata, and to understand how the quality of both the metadata and data should evolve over time, even after initial publication. While much of the information technology and social science research needed to solve these kinds of problems is similar to ongoing research in other domains, there are some issues unique to SDI research (e.g., Dawes and Pardo 2002, de Man 2007). For instance, in addressing the needs of government decision-makers, there must be a recognition of the need to combine quantitative information with qualitative, the social and economic value associated with these decisions, and the risk involved in using information technology to make resource management and environmental decisions that could have significant impacts on public health or must stand up in a court of law (Cushing et al. 2005).

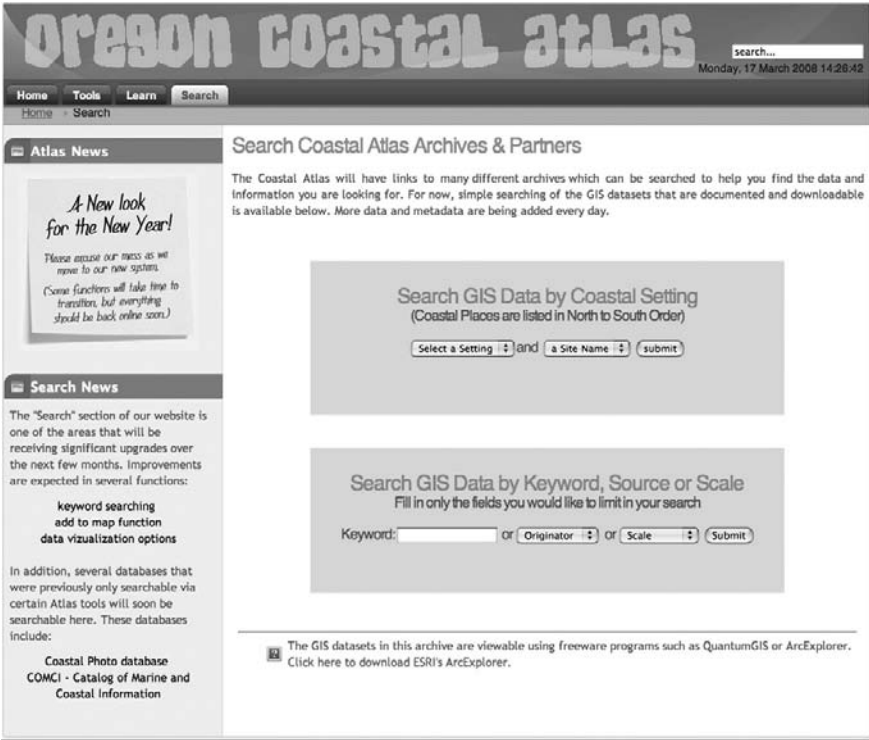


Fig. 5.2 Current search interface for the Oregon Coastal Atlas (OCA), incorporating text menu choices or entry of text keywords

Metadata is at the heart of any search for data within a portal, and searching is the critical first step in the ultimate completion of a task or the making of a decision. Such improvements are also needed in the search mechanism of the OCA (Fig. 5.2). For example, a keyword search in the OCA for “shoreline” returns 197 data sets, but a search for “coastline” returns no data sets. In order to more effectively search among the existing 3380+ data sets in the OCA, we need to incorporate innovative changes to our metadata catalogs. Needed also are updates and additions to the existing toolset, as it does not cover the full range of functions needed by coastal decision-makers. Specific research questions to be addressed in the next phase of work to devise an improved search mechanism include:

- The OCA was designed as a scalable system, and given the usage to this point, as well as anticipated future use, how should we scale in terms of additional data, tools, and educational modules?
- The text-based (keyword) search and downloadable data approach has been successful but is still limited. What are the best ways of improving searches within a portal, and in presenting the results of those improved searches to the user (beyond just a laundry list)?

- As improved search must start with existing metadata (e.g., Wright et al. 2003), what are the practical advantages of having a controlled vocabulary in an ontology (i.e., a dictionary of categories and properties arising from a systematic study of how knowledge is structured), in addition to a database of existing metadata records? What are the best ways to structure a coastal resource decision-making portal, in terms of descriptive elements in text, data properties in numbers, and relationship properties (data derived from? entered by whom? best combined with?).
- Are existing ontologies, such as SWEET (Semantic Web for Earth and Environmental Terminology; <http://sweet.jpl.nasa.gov>) sufficient for research that uniquely combines physical science with social science and decision-making?

By way of further clarification, it is useful here to include more formal definitions of the terms ontology and controlled vocabulary (after the Marine Metadata Interoperability (MMI) project, [marinemetadata.org/guides](http://marinemetadata.org/guides)):

*An ontology may include a catalog (list of terms), glossary (list of terms with definitions), thesaurus (list of terms with definitions and synonyms), and a more formal ontology (list of terms with definitions, synonyms, and other relationships between terms). An ontology therefore provides the structure of the controlled vocabulary similar to a dictionary or a thesaurus (i.e., an ontology could be construed as including the entire spectrum of controlled vocabularies). A controlled vocabulary can be defined as a set of restricted words, used by an information community when describing resources or discovering data. The controlled vocabulary prevents misspellings and avoids the use of arbitrary, duplicative, or confusing words that cause inconsistencies when cataloging data. The vocabulary agreed to by a community is the expression of concepts (i.e. mental abstractions) of their domain. Since a concept can be expressed in different ways and differ in meaning from one person to another, the controlled vocabulary helps to solve semantic incompatibilities.*

Data portals have been criticized as providing data descriptions only at the most basic level, making it difficult for both users and providers to interpret or represent the applicable constraints of data, including the related inputs and outputs of analyses or decisions (e.g., Cabral et al. 2004). A semantic approach has been shown to provide higher quality and more relevant information for improved decision-making (Helly et al. 1999, Sheth 1999, Cabral et al. 2004). Associating formal terms and descriptions captures semantics (e.g., “shoreline” vs. “coastline”), thereby making cross-disciplinary connections between them, in order to attach well-defined meaning to data and to other web resources. In this way, the quality of data retrieval or integration are greatly increased, based on meaning, instead of on mere keywords (Berners-Lee et al. 2001). Basic semantic web research has only recently started to address the support for spatial data and information (Fonseca and Sheth 2002 and references therein, Shi 2005), which is a clear focus of the OCA archive, composed primarily of GIS shapefiles, coverages, raster grids, and images. In order to improve the results of queries for information stored in geographic databases it is necessary to support better definition for spatial concepts and terms used within a discipline such as ocean and coastal management (Eleveld et al. 2003). Equally important is

the development of multiple spatial and terminological ontologies to define and operationalize meanings and formal descriptions (Egenhofer 2002, Goodchild 2003). Building the necessary tools to define, verify and deliver these ontologies is a significant research challenge, as well as understanding the gaps and inconsistencies in ontologies, trust and verification of the content of ontologies, and understanding and handling changes in the material represented by ontologies, all in ways that go beyond simple versioning (e.g., Cushing et al. 2005).

To implement an effective semantic web resource, a data set's ontology should include a controlled vocabulary, ultimately revealing which data sets are interoperable and how. Ontologies can act both as registration mechanisms for vocabularies, and as a means of mapping vocabularies to each other using defined relations. For example, if relations such as "shoreline same as coastline" or "SST same as sea surface temperature" or "seafloor same as seabed" are used to map vocabularies, the results (which can be stored in a collected ontology) can be translated between co-vocabularies, and can also generate other inferences about the relationships between the different vocabularies and their terms. This is the approach that the OCA is building upon, with the expected benefits of:

- better/more complete discovery and filtering of data;
- clearer, more precise, more computable characterization of data;
- contextualization of information, so that it is provided in the right format, place, and language;
- semantic value, where human users but also computerized inference engines and harvesters can make better use of information;
- better display of search results, where terms can be substituted if they are equivalent; and
- integration into additional tools for the OCA, which will then immediately be working with more appropriate data sets.

### **5.2.1.2 A Solution Via Controlled Vocabularies and Ontologies**

The diversity of data sources and data types resident within the OCA are reminiscent of the situation faced at the advent of the SIOExplorer project a few years ago. SIOExplorer is a digital library project of the Scripps Institution of Oceanography (SIO; Miller et al. 2001, Helly et al. 2003, SIOExplorer.ucsd.edu). It sprung from an initial effort to open access to more than 700 SIO expeditions for both research and education. The effort was then formalized by a group of investigators at SIO, the San Diego Supercomputer Center and the University of California-San Diego Libraries as a fully searchable digital library within the National Science Digital Library (NSDL; www.nsdl.org). The collection is rich in complexity with data, images and documents in a wide variety of formats, drawn from 100 years of documents and 50 years of data. General-purpose tools automate collection development, including the harvesting of data and metadata from highly diverse disciplines and three separate data publishing organizations. This collection with approximately 150,000



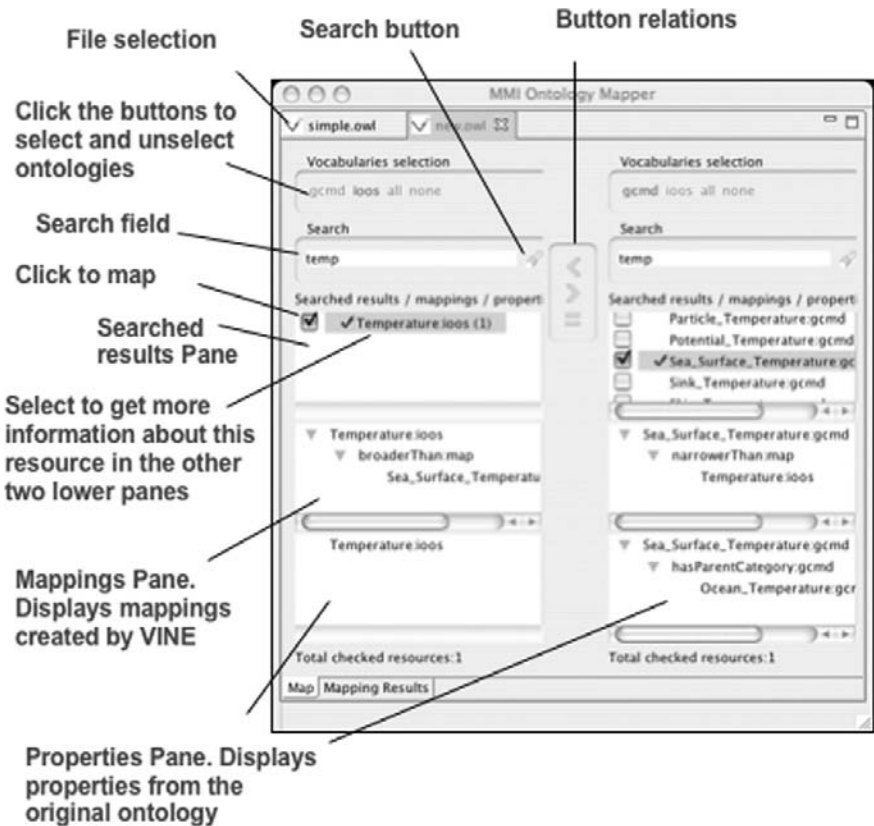
items, requires 1 Tb of storage, and is growing at about 200 Gb per year. It now consists of five federated collections, and new collections from various disciplines are added each year as other funded projects commence.

The technology underlying SIOExplorer has recently been leveraged to create a comprehensive information system for several other communities, thus demonstrating that a similar transformation can be accomplished for portals such as the OCA. For example, SIOExplorer has been implemented at the National Institute of Water and Atmospheric Research (NIWA) in New Zealand. This includes a portable stand-alone version of SIOExplorer, called “Digital Library in a Box,” which operates in real-time aboard the R/V Tangaroa. It is based entirely on public domain code, e.g., using PostgreSQL instead of Oracle. SIOExplorer technology is also being used for managing multibeam holdings at the Center for Ocean and Coastal Mapping (CCOM) at the University of New Hampshire, and plans are underway to implement it at the Monterey Bay Aquarium Research Institute (MBARI). SIOExplorer components are being re-used for hydrological community information within the Hydrologic Information System ([cuahsi.sdsc.edu](http://cuahsi.sdsc.edu)), part of the Consortium of Universities for the Advancement of Hydrological Sciences, Inc. (CUAHSI; [www.cuahsi.org](http://www.cuahsi.org)) initiative. CUAHSI is planning a distributed data network over 24 hydrological observatories across the country with real-time radar feeds, as well as stream and precipitation gauges, remote sensing images, and access to USGS and NOAA archives. Collaborators at University of Texas, Drexel and Virginia Tech are building user-oriented tools based on the flexible SIOExplorer metadata architecture. A number of convenient tools for mapping to FGDC and ISO standards, and for working with controlled vocabularies, will soon be available for download.

By drawing upon the expertise and facilities of the SIOExplorer Digital Library, the OCA partners are moving toward the implementation of a similar, semantically interoperable data archive. The key to the SIOExplorer success was the definition of a Canonical Cruise Data Structure (CCDS), encompassing the scope of all the various data types, valid over the 50 years of the collection. The structure was implemented as a set of nine data directories, plus a few sub-directories. The flexibility and scalability were derived from a template-driven, rules approach that allowed a processing script to harvest data and metadata from arbitrary original data structures in a staging area, and store them in a simple CCDS. A similar approach for the OCA would be to define a Canonical Coastal Atlas Data Structure (CCADS) with a hierarchy of data objects appropriate for the existing OCA data archive, including vector files, digital orthophotoquads, digital raster graphics, and new satellite grids and images. A CCADS also translates the CCDS structure into an XML, OWL-based ontology (OWL Web Ontology Language), thus exposing relationships and dependencies between data sets, science themes, decision-making themes, and geographic locations. OWL is a powerful language that allows the user to encode vocabularies in a way that web browsers and software packages can understand ([www.w3.org/TR/owl-features](http://www.w3.org/TR/owl-features)). OWL also supports the creation of relationships among vocabularies more easily than most other formats.

In order to arrive at the final ontology, it will be important to follow the recommendations of the international Marine Metadata Interoperability initiative (MMI;

www.marinemetadata.org) in order to create initial markup vocabularies that specify the content of OCA data sets and records (i.e., by reading in the current metadata). MMI is a virtual community of marine scientists and engineers led by the Monterey Bay Aquarium Research Institute (MBARI, www.mbari.org), and with a host of U.S. and international partners that provide the coastal/marine community with guidance, background information, tools, standards, cookbooks, vocabulary and ontology tool development (Fig. 5.3), as well as working examples of marine metadata. This is also done in consultation with the ocean observatory community (e.g., the Integrated Ocean Observing System or IOOS at www.ocean.us, and the Ocean Research Interactive Observatory Networks or ORION at www.orionprogram.org). Existing data markup vocabularies (such as the British Oceanographic Data Centre vocabulary for marine applications, www.bodc.ac.uk/data/codes\_and\_formats) provide a means for replacing the cryptic and often meaningless strings used for spreadsheet column headings and data channel labels with clearly defined terms that have the potential to carry metadata rich enough to support true data interoperability



**Fig. 5.3** Example screenshot from the Vocabulary Integration Environment (VINE) Tool developed by MMI to map terms from vocabularies that are represented in ontologies, in the Web Ontology language (OWL) format (from marinemetadata.org/fordevelopers)

([www.marinemetadata.org/vocabularies](http://www.marinemetadata.org/vocabularies), O'Neill et al. 2003). This allows for the automatic generation of a discovery vocabulary, which then leads to improved data search, discovery, documentation, and accessibility.

### 5.2.1.3 The Final Ingredient: Style Sheets

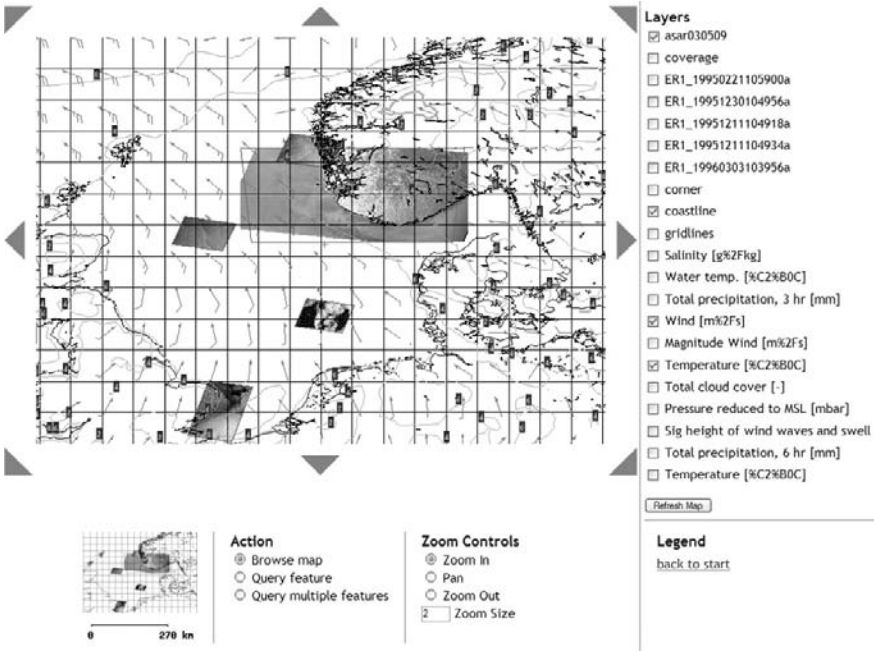
A successful search would display all the viewable data types listed in the OCA, along with the underlying, well-defined vocabularies powering the searches. However, that successful search might return twice the number records to a user than before, a case of “too much of a good thing.” A style sheet must be developed to sort search results for the user, broken out by data set type (e.g., vectors, grids, or satellite images from the existing GIS archive, photos from the new photobase in development or documents/journal references), and by category (e.g., biological, environmental quality, infrastructure, geomorphology). Sorting of records in various ways must be experimented with, based on user feedback (i.e., which categories are most useful?), and input must be sought from state government agencies such as Geospatial Enterprise Office (Oregon’s statewide service center for GIS) or the Oregon Watershed Enhancement Board.

### 5.2.2 *DISMAR/DISPRO*

Another example of a successful SDI implementation is the web-based component of the Data Integration System for Marine Pollution and Water Quality (DISMAR). DISMAR was initiated through a partnership of seventeen organizations from six countries (Norway, Germany, Italy, France, the United Kingdom, and Ireland) and is focused on improving the management of pollution crises in the coastal and ocean regions of Europe. DISMAR supports public administration and emergency services responsible for prevention, mitigation and recovery of crises such as oil spill pollution and harmful algal blooms (HAB). A prototype decision-support system component of DISMAR (named DISPRO) was developed for the integration and distribution of multi-source data, as well as results from ocean numerical models (Hamre et al. 2005). DISPRO is a product of the Coastal and Marine Resources Centre in Cork, Ireland (<http://dispro.ucc.ie/apps/dismar>), and serves as a portal to distributed marine pollution data servers across Europe. Its architecture is therefore consistent with INSPIRE’s general model of an SDI (Hamre et al. 2005).

Similar to the OCA, DISPRO uses the open source web mapping code of Minnesota MapServer. However, additional map services of the Open Geospatial Consortium (OGC, [www.opengeospatial.org](http://www.opengeospatial.org)) are more at the heart of its approach. A web mapping service (WMS) produces a digital raster image of a geospatial data set (not the dataset itself), and is thus quickly transferable and readable in a web browser. In addition, maps may be requested from different servers, enabling the creation of a network of distributed map servers from which users may build customized maps ([www.opengeospatial.org/standards/wms](http://www.opengeospatial.org/standards/wms)). Users do not necessarily





**Fig. 5.5** Screen snapshot of a typical session in DISPRO showing the map viewer controls and the many layers available for browsing and query from INSPIRE datasets. Shown are coastlines, wind vectors, satellite overlays, and temperature data for monitoring harmful algae blooms along northern European coasts. Screen snapshot by E. Ó Tuama and reproduced by permission of the Coastal and Marine Resources Centre, University College Cork, Ireland

added ability to actually see what the data will look like in mapped form. It is also possible to transfer whole directories of data, which is not easy with FTP.

- advantages for datasets that are frequently updated or edited (as opposed to static files). The current practice of mapping a drive allows read-only access, which is fine for a situation where a dataset does not change very often. But if a dataset is consistently updated, a WMS solution is much more efficient.
- With existing data scattered across servers in different counties, states or countries, this approach takes advantage of a distributed network rather than having to have copies of datasets all in one place or having people download duplicate copies from many different places excessively.

### 5.2.3 Other Portals

In addition to the “case studies” discussed above, there are a number of other coastal data portals that have reached a mature or near complete stage, including the Marine Irish Digital Atlas or MIDA (mida.ucc.ie), funded by Ireland’s Higher Education Authority under the Irish National Development Plan, and in Northern Ireland

by the Department of the Environment's Environment and Heritage Service. MIDA has recently emerged as the one of the most comprehensive portals to the coastal and marine regions of Ireland. It is currently the only data portal in Ireland that brings together data from many organizations, and it has thus been identified a key part of Ireland's SDI (Strain et al. 2006, O'Dea et al. 2007). Other examples include the North Coast Explorer of the Oregon Institute for Natural Resources ([northcoastexplorer.info](http://northcoastexplorer.info)), and the Pacific Coastal Resources Atlas of Canada ([www.shim.bc.ca](http://www.shim.bc.ca)). Similar efforts were discussed at length during the CoastGIS '05, the 6th International Symposium on Computer Mapping and GIS for Coastal Zone Management, where the theme was "Defining and Building a Marine and Coastal Spatial Data Infrastructure ([www.abdn.ac.uk/~geo466](http://www.abdn.ac.uk/~geo466)). All of the aforementioned portals have been built and maintained as a result of significant financial and human resource investment as a result of very strong regional partnerships between universities and government agencies. Many technological challenges have been met along the way to provide web-based mapping solutions that meet with end user requirements.

A series of recent workshops (Trans-Atlantic Workshops in Coastal Mapping and Informatics, [workshop1.science.oregonstate.edu](http://workshop1.science.oregonstate.edu)) has examined some of the significant developments in the emergence of these web-based coastal data portals, as well as related issues in coastal/ocean informatics (the general study of the application of computer and statistical techniques to the management of coastal and ocean data and information, including data/metadata vocabularies and ontologies, metadata creation/extraction/cross-walking tools, geographic and information management systems, grid computing) (Wright et al. 2007). Funding was obtained from the National Science Foundation (NSF) to support U.S. participation at two joint workshops designed to identify common research priorities, and focused on specific areas of research collaboration. European efforts were funded in part by the Marine Institute of Ireland's Marine Research, Technology, Development and Innovation (RTDI) Networking and Technology Transfer Initiative under Ireland's National Development Plan. The main objectives of these workshops were to:

- quantify and qualify the strengths and weaknesses of coastal data portals as decision support systems for the integrated coastal zone management process;
- further refine a geo-spatial framework for the coastal zone;
- describe novel and innovative activities in the uptake of geo-spatial tools by coastal managers;
- develop and publish guidelines to the coastal/marine research community and resource decision makers on the development of coastal data portals (including usability of coastal web atlas interfaces, map design, data content and display, attribute tables, and metadata formats, soliciting user feedback, etc.); and
- develop common vocabularies and ontologies to facilitate database searches with coastal data portals of Europe and North America.

The first workshop was held in Cork, Ireland in the summer of 2006, under the theme of "potentials and limitations of coastal web atlases" (O'Dea et al. 2007), and the second was held in Corvallis, Oregon in the summer of 2007, under the theme of "coastal atlas interoperability" (i.e., building a common approach to managing

and disseminating coastal data, maps and information). Both workshops brought together key experts from Europe, both coasts of the United States, and Canada to examine state-of-the-art developments in web-based coastal mapping and informatics, along with future needs in mapping and informatics for the coastal practitioner community. These workshops were intended to advance research in the field by providing recommendations for best practices in coastal web mapping (including the effective translation of science to coastal decision-making). Another goal is to develop a cadre of scientists who will play a leadership role in forging international collaborations of value to the participating nations, especially within the context of the U.S. Coastal SDI and the European INSPIRE.

Another outcome of the workshop series is the formation of the International Coastal Atlas Network (ICAN), a new virtual community of over thirty organizations from ten nations, and growing. The strategic aim of ICAN is to share experiences and to find common solutions to coastal web atlas development (where a coastal web atlas is a special kind of data portal focused solely on the coast), while ensuring maximum relevance and added value for the end users. An initial project of ICAN is the development of a prototype (Wright et al. 2008 and [ican.ucc.ie](http://ican.ucc.ie)) to demonstrate initial interoperability between the OCA and MIDA, with plans to expand the interoperability among all the organizations of ICAN, thereby providing a common point for access and exchange of data instead of having to search aimlessly through each individual portal. The prototype employs a semantic mediation approach (where ontology relationship rules are used order to rewrite the user's query into queries over several distributed information systems, all of which will return more meaningful results), within the interface framework of an OGC catalogue services for the Web (CSW). ICAN activities will be ongoing and progress may be followed at [workshop1.science.oregonstate.edu/join](http://workshop1.science.oregonstate.edu/join).

### 5.3 Conclusion

One may look at an SDI in many different ways and try to separate it into components, but a portal actually integrates many of those separate components (metadata based on standards, data, clearinghouse, all results from good partnerships). This chapter has focused on the portal as the primary means for search, discovery and download of spatial data. It has attempted to lay out some of the most pressing challenges to effective implementation, and then to describe the case studies of interest to practitioners in coastal and estuarine ecosystem assessment and management (i.e., the OCA and DISMAR/DISPRO), along with related efforts and initiatives, all of which might emulated.

It has been argued here that partnerships are absolutely critical for success ("success" being defined, in one sense, as users being able to find what they are searching for – in the form of original data and derived products—to judge the quality of what they have acquired, and what limitations apply to its use). As evidenced by the case studies, successful partnerships involve a variety of players (e.g., government with

academia with non-profit), all of whom ascribe to the vision and principles of an SDI (e.g., use of standards and protocols, allocation of resources to fulfill responsibilities of metadata and data stewardship, development of strategies for advancing geospatial information activities at all levels, etc.). Partnerships also help to reduce the duplication of data through communication and collaboration. And they always bring to bear considerable resources, while still efficiently dividing the labour, and sharing the efforts needed to perform the complex series of tasks required to design, build, test and operate a portal. But one issue for further thought is, if a partnership makes a portal successful, what can help to make a partnership more successful?

In a recent vision document on the closely-related issue of cyberinfrastructure (NSF 2007), the National Science Foundation highlighted what it calls “virtual organizations” for distributed virtual communities, which help to step scientists and social scientists through the nuts-and-bolts of participating in a cyberinfrastructure. The virtual community can show users why their participation is worth the effort, and how it will, in the end, optimize their ability to do their research effectively, to answer scientific questions, or to make decision. I suggest here that virtual communities can have the same positive effect on the partnerships behind the portals. The communities may not be the actual builders of a data portal, but provide the building materials and the know-how. The MMI is one such virtual community as it “promotes the exchange, integration and use of marine data through enhanced data publishing, discovery, documentation and accessibility” (from [www.marinemetadata.org](http://www.marinemetadata.org)) for a distributed community of coastal and ocean scientists, to enable them to recognize the benefits of a marine SDI, and to actually use an SDI. This virtual community provides guides, cookbooks, tools, case studies, and online discussion forums, but perhaps more importantly, hands-on workshops that feature web applications and stand-alone tools that partners can immediately build upon in their own work. It currently enjoys the support and endorsement of the NOAA Coastal Services Center, which shepherds the U.S. Coastal SDI ([www.csc.noaa.gov/shoreline/cnsdi.html](http://www.csc.noaa.gov/shoreline/cnsdi.html)). The MMI is one virtual community that practitioners in coastal and estuarine ecosystem assessment and management should keep abreast of or consider joining. ICAN, though just beginning, will likely develop along a similar trajectory, though with a more specific focus on coastal web atlases and a more targeted audience of coastal zone managers. The International Hydrographic Organization (IHO, [www.iho.int](http://www.iho.int)) may be considering a similar effort (Maratos 2007).

Given the emphasis in this chapter on domain-specific SDIs for the coastal zone, one must also recognize a shift from SDIs for these specific areas (vertical) to more integrated horizontal approaches. Bartlett et al. (2004) have already argued convincingly that it is not possible to develop a coastal SDI in isolation from broader regional, national, and global initiatives. These broader initiatives may connect the coast to the deep ocean, connect science to resource management and policy, bring in the consideration of communities and infrastructures of the built environment, or makes connections between all aspects of the global natural environmental (land, sea, and air). As such, we need to keep looking at efforts within the coastal realm, but most certainly outside of it as well. In this vein it will be important to keep



abreast of the NSDI in the U.S., INSPIRE in Europe, and the GSDI Association. The reader is also directed to the new International Journal of Spatial Data Infrastructures Research (IJSDIR, [ijmdir.jrc.it](http://ijmdir.jrc.it)), which covers the full range of research experiences that advance the theory and practice of SDI development.

**Acknowledgements** The author gratefully acknowledges the support of U.S. National Science Foundation grants OISE-0527216 and OCE-0607372, as well as Tanya Haddad of the Oregon Coastal Management Program, Steve Miller and John Helly of the SIOExplorer team, Luis Bermudez and John Graybeal of MMI, and all members of the Marine Geomatics and Integrated Coastal Zone Management research groups of the Coastal and Marine Resources Centre, University College Cork, Ireland.

## References

- Asante KO, Verdin JP, Crane MP, Tokar SA, Rowland J (2007) Spatial data infrastructures in management of natural disasters. In: Onsrud H (ed) *Research and theory in advancing spatial data infrastructure concepts*. ESRI Press, Redlands, California, pp 279–293
- Bartlett D, Longhorn R, Garriga MC (2004) Marine and coastal infrastructures: a missing piece in the SDI puzzle? Proceedings of the seventh global spatial data infrastructure (GSDI) conference, Bangalore, India, <http://gsdidocs.org/gsdiconf/GSDI-7/papers/FTmcg.pdf> (Last access on 17 March 2008)
- Beard K (2007) Digital library. In: Kemp KK (ed) *The encyclopedia of geographic information science*. Sage Publications, Thousand Oaks, California, pp 109–110
- Berners-Lee T, Hendler J, Lassila O (2001) The semantic web: a new form of web content that is meaningful to computers will unleash a revolution of new possibilities. *Sci Am* 284:34–43
- Buttenfield BP (1998) Looking forward: geographic information services and libraries in the future. *Cartogr Geogr Inform* 25:161–171
- Buttenfield BP, Goodchild MF (1996) The Alexandria Digital Library Project: distributed library services for spatially referenced data. Proceedings of GIS/LIS '96, Denver, Colorado, pp 76–84
- Cabral L, Domingue J, Motta E, Payne T, Hakimpour F (2004) Approaches to semantic web services: an overview and comparisons. In: Bussler C, Davies J, Fensel D (eds) *The semantic web: research and applications: first European semantic web symposium, lecture notes in computer science*, vol 3053. Springer, Berlin, pp 225–239
- Canessa R, Butler M, Leblanc C, Stewart C, Howes D (2007) Spatial information infrastructure for integrated coastal and ocean management in Canada. *Coast Manage* 35:105–142
- Carlson GR, Patel B (1997) A new era dawns for geospatial imagery. *GIS World* 10:36–40
- Cimino JP, Pruett LT, Palmer HD (2000) Management of global maritime limits and boundaries using geographical information systems. *Integ Coastal Zone Mgmt* 1:91–97
- Craglia M, Annoni A (2007) INSPIRE: an innovative approach to the development of spatial data infrastructures in Europe. In: Onsrud H (ed) *Research and theory in advancing spatial data infrastructure concepts*. ESRI Press, Redlands, California, pp 93–106
- Crompvoets J, Bregt A (2007) National spatial data clearinghouses, 2000–2005. In: Onsrud H (ed) *Research and theory in advancing spatial data infrastructure concepts*. ESRI Press, Redlands, California, pp 133–146
- Cushing J, Wilson T, Delcambre L, Hovy E (2005) Preliminary report of eco-informatics & decision making: defining research objectives for digital government for ecology. Workshop on biodiversity and ecosystem informatics, NSF, NASA, USGS-NBII, Olympia, Washington, <http://www.evergreen.edu/bdei/home.php> (Last access on 17 March 2008)

- Dawes SS, Pardo TA (2002) Building collaborative digital government systems: systemic constraints and effective practices. In: McIver W, Elmagarmid AK (eds) *Advances in digital government: technology, human factors, and policy*. Kluwer, Norwell, Massachusetts, pp 259–273
- de Man WHE (2007) Are spatial data infrastructures special? In: Onsrud H (ed) *Research and theory in advancing spatial data infrastructure concepts*. ESRI Press, Redlands, California, pp 33–54
- DeMulder ML, DeLoatch I, Garie H, Ryan BJ, Siderelis K (2004) A clear vision of the NSDI. *GeoSpatial Solutions* 14:30–34
- Egenhofer MJ (2002) Toward the semantic geospatial web. Proceedings of the tenth ACM international symposium on advances in geographic information systems, McLean, Virginia
- Eleveld MA, Schrimpf WBH, Siegert AG (2003) User requirements and information definition for a virtual coastal and marine data warehouse. *Ocean Coast Manage* 46:487–505
- Fonseca F, Sheth A (2002) Geospatial semantic web. UCGIS short-term research priority paper, University Consortium for Geographic Information Science, Washington, DC, <http://www.ucgis.org> (Last access on 17 March 2008)
- Gärtner H, Bergmann A, Schmidt J (2001) Object-oriented modeling of data sources as a tool for the integration of heterogeneous geoscientific information. *Computat Geosci* 27:975–985
- Goodchild MF (2003) The nature and value of geographic information. In: Duckham M, Goodchild MF, Worboys MF (eds) *Foundations of geographic information science*. Taylor and Francis, New York, pp 19–32
- Haddad TC, Wright DJ, Dailey M, Klarin P, Marra J, Dana R, Revell D (2005) The tools of the Oregon Coastal Atlas. In: Wright DJ, Scholz AJ (eds) *Place matters: geospatial tools for marine science, conservation and management in the Pacific Northwest*. Oregon State University Press, Corvallis, Oregon, pp 134–151
- Hamre T, Sandven S, Ó Tuama E (2005) DISMAR: data integration system for marine pollution and water quality. In: Lacoste H (ed) *Proceedings of the MERIS (A)ATSR workshop 2005 (ESA SP-597)*, ESRIN, Frascati, Italy
- Helly J, Elvins TT, Sutton D, Martinez D (1999) A method for interoperable digital libraries and data repositories. *Fut Gen Comp Sys* 16:21–28
- Helly J, Staudigel H, Koppers A (2003) Scalable models of data sharing in Earth sciences. *Geochem Geophys Geosyst* 4:1010, doi:10.1029/2002GC000318
- Katz R, Anderson T, Ousterhout J, Patterson D (1991) *Robo-line storage: low latency, high capacity storage systems over geographically distributed networks*. Sequoia 2000 Technical Report, University of California, Berkeley
- Kracker L (1998) *The quantification and classification of aquatic landscape structure*. PhD thesis, State University of New York at Buffalo, Buffalo, New York
- Lockwood M, Fowler C (2000) Significance of coastal and marine data within the context of the United States National Spatial Data Infrastructure. In: Wright DJ, Bartlett DJ (eds) *Marine and coastal geographical information systems*. Taylor & Francis, London, pp 261–278
- Mapping Science Committee (2001) *National spatial data infrastructure partnership programs: re-thinking the focus*. National Academy Press, Washington, DC
- Maratos A (2007) Marine spatial data infrastructure (MSDI). *Hydro International*, vol 11. [http://www.hydro-international.com/issues/articles/id747-Marine\\_Spatial\\_Data\\_Infrastructure\\_MSDI.html](http://www.hydro-international.com/issues/articles/id747-Marine_Spatial_Data_Infrastructure_MSDI.html) (Last access on 17 March 2008)
- Marra JJ (1998) *Chronic coastal natural hazards model overlay zone: ordinance, planners guide, and practitioners guide*. Report to the Oregon Department of Land Conservation and Development. Shoreland Solutions, Newport, Oregon
- Masser I (1998) *Governments and geographic information*. Taylor and Francis, London
- Masser I (2007) *Building European spatial data infrastructures*. ESRI Press, Redlands, California
- Mayer L, Barbor K, Boudreau P, Chance T, Fletcher C, Greening H, Li R, Mason C, Metcalf K, Snow-Cotter S, Wright D (2004) *A geospatial framework for the coastal zone: national needs for coastal mapping and charting*. National Needs for Coastal Mapping and Charting Committee, National Research Council, National Academies Press, Washington, DC

- Miller HJ, Han J (eds) (2001) *Geographic data mining and knowledge discovery*. Taylor & Francis, London
- Miller SP, Helly J, Koppers A, Brueggeman P (2001) SIOExplorer: digital library project. Proceedings of MTS/IEEE oceans 2001 conference, MTS 0-933957-28-9, vol 4. pp 2288–2296
- Nebert DD (ed) (2000) *Developing spatial data infrastructures: the SDI cookbook*. GSDI Technical Working Group, <http://www.gsdi.org/pubs/cookbook> (Last access on 17 March 2008)
- Nedovic-Budic Z (2002) *Geographic information (GI) partnering*. UCGIS short-term research priority paper, University Consortium for Geographic Information Science, Washington, DC, [http://www.ucgis.org/priorities/research/2002researchPDF/shortterm/m\\_gi\\_partnering.pdf](http://www.ucgis.org/priorities/research/2002researchPDF/shortterm/m_gi_partnering.pdf) (Last access on 17 March 2008)
- NSF (National Science Foundation Cyberinfrastructure Council) (2007) *Cyberinfrastructure vision for 21st century discovery*. Publication NSF07-28, National Science Foundation, Washington, DC, <http://www.nsf.gov/pubs/2007/nsf0728> (Last access on 17 March 2008)
- O'Dea L, Cummins V, Wright D, Dwyer N, Ameztoy I (2007) Report on coastal mapping and informatics Trans-Atlantic workshop 1: potentials and limitations of Coastal Web Atlases. University College Cork, Ireland, [http://workshop1.science.oregonstate.edu/final\\_rpt](http://workshop1.science.oregonstate.edu/final_rpt) (Last access on 17 March 2008)
- O'Neill K, Cramer R, Gutierrez M, van Dam K, Kondapalli S, Latham S, Lawrence B, Lowry R, Woolf A (2003) The metadata model of the NERC DataGrid. Proceedings of the UK all hands meeting, <http://www.nesc.ac.uk/events/ahm2003/AHMCD/pdf/129.pdf> (Last access on 17 March 2008)
- Paul JF, Copeland JL, Charpentier M, August PV, Hollister JW (2003) Overview of GIS applications in estuarine monitoring and assessment research. *Mar Geod* 26:63–72
- Ruggiero P, Komar PD, McDougal WG, Marra JJ, Beach RA (2001) Wave runup, extreme water levels and the erosion of properties backing beaches. *J Coastal Res* 17:407–419
- Sarkar D (2003) Study delves into information sharing. *Government E-Business Weekly*, <http://www.fcw.com/archives/> (Last access on 17 March 2008)
- Sheth A (1999) Changing focus on interoperability in information systems: from system, syntax, structure to semantics. In: Goodchild MF, Egenhofer MJ, Fegeas R, Kottman CA (eds) *Interoperating geographic information systems*. Kluwer, New York, pp 5–30
- Shi X (2005) Semantic communication and integration in geospatial web services. Abstracts of the Association of American geographers Annual Meeting, Denver, Colorado, Session 2403
- Sietzen F (2003) Geospatial preparedness and homeland security. *Geospatial Solutions* 13:18, 20, 22
- Smith CL (2002) Institutional mapping of Oregon coastal watershed management options. *Ocean Coast Manage* 45:357–375
- Strain L, Rajabifard A, Williamson I (2006) Marine administration and spatial data infrastructure. *Mar Policy* 30:431–441
- Valavanis VD (2002) *Geographic information systems in oceanography and fisheries*. Taylor & Francis, London
- Wood NJ, Good JW (2004) Vulnerability of port and harbor communities to Earthquake and tsunami hazards: the use of GIS in community hazard planning. *Coast Manage* 32:243–269
- World Resources Institute (2000) *World resources 2000–2001: people and ecosystems: the fraying web of life*. World Resources Institute, Washington, DC
- Wright DJ, Bartlett DJ (eds) (2000) *Marine and coastal geographical information systems*. Taylor & Francis, London
- Wright DJ, Haddad T, Klarin P, Dailey M, Dana R (2003) The Oregon Coastal Atlas: A Pacific Northwest NSDI contribution. Proceedings of the 23rd annual ESRI user conference, San Diego, California
- Wright DJ, Haddad T, Klarin P, Lavoit T, Cummins V, O'Dea L (2007) U.S./European partnerships in coastal atlases and coastal/ocean informatics. Proceedings of coastal zone '07, Portland, Oregon
- Wright DJ, Lassoued Y, Bermudez L, Nyerges T, Haddad T, Dwyer N (2008) Semantic mediation as a gateway to interoperability, with a case study of the International Coastal Atlas Network

- (ICAN). In: Cova T, Miller H, Beard K, Frank AU, Goodchild MF (eds) *Geographic Information Science: 5th International Conference GIScience 2008*, Park City, Utah, September 23–26, 2008, Extended Abstracts, 201–218
- UÇa ZD, Sunar Erbek F, Kusak L, Yasa F, Oezden G (2006) The use of optic and radar satellite data for coastal environments. *Int J Remote Sens* 27:3739–3747
- Zibordi G, Melin F, Berthon JF (2006) Comparison of SeaWiFS, MODIS and MERIS radiometric products at a coastal site. *Geophys Res Lett* 33 doi:10.1029/2006GL025778

## Web Sites and Acronyms (all sites last accessed 17-March-2008)

- British Oceanographic Data Centre, Code and Format Definitions – [www.bodc.ac.uk/data/codes\\_and\\_formats](http://www.bodc.ac.uk/data/codes_and_formats)
- Canadian Geospatial Data Infrastructure (CGDI) – [cgdi.gc.ca](http://cgdi.gc.ca)
- Coastal National Spatial Data Infrastructure – [www.csc.noaa.gov/shoreline/cnsdi.html](http://www.csc.noaa.gov/shoreline/cnsdi.html)
- CoastGIS '05, 6th International Symposium with theme of “Defining and Building a Marine and Coastal Spatial Data Infrastructure” – [www.abdn.ac.uk/~geo466](http://www.abdn.ac.uk/~geo466)
- Consortium of Universities for the Advancement of Hydrological Sciences, Inc. (CUAHSI) – [www.cuahsi.org](http://www.cuahsi.org)
- CUASI Hydrologic Information System – [cuahsi.sdsc.edu](http://cuahsi.sdsc.edu)
- Data Integration System for Marine Pollution and Water Quality (DISMAR) DISPRO – [dispro.ucc.ie/apps/dismar](http://dispro.ucc.ie/apps/dismar)
- Executive Order 12906 (establishing the U.S. National Spatial Data Infrastructure, NSDI) – [www.archives.gov/federal-register/executive-orders/pdf/12906.pdf](http://www.archives.gov/federal-register/executive-orders/pdf/12906.pdf)
- Federal Geographic Data Committee (FGDC) – [www.fgdc.gov](http://www.fgdc.gov)
- Geospatial One-Stop (GOS) initiative – [gos2.geodata.gov](http://gos2.geodata.gov)
- Geography Network – [geographynetwork.com](http://geographynetwork.com)
- Infrastructure for Spatial Information in Europe (INSPIRE) Directive and Documents – [inspire.jrc.it](http://inspire.jrc.it)
- INSPIRE GeoPortal – [eu-geoportal.jrc.it](http://eu-geoportal.jrc.it)
- Integrated Ocean Observing System (IOOS) – [www.ocean.us](http://www.ocean.us)
- International Coastal Atlas Network (ICAN) – [workshop1.science.oregonstate.edu/join](http://workshop1.science.oregonstate.edu/join), [ican.ucc.ie](http://ican.ucc.ie)
- International Hydrographic Organization (IHO) – [www.iho.int](http://www.iho.int)
- International Journal of Spatial Data Infrastructures Research (IJS DIR) – [ijsdir.jrc.it](http://ijsdir.jrc.it)
- Global Spatial Data Infrastructure (GSDI) Cookbook – [www.gsdi.org/pubs/cookbook](http://www.gsdi.org/pubs/cookbook)
- Marine Irish Digital Atlas (MIDA) – [mida.ucc.ie](http://mida.ucc.ie)
- Marine Metadata Interoperability (MMI) – [marinemetadta.org](http://marinemetadta.org), [marinemetadta.org/vocabularies](http://marinemetadta.org/vocabularies)
- Minnesota MapServer – [mapserver.gis.umn.edu](http://mapserver.gis.umn.edu)
- Monterey Bay Aquarium Research Institute (MBARI) – [www.mbari.org](http://www.mbari.org)
- National Biological Information Infrastructure (NBII) – [nbii.gov](http://nbii.gov)
- National Science Digital Library (NSDL) – [www.nsdll.org](http://www.nsdll.org)
- The National Map – [nationalmap.gov](http://nationalmap.gov)
- North Coast Explorer – [northcoastexplorer.info](http://northcoastexplorer.info)
- Ocean Research Interactive Observatory Networks (ORION) – [www.orionprogram.org](http://www.orionprogram.org)
- Oregon Coastal Atlas (OCA) – [www.coastalatlantlas.net](http://www.coastalatlantlas.net)
- Open Geospatial Consortium (OGC) – [www.opengeospatial.org](http://www.opengeospatial.org)
- OWL Web Ontology Language – [www.w3.org/TR/owl-features](http://www.w3.org/TR/owl-features)
- Pacific Coastal Resources Atlas of Canada – [www.shim.bc.ca](http://www.shim.bc.ca)
- SIOExplorer (of the Scripps Institution of Oceanography and San Diego Supercomputer Center) – [SIOExplorer.ucsd.edu](http://SIOExplorer.ucsd.edu)
- Trans-Atlantic Workshops in Coastal Mapping and Informatics – [workshop1.science.oregonstate.edu](http://workshop1.science.oregonstate.edu)
- Web Mapping Service (WMS) – [www.opengeospatial.org/standards/wms](http://www.opengeospatial.org/standards/wms)
- Also web feature services (WFS) and web coverage services (WCS)

**Part II**  
**Remote Sensing of Coastal Waters**

# Chapter 6

## Airborne Remote Sensing of Chlorophyll in Chesapeake Bay, USA

Lawrence W. Harding, Jr. and W. David Miller

Climatic forcing dominates phytoplankton dynamics in Chesapeake Bay, generating high spatial and temporal variability of chlorophyll (*chl-a*) and primary productivity (PP) in the largest estuary in the USA. Shipboard monitoring of the Bay dates back five decades, providing a long-term context to assess secular change due to nutrient overenrichment. These data lack sufficient coverage, however, to separate change from variability imposed by climate. We have addressed this problem by obtaining data at high resolution to quantify variability of phytoplankton *chl-a* and PP, including drought-flood cycles and event-scale perturbations outside the scope of traditional approaches. Our methods consist of new technologies using aircraft remote sensing since the late 1980s, generating observations for a broad range of conditions. This chapter describes the Chesapeake Bay Remote Sensing Program (CBRSP) and presents results obtained in >400 flights. We analyze and synthesize these data to document the strong role of climate in driving variability of *chl-a* and PP in the Bay. Our findings are discussed with respect to developing water quality ‘criteria’, including *chl-a* as an indicator of ecosystem responses to nutrient loading, that requires consideration of climatic forcing of phytoplankton dynamics.

### 6.1 Introduction

#### 6.1.1 Overenrichment of Chesapeake Bay

Estuaries are rich aquatic ecosystems where high phytoplankton biomass and primary productivity support food chains leading to robust fisheries. One such ecosystem, Chesapeake Bay, has been renowned for its large stocks of crabs, clams, oysters, and finfish since colonial settlement in the 17th century. In the past 40–50

---

L.W. Harding, Jr. (✉)  
Horn Point Laboratory, University of Maryland Center for Environmental Science, Cambridge,  
MD 21613, USA  
e-mail: larry@hpl.umces.edu

years, however, the 'health' of the Bay has declined, precipitating intense study of the ecosystem. Excessive inputs of nitrogen (N) and phosphorus (P) stimulated an overabundance of phytoplankton, leading to a degradation of water quality (D'Elia et al. 1986, Correll 1987, Fisher et al. 1992, Harding 1994, Boynton et al. 1995, Malone et al. 1996, Kemp et al. 2005). Similar to land-sea linkages in other coastal ecosystems, the Bay's degraded water quality traces to landscape changes in an extensive 165,000 km<sup>2</sup> watershed (cf. Bricker et al. 1999, Curtin et al. 2001). Forests once covered >90% of the area surrounding the Bay, but land clearing following European colonization in the 1600s reduced forest cover to 40% by the late 1800s. A significant increase of the human population has led to increased nutrient loading from point and non-point sources, amounting to a 6-fold increase of N and a 17-fold increase of P (Boynton et al. 1995). The increased phytoplankton biomass resulting from overenrichment provides excess organic material to fuel recurrent summer hypoxia, and reduces light penetration affecting habitat suitability for submerged aquatic vegetation (SAV). As a consequence, the Bay has undergone a significant 'state shift' from an ecosystem formerly dominated by large, benthic producers and consumers to one dominated by smaller, planktonic producers and consumers (Cooper and Brush 1991). Notable changes in the ecosystem include: (i) widespread hypoxia or anoxia in bottom waters (Officer et al. 1984, Hagy et al. 2004); (ii) reduced SAV coverage (Orth and Moore 1983); (iii) declines of oysters by overfishing, disease, and habitat destruction (Rothschild et al. 1994); (iv) fluctuations or declines of important finfish stocks (Richkus et al. 1992).

Two highly responsive indicators of overenrichment are chlorophyll (*chl-a*) as a measure of phytoplankton biomass, and photosynthetic carbon assimilation as a measure of primary productivity (PP). An analysis of long-term *chl-a* data reveals a significant increase of phytoplankton biomass since the 1950s that is most strongly expressed in the mid- and lower regions of the Bay that are highly sensitive to seasonal N-depletion (Harding and Perry 1997). Scientists and managers have reached a consensus agreement that increased N and P loadings support the increase of *chl-a* (Fisher et al. 1992, Malone 1992, Harding et al. 2002), culminating in present-day concentrations that are indicative of a highly eutrophic ecosystem. Annual loadings of total N and P to the Bay and its tributaries are approximately 14 g N m<sup>-2</sup> yr<sup>-1</sup> and 1.1 g P m<sup>-2</sup> yr<sup>-1</sup>, respectively, with a 2.5-fold increase of total N from the Susquehanna River between 1945 and 1990 that has abated only slightly in recent years (Boynton et al. 1995).

### **6.1.2 Management Perspective**

Resource managers use *chl-a* and PP as indicators of ecosystem 'health' because both respond positively to increased nutrient loading. Tools to measure these properties on spatial scales from meters to 100s of kilometers and temporal scales from hours to years are essential, yet rarely applied in estuarine and coastal waters.

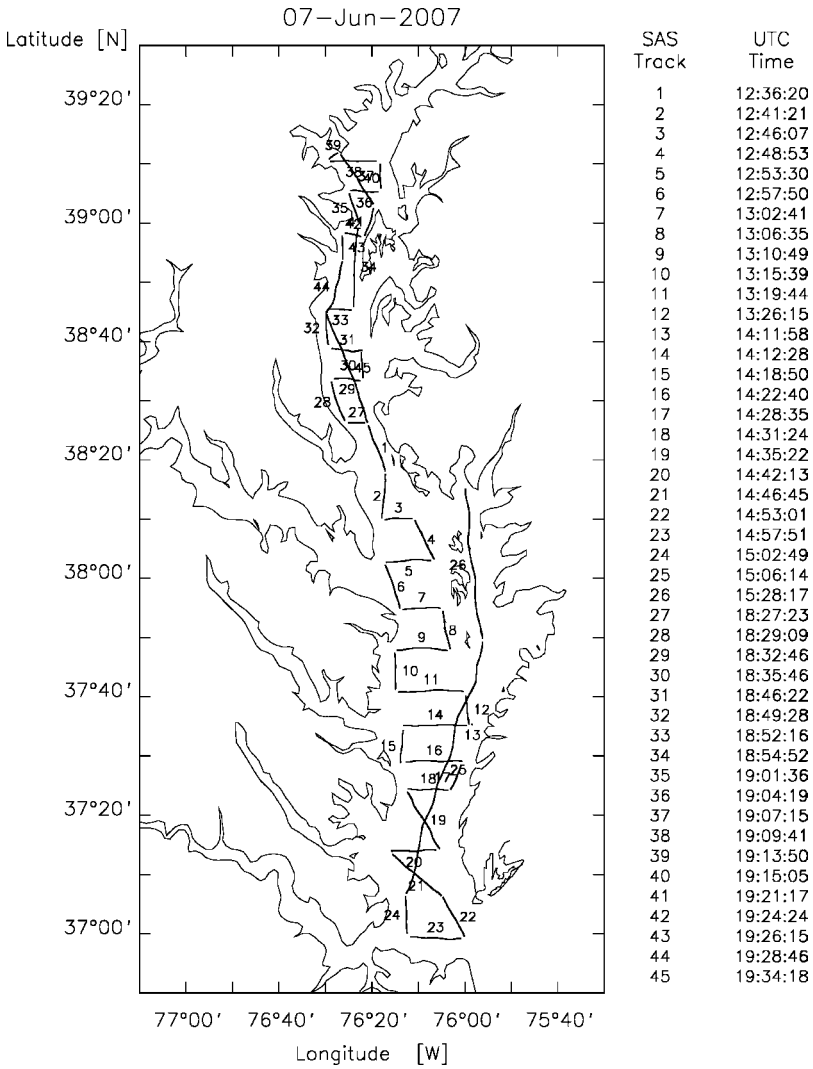
Instead, we have relied for the most part on traditional approaches to measure water quality using in-situ sampling from ships that are both resource-intensive and provide limited coverage. Both *chl-a* and PP can now be retrieved using satellite instruments (Sea-viewing Wide Field-of-view Sensor, SeaWiFS; Moderate Resolution Imaging Spectroradiometer, MODIS), but unfortunately the geographic dimensions, high phytoplankton biomass, spatial and temporal variability, and complex bio-optical characteristics of Case 2 waters that are typically found in estuaries complicate this approach. Some progress has been made to obtain *chl-a* in the Bay using SeaWiFS since its launch in 1997 (Magnuson et al. 2004, Harding et al. 2005), and these advances have aided development of time-series of *chl-a* using SeaWiFS and Aqua-MODIS (Werdell et al. 2007). The main source of remotely sensed *chl-a* for the Bay, however, is airborne remote sensing on low-altitude overflights using ocean color sensors mounted on light aircraft. This long-term program provides a unique data set to complement intensive shipboard monitoring of the Bay. Airborne measurements have advantages in spatial resolution that are not matched by current satellite instruments, and have the operational flexibility to attain repeat coverage of short-lived events such as phytoplankton blooms.

### 6.1.3 Chesapeake Bay Remote Sensing Program

Our group has conducted airborne remote sensing of ocean color on Chesapeake Bay since 1989 when we started the Chesapeake Bay Remote Sensing Program (CBRSP – <http://www.cbrsp.org>) (Fig. 6.1). The motivation for this program was to quantify spatial and temporal variability of phytoplankton biomass as *chl-a* in the main stem Bay, focusing on the spring and summer seasons when *chl-a* and PP reach their respective annual maxima. We conduct Bay-wide flights deploying visible radiometers to measure the spectral quality and quantity of light reflected from the water. The strengths of airborne remote sensing are high spatial and temporal resolution, careful calibration of instruments, generation of local algorithms and models, and independent validation using data from a variety of sources. We estimate the distribution of *chl-a* in the Bay on 20–30 flights per year, totaling >400 flights (to date). The technology for these measurements has evolved from the NASA Ocean Data Acquisition System (ODAS), a three-waveband instrument we used initially, through two generations of instruments manufactured by Satlantic, Inc. of Halifax, Nova Scotia, the SeaWiFS Aircraft Simulator (SAS II, III). We currently use SAS III to collect data at 13 wavebands in the ultraviolet, visible, and near-infrared, including some specific sensors to match capabilities of satellite instruments. CBRSP outputs include interpolated maps of *chl-a* and sea surface temperature (SST). Data are made available to multiple users via the CBRSP web site ([url above](http://www.cbrsp.org)), and support assessments of water quality using *chl-a* criteria that are now being developed by the EPA Chesapeake Bay Program (CBP).

Since CBRSP began, we have documented variability of *chl-a* on a range of spatial and temporal scales, including strong seasonal and interannual variability of





**Fig. 6.1** Flight tracks occupied in the main stem of Chesapeake Bay using airborne remote sensing of ocean color

*chl-a* in the mid- and lower Bay that appears coupled to freshwater flow. Low-flow years are characterized by reduced spring biomass, whereas high-flow years typically have high biomass extending toward the mouth of the Bay. The complete time-series of *chl-a* data from airborne remote sensing has been used to create ‘climatologies’ for a variety of phytoplankton properties, including surface *chl-a*, euphotic-layer *chl-a*, water-column *chl-a*, total *chl-a*, and PP. These long-term data have supported development of predictive models for these key ecosystem properties (cf. Miller and Harding 2007).

### 6.1.4 Organization of this Chapter

In this chapter, we present milestones and results achieved using airborne remote sensing to study phytoplankton dynamics in Chesapeake Bay. Main elements include: (1) programmatic details of the instrumentation, flight operations, data processing, and derived products; (2) lateral and along-axis spatial variability of *chl-a*; (3) short-term variability of *chl-a* associated with events; (4) seasonal and interannual variability of *chl-a*; (5) PP derived from models and remotely sensed measurements; (6) satellite retrievals and future directions.

## 6.2 Methods and Materials

### 6.2.1 Airborne Surveys

Airborne surveys of Chesapeake Bay have been used to measure surface *chl-a* ( $\text{mg m}^{-3}$ ) for nearly twenty years with multispectral radiometers mounted on light aircraft. These instruments include ODAS, SAS II, and SAS III. All three instruments consist of nadir-viewing sensors deployed on a set of  $\sim 40$  flight tracks to provide lateral and along-axis coverage of the Bay (Fig. 6.1). ODAS consists of three radiometers (460, 490, and 520 nm) with 15 nm bandwidths and  $2^\circ$  field-of-view, and was used from 1989 to 1995. SAS II and III consist of seven and 13 radiometers, respectively, with 10 nm bandwidths, and  $3.5^\circ$  field-of-view (SAS II – 412, 443, 490, 510, 555, 670, and 683 nm; SAS III – 380, 400, 412, 443, 470, 490, 510, 555, 670, 685, 700, 780, and 865 nm). SAS II was used from 1995 to 1996 and SAS III from 1997–present. Geo-referenced data (GPS) are collected on flights at an altitude of 500 ft (150 m) and an airspeed of 100 nautical miles  $\text{h}^{-1}$  ( $\sim 50 \text{ m s}^{-1}$ ). Flights are conducted from February through November, with particular emphasis on spring and summer. In-situ observations of *chl-a* for ground-truth of remotely-sensed estimates of *chl-a* are obtained from shipboard sampling on CBP cruises (1989–present), successive NSF programs on Land-Margin Ecosystem Research (LMER) (1989–2000), NASA programs on ocean color and sensor intercomparisons for Case 2 waters, EPA and NASA programs to develop ecological indicators in estuaries (1997–2004), and a NSF Biocomplexity program (2001–2004).

### 6.2.2 Retrievals of *chl-a*

We use matching data from airborne remote sensing and shipboard monitoring to develop relations between the output of a spectral curvature algorithm,  $-\log_{10} G$ , applied to water-leaving radiances in the blue-green region of the visible spectrum (Grew 1981, see Campbell and Esaias 1983) and surface *chl-a* (cf. Harding and Itsweire 1991, Itsweire et al. 1991, Harding et al. 1992, 1994, 1995, 2001).

A 'match' for validation purposes is defined as  $\pm 12$ h on the same day,  $\pm 0.01^\circ$  latitude, and  $\pm 0.005^\circ$  longitude. Regression equations retrieve  $\log_{10} chl-a$  with a root mean square error (RMSE) of 0.21 ( $\log_{10}$  units), and validation is updated regularly with the addition of ground-truth data from subsequent years. Radiometric calibrations are made annually by NASA or Satlantic, Inc. for all sensors. Drift over the course of a flight season is typically  $< 2\%$ . Raw data from ODAS, SAS II, and SAS III are processed using a UNIX workstation (Silicon Graphics, Inc.) or a PC with MATLAB. The sequence of processing steps applies radiometric calibrations, incorporates navigational data, screens for sun glint, and uses regional algorithms to compute *chl-a* and SST. Surface *chl-a* and SST are gridded and contoured using a two-dimensional, octant search with inverse-distance-squared weighting to generate interpolated map products (Harding et al. 1992). Derived *chl-a* products presented in this chapter represent airborne measurements as one- or five-second averages, giving along-track resolutions of 50 and 250 m, respectively, whereas gridded outputs are at a spatial resolution of  $1 \text{ km}^2$  to define major features and trends.

### 6.2.3 Derived Products

Time-series of surface *chl-a* obtained from airborne remote sensing and several derived products have been generated for all flights. The primary product is surface *chl-a* ( $\text{mg m}^{-3}$ ). We combine data on surface *chl-a* with euphotic-layer depth ( $Z_p$ ) to compute euphotic-layer *chl-a* ( $\text{mg m}^{-2}$ ) as the product of surface *chl-a* and  $Z_p$ , with  $Z_p$  estimated as the 1% isolume using Secchi depth readings from CBP monitoring cruises. Significant log-log relationships of depth-weighted integral *chl-a* and surface *chl-a* using vertical profiles from CBP monitoring cruises are used to compute integral, water-column *chl-a* ( $\text{mg m}^{-2}$ ) (cf. Harding et al. 1994). Analysis of variance (ANOVA) shows significant differences in the slopes of regressions for different years, thus we apply equations specific to each year to estimate depth-weighted integral, water-column *chl-a* from remotely sensed *chl-a*. Back-transformed values are combined with water-column depth from a digital bathymetry to give integral, water-column *chl-a*. All three biomass measures – surface *chl-a*, euphotic-layer *chl-a*, and integral, water-column *chl-a* – are log-normally distributed, such that  $\log_{10}$ -transformed data are used in all analyses. A time-series of total phytoplankton biomass as metric tons of *chl-a* is computed as the sum of integral, water-column *chl-a* for three regions in the main stem Bay defined by latitude and average salinity and for the Bay as a whole (Harding 1994, Harding and Perry 1997).

### 6.2.4 Primary Productivity (PP)

Gross PP is estimated using a depth-integrated model (DIM) for the Bay (cf. Harding et al. 2002), modified from the Vertically Generalized Productivity Model

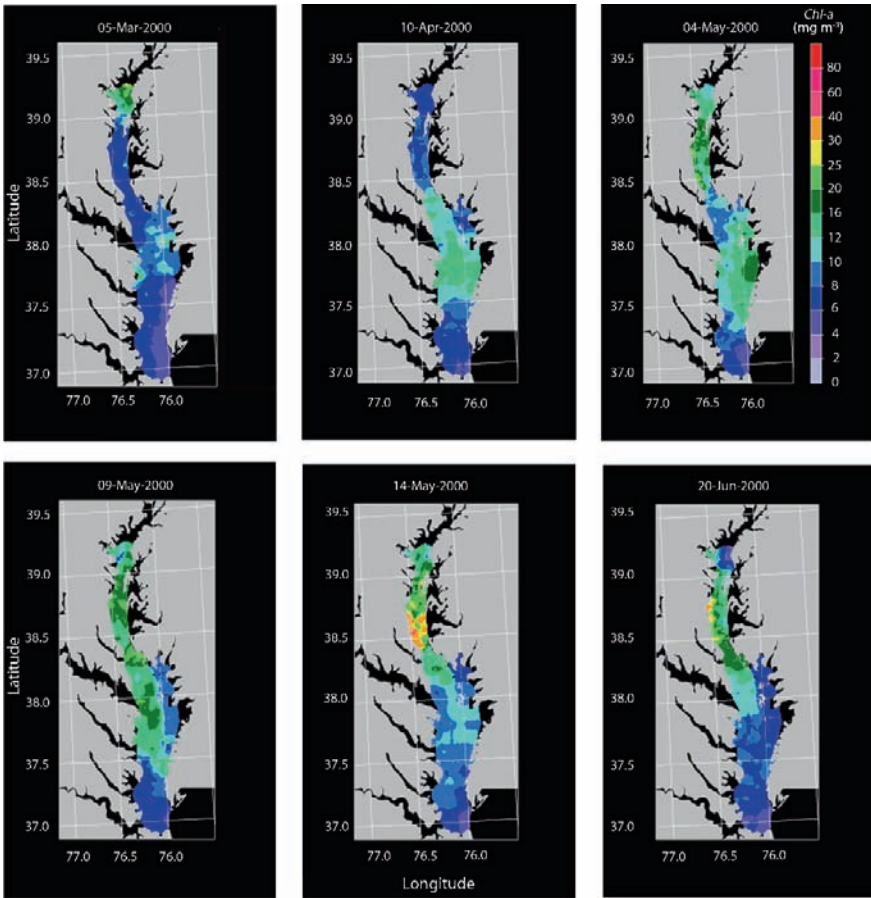
(VGPM) of Behrenfeld and Falkowski (1997). This model, the Chesapeake Bay Productivity Model (CBPM-2), is a log-transformed version of VGPM that allows derivation of locally calibrated coefficients for each independent variable. CBPM-2 embeds a model of the ‘phytoplankton physiology’ term,  $P^B_{opt}$ , making it applicable to remotely sensed data lacking independent measurements of this term. CBPM-2 is calibrated with shipboard measurements collected over 17 years (1982–1998), and produces estimates of PP with RMSE of 49.7%. Validation with data from 1999 to 2000 that were omitted from model calibration produces PP estimates with RMSE of 47.6%. The independent variables in the model include: surface *chl-a* ( $\text{mg m}^{-3}$ ), photosynthetically-available radiation,  $E_0$  ( $\text{E m}^{-2} \text{d}^{-1}$ ) applied as  $tE_0 = (E_0/(E_0 + 4.1))$  to describe the saturating effect of  $E_0$ ,  $Z_p$  (m) estimated as the 1% isolume, daylength,  $D_{irr}$  (h), and SST ( $^{\circ}\text{C}$ ).

We compute daily PP by applying CBPM-2 to data from each flight. Data sources for independent variables are: (1) *chl-a* and SST from airborne remote sensing; (2)  $Z_p$  from bi-weekly to monthly monitoring CBP cruises (<http://www.chesapeakebay.net>); (3)  $E_0$  from a LiCor model 192  $2\pi$  sensor at the Smithsonian Environmental Research Center (SERC, Edgewater, Maryland, USA); (4)  $D_{irr}$  calculated from latitude and day-of-year. All data are mapped onto a common  $1\text{ km}^2$  grid, producing approximately 7000 grid cells for each flight/cruise. Combined data from 18 to 37 flights and cruises per year support computation of PP for 1990–2004. The number of flights varies with weather, instrument function, and aircraft availability. Shipboard *chl-a* were used in place of remotely sensed *chl-a* in 1996 due to instrument malfunctions. Time integrals are obtained by converting irregularly spaced PP outputs to a daily frequency using linear interpolation. Outputs are summed to produce monthly, seasonal, and annual estimates, including summer integral production (SIP) and annual integral production (AIP).

## 6.3 Results

### 6.3.1 Products

The distribution of phytoplankton expressed as surface *chl-a* from airborne remote sensing shows high variability in Chesapeake Bay on a range of spatial and temporal scales. This variability is evident in maps of surface *chl-a* for a sequence of six flights in spring 2000, showing the progression of a well-developed spring bloom (Fig. 6.2). The spring bloom usually consists of large, centric diatoms and is the most prominent feature of the annual phytoplankton cycle in the Bay (cf. Malone 1992, Adolf et al. 2006, Miller and Harding 2007). High biomass develops between March and May as phytoplankton draw on ample nutrients to generate particulate organic matter. This material of phytoplankton origin serves to fuel the Bay’s food web, but also underlies deleterious effects of nutrient overenrichment, including low dissolved oxygen and reduced water clarity.



**Fig. 6.2** Sequence of six *chl-a* images from 2000 to illustrate the progression of the spring bloom between March and June

Scientists and managers recognize that increased nutrient loading has acted to fertilize the Bay, alleviating N-limitation and supporting increased phytoplankton biomass. The response of the ecosystem is apparent as increased *chl-a* in the mid- to lower Bay, particularly from the 1950s to the 1980s. Resource managers have a strong interest in using *chl-a* data from airborne remote sensing to gauge progress in reversing nutrient overenrichment as these data are more highly resolved than other sources. A practical application of the data is to use surface *chl-a* and derived products as indicators of nutrient loading, particularly of the macronutrient N that impacts phytoplankton biomass on a Bay-wide scale (cf. Malone et al. 1996). Detection of a long-term decline of *chl-a* that is expected to accompany nutrient reductions is complicated by spatial and temporal variability of *chl-a*, however, and remotely sensed data better capture the relevant scales of variability expressed in the estuary. An important application is to use remotely sensed data to quantify spatial

and temporal variability of *chl-a* in years of contrasting precipitation and freshwater flow, providing an essential context against which to measure future changes.

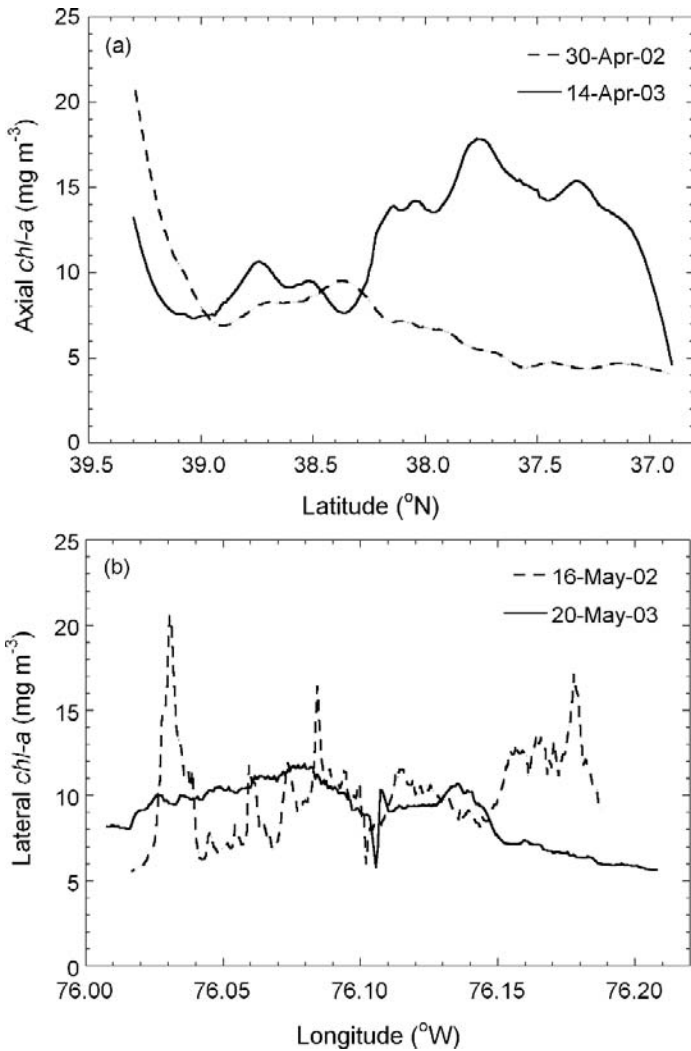
### 6.3.2 Axial and Lateral Variability of Surface *chl-a*

Surface *chl-a* shows spatial variability on scales of 100s of meters to kilometers along the main stem axis of the Bay and on lateral transects. Examples of recent data illustrate gradients in 2002 and 2003, two strongly contrasting years with ‘dry’ and ‘wet’ climate conditions, respectively (Fig. 6.3). These data reveal four-fold axial and lateral variability of surface *chl-a* within 10–50 km. An earlier analysis of lateral gradients quantified significant small-scale variability of surface *chl-a* using ODAS data from 1990 to 1991 (Weiss et al. 1997). Linear models showed negative correlations between  $\log_{10}$  *chl-a* and track distance, indicating a west to east decrease. Steep gradients with west to east decreases of surface *chl-a* up to six-fold were reported for the lower Bay. Interannual differences of surface *chl-a* gradients were also observed during the spring bloom, with higher variability in 1990 than in 1991. Negative correlations were particularly common for lower Bay flight tracks where significant linear decreases of surface *chl-a* occurred on >60% of flights. Positive correlations indicating west to east increases of surface *chl-a* were less common. Correlation lengths ranged from 0.3 to 7.0 km for two flight tracks in the lower Bay, whereas more northerly tracks had correlation lengths ranging from 0.3 to 3.1 km. Predictable values of correlation length were associated with strong linear gradients, and the absence of such a gradient was usually accompanied by a lower and highly variable correlation length.

Based on their spatial analyses, Weiss et al. (1997) concluded that sampling infrequently or with limited spatial resolution poorly recovers information on small-scale or short-term variability of surface *chl-a*, particularly at high concentrations. This finding is consistent with the conclusions of Harding et al. (1994, 1995) that ship-board sampling inadequately recovers high *chl-a* associated with blooms, but does a respectable job estimating mean surface *chl-a* for different regions of the Bay. Sampling that poorly retrieves peaks of surface *chl-a* is likely to introduce error in quantifying the Bay-wide distribution of phytoplankton. This limitation affects computations of seasonal/annual biomass by failing to include extreme values, and has implications for secondary production known to be affected by spatial gradients and localized peaks (cf. Boynton et al. 1997).

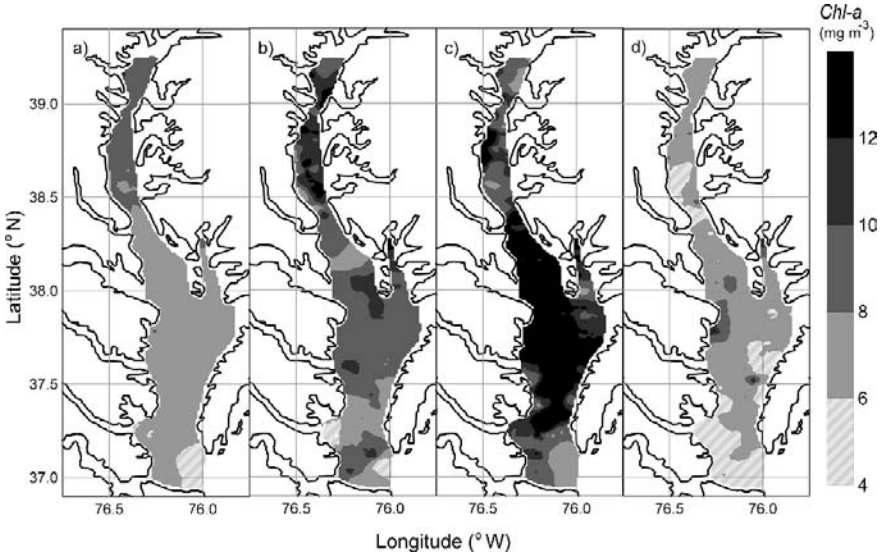
### 6.3.3 Event-Scale Phytoplankton Dynamics

Airborne remote sensing of ocean color quantified a major perturbation of phytoplankton biomass in Chesapeake Bay by Hurricane Isabel (17–19 September 2003) (Fig. 6.4). Mid-Atlantic hurricanes typically produce high precipitation leading to increased freshwater flow and nutrient loading, supporting increased phytoplankton



**Fig. 6.3** (a) Axial *chl-a* from April flights in successive dry (2002) and wet (2003) years, showing the extension of high *chl-a* toward the mouth of Chesapeake Bay driven by high freshwater flow and nutrient loading; (b) lateral *chl-a* from lower Bay track (latitude = 36.99–37.00°N) from May flights in 2002 and 2003

biomass over a period of weeks to months (Paerl et al. 2001). For example, Tropical Storm Agnes in June 1972 led to unprecedented freshwater flow and a protracted increase of phytoplankton biomass in Chesapeake Bay following a massive nutrient pulse (Zubkoff and Warinner 1977). Phytoplankton responses to Isabel were quite distinct from those to Agnes, occurring within days of storm passage by a mechanism wherein hurricane energy eroded the pycnocline and injected nutrients to the surface mixed layer (Davis and Yan 2004, Li et al. 2006).



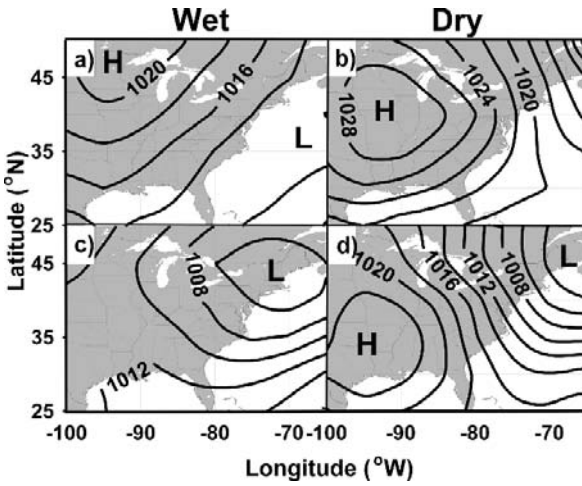
**Fig. 6.4** Effect of Hurricane Isabel (18 September 2003) on the *chl-a* distribution in Chesapeake Bay: (a) long-term average (LTA) for September 1989–04; (b) pre-Isabel, 11 September; (c) post-Isabel, 24 September; (d) two weeks post-Isabel, 2 October

Flights on 11 September 2003 (Fig. 6.4b) and 24 September 2003 (Fig. 6.4c) before and after the passage of Hurricane Isabel showed a significant increase ( $4.7 \text{ mg m}^{-3}$ ) of phytoplankton biomass covering  $>3000 \text{ km}^2$  of the mid- to lower Chesapeake Bay (Miller et al. 2006a). A fall bloom of this magnitude had not been detected in either CBRSP or CBP time-series of *chl-a*. Mass balance calculations showed nutrients in bottom waters were mixed into the surface layer by Hurricane Isabel and incorporated into phytoplankton biomass, leading to a rapid increase of *chl-a* observed by airborne remote sensing. These nutrients were exhausted within two weeks as *chl-a* returned to the long-term average for fall by 2 October 2003 (Fig. 6.4 a,d). This application highlights the usefulness of airborne remote sensing to provide high-resolution, quasi-synoptic coverage of estuarine and coastal waters, allowing the detection of a significant perturbation of phytoplankton dynamics.

### 6.3.4 Seasonal Distribution of Phytoplankton

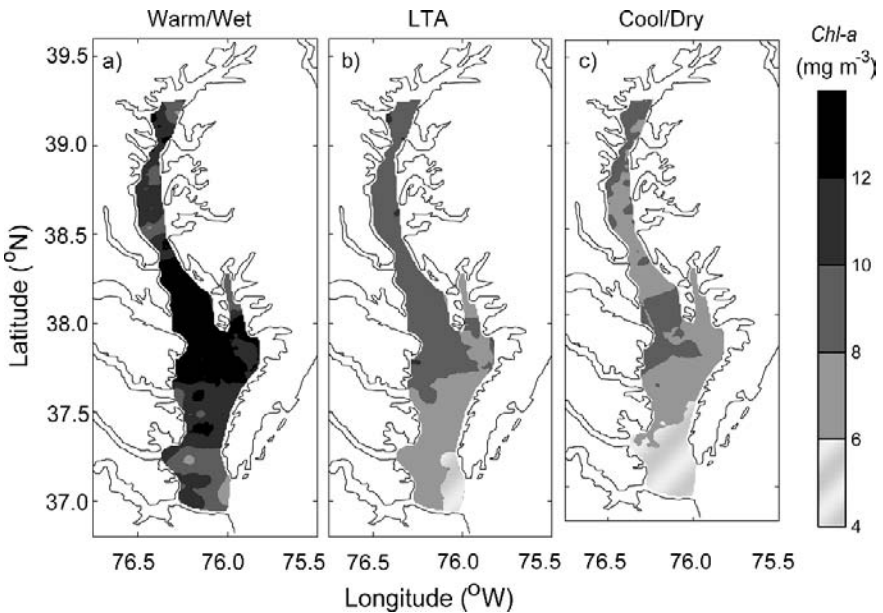
To link climate and phytoplankton, we have used a synoptic climatology developed for the Bay (Miller et al. 2006b) to categorize individual years covered by airborne remote sensing (Fig. 6.5). This approach quantifies regional climate conditions using sea-level pressures (SLP) by computing the frequencies of individual patterns, and relating interannual differences to surface conditions, i.e., precipitation and freshwater flow, that are known to drive phytoplankton dynamics in the Bay. The position of the spring phytoplankton maximum is sensitive to climate forcing as





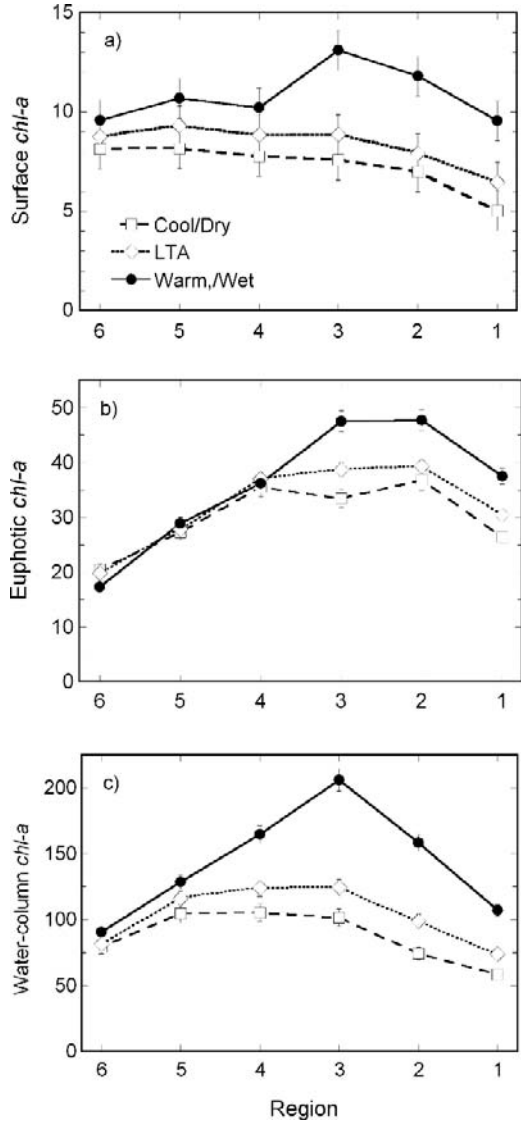
**Fig. 6.5** Sea-level pressure (SLP) patterns for four commonly observed weather patterns in the Chesapeake Bay region identified using synoptic climatology. Patterns (a) and (c) correspond to ‘wet’ conditions, and patterns (b) and (d) to ‘dry’ conditions

documented by interannual variability in the distribution of surface *chl-a*, euphotic-layer *chl-a*, and integral, water-column *chl-a* derived from airborne remote sensing (Figs. 6.6 and 6.7). In warm/wet years, maxima of these three biomass measures occur seaward of maxima for cool/dry years. Long-term data (1989–2004) show



**Fig. 6.6** Surface *chl-a* from airborne remote sensing of Chesapeake Bay for: (a) warm/wet, (b) long-term average (LTA), and (c) cool/dry conditions

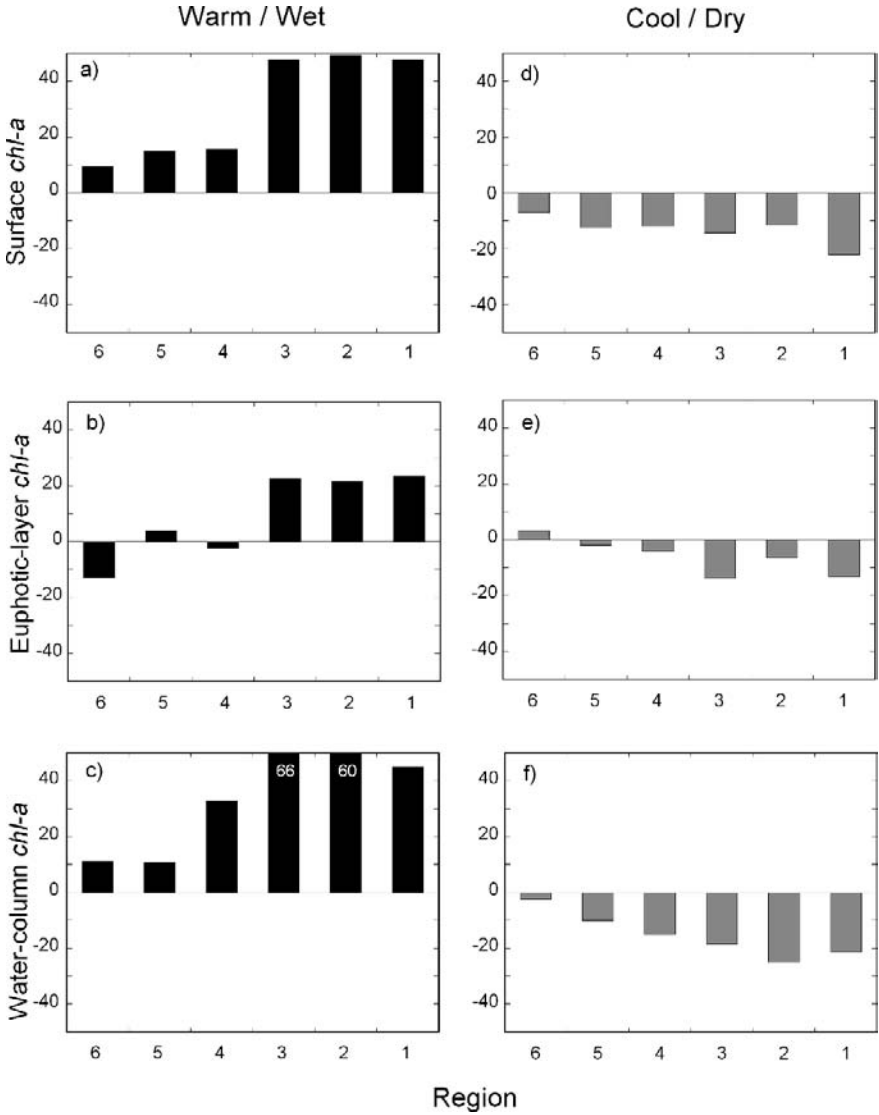
**Fig. 6.7** Regional means of surface *chl-a*, euphotic-layer *chl-a*, and integral, water-column *chl-a* for six regions along the main stem Chesapeake Bay. The region designations progress from seaward (1) to landward (6) per Harding and Perry (1997)



surface *chl-a* reaches a maximum of  $13.1 \text{ mg m}^{-3}$  positioned in the mid-Bay in warm/wet years, but is only  $8.2 \text{ mg m}^{-3}$  in the upper Bay in cool/dry years. Peaks of euphotic-layer *chl-a* occur in the lower Bay for both warm/wet and cool/dry climate modes, whereas the magnitude of the peak is  $47.7 \text{ mg m}^{-2}$  in warm/wet years and  $36.8 \text{ mg m}^{-2}$  in cool/dry years. A maximum of integral, water-column *chl-a* occurs in the mid-Bay in warm/wet years, distinct from a broad plateau of water-column *chl-a* that is found in the mid- to upper Bay in cool/dry years (Fig. 6.7).

Differences in surface *chl-a*, euphotic-layer *chl-a*, and integral, water-column *chl-a* between warm/wet and cool/dry years expressed as deviations from long-term

averages (LTA) for 1989–2004 display consistent responses to climatic forcing (Fig. 6.8). Largest positive anomalies for all three measures of phytoplankton biomass occur in the mid- to lower Bay in warm/wet years. These regions average 49, 22, and 57% above the LTA for surface *chl-a*, euphotic-layer *chl-a*, and integral, water-column *chl-a*, respectively. A negative anomaly for euphotic-layer *chl-a* is found in the upper Bay during warm/wet years. The largest negative anomalies for



**Fig. 6.8** Climate effects on phytoplankton biomass expressed as percent differences by re-gion for surface *chl-a* (a, d), euphotic-layer *chl-a*, (b, e), and integral, water-column *chl-a* (c, f) from LTA for warm/wet and cool/dry years. Regions are as defined in Fig. 6.7

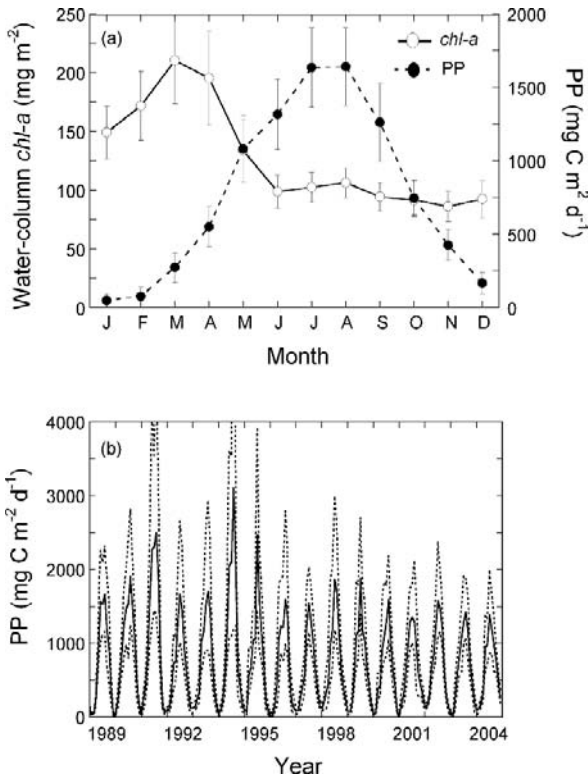
the three biomass measures occur in the mid- to lower Bay during cool/dry years. Positive anomalies during warm/wet years are greater than negative anomalies during cool/dry years for all regions and biomass measures.

Climatic forcing also affects the timing of the spring phytoplankton maximum expressed as total *chl-a* biomass (Miller and Harding 2007). The highest value of total *chl-a* biomass reaches  $\sim 717$  metric tons in late May during warm/wet years and is significantly greater ( $p < 0.01$ ) than the LTA of 455 metric tons. Total *chl-a* biomass shows a broad peak of 383–445 metric tons in April–May in cool/dry years and is significantly ( $p < 0.05$ ) less than the LTA. Spring bloom intensity using the metric of total *chl-a* biomass averages 276 metric tons greater in warm/wet than in cool/dry years. The spatial extent of high biomass in the Bay also differs in warm/wet and cool/dry climate conditions. Spatially averaged surface *chl-a* in spring is  $8.0 \text{ mg m}^{-3}$  and the area with  $> 8 \text{ mg m}^{-3}$  averages  $\sim 3800 \text{ km}^2$ . During warm/wet years the  $8 \text{ mg m}^{-3}$  isopleth extends to the Bay's mouth, expanding the area with *chl-a*  $> 8 \text{ mg m}^{-3}$  to  $6836 \text{ km}^2$ . Conversely, during cool/dry years the area with surface *chl-a*  $> 8 \text{ mg m}^{-3}$  is only  $1872 \text{ km}^2$ .

The contrasting responses to climate evident in data from airborne remote sensing are useful to resource managers as they represent natural experiments wherein warm/wet and cool/dry conditions mimic the effects of different nutrient loadings. A cool/dry year with decreased nutrient loading leads to a commensurate decrease of phytoplankton biomass and a *chl-a* distribution resembling that of a bygone decade. Thus, analyses of phytoplankton dynamics that take account of climatic forcing are valuable as a window to the past. Moreover, extensive research shows that the phytoplankton biomass accumulating in spring provides a significant fraction of the fuel for summer hypoxia in the Bay. This link of phytoplankton biomass to hypoxia accentuates the usefulness of synoptic and spatially explicit *chl-a* retrievals from airborne remote sensing to the successful management of the ecosystem.

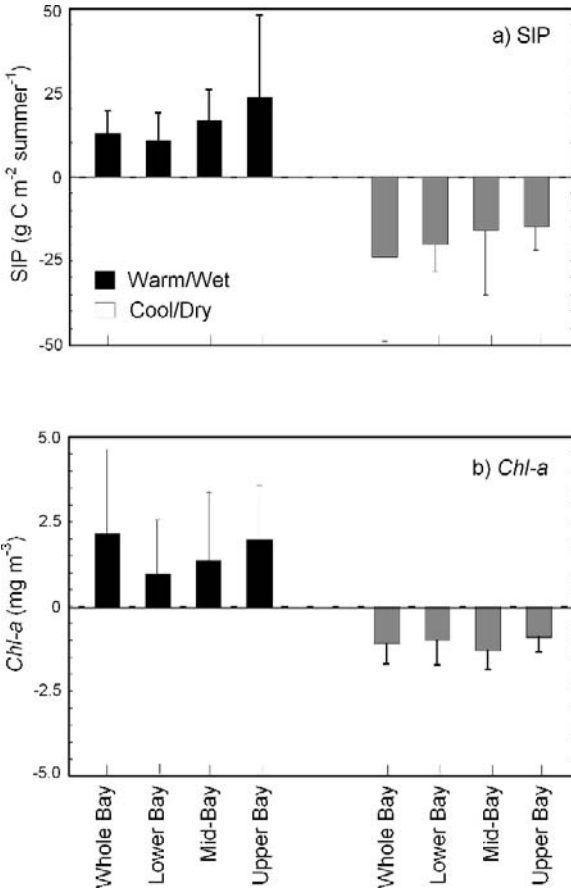
### 6.3.5 Primary Productivity From Remote Sensing and Models

PP derived from CBPM-2 applied to data from airborne remote sensing are in good agreement with PP measurements over a broad range ( $346\text{--}3197 \text{ mg C m}^2 \text{ d}^{-1}$ ; Miller 2006). Data binned by season (spring, summer, fall) and year (1995–2000) show a highly significant ( $p < 0.001$ ,  $r^2 = 0.55$ ,  $n = 18$ ) relationship, despite differences in sample density and timing. Time series of monthly, average PP for 16 years (1989–2004) reveal high interannual variability that is dominated by summer (June–September) (Fig. 6.9). Annual averages show highest values of 840 and  $828 \text{ mg C m}^{-2} \text{ d}^{-1}$  in the mid- to lower regions of the Bay, respectively, whereas the light-limited upper Bay is lower at  $698 \text{ mg C m}^{-2} \text{ d}^{-1}$ . Summer maxima show two- to three-fold differences among years, averaging  $1653 \text{ mg C m}^{-2} \text{ d}^{-1}$  for the upper Bay,  $1957 \text{ mg C m}^{-2} \text{ d}^{-1}$  for the mid-Bay, and  $1860 \text{ mg C m}^{-2} \text{ d}^{-1}$  the lower Bay. Secondary spring peaks of PP occur during several years.



**Fig. 6.9** Annual and multi-year patterns of PP in Chesapeake Bay: (a) assembled data on integral, water-column *chl-a* and PP from shipboard observations, 1982–1998 ( $n = 455$ ), showing displacement of peak biomass and PP (modified from Harding et al. 2002); (b) interannual variability of PP derived from airborne remote sensing, 1989–2004 (modified from Miller 2006)

Miller (2006) computed integral PP as SIP and AIP using data from airborne remote sensing, reporting two-fold interannual variability of SIP and AIP with the largest range in the lower Bay and the smallest range in the upper Bay at 226 and 96 g C m<sup>-2</sup> yr<sup>-1</sup>, respectively. Average Bay-wide AIP is 301 g C m<sup>-2</sup> yr<sup>-1</sup> for the 16-yr time series. AIP is highest in the mid-Bay (306 g C m<sup>-2</sup> yr<sup>-1</sup>) and lowest (256 g C m<sup>-2</sup> yr<sup>-1</sup>) in the upper Bay. Bay-wide SIP averages 189 g C m<sup>-2</sup> summer<sup>-1</sup>, whereas regional values range from a minimum of 164 g C m<sup>-2</sup> summer<sup>-1</sup> in the upper Bay to 193 g C m<sup>-2</sup> summer<sup>-1</sup> in the mid-Bay. On a Bay-wide scale, the lower Bay is responsible for 52.6% of AIP, the mid-Bay for 42.5%, and the upper Bay for only 4.8%. There are regional differences in AIP and SIP, but the proportion of Bay-wide PP associated with each region is primarily a function of area. SIP constitutes a large and consistent fraction of AIP, ranging from 55 to 79% with an average of 62%. Simple linear regression of AIP on SIP for all regions produces a highly significant relationship ( $p < 0.001$ ) that explains 92% of the variance of AIP.



**Fig. 6.10** SIP and chl-a in Chesapeake Bay regions for warm/wet and cool/dry conditions from airborne remote sensing

Examined regionally, SIP explains 75% of the variance of AIP in the upper Bay, and 94–95% of the variances in the mid- and lower Bay, respectively. Climatic forcing exerts similar control on SIP as on surface *chl-a*, shown as deviations from LTA for regional data grouped by warm/wet and cool/dry conditions (Fig. 6.10).

### 6.3.6 Satellite Remote Sensing

Satellite retrievals of surface *chl-a* from orbital ocean color missions are increasingly useful for Chesapeake Bay (Magnuson et al. 2004, Harding et al. 2005, Acker et al. 2005). Recent advances stem from a detailed analysis of algorithm performance in the Bay, using ocean color data from SeaWiFS and in-situ observations from CBP monitoring cruises (Werdell et al. 2007). Both radiance-ratio and

semi-analytical algorithms are effective to capture seasonal and regional distributions of surface *chl-a* in the mid- to lower Bay, whereas accuracy in the upper Bay remains problematic due to high concentrations of chromophoric dissolved organic matter (CDOM) and suspended particulate material (SPM). There are several advantages to using a satellite system for environmental monitoring if current technological and logistical difficulties can be overcome. Sun-synchronous orbiting satellites such as SeaWiFS and MODIS provide 100–120 cloud-free images per year for the Bay region, have fewer day-to-day operational considerations, and cover a much broader region that includes the adjacent coastal ocean. Limitations of the current generation of satellite sensors include pixels that are too large for relatively small bays and rivers, atmospheric correction that cannot rely on assumptions used in the open ocean, and complex and non co-varying absorption and scattering properties that require local, empirically derived algorithms for most products (Magnuson et al. 2004, Harding et al. 2005). NASA's Ocean Biology Processing Group is addressing this last issue by comparing surface *chl-a* retrievals from nine different ocean color algorithms to ground truth data collected in the Bay (Werdell et al. 2007).

## 6.4 Discussion

Since the beginning of airborne remote sensing in Chesapeake Bay nearly two decades ago, we have improved spatial and temporal resolution of surface *chl-a*, significantly adding to our understanding of phytoplankton dynamics previously based on shipboard observations alone. Our focus has been on two pivotal periods in the annual phytoplankton cycle – the spring diatom bloom that accounts for the annual biomass peak, and spring-summer dinoflagellate outbreaks that often attain 'red tide' proportions – while collecting data at other times of year to give annual coverage. Surface *chl-a* and derived products have been obtained at much finer resolution than previously accomplished for an estuary by flying ocean color instruments at a frequency of up to twice per week, collecting data at a spatial resolution of 10s of meters along regular flight tracks. Images derived from a sequence of flights in spring 2000 exemplify products we have attained for >400 dates between 1989 and 2007 (Fig. 6.2). The assembled data and images constitute a 'climatology' of remotely-sensed surface *chl-a* that has been used in conjunction with in-situ observations to describe the links of freshwater flow and nutrient loading to variability of phytoplankton biomass (cf. Harding 1994, Harding et al. 1994).

Small-scale variability of surface *chl-a* observed using airborne remote sensing falls outside the sampling capabilities of shipboard monitoring, even by a concerted long-term effort such as the CBP monitoring cruises. Each CBRSP flight generates 1000s of observations in a single day, whereas monitoring requires two ships, occupies 49 main stem Bay stations, and occurs at a monthly frequency. Lateral variability of surface *chl-a* detailed by Weiss et al. (1997) using ODAS data points out the effectiveness of airborne remote sensing to quantify gradients on scales of 10s of meters to kilometers. We analyzed surface *chl-a* for a series of flight tracks normal

to the main axis of the Bay, showing high spatial variability that was most apparent during phytoplankton blooms with high surface *chl-a*. Strong gradients observed using ODAS data consisted predominantly of west-to-east decreases of surface *chl-a*, occurring commonly in spring and summer. Axial and lateral transects from more recent flights using SAS III show strong gradients of surface *chl-a* consistent with those earlier findings on small-scale variability (Fig. 6.3).

One of the unmatched strengths of airborne remote sensing in Chesapeake Bay is resolving patchiness of surface *chl-a*. We found the magnitude of axial and lateral variability of surface *chl-a* is comparable to Bay-wide variability, thus infrequent sampling that does not address small-scale variability misses important information about phytoplankton dynamics, such as the timing, position, and magnitude of blooms. This limitation applies to harmful algal blooms (HABs) that are ephemeral and of limited spatial extent. We reached a similar conclusion earlier that shipboard sampling inadequately recovers information about high surface *chl-a* in the Bay (Harding et al. 1994, 1995), and it is increasingly evident that quantifying small-scale variability is essential to an accurate, complete characterization of phytoplankton dynamics in the Bay. We submit that airborne remote sensing generates data providing axial and lateral coverage of high spatial resolution that are appropriate to this need.

Climatic perturbations such as tropical storms and hurricanes force significant ecosystem responses that can be difficult or impossible to detect using shipboard measurements. Our research on Hurricane Isabel in Chesapeake Bay represents an example of the superiority of airborne remote sensing to capture such responses (Fig. 6.4). N is usually limiting to phytoplankton growth by early fall in the mid- to lower Bay, leading to low phytoplankton biomass toward the mouth (Fisher et al. 1992). This observation is consistent with long-term data from shipboard and airborne sampling showing a strong gradient along the main stem axis with low surface *chl-a* ( $<5 \text{ mg m}^{-3}$ ) in southerly regions. Physical mixing of the Bay and the consequent delivery of N to the surface mixing layer by Hurricane Isabel led to an extensive fall bloom consisting of increased *chl-a*, a shift of floral composition to diatoms, and increased PP commensurate with increased phytoplankton biomass in a region usually characterized by seasonally low surface *chl-a* (Miller et al. 2006a).

Despite covering  $3232 \text{ km}^2$ , this unprecedented fall bloom would probably have gone undetected by shipboard monitoring as it formed and dissipated rapidly. The ability to undertake airborne remote sensing soon after Isabel provided a unique data set bracketing this major climatic perturbation. Miller et al. (2006a) reconciled N input associated with physical mixing with the *chl-a* increase. We estimated the 61.9 tons of *chl-a* that developed in the bloom area would require  $192 \text{ mg N m}^{-2}$ , assuming N: *chl-a* (w/w) = 10 (Malone 1992). CBP monitoring cruises determined vertical profiles of dissolved inorganic nitrogen (DIN) and a  $Z_p$  of 3.8 m for the northern half of the bloom region ( $<37.9^\circ\text{N}$ ). These data were used to compute N supplied to the euphotic layer by mixing of the water column as  $387 \text{ mg N m}^{-2}$ , more than sufficient N to support the increase of *chl-a* we observed. The use of airborne remote sensing to detect phytoplankton responses to Hurricane Isabel draws on the unique capabilities of aircraft to give high-resolution, quasi-synoptic coverage of estuarine



and coastal waters. These findings have implications for detecting event-scale climatic forcing using sustained, long-term observations of key ecosystem variables.

Data from airborne remote sensing contribute to our understanding of seasonal and interannual variability of phytoplankton dynamics, allowing us to link processes in the Bay's extensive 165,000 km<sup>2</sup> watershed to those in receiving waters of the estuary proper. Our findings are consistent with earlier work on the effects of freshwater flow, nutrient loading, and turbidity (cf. Malone 1992), but draw on data of unmatched spatial and temporal resolution to explicitly relate climatic forcing to ecosystem responses. Recent analyses of shipboard observations show that freshwater flow and attendant properties, such as nutrient loading and light attenuation, exert coincident effects on phytoplankton biomass, floral composition, and PP, suggesting that climatic forcing significantly controls these properties (cf. Adolf et al. 2006). The link of climate to phytoplankton dynamics suggested by detailed statistical analyses of shipboard data has been extended recently by applying a synoptic climatology to identify, categorize, and quantify regional climate patterns (Fig. 6.5). An analysis of data from airborne remote sensing by Miller and Harding (2007) shows predominantly warm/wet or cool/dry climate patterns affect the position and magnitude of the surface *chl-a* maximum during spring (Fig. 6.6). Several derived measures of phytoplankton biomass for spring are also responsive to climate, evident in regional distributions (Fig. 6.7) and deviations from the LTA (Fig. 6.8) for contrasting climate modes. Integrated biomass of the spring bloom expressed as metric tons of *chl-a* using data from airborne remote sensing is also responsive to climatic forcing. Total *chl-a* during warm/wet years peaked at ~717 metric tons in late May, significantly higher ( $p < 0.01$ ) than the LTA of 455 metric tons. A broad maximum of total *chl-a* of 383–445 metric tons during April–May occurs in cool/dry years, significantly lower ( $p < 0.05$ ) than the LTA. Intensity of the spring bloom expressed as total *chl-a* averages 276 metric tons higher in warm/wet than in cool/dry years, documenting climatic forcing of the production of organic material during spring.

The annual pattern of PP in the Bay resolved with data from airborne remote sensing is essentially consistent with shipboard observations from >80 cruises spanning 1982–2004 (Harding et al. 2002). Both sources of data show a spring maximum of euphotic-layer *chl-a* displaced from a summer maximum of PP, consistent with the previous description by Malone (1992). A limitation of shipboard data that is overcome by analyses based on airborne remote sensing is increased spatial and temporal resolution. Shipboard data on PP we have collected give only seasonal coverage and computations of AIP are thereby based on a few measurements spaced over the year, supporting the textbook pattern of PP and euphotic-layer *chl-a* we developed by compiling data spanning many years (Fig. 6.9a; cf. Harding et al. 2002). Recent analyses based on data from airborne remote sensing reveal attributes of the annual cycle of PP that are not apparent in shipboard data alone. AIP derived from a combination of remotely sensed data and models shows two-fold interannual variability not resolved with computations based on seasonal cruises (Fig. 6.9b). These data also identify a significant correlation between AIP and euphotic-layer *chl-a* (Miller 2006) that has pragmatic applications beyond the study of phytoplankton dynamics.

One such application is the use of PP data from airborne remote sensing to address recruitment variability of young-of-year (YOY) Atlantic menhaden, an important commercial fishery in the U.S. that has shown recent declines. AIP computed using time-series of PP (1989–2005) from airborne remote sensing and models (Harding et al. 2002) allows us to relate interannual variability of recruitment to AIP and *chl-a* using highly resolved data instead of those from sparse cruises. These analyses show significant correlations of YOY menhaden to AIP and euphotic-layer *chl-a*, suggesting a strong role of ‘bottom-up’ control in recruitment. These data have also proven effective in developing a bioenergetics model for menhaden, adapting the methods of Hewitt and Johnson (1992) to evaluate mechanistic links of PP to menhaden recruitment and growth (Annis et al. in prep). We tailor the model to use *chl-a* from airborne remote sensing as an input, and derive estimates of the growth potential for YOY menhaden based on water temperature and physiological parameters defined in previous laboratory studies (Rippeto 1993). This application supports derivations of growth curves for Atlantic menhaden that are specific to *chl-a* and temperature conditions for individual years. These estimates are subsequently compared to YOY menhaden collected on trawl surveys, providing a unique opportunity to calibrate model outputs to field observations.

A recently developed hydrodynamic-biogeochemical model of the Bay is also benefiting from the use of data from airborne remote sensing. The coupled three-dimensional model is based on the Regional Ocean Modeling System (ROMS), using a biogeochemical model adapted from a five-component plankton model. Data from airborne remote sensing are used to validate the coupled model, showing that it captures observed seasonal and regional distributions of plankton in the Bay and predicts the phase lag between the spring *chl-a* maximum and peak summer PP. Quantitative comparisons between predicted and observed annual time series of euphotic-layer *chl-a* and PP show the model has good predictive capability with regression coefficients and skill scores falling in the range 0.5–0.9. Sensitivity analysis of model simulations for different parameter values and alternative formulations of biogeochemical processes suggest that model predictions are robust, with outputs for annual-mean euphotic-layer *chl-a* within 30% of  $27.2 \text{ mg m}^{-2}$ , and AIP within 15% of  $246 \text{ g C m}^{-2} \text{ yr}^{-1}$ .

The success of airborne remote sensing in Chesapeake Bay is strong evidence of the usefulness of this approach to collect data on phytoplankton dynamics in estuarine and coastal waters. Applications of the data are many and varied, as described herein, and are especially relevant to support evaluations of ecosystem state and trajectory. Increased spatial and temporal resolution of key ecosystem properties, including phytoplankton biomass and productivity, is essential as we embark on setting numerical criteria as mandated goals for water quality improvement. Such efforts are well underway as a partnership of scientists and managers in the Bay. But to develop and apply indicators of ecosystem health that express responses at the primary producer level broadly, the singular success with this one estuary must be extended to other systems, building data sets of sufficient spatial and temporal resolution to detect trends.

## 6.5 Conclusions

Metrics of phytoplankton *chl-a* clearly integrate the effects of watershed activities that result from nutrient overenrichment of estuarine and coastal ecosystems. High spatial and temporal variability of *chl-a* and PP in estuaries, however, makes it essential to use new technologies to assess secular changes and separate them from signals of lesser duration related to short-term forcing. CBRSP provides a unique data source for the nation's largest estuary, generating highly resolved *chl-a* and PP data unattained previously. These data support progress in detailing the role of freshwater flow/climate in regulating phytoplankton dynamics. The ecosystem-scale measurements of *chl-a* and PP we acquire are at sufficiently fine spatial scales and temporal frequency to serve as proximal indicators of nutrient loading for charting the state and trajectory of water quality in the Bay. The combination of remotely sensed and in-situ data reflects valuable sampling partnerships that enable us to validate products derived from long-term ocean color measurements for waters of complex optical properties.

## References

- Acker JG, Harding LW, Leptoukh G, Zhu T, Shen S (2005) Remotely-sensed chl a at the Chesapeake Bay mouth is correlated with annual freshwater flow to Chesapeake Bay. *Geophys Res Lett* 32:L05601, doi:10.1029/2004GL021852
- Adolf JE, Yeager CL, Miller WD, Mallonee ME, Harding LW (2006) Environmental forcing of phytoplankton floral composition, biomass, and primary productivity in Chesapeake Bay, USA. *Estuar Coast Shelf Sci* 67:108–122
- Annis E, Houde ED, Harding LW Bioenergetics model of the mechanistic linkages between primary production and the recruitment and growth of Atlantic menhaden. (In preparation)
- Behrenfeld MJ, Falkowski PG (1997) Photosynthetic rates derived from satellite-based chlorophyll concentration. *Limnol Oceanogr* 42:1–20
- Boynton WR, Boicourt W, Brandt S, Hagy J, Harding L, Houde E, Holliday DV, Jech M, Kemp WM, Lascara C, Leach SD, Madden AP, Roman M, Sanford L, Smith EM (1997) Interactions between physics and biology in the estuarine turbidity maximum (ETM) of Chesapeake Bay, USA. International Council for the Exploration of the Sea, CM 1997/S:11
- Boynton WR, Garber JH, Summers R, Kemp WM (1995) Inputs, transformations, and transport of nitrogen and phosphorus in Chesapeake Bay and selected tributaries. *Estuaries* 18:285–314
- Bricker SB, Clement CG, Pirhalla DE, Orlando SP, Farrow DRG (1999) Effects of nutrient enrichment in the nation's estuaries: national estuarine eutrophication assessment. NOAA, Silver Spring, Maryland
- Campbell JW, Esaias WE (1983) Basis for spectral curvature algorithms in remote sensing of chlorophyll. *Appl Optics* 22:1084–1093
- Cooper SR, Brush GS (1991) Long-term history of Chesapeake Bay anoxia. *Science* 254:992–996
- Correll DW (1987) Nutrients in Chesapeake Bay. In: Majumdar SK, Hall LW, Austin HM (eds) Contaminant problems and management of living Chesapeake Bay resources. Pennsylvania Academy of Science, Philadelphia, Pennsylvania, pp 298–320
- Curtin PD, Brush GS, Fisher GW (eds) (2001) *Discovering the Chesapeake: The history of an ecosystem*. Johns Hopkins University Press, Baltimore, Maryland
- Davis A, Yan X-H (2004) Hurricane forcing on chlorophyll-a concentration off the northeast coast of the U.S. *Geophys Res Lett* 31:L17304, doi:10.1029/2004GL020668

- D'Elia CF, Sanders JG, Boynton WR (1986) Nutrient enrichment studies in a coastal plain estuary: phytoplankton growth in large-scale, continuous cultures. *Can J Fish Aquat Sci* 43:397–406
- Fisher TR, Peele ER, Ammerman JW, Harding LW (1992) Nutrient limitation of phytoplankton in Chesapeake Bay. *Mar Ecol Prog Ser* 82:51–63
- Grew GW (1981) Real-time test of MOCS algorithm during Superflux 1980. NASA Pub CP\_2188:301
- Hagy JD, Boynton WR, Wood CW, Wood KV (2004) Hypoxia in Chesapeake Bay, 1950–2001: long-term changes in relation to nutrient loading and river flow. *Estuaries* 27:634–658
- Harding LW (1994) Long-term trends in the distribution of phytoplankton in Chesapeake Bay: roles of light, nutrients and streamflow. *Mar Ecol Prog Ser* 104:267–291
- Harding LW, Itsweire EC (1991) Synoptic measurements of the distribution of chlorophyll in the Chesapeake Bay using aircraft remote sensing. In: Mihursky JA, Chaney A (eds) *New perspectives in the Chesapeake system: a research and management partnership*. Chesapeake Research Consortium, Baltimore, Maryland, pp 147–160
- Harding LW, Itsweire EC, Esaias WE (1992) Determination of phytoplankton chlorophyll concentrations in the Chesapeake Bay using aircraft remote sensing. *Remote Sens Environ* 40:79–100
- Harding LW, Itsweire EC, Esaias WE (1994) Estimates of phytoplankton biomass in the Chesapeake Bay from aircraft remote sensing of chlorophyll concentrations. *Remote Sens Environ* 49:41–56
- Harding LW, Itsweire EC, Esaias WE (1995) Algorithm development for recovering chlorophyll concentrations in the Chesapeake Bay using aircraft remote sensing, 1989–1991. *Photogramm Eng Rem S* 61:177–185
- Harding LW, Magnuson A, Mallonee ME (2005) SeaWiFS retrievals of chlorophyll in Chesapeake Bay and the mid-Atlantic bight. *Estuar Coast Shelf S* 62:75–94
- Harding LW, Mallonee ME, Perry ES (2002) Toward a predictive understanding of primary productivity in a temperate, partially stratified estuary. *Estuar Coast Shelf S* 55:437–463
- Harding LW, Miller WD, Swift RN, Wright CW (2001) Aircraft remote sensing. In: Steele JH, Thorpe SA, Turekian KK (eds) *Encyclopedia of ocean sciences*. Academic Press, London, pp 113–122
- Harding LW, Perry ES (1997) Long-term increase of phytoplankton biomass in Chesapeake Bay, 1950–1994. *Mar Ecol Prog Ser* 157:39–52
- Hewitt SW, Johnson BL (1992) A generalized bioenergetics model of fish growth for microcomputers. University of Wisconsin Sea Grant Institute, Madison, Wisconsin. UW Sea Grant Tech. Rep. WIS-SG-92-250
- Itsweire EC, Harding LW, Bahner LH (1991) Comparison of phytoplankton biomass estimates for the Chesapeake Bay using aircraft remote sensing and in-situ chlorophyll data. In: Mihursky JA, Chaney A (eds) *New perspectives in the Chesapeake system: a research and management partnership*. Chesapeake Research Consortium, Baltimore, Maryland, pp 161–168
- Kemp WM, Boynton WR, Adolf JE, Boesch DF, Boicourt WC, Brush G, Cornwell JC, Fisher TR, Glibert PM, Hagy JD, Harding LW, Houde ED, Kimmel DG, Miller WD, Newell REI, Roman MR, Smith EM, Stevenson JC (2005) Eutrophication of Chesapeake Bay: historical trends and ecological interactions. *Mar Ecol Prog Ser* 303:1–29
- Li M, Zhong L, Boicourt WC, Zhang S, Zhang D (2006) Hurricane induced storm surges, currents, and destratification in a semi-enclosed Bay. *Geophys Res Lett* 33:L02604, doi:10.1029/2005GL024992
- Magnuson A, Harding LW, Mallonee ME, Adolf JE (2004) Bio-optical model for Chesapeake Bay and the Middle Atlantic Bight. *Estuar Coast Shelf S* 61:403–424
- Malone TC (1992) Effects of water column processes on dissolved oxygen: nutrients, phytoplankton and zooplankton. In: Smith D, Leffler M, Mackiernan G (eds) *Oxygen dynamics in Chesapeake Bay: a synthesis of research*. Maryland Sea Grant, College Park, pp 61–112
- Malone TC, Conley DJ, Fisher TR, Glibert PM, Harding LW, Sellner KG (1996) Scales of nutrient-limited phytoplankton productivity in Chesapeake Bay. *Estuaries* 19:371–385
- Miller WD (2006) Climate forcing of phytoplankton dynamics in Chesapeake Bay. PhD dissertation, University of Maryland, College Park

- Miller WD, Harding LW (2007) Climate forcing of the spring bloom in Chesapeake Bay. *Mar Ecol Prog Ser* 331:11–22
- Miller WD, Harding LW, Adolf JE (2006a) Hurricane Isabel generated an unusual fall bloom in Chesapeake Bay. *Geophys Res Lett* 33:L06612, doi:10.1029/2005GL025658
- Miller WD, Kimmel DG, Harding LW (2006b) Predicting spring discharge of the Sus-quehanna River from a synoptic climatology for the eastern United States. *Water Resour Res* 42:W05414, doi:10.1029/2005WR004270
- Officer CB, Biggs RB, Taft JL, Cronin LE, Tyler MA, Boynton WR (1984) Chesapeake Bay anoxia: origin, development and significance. *Science* 223:22–27
- Orth RJ, Moore KA (1983) Chesapeake Bay: an unprecedented decline in submerged aquatic vegetation. *Science* 222:51–53
- Paerl HW, Bales JD, Ausley LW, Buzzelli CP, Crowder LB, Eby LA, Fear JM, Go M, Peierls BL, Richardson TL, Ramus JS (2001) Ecosystem impacts of three sequential hurricanes (Dennis, Floyd, and Irene) on the United States' largest lagoonal estuary, Pamlico Sound, NC. *Proc Natl Acad Sci USA* 98:5655–5660
- Richkus WA, Austin HM, Nelson SJ (1992) Fisheries assessment and management synthesis: lessons for Chesapeake Bay. In: perspectives on Chesapeake Bay, 1992: advances in estuarine sciences. Chesapeake Bay Program, Chesapeake Research Consortium, Baltimore, pp 75–114
- Rippetoe TH (1993) Production and energetics of Atlantic menhaden in Chesapeake Bay. Master thesis, University of Maryland, College Park, Maryland
- Rothschild BJ, Ault JS, Gouletquer P, Heral M (1994) Decline of the Chesapeake Bay oyster population: a century of habitat destruction and overfishing. *Mar Ecol Prog Ser* 111:29–39
- Weiss GM, Harding LW, Itsweire EC, Campbell JC (1997) Assessing lateral variations of surface chlorophyll concentrations in the Chesapeake Bay using aircraft remote sensing. *Mar Ecol Prog Ser* 149:183–199
- Werdell JP, Franz BA, Bailey SW, Harding LW, Feldman GC (2007) Approach for the long-term spatial and temporal evaluation of ocean color satellite data products in a coastal environment. *Proc SPIE*.
- Zubkoff PL, Warinner III JE (1977) The effect of Tropical Storm Agnes as reflected in chlorophyll a and heterotrophic potential of the lower Chesapeake Bay. In: Davis J, Laird B (eds) The effects of tropical storm agnes on the Chesapeake Bay estuarine system. The Johns Hopkins University Press, Baltimore, pp 368–387

## Chapter 7

# Bio-Optical Characteristics and Remote Sensing in the Mid Chesapeake Bay Through Integration of Observations and Radiative Transfer Closure

Maria Tzortziou, Charles L. Gallegos, Patrick J. Neale, Ajit Subramaniam, Jay R. Herman and Lawrence W. Harding, Jr.

Remotely sensed ocean color is an essential tool for studying water quality and biogeochemical processes, and applying results for coastal ecosystem assessment and management. Successful interpretation and application of remote sensing data depends to a large extent on the accuracy of, and consistency among, the in-situ data used in the calibration and validation of satellite measurements and in algorithm development. Thus, the degree of closure among bio-optical quantities independently measured in the field becomes critical for remote sensing applications. Optical closure results can be used to identify sources of errors associated with different measurement methodologies, investigate uncertainties in relations between inherent and apparent optical properties used in bio-optical models, and examine the relative importance of certain processes in determining ocean color. Here, we discuss how remote sensing of water quality in optically complex environments can be improved by integrating optical measurements and radiative-transfer model calculations. This approach is illustrated with recent findings on the bio-optical characteristics of Chesapeake Bay waters, including measurements of the magnitude and spectral characteristics of particulate backscattering. We then discuss progress on optical closure studies in coastal regions and propose bio-optical relations for remote sensing retrieval of water quality indicators in the Chesapeake Bay ecosystem.

### 7.1 Remote Sensing of Ocean Color in the Chesapeake Bay: Progress and Challenges

The Chesapeake Bay is the largest estuary in the U.S. with about 150 rivers and streams draining into the Bay. Its drainage basin is 166,000 km<sup>2</sup> in area, supports more than 3,000 species of plants, fish and animals, and has over 15 million people living nearby. In addition to its great socio-economic significance, Chesapeake

---

M. Tzortziou (✉)

Earth System Science Interdisciplinary Center, University of Maryland, College Park, MD 20740, USA

e-mail: Maria.A.Tzortziou@nasa.gov

Bay has significant commercial, recreational, and national security value directly related to the productivity and quality of its water. In recent years the water quality of the Chesapeake Bay has suffered as a consequence of growing human activity on the surrounding land and from excessive fishing in the bay. Nutrients entering the bay from agricultural runoff and inadequate sewage treatment often cause extensive phytoplankton blooms, leading to increased biological oxygen demand and reduced light penetration into the water column. Depleted fisheries, resulting from excess removals, increased pollution, and loss of submerged aquatic vegetation (SAV), associated with reduced water clarity, are major problems in these waters (e.g. Boesch 2000).

Improving the Bay's water quality has been a primary objective of management agencies for several decades. Because the composition and concentrations of water constituents (e.g. dissolved organic matter, phytoplankton and suspended sediments) influence the water optical characteristics, optical measurements can be applied to monitor changes in water quality in the Bay (e.g. Glibert et al. 1995, Harding et al. 2004, Gallegos and Bergstrom 2005). Monitoring methods that include aircraft, satellite, and in situ optical instruments are being used to assess ecosystem state and detect changes in response to management actions (Harding et al. 2004). Recently, our ability to detect these changes has been augmented by technological advances in optical sensors and radiative transfer modeling techniques. Here, we discuss how remote sensing of water quality in this optically complex environment can be improved by integrating optical measurements and radiative transfer calculations. This approach is illustrated with recent findings on the bio-optical characteristics of the middle region of the Chesapeake Bay.

Incorporating new techniques with in situ and remotely-sensed measurements into the Chesapeake Bay monitoring activities is challenging, but also a critical step for taking advantage of the strengths offered by the different approaches (e.g. Boesch 2000, Harding et al. 2004). In situ measurements of optical properties, as well as physical, chemical, and biological indicators of the Bay's health, have been performed by several ship-based programs during the last decades. By providing observations at high spatial resolution and information on diurnal changes or vertical distribution of water constituents, these field efforts have resulted in an extensive monitoring network that has evolved to provide important information for sustainable management of the Chesapeake Bay natural resources. Yet, the spatial and temporal coverage of in situ measurements is often insufficient for resolving important estuarine processes. Because in situ measurements are essentially point observations, tides and advection can further complicate their interpretation.

Remote sensing of ocean color, using airborne or satellite sensors, offers the capability of extending field observations beyond the restricted in situ sampling domain. Aircraft surveys provide surface maps at high spatial (less than 1 m) and spectral (up to 256 channels in the visible) resolution. Since aircrafts can be flown under clouds, they can provide data even on cloudy days. The Chesapeake Bay is probably the best-studied water body in the world using aircraft remote sensing, with over 300 flights flown between 1989 and 2002 (e.g. Hoge and Swift 1981, Harding et al. 1994, Lobitz et al. 1998). However, aircraft surveys, similar to shipboard surveys,

are expensive to conduct, and only apply to the region within the flight range of the aircraft. Satellite remote sensing provides nearly daily coverage over all coastal regions using a common instrument with a single calibration. However, current ocean-color satellite sensors have a spatial resolution of about 1 km at nadir view (satellite directly overhead). Moreover, the sensor cannot 'see' through clouds, effectively reducing the amount of available data in a particular region. To derive water optical properties from remote sensing requires the determination of the fraction of the total backscattered signal that originates from within the water by removing the atmospheric component and that resulting from surface Fresnel reflection. Determining these corrections to derive accurate estimates of the water leaving radiances is a major issue for remote sensing of near-shore waters. The atmosphere over such water bodies is heavily influenced by rapidly changing atmospheric pollution from natural and anthropogenic input, and is more complex than the relatively homogenous atmosphere over open oceans. Accounting for absorbing aerosols, ozone,  $\text{NO}_2$ , and other pollutants that change rapidly with time and space (e.g. Ahmad et al. 2007) may require more complicated atmospheric correction schemes than the static climatologic look up tables used for open ocean conditions. Despite these difficulties, satellite remote sensing of ocean color is an extremely valuable tool that complements traditional ship and aircraft surveys with synoptic monitoring of surface coastal waters at temporal and spatial scales unattainable with field measurements alone (Dickey et al. 2006).

Ocean remote sensing reflectance,  $R_{rs}$ , is related to backscattering, the scattering of light in the opposite direction of the incident light, and absorption, the conversion of photons to heat or chemical energy. In order to use satellite measurements of ocean color to extract information on water composition it is necessary to develop bio-optical algorithms relating  $R_{rs}$  either directly to the surface concentrations of optically significant water constituents (empirical algorithms; e.g. Clark 1997, O'Reilly et al. 2000), or to their optical properties based on principles derived from radiative transfer theory (semi-analytical inversion models; e.g. Garver and Siegel 1997, Maritorena et al. 2002). Since the launch of the Coastal Zone Color Scanner (CZCS) in October 1978, satellite ocean color observations have contributed significantly to gaining a better understanding of biological activity in open-ocean 'Case 1' waters where phytoplankton chlorophyll-*a* (chl-*a*) pigments and co-varying material are the major optical components (e.g. Yentsch 1993, Longhurst et al. 1995, Gregg and Conkright 2001). With more channels in the visible part of the spectrum, CZCS's follow-on sensor SeaWiFS (Sea-viewing Wide Field of view Sensor, launched in 1997) and newer instruments, including MODIS (MODerate resolution Imaging Spectroradiometer, launched in 1999) and MERIS (MEDium Resolution Imaging Spectrometer, launched in 2002), allowed for further improvements in satellite retrievals of biogeochemical variables in Case 1 waters (e.g. Yoder and Kennelly 2003, Carder et al. 2004, McClain et al. 2004, Curran and Steele 2005). A more difficult challenge, however, has been developing bio-optical algorithms suitable for use in optically complex 'Case 2' waters, such as the Chesapeake Bay, where multiple, independently varying, dissolved and particulate, marine- and terrestrially-derived substances affect ocean color (e.g. Morel and



Prieur 1977, Ruddick et al. 2001, Binding et al. 2003, Hu et al. 2003, Darecki and Stramski 2004, Dall'Olmo et al. 2005).

Harding et al. (2005) examined the applicability of the SeaWiFS chl-*a* empirical algorithm OC4v4, a model relating variability in blue-green  $R_{rs}$  ratios to chl-*a* changes (O'Reilly et al. 2000), for the Chesapeake. They found that SeaWiFS reliably captured seasonal and inter-annual variability of phytoplankton biomass in the lower Bay. However, the OC4v4 algorithm significantly overestimated chl-*a* in the upper Bay due to strong absorption by non-covarying dissolved organic matter and non-algal particles that are not sufficiently accounted for in this empirical algorithm. Magnuson et al. (2004) used an extensive set of bio-optical data to parameterize the semi-analytical Garver-Siegel-Maritorena (GSM01) model (Maritorena et al. 2002) for the Chesapeake Bay and the adjacent Middle Atlantic Bight waters (model version GSM01-CB). The GSM01 model allows for independent variation of several sources of absorption and backscatter and uses multiple SeaWiFS wavebands in the 412–670 nm spectral region. However, the lack of sufficient measurements of backscattering,  $b_b$ , for Bay waters affected backscattering parameterizations in the GSM01-CB model and limited the authors' ability to evaluate the model's backscattering product (Magnuson et al. 2004). Zawada et al. (2007) used a spectra-matching optimization algorithm (Lee et al. 1999, Hu et al. 2003) to estimate  $b_b$  in the Bay from SeaWiFS data. In this case too, validation of the satellite  $b_b$  estimates was hindered by the lack of in situ  $b_b$  measurements.

These studies underscore the need to improve our understanding on how certain optical properties (e.g. particulate backscattering) affect remotely sensed quantities in the Chesapeake Bay, and develop more accurate algorithms for these Case 2 waters based on detailed in situ bio-optical characteristics. Development of effective coastal bio-optical algorithms and validation of remote sensing observations using in situ bio-optical data require testing the accuracy of the data and the consistency, or 'optical closure', among the independently measured quantities. Demonstration of optical closure involves solution of the equations of radiative transfer using measured boundary conditions (e.g. downwelling surface radiance,  $E_s(\lambda)$ ) inherent optical properties (IOPs), such as absorption ( $a(\lambda)$ ) and scattering ( $b(\lambda)$ ), and concentrations of in-water constituents, to predict apparent optical properties (AOPs), such as downwelling in-water irradiance ( $E_d(\lambda, z)$ ) or above-water remote sensing reflectance  $R_{rs}(\lambda)$ . Closure is obtained to the extent that model predictions match independent measurements (schematic illustration shown in Fig. 7.1). Optical closure results can be used to investigate errors in measurement methodology and uncertainties in relations between IOPs and AOPs used in bio-optical models, as well as examine the relative importance of several bio-optical properties in determining coastal ocean color (Tzortziou et al. 2006).

In the following sections, we present some recent findings on the bio-optical characteristics of Chesapeake Bay waters, including direct measurements of the magnitude, variability and spectral characteristics of particulate backscattering. We then discuss progress on optical closure studies in coastal regions and propose bio-optical relations for remote sensing retrieval of water quality indicators in the Chesapeake Bay estuarine ecosystem.

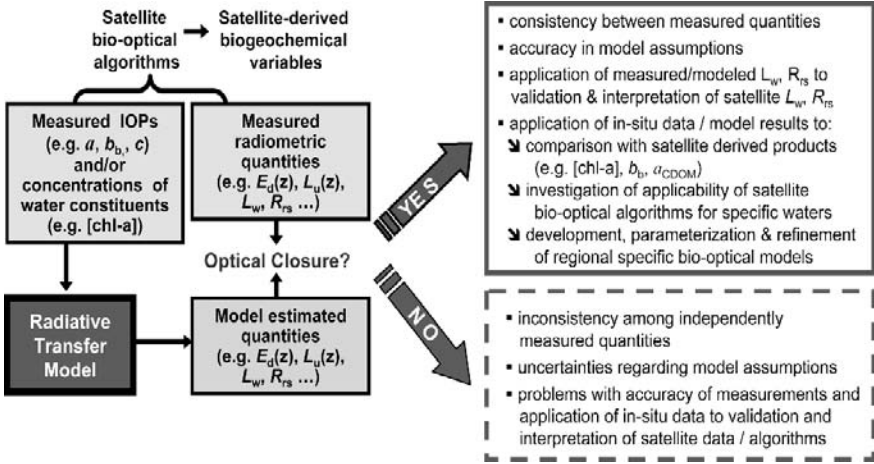
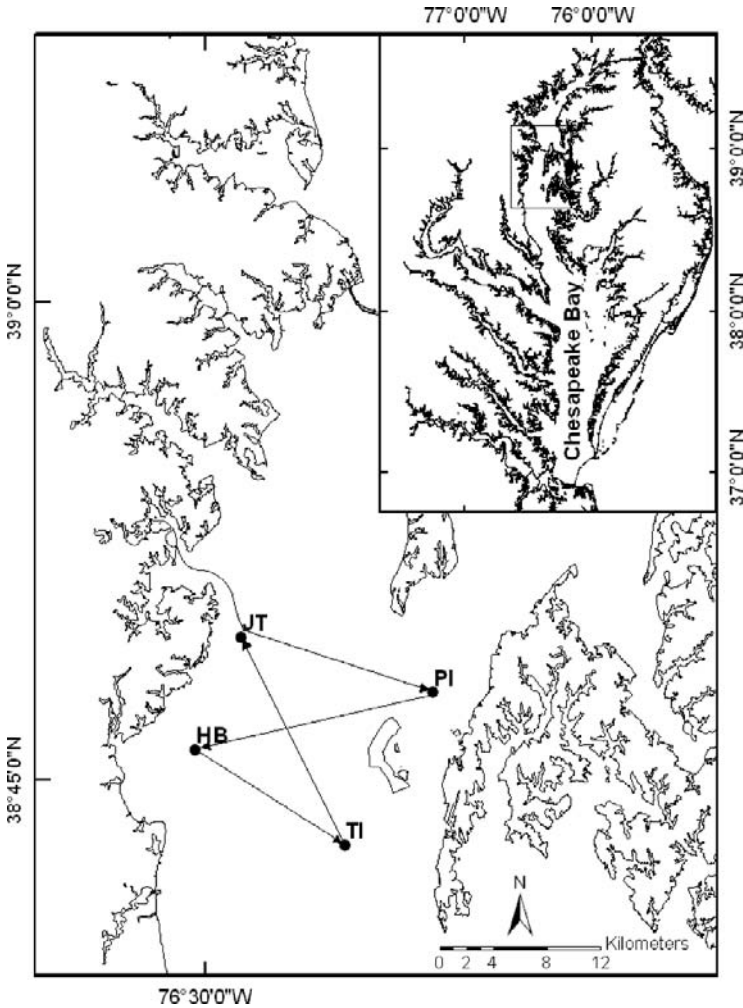


Fig. 7.1 Radiative transfer closure and its role in the interpretation of remote sensing ocean color observations

## 7.2 Bio-Optical Characteristics of the Chesapeake Bay

In the Chesapeake Bay, phytoplankton biomass and primary productivity, nutrient concentrations, and distributions of suspended particles and dissolved organic substances are highly variable. Their strong temporal and spatial variability are mainly driven by seasonal changes in environmental conditions, freshwater inputs, frontal features and tides and lateral gradients driven by estuarine circulation (e.g. Hood et al. 1999, Harding et al. 2005, Adolf et al. 2006). The annual cycle of phytoplankton in Chesapeake Bay typically consists of a winter–spring diatom bloom characterized by high chl- $a$  concentrations and low primary productivity, followed by a summer maximum of picoplankton and flagellates coinciding with the annual primary productivity maximum (e.g. Malone et al. 1991, Malone 1992, Harding et al. 2002). The timing, position, and magnitude of the spring bloom are strongly influenced by freshwater flow (Malone et al. 1988, Harding et al. 1994, Harding et al. 2002), dominated by the Susquehanna River located at the northern head of the estuary. The summertime productivity is largely supported by regenerated nutrients derived from metabolism of the spring bloom to support high primary productivity (Malone 1992, Harding et al. 2005).

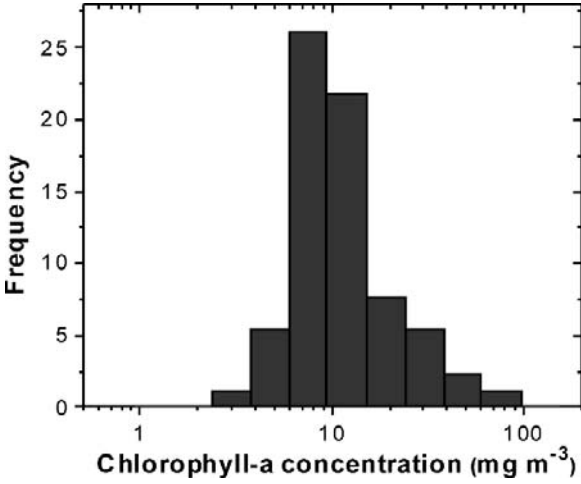
Consistent with studies in other areas of the Bay, measurements performed during 2001–2002 in a region of the mid Chesapeake Bay (Fig. 7.2) revealed a wide range of chl- $a$  concentrations, [chl- $a$ ], and water optical characteristics. Details on the methods for these measurements can be found in Tzortziou et al. (2006, 2007). Relatively clear waters were observed during the fall, with low biological activity and relatively low absorption, scattering, and [chl- $a$ ] values. Higher [chl- $a$ ] values, associated with large surface phytoplankton bloom events, were observed in spring



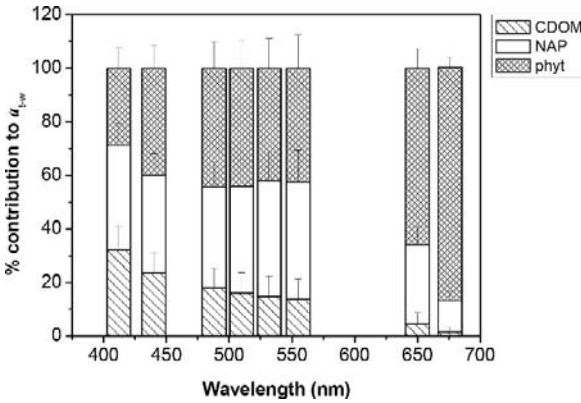
**Fig. 7.2** Location of in situ measurements (stations HB, PI, TI and JT) and a typical cruise track, for measurements performed in the mid Chesapeake Bay during 2001–2002 (from Tzortziou et al. 2006)

and summer (Tzortziou et al. 2007). Surface [chl-*a*] ranged from  $3.5 \text{ mg m}^{-3}$  to  $74 \text{ mg m}^{-3}$  with an average value of  $14.7 \text{ mg m}^{-3}$  (Fig. 7.3).

Colored dissolved organic matter (CDOM) and non-algal particles (NAP) in the Chesapeake Bay contribute considerably to light attenuation at blue-green wavelengths often used in satellite chl-*a* retrievals (Fig. 7.4). Combined contribution by CDOM and NAP to surface (0–1 m) total (minus pure water) absorption,  $a_{t-w}$ , was on average 61% at 532 nm and 59% at 488 nm in the mid Bay waters. Absorption by non-algal particles alone was as high as 56% and averaged 41% of  $a_{t-w}$  at 488 nm. Contribution by CDOM and NAP to surface  $a_{t-w}$  was even larger at shorter



**Fig. 7.3** Frequency histogram of surface [chl-*a*] ( $\text{mg m}^{-3}$ ) measured in the mid Chesapeake Bay, 2001–2002 (from Tzortziou et al. 2007)



**Fig. 7.4** Average percent contribution of CDOM ( $a_{\text{CDOM}}$ ) phytoplankton ( $a_{\text{phyt}}$ ) and NAP ( $a_{\text{NAP}}$ ) to surface total (minus pure water) absorption, along with the  $\pm 1$  standard deviation ( $n = 136$ ). Results are shown at wavelengths 412, 443, 488, 510, 532, 555, 650, and 676 nm

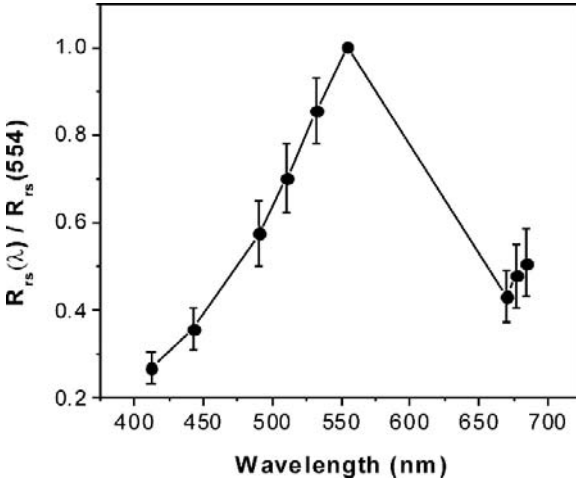
wavelengths (e.g. 73% at 412 nm) because of the exponential increase in the absorption of both substances with decreasing wavelength.

Although both CDOM and NAP absorption increase exponentially with decreasing wavelength, their absorption exponential spectral slopes,  $S$ , can be quite different. Tzortziou et al. (2007) reported an average value of  $0.018 \text{ nm}^{-1}$  for the  $S_{\text{CDOM}}$  in the mid Bay waters, and considerable variability ( $\text{SD} = 0.0032 \text{ nm}^{-1}$ ) among sampling dates and locations.  $S_{\text{NAP}}$  varied only slightly, having an average value of  $0.011 \text{ nm}^{-1}$  ( $\text{SD} = 0.001 \text{ nm}^{-1}$ ) (Tzortziou et al. 2007). Because of the many different sources of dissolved and particulate compounds in the Bay and the different processes affecting their quality, CDOM, NAP and phytoplankton amounts do not

covary (Magnuson et al. 2004). According to Tzortziou et al. (2007), estimated coefficients of determination ( $R^2$  values) in linear regressions between phytoplankton and CDOM, phytoplankton and NAP, and NAP and CDOM absorption at 440 nm were 0.01, 0.28 and 0.08, respectively. The observed non-covariation between CDOM and NAP and their largely different absorption spectral slopes complicate monitoring of these biogeochemically important water components using remote-sensing data, especially since most satellite Case 2 bio-optical algorithms combine CDOM and NAP into one term (e.g. Carder et al. 2002, Maritorena et al. 2002).

The number of measurements of particulate backscattering,  $b_{bp}$ , characteristics in coastal and estuarine waters has increased rapidly in recent years (Loisel et al. 2007, Snyder et al. 2008), but the implications of this in situ information for remote retrieval of particulate composition and distribution in Case 2 waters has not been fully explored. Tzortziou et al. 2007 observed high  $b_{bp}$  variability in the mid Chesapeake Bay, depending on particulate loading, distance from land and mixing processes. Surface  $b_{bp}$  at 530 nm ranged from 0.013 to 0.166  $m^{-1}$ . Higher  $b_{bp}$  values were observed consistently near station Jetta (JT), which is located closest to the land among the four sampling stations (Fig. 7.2) and is more strongly influenced by shoreline erosion and resuspension of bottom sediments due to tidal and land boundary effects. Considerable variation was also observed in the estimated particulate backscattering fraction (or backscattering probability), which is defined as the ratio of backscattering to total scattering by particles,  $b_{bp}/b_p$ . Backscattering fraction at 530 nm ranged from 0.006 to 0.036. Large values were measured close to the bottom, consistent with an increase in the proportion of resuspended inorganic sediments relative to organic particles with depth. In their measurements, performed in three optically distinctive coastal regions off the coast of New Jersey, in the Northern Gulf of Mexico and in Monterey Bay in California, Snyder et al. (2008) also observed high variability in the particulate backscattering fraction, with values at 550 nm in the range  $\sim 0.005$ – $0.06$ . The wavelength dependence they found for  $b_{bp}/b_p$  varied from site to site and within each site. Averaged over all depths at the four stations in the mid Chesapeake Bay,  $b_{bp}/b_p$  was 0.0128 (SD = 0.0032) at 530 nm (Tzortziou et al. 2007). These results for the Chesapeake Bay were in good agreement with  $b_{bp}/b_p$  values reported by Sydor and Arnone (1997) for the near shore waters off Mississippi. Spectral dependence of  $b_{bp}/b_p$  in Chesapeake Bay was weak, with average  $b_{bp}/b_p$  equal to 0.0133 (SD = 0.0032) at 450 nm and 0.0106 (SD = 0.0029) at 650 nm. This is in agreement with Mobley et al. (2002), who measured a decrease in the backscattering fraction from 442 to 555 nm by less than 24%, for the Case 2 waters offshore of New Jersey.

The large variability in water IOPs that characterizes the Chesapeake Bay results in large spatial and temporal variability in the magnitude of measured water leaving radiance,  $L_w$  (the upwelling radiance just above the water surface), and  $R_{rs}$ . However,  $R_{rs}$  spectra (and also  $L_w$  spectra) are similar in shape throughout the Bay (Fig. 7.2 in Magnuson et al. 2004), with maximum values typically occurring at green wavelengths (i.e. 554 nm, Fig. 7.5) because of the large pure-water absorption in the red and the large CDOM and NAP absorption in the blue region of the spectrum.



**Fig. 7.5** Average  $R_{rs}$  spectrum for the mid Chesapeake Bay waters, estimated after normalizing individual  $R_{rs}$  spectra to  $R_{rs}$  at 554 nm ( $N = 44$ ). Standard deviation is shown as y-error bars (from Tzortziou et al. 2007)

### 7.3 Role of Radiative Transfer Closure in Bio-Optical Modeling of Coastal Waters

Successful remote retrieval of biogeochemical variables in near-shore waters relies on accurate determination of the remotely sensed water reflectance, proper modeling of the underwater light field, and on establishing robust algorithms relating amounts of in-water constituents with water inherent and apparent optical properties based on in situ information. Thus, successful applications and understanding of coastal ocean color depend to a large extent on the accuracy of, and consistency among, the in situ data used in the calibration and validation of satellite measurements and in algorithm development. It is in this sense that the degree of closure between modeled and measured radiometric quantities is critical for remote sensing applications.

Radiative transfer modeling can be used to investigate errors in measurement methodology and uncertainties in relations between inherent and apparent optical properties used in bio-optical models (Fig. 7.1). It can also be applied to examine the relative importance of certain processes, such as CDOM and chl-*a* fluorescence, in determining coastal ocean color (e.g. Bulgarelli et al. 2003, Tzortziou et al. 2006). Through a closure experiment, it is possible to evaluate how uncertainties in the modeling of the atmosphere–water system affect computations of underwater radiance distributions used in the generation of look-up tables for remote-sensing applications. Bulgarelli et al. (2003) performed a closure experiment to quantify how uncertainties in measurements of IOPs and bottom reflectance translate into uncertainties in the numerical modeling of radiometric quantities in coastal waters. Chang et al. (2003) used optical closure to understand the errors associated with different in situ methods for the determination of  $R_{rs}(\lambda)$  in turbid coastal waters.

Three bio-optical properties, for which in-situ determinations are still rare in many coastal regions despite their importance in obtaining closure between measured IOPs and light fields, are: (i)  $b_{bp}$  and  $b_{bp}/b_p$  (e.g. Mobley et al. 2002); (ii) long wavelength ( $> 700\text{nm}$ ) non-algal particulate absorption (e.g. Babin and Stramski 2002, Tassan and Ferrari 2003); and (iii) contribution of solar-induced chl-*a* fluorescence to remotely-sensed water reflectance (e.g. Gower 1980, Maritorena et al. 2000). Inadequate characterization and uncertainties in the modeling of these processes for the Bay waters complicate retrievals of key environmental parameters from remote sensing data (e.g. Magnuson et al. 2004). Tzortziou et al. (2006) showed that an approach combining new in situ measurements of particulate backscattering and absorption with radiative transfer calculations can help address some of the bio-optical modeling challenges imposed by the optical complexities of the Chesapeake Bay waters.

### 7.3.1 Modeling of Backscattering Properties

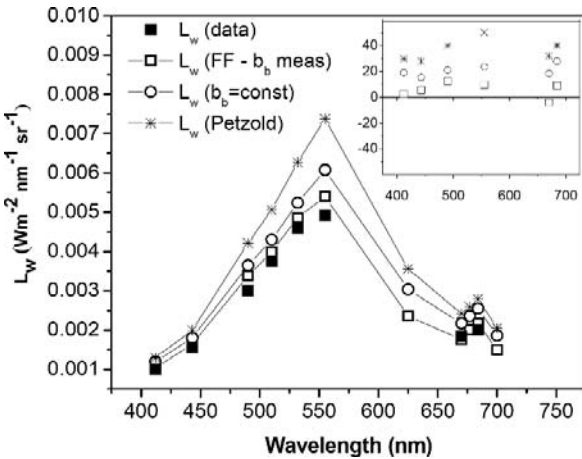
The remote sensing reflectance,  $R_{rs}$ , is, to a first approximation, proportional to the ratio of backscattering to the sum of backscattering and absorption [ $b_b/(a + b_b)$ ] (e.g. Morel and Prieur 1977). Thus, backscattering processes are of primary importance in determining the magnitude and spectral shape of water reflectance. However, measurements of particulate backscattering probability, magnitude and spectral shape, or of the volume scattering function, VSF, which describes the directional dependence of scattering, are still rare in estuarine and coastal environments (Snyder et al. 2008). As a result, modeling of backscattering processes in many studies has been largely based on a few existing datasets and assumptions regarding  $b_b/b$  variability. For example, the Petzold ‘average particle’ VSF (Petzold 1972), derived from three measurements of VSF in San Diego Harbor and with an estimated particulate backscattering fraction,  $b_{bp}/b_p$ , of  $\sim 0.018$ , has been widely assumed for modeling  $b_b$  in coastal areas. The scarcity of  $b_{bp}$  measurements in the mid Chesapeake Bay waters poses a significant limitation in the development of appropriate backscattering parameterizations for satellite algorithms, or the evaluation of satellite backscattering products (e.g. Magnuson et al. 2004, Zawada et al. 2007). Due to the lack of in situ information on  $b_b$ , Magnuson et al. (2004) parameterized the  $b_{bp}$  spectral shape in the GSM01-CB model based on literature values (e.g. Stramski and Kiefer 1991, Gould et al. 1999) and assuming zero wavelength dependence for  $b_{bp}$ . To evaluate the model performance, Magnuson et al. (2004) compared the model-derived  $b_{bp}$  coefficients to  $b_{bp}$  values estimated from particulate scattering,  $b_p$ , assuming a constant  $b_{bp}/b_p$  of 0.018 (from Petzold data). This approach resulted in an overestimation of  $b_{bp}$  compared to the  $b_{bp}$  product of the GSM01-CB model.

Tzortziou et al. (2006) applied detailed measurements of IOPs and radiometric quantities for the mid Chesapeake Bay waters to investigate the effect of the

choice of VSF and the importance of variability in  $b_b$  magnitude and spectral shape for accurate modeling of underwater light fields and water-leaving radiance,  $L_w$ , in these waters. Radiative transfer model simulations, performed using the extensively validated Hydrolight underwater radiative transfer program (Mobley 1988), showed that information on the spectral shape and vertical structure of  $b_{bp}/b_p$  is important when modeling backscattering processes. It was also shown that the Petzold ‘average particle’ assumption is usually not applicable for the Chesapeake Bay. Alternative formulations for backscattering processes were necessary for accurate bio-optical modeling in these waters.

Model calculations are shown here for an example data set when measured  $b_{bp}/b_p$  in the blue-green was close to 0.015. Use of a Petzold phase function in model simulations led to an underestimation of  $E_d(443)$  by  $\sim 20\%$  at 3–5 m depths compared to measurements. Upwelling radiance just below the water surface,  $L_u(0^-)$ , and  $L_w$  were overestimated by 30% at 443 nm and by 30–50% in the 550–650 nm wavelength region (Fig. 7.6, stars). This large disagreement, and the opposite signs in the estimated  $E_d$  and  $L_u$  differences, resulted mainly because the assumed  $b_{bp}/b_p$  of 0.018 was too large for the specific waters.

The agreement between model results and measurements was improved considerably when information on  $b_{bp}/b_p$  magnitude was incorporated into the model by using a Fournier Forand (FF) phase function scaled to measured  $b_{bp}/b_p$  profiles (Mobley et al. 2002). The FF VSF is an analytical representation of the angular scattering of light that is determined by the particle index of refraction and the particle-size distribution (Fournier and Forand 1994). Mobley et al. (2002) demonstrated



**Fig. 7.6**  $L_w$  spectra estimated using: (i) a Petzold ‘average particle’ scattering phase function (stars), (ii) a FF scattering phase function with a constant backscattering ratio,  $b_{bp}/b_p = 0.015$  (open circles); and (iii) a FF scattering phase function as determined by measured wavelength- and depth- dependent  $b_{bp}/b_p$  (open squares). Measured  $L_w$  are shown as filled squares. Percent differences in  $L_w$  between measurements and model estimations are shown in the inset Fig. 7.7. (percent differences estimated as  $(L_{wmodel} - L_{wdata})/L_{wdata}$ ) (from Tzortziou et al. 2006)



that the FF VSF can be specified mainly by the backscattering fraction. Use of a FF phase function with a backscattering fraction constant with wavelength and depth and equal to the average value measured in the blue-green ( $b_{bp}/b_p = 0.015$ ) resulted in an overestimation of  $L_w$  by  $\sim 15\%$  in the blue-green spectral region (compared to  $\sim 30\%$  when using the Petzold assumption). Overestimates were larger,  $\sim 20\text{--}30\%$ , at the red wavelengths because measured  $b_{bp}/b_p$  showed a small decrease with increasing wavelength (Fig. 7.6, open circles).

Modeling  $b_{bp}$  using a FF phase function and accounting for the  $b_{bp}/b_p$  spectral shape and vertical structure further improved the agreement between data and model simulations. Absolute percent differences between model estimated and measured  $L_w(\lambda)$  were reduced to less than 10% at all wavebands (Fig. 7.6, open squares). Use of FF VSF constrained by measured wavelength- and depth-dependent  $b_{bp}/b_p$  consistently improved agreement between model and data for a wide range of bio-optical conditions in the Chesapeake Bay waters (Table 7.1).

Chang et al. (2003) examined optical closure in the near shore waters off New Jersey by performing radiative transfer calculations using measured VSFs constant with wavelength and depth. Their average absolute percent differences between measured and model-estimated  $L_w(\lambda)$  were 20% at 443 nm, 22% at 554 nm, and 17% at 682 nm, similar to the results in Tzortziou et al. (2006) when using vertically and spectrally constant  $b_b/b$  (Table 7.2, step 2). The use of a FF scattering phase function constrained by measured  $b_b/b$  allowed to incorporate information on  $b_b/b$  magnitude, spectral shape, and vertical structure into the radiative transfer model, and account for the  $b_b/b$  spatial and temporal variability observed in the Bay waters. This approach reduced differences between measured and model-estimated  $L_w$ , improving optical closure in coastal waters (Tzortziou et al. 2006). Moreover, when Magnuson et al. (2004) used a  $b_{bp}/b_p$  of 0.0125 (instead of 0.018), which is close to the average surface  $b_{bp}/b_p$  reported for the mid Chesapeake Bay waters by Tzortziou et al. (2006), the bias between their estimated  $b_{bp}$  values and the GSM01-CB  $b_{bp}$  product for the Chesapeake Bay was reduced (Fig. 11(g,h) in Magnuson et al. 2004). Therefore, detailed information on backscattering variability, including vertical and spectral resolution of backscattering processes, is necessary for radiative transfer modeling of water reflectance in the Chesapeake Bay and application of both data and model results to satellite algorithm development.

**Table 7.1** Range of values (min-max) of wavelength specific total-water absorption ( $a_{t-w}$ ), attenuation ( $c_{t-w}$ ), the backscattering to scattering ratio ( $b_b/b$ ) and concentration of chl-*a* for those days for which Hydrolight simulations were performed (from Tzortziou et al. 2006)

	$a_{t-w}(440)$ ( $m^{-1}$ )	$a_{t-w}(676)$ ( $m^{-1}$ )	$c_{t-w}(440)$ ( $m^{-1}$ )	$c_{t-w}(676)$ ( $m^{-1}$ )	$b_b/b$ (530)	[chl- <i>a</i> ] ( $mg\ m^{-3}$ )
<b>Min</b>	0.6	0.12	2.5	1.6	0.006	4.8
<b>Max</b>	1.44	0.44	8.5	6.3	0.020	23

**Table 7.2** Improvement of agreement between measured and model-estimated  $L_w$  as information on the specific IOPs measured at station PI (28 September 2001) is successively incorporated into the radiative transfer model. The final agreement between data and model (step 4) demonstrates the good optical closure obtained at this study site after applying measurement results to properly model optical properties in the complex Chesapeake Bay waters (from Tzortziou et al. 2006)

Radiative transfer modeling	Absolute % difference between model and data
1. $a_{t-w}(715) = 0$ , fluorescence included, Petzold VSF	for $L_w(554)$ : 50%
2. FF VSF with $b_b/b = 0.015$ (otherwise 1)	for $L_w(554)$ : 20%
3. FF VSF with measured $b_b/b(\lambda, z)$ (otherwise 1)	for $L_w(554)$ : 9%
4. $a_{t-w}(715) = a_p(715)$ (otherwise 3)	for $L_w(554)$ : 0.6%
	for $L_w(685)$ : 4%
5. chl- <i>a</i> fluorescence not included (otherwise 4)	for $L_w(685)$ : 40%

### 7.3.2 Long Wavelength Particulate Absorption

Water absorption coefficients are frequently measured as part of near shore bio-optical studies. However, current understanding of variations in the non-algal particulate absorption spectra is still limited (Babin et al. 2003) and uncertainties remain about the long-wavelength particulate absorption in highly turbid waters, which can affect model calculations of reflectance spectra and underwater light fields (Tzortziou et al. 2006).

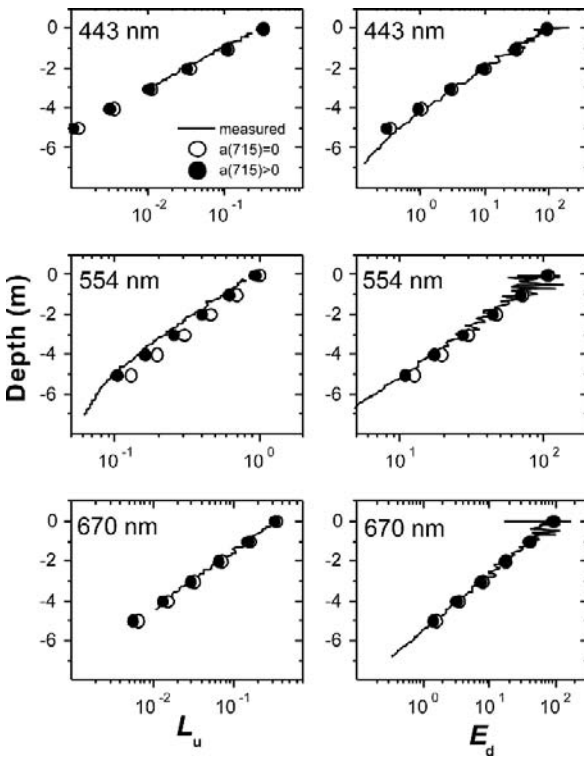
In situ measurements of water absorption are typically made using reflecting tube absorption meters and spectrophotometers (e.g. WetLabs Inc. AC9 instrument). One common assumption when correcting these measurements for scattering errors, due to uncollected scattered light, is that particulate absorption at 715 nm is zero (Zaneveld et al. 1994). Based on this assumption, a correction is typically applied to absorption data by subtracting a fraction of the measured scattering from the whole measured absorption spectrum. The fraction is scaled to set non-water absorption at 715 nm to zero. That is,

$$a_{t-w}(\lambda)_{corrected} = a_{t-w}(\lambda)_{measured} - \frac{a_{t-w}(715)_{measured}}{b_p(715)_{measured}} b_p(\lambda)_{measured} \quad (7.1)$$

However, this assumption is not always valid, especially in turbid coastal waters, resulting in negative bias in estimated absorption values and inaccuracies in AOPs computed by radiative transfer models. Indeed, measurements in the mid Bay waters revealed low, but non-zero, particulate absorption in the wavelength region 700–730 nm (example data shown in Fig. 4 in Tzortziou et al. 2006). Measurements were performed both for particulates on glass fiber filters (standard method) and for particle suspensions inside an integrating sphere (Tzortziou et al. 2006). Measured  $a_{t-w}(715)$  values for the studied region of the Bay were typically  $0.03 \text{ m}^{-1}$  (S.D. = 0.01), commensurate with expectations based on measured absorption characteristics (absorption magnitude,  $a_{NAP}(440)$ , and spectral shape,

$S_{\text{NAP}}$ ) of non-algal particles in these waters. Weak particulate absorption in the 700–730 nm was also shown by Gallegos and Neale (2002) for the Rhode River sub-estuary on the western shore of the mid Chesapeake Bay, and by Babin and Stramski (2002), Tassan and Ferrari (2003), and Babin et al. (2003) for other coastal waters.

Ramifications of this long-wavelength residual particulate absorption for estimation of radiometric quantities in the visible, were examined more thoroughly for an example data set when measured particulate absorption at 715 nm was close to  $0.02 \text{ m}^{-1}$  (Tzortziou et al. 2006). When model simulations were performed using in situ absorption data corrected assuming zero  $a_{t-w}(715)$  (Eq. 7.1), differences between model-estimated and measured  $L_u$  values at 1 m depth were as large as 17% at 490 nm and 17.2% at 554 nm (Fig. 7.7). The model overestimated both  $E_d(z)$  and  $L_u(z)$ , due to the negative bias in  $a_{t-w}(\lambda)$ , and the disagreement between measurements and model estimations increased with increasing depth. Similar results were observed when comparing measurements and model estimates for other days and



**Fig. 7.7** (Left column) Comparison between measured (solid lines) and model-estimated  $L_u(z)$  (in  $\mu\text{W nm}^{-1} \text{cm}^{-2} \text{sr}^{-1}$ ) at 443, 554 and 670 nm, assuming  $a_{t-w}(715) = 0$  (open circles) and assuming  $a_{t-w}(715) = a_p(715)$  (filled circles).  $L_u$  values are truncated at  $0.01 \mu\text{W nm}^{-1} \text{cm}^{-2} \text{sr}^{-1}$ , due to large measurement uncertainty at low light levels. (Right column) Similarly for  $E_d(z)$  (in  $\mu\text{W nm}^{-1} \text{cm}^{-2}$ ). Data are shown for measurements performed at station PI, on 28 September 2001 (from Tzortziou et al. 2006)

stations. The overestimation of both  $L_u$  and  $E_d$  by the model could not be explained only by errors in measured  $b_b$ , as overestimation, for example, of  $b_b$  would result in overestimation of  $L_u$  but underestimation of  $E_d$ .

Accounting for the small particulate absorption at 715 nm when correcting in situ absorption data improved radiative transfer closure in the Bay waters by reducing the model's systematic overestimation of both  $E_d$  and  $L_u$  (Fig. 7.7, Table 7.2 step 4). In this case, a modified in situ absorption correction for scattering errors was performed according to:

$$a_{t-w}(\lambda)_{corrected} = a_{t-w}(\lambda)_{measured} - \frac{a_{t-w}(715)_{measured} - a_p(715)}{b_p(715)_{measured}} b_p(\lambda)_{measured} \quad (7.2)$$

where  $a_p(715)$  is the total particulate absorption at 715 nm measured spectrophotometrically. Percent differences between model-estimated and measured  $L_u$  values at 1 m depth improved to 9% at 490 nm and 5.8% at 554 nm (compared to 17% and 17.2%, respectively, without allowing for small positive  $a_p(715)$ ). Similar improvement in the agreement between model and data was observed for samples representing other bio-optical conditions in the Bay.

Due to strong absorption by CDOM and NAP at blue wavelengths, and water itself at red wavelengths, the effect was most noticeable at green wavelengths (i.e. 554 nm). In this wavelength region, total absorption is relatively small, and small changes, equal to the observed particulate absorption at 715 nm, have a relatively large effect on model simulations (Fig. 7.7). Failure to account for the small near-infrared particulate absorption when correcting field measurements used as inputs for the radiative transfer model, leads to consistent, though variable, model overestimation of  $R_{rs}$  around 554 nm. This is important when applying these model results to algorithm development, as this is a key wavelength region that is being used in both empirical and semi-analytical satellite algorithms for remote chl-*a* retrievals (e.g. O'Reilly et al. 2000, Carder et al. 2002, Maritorena et al. 2002).

### 7.3.3 Modeling Fluorescence in the Chesapeake Bay

Sun-induced chl-*a* fluorescence emission at wavelengths close to 685 nm affects the magnitude and spectral shape of reflectance in natural waters (e.g. Gordon 1979, Maritorena et al. 2000). As fluorescence is an indicator of both the amount of chl-*a* and the rate of photosynthesis, much attention has been focused on the use of the remotely sensed chl-*a* fluorescence signal for inferring information on primary productivity and phytoplankton physiological state in coastal waters (e.g. Gower and Borstad 1981, Abbott and Letelier 1999, Huot et al. 2005). This signal can be particularly strong in estuaries that, similar to the Chesapeake Bay, are characterized by high chl-*a* concentrations.

Radiative transfer studies provide a means of evaluating the effect of chl-*a* fluorescence on  $R_{rs}$  and, consequently, a basis for remote sensing retrieval of chl-*a* distributions. Model simulations for the Chesapeake Bay showed that accounting

for chl-*a* fluorescence removes large errors in modeling  $R_{rs}$  in the red wavelengths (Tzortziou et al. 2006). Neglecting fluorescence for a [chl-*a*] of  $7.3 \text{ mg m}^{-3}$  resulted in model underestimations of  $L_u(0^-)$ ,  $L_w$  and  $R_{rs}$  by as much as 30–40% in the wavelength region around the chl-*a* fluorescence maximum at 685 nm compared to measurements. Including chl-*a* fluorescence in the radiative transfer modeling, using the Hydrolight default fluorescence efficiency of 2% (Mobley 1994), considerably improved agreement between model and data, reducing absolute percent differences to 4–8% (Table 7.2).

Assumptions regarding the chl-*a* fluorescence efficiency affect model calculations near 685 nm. Maritorena et al. (2000) found that vertical profiles of fluorescence quantum yield in the Case 1 Pacific waters were strongly structured, with relatively low (1%) values close to the surface and maximal (5–6%) values at larger depths. Similar in situ determinations of chl-*a* fluorescence efficiency variability for the Chesapeake Bay waters could further improve model estimates of reflectance at red wavelengths. Obtaining good closure of model and measurements in the red supports the use of these wavelengths for chl-*a* retrieval from remotely sensed reflectance of Bay waters, as opposed to using  $R_{rs}$  in the blue and green where absorption is dominated by CDOM and non-algal particles.

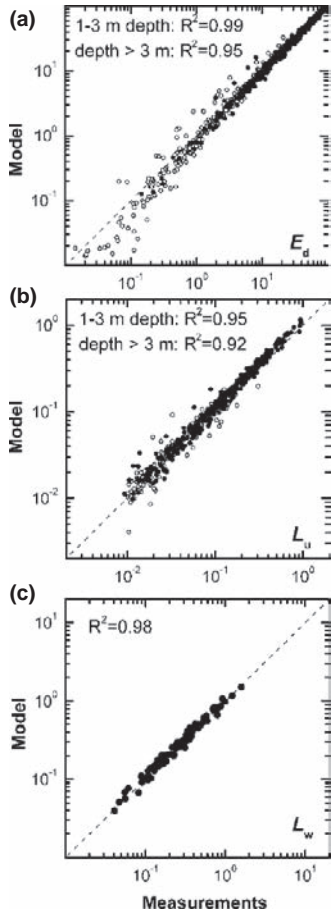
### 7.3.4 Overall Radiative Transfer Model Performance

Based on the foregoing results for a single station, which are summarized in Table 7.2, Tzortziou et al. (2006) performed radiative transfer calculations for more stations in the mid Chesapeake Bay by: (i) using a FF phase function as determined by measured profiles of  $b_{bp}/b_p$  spectra to account for the observed temporal and spatial variability of  $b_{bp}/b_p$ , (ii) allowing for a small particulate absorption at the 715 nm wavelength region (equal to the measured  $a_p(715)$ ) when correcting in situ absorption estimates used as input to the model, and (iii) including chl-*a* fluorescence. For completeness, fluorescence by CDOM was also included (using a fluorescence efficiency based on Hawes (1992)), though neglecting CDOM fluorescence in model simulations had a relatively small effect on  $R_{rs}$  and  $L_w$  estimations (i.e. 2–5% underestimation at the blue wavelengths and negligible effect at longer wavelengths; Tzortziou et al. 2006). Application of these measurement results to modeling of bio-optical processes in the Chesapeake Bay, allowed for improved optical closure between independently measured inherent and apparent optical properties over a wide range of observed bio-optical conditions (Table 7.1).

Model  $E_d$  and  $L_u$  values, estimated from measured IOPs, were in good agreement with measurements (Fig. 7.8). The agreement between model and data extended for over three orders of magnitude dynamic range in radiance and irradiance values. In the upper three meters, coefficients of determination assuming a 1:1 relation between model and observed values were 0.99 and 0.95 for  $E_d$  and  $L_u$  respectively. For average values of attenuation ( $c(412) = 5.5 \text{ m}^{-1}$  and  $c(532) = 4.2 \text{ m}^{-1}$ ) measured in the Chesapeake Bay (Tzortziou et al. 2006), the upper three meters correspond to

optical depths ( $\zeta = cz$ ) of 16.5 and 12.5, at wavelengths 412 and 532 nm, respectively. In these optically thick waters, the upper 3-meter layer is the most important for remote sensing. For depths greater than 3 meters ( $N = 315$ ), estimated  $R^2$  was smaller, 0.95 and 0.92 for  $E_d$  and  $L_u$  respectively. Closer to the bottom, larger percent differences between model and data typically occur, since both measurements and model results have relatively high levels of uncertainties due to very low light levels, problems with dark signal correction and small model-input errors that propagate in the model calculations.

Although measured  $L_w$  spectra in the Bay are highly variable because of large variation in  $E_s$  and water IOPs,  $L_w(\lambda)$  measurements were consistently in good agreement with model results (Tzortziou et al. 2006). Average absolute percent differences between measured and model-estimated  $L_w$  were smaller than 10% in the 412–670 nm wavelength region, with a standard deviation in the percent differences ranging between 5 and 7%. The coefficient of determination assuming a 1:1 relation



**Fig. 7.8** Comparison between model-estimated and in situ measured  $E_d(z)$  (in  $\mu\text{W nm}^{-1} \text{cm}^{-2}$ ),  $L_u(z)$  (in  $\mu\text{W nm}^{-1} \text{cm}^{-2} \text{sr}^{-1}$ ), and  $L_w$  (in  $\mu\text{W nm}^{-1} \text{cm}^{-2} \text{sr}^{-1}$ ) for all cruises-stations that comparisons with the radiative transfer model were performed. Comparisons within the first 3 meters for  $E_d$  and  $L_u$  are shown as dark circles ( $R^2 = 0.99$  for  $E_d$ ,  $R^2 = 0.95$  for  $L_u$ ), while comparisons for depths below 3 m are shown as open circles ( $R^2 = 0.95$  for  $E_d$ ,  $R^2 = 0.92$  for  $L_u$ ), (the 1:1 line is also shown for comparison)

between model and measured  $L_w$  values (Fig. 7.8) was  $R^2 = 0.98$  ( $N = 112$ ). These differences are considerably smaller than those presented in the few studies of optical closure performed previously in near shore waters of similar optical complexity (e.g. Bulgarelli et al. 2003, Chang et al. 2003).

The improved optical closure in the Chesapeake Bay waters was obtained after using depth and wavelength resolved measurements of  $b_b/b$ , properly correcting absorption measurements in a way that allowed a small residual particulate absorption at 715 nm, and including chl-*a* fluorescence in model simulations. Given that average values for  $b_b/b$  and  $S_{NAP}$  in this study were within the range of values reported in previous studies (e.g. Mobley et al. 2002, Babin et al. 2003, Ferrari et al. 2003, Boss et al. 2004a, Magnuson et al. 2004), and that chl-*a* concentrations were not excessively high for estuaries, we expect that proper accounting for these optical characteristics would be equally important in optical modeling of other coastal and estuarine waters.

## 7.4 Remote Sensing of Chl-*a* and Non-Algal Particles in the Chesapeake Bay

Obtaining synoptic-scale information on the concentration and dynamics of dissolved and particulate, organic and inorganic water constituents using remotely sensed ocean color is critical for primary production studies, coastal water quality monitoring, and carbon cycle modeling in Chesapeake Bay. However, application of currently operational satellite algorithms in these waters often results in erroneous retrievals (as shown in Harding et al. 2005 and Tzortziou et al. 2007), which underscores the need to examine alternative, regionally specific algorithms based on detailed in situ bio-optical measurements. As discussed in Sect. 7.3, integration of observations with optical closure results is essential for examining the accuracy of the in situ data and determining the contribution of various water constituents to the backscattering and absorption characteristics of the Chesapeake Bay. Measurements and radiative transfer model results can, then, be applied to the development, parameterization, and refinement of bio-optical algorithms towards improved remote retrieval of biogeochemical quantities, such as chl-*a* and suspended inorganic particles, in this estuarine ecosystem.

### 7.4.1 Remote Sensing of chl-*a* in the Chesapeake Bay

Chlorophyll-*a* concentrations in the mid and upper Chesapeake Bay are typically considerably larger than  $2 \text{ mg m}^{-3}$  (e.g. Magnuson et al. 2004, Tzortziou et al. 2007, Gitelson et al. 2007). For  $[\text{chl-}a] > 2 \text{ mg m}^{-3}$ , extant satellite chl-*a* algorithms like the SeaWiFS OC4V4 (O'Reilly et al. 2000), the MODIS semi-analytical algorithm (Carder et al. 2002) and the MODIS OC3M (O'Reilly et al. 2000) are all

based on empirical relations between [chl-*a*] and reflectance ratios in the blue-green spectral region (i.e. 443–555 nm). The specific wavelengths in these algorithms are chosen on the basis of strong absorption by algal pigments at blue wavelengths (e.g. 443 nm) and their weak absorption around 550–580 nm. These algorithms, however, do not account sufficiently for any interference from other water components that are optically significant in coastal waters. When considering previous results for the Chesapeake Bay (e.g. Magnuson et al. 2004, Tzortziou et al. 2007) showing large contributions by non-covarying CDOM and NAP to total light attenuation at blue and green wavelengths, the weak performance of MODIS and SeaWiFS chl-*a* retrievals in these Case 2 waters is not surprising. Using Mie scattering calculations, Wozniak and Stramski (2004) showed that even relatively low concentrations of mineral particles of the order of  $0.1 \text{ g m}^{-3}$  can considerably affect chl-*a* estimates from standard SeaWiFS and MODIS algorithms that are based on blue-green reflectance ratios. In the Chesapeake Bay turbid waters, mineral particulate concentrations are typically much larger (average concentration of  $4.8 \text{ g m}^{-3}$  reported in Tzortziou et al. 2007), strongly affecting the  $R_{rs}$  signal in the blue-green.

Because of the strong interference from CDOM and non-algal particulate absorption in the blue-green, regionally-specific algorithms based on the strong chl-*a* fluorescence signal at around 685 nm or the chl-*a* absorption feature at 675 nm have been proposed for improving chl-*a* retrievals in highly turbid, coastal and inland waters (e.g. Gower and Borstad 1981, Letelier and Abbott 1996, Ruddick et al. 2001, Dall’Olmo and Gitelson 2005, Dall’Olmo et al. 2005). Tzortziou et al. (2007) examined the correlation between surface [chl-*a*] and various two-band MODIS  $R_{rs}$  ratios using in situ data for the mid Chesapeake Bay, and found that variability in surface [chl-*a*] was most strongly correlated with changes in the ratio  $R_{rs}(677)/R_{rs}(554)$  ( $N = 40$ ,  $R^2 = 0.54$ ). The derived relation between [chl-*a*] and this  $R_{rs}$  ratio was consistent with predictions based on radiative transfer calculations and observed relations between in situ data of [chl-*a*] and IOPs ( $b_b$  and  $a$ ) at the two specific wavelengths. Based on a seasonally-limited but detailed in-situ dataset of water IOPs and radiance reflectance spectra, collected from a number of stations in tributary rivers and the main stem of the Chesapeake Bay during 11–18 July 2005, Gitelson et al. (2007) also proposed the use of red and near-infrared spectral bands for chl-*a* retrievals in the Chesapeake Bay waters (i.e. a two-band model with SeaWiFS 670 and 765 nm bands ( $R^2 = 0.65$ ) and MODIS 667 and 748 nm bands ( $R^2 = 0.68$ ), and a three-band model with MERIS 665, 705 and 754 nm bands ( $R^2 = 0.75$ )).

These results strongly suggest that further exploitation of the ocean color signal in the red and near-infrared, where interference from CDOM and NAP absorption is minimal, is necessary for improving satellite monitoring of biological activity in these turbid and productive waters. Moreover, one of the main factors affecting the accuracy of satellite chl-*a* retrievals in near shore waters is correction for the atmosphere’s optical characteristics. Problems with atmospheric correction of satellite data in the blue due to extrapolation of aerosol properties from near-infrared to shorter wavelengths (Gordon and Voss 1999) are avoided when using information in the red wavelengths for chl-*a* retrievals.



### 7.4.2 Remote Sensing of Backscattering and Non-Algal Particles

Particulate backscattering in the water depends on the concentration, size, shape, internal structure and refractive index of suspended, organic and inorganic particles (van de Hulst 1981). Thus,  $b_{bp}$  carries useful information about the abundance and the types of seawater constituents that affect carbon fluxes and biogeochemical cycling in coastal ecosystems (Boss et al. 2004b). As carbon content in individual plankton cells is coupled with particle size (Verity et al. 1992, Montagnes et al. 1994) and refractive index (Stramski et al. 1999), Stramski et al. (1999) reported high correlation between surface  $b_{bp}$  at 510 nm and surface concentration of particulate organic carbon (POC) in the Southern Ocean. In coastal waters, however, strong correlation between backscattering and the organic component of particulate matter is not to be expected, as in these regions a significant fraction of suspended particles consists of inorganic material derived from various sources, such as river discharges, bottom resuspension, atmospheric deposition, or coastal erosion by wave and current action (Stramski et al. 2004).

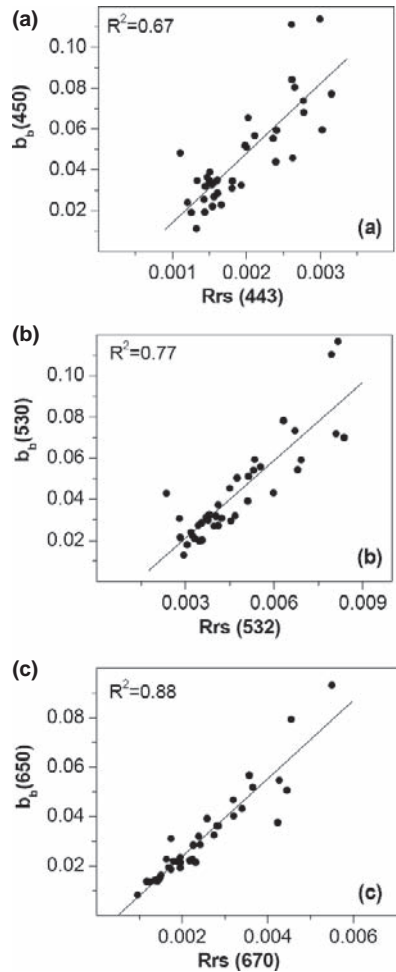
Particulate backscattering in the Chesapeake Bay is typically highly variable (Tzortziou et al. 2007). This variation in surface  $b_{bp}$  significantly affects  $R_{rs}$  at all wavelengths (Fig. 7.9) and, in the mid Chesapeake Bay, was found to be the main factor driving observed variability in the  $R_{rs}$  at 670 nm ( $N = 37$ ,  $R^2 = 0.88$ ),

$$b_b(650) = 15.82 \cdot R_{rs}(670) - 0.008 \quad (7.3)$$

Although  $R_{rs}$  magnitude is affected by both backscattering and absorption ( $R_{rs} \sim b_b/a$ ), variability in  $R_{rs}$  at 670 nm is driven more by changes in particulate backscattering than by changes in particulate absorption because of the relatively large contribution by pure water to total absorption at 670 nm. In Tzortziou et al. (2007), surface  $b_b$  in the red varied by more than an order of magnitude (measured range 0.008–0.13  $m^{-1}$ ), corresponding to more than an order of magnitude changes in  $R_{rs}(670)$ . Particulate absorption in the red was also highly variable ( $a_{t-w}(670)$  ranged between 0.1 and 1  $m^{-1}$ ). However, when  $a_{t-w}(670)$  was added to the relatively large pure water absorption ( $a_w(670) = 0.44 m^{-1}$ ; Pope and Fry 1997) total absorption varied by less than a factor of 3. At shorter visible wavelengths, the contribution of pure water absorption is minimal. Therefore,  $R_{rs}$  at 443 and 532 nm is affected strongly by changes in both total absorption (strong contribution by non-covarying particulate and dissolved components) and total backscattering (contribution by suspended particles). The strong correlation found between  $b_b$  and  $R_{rs}(670)$  indicates that satellite measured  $R_{rs}$  at 670 nm can be applied to remotely retrieve particulate backscattering in these Case 2 waters (Tzortziou et al. 2007). This could, subsequently, be used to derive information on the major water constituents that regulate backscattering variability in the Bay.

Backscattering fraction can provide a proxy to the particulate bulk refractive index, which in turn is an indicator of the particulate composition in the water (Twardowski et al. 2001, Stramski et al. 2004). Because of their high water content, phytoplankton cells have relatively low refractive index and low backscatter signal

**Fig. 7.9** Relation between measured  $b_b$  ( $\text{m}^{-1}$ ) and  $R_{rs}$  ( $\text{sr}^{-1}$ ) at wavelengths (a) 443 nm ( $b_b$  measured at 450 nm), (b) 532 nm ( $b_b$  measured at 530 nm) and (c) 670 nm ( $b_b$  measured at 650 nm)



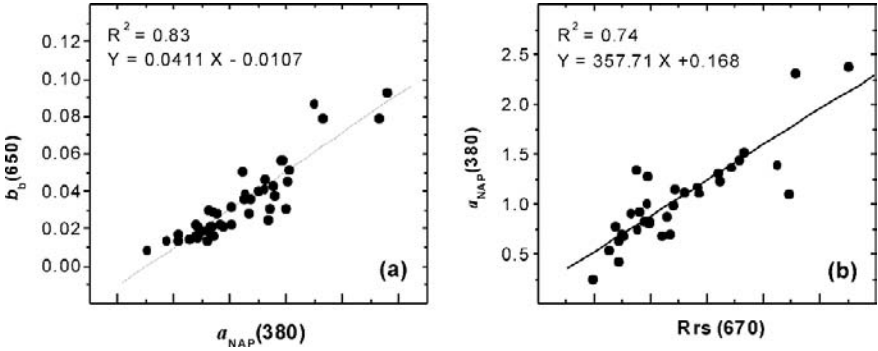
compared to inorganic particles (e.g. Carder et al. 1974, Stramski et al. 1988, Aas 1996). As particulate backscattering increases with increasing particulate refractive index,  $b_{bp}/b_p$  values for phytoplankton-dominated waters are typically lower than those of waters where suspended inorganic particles dominate (Twardowski et al. 2001). Measurements by Twardowski et al. (2001) in the Gulf of California and by Boss et al. (2004a) off the New Jersey coast showed that phytoplankton-dominated surface waters with high chl-*a* concentrations had  $b_{bp}/b_p$  values of  $\sim 0.005$ – $0.006$ , while  $b_{bp}/b_p$  exceeded 0.012 in regions where highly refractive re-suspended inorganic particles dominated. The  $b_{bp}/b_p$  values measured in the Bay, with an average of 0.0125 at 530 nm (Tzortziou et al. 2007), were considerably larger than previously reported values for phytoplankton-dominated waters, suggesting that particulate backscattering in mid Chesapeake Bay is dominated by suspended inorganic particles despite the large concentration of chl-*a* in these waters.

Non-algal particles contributed significantly to total in-water absorption in the studied region of the Bay (Fig. 7.4). The magnitude of NAP absorption showed strong seasonal and temporal variability. However, the spectral shape of NAP absorption showed little variation, with  $S_{\text{NAP}}$  values having a narrow range around an average of  $0.011 \text{ nm}^{-1}$  ( $\text{SD} = 0.001 \text{ nm}^{-1}$ ). According to previous studies that attempted to infer qualitative information on non-algal particles from their absorption characteristics,  $S_{\text{NAP}}$  values of about  $0.011 \text{ nm}^{-1}$  are typical for mineral-dominated waters. Bowers et al. (1996) estimated an average  $S_{\text{NAP}}$  value of  $0.011 \text{ nm}^{-1}$  ( $\text{SD} = 0.0002 \text{ nm}^{-1}$ ) for the absorption spectra of over 100 samples of mineral suspended solids collected from the Menai Strait in the Irish Sea. Measurements by Babin et al. (2003) at about 350 stations in European coastal waters showed that  $S_{\text{NAP}}$  was on average  $0.0117 \text{ nm}^{-1}$  for the mineral-dominated waters in the North Sea and English Channel. Ferrari et al. (2003) measured  $S_{\text{NAP}}$  in the range  $0.0095\text{--}0.0125 \text{ nm}^{-1}$  for the coastal waters of the North Sea and German Bight where 76% of total suspended particulate matter was inorganic. Relatively higher  $S_{\text{NAP}}$  values, in the range  $0.0115\text{--}0.0145 \text{ nm}^{-1}$ , were reported for the Baltic Sea, which is known for its high organic matter content (Voipo 1981, Ferrari et al. 2003). Similarly, Babin et al. (2003) found that highly organic samples collected from the Baltic Sea had significantly higher  $S_{\text{NAP}}$  compared to mineral-dominated waters, suggesting that observed variation in  $S_{\text{NAP}}$  may be related to the proportion of mineral and organic matter. The close agreement between the  $S_{\text{NAP}}$  values reported in Tzortziou et al. (2007) and those reported in studies for suspended inorganic particles, and the high particulate backscattering ratio measured relative to phytoplankton-dominated waters, indicate that highly-refractive non-algal particles with high inorganic content are the major water constituents controlling changes in both  $a_{\text{NAP}}$  and  $b_{\text{bp}}$  in the mid Chesapeake Bay waters.

Consistent with these results,  $b_{\text{b}}$  in the mid Bay, although highly variable, was found to be strongly correlated with the magnitude of non-algal particulate absorption at 380 nm (Fig. 7.10a) ( $N = 44$ ,  $R^2 = 0.83$ ), according to:

$$b_{\text{b}}(650) = 0.0411 \cdot a_{\text{NAP}}(380) - 0.0107 \quad (7.4)$$

Because  $S_{\text{NAP}}$  was only slightly variable in the Chesapeake Bay, suggesting little variability in composition, the magnitude of NAP absorption can be used as a proxy for non-algal particles abundance in these waters. Zawada et al. (2007) used  $b_{\text{b}}(440)$  derived from SeaWiFS satellite data (Lee et al. 1999, Hu et al. 2003) as a proxy for total suspended solids (TSS) concentrations in the Chesapeake Bay. Their derived coefficient of determination between field measurements of TSS and satellite  $b_{\text{b}}$  was  $R^2 = 0.4$ , which is considerably lower than the  $R^2$  of 0.83 that was derived between  $b_{\text{b}}(650)$  and  $a_{\text{NAP}}$  in Tzortziou et al. (2007). Several factors can limit the degree of correlation between satellite-derived  $b_{\text{b}}$  and in situ measurements of TSS, e.g. scale mismatches between satellite and field data, uncertainties in satellite algorithm parameterizations, errors in the in situ TSS data. However, the variability in the size and composition of particles included in the TSS pool, and the large differences in the contribution of phytoplankton cells and inorganic particles to total



**Fig. 7.10** (a) Relation between surface measurements of  $b_b(650)$  ( $\text{m}^{-1}$ ) and  $a_{\text{NAP}}$  ( $\text{m}^{-1}$ ) at 380 nm. (b) Linear regression between  $R_{\text{rs}}(670)$  ( $\text{sr}^{-1}$ ) and surface measurements of absorption by non-algal particles ( $\text{m}^{-1}$ ) at 380 nm

$b_{\text{bp}}$  (e.g. Twardowski et al. 2001), are probably the most important factors contributing to the relatively low  $R^2$  derived by Zawada et al. (2007). In the mid Chesapeake Bay, the relation between surface [chl- $a$ ] and particulate backscattering showed high variability at all measured  $b_b$  wavelengths (450, 530, 650 nm; Tzortziou et al. 2007), and correlation between  $b_b(650)$  and [chl- $a$ ] was considerably smaller ( $R^2 = 0.42$ ) compared to that between  $b_b(650)$  and  $a_{\text{NAP}}(380)$  ( $R^2 = 0.83$ ).

The strong correlation between particulate  $b_b$  and  $a_{\text{NAP}}$ , in conjunction with remote retrieval of surface  $b_b$  from  $R_{\text{rs}}$  measurements in the red, suggest that  $R_{\text{rs}}(670)$  can be applied to remotely determine abundance and distribution of non-algal particulate matter in near-shore regions where suspended inorganic particles strongly affect ocean color. Indeed,  $R_{\text{rs}}(670)$  in the Chesapeake Bay surface waters was strongly correlated with NAP absorption (Fig. 7.10b). Coefficients of determination for the linear least-squares regression between  $R_{\text{rs}}(670)$  and surface  $a_{\text{NAP}}$  were 0.7 and 0.74 for absorption measurements at 412 and 380 nm, respectively (only results at 380 are shown in Fig. 7.10b). Binding et al. (2003) found good correlation between surface irradiance reflectance ( $R = E_u/E_d$ ) at 665 nm and concentration of mineral suspended sediments for the Irish Sea waters.

Because of the similarities in the absorption spectral shapes of dissolved organic matter and non-algal particles, separating contribution by these two components to total light absorption in Case 2 waters is a difficult task. As a result, most satellite Case 2 algorithms (e.g. Lee et al. 1999, Carder et al. 2002, Maritorena et al. 2002, Hu et al. 2003) combine CDOM and NAP into one term even though the two components do not covary in coastal waters. Regionally specific relations, such as those discussed here between  $a_{\text{NAP}}(380)$ ,  $b_b(650)$ , and  $R_{\text{rs}}(670)$ , allow a separate estimate of the contribution by NAP to total light absorption based on the backscattering properties of non-algal particles and the remote retrieval of particulate  $b_b$  from satellite-measured  $R_{\text{rs}}$ .

## 7.5 Conclusions

The extended areal and nearly daily coverage afforded by remote sensing is essential for detecting and monitoring changes in water quality. Effective interpretation of remotely sensed ocean color, however, is still a major challenge in near shore waters such as the Chesapeake Bay where the quality and quantity of optically and biogeochemically important water constituents are affected by a number of different sources as well as complex physical, photochemical and biological processes. Improvements in remote sensing of water composition arise from advances in technology and from better algorithms. Both the improved hardware sensitivity and algorithmic interpretation must be tested against appropriately designed in situ measurements. Comparison between field observations and radiative transfer model simulations and demonstration of good optical closure is a critical step towards improving our knowledge of the bio-optical characteristics of these waters and applying results to the development and refinement of remote-sensing algorithms for accurate assessments of water quality.

Field observations and radiative transfer model calculations in the Chesapeake Bay suggest that exploiting further the ocean color signal in the red and near-infrared spectral region, where interference from CDOM and NAP absorption is minimal, is necessary for improving satellite monitoring of chlorophyll-*a* variability. Measurements of  $b_b/b$  and  $S_{\text{NAP}}$  indicate a dominant role by highly refractive inorganic particles in regulating backscattering variability in these waters, and particulate backscattering was the main factor driving observed variability in the remotely sensed quantity  $R_{\text{rs}}(670)$ . Retrieval of particulate  $b_b$  from satellite measured  $R_{\text{rs}}(670)$  can be applied to remotely monitor distribution and concentrations of highly refractive suspended particles in this region of the Bay. Moreover, retrieval of NAP absorption from the remotely-sensed reflectance signal at 670 nm could be used in conjunction with inversion of blue (and, in future planned satellites, of UV) wavelengths to derive CDOM absorption in these Case 2 waters. Separating contribution by these two similarly absorbing, but non-covarying, components of total light absorption would be particularly useful for remote sensing of CDOM and studies on dissolved organic carbon cycling and biogeochemical processing in coastal waters. Quantitative analysis of particulate composition and measurements of the differences in the optical characteristics (i.e.  $S_{\text{NAP}}$  and  $b_b$ ) between organic detrital and inorganic mineral suspended particles are needed to improve interpretation of remote sensing in coastal regions where non-algal particles often dominate the backscattered signal (Tzortziou et al. 2007).

Re-establishment of water clarity sufficient to support submerged vascular plants to their historically observed extent is one major goal of the Chesapeake Bay restoration effort (Chesapeake 2000 interagency agreement). Absorption and scattering by non-algal particulates is the major contribution to light attenuation in the shallow, near-shore regions that bay grasses inhabit (Gallegos 2001). Further development of the ability to estimate synoptically and repetitively the NAP absorption in shallow turbid waters will contribute greatly to gauging progress toward successful restoration.

## List of Symbols

$a$	total absorption
$a_{\text{CDOM}}$	absorption by Colored Dissolved Organic Matter (CDOM)
$a_{\text{NAP}}$	absorption by Non Algal Particles (NAP)
$a_{\text{p}}$	particulate absorption
$a_{\text{t-w}}$	total (minus pure water) absorption
$a_{\text{w}}$	pure water absorption
$b$	total scattering
$b_{\text{p}}$	particulate scattering
$b_{\text{b}}$	total backscattering
$b_{\text{bp}}$	particulate backscattering
$b_{\text{b}}/b$	total backscattering fraction
$b_{\text{bp}}/b_{\text{p}}$	particulate backscattering fraction
$c$	total attenuation
$c_{\text{t-w}}$	total (minus pure water) attenuation
$\text{chl-}a$	chlorophyll- $a$
$[\text{chl-}a]$	chlorophyll- $a$ concentration
$E_{\text{d}}$	downwelling irradiance
$E_{\text{s}}$	downwelling surface irradiance
$E_{\text{u}}$	upwelling irradiance
$L_{\text{u}}$	upwelling radiance
$L_{\text{w}}$	water-leaving radiance
$R$	irradiance reflectance
$R_{\text{rs}}$	remote sensing reflectance
$S_{\text{CDOM}}$	CDOM absorption exponential spectral slope
$S_{\text{NAP}}$	NAP absorption exponential spectral slope
$z$	geometric depth
$\lambda$	wavelength
$\zeta$	optical depth

## List of Acronyms and Abbreviations

AOPs	Apparent Optical Properties
CDOM	Colored Dissolved Organic Matter
CZCS	Coastal Zone Color Scanner
FF	Fournier Forand
IOPs	Inherent Optical Properties
MERIS	MEDium Resolution Imaging Spectrometer
MODIS	MODERate resolution Imaging Spectroradiometer
NAP	Non Algal Particles
POC	Particulate Organic Carbon
SAV	Submerged Aquatic Vegetation

SeaWiFS	Sea-viewing Wide Field of view Sensor
TSS	Total Suspended Solids
VSF	Volume Scattering Function

## References

- Aas E (1996) Refractive index of phytoplankton derived from its metabolite composition. *J Plankton Res* 18:2223–2249
- Abbott MR, Letelier RM (1999) Chlorophyll fluorescence (MODIS product number 20). MODIS algorithm theoretical basis document, version 3, NASA
- Adolf JE, Yeager CL, Miller WD, Mallonee ME, Harding LW (2006) Environmental forcing of phytoplankton floral composition, biomass, and primary productivity in Chesapeake Bay, USA. *Estuar Coast Shelf Sci* 67:108–122
- Ahmad Z, McClain C, Herman JR, Franz B, Kwiatkowska E, Robinson W, Bucsela E, Tzortziou M (2007) Atmospheric correction for NO<sub>2</sub> absorption in retrieving water-leaving reflectances from the SeaWiFS and MODIS measurements. *Appl Opt* 46:6504–6512
- Babin M, Stramski D (2002) Light absorption by aquatic particles in the near-infrared spectral region. *Limnol Oceanogr Notes* 47:911–915
- Babin M, Stramski D, Ferrari G, Clauster H, Bricaud A, Obelensky G, Hoepffner N (2003) Variations in the light absorption coefficients of phytoplankton, nonalgal particles, and dissolved organic matter in coastal waters around Europe. *J Geophys Res* 108(C7):3211 doi: 10.1029/2001JC000882
- Binding CE, Bowers DG, Mitchelson-Jacob EG (2003) An algorithm for the retrieval of suspended sediment concentrations in the Irish Sea from SeaWiFS ocean colour satellite imagery. *Int J Remote Sens* 24:3791–3806
- Boesch DF (2000) Measuring the health of the Chesapeake Bay: toward integration and prediction. *Environ Res* 82:134–142
- Boss E, Pegau WS, Lee M, Twardowski MS, Shybanov E, Korotaev G, Baratange F (2004a) The particulate backscattering ratio at LEO 15 and its use to study particles composition and distribution. *J Geophys Res* 109 C01014 doi:10.1029/2002JC001514
- Boss E, Stramski D, Bergmann T, Pegau WS, Lewis M (2004b) Why should we measure the optical backscattering coefficient? *Oceanography* 17:44–49
- Bowers DG, Harker GEL, Stephan B (1996) Absorption spectra of inorganic particles in the Irish Sea and their relevance to remote sensing of chlorophyll. *Int J Remote Sens* 17:2449–2460
- Bulgarelli B, Zibordi G, Berthon JF (2003) Measured and modeled radiometric quantities in coastal waters: toward a closure. *Appl Opt* 42:5365–5381
- Carder KL, Betzer PR, Eggimann DW (1974) Physical, chemical, and optical measures of suspended particle concentrations: their intercomparison and application to the West African shelf. In: Gibbs RJ (ed) *Suspended solids in water*. Plenum, New York, pp 173–193
- Carder KL, Chen FR, Cannizzaro JP, Campbell JW, Mitchell BG (2004) Performance of the MODIS semi-analytical ocean color algorithm for chlorophyll-a. *Advances in Space Res* 33:1152–1159
- Carder KL, Chen RF, Cannizzaro JP (2002) Case 2 Chlorophyll a. MODIS algorithm theoretical basis document, ATBD 19, version 6, NASA
- Chang GC, Dickey TD, Mobley CD, Boss E, Pegau WS (2003) Toward closure of upwelling radiance in coastal waters. *Appl Opt* 42:1574–1582
- Clark DK (1997) Bio-optical algorithms case 1 waters. MODIS algorithm theoretical basis document (MOD-18), NASA
- Curran PJ, Steele CM (2005) MERIS: the re-branding of an ocean sensor. *Int J Remote Sens* 26:1781–1798

- Dall'Olmo G, Gitelson AA (2005) Effect of bio-optical parameter variability on the remote estimation of chlorophyll-a concentration in turbid productive waters: experimental results. *Appl Opt* 44:412–422
- Dall'Olmo G, Gitelson AA, Rundquist DC, Leavitt B, Barrow T, Holz JC (2005) Assessing the potential of SeaWiFS and MODIS for estimating chlorophyll concentration in turbid productive waters using red and near-infrared bands. *Remote Sens Environ* 96:176–187
- Darecki M, Stramski D (2004) An evaluation of MODIS and SeaWiFS bio-optical algorithms in the Baltic Sea. *Remote Sens Environ* 89:326–350
- Dickey T, Lewis M, Chang G (2006) Optical oceanography: recent advances and future directions using global remote sensing and in situ observations. *Rev Geophys* 44 Art. No. RG1001
- Ferrari GM, Bo FG, Babin M (2003) Geo-chemical and optical characterizations of suspended matter in European coastal waters. *Estuar Coast Shelf Sci* 57:17–24
- Fournier GR, Forand JL (1994) Analytical phase function for ocean water. In: Jaffe JS (ed) *Ocean optics XII, SPIE*, vol 2258. pp 194–201
- Gallegos CL (2001) Calculating optical water quality targets to restore and protect submersed aquatic vegetation: Overcoming problems in partitioning the diffuse attenuation coefficient for photosynthetically active radiation. *Estuaries* 24:381–397
- Gallegos CL, Bergstrom PW (2005) Effects of a *Prorocentrum* minimum bloom on light availability for and potential impacts on submersed aquatic vegetation in upper Chesapeake Bay. *Harmful Algae* 4:553–574
- Gallegos CL, Neale PJ (2002) Partitioning spectral absorption in case 2 waters: discrimination of dissolved and particulate components. *Appl Opt* 41:4220–4233
- Garver SA, Siegel DA (1997) Inherent optical property inversion of ocean color spectra and its biogeochemical interpretation. I. Time series from the Sargasso Sea. *J Geophys Res* 102:18607–18625
- Gitelson AA, Schalles JF, Hladik CM (2007) Remote chlorophyll-a retrieval in turbid, productive estuaries: Chesapeake Bay case study. *Remote Sens Environ* 109:464–472
- Glibert PM, Conley DJ, Fisher TR, Harding LW, Malone TC (1995) Dynamics of the 1990 winter/spring bloom in Chesapeake Bay. *Mar Ecol Prog Ser* 122:22–43
- Gordon HR (1979) Diffuse reflectance of the ocean: the theory of its augmentation by chlorophyll a fluorescence at 685 nm. *Appl Opt* 18:1161–1166
- Gordon HR, Voss KJ (1999) MODIS normalized water-leaving radiance. MODIS algorithm theoretical basis document, version 4 (MOD-17), NASA
- Gould RW, Arnone RA, Martinolich PM (1999) Spectral dependence of the scattering coefficient in case 1 and case 2 waters. *Appl Opt* 38:2377–2383
- Gower JFR (1980) Observations of in situ fluorescence of chlorophyll a in Saanich Inlet. *Boundary Layer Meteorol* 18:235–245
- Gower JFR, Borstad GA (1981) Use of in vivo fluorescence line at 685 nm for remote sensing surveys of surface chlorophyll a. In: Gower JFR (ed) *Oceanography from space*. Plenum, New York, pp 329–338
- Gregg WW, Conkright ME (2001) Global seasonal climatologies of ocean Chlorophyll: blending in situ and satellite data for the CZCS era. *J Geophys Res* 106:2499–2515
- Harding LW Jr, Itsweire EC, Esaias WE (1994) Estimates of phytoplankton biomass in the Chesapeake Bay from aircraft remote sensing of chlorophyll concentrations. *Remote Sens Environ* 49:41–56
- Harding LW Jr, Kramer JG, Phinney J (2004) Estuarine and watershed monitoring using remote sensing technology present status and future trends. Maryland Sea Grant publication number UM-SG-TS-2004-03
- Harding LW Jr, Mallonee A, Mallonee ME (2005) Bio-optical and remote sensing observations in Chesapeake Bay. *Estuar Coast Shelf Sci* 62:75–94
- Harding LW Jr, Mallonee ME, Perry ES (2002) Toward a predictive understanding of primary productivity in a temperate, partially stratified estuary. *Estuar Coast Shelf Sci* 55:437–463
- Hawes SK (1992) Quantum fluorescence efficiencies of marine fulvic and humic acids. Master's thesis, Department of Marine Science, University of South Florida, St. Petersburg, FL



- Hoge FE, Swift RN (1981) Application of the NASA Airborne Oceanographic Lidar to the mapping of chlorophyll and other organic pigments. In: Campbell JW, Thomas JP (eds) Chesapeake Bay plume study – superflux 1980. NASA Conf. Publ. 2188, NOAA/NEMP III 81 ABCDFG 0042
- Hood RR, Wang HV, Purcell JE, Houde ED, Harding LW (1999) Modeling particles and pelagic organisms in Chesapeake Bay: convergent features control plankton distributions. *J Geophys Res* 104:1223–1243
- Hu C, Lee Z, Muller-Karger FE, Carder KL (2003) Application of an optimization algorithm to satellite ocean color imagery: a case study in southwest Florida coastal waters. *Proc. Ocean Remote Sensing and Applications, SPIE – The International Society for Optical Engineering* 4892, pp 70–79
- Huot Y, Brown CA, Cullen JJ (2005) New algorithms for MODIS sun-induced chlorophyll fluorescence and a comparison with present data products. *Limnol Oceanogr Methods* 3:108–130
- Lee Z, Carder KL, Mobley CD, Steward RG, Patch JS (1999) Hyperspectral remote sensing for shallow waters: 2. Deriving bottom depths and water properties by optimization. *Appl Opt* 38:3831–3843
- Letelier RM, Abbott MR (1996) An analysis of chlorophyll fluorescence algorithms for the Moderate Resolution Imaging Spectrometer (MODIS). *Remote Sens Environ* 58:215–223
- Lobitz B, Johnson L, Mountford K, Stokely P (1998) AVIRIS analysis of water quality in the Chesapeake Bay. *Proc fifth int'l conference remote sensing for marine and coastal environments*, 1:450
- Loisel H, Mériaux X, Berthon JF, Poteau A (2007) Investigation of the optical backscattering to scattering ratio of marine particles in relation to their biogeochemical composition in the eastern English Channel and southern North Sea. *Limnol Oceanogr* 52:739–752
- Longhurst A, Sathyendranath S, Platt T, Caverhill C (1995) An estimate of global primary production in the ocean from satellite radiometer data. *J Plankton Res* 17:1245–1271
- Magnuson A, Harding LW, Mallonee ME, Adolf JE (2004) Bio-optical model for Chesapeake Bay and the middle Atlantic bight. *Estuar Coast Shelf Sci* 61:403–424
- Malone TC (1992) Effects of water column processes on dissolved oxygen: nutrients, phytoplankton and zooplankton. In: Smith D, Leer M, Mackiernan G (eds) *Oxygen dynamics in Chesapeake Bay: a synthesis of research*, University of Maryland Sea Grant, College Park, MD, pp 61–112
- Malone TC, Crocker LH, Pike SE, Wendler BW (1988) Influences of the river flow on the dynamics of the phytoplankton production in a partially stratified estuary. *Mar Ecol Prog Ser* 48:235–249
- Malone TC, Ducklow HW, Peele ER, Pike SE (1991) Picoplankton carbon flux in Chesapeake Bay. *Mar Ecol Prog Ser* 78:11–22
- Maritorena S, Morel A, Gentili B (2000) Determination of the fluorescence quantum yield by oceanic phytoplankton in their natural habitat. *Appl Opt* 39:6725–6737
- Maritorena S, Siegel DA, Peterson AR (2002) Optimization of a semianalytical ocean color model for global-scale applications. *Appl Opt* 41:2705–2714
- McClain CR, Feldman GC, Hooker SB (2004) An overview of the SeaWiFS project and strategies for producing a climate research quality global ocean bio-optical time series. *Deep Sea Res (II. Top Stud Oceanogr)* 51:5–42
- Mobley CD (1988) A numerical model for the computation of radiance distribution in natural waters with wind-roughened surfaces, part II: User's guide and code listing. NOAA Tech. Memo ERL PMEL-81 (NTIS PB88-246871). (Pacific Marine Environmental Laboratory, Seattle, Wash.)
- Mobley CD (1994) *Light and water: radiative transfer in natural waters*. Academic Press, San Diego, California
- Mobley CD, Sundman LK, Boss E (2002) Phase function effects on oceanic light fields. *Appl Opt* 41:1035–1050
- Montagnes DJ, Berges JA, Harrison PJ, Taylor FJR (1994) Estimation of carbon, nitrogen, protein, and chlorophyll a from volume in marine phytoplankton. *Limnol Oceanogr* 39:1044–1060
- Morel A, Prieur L (1977) Analysis of variations in ocean color. *Limnol Oceanogr* 22:709–722

- O'Reilly JE, Maritorea S, Siegel D, O'Brien MC, Toole D, Mitchell BG, Kahru M, Chavez FP, Strutton P, Cota G, Hooker SB, McClain CR, Carder KL, Muller-Karger F, Harding L, Magnuson A, Phinney D, Moore GF, Aiken J, Arrigo KR, Letelier R, Culver M (2000) Ocean color chlorophyll a algorithms for SeaWiFS, OC2, and OC4: Version 4. In: Hooker SB, Firestone ER (eds) SeaWiFS postlaunch technical report series, vol 11. SeaWiFS postlaunch calibration and validation analyses, part 3, NASA, pp 9–23
- Petzold TJ (1972) Volume scattering functions for selected ocean waters. SIO Ref. 72–78, Scripps Inst. Of Oceanography, Visibility Laboratory, La Jolla
- Pope RM, Fry ES (1997) Absorption spectrum (380–700 nm) of pure water. II. Integrating measurements. *Appl Opt* 36:8710–8723
- Ruddick KG, Gons HJ, Rijkeboer M, Tilstone G (2001) Optical remote sensing of chlorophyll a in case 2 waters by use of an adaptive two-band algorithm with optimal error properties. *Appl Opt* 40:3575–3585
- Snyder WA, Arnone RA, Davis CO, Goode W, Gould RW, Ladner S, Lamela G, Rhea WJ, Stavn R, Sydor M, Weidemann A (2008) Optical scattering and backscattering by organic and inorganic particulates in U.S. coastal waters. *Appl Opt* 47:666–677
- Stramski D (1999) Refractive index of planktonic cells as a measure of cellular carbon and chlorophyll a content. *Deep Sea Res (I Oceanogr Res Pap)* 46:335–351
- Stramski D, Boss E, Bogucki D, Voss KJ (2004) The role of seawater constituents in light backscattering in the ocean. *Prog Oceanogr* 61:27–55
- Stramski D, Kiefer DA (1991) Light scattering by microorganisms in the open ocean. *Prog Oceanogr* 28:343–383
- Stramski D, Morel A, Bricaud A (1988) Modeling the light attenuation and scattering by spherical phytoplankton cells: A retrieval of the bulk refractive index. *Appl Opt* 27:3954–3956
- Stramski D, Reynolds RA, Kahru M, Mitchell BG (1999) Estimation of particulate organic carbon in the ocean from satellite remote sensing. *Science* 285:239–242
- Sydor M, Arnone RA (1997) Effect of suspended particulate and dissolved organic matter on remote sensing of coastal and riverine waters. *Appl Opt* 36:6905–6912
- Tassan S, Ferrari GM (2003) Variability of light absorption by aquatic particles in the near-infrared spectral region. *Appl Opt* 42:4802–4810
- Twardowski M, Boss E, Macdonald JB, Pegau WS, Barnard AH, Zaneveld JRV (2001) A model for estimating bulk refractive index from the optical backscattering ratio and the implications for understanding particle composition in case I and case II waters. *J Geophys Res* 106:14129–14142
- Tzortziou M, Herman JR, Gallegos C, Neale P, Subramaniam A, Harding L, Ahmad Z (2006) Bio-optics of the Chesapeake Bay from measurements and radiative transfer closure. *Estuar Coast Shelf Sci* 68:348–362
- Tzortziou M, Subramaniam A, Herman JR, Gallegos C, Neale P, Harding L (2007) Remote sensing reflectance and inherent optical properties in the Mid Chesapeake Bay. *Estuar Coast Shelf Sci* 72:16–32
- van de Hulst HC (1981) *Light scattering by small particles*. Dover, Mineola, New York
- Verity PG, Robertson CY, Tronzo CR, Andrews MG, Nelson JR, Sieracki ME (1992) Relationships between cell volume and the carbon and nitrogen content of marine photosynthetic nanoplankton. *Limnol Oceanogr* 37:1434–1446
- Voipio A (1981) *The Baltic Sea*. Elsevier Science, New York
- Wozniak SB, Stramski D (2004) Modeling the optical properties of mineral particles suspended in seawater and their influence on ocean reflectance and chlorophyll estimation from remote sensing algorithms. *Appl Opt* 43:3489–3503
- Yentsch CS (1993) CZCS: Its role in the study of the growth of oceanic phytoplankton. In: Barale V, Schlittenhardt PM (eds) *Ocean colour: theory and applications in a decade of CZCS experience*. Kluwer Academic Publishers, Dordrecht, The Netherlands, pp 17–32
- Yoder JA, Kennelly MA (2003) Seasonal and ENSO variability in global ocean phytoplankton chlorophyll derived from 4 years of SeaWiFS measurements. *Global Biogeochem Cycles* 17:(4)1112, doi:10.1029/2002GB001942

- Zaneveld JRV, Kitchen JC, Moore C (1994) The scattering error correction of reflecting-tube absorption meters. In: Jaffe JS (ed) *Ocean optics XII*, SPIE – International Society for Optical Engineering, vol 2258, pp 44–55
- Zawada DG, Hu C, Clayton T, Chen Z, Brock JC, Muller-Karger FE (2007) Remote sensing of particle backscattering in Chesapeake Bay: A 6-year SeaWiFS retrospective view. *Estuar Coast Shelf Sci* 73:792–806

**Part III**  
**Mapping Submerged Aquatic Vegetation  
and Benthic Habitats**

## Chapter 8

# High-Resolution Ocean Color Remote Sensing of Coral Reefs and Associated Benthic Habitats

Deepak R. Mishra

This chapter discusses a research aiming to develop semi-analytical models that resolve the confounding influence of water column attenuation on substrate reflectance to characterize benthic habitats from high-resolution remotely sensed imagery. We used high-resolution satellite and airborne imagery as inputs in the models to derive water depth and water column optical properties. Then, we used these parameters in various bio-optical algorithms to deduce bottom albedo and then to classify the benthos, generating a detailed map of benthic habitats. We used IKONOS and QuickBird multispectral satellite data and AISA Eagle hyperspectral airborne data for benthic habitat mapping along the north shore of Roatan Island, Honduras. We found that the hyperspectral data consistently outperform the high-resolution satellite imagery in terms of classification accuracy; however, the hyperspectral data and satellite imagery show similar accuracies when the classification is at the coarse level. These findings reveal the need of data fusion from high spectral and spatial resolution sensors for accurate benthic habitat mapping.

### 8.1 Introduction

Environmental stress on coral reefs and associated benthic habitats can result from natural and human influences. Natural causes include global rise in temperature and sea level (Pittock 1999), increased frequency of the El Niño Southern Oscillation (ENSO) events (Timmermann et al. 1999), tropical cyclones (Knutson et al. 1998), and increased concentrations of atmospheric CO<sub>2</sub> (Kleypas et al. 1999), while human activities include coastal development, destructive fishing, marine pollution, runoff from deforestation, and industrial/agricultural discharge. The net effect of most disturbances is a decline in the percent cover of living benthic habitats over time that has raised alarms in the scientific, recreational, tourism, and political sectors. As a result there is an emerging consensus to map out the spatial distribution

---

D.R. Mishra (✉)

Pontchartrain Institute for Environmental Sciences and Department of Earth & Environmental Sciences, University of New Orleans, New Orleans, LA 70148, USA  
e-mail: dmishra@uno.edu

of benthic habitats so that protection, preservation, and monitoring measures can be implemented (NOAA 2002). However, mapping benthic habitats over large areas using field surveys can be extremely expensive. Therefore, alternative methods such as remote sensing may be preferred by resource managers because they are economical and provide a synoptic view that is unmatched by surface data collection. However, it is not a simple task because coral reef environments are optically, spatially, and temporally complex. To extract meaningful information from remotely sensed data, techniques must be developed that relate the signals received by a remote sensor to the optical properties of the reef community and its associated habitats.

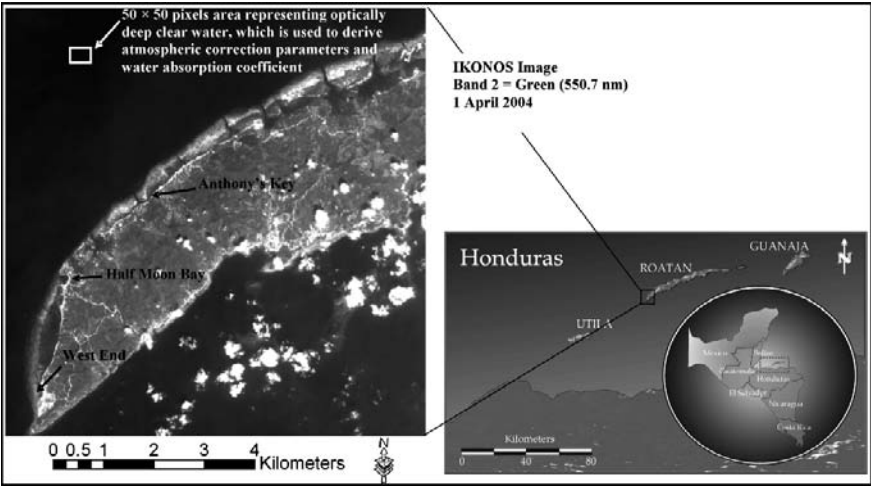
Accurate characterization of benthic features in shallow, near-shore waters can be challenging for remote sensing because of the scattering, attenuation, and differential absorption of light by the water column. The presence of suspended organic and inorganic materials and a heterogeneous benthos comprised of coral reefs, seagrasses, and other benthic features makes mapping and interpretation an extremely difficult task (LeDrew et al. 1995, Mumby et al. 2001). Accurate benthic mapping requires thorough analysis of substrate reflectance but it is always intimately associated with water column properties (depth, absorption, and scattering). Conventional analytical methods are unable to resolve one measure accurately unless the other is already known (Mishra et al. 2005, 2006, 2007). For example, if the water column diffuse attenuation coefficients are known for each spectral band and the depth for each pixel has been measured independently, the at-surface reflectance of the substrate can be predicted, thus permitting spectral classification and benthic mapping (LeDrew et al. 1995, Maritorena and Guillocheau 1996, Mumby et al. 2001)

The signals measured by a sensor from above the water surface of a shallow marine environment are highly coupled with phytoplankton abundance (chlorophyll absorption), water column interactions (absorption by water and scattering by suspended sediments), and radiance reflected from the bottom i.e., bottom albedo. To map the benthic habitats accurately, the bottom albedo needs to be known or at least be derivable (Mumby et al. 1998b). The research question identified in this chapter was: will incorporation of important parameters such as water depth, absorption and scattering coefficients allow for an accurate estimation of bottom albedo?

This chapter is based on the work of Mishra et al. (2005, 2006, 2007) and focuses on the development of semi-analytical models that can be used to map the spatial distribution of coral reefs and associated habitats from remote measurements of water reflectance. The models used high spatial resolution remotely sensed data, water depth and water column optical properties (absorption and scattering) to remove the effect of overlying water column, and derive a bottom image. Specific objectives included, mapping the spatial distribution of these benthic habitats using high resolution multi- and hyperspectral sensors as well as comparison of results derived from these sensors.

## 8.2 Study Area

Roatan Island lies between  $16^{\circ} 15'$  to  $16^{\circ} 25'$  N and  $86^{\circ} 22'$  to  $86^{\circ} 37'$  W. It is the largest of the Bay Islands of Honduras, and is located in the western portion of the Caribbean Sea approximately 50 km north of the mainland. Our study was



**Fig. 8.1** Location of Roatan Island, Honduras in Central America (circle inset), and a grayscale image-map of the IKONOS scene acquired on 1 April 2001 (Mishra et al. 2005)

conducted in the vicinity of Anthony's key and Man of War key resorts in the north shore of the island (Fig. 8.1).

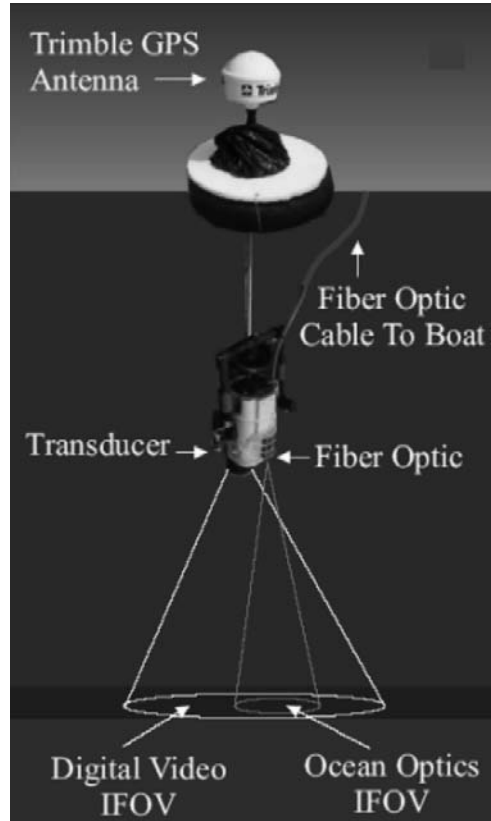
Roatan's climate is typical of the hot and humid tropical environments, with an average annual precipitation of 215 cm per year. Mean monthly temperatures range from 25.4°C in January to 28.9°C in September (Davidson 1974). The reefs of the Bay Islands contain at least 52 species of stony corals, at depths ranging from 2 to 15 m (Keck 2000). Coral species include Star corals (*Montastrea annularis*, *M. franksi*, *M. faveolata*, *M. cavernosa*), Brain corals (*Colpophyllia natans*, *Diploria spp.*), Sheet and Lettuce corals (*Agaricia agaricites*, *A. larcki*, *A. undata*, *A. fragilis*, and *Leptosiris cuculatta*), Flower coral (*Eusmilia fastigiata*), Pillar coral (*Dendrogyra cylindrus*), Boulder Brain coral (*Colpophyllia natans*), Symmetrical Brain coral (*Diploria strigosa*) and Massive Starlet coral (*Siderastrea siderea*). The bays contain highly productive seagrass beds, with Turtle Grass (*Thalassia testudinum*) being the most abundant species at Roatan. The seagrasses provide habitat for anemones, mossusks, crabs, shrimp, and many other organisms.

## 8.3 Data Acquisition

### 8.3.1 In Situ Data

Two independent *in situ* datasets were collected for model calibration and validation respectively. The model calibration datasets were obtained from a vertically stable buoy guided by a snorkeler along a series of transects. This buoy served as a platform for a Trimble TDC1 Asset Surveyor GPS antenna, a Sony Hi-8 mm TRV-320

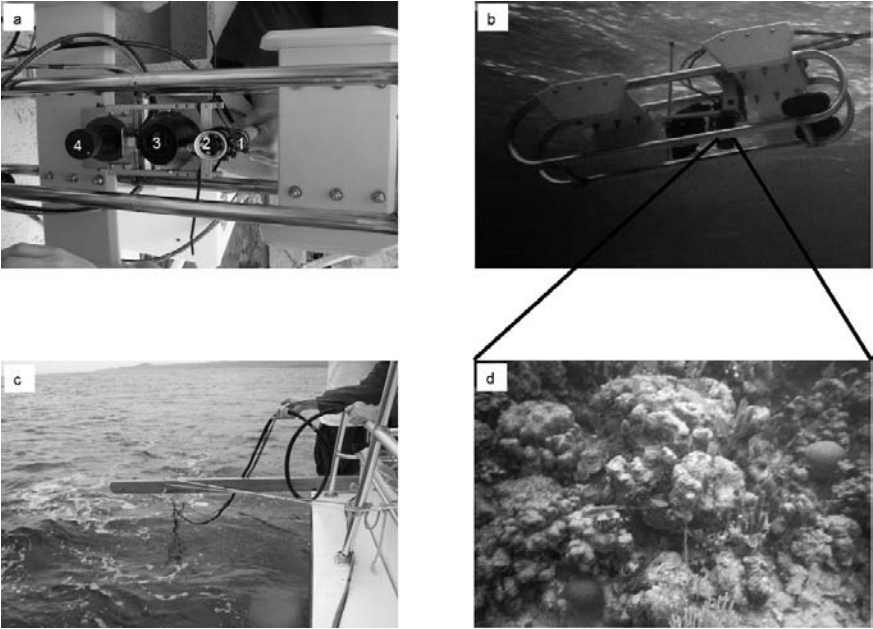
**Fig. 8.2** Components of a vertically stable GPS buoy used *in situ* data collection for bathymetry model calibration (Mishra et al. 2005, 2006, 2007)



digital video camera encased in a T-9 housing (Undersea Video Housings), and a Lowrance depth transducer (Fig. 8.2). The data were collected simultaneously 1-m below the air/water interface. Consequently, the instantaneous field of view (IFOV) of the images and hyperspectral readings varied as a function of depth and ranged from 0 to 25 m. However, recorded images and the GPS synchronous time stamp were of suitable quality to determine the primary benthic cover at sample locations and the IFOV was calculated based on depth measured by the Lowrance sonar.

A towed sensor platform (the “towfish”) built by Shark Marine (St. Catharines, Ontario, Canada) was used to acquire the bathymetric model validation data sets (Fig. 8.3a,b). The towfish was constructed to resist wave action, so it moved through the water at a relatively constant, horizontal position while being towed at a speed of approximately 3 km/h (Fig. 8.3c). Depths were logged continuously along selected transects and a high-resolution “mini-camera” imaged the bottom at the locations where these readings were acquired (Fig. 8.3d). A differential GPS was placed on the boat and the offset to the towfish was calculated. Mathematically, the exact location of the transducer was determined by correcting for the distance between the





**Fig. 8.3** (a) Components of towfish, a multi-sensor platform designed by CALMIT includes 1. ocean optics hyperspectral sensor, 2. camera one, 3. camera two, 4. transducer; (b) view of towfish from under water; (c) towfish in action; (d) typical coral bottom types photograph taken by towfish camera (Mishra et al. 2005, 2006, 2007)

GPS unit and the transducer (6.2 m), the angle at which the boat was moving (variable), and the position of the transducer relative to the surface of the water (0.3048 m below).

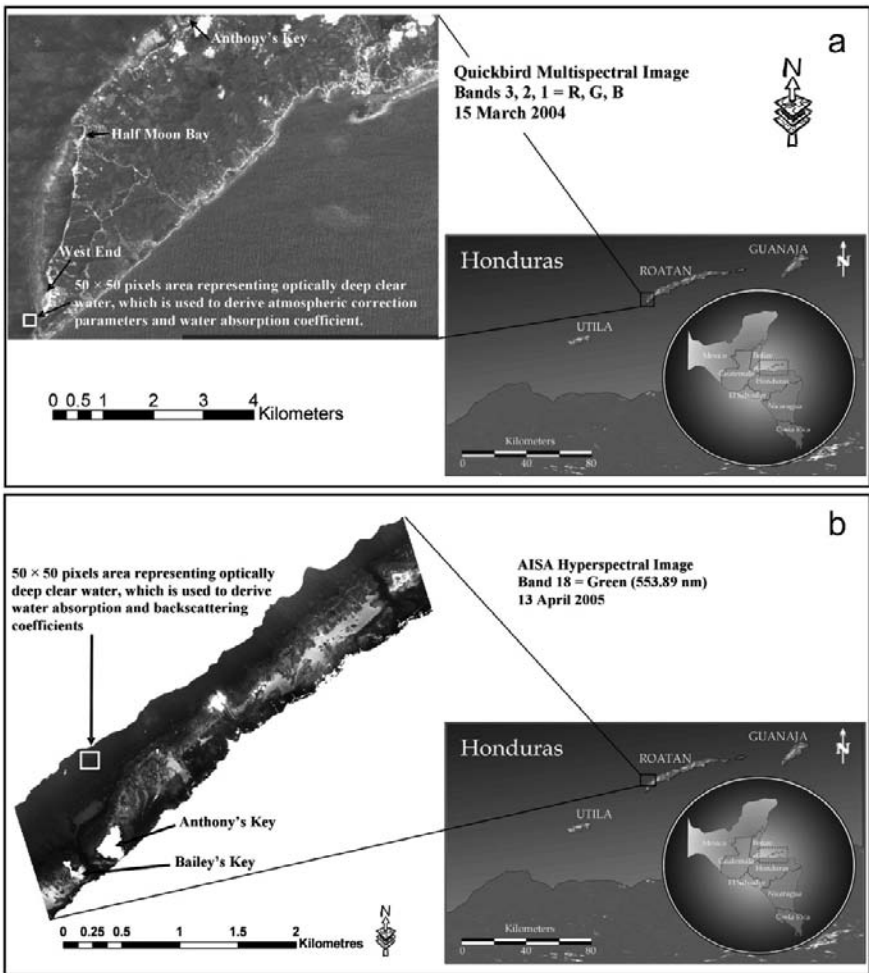
During subsequent field surveys in 2005, two pairs of Ocean Optics USB 2000 hyperspectral radiometers were added to the towfish (i.e., upward looking and downward looking Ocean Optics sensor) for acquiring upwelling radiance ( $L_u$ ) and downwelling irradiance ( $E_d$ ) just above and below the water surface. In essence the towfish provided us with four different kinds of datasets at a particular geographic location, including bottom type (photograph from the camera), depth (transducer), above water remote sensing reflectance,  $R_{rs}(\lambda)$  (Ocean Optics), and underwater remote sensing reflectance,  $r_{rs}(\lambda)$  (Ocean Optics).

### 8.3.2 Spaceborne Multispectral Data

IKONOS panchromatic and multispectral images were collected for the Roatan study site on 1 April 2001 (Fig. 8.1). Primary radiometric corrections by Space Imaging, Inc., Colorado, USA, were designed to remove any spatial variations in digital output or artifacts that may occur in the image data. In addition, Space

Imaging had performed geometric corrections ( $\pm 1$  pixel; nearest neighbor) on the image to remove any optical or positional distortions. The brightness values (BVs) for each band were converted to top of the atmosphere (TOA) radiance by applying calibration coefficients referenced to well-characterized spectro-radiometric targets (Space Imaging 2001).

Two Quickbird multispectral images were collected for the Roatan study site on 15 March 2004 (Fig. 8.4a). The QuickBird sensor system has three visible bands centered at 485 nm (450–520 nm), 560 nm (520–600 nm), and 660 nm (630–690 nm), which can be used for shallow marine applications. Primary radiometric corrections, performed by Digital Globe, Inc., Longmont, Colorado, USA, were designed



**Fig. 8.4** Location of Roatan Island, Honduras in Central America (*circle inset*), and (a) A grayscale image-map of the QuickBird scene acquired on 15 March 2004; (b) A grayscale image-map of the AISA Eagle acquired in April 2005 (Mishra et al. 2006, 2007)

to remove any spatial variations in digital output or artifacts that may occur in the image data. Geometric corrections ( $\pm 1$  pixel; nearest neighbor) were performed by Digital Globe, Inc. to remove any optical or positional distortions in the imagery. The brightness values (BVs) for each band were converted to the top of atmosphere (TOA) radiance by applying calibration coefficients derived from the image metadata.

### ***8.3.3 Airborne Hyperspectral Data***

An aerial remote sensing platform for hyperspectral data collection was used for this investigation. The instrument array included an AISA Eagle hyperspectral imager from Visible to Near Infrared (VNIR), a system which can provide high spatial and spectral resolution. The AISA Eagle is a solid-state, push-broom instrument that has the capability of collecting data within a spectral range of 390–1000 nm in up to 512 bands. The placement of the spectral bands may be configured by the user and the selected bandwidths can range anywhere from  $\sim 2$  nm to  $\sim 10$  nm. The AISA Eagle pre-processing software provides for the automatic geometric correction, rectification, mosaicking, and calculation of at-platform radiance by applying calibration coefficients referenced to well-characterized spectroradiometric targets. The algorithm uses the DGPS and attitude information from the INS to perform geometric, georeferencing and mosaicking operations. AISA Eagle data were acquired between 0330 and 0430 h (CST) on 13 April 2005 when the solar zenith angle was close to  $70^\circ$ . Ground data indicated low wind ( $\sim 3$  m s $^{-1}$ ), minimal ocean swell, high visibility (30 km), and clear skies. The sensor altitude was (2.073 km), and the image was acquired at nadir at a spatial resolution of 2 m and spectral resolution of 62 bands ranging from 392.39 to 981.68 nm with a 12-bit radiometric output and the flight lines covered an area of approximately 1.6 km $^2$  in the vicinity of Anthony's Key and Man of War Key (Fig. 8.4b). The image data were converted to at-platform radiance by applying the calibration coefficients provided by AISA processing software 'Caligeo' for subsequent processing.

## **8.4 Methodology**

### ***8.4.1 Land and Cloud Masking***

When extracting aquatic information, it is useful to eliminate all upland and terrestrial features (Jensen et al. 1991); thus all upland features, as well as boats, piers, and clouds were masked out of all the images. The "land-mask" restricts the spectral range of radiance values to aquatic features and allows for detailed feature discrimination. Radiance values of the NIR band were used to prepare the binary mask which was subsequently applied to all the channels.

### 8.4.2 First-Order Atmospheric Correction

The atmospheric correction method employed herein follows the approach adopted for Coastal Zone Color Scanner (CZCS) protocol (Gordon et al. 1983). The Rayleigh and aerosol contributions to the total radiance measured by the sensors were removed from the images. Rayleigh scattering was computed for each pixel, whereas the aerosol scattering was calculated for offshore pixels assuming a marine-type of aerosol. Water-leaving radiance is a radiometric quantity resulting from the atmospheric correction and is a measure of the total signal recorded at the top of the water column.

In the case of oceanic remote sensing, the total signal received at the sensor altitude is dominated by radiance contributed by atmospheric scattering processes and only 8–10% of the signal corresponds to the oceanic reflectance (Kirk 1994). Therefore, it is advisable to correct for atmospheric effects to retrieve any quantitative information for surface waters from the image. The radiance received by a sensor,  $L_t(\lambda_i)$ , at the top of the atmosphere (TOA) in a spectral band centered at a wavelength  $\lambda_i$  can be divided into the following components (Gordon et al. 1983):

$$L_t(\lambda_i) = L_r(\lambda_i) + L_a(\lambda_i) + T(\lambda_i)L_g(\lambda_i) + t(\lambda_i)L_w(\lambda_i) \quad (8.1)$$

where,

$L_r(\lambda_i)$  and  $L_a(\lambda_i)$  = radiances generated along the optical path in the atmosphere by Rayleigh and aerosol scattering respectively;

$L_g(\lambda_i)$  = contribution arising from the specular reflection of direct sunlight from the sea surface or the sun glint component;

$L_w(\lambda_i)$  = desired water leaving radiance;

$T$  = direct atmospheric transmittance; and

$t$  = diffuse atmospheric transmittance of the atmosphere.

Note that for a high visibility environmental condition (in our case visibility >40 km), we ignore any Rayleigh-aerosol multiple scattering and use a quasi-single-scattering approximation. According to Gordon and Voss (1999), for areas around the sun glint pattern,  $T(\lambda_i)L_g(\lambda_i)$  is so large that the imagery is virtually useless and must be discarded. The images had negligible sun glint effects, and hence  $T(\lambda_i)L_g(\lambda_i)$  may be ignored, leaving the largest and most difficult terms to estimate (i.e., the path radiances due to Rayleigh and aerosol scattering).

Rayleigh atmospheric scattering affects the direction of short wave radiation, resulting in haze that affects primarily the blue and green bands. Using the algorithm developed by Gordon and Clark (1981), the Rayleigh path radiance was computed and applied to the image. Similarly, the aerosol scattering for the scene, was derived by subtracting the Rayleigh path radiance from TOA radiance in clear water pixels (Figs. 8.1, 8.4a,b) of the NIR band. Gordon and Wang (1994) proposed an exponential relationship for the spectral behavior of aerosol optical depth which has been used for the SeaWiFs atmospheric correction algorithm. The algorithm uses an Angstrom exponent ( $\epsilon$ ) based on an exponential relation using spectral data at

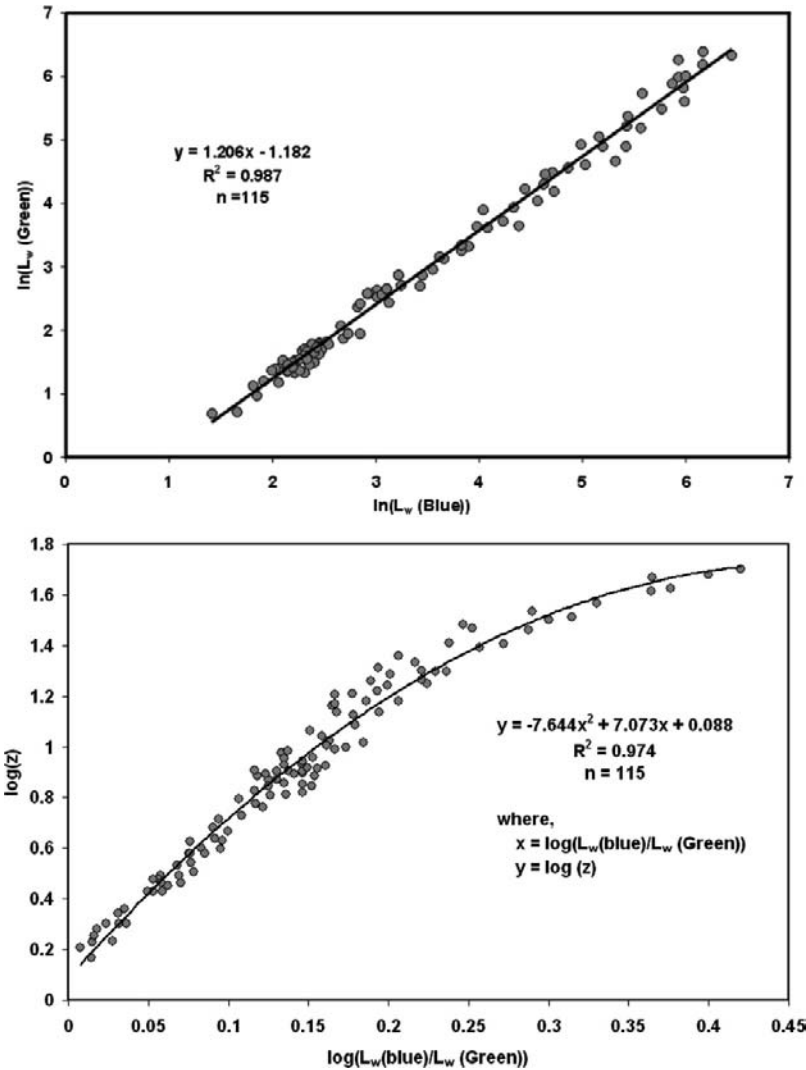
765 and 865 nm for each pixel. The aerosol optical thickness was extrapolated to the visible channels using this relationship. Because IKONOS and Quickbird sensor do not have two bands in the NIR to calculate the Angstrom exponent,  $\varepsilon(\lambda_i, \lambda_4)$ , it was set to unity, which is characteristic of maritime aerosols at high relative humidities (Gordon and Voss 1999, Hu et al. 2001). It was also assumed that the aerosols are homogeneously distributed over the entire area of interest, so that it was implicit that aerosol path radiance, computed over the clear water was constant for the entire scene. The final component, diffuse transmittance ( $t(\lambda_i)$ ), which is defined as the water leaving radiance in a particular viewing direction transmitted to the TOA, was computed as recommended by Gordon et al. (1983). By applying the method described in this section it was observed that approximately 85–90% of the radiance was removed as a result of atmospheric correction from all the images.

AISA Eagle data were atmospherically corrected by using FLAASH (Fast Line-of-sight Atmospheric Analysis of Spectral Hypercubes), a first-principles atmospheric correction algorithm for visible to shortwave infrared (SWIR) hyperspectral data. The solar zenith and azimuth angles were calculated in the FLAASH algorithm from the AISA flight date, time, latitude, and longitude and were used to predict incident solar irradiance at the top of the atmosphere. A scale factor file for the input radiance image was provided to the algorithm. The input atmospheric and aerosol models were chosen to be tropical and maritime respectively with initial visibility of 30 km. Then 820 nm band was selected as the water absorption feature, and the aerosol scale height and CO<sub>2</sub> mixing ratio were kept as default, which is 2.0 km and 390 ppm respectively.

### 8.4.3 Shallow Marine Bathymetry Estimation

The ultimate goal of this research was to derive the bottom albedo and carry out benthic mapping of shallow marine habitats in Roatan Island, Honduras. To derive bottom albedo, water depth should be known for the study area. The depths will be used to eliminate the change in reflectance that is attributable to variable depth, and water column attenuation effects. Researchers have been attempting to estimate depth of shallow water using remote sensing for several years (e.g., Lyzenga 1978). A common problem among most studies is that the seafloor is covered by a patchwork of organisms and substrates that have different albedos, ranging from very dark (e.g., coral  $\sim 0.12$ ) to very bright (e.g., sand  $\sim 0.3$ ). The difficulty is that a dark object strongly absorbs light and will appear to be deeper than it really is. This effect is not as severe for bright objects, which absorb less strongly. Thus, for coral and sand at the same true depth, the coral virtually always appears to be deeper than the sand. Previous researchers have mapped water depth by assuming that a pair of wavebands can be identified such that the ratio of the radiances in these two bands was the same for all the bottom types within a given scene (Polcyn et al. 1970, Lyzenga 1978). Following this assumption, three site-specific algorithms were developed to map high resolution bathymetry using the radiance measured by the three sensors. For example, in the IKONOS image essentially a ratio of wavebands (blue

and green) was identified that is constant for all bottom types (Fig. 8.5a). With these bands having different water absorptions, one band will have arithmetically lesser values than the other. As the depth increased, radiance of the band with higher absorption (green) decreased proportionally faster than the band with lower absorption (blue) and the radiance ratio of the blue to the green increased. This method also compensate implicitly for variable bottom types. A change in bottom albedo affects both bands similarly, but changes in depth affect the high absorption band more



**Fig. 8.5** (a) Model calibration dataset taken from GPS buoy showing the regression between log-transformed water-leaving *blue* versus *green* radiance values for several bottom types; (b) Relationship between bottom depth and ratio of blue to green water leaving radiance (Eq. 8.2). The polynomial equation shown in the graph was used to derive bathymetry map from the IKONOS image (Mishra et al. 2005)

(Philpot 1989). Accordingly, the change in ratio because of depth is much greater than that caused by change in bottom albedo, suggesting that different bottom albedos at a constant depth will still have the same ratio. The log transformed radiance ratio of the two bands (blue, green) in the IKONOS image was plotted against known depth data ( $z$ ) to develop a second order polynomial bathymetry models (Fig. 8.5b). The models were different for different sensors. For example, given below is the polynomial model for the IKONOS sensor:

$$y = -7.6439x^2 + 7.0734x + 0.0876 \quad (8.2)$$

where,

$$y = \log(z) \quad (8.3)$$

$$x = \log \left[ \frac{L_w(\text{blue}; 480.3 \text{ nm})}{L_w(\text{green}; 550.7 \text{ nm})} \right] \quad (8.4)$$

The above polynomial equation explained  $> 97\%$  of variation ( $p < 0.001$ ) in water depth calibration dataset collected over five transects of various bottom types (coral, sand, seagrass, Mixed: sand/coral/seagrass/algae). Approximately 50% of the predictions were within  $\pm 0.033$  m and the mean residual was  $\pm 0.13$  m. Equation (8.2) was used for the IKONOS image to derive a map of bathymetry across the study site. Similarly a different polynomial model was used for AISA Eagle and a single band model (taken from Mishra et al. 2006) was used for QuickBird to derive the bathymetric maps.

#### 8.4.4 Deriving Bottom Albedo

The signals measured by an airborne sensor from above the water surface of a shallow marine environment are highly coupled with phytoplankton abundance (chlorophyll absorption), water column interactions (water depth, absorption by water column and scattering by suspended sediments), and bottom albedo. The apparent optical properties of water such as absorption ( $a$ ) and backscattering coefficient ( $b_b$ ) are the main physical agents governing the magnitude and spectral composition of the backscattered flux from the ocean surface (Maritorena et al. 1994). Derivation or approximation of these parameters are necessary in order to determine the optical bottom albedo and ultimately to map the spatial distribution of benthic habitats for shallow ocean waters. Lee et al. (1994, 1996) and Zhang et al. (1999) proposed analytical models to derive water optical properties ( $a$  and  $b_b$ ) from remotely sensed data. Using AVIRIS imagery and spaceborne spectrometers with high spatial and spectral resolution, they successfully separated various shallow water constituents based on their unique spectral contributions. The work described in this section of the paper demonstrates analytically how to derive bottom albedo using multi- and hyperspectral data, after the removal of atmospheric interferences. Given the limited number of visible bands on the IKONOS and QuickBird sensors, the model has been necessarily simplified.

Remote sensing reflectance ( $R_{rs}$ ) is defined as a ratio of the water-leaving radiance ( $L_w$ ) to downwelling irradiance ( $E_d$ ) just above the surface.  $R_{rs}$  is an apparent optical property (Mobley 1994) controlled by the absorption and scattering properties of the constituents in the water and the bottom albedo, and can be written as:

$$R_{rs}(\lambda) = R_{rs}^w(\lambda) + R_{rs}^b(\lambda) \quad (8.5)$$

where,

$R_{rs}^w(\lambda)$  = remote sensing reflectance from water column; and

$R_{rs}^b(\lambda)$  = remote sensing reflectance from the bottom

Lee et al. (1994) have further approximated the two terms,  $R_{rs}^w(\lambda)$ ,  $R_{rs}^b(\lambda)$ , as follows:

$$R_{rs}^w(\lambda) \approx 0.05 \frac{b_b(\lambda)}{a(\lambda) + b_b(\lambda)} \left[ 1 - e^{-3.2(a(\lambda) + b_b(\lambda))H} \right] \quad (8.6)$$

$$R_{rs}^b(\lambda) \approx 0.173\rho(\lambda) e^{[-2.7(a(\lambda) + b_b(\lambda))H]} \quad (8.7)$$

where,

$a(\lambda)$  = total absorption coefficient in  $m^{-1}$ ;

$b_b(\lambda)$  = backscattering coefficient in  $m^{-1}$ ;

$H$  = depth of water in m; and

$\rho(\lambda)$  = bottom albedo.

The angular dependency of the remote sensing reflectance (subsurface solar zenith angle, sensor zenith angle) are not explicitly stated in the Eqs. (8.6) and (8.7); however, they are included in the coefficients of the equations.

The backscattering coefficient may be expressed as:

$$b_b(\lambda) = b_{bp}(\lambda) - b_{bw}(\lambda) \quad (8.8)$$

where,

$b_{bp}$  = backscattering by particles in  $m^{-1}$ ; and

$b_{bw}$  = backscattering by water molecules in  $m^{-1}$  taken from Morel (1974).

Gordon et al. (1998) and Morel (1988) proposed different forms of bio-optical algorithms to approximate the backscattering by particles and is incorporated in the Eq. (8.8) as:

$$b_b(\lambda) = b_{bp}(660) \left( \frac{660}{\lambda} \right)^\eta + b_{bw}(\lambda) \quad (8.9)$$

where,

$\eta$  = a coefficient whose values for ocean particles range from 0.0 to 3.0;

$\eta = 0.5$  is chosen for this coastal study because it is Case-1 water, where concentration of chlorophyll and other biogenic materials is higher compared to non-biogenic particles.



To estimate  $b_{bp}(660)$ , we assume there is no contribution from the bottom to the upwelling signal in 660 nm, where the absorption is large ( $>0.4\text{ m}^{-1}$ ) and dominated by water molecules. Hence, for relatively clear water deeper than  $1.5/a_w(660)$ , where bottom effects are small, the backscattering coefficients by particles can be expressed as (Morel and Gentili 1993):

$$b_{bp}(660) \approx \frac{a_w(660)}{0.05} R_{rs}(660) \quad (8.10)$$

where,

$a_w$  = pure-water absorption coefficient of water taken from Pope and Fry (1997).

The total absorption coefficient,  $a(\lambda)$ , can be derived by modification of Austin and Petzold (1986) as:

$$a(\lambda) = M(\lambda)[a(485) - a_w(485)] + a_w(\lambda) \quad (8.11)$$

where,

$M$  = statistically derived coefficients taken from Austin and Petzold (1986);

$a(485)$  = total absorption coefficient at 485 nm; and

$a_w(485)$  = pure-water absorption coefficient at 485 nm.

According to Lee et al. (1998), the total absorption coefficient at 440 nm,  $a(440)$ , over deep water, can be empirically determined by the following equation:

$$a(440) = 10^{-0.619 - 1.969 \left( \log_{10} \left( \frac{R_{rs}(485)}{R_{rs}(560)} \right) \right) + 0.790 \left( \log_{10} \left( \frac{R_{rs}(485)}{R_{rs}(560)} \right) \right)^2} \quad (8.12)$$

where,

$R_{rs}(485)$  = remote sensing reflectance at 485 nm; and

$R_{rs}(560)$  = remote sensing reflectance at 560 nm.

We can thus rewrite the Eq. (8.11) to compute the total absorption coefficient at 485 nm as:

$$a(485) = \frac{a(440) - a_w(440)}{M(440)} + a_w(485) \quad (8.13)$$

Note that, the models to derive absorption and backscattering coefficients discussed above uses wavelengths such as 485, 560, 660 nm, and in our case, applied to IKONOS, QuickBird, and AISA Eagle blue, green, red band centers respectively. Equation (8.11) is applied over deep water pixels (white square in Figs. 8.1, 8.4a,b) to compute the water absorption coefficients for the blue, green, and red bands of the IKONOS and QuickBird datasets as well as for 33 bands of the AISA Eagle dataset. Deep water pixels were defined as those having very little upwelling signal in the visible bands of the dataset and are not affected by bottom albedo; i.e., they comprise optically deep areas. A  $50 \times 50$  pixel window was identified (white square in white square in Figs. 8.1, 8.4a,b) as having very little water leaving radiance values

in all visible bands. The total absorption coefficients derived from that region were assumed to be constant over the entire scene. Absorption and backscattering coefficients for each image were derived using Eqs. (8.9, 8.11, and 8.13) (Table 8.1a,b,c). The water depth and optical parameters were used to derive the bottom albedo im-

**Table 8.1** Absorption and backscattering coefficients derived from the  $50 \times 50$  optically deep water pixel window (shown in Figs. 8.1, 8.4a,c) of (a) IKONOS; (b) QuickBird; and (c) AISA Eagle images (Mishra et al. 2005, 2006, 2007)

Sensors		Total absorption coefficients ( $a(\lambda)$ ) ( $m^{-1}$ )	Total backscattering coefficients ( $bb(\lambda)$ ) ( $m^{-1}$ )	Coefficients ( $M(\lambda)$ )
Name	Wavelength- $\lambda$ (nm)			
<b>IKONOS</b>	480.3	0.0216	0.0049	1.0955
	550.7	0.0617	0.0039	0.586
	664.8	0.4310	0.0031	0.7301
<b>Quick Bird</b>	485	0.0366	0.0125	1.0469
	560	0.0743	0.0067	0.5457
	660	0.4266	0.0033	0.7101
<b>AISA Eagle</b>	401.15	0.2502	0.00387	1.7383
	409.91	0.2425	0.00377	1.7591
	418.67	0.2315	0.00368	1.6974
	427.42	0.2262	0.00359	1.6108
	436.22	0.2138	0.00350	1.5648
	445.23	0.2002	0.00342	1.4673
	454.27	0.1858	0.00333	1.3627
	463.31	0.1719	0.00326	1.2521
	472.35	0.1660	0.00318	1.1460
	481.39	0.1544	0.00311	1.0955
	490.42	0.1448	0.00304	1.0000
	499.46	0.1385	0.00297	0.9118
	508.50	0.1363	0.00291	0.8310
	517.54	0.1410	0.00285	0.7578
	526.58	0.1346	0.00279	0.7241
	535.61	0.1317	0.00274	0.6627
	544.67	0.1320	0.00268	0.6094
	553.89	0.1366	0.00263	0.5647
	563.17	0.1407	0.00258	0.5289
	572.45	0.1473	0.00253	0.5146
	581.78	0.1680	0.00248	0.4935
	591.18	0.2089	0.00243	0.4840
	600.58	0.3002	0.00238	0.4903
	609.98	0.3438	0.00234	0.5090
	619.39	0.3663	0.00230	0.5380
	628.79	0.3911	0.00226	0.6231
	638.19	0.4090	0.00222	0.7001
	647.59	0.4280	0.00218	0.7300
656.99	0.4573	0.00214	0.7323	
666.39	0.5015	0.00210	0.7205	
675.80	0.5008	0.00207	0.6693	
685.20	0.5055	0.00204	0.5651	
694.60	0.5158	0.00200	0.3984	

age (Eq. 8.7) from which the spatial distribution of benthic habitats was extracted using standard image processing procedures.

#### ***8.4.5 IKONOS and QuickBird Image Classification***

Prior to implementing a spectral pattern recognition algorithm, a classification scheme was developed that included the following categories: (1) dense seagrass, (2) Mixed: seagrass/sand/algae, (3) Mixed: coral/sand, (4) sand, (5) coral, and (6) deep water. These six aquatic feature classes were selected based on the availability of sufficient replication of ground control data to verify feature locations in a later classification analysis. The Iterative Self Organizing Data (ISODATA) algorithm was used on the bottom albedo image composed of three bands to derive 150 statistically different clusters (Jensen 1996). Using *in situ* data these clusters were assigned to the benthic categories with the highest probability of being a member. Finally a comprehensive evaluation of the classification accuracy was performed based on 651 and 383 reference points for IKONOS and QuickBird respectively. The reference points included digital still photographs, and digital video images taken by the towfish, as well as photos taken by the divers comprising our field team.

#### ***8.4.6 AISA Eagle Noise Reduction and Image Classification***

Since bottom-reflected light is negligible (specifically wavelengths  $> 600$  nm) compared to the total reflectance received at sensor level, the signal to noise ratio in the bottom albedo image, generated after the atmospheric and water column correction to the AISA-Eagle hyperspectral image, was found to be low. Therefore a noise reduction technique referred as “minimum noise fraction” (MNF) was applied to the bottom albedo image before performing image classification. MNF determines the inherent dimensionality, identifies and segregates noise in the image, and reduces the computational requirements for subsequent processing (Boardman and Kruse 1994). It is essentially two cascaded principal components transformation. The first transformation, based on an estimated noise covariance matrix, decorrelates and rescales the noise in the data. This results in transformed data where the noise has unit variance and no band-to-band correlations. The second transform is a standard principal component transformation of the noise-whitened data. For further spectral processing, the inherent dimensionality of the data is determined by examining the final eigenvalues and the associated images. Once a threshold eigenvalue value was established, the noise bands were clipped out and a spectral segmentation algorithm was used on the information bands to map out the benthic habitats.

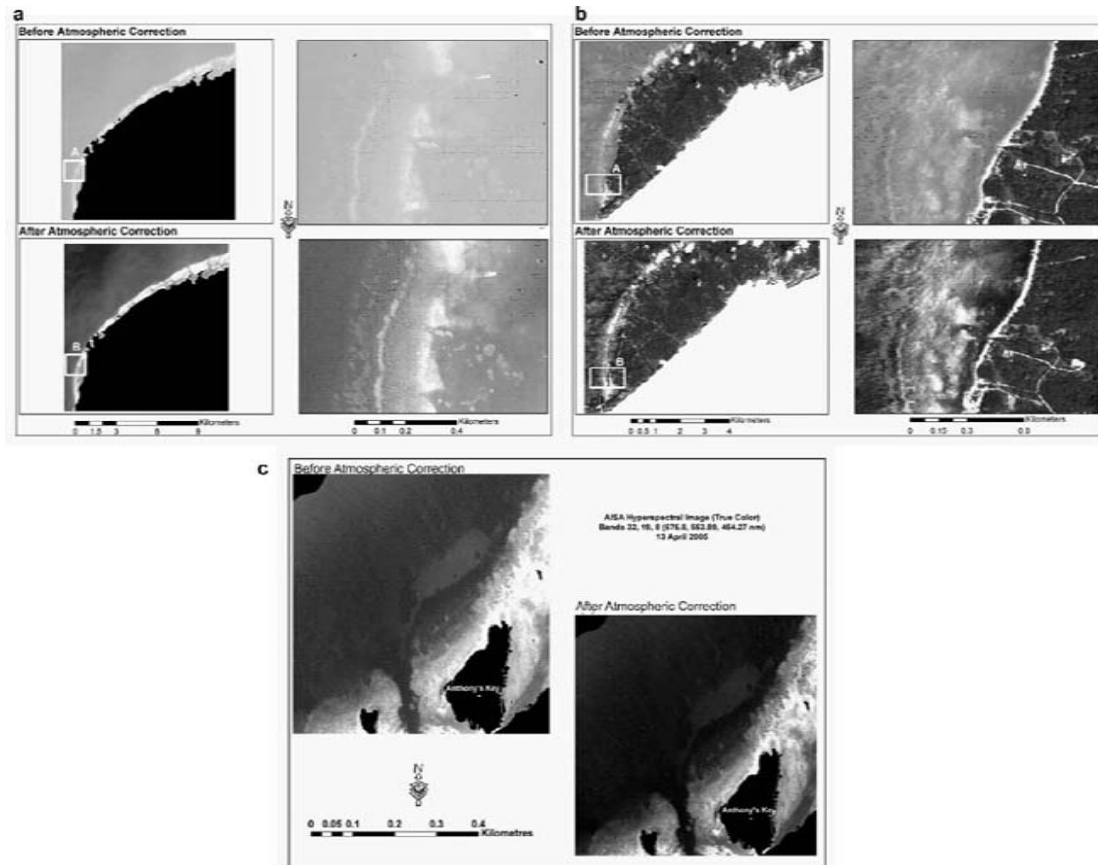
The classification scheme developed for AISA Eagle data had few more classes because of the detailed field work and included the following categories: (1) Sand, (2) Seagrass with Sand (3) Dense Seagrass (4) Sand with Benthic Algae, (5) Coral,

(6) Coral with Sand, (7) Hard Bottom, (8) Mixed: Sand/Hard Bottom/Coral, and (9) Deep Water. The ISODATA algorithm was used on the MNF information bands to derive 300 clusters (Jensen 2004). Subsequently, *in situ* data were used to assign each cluster to the category to which it had the highest probability of being a member. Finally a comprehensive evaluation of the classification accuracy was performed based on 1208 reference points, digital still photographs, and digital video images taken by the towfish, as well as photos taken by the divers comprising our field team.

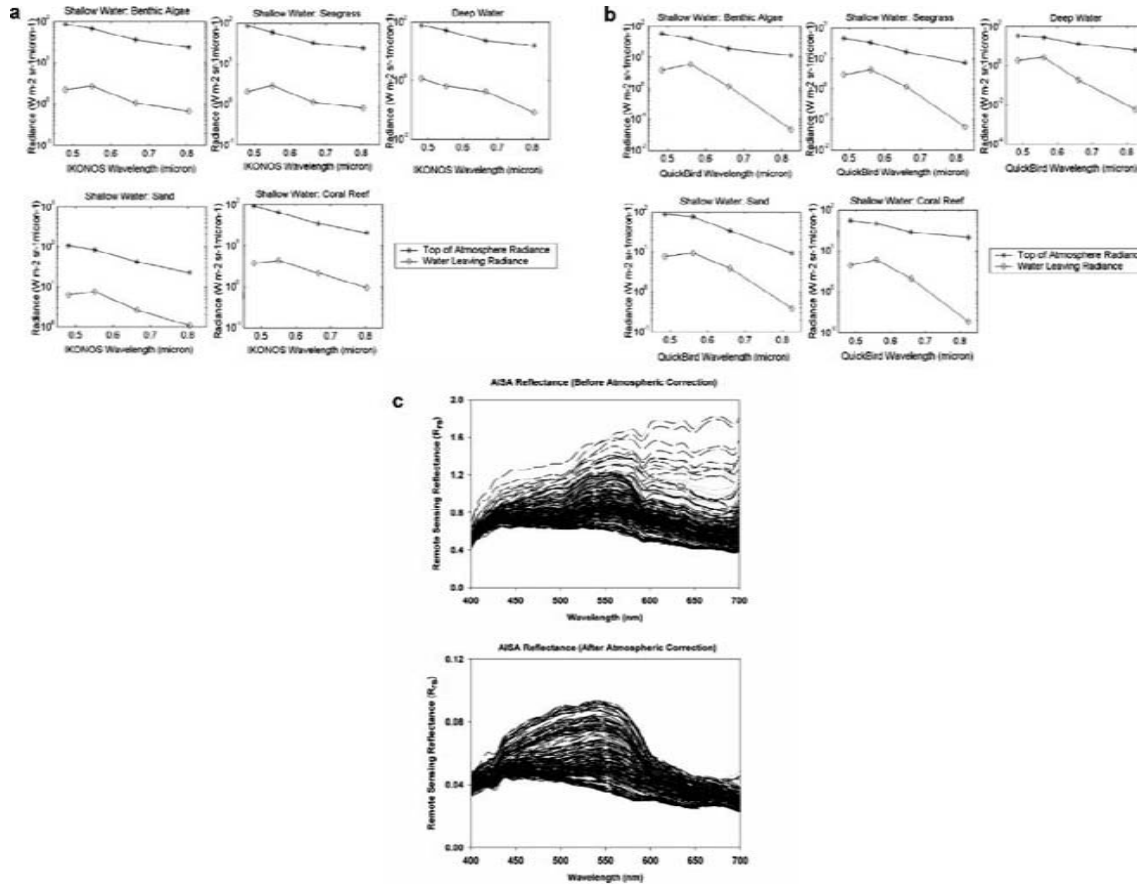
## 8.5 Results and Discussion

The most common method for evaluating atmospheric correction is to compare  $R_{rs}$  spectra retrieved from the images before and after the procedure for all sampling areas as well as with ground-based measurements for a variety of targets. Visual examination of the IKONOS and QuickBird images before and after the atmospheric correction procedure showed sharp differences between them (Fig. 8.6a,b). For example in the IKONOS image the coral areas in the zoomed insets (light brown) showed a linear trend (N-S) after the atmospheric correction (Fig. 8.6a). In general the haziness depicted in the original images, attributed to Rayleigh and aerosol scattering, was eliminated resulting in visually clear images (see comparison of Fig. 8.6a,b zoomed insets). Radiance values of water over different bottom types were analyzed before and after the atmospheric correction. Because TOA radiance values are dominated by Rayleigh and aerosol path radiance, it becomes difficult to infer the spectral properties of water over different benthic substrates. To fully understand this concept, known pixels depicting water over five locations including benthic algae, seagrass, deep water, sand, and coral reef areas were selected (Fig. 8.7a,b). After the atmospheric correction was implemented, the corrected profiles showed the spectral variability in greater detail. For example, water leaving radiance in the NIR became  $\approx 0$  in all the cases because of high NIR absorption by water. Similarly, dark targets such as seagrass areas and deep water showed low radiance values in all visible bands. Water leaving radiance in shallow waters always contains a fraction of upwelling radiance of the underlying benthic habitat. When comparing water leaving radiance over shallow areas, submerged sand or coral reefs to seagrass areas, it can be observed that the seagrass substrate, being darker, has low upwelling radiance. Conversely, submerged sand (being the brightest substrate) had the maximum radiance values. In general, the blue and green bands were found to have the highest water leaving radiance amongst all IKONOS and QuickBird bands. Specific absorption features of different benthic bottom types were not identifiable because of the water column attenuation and the broadband nature of the sensors.

For the AISA hyperspectral image,  $R_{rs}$  spectra for all sampling locations before the FLAASH atmospheric correction when compared with the retrieved  $R_{rs}$  spectra after applying the atmospheric correction model showed a significant decrease in the  $R_{rs}$  values (70–80%) (Fig. 8.7c). In the red band (600–700 nm) the  $R_{rs}$  values



**Fig. 8.6** Visual differences in (a) IKONOS image before and after the atmospheric correction; (b) QuickBird image before and after the atmospheric correction; (c) AISA Eagle hyperspectral image before and after the FLAASH atmospheric correction. Note that the atmospheric haziness is eliminated after the correction is applied in all cases (Mishra et al. 2005, 2006, 2007)

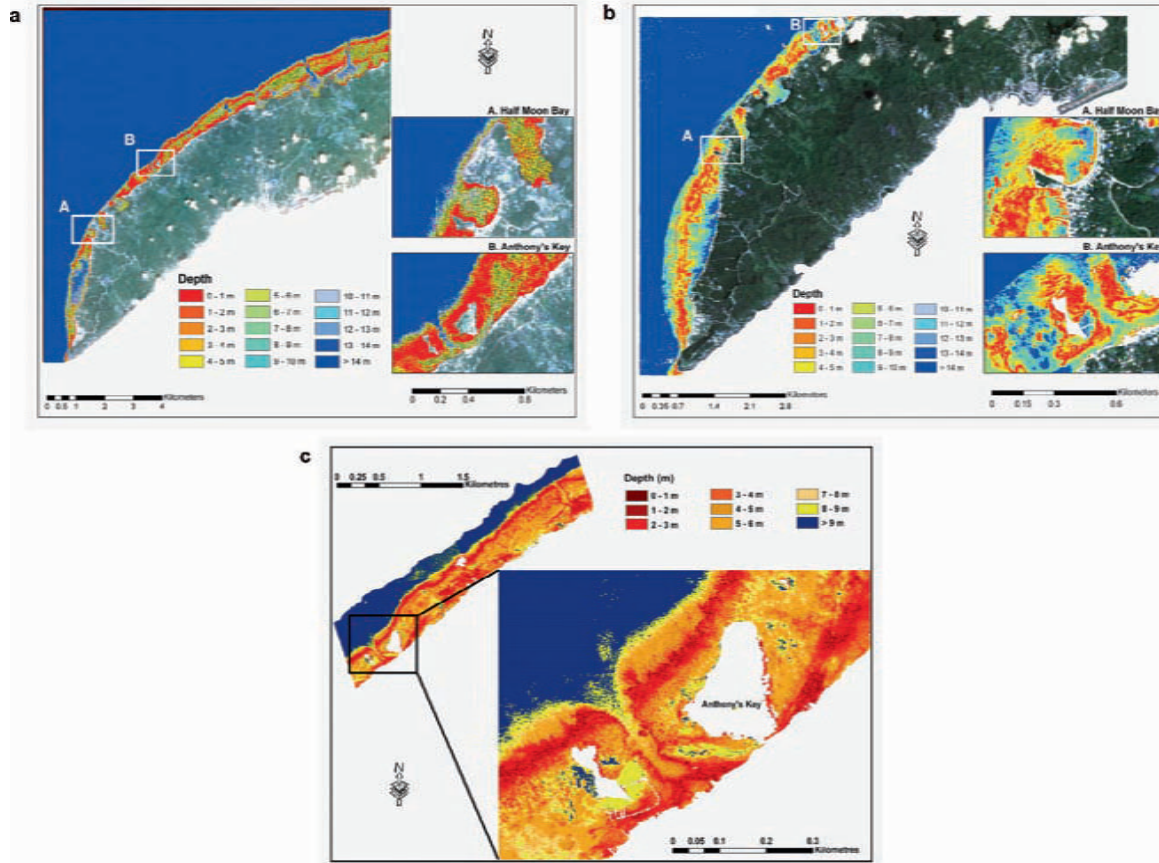


**Fig. 8.7** Top of atmosphere and water leaving radiances ( $Wm^{-2}sr^{-1}\mu m^{-1}$ ) derived from (a) IKONOS image over different bottom types; (b) QuickBird image over different bottom types. (c)  $R_{rs}$  spectra of AISA Eagle pixels at all sampling locations before and after the atmospheric correction (Mishra et al. 2005, 2006, 2007)

decreased after atmospheric correction indicating high absorption by water itself, whereas the reflectance peak in the green is caused by the scattering of suspended sediments and chlorophyll present in phytoplankton cells. To validate the accuracy of atmospheric correction, above water  $R_{rs}$  *in situ* spectra acquired by the Ocean Optics hyperspectral sensor was compared with the AISA atmospherically corrected reflectance data over different benthic habitats. Overall the  $R_{rs}$  spectra of AISA and Ocean Optics sensor for all the targets were in close agreement. Visual examination of the images before and after atmospheric correction procedure showed sharp differences (Fig. 8.6c). For example, coral areas towards the northeast of Anthony's Key, which appeared to be white before the correction, showed up clearly (light brown) after the atmospheric correction. In addition, the haziness depicted in the original AISA image, attributed to Rayleigh and aerosol scattering, and water vapor content (3.3081 cm; 820 nm), was eliminated thus resulting in a visually clear image.

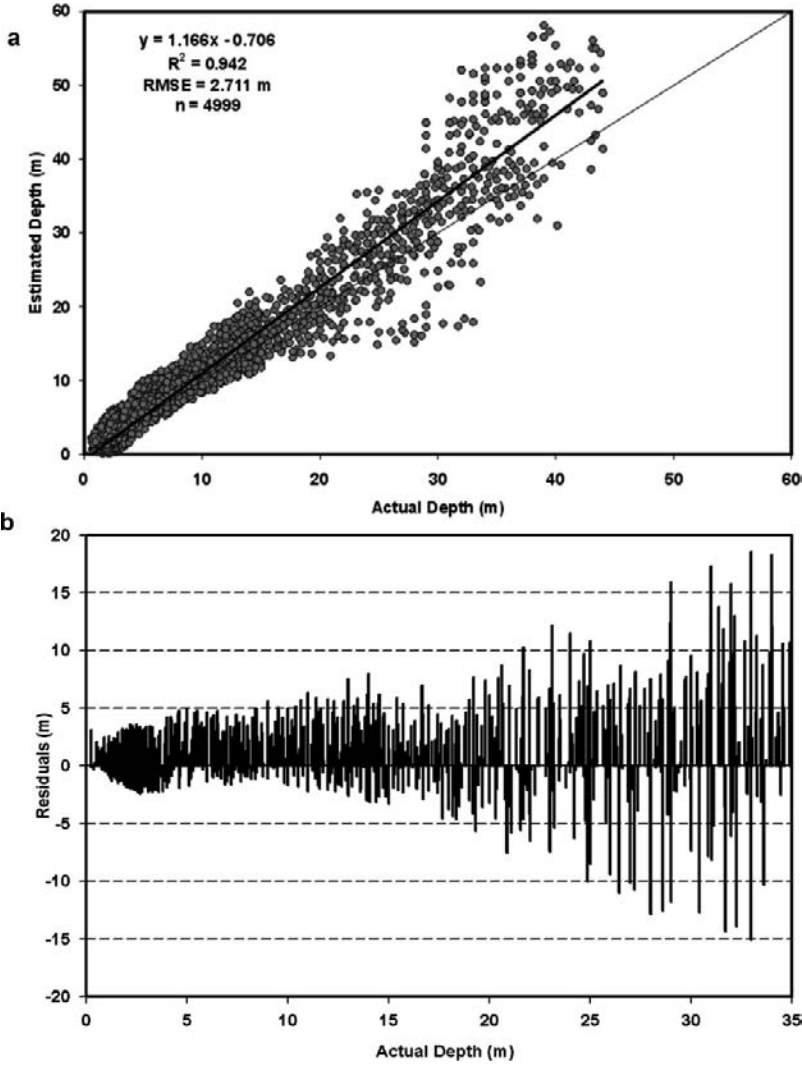
A bathymetric map generated using Eq. (8.2), when compared to the original IKONOS image (i.e., Fig. 8.1), visual observations of similarities in bottom patterns can be made in both the image and the map (Fig. 8.8a). Two areas – Half-Moon Bay (A) and Anthony's Key (B) are depicted in a large format because our research team has collected *in situ* data there annually since 1999. The depth variation around the zoomed areas of Half-Moon Bay and Anthony's Key was high, which is generally true in the coral reef marine environment because of their uneven morphological structure. Using 4999 *in situ* depth points, the bathymetric map was validated for its accuracy and the root mean square (rms) error was calculated. When analyzing the accuracies of estimated depths, it was found that the correlation coefficient between actual depth and estimated depth was 0.942 with an rms error of 2.711 m (Fig. 8.9a). The slope and intercept of the trend line were found to be 1.166 and 0.706 respectively. From the errors in modeling the dependence of depth with band ratio  $L_w(\text{blue})/L_w(\text{green})$  it was observed that  $x \leq 0.25$ , the calibration points are roughly evenly distributed about the curve (Fig. 8.5b). However, for  $x > 0.25$ , the points are mostly below the calibration curve thus indicating that the model overestimates depths beyond 21 m. Residuals were calculated by subtracting estimated depths from actual depths and revealed no clear pattern of over/under estimation (Fig. 8.9b).

A visual examination of the QuickBird bathymetric image-map reveals the details of variations in depth at two study sites including Half-Moon Bay (A) and Anthony's Key (B) (Fig. 8.8b). The deep channel near the Anthony's Key shows a depth of  $> 7$  m, which is appropriate given our knowledge of the site. Using 620 *in situ* depth points, the bathymetric map was validated for its accuracy revealing a correlation coefficient of 0.845 and a rms error of 2.819 m between actual and estimated depth (Fig. 8.10a). The slope and intercept of the trend line were found to be 0.845 and 1.616 respectively. It was evident that the RMS error increased with depth, and based on further analysis it was observed that after 18-m there was significant deviation of the estimated depths from actual depths. To quantify this deviation, we separated the validation datasets as  $< 18$  m and  $> 18$  m where the correlation coefficient for depths less than 18-m was 0.906 with a RMS of 1.316 and



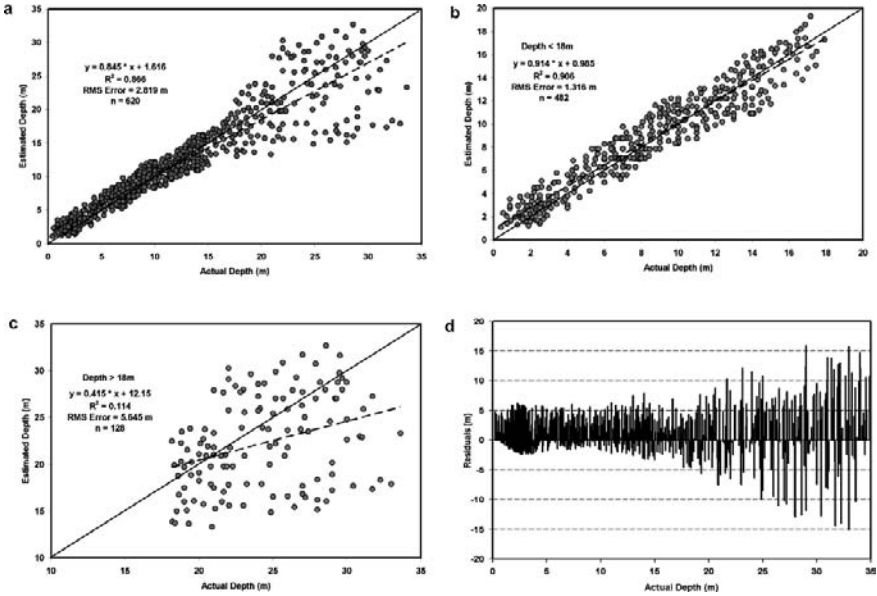
**Fig. 8.8** Bathymetric image-map of part of Roatan Island derived from (a) IKONOS image; (b) QuickBird image; and (c) AISA Eagle hyperspectral image based on the polynomial model (Mishra et al. 2005, 2006, 2007)





**Fig. 8.9** IKONOS depth validation: (a) Plot of actual versus estimated depths using model validation dataset taken from the towfish; (b) Histogram plot of depth residuals from the regression model versus actual depth (Mishra et al. 2005)

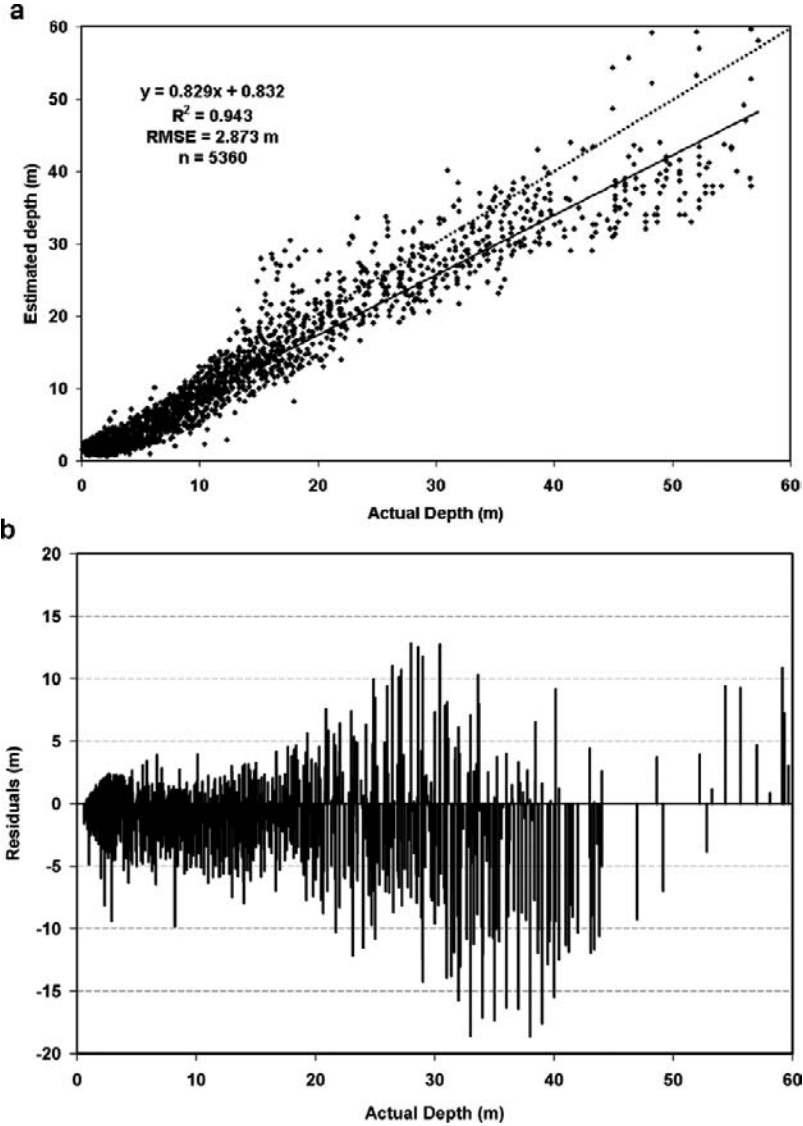
a slope of 0.914 (Fig. 8.10b). Conversely, for depths greater than 18-m, the correlation coefficient between actual and estimated depth was 0.114 (Fig. 8.10c) with a RMS of 5.648 and a slope of 0.415, which is significantly different from slope of 1:1 line. The reason for these differences is simply because the path length of the photons increase as depth increases, thereby resulting in increased light attenuation and reduced light propagation. Reduced propagation decreases the signal to noise ratio causing higher estimation error in the deep water. However, the residuals did not have a clear pattern of over/under estimation (Fig. 8.10d).



**Fig. 8.10** QuickBird depth validation: (a) Plot of actual versus estimated depths using model validation dataset taken from the towfish; (b) Validation result for depths < 18 – m; (c) Validation result for depths > 18 – m and (d) Histogram plot of depth residuals from the regression model versus actual depth (Mishra et al. 2006)

Comparing a bathymetric map generated using AISA Eagle data with the original AISA image, visual observations of similarities in bottom patterns can be made in both the image and the map (Fig. 8.4b,c). A close examination of the image map revealed that most shallow vertical features around the Key were reproduced, including a shallow “basin” of sand waves, fore reef, patch reef, and step narrow reticulated reef structure. The image map also showed a clear distinction of the drop off point (depicted in blue) separating the submerged shelf-edge reef from the deep water (Fig. 8.8c). The barrier reef, which is separated from the shoreline by a moderately deep (usually) body of water, depicted in red color and runs SW-NE through the entire image, was the most distinct feature of the bathymetric map (Fig. 8.8c). Using 5360 *in situ* depth points, the bathymetric map was validated for its accuracy and the rms error was calculated. When analyzing the accuracies of estimated depths, it was found that the  $R^2$  between actual depth and estimated depth was 0.943 with an rms error of 2.873 m (Fig. 8.11a). The slope of the trend line was found to be 0.829, which is not significantly different from the slope of 1:1 line. Residuals were calculated by subtracting estimated depths from actual depths and revealed no clear pattern of over/underestimation (Fig. 8.11b). However, for depths > 20m the estimation error increased noticeably and the ratio transform rarely retrieved meaningful depths.

The absorption and backscattering parameters for the three IKONOS and Quick-Bird bands are specified at the band centers (Table 8.1). As the wavelength increased, there was an increase in the total absorption coefficient in both cases,

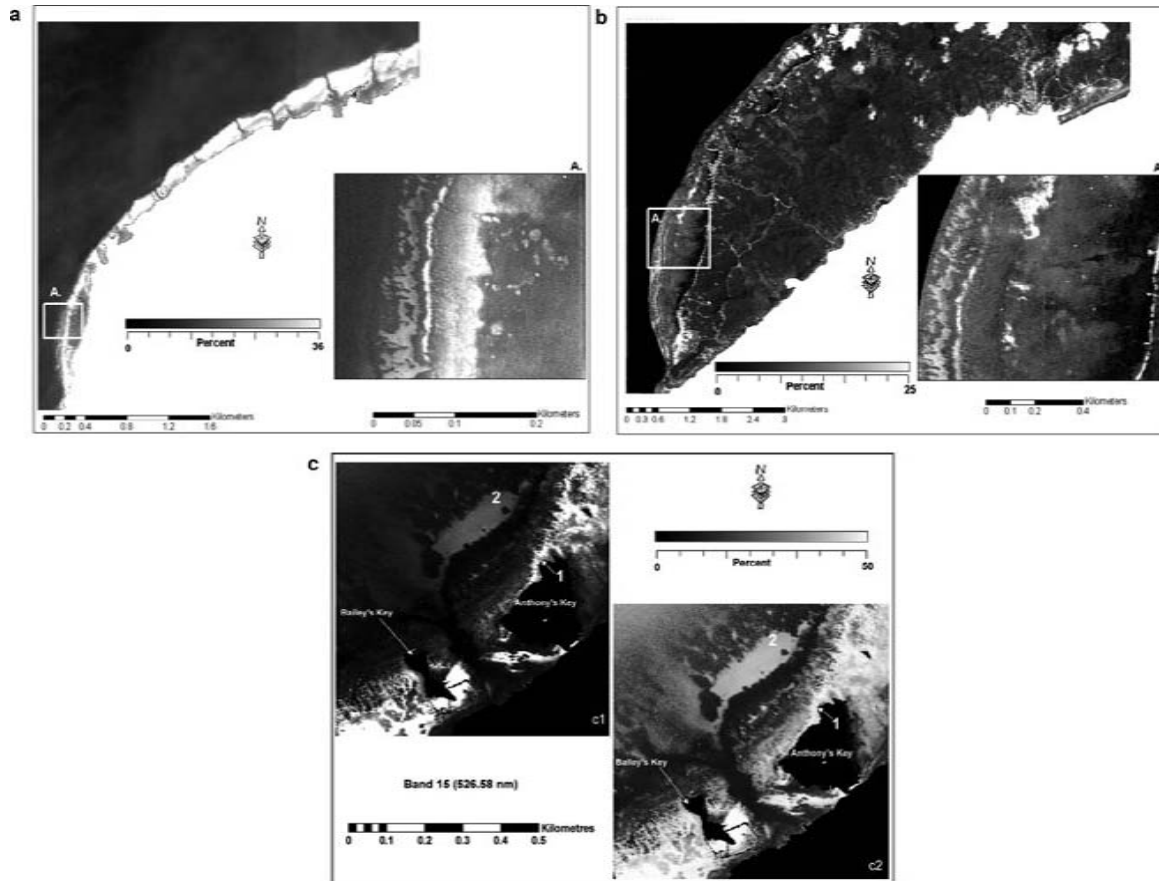


**Fig. 8.11** AISA Eagle depth validation: (a) Plot of actual versus estimated depths using model validation dataset taken from the towfish; (b) Histogram plot of depth residuals from the regression model versus actual depth (Mishra et al. 2007)

which is due to the fact that the phytoplankton pigments and water itself shows high absorption in the red spectrum. The waters off Roatan Island, where the concentration of phytoplankton (chlorophyll range: 0.031–1.81 mg/l, seston range: 0.319–4.091 mg/l, based on field measurements) is greater than non-biogenic particles, are considered as Case-1 waters. Absorption by chlorophyll and related pigments therefore plays a major role in determining the total absorption coefficient

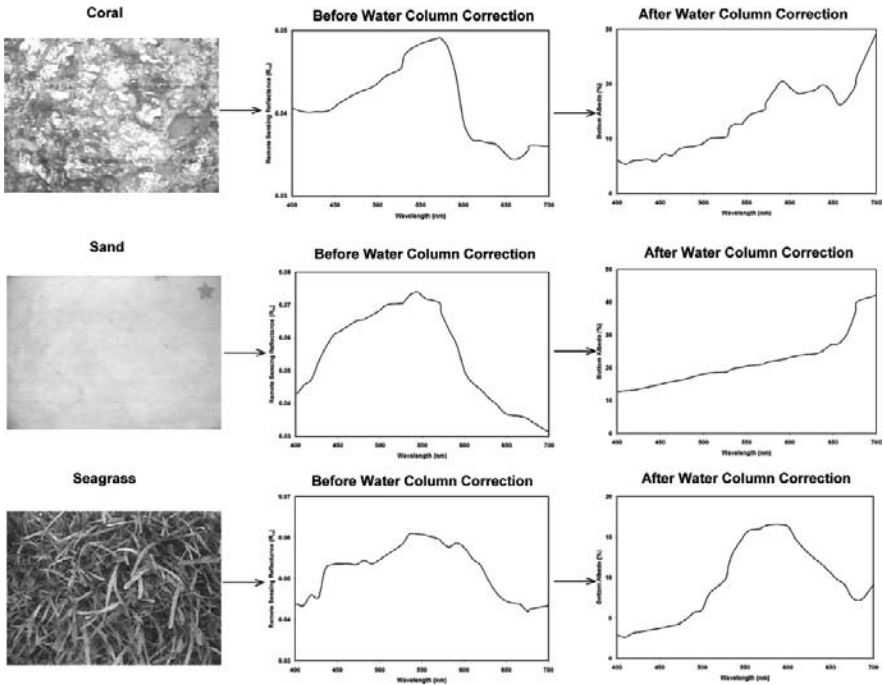
in such waters; although detritus and dissolved organic matter derived from the phytoplankton also contribute to absorption in Case-1 waters. Because backscattering is wavelength dependent, a higher coefficient was observed in blue band than in the red. Absorption and backscattering coefficients along with water depth were incorporated in Eq. (8.7) to generate bottom albedo images of IKONOS and QuickBird data respectively (Fig. 8.12a,b). The dark region on the IKONOS albedo image (Green band) is the deep water region with depths deeper than 21 m. The zoomed inset shows the detailed variation in bottom albedo based on the substrate reflectance. In the IKONOS bottom albedo image, the dark regions are comprised of seagrasses with albedo  $\leq 12\%$ , while the bright regions represent sand dominated areas with albedo  $\geq 24\%$ . Coral dominated areas manifested albedos in the range of 12–24% depending upon the percent of live coral cover occurring in each pixel (Fig. 8.12a). In the QuickBird bottom albedo image, the dark regions are comprised of seagrasses with albedo  $\leq 8\%$ , while the bright regions represent sand dominated areas with albedo  $\geq 18\%$  and the coral dominated areas manifested albedos in the range of 8–18% depending upon the percent of live coral cover occurring in each pixel (Fig. 8.12b). The effectiveness of the water column correction in both cases is evident from the fact that the differences in radiance between deep and shallow sand for the IKONOS and QuickBird scene observed in Figs. 8.1 and 8.4a are eliminated in the albedo images, and all sand dominated areas have approximately the same albedo.

The absorption and backscattering parameters for the 33 AISA bands are specified at the band centers (Table 8.1c). Absorption coefficients showed exponential increase toward the higher wavelengths ( $> 600\text{nm}$ ). However, there was significant increase in absorption values observed at blue band because the chlorophyll present in the phytoplankton cells absorbs blue light. Absorption by chlorophyll itself is characterized by strong absorption bands in the blue and in the red (peaking at  $\lambda \approx 430$  and  $665$  nm, respectively, for chlorophyll *a*), with very little absorption in the green. Overall, as the wavelength increased, there was an increase in the total absorption coefficient, which is due to the fact that the phytoplankton pigments and water itself shows high absorption with increasing wavelength. Phytoplankton cells are strong absorbers of visible light and therefore play a major role in determining the absorption properties of Case-1 waters such as Roatan waters; although detritus and dissolved organic matter derived from the phytoplankton also contribute to absorption in Case-1 waters. Overall backscattering is inversely proportional to wavelength; therefore a higher coefficient was observed in blue band than in the red. Backscattering coefficients of pure water (from Morel 1974) showed lower values when compared with Roatan water which was expected because of several reasons. Firstly, sea water consists of pure water plus various dissolved salts, which average about 35 parts per thousand (35‰) by weight (Mobley 1994). These salts increase scattering above that of pure water by about 30% (Mobley 1994) but have a negligible effect on absorption at visible wavelengths. Secondly, particles present in the Roatan water are generally much larger than the wavelength of visible light and are efficient scatterers, especially via diffraction, thus strongly influencing the total scattering properties of sea water. Absorption and backscattering coefficients along



**Fig. 8.12** (a) IKONOS image showing bottom albedo (Band 2: green band) varying from 0 to 36%; (b) QuickBird image showing bottom albedo (Band 2: green band) varying from 0 to 25%; (c) AISA Eagle image showing bottom albedo (band 15: 526.58 nm) varying from 0 to 50% (Mishra et al. 2005, 2006, 2007)

with water depth were incorporated in Eq. (8.7) to generate a bottom albedo image (Fig. 8.12c). Visual comparison of the atmospherically corrected image with the bottom albedo image (image generated after water column correction; Fig. 8.12c: part c1 & c2) revealed apparent differences. For example, areas 1 and 2 (Fig. 8.12c: part c1) are both sand bottoms, approximately 3–4 m and 9–11 m deep respectively, and showed a high contrast in their brightness values because of their occurrence at different depths. Whereas after the water column correction i.e., after eliminating the depth factor, the contrast between the two areas was similar ( $\rho \approx 40\%$ ) (Fig. 8.12c: part c2). The zoomed inset showed the detailed variation in bottom albedo based on the substrate reflectance. Dark regions are comprised of seagrasses, benthic algae with  $\rho \approx 15\%$ , while the bright regions represent sand-dominated areas with  $\rho > 30\%$ . Coral-dominated areas manifested albedos in the range of 15–35% depending upon the percent of live coral cover occurring in each pixel. Figure 8.13 shows the remarkable effect of water column attenuation while comparing above water  $R_{rs}$  spectra (after atmospheric correction) with the bottom albedo for three primary benthic features. Before the water column correction the three features showed similar spectral characteristics; i.e., high reflectance in green, low reflectance in blue (chlorophyll absorption) and red (chlorophyll and water absorption). Any specific absorption and reflectance features for the three bottoms were not identifiable. After



**Fig. 8.13** Comparison of AISA Eagle above water  $R_{rs}$  spectra (after atmospheric correction) with the bottom albedo spectra for 3 primary benthic features (coral, seagrass, sand) showing the effect of water column attenuation (taken from Mishra et al. 2007)

the water column correction bottom albedo spectra for coral exhibited relatively low  $\rho$  between 400 and 500 nm, higher  $\rho$  between 550 and 650 nm, a narrow chlorophyll absorption feature at 675 nm, and very rapidly increasing  $\rho$  at wavelengths greater than 680 nm. This variability in the shape of coral  $\rho$ , determined by spectral absorption and fluorescence properties of multiple pigments residing at various locations in a coral colony, including the zooxanthellae and ectodermal and endodermal host tissues (Dove et al. 1995), were absent in the spectra before water column correction. All those spectral features became prominent after removing the water attenuation factor from the spectra. For sand bottom, a gradual increase in  $\rho$  was observed with increasing wavelength, which is a typical sand reflectance characteristic. Seagrass bottom exhibited a reflectance peak at around 550 nm, and chlorophyll absorption features at  $\sim 675$  nm and both chlorophyll and carotenoid absorption in blue band. Overall water absorption and suspended sediment scattering played an important role and photons reflected back from benthos were basically mixed spectra with significant contributions from water column, specifically in the red wavelengths. After water column removal the same set of spectra showed spectral features and the magnitude of the  $\rho$  was comparable to the *in situ* spectra.

Because of the absence of the required field measurements, the validation for water column correction i.e., for the estimated bottom albedo was performed in a unique way. For this purpose the hypothesis was, if the water column correction to derive bottom albedo was accurately performed, then the depth factor on the bottom reflectance would have been eliminated and the bottom albedo for a particular bottom at various depths would be similar. For this purpose, five bottom albedo spectra of coral, sand, and seagrass at different depths were plotted and compared with their corresponding reflectance spectra before the water column correction (Fig. 8.14). Before the water column correction, the water depth played an important role in determining the reflectance values of the bottom; for example, the deeper the bottom the lower the reflectance values. After the water column correction, the albedo values for a particular bottom were close to each other irrespective of their depths. However, it was noted that with increasing depth, dark bottoms or bottoms with high phytoplankton content (corals and seagrass) showed that influence of water column is not completely eliminated. For example, the coral albedo at 5.632 m and 7.421 m and the seagrass albedo at 4.868 m did not reveal the 675 nm chlorophyll absorption feature which was clearly present at other depths (Fig. 8.14). Sand, being the bright bottom, showed a close match for albedos at different depths indicating an accurate water column correction. Another concern with the bottom albedo image was the low signal to noise ratio for dark bottoms at longer wavelengths (specifically  $\lambda > 600$  nm). This noise was introduced to the image during subsequent calculation and needed to be removed before applying the clustering algorithm to map the benthic habitat.

An ISODATA classification algorithm was applied to the bottom IKONOS and QuickBird albedo images resulting 150 and 100 clusters respectively and each cluster was assigned to a particular benthic class with the help of *in situ* data, towfish images, and still photographs derived from the video camera to derive benthic habitat image-maps (Fig. 8.15a,b). A comparative evaluation of the IKONOS classified

**Table 8.2** Results of accuracy assessment of (a) IKONOS image based on 651 underwater reference points; (b) QuickBird image based on 383 underwater reference points; and (c) AISA Eagle image based on 1208 underwater reference points (Mishra et al. 2005, 2006, 2007)  
(a)

IKONOS benthic type	Dense seagrass	Mixed: seagrass/sand/algae	Mixed: coral/sand	Sand	Coral	Deep water	Row total	Produces accuracy (%)	Users accuracy (%)	Kappa coefficient
Dense Seagrass	69	18	4	0	7	6	104	75.82	66.35	0.810
Mixed: Seagrass/Sand/Algae	11	95	5	0	2	0	113	72.52	84.07	0.808
Mixed: Coral/Sand	0	9	43	0	8	0	60	57	72	0.813
Sand	0	0	11	109	5	0	125	95.61	87.20	0.808
Coral	4	9	12	5	131	0	161	83.97	81.37	0.803
Deep Water	7	0	0	0	3	78	88	92.86	88.64	0.811
<b>Column Total</b>	<b>91</b>	<b>131</b>	<b>75</b>	<b>114</b>	<b>156</b>	<b>84</b>	<b>Total = 651</b>	<b>Overall Accuracy = 80.645%;</b>		<b>Overall Kappa = 0.765</b>



(b)

<b>IKONOS benthic type</b>	<b>Dense seagrass</b>	<b>Mixed: seagrass/ sand/algae</b>	<b>Mixed: coral/sand</b>	<b>Sand</b>	<b>Coral</b>	<b>Deep water</b>	<b>Row total</b>	<b>Produces accuracy (%)</b>	<b>Users accuracy (%)</b>	<b>Kappa coefficient</b>
<b>Dense Seagrass</b>	45	14	2	0	5	4	<b>70</b>	78.94	64.28	0.809
<b>Mixed: Seagrass/ Sand/ Algae</b>	7	49	2	0	1	0	<b>59</b>	66.21	83.05	0.809
<b>Mixed: Coral/Sand</b>	0	5	24	0	3	0	<b>32</b>	60.00	75.00	0.813
<b>Sand</b>	0	0	3	51	1	0	<b>55</b>	94.44	92.72	0.811
<b>Coral</b>	2	6	9	3	81	0	<b>101</b>	88.04	80.19	0.802
<b>Deep Water</b>	3	0	0	0	1	62	<b>66</b>	93.93	93.93	0.809
<b>Column Total</b>	<b>57</b>	<b>74</b>	<b>40</b>	<b>54</b>	<b>92</b>	<b>66</b>	<b>Total = 383</b>	<b>Overall Accuracy = 81.462%</b>		<b>Overall Kappa = 0.774</b>

(c)

<b>IKONOS benthic type</b>	<b>Sand</b>	<b>Seagrass with sand</b>	<b>Dense seagrass</b>	<b>Sand with benthic algae</b>	<b>Coral</b>	<b>Coral with sand</b>	<b>Hard bottom</b>	<b>Mixed: sand/hard bottom/coral</b>	<b>Deep water</b>	<b>Row total</b>	<b>Produces accuracy (%)</b>	<b>Users accuracy (%)</b>	<b>Kappa coefficient</b>
<b>Sand</b>	228	5	1	3	5	5	6	1	0	<b>254</b>	87.692	89.764	0.828
<b>Seagrass with Sand</b>	5	138	4	4	4	9	3	1	2	<b>170</b>	86.250	81.176	0.833
<b>Dense Seagrass</b>	0	4	114	7	4	2	1	0	7	<b>139</b>	87.023	82.014	0.834
<b>Sand with Benthic Algae</b>	3	3	2	39	2	0	1	2	1	<b>53</b>	65.000	73.585	0.836
<b>Coral</b>	5	2	3	3	187	8	4	3	2	<b>217</b>	85.780	86.175	0.831
<b>Coral with Sand</b>	11	5	3	2	11	165	3	5	0	<b>205</b>	85.938	80.488	0.832
<b>Hard Bottom</b>	6	2	0	1	3	2	59	3	1	<b>77</b>	75.641	76.623	0.835
<b>Mixed: Sand/Hard Bottom/Coral</b>	2	1	0	0	2	1	1	28	0	<b>35</b>	63.636	80.000	0.836
<b>Deep Water</b>	0	0	4	1	0	0	0	1	52	<b>58</b>	80.000	89.655	0.836
<b>Column Total</b>	<b>260</b>	<b>160</b>	<b>131</b>	<b>60</b>	<b>218</b>	<b>192</b>	<b>78</b>	<b>44</b>	<b>65</b>	<b>Total = 1208</b>	<b>Overall Accuracy =</b>		<b>Overall Kappa = 0.808</b>
											<b>83.609%</b>		

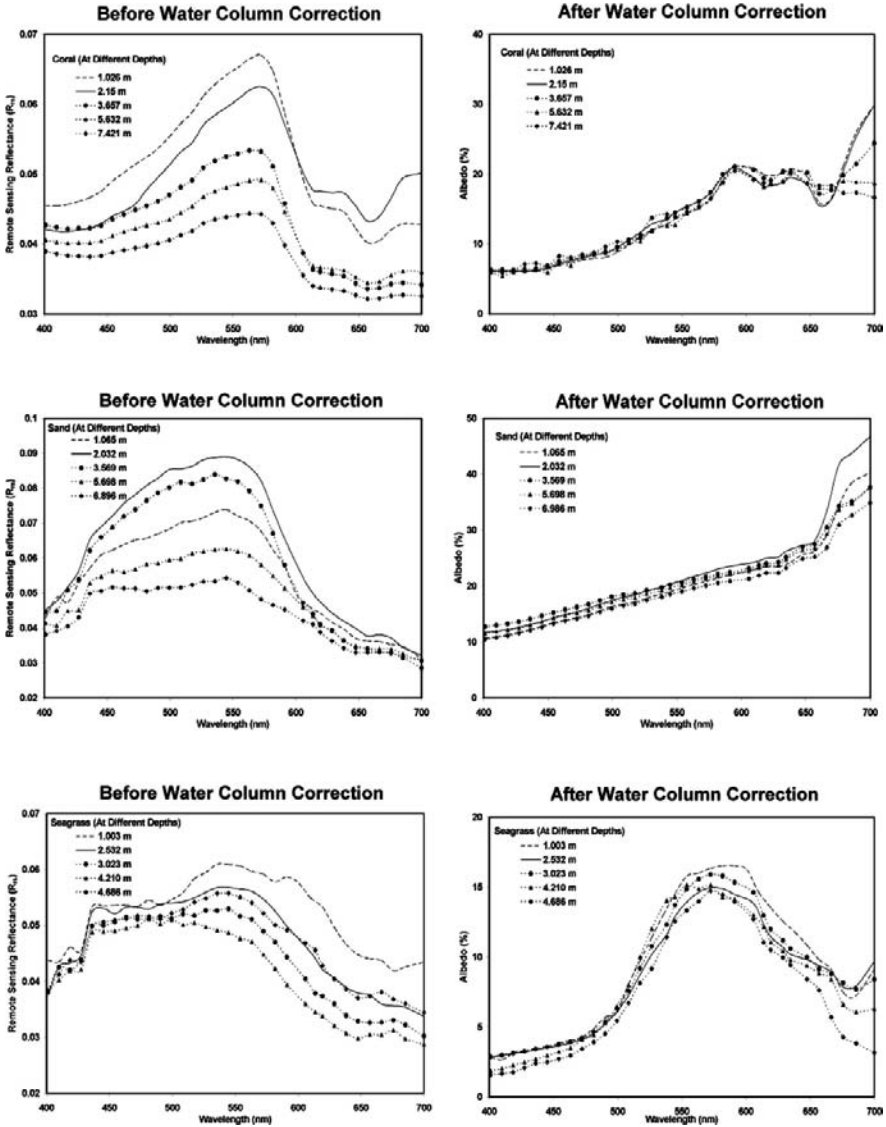
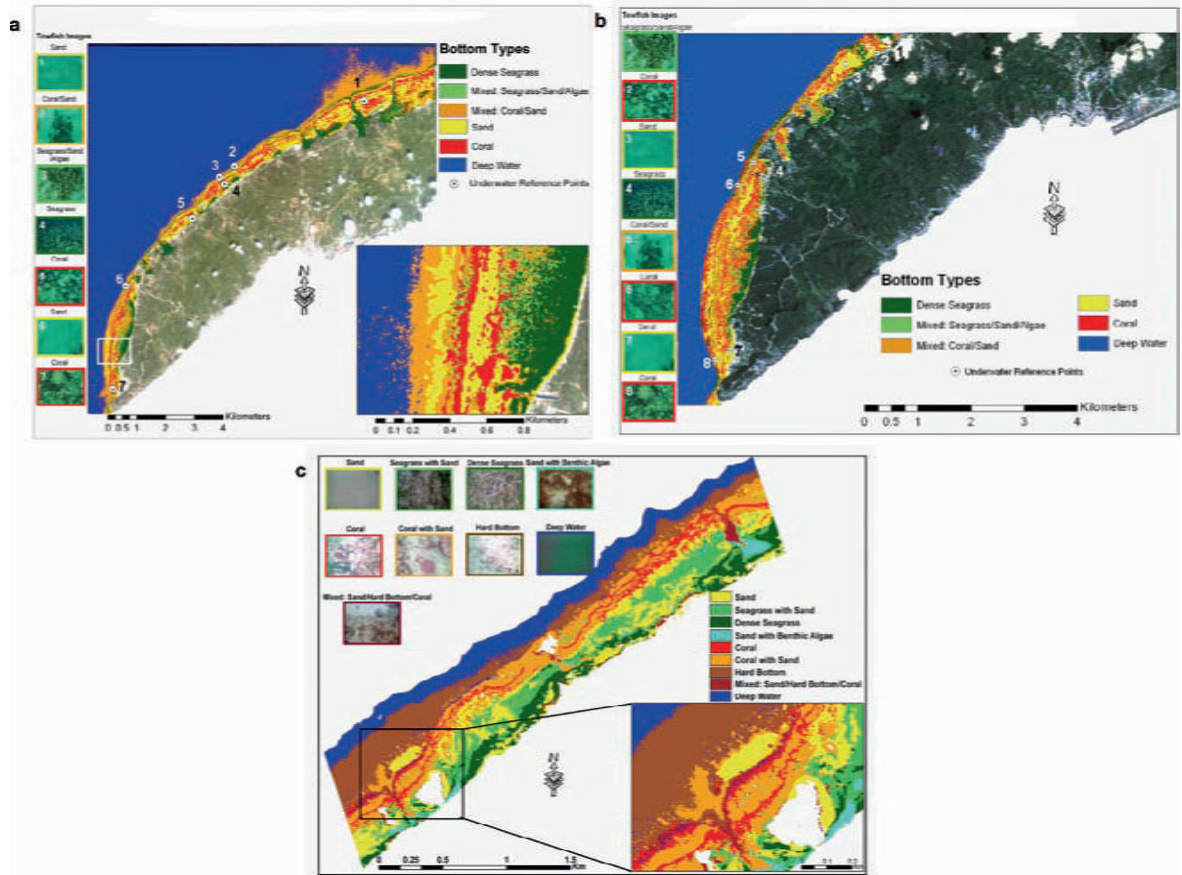


Fig. 8.14 Validation of AISA Eagle water column correction procedure: Comparison of bottom albedo spectra of different bottom types at different depths before and after the water column correction (Mishra et al. 2007)

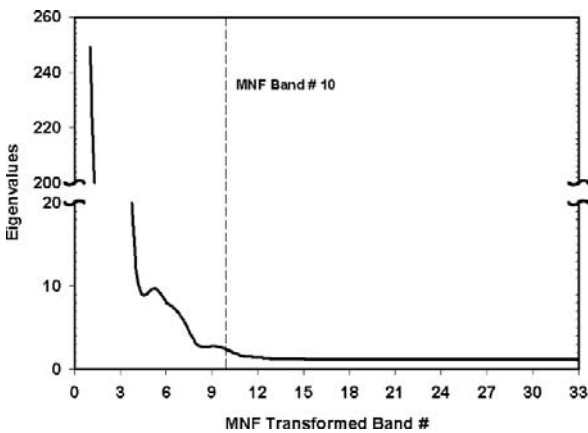
image map versus 651 independent *in situ* points (GPS location, towfish image) revealed an overall accuracy of 80.645% (Table 8.2a), whereas similar comparative evaluation of the QuickBird classified image map versus 383 independent *in situ* points revealed an overall accuracy of 81.46% (Table 8.3b). In both cases sand and deep water areas showed the highest producer's and user's accuracies, when



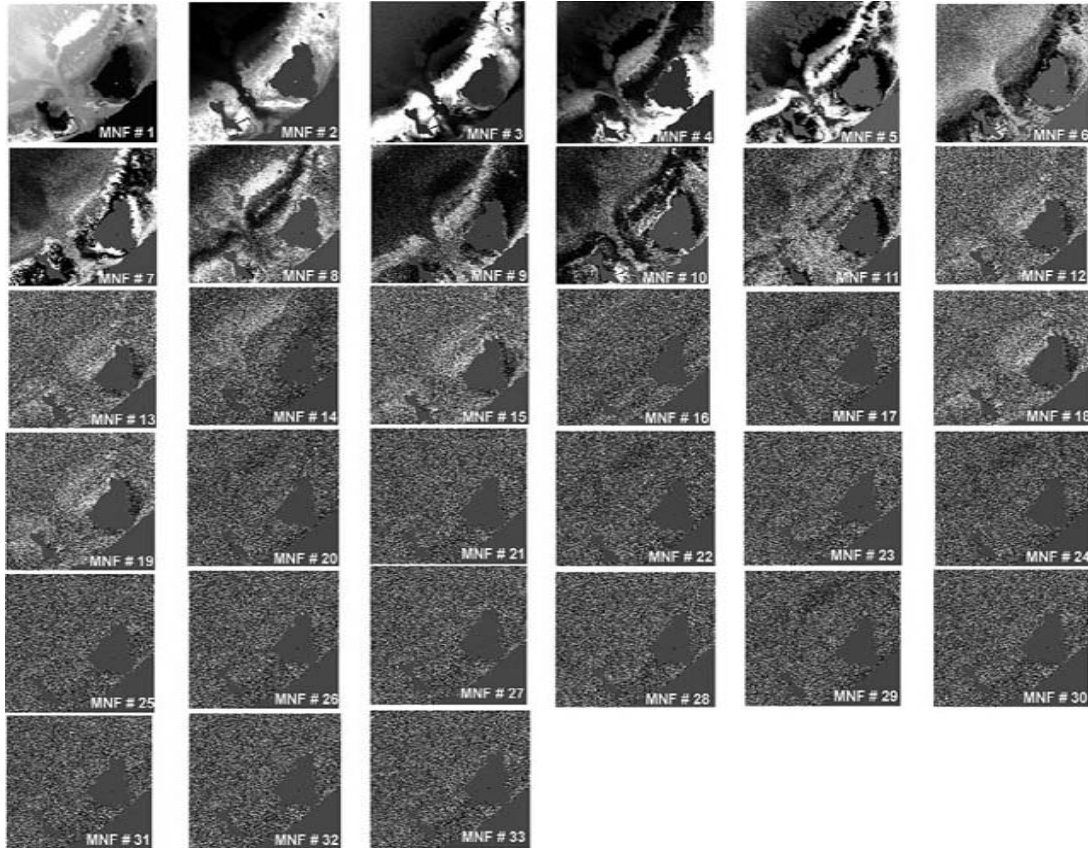
**Fig. 8.15** Color coded map showing different benthic habitats off the northwest coast of Roatan Island, Honduras resulted from an unsupervised classification of the (a) IKONOS; (b) QuickBird; and (c) AISA Eagle bottom albedo images. The border color of each representative photograph of bottom types (acquired by towfish) matches the color given to a particular class (Mishra et al. 2005, 2006, 2007)

compared to dense seagrass, Mixed: seagrass/sand, and Mixed: coral/sand areas. Sand (very bright), and deep water (very dark) are the two most spectrally distinct classes and yielded the lowest classification errors, whereas the mixed benthos areas had higher error because of the spectral similarities between various features. The overall Kappa statistic, a discrete multivariate accuracy assessment technique described by Congalton and Mead (1983), was 0.765 and 0.774 for IKONOS and QuickBird maps respectively. This statistic estimates the percent of successful classifications compared to a random, chance classification assignment (Jensen 2004). There are several reasons for the confusion in the three classes, including limitations of the spectral sensitivity of the broad band IKONOS and QuickBird satellites, and spectral overlaps between optically similar objects. For example, the calcium carbonate skeleton of a dead coral is optically similar to sparse seagrass with a sand background, while algal overgrowth is often similar to zooxanthalle densities and pigmentation occurring in coral features. Depending on the level of classification, previous studies using coarser resolution satellite data (e.g., Landsat TM) have normally achieved accuracies that have ranged from 37% (Mumby et al. 1998a) to 73% (Mumby and Edwards 2002), even when compensating for the confounding effects of variable water depths. The problems with our classification were primarily due to the presence of sand in reef areas, and the rapid changes in coral diversity and reef features over relatively short distances.

A noise reduction technique called MNF was applied on the AISA Eagle bottom albedo image before running the ISODATA classification algorithm. MNF is a linear transformation related to principal components that orders the data according to signal-to-noise-ratio (Green et al. 1988) and can be used to partition the data space into two parts: one associated with large eigenvalues and coherent eigenimages, and a second with near-unity eigenvalues and noise-dominated images. By using only the coherent portions in subsequent processing, the noise is



**Fig. 8.16** Eigenvalues of the MNF transformed AISA Eagle bands separating signal from noise at band 10 (Mishra et al. 2007)



**Fig. 8.17** Visual comparison of MNF transformed AISA Eagle bands to identify information bands (Mishra et al. 2007)

separated from the data, thus improving spectral processing results. The MNF algorithm was used to separate information from noise based on eigenvalues which showed high variability (standard deviation,  $\sigma > 46.671$ ) ranging from 249.005 (component 1) to 1.119 (component 33) (Fig. 8.16). The threshold band separating signal from noise was set on MNF band #10 after examining the  $\sigma$  of eigen values and the image. The eigen values showed significant variation from band 1 to 10 (range = 249.005 – 2.318;  $\sigma = 79.010$ ) whereas remained fairly constant (near-unity) from band 11 to 33 (range = 1.558 – 1.119;  $\sigma = 0.103$ ). Visual examination of all the 33 MNF bands also exhibited a clear distinction between bottom albedo signal or coherent eigenimage (MNF band 1–10) and noise dominated images (MNF bands 11–33) (Fig. 8.17). The first 10 MNF bands were subset from MNF image and were then used in the ISODATA clustering algorithm. An ISODATA classification algorithm was applied to the bottom albedo image resulting 300 clusters and each cluster was assigned to a particular benthic class with the help of *in situ* data, towfish images, and still photographs derived from the video camera to produce a benthic habitat map (Fig. 8.15c). A comparative evaluation of the classified image versus 1208 independent *in situ* points (GPS location, towfish image) revealed an overall accuracy of 83.609% (Table 8.2c). An examination of producer's and user's accuracies also showed better classification results with AISA hyperspectral data versus those derived from IKONOS and QuickBird (Mishra et al. 2005, 2006), and Landsat TM or SPOT XS data (Mumby et al. 1998a). Sand, seagrass sand, coral, and deep water areas showed the higher producer's and user's accuracies, when compared to sand with benthic algae, hard bottom, and Mixed: sand/hard bottom/coral areas. This indicates that confusion between the latter classes during the ISODATA classification were high, due to their similar spectral characteristics. Sand (very bright), seagrass, coral, and deep water (very dark) are the spectrally distinct classes, with the highest spectral separability and lowest classification error. The overall kappa statistic was 0.808 which showed better classification results compared to IKONOS and QuickBird sensors.

## 8.6 Conclusion

This research contributes to our understanding of how electromagnetic radiation interacts with coastal waters and also adds to the limited number of existing benthic habitat mapping studies. The most significant aspect of the study is that it provides detailed techniques on extracting per-pixel bathymetry, and water column optical properties from remotely sensed data. These lead to the correction of the water column effect, the strongest component of accurate benthic habitat mapping. However, these techniques are dependent on the extraction of dark water pixels as well as depth sounding data which may not be available in a particular scene or for a given site.

The bathymetric maps produced using IKONOS, QuickBird, and the AISA Eagle revealed that most of the shallow vertical features around the Anthony's Key area

were reproduced, including a shallow “basin” of sand waves, fore reef, patch reef, and steep narrow reticulated reef structure. All three bathymetric maps showed clear distinction of the drop off point separating submerged shelf-edge reef from the deep water. The barrier reef, which is separated from the shoreline by a moderately deep body of water, runs SW-NE through the entire image, was distinctly revealed in these bathymetric maps.

The water column correction technique used to produce the bottom albedo images showed similar results for both satellite datasets, whereas the albedo values increased for the hyperspectral data. Albedo images derived from satellite data revealed that seagrass areas are associated with low albedo values ( $\approx 8\text{--}12\%$ ), while albedo values ranged from 18 to 24% in sand dominated areas. Coral areas manifested albedos in the range of  $\approx 12\text{--}24\%$  depending upon the percent of live coral cover occurring in each pixel. In case of the hyperspectral data, the dark regions comprised of seagrasses and benthic algae with albedo values  $\approx 15\%$ ; whereas sand and coral dominated areas showed albedo  $> 30\%$  and  $\approx 15\text{--}35\%$  respectively. This increase in the albedo values could be attributed to the reduced atmospheric interferences observed in airborne data compared to spaceborne data. The effectiveness of the water column correction was evident from the fact that differences in radiance between deep and shallow homogenous substrate (i.e., shallow sand, large patch of seagrass) were eliminated in the albedo image, and all homogenous substrate had approximately the same albedo irrespective of their depth of occurrence.

Significantly varying in both spatial and spectral resolution, the satellite sensors rendered considerable discrepancies for benthic habitat classification relative to airborne hyperspectral sensor. Overall, AISA Eagle image classification was consistently more accurate (84%) including finer definition of geomorphological features (9 classification levels) than the satellite sensors. IKONOS (81%) and QuickBird (81%) classifications showed some correspondence to the AISA Eagle, however, only at a coarse classification level of 5 and 6 habitats. This coarse classification with satellite data is because of the limitation in the spectral sensitivity of the broad band sensors, and spectral overlaps between optically similar objects. Depending on the level of classification, previous studies using coarser resolution satellite data (e.g., Landsat TM) have normally achieved accuracies ranging from 37% (Mumby et al. 1998b) to 73% (Mumby and Edwards 2002), even when compensating for the confounding effects of variable water depths. These results confirm the potential of an effective combination of high spectral and spatial resolution satellite sensor for the degree of accuracy required in coral reef habitat mapping.

A satellite sensor with high spectral resolution and an appropriate synoptic coverage will help to address more efficiently the different signs of worldwide coral reef degradation and accurate coral reef habitat inventorying, mapping, and monitoring. These submerged and highly heterogeneous environments impose challenges for benthic habitat mapping and require a specialized sensor. Such challenges not only include dealing with the intervening atmosphere (Gordon 1992), but also the contribution of the water column (Smith and Baker 1981, Mobley 1994, Fraser et al. 1997, Mobley 1999, Morel and Maritorena 2001, Hochberg et al. 2003b), and depth variation effects (Lyzenga 1978, 1981, Philpot 1989, Maritorena 1996, Stumpf et al.



2003, Mishra et al. 2004) to the measured signal. The spectral resolution of a sensor designed to better discriminate reef biological communities requires a high number of narrow, properly placed, bands which are not currently available in existing satellite sensors (Mumby and Edwards 2002, Hochberg and Atkinson 2003). Optical hyperspectral sensors mounted on aerial platforms seem to be more appropriate for overcoming the lack of high spectral resolution of satellite sensors. However, the latter lacks the synoptic coverage for large-scale studies and usually cost more. Mumby and Edwards (2002) suggest that in dealing with similar spectral bands at different spatial scales, a higher spatial resolution increases the classification accuracy for fine level habitat mapping. Hochberg et al. (2003a) compared coral reef spectral reflectances collected *in situ* around the world to those provided by simulated broadband spaceborne sensors, and pointed out the limitations of the latter to spectrally discriminate between sand, coral and algae independent of geographic location. Further, Capolsini et al. (2003), and Mumby et al. (1998a) demonstrated the advantages of considering the reef morphology and habitat zonation at reef level (e.g., contextual knowledge) to improve image classification accuracy. Additional efforts to validate or unveil trends in terms of thematic map accuracy relative to sensors specification should clarify the relative potential of individual sensors for coral reef habitat mapping.

## 8.7 Future Research

It is widely suggested that reef communities around the world are currently undergoing a phase shift, with previously coral-dominated areas being permanently replaced by algae (Wilkinson 2000). Further research should focus on using the hyperspectral data to address certain key issues that are of vital interest to the biological community, especially the detection of stress effects (i.e., bleaching, disease) and structural changes in coral reef habitat. Researchers have had some success in calculating percent live cover from airborne remote sensing (Mumby et al. 2004) using clustering and derivative analyses. One of the main factors affecting consistent results is the effect of water column on the reflectance properties of corals. There is always a temptation to interpret readily observable variations in remotely sensed signal of water as a direct indicator of water quality, or benthic type, without correcting for water column effects. Initially, remote sensing specialists attempted to develop strategies to monitor the extent and vitality of coral reefs, often by assuming the effects of the water column above to be horizontally and vertically homogeneous (Holden and LeDrew 2001). More recently, investigators have determined these assumptions of homogeneity to be overly simplistic. This research provides innovative techniques that will allow further processing (i.e., water column correction) of airborne or space-borne remotely sensed images necessary for mapping health and live cover of sensitive benthic habitats. Future research should also focus on the generation of a large number of lookup tables for atmospheric correction and air-water interface correction; and the generation of spectral libraries that simulate most coral

reef, seagrass, macro-algae species, and other substrate types at varying depths and types of water column. Once such data are available, fast processing methodologies such as neural networks can be automated to process the satellite remote sensing data and prepare accurate benthic habitat maps at a faster speed. This spectral library could require a period of 2–5 years to accomplish (depending on the level of involvement by different agencies and developers) (Mobley et al. 2005). Once accomplished it could be easily applied to all marine environments.

## References

- Austin RW, Petzold TJ (1986) The determination of the diffuse attenuation coefficient of sea water using the Coastal Zone Color Scanner. In: Gower JFR (ed) *Oceanography from space*. Plenum Press, New York, pp 239–256
- Boardman JW, Kruse FA (1994) Automated spectral analysis: a geologic example using AVIRIS data, north Grapevine Mountains, Nevada. *Proceedings of tenth thematic conference on geologic remote sensing*. Environmental Research Institute of Michigan, Ann Arbor, I:407–418
- Capolsini P, Andréfouët S, Rion C, Payri C (2003) A comparison of Landsat ETM+, SPOT HRV, Ikonos, ASTER, and airborne MASTER data for coral reef habitat mapping in South Pacific islands. *Can J Remote Sens* 29:187–200
- Congalton RG, Mead RA (1983) A quantitative method to test for consistency and correctness in photointerpretation. *Photogramm Eng Rem S* 49:69–74
- Davidson WV (1974) *Historical geography of the Bay Islands, Honduras*. Southern University Press, Birmingham, Alabama
- Dove SG, Takabayashi M, Hoegh-Guldberg O (1995) Isolation and partial characterization of the pink and blue pigments of Pocilloporid and Acroporid corals. *Biol Bull* 189:288–297
- Fraser RS, Mattoo S, Yeh E, McClain C (1997) Algorithm for atmospheric and glint corrections of satellite measurements of ocean pigment. *J Geophys Res* 102:107–118
- Gordon HR (1992) Radiative transfer in the atmosphere for correction of ocean color remote sensors. In: Barale V, Schlittenhardt PM (eds) *Ocean colour: theory and applications in a decade of CZCS experience*. Kluwer Academic, Dordrecht, pp 33–77
- Gordon HR, Brown OB, Evans RH, Brown JW, Smith RC, Baker KS, Clark DK (1998) A semianalytic radiance model of ocean color. *J Geophys Res* 93:10909–10924
- Gordon HR, Clark DK (1981) Clear water radiances for atmospheric correction of Coastal Zone Color Scanner imagery. *Appl Optics* 20:4175–4180
- Gordon HR, Clark DK, Brown JW, Brown OB, Evans R, Broenkow WW (1983) Phytoplankton pigment concentrations in the Middle Atlantic Bight: comparison of ship determinations and CZCS estimates. *Appl Optics* 22:20–36
- Gordon HR, Voss KJ (1999) MODIS normalized water-leaving radiance algorithm theoretical basis document. Tech Rep MOD 18, NAS5-31363, University of Miami, Coral Gables, Florida
- Gordon HR, Wang MH (1994) Retrieval of water-leaving radiance and aerosol optical-thickness over the oceans with SeaWiFS – a preliminary algorithm. *Appl Optics* 33:443–452
- Green AA, Berman M, Switzer B, Craig MD (1988) A transformation for ordering multispectral data in terms of image quality with implications for noise removal. *IEEE T Geosci Remote* 26:65–74
- Hochberg EJ, Andréfouët S, Tyler MR (2003a) Sea surface correction of high spatial resolution Ikonos images to improve bottom mapping in near-shore environments. *IEEE T Geosci Remote* 41:1724–1729
- Hochberg EJ, Atkinson MJ (2003) Capabilities of remote sensors to classify coral, algae, and sand as pure and mixed spectra. *Remote Sens Environ* 85:174–189

- Hochberg EJ, Atkinson MJ, Andréfouët S (2003b) Spectral reflectance of coral reef bottom-types worldwide and implications for coral reef remote sensing. *Remote Sens Environ* 85:159–173
- Holden H, LeDrew E (2001) Effects of the water column on hyperspectral reflectance of submerged coral reef features. *B Mar Sci* 69:685–699
- Hu C, Müller-Karger FE, Andréfouët S, Carder KL (2001) Atmospheric correction and cross-calibration of LANDSAT-7/ETM+ imagery over aquatic environments: a multiplatform approach using SeaWiFS/MODIS. *Remote Sens Environ* 78:99–207
- Jensen JR (1996) *Introductory digital image processing: a remote sensing perspective*, 3rd edn. Prentice-Hall, Upper Saddle River, New Jersey
- Jensen JR (2004) *Introductory digital image processing: a remote sensing perspective*. Prentice-Hall, Upper Saddle River, New Jersey
- Jensen JR, Narumalani S, Weatherbee O, Mackey HE (1991) Remote Sensing offers an alternative for mapping wetlands. *Geo Info Sys* 1:46–53
- Keck J (2000) *Instructor's Guide*. The Roatan Institute for Marine Sciences, Roatan, Bay Islands, Honduras
- Kirk JTO (1994) *Light and photosynthesis in aquatic ecosystems*. Cambridge University Press, Cambridge, UK
- Kleypas JA, Buddemeier RW, Archer D, Gattuso JP, Langdon G, Opdyke B (1999) Geochemical consequences of increased atmospheric carbon dioxide on coral reefs. *Science* 284:118–120
- Knutson TR, Tuleya RE, Kurihara Y (1998) Simulated increase of hurricane intensities in a CO<sub>2</sub>-warmed climate. *Science* 279:1018–1020
- LeDrew E, Holden H, Peddle D, Morrow J, Murphy R, Bour W (1995) Towards a procedure for mapping coral stress from SPOT imagery with in situ optical correction. *Proceedings of third thematic conference on remote sensing of the marine coastal environment, Seattle, Washington*, 1:211–219
- Lee ZP, Carder KL, Hawes SK, Steward RG, Peacock TG, Davis CO (1994) A model for interpretation of hyperspectral remote-sensing reflectance. *Appl Optics* 33:5721–5732
- Lee ZP, Carder KL, Mobley CD, Steward RG, Patch JS (1998) Hyperspectral remote sensing for shallow waters: 1. a semi-analytical model. *Appl Optics* 37:6329–6228
- Lee ZP, Carder KL, Steward RG, Peacock TG, Davis CO, Mueller JL (1996) Remote-sensing reflectance and inherent optical properties of oceanic waters derived from above-water measurements. *SPIE* 2963:160–166
- Lyzenga D (1978) Passive remote sensing techniques for mapping water depth and bottom features. *Appl Optics* 17:379–383
- Lyzenga D (1981) Remote sensing of bottom reflectance and water attenuation parameters in shallow water sign aircraft and Landsat data. *Int J Remote Sens* 2:71–82
- Maritorena S (1996) Remote sensing of the water attenuation in coral reefs: a case study in French Polynesia. *Int J Remote Sens* 17:155–166
- Maritorena S, Guillocheau N (1996) Optical properties of the water and spectral light absorption by living and non-living particles and by yellow substances in coral reef waters of French Polynesia. *Mar Ecol-Prog Ser* 131:245–255
- Maritorena S, Morel A, Gentili B (1994) Diffuse reflectance of oceanic shallow waters: Influence of water depth and bottom albedo. *Limnol Oceanogr* 39:1689–1703
- Mishra DR, Narumalani S, Lawson MP, Rundquist D (2004) Bathymetric mapping using IKONOS multispectral data. *GISci Remote Sens* 41:301–321
- Mishra DR, Narumalani S, Rundquist D, Lawson MP (2005) High resolution ocean color remote sensing of benthic habitats: A case study at the Roatan Island, Honduras. *IEEE T Geosci Remote* 43:1592–1604
- Mishra DR, Narumalani S, Rundquist D, Lawson MP (2006) Benthic habitat mapping in tropical marine environments using QuickBird imagery. *Photogramm Eng Rem S* 72:1037–1048
- Mishra DR, Narumalani S, Rundquist D, Lawson MP, Perk R (2007) Enhancing the detection and classification of coral reef and associated benthic habitats: A hyperspectral remote sensing approach. *J Geophys Res* 112, C08014, doi:10.1029/2006JC003892

- Mobley CD (1994) *Light and Water: Radiative transfer in natural waters*. Academic Press, San Diego, California
- Mobley CD (1999) Estimation of the remote-sensing reflectance from above-water surface measurements. *Appl Optics* 38:7442–7455
- Mobley CD, Sundman LK, Davis CO, Bowles JH, Downes TV, Leathers RA, Montes MJ, Bissett WP, Kohler DD, Reid RP, Louchard EM, Gleason A (2005) Interpretation of hyperspectral remote-sensing imagery by spectrum matching and look-up tables. *Appl Optics* 44: 3576–3592
- Morel AY (1974) Optical properties of pure water and pure seawater. In: Jerlov NG, Steeman Nielsen E (eds) *Optical aspects of oceanography*. Academic Press, New York, pp 1–24
- Morel AY (1988) Optical modeling of the upper ocean in relation to its biogenous matter content (case 1 waters). *J Geophys Res* 93:10749–10768
- Morel AY, Gentili B (1993) Diffuse reflectance of oceanic waters II. Bi-directional aspects. *Appl Optics* 32:6864–6879
- Morel AY, Maritorena S (2001) Bio-optical properties of oceanic waters: a reappraisal. *J Geophys Res* 106:7163–7180
- Mumby PJ, Chisholm JRM, Hedley JD, Clark CD, Jaubert J (2001) A bird's-eye view of the health of coral reefs. *Nature* 413:36–36
- Mumby PJ, Clark C, Green E, Edwards A (1998a) Benefits of water column correction and contextual editing for mapping coral reefs. *Int J Remote Sens* 19:203–210
- Mumby PJ, Edwards A (2002) Mapping marine environments with IKONOS imagery: enhanced spatial resolution does deliver greater thematic accuracy. *Remote Sens Environ* 82:248–257
- Mumby PJ, Edwards A, Clark C, Green E (1998b) Managing tropical coastal habitats. *Backscatter* 9:22–24
- Mumby PJ, Hedley JD, Chisholm JRM, Clark CD, Jaubert J (2004) The cover of living and dead corals using airborne remote sensing. *Coral Reefs* 23:171–183
- NOAA (National Oceanic and Atmospheric Administration) (2002) *A National Coral Reef Action Strategy: Report to Congress on implementation of the Coral Reef Conservation Act of 2002 and the National Action Plan to Conserve Coral Reefs in 2002–2003*. NOAA, Silver Spring, Maryland
- Philpot WD (1989) Bathymetric mapping with passive multispectral imagery. *Appl Optics* 28:1569–1578
- Pitcock BA (1999) Coral reefs and environmental change: Adaptation to what? *Am Zool* 39:10–29
- Polcyn FC, Brown WL, Sattinger IJ (1970) The measurement of water depth by remote sensing techniques. Rep. 8973-26-F, Willow Run Laboratories, University of Michigan, Ann Arbor, Michigan
- Pope RM, Fry ES (1997) Absorption spectrum (380–700 nm) of pure water. 2. integrating cavity measurements. *Appl Optics* 36:8710–8723
- Smith RC, Baker KS (1981) Optical properties of the clearest natural waters (200–800 nm). *Appl Optics* 20:177–184
- Space Imaging (2001) IKONOS relative spectral response and radiometric calibration coefficients. Space Imaging Corp, Colorado. <http://www.spaceimaging.com/products/ikonos/spectral.htm> (last access on 31 May 2007)
- Stumpf RP, Holderied K, Sinclair M (2003) Determination of water depth with high-resolution satellite imagery over variable bottom types. *Limnol Oceanogr* 48:547–556
- Timmermann A, Latif M, Bacher A, Oberhuber J, Roeckner E (1999) Increased El Nino frequency in a climate model forced by future greenhouse warming. *Nature* 398:694–696
- Wilkinson C (2000) *Status of coral reef of the world*. Australian Institute of Marine Science, Townsville, Queensland, Australia
- Zhang M, Carder KL, Muller-Karger FE, Lee Z, Goldhof DB (1999) Noise reduction and atmospheric correction for coastal applications of Landsat Thematic Mapper imagery. *Remote Sens Environ* 70:167–180

## Chapter 9

# An Integrated Approach to Benthic Habitat Mapping Using Remote Sensing and GIS: An Example from the Hawaiian Islands

Ann E. Gibbs and Susan A. Cochran

This chapter documents our effort to map benthic habitats within the Kaloko-Honokohau National Historic Park, Hawai'i, USA. We produce detailed benthic-habitat maps by using a combination of color aerial photography, high-resolution bathymetry, and georeferenced underwater video and still photography. We classify individual habitat polygons using five basic attributes and additional information regarding geology, morphology, and coral species. Derivative data sets including isobaths, hillshades, and slope maps are also generated. The mapping shows that benthic habitat and seafloor morphology varies greatly throughout the study area. Nearly 73% of the study area consists of a hardbottom structure that is potentially available for coral habitation; the remaining 27% includes unconsolidated sediment and artificial or historical features. Coral cover is generally low and increases with water depth. The offshore geology is predominantly composed of smooth to undulating *pahoehoe*-type basalt flows that form flat to gently sloping benches, vertical walls, and steep escarpments. In some locations the basalt surface is irregular and mounded into ridges, pinnacles, and arches. Large rounded basaltic boulders and smaller scattered rocks are common throughout the marine portions of the park. Coral or accreted carbonate reef obscures the underlying volcanic surface in only a few areas. The underlying geologic framework and morphology of the submerged volcanic flows within Kaloko-Honokohau National Historical Park provide the primary control on benthic habitats within the park. The habitat maps and associated data can be used as a stand-alone product or in a GIS to provide useful baseline information to scientists, managers and the general public.

### 9.1 Introduction

Coral reefs are an essential part of the earth's ecosystem. They are sensitive indicators of the health of marine environments and are important economically, providing people around the globe with food, jobs, coastal storm protection, and

---

A.E. Gibbs (✉)

Pacific Science Center, U.S. Geological Survey, Santa Cruz, CA 95060, USA  
e-mail: agibbs@usgs.gov

recreational opportunities. Many of the world's reefs have been severely damaged over the past few decades due to a combination of factors including habitat destruction, land-based pollution, sedimentation, overfishing, vessel groundings, coastal development, disease, and climate change.

In contrast to many coral reefs around the world, where nearly 70% are threatened or destroyed, Hawai'i's coral reefs are generally in good condition, with most degradation occurring near urban areas and at popular tourist destinations in response to land-based sources of pollution, overfishing, recreational overuse, and invasive species (Wilkinson 2004, Friedlander et al. 2005).

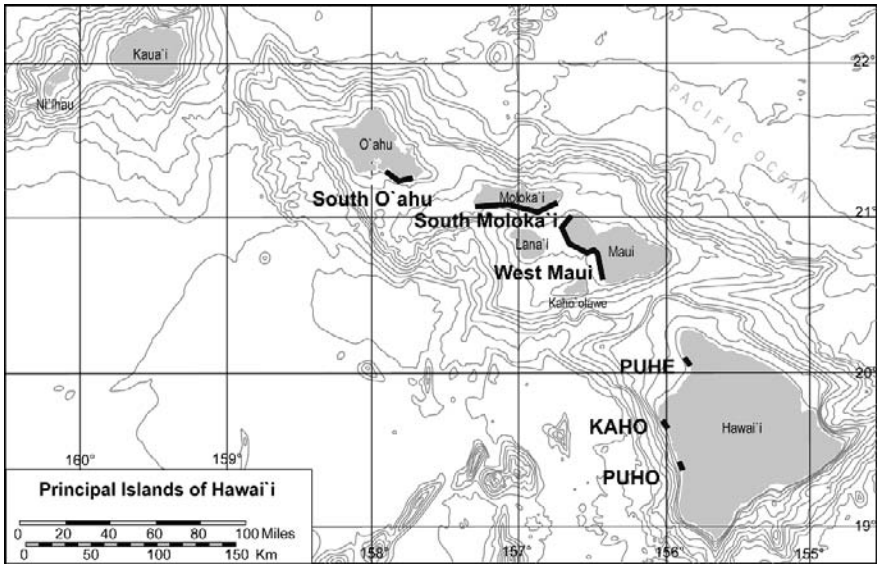
With escalating population and development pressures, Hawai'i's coral reefs will increasingly become threatened. Baseline habitat maps and monitoring programs are an essential step toward evaluating reef health and assisting in management of these important resources. Prior to the 1990s, however, very few maps of the modern, shallow-water coral reefs of Hawai'i existed.

### ***9.1.1 History of Coral Reef Mapping in the Hawaiian Islands***

Early works were merely descriptive in their nature (for example, MacCaughey 1918, Pollock 1928). Beginning around 1960, the coral reefs in Kane'ohe Bay, O'ahu became some of the most heavily studied in the islands due to tremendous degradation, as well as their proximity to researchers at the University of Hawai'i marine lab on Coconut (Moku O Lo'e) Island. While the body of work in Kane'ohe Bay is extensive, most of these coral reef surveys, and others conducted around the state during the late 20th century, used a line-transect method to assess coral health and coverage for various other studies (for example, Banner 1968, Fitzhardinge 1985, Alifio 1986), and as such, provided no maps or method of quantifying the spatial extent of Hawaiian reefs.

In 1984, the University of Hawai'i Marine Options Program undertook a coral reef mapping effort on the island of Moloka'i for the U.S. Army Corps of Engineers (Manoa Mapworks 1984). Qualitative field data were collected over a two-week period using scuba and snorkel, and maps were plotted using 1:6 K and 1:24 K black-and-white aerial photography from 1975 as a base layer. These maps provide a useful background to the Moloka'i reef ecosystem, however, the aerial photographs were not georeferenced, and thus no accurate measurements of scale and distribution can be made from them.

In 1998, the U.S. Geological Survey (USGS) recognized the need for accurate maps of Hawai'i's coral reefs to provide a baseline for future change assessments and that these maps should include the geometry and distribution of coral cover (Field and Reid 1998). In order to be useful for management decisions, the accuracy of the maps would need to be verified using ground-truth methods. Concurrently, in response to the mandate set forth by Executive Order 13089, the National Oceanic and Atmospheric Administration (NOAA) National Ocean Service (NOS) implemented a program to provide digital maps of coral reefs within U.S. waters, including territories, for use in a Geographic Information System (GIS). A digital



**Fig. 9.1** Map of the main eight Hawaiian islands. The dark black lines show the locations of recent coral reef mapping efforts by the USGS

atlas of the benthic habitats of the main Hawaiian Islands was completed by NOAA’s Biogeography team in 2003 (Coyne et al. 2003).

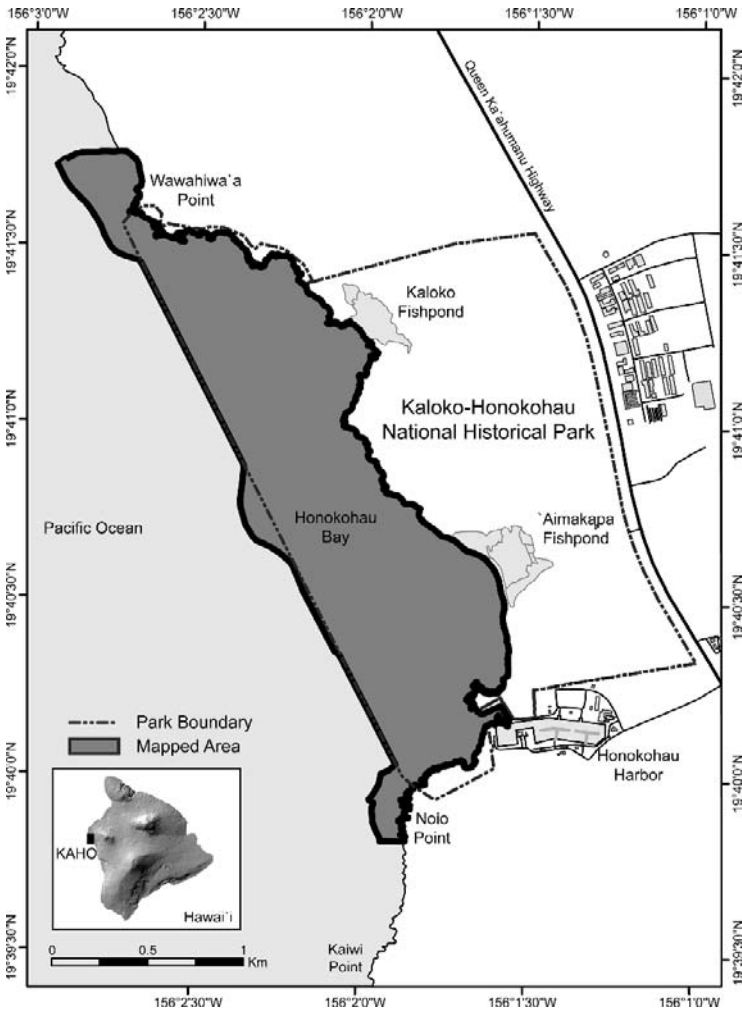
Coral reef mapping efforts by the USGS in the Hawaiian islands include major efforts on the south coast of Moloka’i (Cochran-Marquez 2005) and within or adjacent to three National Park lands along the Kona coast of Hawai’i: Pu’ukohola Heiau National Historic Site (PUHE), Kaloko-Honokohau National Historical Park (KAHO), and Pu’uhonua O Honaunau National Historical Park (PUHO) (Gibbs et al. 2007, Cochran et al. 2007a,b). Limited reconnaissance mapping was also conducted off the south shore of O’ahu and the west coast of Maui (Gibbs et al. 2005) (Fig. 9.1). A combination of aerial photography, high-resolution lidar bathymetry, and *in situ* observations were utilized in each of these mapping efforts. The methodologies employed and general results from one of the National Park studies, Kaloko-Honokohau, are presented here.

### 9.1.2 The Kaloko-Honokohau Study Area

Kaloko-Honokohau National Historical Park is one of three National Park lands located along the western coast of the island of Hawai’i and the only one to include submerged lands and marine resources within its official boundaries. The park was established in 1978 and is 1,160 acres in size, including 596 acres of marine area. KAHO is located adjacent to a moderately well-developed area of the Kona coast. The park is bordered on the south by the Honokohau small boat harbor and on the north by a luxury residential/resort and golf course development near Wawahiwa’a

Point (Fig. 9.2). Future development slated for lands adjacent to the southern boundary of the park include a 300% expansion of the small boat harbor along with construction of hotels, condominiums, and a light industrial park.

Marine resources located within KAHO include coral reef and habitat for many marine animals such as the green sea turtle and a variety of fish and invertebrates. In addition, many archeological, cultural, and recreational resources are located within the marine realm of the park, including ancient fishponds and popular scuba diving destinations. Potential threats and stressors to the modern marine environment include groundwater and surface-water contamination, invasive plants and algae, fishing pressure, use of monofilament gill nets (which can ensnare marine life or



**Fig. 9.2** Location map showing the boundaries of Kaloko-Honokohau National Historical Park and the area mapped as part of this study



become tangled on reefs and left behind as fishing debris), and visitor use impacts, such as scuba diving and snorkeling. Illegal dumping, oil releases, boat groundings, and other physical damage to reef resources are potential threats from users of the nearby harbor. A specific issue of concern for the park includes establishing baseline conditions of the offshore resources prior to the development of adjacent coastal lands.

In 2003, the U.S. Geological Survey (USGS) Coastal and Marine Geology Program, in cooperation with the National Park Service (NPS), was tasked with developing a detailed benthic-habitat classification map for the marine lands within and adjacent to the park. The intent of this project was to provide baseline maps, a GIS database, and a report summarizing the biological and geological resources of these marine lands in order to facilitate the management, interpretation, and understanding of park resources. The report (Gibbs et al. 2007) and data generated are available online at: <http://pubs.usgs.gov/sir/2006/5256/> (last access on 11 March 2008).

## **9.2 Data and Methods**

### ***9.2.1 Classification Standards***

A standard for characterization of coral-reef environments was first implemented by NOAA for mapping the Florida Keys (Rohman and Monaco 2005) and Puerto Rico and the Virgin Islands (Kendall et al. 2001). This standard for mapping coral reefs in the United States and its territories characterizes benthic habitats on the basis of their sea-floor geomorphology, geographic zones, and biological cover using a minimum mapping unit of one acre. Typically, only color aerial photography or satellite imagery is used to define habitat boundaries and field reference checks are conducted using shipboard video or scuba transects.

In the study presented here, benthic-habitat classification maps were created using the standards established by NOAA but at a larger scale (minimum mapping unit of 100m<sup>2</sup> versus 1 acre) and with additional data sources, including existing color aerial photography, Scanning Hydrographic Operational Airborne Lidar Survey (SHOALS) bathymetric data, and georeferenced underwater video and still photography. Maps were generated using both ArcView and ArcMap GIS software by ESRI (<http://www.esri.com>; last access on 11 March 2008), and a statistical analysis of accuracy of the resultant maps was performed.

### ***9.2.2 Base Imagery and Data***

#### **9.2.2.1 Aerial Photography**

High-resolution aerial photomosaics offer a relatively inexpensive and easily acquired foundation for mapping shallow-water structures and features of coral reefs. As a passive form of remote sensing, aerial photography can provide an excellent

overview of reef habitats due to the typically clear, shallow-water environments in which reefs are found. Two of the primary limitations in the use of aerial photography for mapping coral reefs are: (1) the absorption of light by the water column precludes interpretation of bottom habitats in water depths greater than approximately 20 m, and (2) the remotely sensed data must be integrated with actual in-the-water field (groundtruth) observations in order to determine actual sediment type and live coral abundance, type, and distribution.

In this study, color aerial photographs were used as the base layers for mapping. The images were scanned, orthorectified, and a digital mosaic with a resolution of 0.16 m per pixel was produced. The horizontal accuracy of this photography was better than 2 m and most seafloor features were recognizable to a water depth between 15 and 25 m.

### 9.2.2.2 High-Resolution Bathymetry

High-resolution bathymetry was a second integral base data type used for delineating the habitat and morphological environments in this study. Scanning Hydrographic Operational Airborne Lidar Survey (SHOALS) bathymetric data were collected over the Hawaiian islands during 1999 and 2000 by the U.S. Army Corps of Engineers. Lidar is an active remote sensing technology that utilizes laser energy to detect distance between source and receiver. The SHOALS technology (see also Lillycrop et al. 1996, Guenther et al. 2000, Irish et al. 2000) determines water depth by comparing the time difference between a pulse of laser energy reflected off the surface of the water and one reflected off the sea floor. This time difference is difficult to resolve in shallow water ( $< \sim 1$  m) or where waves are breaking. The maximum water depth of data collection is limited by the combined effects of the incident sun angle and intensity, the reflectance or radiance of bottom material, and water clarity—including the type and quantity of particles in the water column. The SHOALS system is typically capable of sensing bottom depths equal to two or three times the Secchi depth—the depth to which an 8-inch (20-cm) disk with alternating black and white quadrants can be seen from the surface (Tyler 1968). In the KAHO study area, the maximum water penetration was 42 m. The bathymetric data have a nominal horizontal point spacing of 4 m ( $\pm 3$  m) and a vertical resolution of  $\pm 15$  cm. For further details regarding SHOALS data, see <http://shoals.sam.usace.army.mil> (last access on 11 March 2008).

Continuous bathymetric data were obtained for nearly the entire park area, with the exception of the shallow coastal waters in Honokohau and Kaloko Bays and a swath of missing data in the central part of Honokohau Bay. Bathymetry in this central area was obtained from the historical National Ocean Service (NOS) survey H09336 of 1968 (<http://www.ngdc.noaa.gov/mgg/bathymetry/hydro.html>; last access on 11 March 2008). From the combined SHOALS/NOS data, a triangulated irregular network (TIN) of the point data was generated, from which gridded surfaces were created. Isobaths, hillshades, and slope maps were derived from these grids using standard ArcMap functions and then used to assist in the interpretation of seafloor morphology and benthic habitat distribution.

### 9.2.3 Groundtruth Data

#### 9.2.3.1 Underwater Video and Still Photography

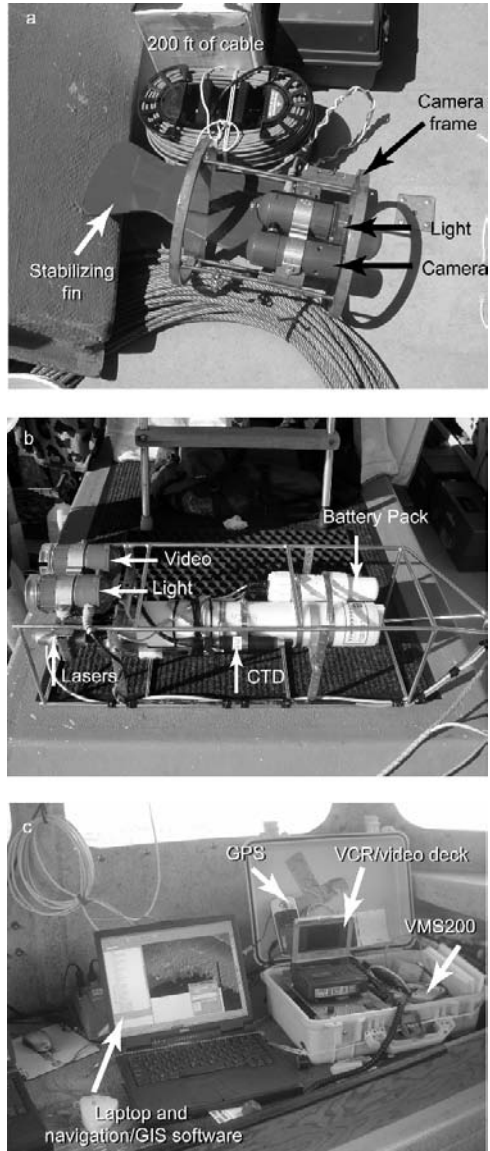
Several types of camera systems and collection methods were used to collect the groundtruth data. In water depths shallower than a boat could navigate, and along scuba transects, video and still photography were collected by snorkelers and scuba divers using hand-held video recorders and digital still cameras. A Global Positioning System (GPS) unit mounted on a surface float tethered to the snorkeler or diver provided positional information for the imagery.

In deeper water, video imagery was obtained by either towing a camera behind a moving vessel or dropping it over the side of the vessel while remaining on a fixed station or drifting slowly. Camera tows were designed to rapidly collect video imagery over large geographical areas. To avoid collisions with the seafloor, however, the camera had to be towed several meters above the bottom. This limited the observable detail of the seafloor in the video and these images were thus most useful for providing information regarding spatial transitions in coral cover and habitat. In contrast, during collection of video using the on-station drop or drift configuration, the camera could be lowered to within centimeters of the seafloor, which provided exceptionally detailed information on substrate type, benthic cover, and habitat diversity.

The camera system used for shipboard operations was a watertight video camera illuminated with a light-emitting diode (LED) light ring designed by SeaViewer Underwater Video Systems (<http://www.seaviewer.com>; last access on 11 March 2008). When rigged for towing, the camera was mounted in a small aluminum frame with a rear-mounted plastic fin (Fig. 9.3A). When rigged for on-station dropping, the camera and light were integrated with two battery-powered lasers and a Seabird CTD (Conductivity, Temperature, Depth) instrument in a steel frame (Fig. 9.3B). Live video from both systems was viewed in a shipboard laboratory on a monitor and recorded directly to miniDV tape (Fig. 9.3C). Time, date, location, and ship speed were overlaid on the video using Sea-Trak GPS Video Overlay, also developed by the SeaViewer Company.

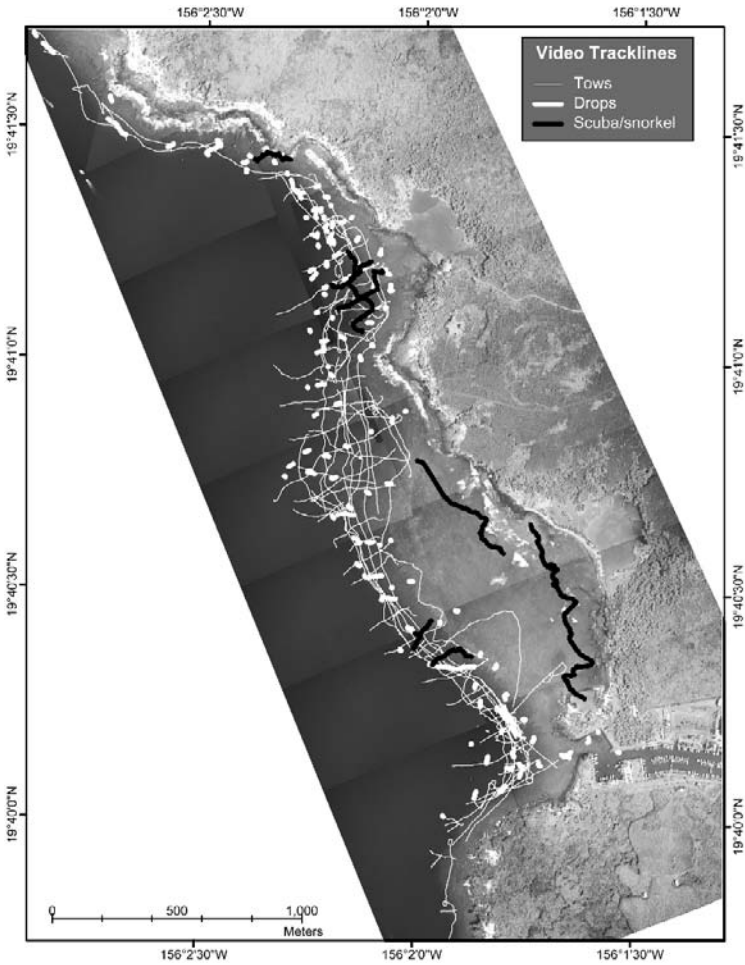
Simultaneous navigation, recording of ship position, and feature annotation were conducted in real time using hardware and software developed by Red Hen Systems (RHS; <http://www.redhensystems.com>; last access on 11 March 2008) on a PC laptop. Location data were recorded using a hand-held GPS receiver. The RHS hardware transmitted NMEA-formatted GPS data at two-second intervals to the first audio channel of the video tape. A database was simultaneously created to cross-reference the GPS locations and video time codes. This technique allowed for navigation and video to be viewed in real time and the location of features of interest and comments (for example, start/end of lines, substrate types) to be added to the database during data collection. For post-survey analyses, this technique allowed rapid random access to the original video by selecting locations along the navigation trackline within MediaMapper and GeoVideo (an extension developed by Red

**Fig. 9.3** Photograph of the (A) SEAVIEWER camera system rigged to collect towed video, and (B) with SeaBird CTD acquisition system rigged to collect drop or drift video and CTD information. (C) Photograph of shipboard laboratory set up for navigation, recording of ship's position, and annotation of bottom features



Hen Systems for integration with the ESRI ArcMap platform) software packages. Video could be interactively queried and geographically referenced feature annotations could be added to the database.

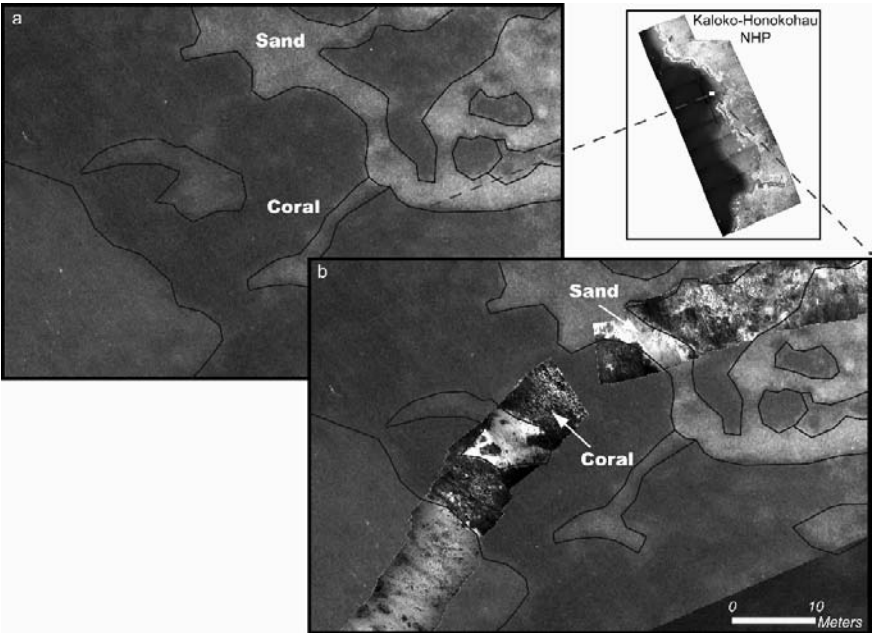
Nearly 48 trackline kilometers (22 h) of underwater video footage and more than 500 still images (89 towed lines, 124 on-station drop/drift sites, 5 scuba transects, and 3 snorkel transects), were collected during three field surveys between December 2003 and August 2004 (Fig. 9.4).



**Fig. 9.4** Aerial photomosaic of the study area overlain with video trackline locations

### 9.2.3.2 Video Mosaics

Recent advances in software development have allowed digital video to be converted to georeferenced image strips that can be imported into a GIS. Researchers at the University of New Hampshire (UNH) are developing software tools for pattern recognition from one video frame to the next, which results in a continuous image mosaic made from overlapping video frames (Rzhanov et al. 2004). Collaborators from the USGS and UNH used the sea-floor video acquired from KAHO to make georeferenced mosaics of selected tracklines within the study area. Original video on miniDV tape was converted into Audio Video Interleave (AVI) format using commercial software and then divided into 2-min sections in order to limit file size and to minimize propagation errors. Using the suite of UNH-developed software, the



**Fig. 9.5** Example of an underwater video mosaic overlain on aerial photography. (A) Aerial photomosaic with habitat polygon boundaries, and (B) with video mosaic added

video was then de-sampled, keeping every 15th–20th frame (depending on camera sled speed), and the outer edges of the AVI were cropped to remove the navigation and time stamps (Sea-Trak) that were superimposed on the video. With the clean AVI, both automatic and manual pattern recognition were performed, calculating the X-Y shift and rotation from one frame to the next. An image mosaic was generated using the video frames and the offset information. Finally, the image mosaics were georeferenced using a combination of GIS techniques, the navigation information on the original video, and comparison with the aerial photography where shallow portions of the reef were visible. Once the imagery was properly georeferenced, it was available within the GIS for direct comparison and groundtruthing of the benthic habitats (Fig. 9.5).

#### ***9.2.4 Benthic Habitat Mapping Using GIS***

Digital benthic habitat maps were created using ESRI's ArcMap 8.3 and ArcView 3.2 software with a habitat digitizing extension created by NOAA (see <http://www.ccma.nos.noaa.gov/products/biogeography/digitizer/> to download the extension; last access on 11 March 2008). The habitat digitizing extension allows users to delineate habitat areas and assign attributes to the habitat polygons based on a predetermined classification scheme using a point-and-click menu system.

We delineated and classified 1,185 polygons, covering more than 2,479 km<sup>2</sup>. A minimum mapping unit (MMU) of 100 m<sup>2</sup> was used; however, smaller features were mapped if they carried habitat significance (for example, an individual coral colony 2 m in diameter located in an otherwise uncolonized area). Features were digitized and interpreted primarily using the orthomosaics. In areas where seafloor features were too deep to be resolved in the aerial photograph, the morphological characteristics of the sea floor observed in the bathymetry, combined with underwater imagery, were used to define and classify the habitat polygons.

### 9.2.5 Classification Scheme

The classification scheme used was based on a scheme established by NOAA’s biogeography program in 2002 (Coyne et al. 2003) for the main eight Hawaiian islands and subsequently revised in 2004 (NOAA 2005). Developed with input from coral

**Table 9.1** List of individual habitat components in the classification scheme. Numbers represent the 4-digit identifier (ABCD)

Major structure (A)	Dominant structure (B)
1 Unconsolidated Sediment	1 Mud 2 Sand
2 Reef and Hardbottom	1 Aggregate Reef 2 Spur-and-Groove 3 Individual Patch Reef 4 Aggregated Patch Reef 5 Volcanic Pavement with 10–50% Rocks/Boulders 6 Volcanic Pavement 7 Volcanic Pavement with > 50% Rocks/Boulders 8 Volcanic Pavement with Sand Channels 9 Reef Rubble
3 Other	0 Unknown 1 Land 2 Artificial 3 Artificial/Historical
9 Unknown	0 Unknown
Major biologic cover (C)	Percent cover (D)*
0 Unknown	0 Unknown
1 Uncolonized	2 10– < 50%
2 Macroalgae	3 50– < 90%
3 Seagrass	4 90–100%
4 Coralline Algae	* Because < 10% coverage is considered to be uncolonized, percent category (1) < 10% is not used.
5 Coral	
6 Turf	
7 Emergent Vegetation	
8 Mangrove	
9 Octocoral	

reef scientists, managers, local experts, and others, the hierarchical scheme allows users to expand or collapse the level of thematic detail as necessary. We used the NOAA definition of benthic habitats and classification scheme as a starting point to provide continuity with other habitat maps. We then made modifications to the classification scheme where necessary to improve the characterization of benthic habitats and geologic substrates found along the Kona coast.

The classification scheme uses four basic attributes to describe each mapped polygon: (A) the major structure of the substrate, (B) the dominant structure (a subset of the major structure), (C) the major biologic cover found on the substrate, and (D) the percentage of major biological cover. The structure combined with the overlying biologic cover is referred to as a “habitat”. Each polygon is coded with a 4-digit identifier (ABCD) that reflects the combination of the individual habitat components. See Table 9.1 for a list of habitat components. If a polygon includes two or more substrate or coverage types, the polygon is identified with the dominant one. Each polygon is also coded with a fifth attribute, “zone”, which refers to the location of the habitat community within the coral reef ecosystem. These zones correspond to typical reef geomorphology (for example, reef flat, reef crest, fore reef, shelf, etc.; Spaulding et al. 2001, Kendall et al. 2001, Coyne et al. 2003). Detailed descriptions of habitats and zones, including example photographs, may be found in Gibbs et al. (2007).

## 9.3 Application of Techniques and Habitat Classification

### 9.3.1 *Habitat and Geology*

A thematic map showing the distribution of benthic habitats within the study area is shown in Fig. 9.6. This 2-dimensional thematic map provides a highly detailed representation of the aerial extent and distribution of the various benthic habitats. The ability to directly query the digital data and view the data in 3 dimensions, however, expands the utility and usefulness of the information, allowing for a more complete assessment of the environment and the interpretation of potential controls on the distribution of corals in this environment.

Evaluation of the bathymetric data, including the development of shaded relief (hillshades) and slope maps, along with profile transects or cross-sections, provided information on the shape or morphology of the seafloor (Fig. 9.7). Groundtruth data provided additional detail on the structures at a finer scale than the bathymetric data allowed. Gibbs et al. (2007) describe the geology of the marine region of the park and suggest that the underlying geologic framework and morphology of the submerged volcanic flows provide the primary control on benthic habitats within the park. The seafloor of KAHO is composed of multiple, smooth to undulating *pahoehoe*-type basalt flows that form flat to gently sloping benches, shear vertical walls, and steep flow-front escarpments. In some locations the basalt surface



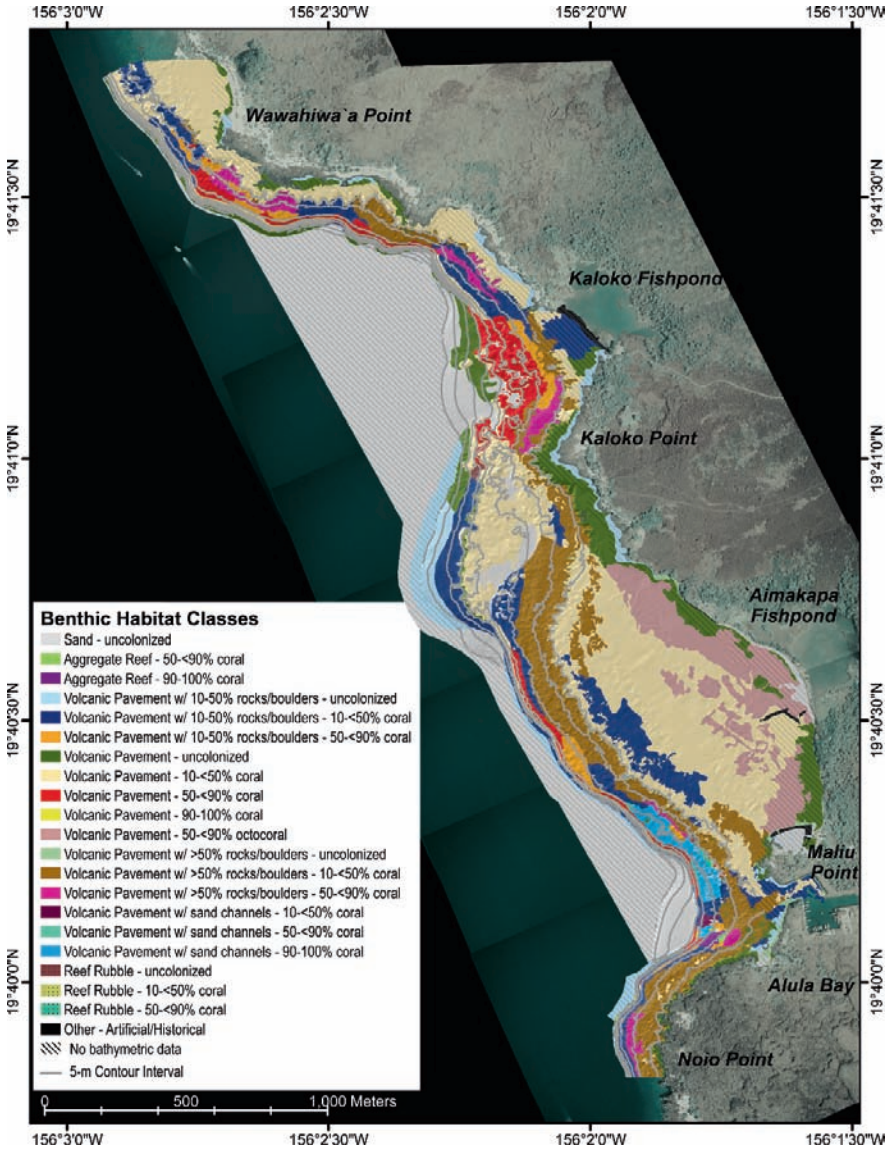
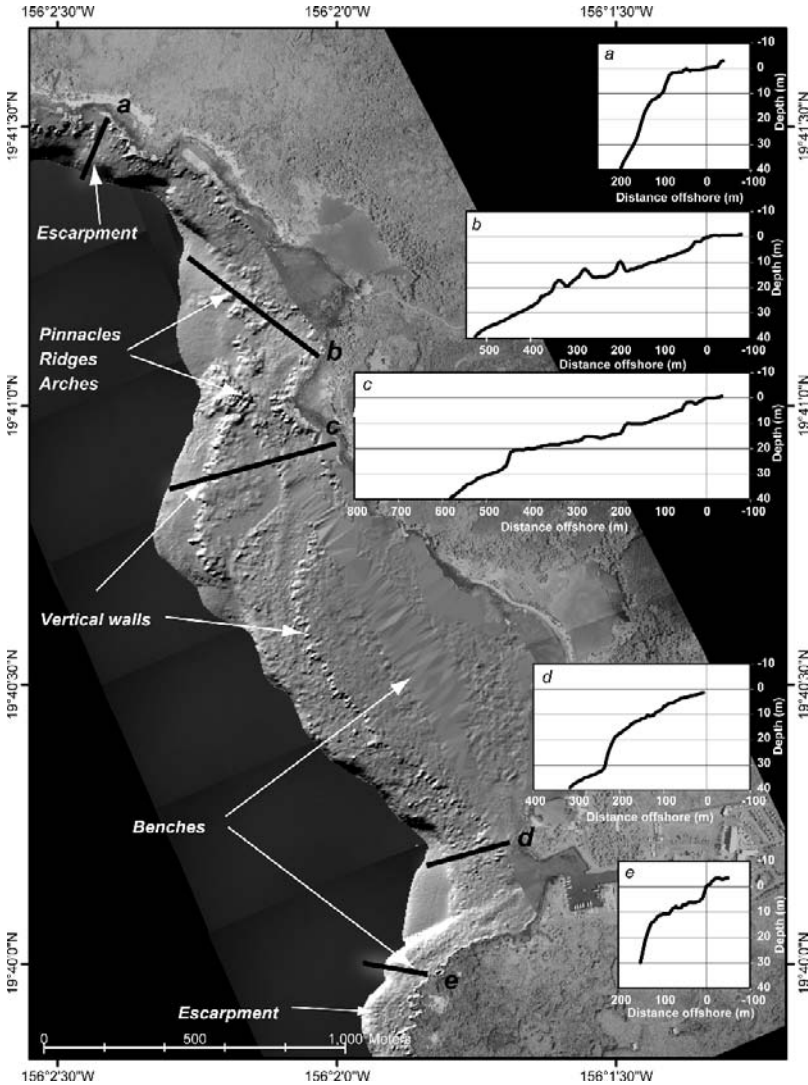


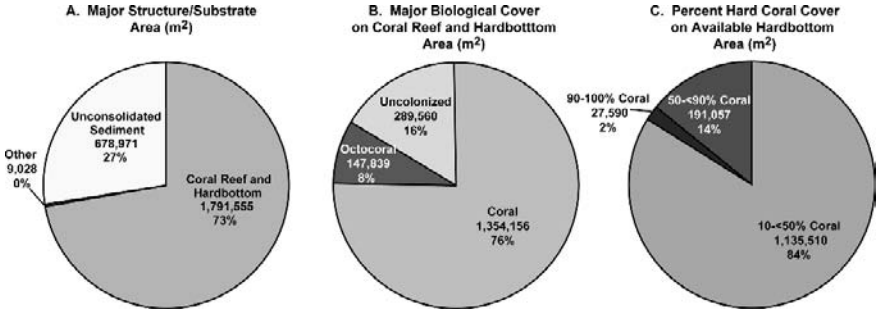
Fig. 9.6 A thematic map showing the distribution of benthic habitat classes in the KAHO area draped on shaded relief bathymetry and aerial photomosaic. Hatched lines indicate areas lacking bathymetric data

is irregular and mounded into ridges, pinnacles, and arches. Large rounded boulders and smaller scattered rocks are common throughout the marine portions of the park. In only a few locations does coral cover or accreted carbonate reef obscure the underlying volcanic surface (Fig. 9.7).



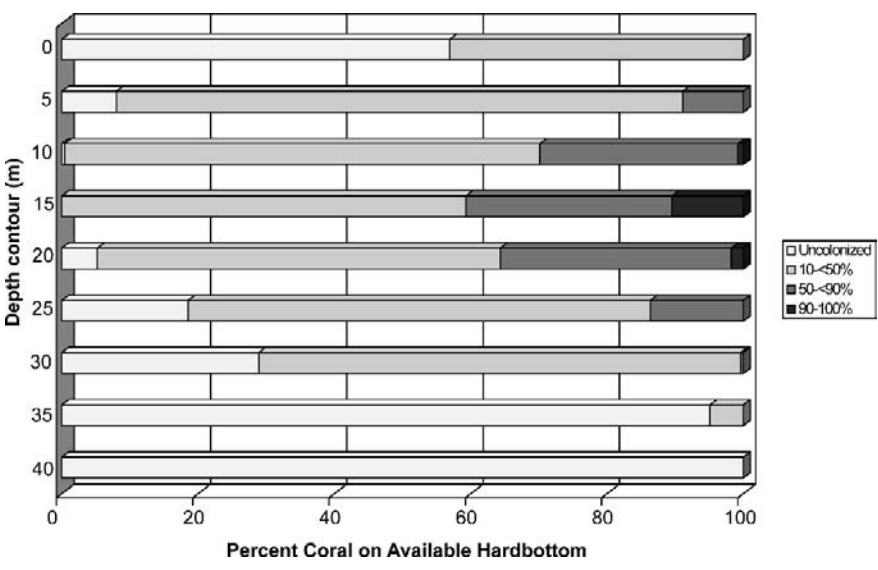
**Fig. 9.7** Shaded-relief map (hillshade) of the combined SHOALS and NOS bathymetry gridded data, aerial photomosaic, and selected cross-sections illustrating the complex seafloor morphology of the study area

Combination analyses of attributes, such as the structure/substrate with major biological cover, or percent coral cover with depth, provide information on the success or failure of corals to colonize different environments. For example, pie charts show the relative percent of seafloor potentially available for coral colonization (“available hardbottom” =73%) versus that covered with unconsolidated sand or other structures (27%) (Fig. 9.8A). Of the available hardbottom, 76% is covered with at



**Fig. 9.8** Relative abundance of (A) major substrate structures, (B) major biological coverage on coral reef and hardbottom, and (C) percent hard coral cover on available hardbottom in the KAHO study area. All unconsolidated sediment (27% of the study area) is sand (A). The remaining 73% of the study area is reef and hardbottom available for coral habitat (B). Of this available hardbottom, 76% is covered with a minimum of 10% coral (B). The majority of the study area is colonized with less than 50% live coral (C). In this study, soft octocoral is considered separately from hard scleractinian coral

least 10% coral (Fig. 9.8B). Overall, however, hard (scleractinian) coral cover is low, with 84% of the total hardbottom classified with 10 to < 50% hard coral cover. Only 14% is classified with moderately high (50–< 90%) hard coral cover and 2% is classified with high (90–100%) hard coral cover (Fig. 9.8C). Comparing coral



**Fig. 9.9** Bar graph showing the percent coral cover by depth. The highest coral cover is located in water depths between 10 and 20 m

cover with water depth shows that, in general, coral cover increases with depth and reaches maximum values between about 10 and 20 m (Fig. 9.9).

### ***9.3.2 Accuracy of Maps***

The validity, or usefulness, of any classification or interpretation can be determined with an accuracy assessment, which compares the mapped interpretation with actual reference conditions found in the field. In this project, the overall accuracy of the benthic habitat map and its accuracy from both the producer and user points of view were determined.

Overall accuracy indicates which points on the map are classified correctly according to a field check (Lillesand and Keifer 1994). Producer accuracy indicates how well the map producer classified the different cover types (that is, what percentage of a particular class was correctly classified). User accuracy is a measure of the reliability of an output map generated from a classification scheme (that is, the probability a map user will actually find that class in the field).

For this study, 185 randomly generated sample points were visited by third-party coral reef research biologists from the University of Hawai'i who were familiar with the classification scheme. An accuracy assessment was performed for the major biological covers (Table 9.2). The overall accuracy of 90.3% (with a 95% confidence interval of  $\pm 1.3$ ) indicates which points on the map were classified correctly according to the reference field check. Producer's and User's accuracies were generally greater than 60%, except for macroalgae, which was incorrectly classified 100% of the time. A tau coefficient of 0.878 was calculated as described by Ma and Redmond (1995) and indicates that 87.8% more points were classified correctly than would be expected by chance alone. After accuracy assessment calculations were performed, any misinterpreted polygons identified on the map were corrected using the field reference data, thus increasing the accuracy of the final map.

### ***9.3.3 Integration of Data Sets***

The unique aspect of this study was the integration of multiple remotely-sensed and groundtruth data sets to map coral reef habitat. Previous mapping efforts used solely aerial photography as a data source, with limited data for the purpose of accuracy assessment (Coyne et al. 2003). The lack of light penetration in standard aerial photography limits its usefulness as the sole source for interpretation of underwater features. By incorporating high-resolution bathymetry and field observations with the aerial photography, the mappable depth can be increased to about 40 m, nearly twice the depth that can be mapped with aerial multispectral or hyperspectral data

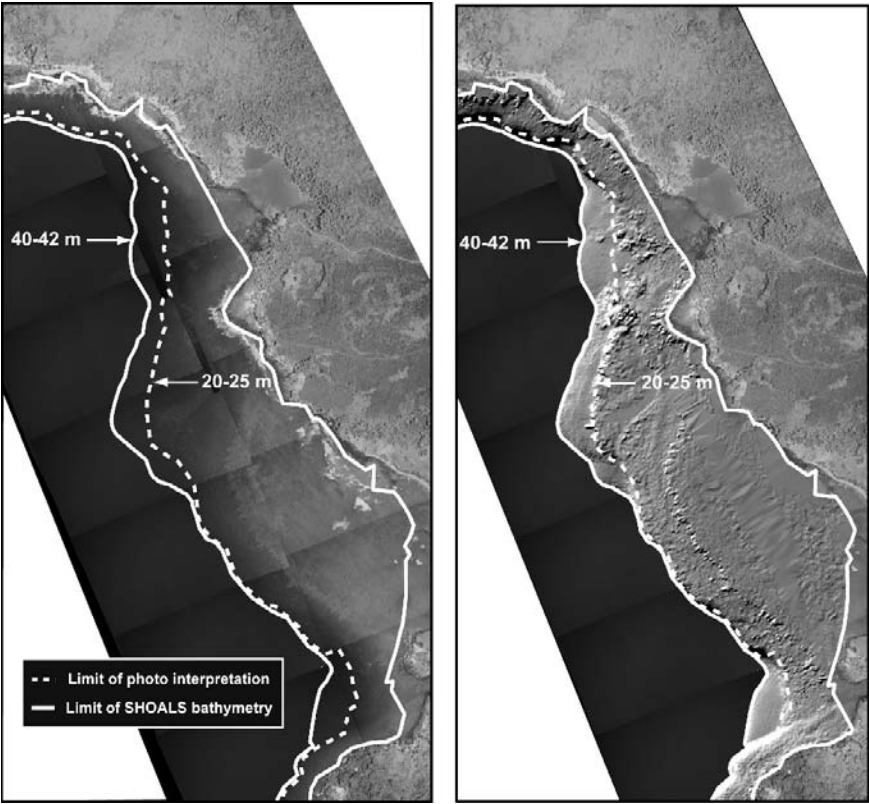
**Table 9.2** Accuracy assessment matrix for the major biological cover classes

		Reference									Total	User's Accuracy
		Unknown	Uncolonized	Macroalgae	Seagrass	Coralline Algae	Coral	Turf	Emergent Vegetation	Mangrove		
Mapped	Unknown	0	0	0	0	0	0	0	0	0	0	100
	Uncolonized	0	30	0	0	0	6	0	0	0	36	83
	Macroalgae	0	3	0	0	0	0	0	0	0	3	0
	Seagrass	0	0	0	0	0	0	0	0	0	0	100
	Coralline Algae	0	0	0	0	0	0	0	0	0	0	100
	Coral	0	6	0	0	0	134	0	0	0	141	95
	Turf	0	0	0	0	0	0	0	0	0	0	100
	Emergent Vegetation	0	0	0	0	0	0	0	0	0	0	100
	Mangrove	0	0	0	0	0	0	0	0	0	0	100
	Octocoral	0	1	1	0	0	0	0	0	0	3	60
Total		0	40	1	0	0	140	0	0	0	4	185
Producer's Accuracy (%)		100	75	0	100	100	96	100	100	100	75	
Diagonal Sum =167 Overall Accuracy=90.3% Tau=0.878												

alone (Fig. 9.10). In order to map to greater depths from a platform on or above the water surface, non-optical methodologies (e.g., single-beam or multi-beam sonar) would need to be employed.

### 9.3.4 Bathymetry and 3-D Visualization

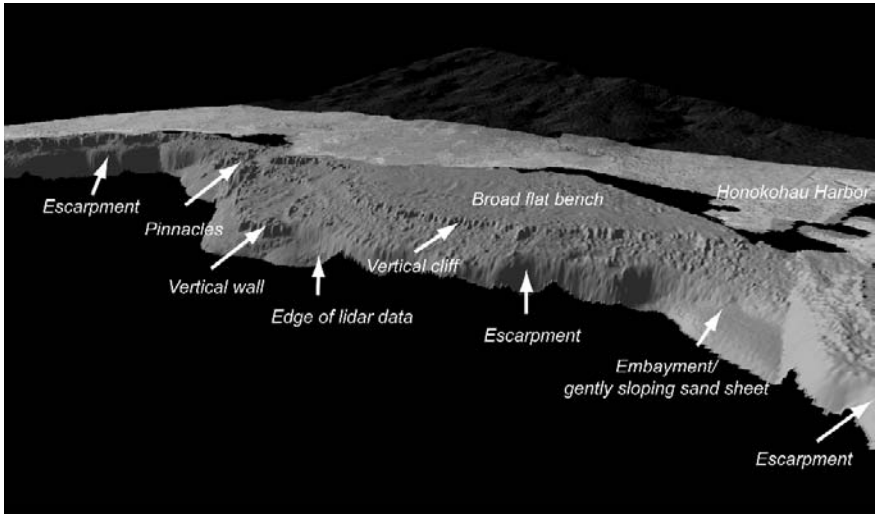
The inclusion of high-resolution bathymetric data allows for 3-dimensional visualization of the maps, assisting in both habitat interpretation and management decision-making. The integration of thematic maps with 3-dimensional data allows the scientist or manager to view data with a real-world perspective, rather than in a simple planar 2-dimensional perspective as is typical with conventional map products. A variety of software viewing packages exist (e.g., ArcScene, Fledermaus) that allow the user to view the data from different perspectives and scales, stack layers, and so on, to examine relationships between habitats and geology. For example, if only 2-dimensional, planar information had been used in this study, the detection of the complex seafloor morphology, including steep escarpments, vertical walls, and pinnacled regions, and its control on coral distribution would not have been possible (Fig. 9.11).



**Fig. 9.10** Lines showing the limit of mappable area using aerial photography alone (*dashed line*) and using a combination of aerial photography, high-resolution bathymetry, and field observations (*solid line*), overlain on the aerial photomosaic (*left*) and shaded relief bathymetry (*right*)

## 9.4 Summary and Conclusions

The integration of multiple data sets within a GIS allows for a multitude of analytical and visualization approaches to understanding, interpreting, and quantifying a particular physical environment. In this study, we combined aerial photography, high-resolution bathymetry, and georeferenced video and still imagery to produce a high quality, multi-faceted data set on benthic habitats and submerged geological resources in Kaloko-Honokohau National Historical Park. The integration of multiple data sources allowed us to map the park area at a finer scale and to a deeper depth than previously available. By using similar classification schemes our higher resolution maps nest easily within the smaller scale (lower resolution) benthic habitat maps developed for all of the main eight Hawaiian islands (Coyne et al. 2003). The habitat maps and other data sources can be used by park managers and scientists as stand-alone maps or can be digitally viewed and queried in a GIS for purposes of



**Fig. 9.11** A 3-dimensional perspective figure showing the complex seafloor morphology off Kaloko-Honokohau NHP. View is toward the north east. Vertical exaggeration is x4. Approximate distance along the bottom of the figure is 3 km

inventorying and evaluating existing park resources. The data and maps also provide a baseline for monitoring the status and sustainability of the habitats and resources they are tasked with managing.

**Acknowledgements** This project was funded by the U.S. Geological Survey (Coral Reef Project, Coastal and Marine Geology Program – Mike Field, coordinator) and by the National Park Service (Kaloko-Honokohau NHP). The authors thank Pat Chavez and his group from the USGS in Flagstaff for coordinating our acquisition of the SHOALS bathymetric data. Josh Logan and Eric Grossman (USGS) were invaluable in the field and provided many insightful conversations during the course of the study. Will Smith and colleagues from the University of Hawai'i Coral Reef Assessment and Monitoring Program (CRAMP) team performed the third-party field-check observations and provided the accuracy assessment calculations. Sallie Beavers from Kaloko-Honokohau NHP was instrumental in bringing the project to fruition and assisted with logistics while we were on island. Cheryl Hapke, Katie Farnsworth, and Alan Allwardt (all USGS) provided very helpful reviews of this paper. Mahalo nui loa.

## References

- Alifio PM (1986) A comparison of coral community structure on reef flats in Kane'oh'e Bay, Hawai'i. In: Jokiel PL, Richmond RH, Rogers RA (eds) Coral reef population biology: Hawai'i Institute of Marine Biology technical report, vol 37. pp 91–100
- Banner AH (1968) A fresh water kill on the coral reefs of Hawai'i. In: Hawai'i Institute of Marine Biology Technical Report, vol 15. pp 1–29
- Cochran-Marquez SA (2005) Moloka'i benthic habitat mapping. U.S. Geological Survey Open-File Report 2005-1070. <http://pubs.usgs.gov/of/2005/1070/> (last access on 11 March 2008)

- Cochran SA, Gibbs AE, Logan JB (2007a) Geologic resource evaluation of Pu'ukohola Heiau National Historic Site, part II: benthic habitat mapping. U.S. Geological Survey Scientific Investigations Report 2006-5254. <http://pubs.usgs.gov/sir/2006/5254/> (last access on 11 March 2008)
- Cochran SA, Gibbs AE, Logan JB (2007b) Geologic resource evaluation of Pu'uhonua O Honau-nau National Historical Park, part II: benthic habitat mapping. U.S. Geological Survey Scientific Investigations Report 2006-5258. <http://pubs.usgs.gov/sir/2006/5258/> (last access on 11 March 2008)
- Coyne MS, Battista TA, Anderson M, Waddell J, Smith W, Jokiel P, Kendall MS, Monaco ME (2003) Benthic habitats of the main Hawaiian Islands. NOAA Technical Memorandum NOS NCCOS CCMA 152. [http://www.ccma.nos.noaa.gov/products/biogeography/hawaii\\_cd/](http://www.ccma.nos.noaa.gov/products/biogeography/hawaii_cd/) (last access on 11 March 2008)
- Field ME, Reid JA (1998) America's coral reefs; a program for mapping, research and assessment to insure vitality, protect resources, and understand change. U.S. Geological Survey Administrative Report, unpublished, Menlo Park, CA
- Fitzhardinge R (1985) Spatial and temporal variability in coral recruitment in Kane'ohe Bay (Oahu, Hawai'i). Proceedings of the Fifth International Coral Reef Symposium, vol 4. pp 373–378
- Friedlander AM, Aeby G, Brown E, Clark A, Coles S, Dollar S, Hunter C, Jokiel P, Smith J, Walsh B, Williams I, Wiltse W (2005). The state of coral reef ecosystems of the main Hawaiian Islands. In: Waddell J (ed) The state of coral reef ecosystems of the United States and Pacific freely associated states: 2005. NOAA Technical Memorandum NOS NCCOS 11. NOAA/NCCOS Center for Coastal Monitoring and Assessment's Biogeography Team. Silver Spring, MD, pp 222–269
- Gibbs AE, Cochran SA, Logan JB, Grossman EE (2007) Benthic habitats and offshore geological resources of Kaloko-Honokohau National Historical Park. U.S. Geological Survey Scientific Investigations Report 2006-5256. <http://pubs.usgs.gov/sir/2006/5256/> (last access on 11 March 2008)
- Gibbs AE, Grossman EE, Richmond BM (2005) Summary and preliminary interpretations of USGS Cruise A202HW: underwater video surveys collected off of Oahu, Molokai, and Maui, Hawaii - June–July 2002. U.S. Geological Survey Open-File Report 2005–1244
- Gunther GC, Cunningham AG, LaRocque PE, Reid DJ (2000) Meeting the accuracy challenge in airborne lidar bathymetry. Proceedings of EARSeL-SIG-Workshop LIDAR, Dresden/FGR, 16–17 June 2000
- Irish JL, McClung JK, Lillycrop WJ (2000) Airborne lidar bathymetry: the SHOALS system. PI-ANC Bulletin, vol 103. pp 43–53
- Kendall MS, Monaco ME, Buja KR, Christensen JD, Kruer CR, Finkbeiner M, Warner RA (2001) Methods used to map the benthic habitats of Puerto Rico and the U.S. Virgin Islands. U.S. National Oceanic and Atmospheric Administration. <http://ccma.nos.noaa.gov/products/biogeography/benthic/> (last access on 11 March 2008)
- Lillesand TM, Keifer RW (1994) Remote sensing and image interpretation, 3rd edn. John Wiley and Sons, New York
- Lillycrop WJ, Parson LE, Irish JL (1996) Development and operation of the SHOALS airborne lidar hydrographic survey system. In: Feigles VI, Kopilevich YI (eds) laser remote sensing of natural waters: from theory to practice. SPIE Selected Papers, St. Petersburg, Russia, vol 2694. pp 26–37
- Ma Z, Redmond RL (1995) Tau coefficients for accuracy assessment of classification of remote sensing data. Photogramm Eng and Rem S 61:435–439
- MacCaughy V (1918) A survey of the Hawaiian coral reefs. Am Nat 52(620/621):409–438
- Manoa Mapworks (1984) Moloka'i Coastal Resource Atlas. U.S. Army Corps of Engineers, Pacific Ocean Division
- NOAA (National Centers for Coastal Ocean Science) (2005) Shallow-water benthic habitats of American Samoa, Guam, and the Commonwealth of the Northern Mariana Islands. NOAA Technical Memorandum NOS NCCOS 8. [http://ccma.nos.noaa.gov/products/biogeography/us\\_pac\\_terr/index.htm](http://ccma.nos.noaa.gov/products/biogeography/us_pac_terr/index.htm) (last access 11 March 2008)



- Pollock JB (1928) Fringing and fossil coral reefs of O`ahu. Bernice Pauahi Bishop Museum Bulletin 55
- Rohman SO, Monaco ME (2005) Mapping Southern Florida's shallow-water coral ecosystems; an implementation plan. National Oceanic and Atmospheric Administration Technical Memorandum NOS NCCOS 19. <http://ccma.nos.noaa.gov/publications/biogeography/FloridaTm19.pdf> (last access 11 March 2008)
- Rzhanov Y, Mayer L, Fornari D (2004) Deep-sea image processing. Oceans'04 Conference, Kobe, Japan
- Spaulding MD, Ravilious C, Green EP (2001) World Atlas of Coral Reefs. Prepared at the UNEP World Conservation Monitoring Centre. University of California Press, Berkeley, USA
- Tyler JE (1968) The Secchi disc. *Limnol Oceanogr* 13:1–6
- Wilkinson C (ed) (2004) Status of coral reefs of the world: 2004. Australian Institute of Marine Science. <http://www.aims.gov.au/pages/research/coral-bleaching/scr2004/> (last access 11 March 2008)

## Chapter 10

# Assessment of the Abundance of Submersed Aquatic Vegetation (SAV) Communities in the Chesapeake Bay and its Use in SAV Management

Kenneth A. Moore, Robert J. Orth and David J. Wilcox

Broad declines in Chesapeake Bay submerged aquatic vegetation (SAV) populations that were first observed in the late 1960s and 1970s prompted the initiation of a comprehensive aerial mapping program to assess the status of the resource. This mapping program which began in 1978 has continued on an annual basis since 1984. The imagery used has primarily consisted of high resolution black and white photographs taken at a scale of 1:24,000. Mapping missions have been flown under guidelines addressing frame overlap, tidal stage, seasonal plant development, sun angle, atmospheric transparency, water turbidity and wind speed and direction to maximize SAV bed signatures. Currently 173 flight lines, which cover approximately 3,800 flight line km, are photographed and mapped for SAV each year. Scanned aerial photography images are geo-rectified and orthographically corrected to produce a series of aerial mosaics at 1 m resolution. The SAV beds are interpreted on-screen using in a GIS environment. Extensive ground survey data is also collected to verify the SAV photo-interpretation. A bay wide analysis of SAV distributions since the 1930s was also undertaken with archival aerial photographs using similar procedures to develop a composite historical coverage of SAV. Both the current and historical mapping results have been used for a variety of purposes. The composite historical coverages have been used to set SAV restoration goals and direct SAV restoration efforts. In addition, analyses of the historical SAV growth and bay bathymetry have been used to set seasonal water clarity targets for shallow water historically vegetated SAV areas throughout the bay. Comparisons of current SAV mapping results with historically based restoration targets are used annually to provide important indexes of bay condition and trends that are used to assess the effectiveness of nutrient and sediment reduction strategies for the bay and its watershed. In addition, the photographic imagery and the resultant SAV delineations have been widely used by managers to identify and minimize direct impacts to the SAV.

---

K.A. Moore (✉)

Virginia Institute of Marine Science, College of William and Mary, Gloucester Point,  
VA 23062, USA

e-mail: moore@vims.edu

## 10.1 Introduction

Throughout many littoral regions of the Chesapeake Bay and its tributaries both direct observation and other evidence have indicated that broad declines of seagrasses and other submersed aquatic vegetation (SAV) have occurred since the 1930s, with precipitous declines beginning in the 1970s (Orth and Moore 1983a). These declines have been thought to be principally the result of increasing inputs of nutrients and sediments into the estuarine waters from the watershed and directly from the atmosphere (Kemp et al. 1983, Twilley et al. 1985, Kemp et al. 2005). These contribute to reduced light availability for plant photosynthesis by increasing water column turbidity and periphyton fouling of the aquatic plant leaves (Neckles et al. 1993, Moore et al. 1996, 1997). Recent losses of SAV have not just been observed in the Chesapeake Bay, but broad-scale declines attributed to human influences have been documented in populations worldwide (Orth et al. 2006a, Ralph et al. 2006).

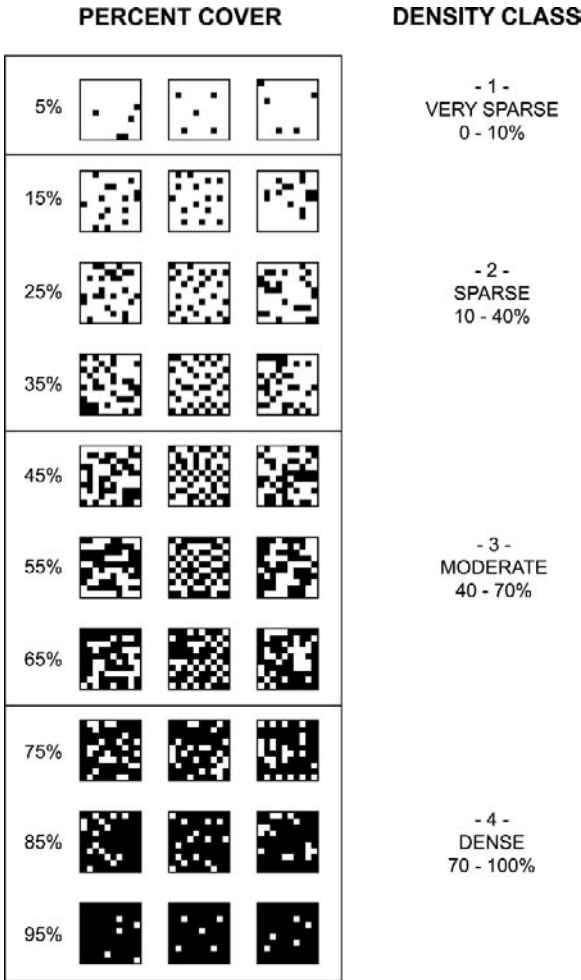
SAV is a highly valuable bay resource whose presence serves as an important indicator of local water quality conditions (Dennison et al. 1993, Batiuk et al. 2000). Throughout most of the Chesapeake Bay SAV are currently found growing at water depths of 2 m mean low water (MLW) or less. Even in these shallow depths high levels of nutrient and suspended sediments can decrease SAV growth and survival; and because SAV beds are non-motile, their presence or absence can serve as an integrating measure of variable water quality conditions in local areas (Moore et al. 1996, Kemp et al. 2005, Rybicki and Landwehr 2007). Research indicates that the growth, survival and depth limits of SAV can be directly related to water column light levels (Duarte 1991, Dennison et al. 1993, Nielsen et al. 2002). Water quality requirements for SAV growth are particularly crucial as barometers of the health of the Chesapeake Bay littoral environment and because of the direct relationships between SAV and water quality (Kemp et al. 2005), trends in the distribution and abundance of Chesapeake Bay SAV over time are very useful in understanding trends in water quality and bay restoration in general (Batiuk et al. 2000, Kemp et al. 2005).

Because of the value of SAV in the Chesapeake Bay ecosystem and their apparent large scale declines, a SAV mapping program was instituted in the late 1970s to assess the status of the resource. Archived black and white photography available from agencies such as the U.S. Geological Survey, U.S. Department of Agriculture Soil Conservation Service, National Oceanic and Atmospheric Administration and the Virginia and Maryland Departments of Highways was used to develop a historical composite picture of a few selected areas dating back to the 1930s (Orth and Moore 1983b). This provided the initial evidence that the low abundances first observed in 1960s and continuing into the early 1970s in all sections of the bay were likely unprecedented in recent bay history (Orth and Moore 1983a). The intensity of the decline was greatest in upper bay and western tributaries, suggesting a direct link with watershed processes and watershed development.

## 10.2 The Aerial Photographic Mapping Process

The comprehensive aerial photographic mapping inventory of SAV in the Chesapeake Bay began in 1978 and has been conducted on an annual basis since 1984, by the SAV Mapping Laboratory at the Virginia Institute of Marine Science (VIMS, Gloucester Point, VA). The mapping project has been funded by a variety of state and federal partners with the support of the Chesapeake Executive Council consisting of the Governors of Virginia, Maryland, Pennsylvania, the Mayor of the District of Columbia and the United States Environmental Protection Agency (USEPA) Administrator. In the initial years, high resolution black and white, aerial photographs were taken using 9.5 in. square negative Aerographic type 2405 or Aerochrome MS type 2448 film at scales of 1:12,000–1:24,000. Prints of these photographs were analyzed directly with analog interpretation techniques based on photo-interpretation by a seagrass biologist (Orth and Moore 1983b). The bed outlines were then transferred directly to mylar, 7.5 min series, 1:24,000 scale, United States Geodetic Survey (USGS) topographic quadrangles for area determinations and perimeter digitization. In addition to the boundaries of the SAV beds, estimates of percent cover for each bed were visually classified into four categories using a standard scale (Fig. 10.1) to estimate cover of the vegetation. A black and white film type was and continues to be used for the delineations despite the potential advantages of normal-color imagery for seagrass mapping (Pasqualini et al. 2001), due principally to the finer grain, smaller storage requirements for scanned images, and lower cost. Currently Aviphot Pan 80 black and white film is used to obtain the images flown at 12,000 ft, yielding 1:24,000 scale photographs.

Guidelines for acquisition of aerial photography used in this monitoring program were initially developed to address tidal stage, seasonal plant development, sun angle, atmospheric transparency, water turbidity, wind, sensor operation and sufficient land features for geographic orientation (Orth and Moore 1983b) and these continued to be used to the present (Orth et al. 2006b). For example, for SAV in the Chesapeake Bay: photography must be acquired at low tide,  $\pm 0$ –1.5 ft, as predicted by the National Ocean Survey tables; imagery must be acquired when growth stages ensure maximum delineation of SAV, and when SAV species phenologic state overlap is greatest; photography must be acquired when surface reflection from sun glint does not cover more than 30% of frame; sun angle is between 20° and 40° to minimize water surface glitter; there is at least 60% line overlap and 20% side lap; photography must be acquired during periods of no or low haze and/or clouds below the aircraft as well as no more than scattered or thin broken clouds, or thin overcast above the aircraft to ensure maximum SAV to bottom contrast; turbidity must be low enough that when viewed from the aircraft the SAV can be seen by the observer; there should be little or no wind, with offshore winds preferred to onshore winds when slight wind conditions cannot be avoided; photography must be acquired in the vertical mode with less than 5° tilt; scale, altitude, film and focal length combination must permit resolution and identification of one square meter area of SAV at the surface; each flight line must include sufficient identifiable land area to



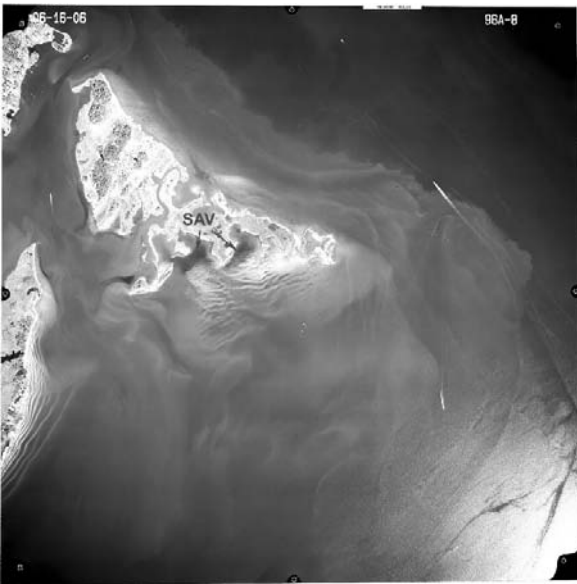
**Fig. 10.1** Categories used for estimating density of SAV from aerial photography. Rows of squares with black and white patterns represent three different arrangements of vegetated cover for a given percentage. <10% = Category 1; 10–40% = Category 2; 40–70% = Category 3; 70–100% = Category 4. (Reproduced from Moore et al. 2000, by permission)

assure accurate location of grass beds. These guidelines have become a standard for mapping SAV (Dobson et al. 1995). Adherence to the guidelines assures acquisition of photography under as optimal conditions as possible for detection of SAV, thus ensuring accurate photo interpretation. Deviation from any of these guidelines requires prior approval by VIMS staff. Quality assurance and calibration procedures are consistently followed. The altimeter is calibrated annually by the Federal Aviation Administration and the aerial camera is calibrated by USGS.

Camera settings are currently selected by automatic exposure control. Flights are scheduled within a sun angle window of 20°–40° to minimize sun glint in the

frame. In addition, the camera is equipped with a computer controlled intervalometer that establishes 60% line overlap and 20% sidelap providing duplicate coverage for areas obscured by glint. An automatic bubble level holds the camera to within one-degree tilt. The scale, altitude, film, and focal length combination is coordinated so that SAV patches of one square meter can be resolved. Ground-level wind speed is monitored with realtime data available on the web. Under normal operating conditions, flights are usually conducted under wind speeds less than 10 mph. Above this speed, wind-generated waves stir bottom sediments, which can easily obscure SAV beds in less than one hour. During the flight the pilot evaluates water clarity conditions. During optimum flight conditions where the turbidity is sufficiently low to permit complete delineation of the SAV beds, the shoals are clearly visible and the pilot is usually able to distinguish bottom features such as SAV or algae.

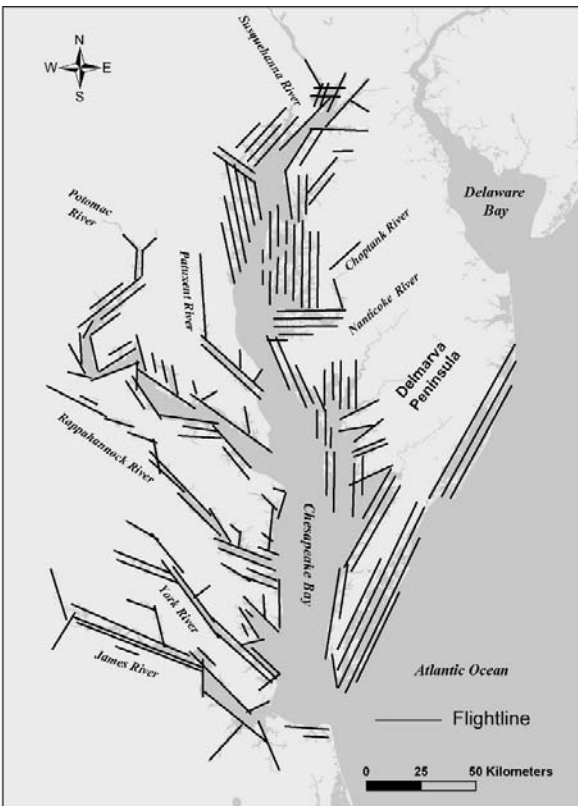
Excessively turbid conditions generally preclude photography and the determination of optimum cloud cover level is based on pilot experience. Records of pilot observation are kept in a flight notebook. Cloud cover below 12,000 ft is limited to 5% of the area covered by the camera frame, but a thin haze layer above 12,000 ft is acceptable. Experience with the Chesapeake Bay has shown that optimal atmospheric conditions generally occur two to three days following passage of a cold front, when winds have shifted from north-northwest to south and have moderated to less than 10 mph. Within the guidelines for prioritizing and executing the photography, the flights are planned to coincide with these atmospheric conditions where possible. A 9-inch by 9-inch, black-and-white contact print is produced for each exposed frame and reviewed by a scientist/photointerpreter to determine if each



**Fig. 10.2** A Typical aerial image used for mapping with arrows indicating several areas of dark SAV signatures near the island

flight line is suitable for SAV delineation. Each photograph is labeled with the date of acquisition as well as the flight line number and frame number (Fig. 10.2). Film and photographs are stored under appropriate environmental conditions to prevent degradation.

Currently the Chesapeake Bay SAV aerial photography (Orth et al. 2006b) consists of 173 flight lines, which cover approximately 3,800 flight line km (Fig. 10.3). These flight lines are positioned to include all areas known to recently or historically support SAV, as well as other areas of appropriate depths of less than 2 m mean low water (MLW) that have the potential for SAV growth. Typically, the flight lines are similar from year to year so as to provide a consistent image base. Flight lines are prioritized by sections and flights timed to occur during the peak growing season of the SAV species known to occur in each section. Specific areas known to have had significant SAV coverage are given a high priority. Higher salinity seagrass dominated regions in the lower bay are generally flown during May through June. Here, the dominant seagrass species, eelgrass (*Zostera marina*), reaches maximum biomass during this late spring-early summer period (Moore et al. 2000). Mid-bay



**Fig. 10.3** Chesapeake Bay and coastal bays annual aerial photography flight lines. Solid lines indicate flightlines

and upper bay areas that are dominated by a mix of freshwater and oligohaline tolerant species which reach peak biomass in the late summer (Moore et al. 2000) are flown later.

### 10.3 Orthorectification and Mosaic Production

Scanned aerial photography negatives are georectified and orthographically corrected to produce a seamless series of aerial mosaics following standard operating procedures. Leica LPS image processing software (Leica Geosystems GIS & Mapping, LLC. Atlanta, Ga. 2005) is used to orthographically correct the individual flight lines using a bundle block solution. Camera lens calibration data is matched to the image location of fiducial points to define the interior camera model. Control points from USGS DOQQ images provide the exterior control, which is enhanced by a large number of image-matching tie points produced automatically by the software. The exterior and interior models are combined with a 30-m resolution digital elevation model (DEM) from the USGS National Elevation Dataset (NED) to produce an orthophoto for each aerial photograph.

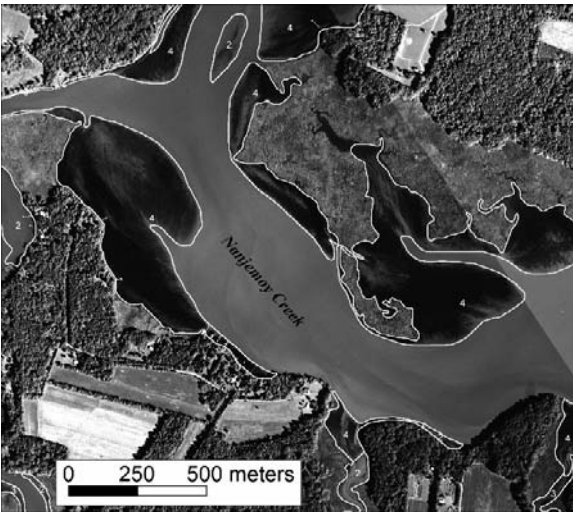
The orthophotographs that cover each USGS 7.5 min quadrangle area are adjusted to approximately uniform brightness and contrast and are mosaicked together using the ERDAS Imagine mosaic tool to produce a one-meter resolution quad-sized mosaic.

### 10.4 Photo-Interpretation and Bed Delineation

The SAV beds are interpreted on-screen from the orthophoto mosaics using commercial GIS software and a custom tool, which includes editing palettes, that was developed to facilitate the process. The identification and delineation of SAV beds by photo interpretation utilizes all available information including: knowledge of aquatic grass signatures on film, distribution of SAV from aerial photography, ground survey information, and aerial site surveys. In addition to delineating SAV bed boundaries, an estimate of SAV density within each bed is made by visually comparing each bed to an enlarged crown density scale (Fig. 10.1) similar to those developed for estimating forest tree crown cover from aerial photography (Paine 1981). Bed density is categorized into one of four classes based on a subjective comparison with the density scale. These are: 1, very sparse (<10% coverage); 2, sparse (10–40%); 3, moderate (40–70%); or 4, dense (70–100%). Substantial sections of larger beds that differ in density are delineated separately. Either the entire bed or sections within the bed are assigned a bed density number (1–4) corresponding to the above density classes. Additionally, each distinct SAV unit (bed or bed section) is assigned an identifying one or two letter designation unique to its map. Coupled with the appropriate SAV map number and year of photography, these one or two letter designations uniquely identify each SAV bed in the database.



Interpreting the outer, deeper edges of the SAV beds can be problematic especially in turbid systems. Mount (2003) has determined that the detection depth of SAV bed boundaries is approximately 60% of the in situ water transparency secchi depth. Typically, SAV in the Chesapeake Bay are found growing below mean sea level to depths equal to 100% of the local secchi depth (Dennison et al. 1993), which in the Chesapeake Bay commonly ranges from 0.5 m to 2.0 m. Given tidal ranges throughout the bay of approximately 0.5–1.0 m, aerial photography taken around the low tidal stage is usually sufficient to identify the deeper bed boundaries (Fig. 10.4). Local constraints such as wind generated turbidity or phytoplankton blooms can obscure the evidence of SAV in some areas; however, most SAV boundaries can be mapped with precision. Other constraints such as weather patterns, including summer atmospheric haze and restricted fly zones, typically provide a number of challenges for the acquisition of imagery suitable for mapping SAV. Timely and direct communication between the aerial photography contractor and the SAV mapping program scientist is critical in directing the aerial photography missions to the most appropriate flight lines for the local conditions. Strict adherence to mission constraints as well as pilot and other mission personnel experience and knowledge of the SAV natural resource also are extremely important in the acquisition of useful imagery.



**Fig. 10.4** SAV beds on aerial black and white photograph showing photointerpreted bed boundaries and individual bed numeric density category (1–4) classifications

## 10.5 Ground Survey Sampling

Ground survey information is collected annually by a variety of partners including researchers, state and federal management agency personnel, and trained individuals including private citizens and non-profit groups. The data are submitted in a variety

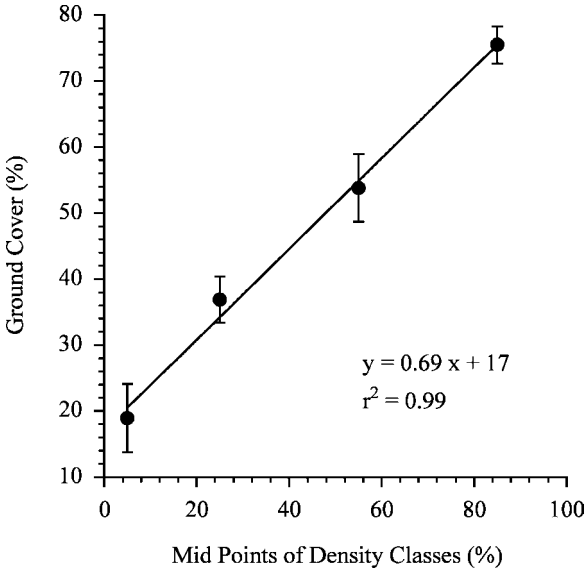
of formats including direct correspondence, transfer of GIS data files, and an interactive website. These reports of species presence and abundance and location are reviewed by scientific personnel at VIMS, tabulated and entered into a SAV geographic information system database. Based on eleven years of ground survey information from 1985 to 1996 Moore et al. (2000) were able to identify four distinct species associations (ZOSTERA, RUPPIA, POTAMOGETON, FRESHWATER MIXED) that were distributed throughout the Bay and its tidal tributaries principally by decreasing salinity regimes (Table 10.1).

Evaluation of the how well the photo-interpreted density classification (Fig. 10.1) represents actual SAV coverage has been investigated using transects consisting of point-intercept sampling by divers made across a range of SAV beds of different densities and species at 35 locations throughout the Bay system (Moore et al. 2000). These ground survey cover measurements were then compared to the photo-interpreted density class zones comprising each sampling area (Fig. 10.5). This relationship indicates that the photo-interpreted density class zones provide good measures of SAV abundance with a slight under estimate of SAV abundance by photo-interpretation in lower density areas, and over estimate in higher density areas. No effects of community type or depth of SAV growth on the relationship between measured ground cover and density class assignment could be determined. Therefore, the photo-interpreted density classification is applicable throughout the Bay system. Ground survey field measurements of SAV bottom cover

**Table 10.1** Chesapeake Bay SAV Communities. Species occurrence in community exceeds 10% of species observations. Reprinted with permission from Moore et al. 2000

ZOSTERA Community	<i>Zostera marina</i> *
	<i>Ruppia maritima</i>
RUPPIA Community	<i>Ruppia maritima</i> *
	<i>Potamogeton perfoliatus</i>
	<i>Potamogeton pectinatus</i>
	<i>Zannichellia palustris</i>
POTAMOGETON Community	<i>Potamogeton perfoliatus</i> *
	<i>Potamogeton pectinatus</i> *
	<i>Elodea canadensis</i>
	<i>Potamogeton crispus</i>
FRESHWATER Community	<i>Myriophyllum spicatum</i> *
	<i>Hydrilla verticillata</i> *
	<i>Vallisneria americana</i> *
	<i>Ceratophyllum demersum</i>
	<i>Heteranthera dubia</i>
	<i>Najas minor</i>
	<i>Elodea canadensis</i>
	<i>Najas guadalupensis</i>
	<i>Potamogeton crispus</i>
	<i>Najas gracillima</i>
	<i>Potamogeton pusillus</i>

\*Dominant species.



**Fig. 10.5** Comparison of SAV aerial density classifications to ground survey measurements. (Reproduced from Moore et al. 2000 by permission)

have previously been demonstrated to provide very good estimates of SAV density and biomass ( $r^2 > 0.86$ ; Orth and Moore 1988), and therefore the combination of ground survey information, aerial photography and density classification has been used to quantify both current as well as historical SAV community biomass throughout the growing season of multiple years (Moore et al. 2000).

## 10.6 Mapping Historical SAV Beds

To develop reasonable SAV restoration targets and to formulate the strategies for achieving these targets, it is necessary to first identify the potential for SAV restoration. Some shallow areas that may meet SAV water quality requirements are subject to high currents and wave activity or contain sediments that are very high in organic content and may not have a high potential for SAV growth (Koch 2001). Identification of those areas with previous evidence of SAV growth is an important step in quantifying that potential. In addition, because of the direct relationships between SAV and water quality, especially nutrient levels and water clarity, trends in the distribution and abundance of SAV over time are also very useful in understanding trends in water quality. Initial reviews of photographic evidence from a number of sites dating back to 1937 suggested that SAV, once abundant throughout the Chesapeake Bay system, had declined from historic levels (Orth and Moore 1984) and therefore water quality conditions may have similarly deteriorated (Orth and Moore 1983b). Although the absence of SAV on historical aerial photographs

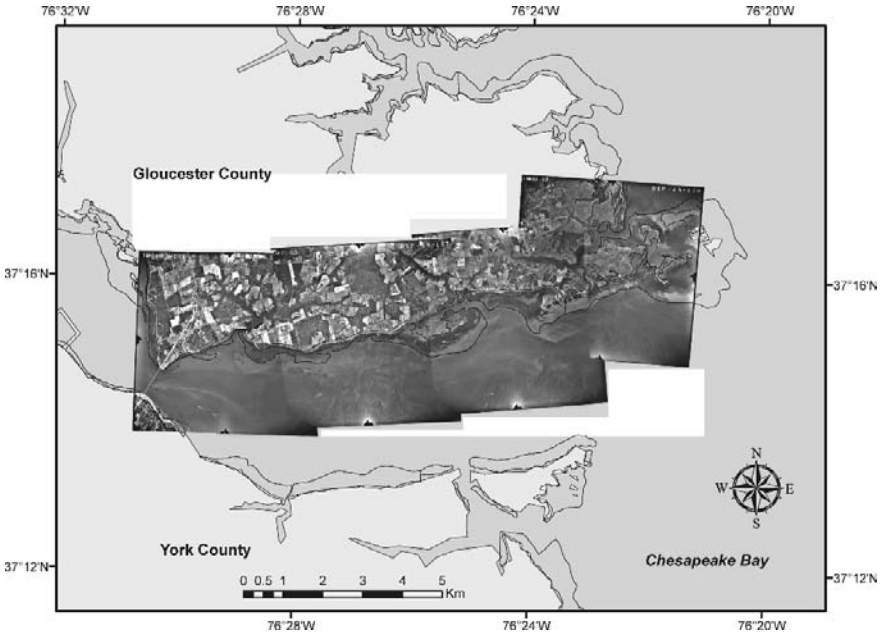
does not necessarily preclude SAV occurrence, SAV signatures are strong supporting evidence for the previous occurrence of SAV (Orth and Moore 1983b).

Photographic databases ranging from the 1930s through the early 1970s were analyzed to develop a comprehensive evaluation of historical SAV abundances throughout all littoral areas of the bay to serve as goals for SAV and water quality restoration (Naylor 2002, Moore et al. 1999, 2001, 2003b, 2004). Key photographic databases, including those of the Virginia and Maryland Departments of Transportation, local city and county photographic archives, National Oceanic and Atmospheric Administration (NOAA), United States Department of Agriculture (USDA), United States Geological Survey (USGS), and the Virginia Institute of Marine Science (VIMS) archives as well as other published reports, were initially searched by direct visits to local, state and federal repositories to view paper prints and color transparencies for photography and other documentation relative to SAV ground survey information. Web-based USGS and NOAA databases were also searched online using a web browser. Photographs that contained images of SAV were purchased and then scanned, photo-interpreted and digitized. Photo-interpretation of the selected aerial photographs followed as closely as possible the methods currently used to delineate SAV beds throughout the Chesapeake Bay in the annual aerial mapping SAV surveys (e.g., Orth et al. 2006b).

Initial screening of photographic prints was accomplished by viewing under a 10X magnification viewer. Each print was searched for SAV signatures, and the quality of the imagery for SAV delineation was estimated as "Good," "Fair," or "Poor." Those prints that showed some evidence of SAV signatures were scanned at a resolution of 600 dpi and viewed using ERDAS Imagine<sup>TM</sup> image processing software.

The aerial photography that was determined to have SAV signatures was processed using a heads-up, on-screen digitizing system. The system increases accuracy by combining the series of images into a single geographically registered image permitting the final SAV interpretation to be completed seamlessly in a single step (Fig. 10.6). In addition, the images are available digitally and can be printed along with the interpreted lines to show the precise character of the SAV beds.

The standard 9 inch  $\times$  9 inch, 1:24,000 scale black and white historical aerial photographs, were scanned at a resolution of 600 dpi, forming pixels approximately one meter in width. This was the minimum resolution required to accurately delineate SAV beds and resulted in files that were approximately 30 megabytes in size. The scanned images were then transferred to a Windows 2000 workstation for registration using ERDAS Orthobase<sup>TM</sup> (ERDAS, Atlanta, Ga.). Horizontal control was taken from USGS digital orthophoto quarter quads (DOQQ) and USGS 1:24,000 scale topographic quadrangles. USGS DEMs for the region were merged and used for vertical control. The Orthobase<sup>TM</sup> software combined both sources of control with a set of common "tag" points that were identified on pairs of photos to generate a photogrammetric solution and orthorectify the images, producing a single geographically corrected product that was used for interpretation. The total RMS error for the solution varied among images from 2.6 m to 4.1 m with a mean of 3.5 m.



**Fig. 10.6** Compositd 1953 historical photographs of SAV along the northern shoreline of the York River, Va. Lines indicate photo-interpreted SAV bed polygons

SAV bed outlines were traced directly from the combined image displayed on the computer screen into a GIS polygon file. The image scale was held fixed at 1:12,000 and line segments for polygons characterizing the beds were set to be no shorter than 20 m to maintain consistency with previous historical SAV surveys. The interpreted boundaries were drawn to include all visible SAV areas regardless of patchiness or density (Fig. 10.6).

A variety of historical aerial photographic images were located and reviewed, however the quality of the imagery for determination of SAV abundance ranged from good to poor. As previously described, a number of criteria must be met for acquisition of aerial photographs that are optimum for delineation of estuarine SAV (e.g., Orth and Moore 1983b, Orth et al. 2006b). Most imagery used for historical SAV analyses was obtained for other purposes, usually land use or farming analyses, and therefore, while criteria for atmospheric conditions were usually met (e.g. sun elevation, atmospheric transparency, etc.), those important for SAV delineation (e.g., tidal stage, water transparency, plant growth stage) may not have been met. In addition, while standard black and white, and color photographs are useful for SAV delineation (Orth and Moore 1984) other film types such as infrared or color infrared photography, which effectively delineates upland vegetation, are less useful in delineating submerged vegetation because of the rapid absorption of the infrared wavelengths of sunlight in water.

The most useful historical photography found for delineation of SAV in the Bay came from USDA. This photography acquired for land use and agricultural purposes was primarily black and white format at scales of approximately 1:20,000. The earliest photography from USDA and other sources consisted of over-flights conducted during 1936 and 1937. However much of this 1930s photography was found to show less SAV coverage than similar photography from the 1950s. Qualitatively, in many areas the difference appeared to be related to overall poorer atmospheric and water clarity conditions making SAV less apparent in the 1930s. In many other areas it appeared that the SAV were generally less abundant during the periods of the over-flights during the 1930s. Seasonal differences may have also been a factor; however, photography was constrained to that taken during the principal SAV growing season (April-October). Reduced abundance of SAV in the lower bay during the 1930s may have been the result of a worldwide decline of eelgrass that occurred in the early 1930s as well as a catastrophic un-named hurricane which struck the region in 1933 (Orth and Moore 1984). Given these constraints the 1950s period of photographs were generally chosen to delineate historical coverage of SAV in the bay region. In regions where data was available for more than one year, data from the year with maximum coverage was selected. Datasets were joined to form a comprehensive, composite, historical bay-wide SAV coverage. This GIS data layer represented the SAV that was visible on the available historical aerial photography for the Chesapeake Bay. Areas that were not visible on any of the available photography were not included. In some cases this was due to limited and poor quality of the available photography. Ground survey data were gathered from a variety of sources including reports, field survey sheets and interviews with local residents to substantiate SAV occurrence. Typically, the signatures on the imagery were very similar to those observed on current photography, and this combined with local knowledge and other information such as location and bathymetry, provided a reasonable degree of photo-interpretive confidence.

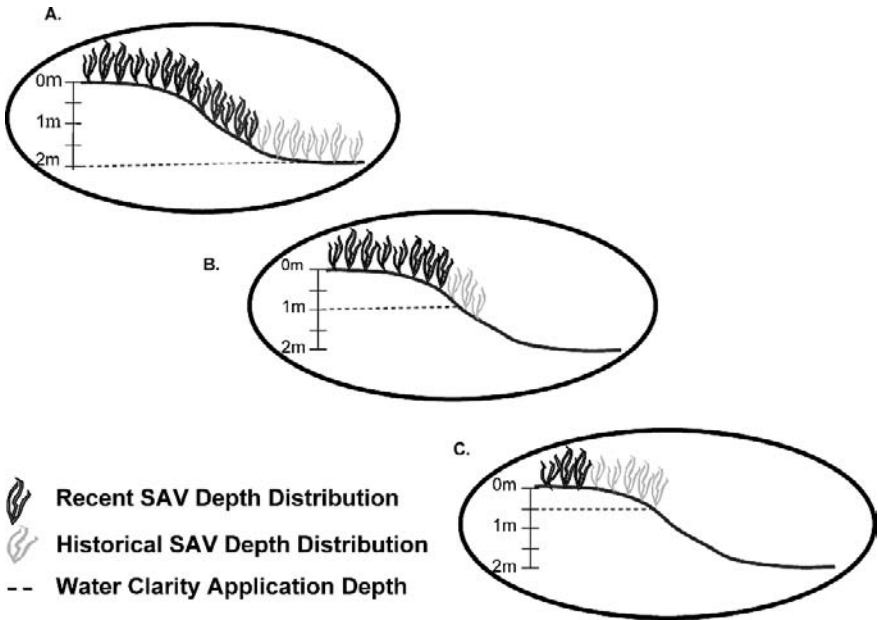
## **10.7 Setting Water Clarity Goals Based on SAV Distribution and Abundance**

Because of the strong relationships between light availability and SAV distribution and abundance (Batiuk et al. 1992, 2000, Dennison et al. 1993) and because of the importance of SAV as a critical designated use of the shallow water bay environment, the US EPA Chesapeake Bay Program (US EPA, Annapolis, MD) along with its state partners has established water clarity criteria for shallow water (<2 m MLW) designated use based on SAV water column light requirements (USEPA 2003a). In addition, it has developed and implemented a novel approach where water clarity criteria and state water clarity standards for shallow water areas can be met by either achieving the specific water clarity criteria, restoring the local SAV abundance to historical acreage levels, or achieving a combination of both (US EPA 2007).

### 10.7.1 Water Clarity Criteria

Research has determined that the mean SAV growing season light level at the deepest edge of a SAV bed necessary for continuing SAV survival is approximately 22% of surface irradiance through the water column (PLW) for SAV growing in polyhaline and mesohaline areas, and 13% for SAV communities in oligohaline and fresh-water tidal areas (Batiuk et al. 1992, 2000, Kemp et al. 2004). One of these PLW criteria has been set for every area of the bay depending on the salinity regime. It is understood, however, that the bottom depths to which the PLW criteria are applied, can and should be different for different areas depending on the natural conditions. Duarte (1991) has demonstrated that while this 22% light level at the deepest edge of a bed can be consistent for any one type of SAV or seagrass community found throughout the world, the actual depth of bed growth can vary greatly dependent on the local water clarity. For example, in coastal areas with historically very clear water the seagrass beds dominated by one species such as eelgrass (*Zostera marina*) can be found growing to 30 ft. depths or greater and at another, where the natural background turbidity is much higher, eelgrass growth may be only to 3–6 ft (Dennison et al. 1993). Applying the PLW over a specific maximum restoration depth will determine the exact water clarity requirement for a specific area. Water clarity can be approximated by measuring the turbidity (NTU units) or visibility (secchi disk depth) of the local water. It can also be determined more directly by measuring a depth profile of photosynthetically available radiation (PAR) and calculating the negative exponential decay of the light field according to the Lambert-Beer equation (Kirk 1994). Light at any depth can then be calculated using this resultant downwelling light attenuation coefficient ( $K_d$ ).

To assign an appropriate water depth (also called either “application” or “designated use” depths) for the PLW criteria as well as to set the targets for SAV designated use attainment, the historical composite distributions of SAV were used (US EPA 2003b). First, the historical SAV composite GIS coverage developed for the entire bay was divided into three bathymetry zones (0–0.5 m, 0.5–1.0 m, and 1.0–2.0 m) that had been established by the USEPA Chesapeake Bay Program for all bay shallow water areas. For the SAV restoration goals or SAV designated use abundances, all historical SAV areas including those observed growing deeper than the 2.0 m boundary were used. Next, water clarity restoration depths for the assessment of PLW levels were set at 0.5 m, 1.0 m, or 2.0 m based on the maximum depths of the historical SAV growth (Fig. 10.7), or more recent growth where either the historical imagery was limited or the more recent abundances up to 2002 were greater than the historical. A salinity-based segmentation scheme consisting of 78 bay segments (US EPA 2004a) was used to determine local spatial boundaries for the water clarity application depth determinations. In setting the designated use application depths for the PLW criteria a conservative estimate of SAV coverage within a depth interval was used (US EPA 2004b). For the use of historical SAV aerial coverage, at least 20% of the potential habitat in a depth interval for a segment was required for the application depth to be set at the next greater depth interval. For example, a historical SAV abundance in a segment would have to equal 20% or greater of the



**Fig. 10.7** Depiction of recent and historical depth distributions of Chesapeake Bay SAV in areas with different historical and current SAV colonization depths and water clarity application depths. (A) Water clarity depth 2 m. (B) Water clarity depth 1 m (C) Water clarity depth 0.5 m

available bottom bounded by the 1.0–2.0 m depth contours and the upstream and downstream segment boundaries in order for the water clarity goal to be set to 22% of light to the bottom at 2 m for that segment. If the 20% rule was not met, the water clarity application depth was set at 1 m depending on SAV abundance in that segment. For those segments where more recent aerial photography was used to set the application depths, a 10% coverage of the bottom habitat by SAV for an extended period of time was required (US EPA 2003b). If none of the SAV acreage thresholds were met, but some SAV growth was identified or considered possible, then a minimum application depth of 0.5 m could be set for that segment. In all of these analyses “No Grow Zones” were established and these areas were excluded from the calculations if it was thought that high energy conditions or other factors unrelated to water clarity (Koch 2001) precluded SAV growth in those areas. Table 10.2 provides a listing of Chesapeake Bay segments for Virginia and their restoration acreages as well as their restoration or water clarity designated use depths.

**10.7.2 SAV Shallow Water Designated Use Criteria**

Criteria for shallow water SAV designated use attainment set for the shallow water designated use areas of each bay segment are based on the composite historical



**Table 10.2** Virginia Shallow Water SAV Designated Use and Water Clarity Standards (from 9 VAC 25-260 Virginia Water Quality Standards, January 12, 2006)

Chesapeake bay program segment name	CBP segment	SAV acres	Water clarity criteria (%)	Designated use depth (m) <sup>1</sup>	Water clarity acres	Water clarity temporal application
Lower Central Chesapeake Bay	CB5MH	7,633	22	2	14,514	April 1–October 31
Western Lower Chesapeake Bay	CB6PH	1,267	22	1	3,168	March 1–November 30
Eastern Lower Chesapeake Bay	CB7PH	15,107	22	2	34,085	March 1–November 30
Mouth of the Chesapeake Bay	CB8PH	11	22	0.5	28	March 1–November 30
Upper Potomac River	POTTF	2,093	13	2	5,233	April 1–October 31
Middle Potomac River	POTOH	1,503	13	2	3,758	April 1–October 31
Lower Potomac River	POTMH	4,250	22	2	10,625	April 1–October 31
Upper Rappahannock River	RPPTF	66	13	0.5	165	April 1–October 31
Middle Rappahannock River	RPPOH	*	13	0.5	*	*
Lower Rappahannock River	RPPMH	1700	22	0.5	5000	April 1–October 31
Corrotoman River	CRRMH	768	22	1	1,920	April 1–October 31
Piankatank River	PIAMH	3,479	22	2	8,014	April 1–October 31
Upper Mattaponi River	MPNTF	85	13	0.5	213	April 1–October 31
Lower Mattaponi River	MPNOH	*	13	0.5	*	*
Upper Pamunkey River	PMKTF	187	13	0.5	468	April 1–October 31
Lower Pamunkey River	PMKOH	*	13	0.5	*	*
Middle York River	YRKMH	239	22	0.5	598	April 1–October 31
Lower York River	YRKPH	2,793	22	1	6,982	March 1–November 30
Mobjack Bay	MOBPH	15,901	22	2	33,990	March 1–November 30

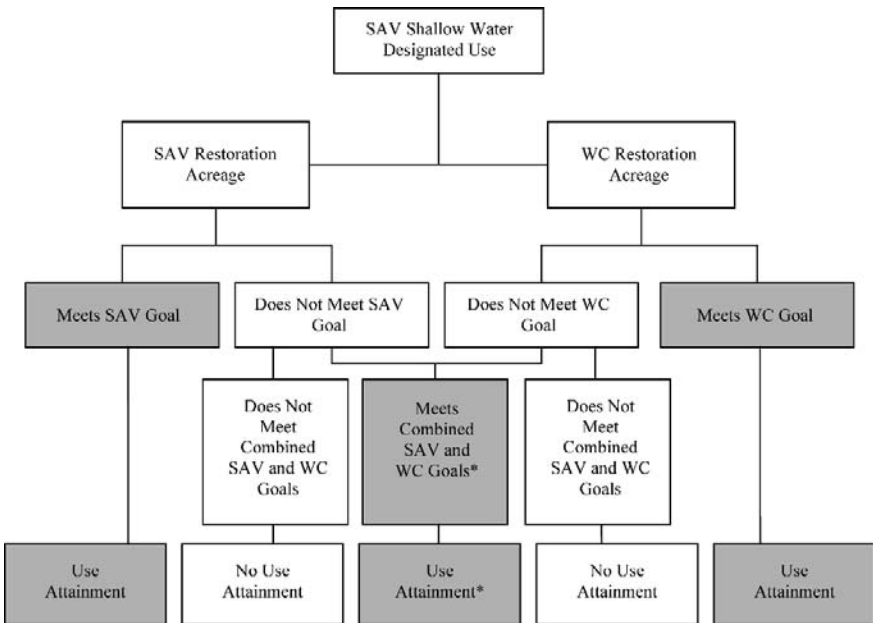
**Table 10.2** (continued)

Chesapeake bay program segment name	CBP segment	SAV acres	Water clarity criteria (%)	Designated use depth (m) <sup>1</sup>	Water clarity acres	Water clarity temporal application
Upper James River-2	JMSTF2	200	13	0.5	500	April 1–October 31
Upper James River – 1	JMSTF1	1000	13	0.5	2500	April 1–October 31
Appomattox River	APPTF	379	13	0.5	948	April 1–October 31
Middle James River	JMSOH	15	13	0.5	38	April 1–October 31
Chickahominy River	CHKOH	535	13	0.5	1,338	April 1–October 31
Lower James River	JMSMH	200	22	0.5	500	March 1–November 30
Mouth of the James River	JMSPH	300	22	1	750	March 1–November 30
Western Branch Elizabeth River	WBEMH	*	*	*	*	*
Southern Branch Elizabeth River	SBEMH	*	*	*	*	*
Eastern Branch Elizabeth River	EBEMH	*	*	*	*	*
Lafayette River	LAFMH	*	*	*	*	*
Mouth of the Elizabeth River	ELIPH	*	22	0.5	*	*
Lynnhaven River	LYNPH	107	22	0.5	268	March 1–November 30
Middle Pocomoke River	POCOH	*	13	0.5	*	*
Lower Pocomoke river	POCMH	4,066	22	1	9,368	April 1–October 31
Tangier Sound	TANMH	13,579	22	2	22,064	April 1–October 31
Total		75,463			167,035	

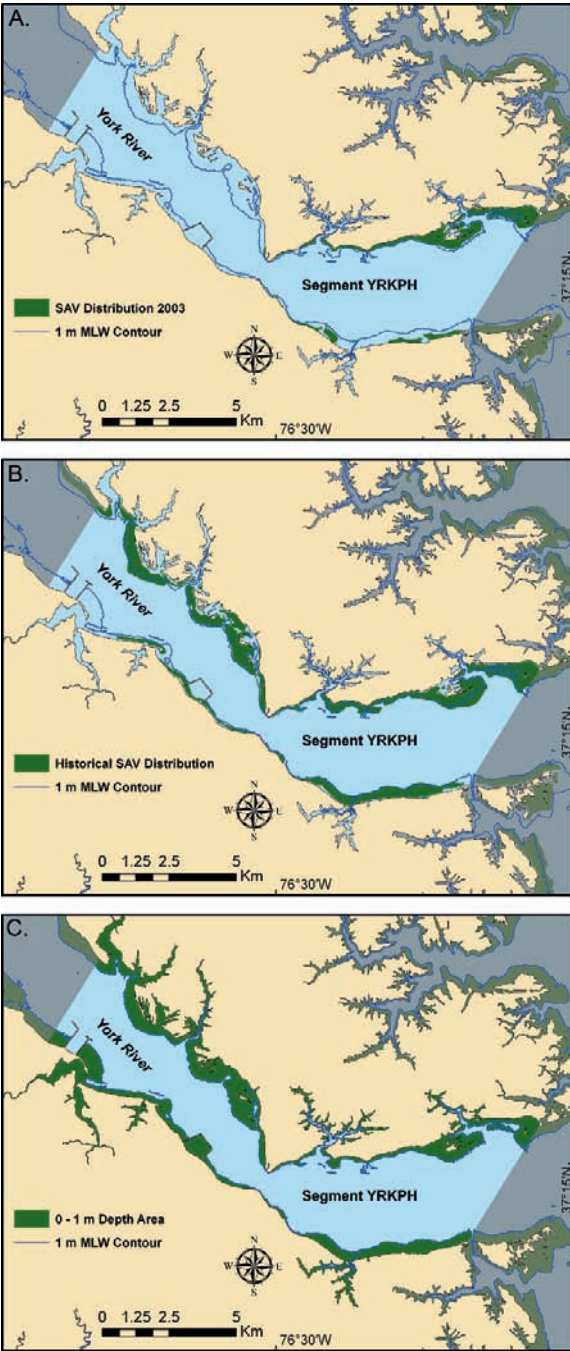
\*No specific numeric criteria developed.

<sup>1</sup>Recommended by EPA 2003. Not included in 9 VAC 25-260.

or current SAV abundances determined through the use of the historical and recent (through 2002) photography analyses described previously. The SAV designated use is considered in attainment if there are sufficient acres of SAV observed within the segment (determined as maximum single best year over the previous three years) or if there are enough acres of shallow-water habitat meeting the applicable water clarity criteria to support restoration of the desired acres of SAV for that segment (US EPA 2005, 2007). Assessment of either measure or a combination of both can be used as the basis for determining attainment or impairment of the shallow-water bay SAV designated use (Fig. 10.8). Acreage of shallow water habitat required to meet the water clarity goal is simply set at 2.5 times each acre of SAV required to meet the SAV restoration goal for the segment or the total area of available shallow bottom, whichever is less (US EPA 2003b). This is a bay-wide average of the ratio of available bottom to the historical composite SAV abundance determined from the historical photography. Attainment of a segment's water clarity goal is based on a calculation of the arithmetic mean of the year-by-year arithmetic means of a month-by-month accounting of water clarity acres over the three year SAV growing season assessment period. If neither the water clarity acreage (determined by measuring and then interpolating numerous water clarity measurements for each segment) nor the single best year SAV acreage meets their respective goals, then a combination of SAV acreage and water clarity acreages may be summed to achieve a total that must be equal to 2.5 times the SAV restoration acreage (US EPA 2007).



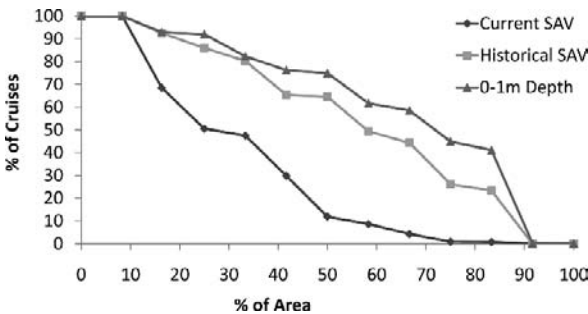
**Fig. 10.8** Decision process used to determine shallow water SAV use attainment for each bay segment. Use attainment can be met by meeting either SAV or water clarity (WC) restoration acreages, or a combination of both. \*Combination of SAV and WC not currently used in Virginia in 2007



**Fig. 10.9** Lower York River, Va (YRKPH) segment. (A) Mapped SAV distribution in 2003. (B) Mapped composite historical SAV distribution. (C) 0–1 m shallow water area. Green areas indicate SAV. Blue lines indicate 1 m bathymetry contour

Currently, high speed continuous mapping of water clarity for individual bay segments is being conducted using flow-through systems from surface vessels that make water quality measurements of turbidity every 25 m (Moore et al. 2003a). These individual measurements are interpolated using a standard krieging procedure (ArcGIS) and water clarity determined at a spatial grid of 25 m. Potentially any accurate spatial measure of water turbidity including aerial mapping or satellite imagery could be used to assess the water clarity attainment coverage. The current methods using mapping from surface vessels allow for regular calibration sampling, are detailed spatially, including near shore regions, and are not affected by atmospheric or other interferences.

Another potential approach to the determination of the attainment of SAV designated use in shallow waters is the use of cumulative frequency distribution methodology (US EPA 2003a 2007). Here the proportion of each segment that exceeds the water clarity criteria for that segment is plotted in ascending order for each cruise. This curve is compared to a reference curve which accounts for the allowable exceedance of the criteria under natural conditions. Significant difference between the curves can be tested statistically using empirical distribution functions, such as the Kolmogorov-Smirnov test (Zar 1996) to determine if the distribution of water clarity exceedances, if any, is significantly different from the reference. A reference curve can be developed by calculating the proportion of water clarity exceedances of areas that have been both mapped for SAV with aerial photography and measured for water clarity. An example of how this can be applied among three different classes of shallow water bottom is presented here. Figure 10.9 shows for Lower York River segment (YRKPH) a recently mapped distribution of SAV (A), the composite historical SAV areas (B), and the shallow water areas out to the water clarity application depth of 1 m for that segment (C). The recently mapped SAV can be observed to comprise significantly less area than the historical SAV coverage, which is, in turn, less than the potentially available shallow water bottom out to a depth of 1 m. In Fig. 10.10, CFD curves of interpolated monthly water clarity sampling from 2002 to 2003 for each of these three areas are compared. Both the CFDs for

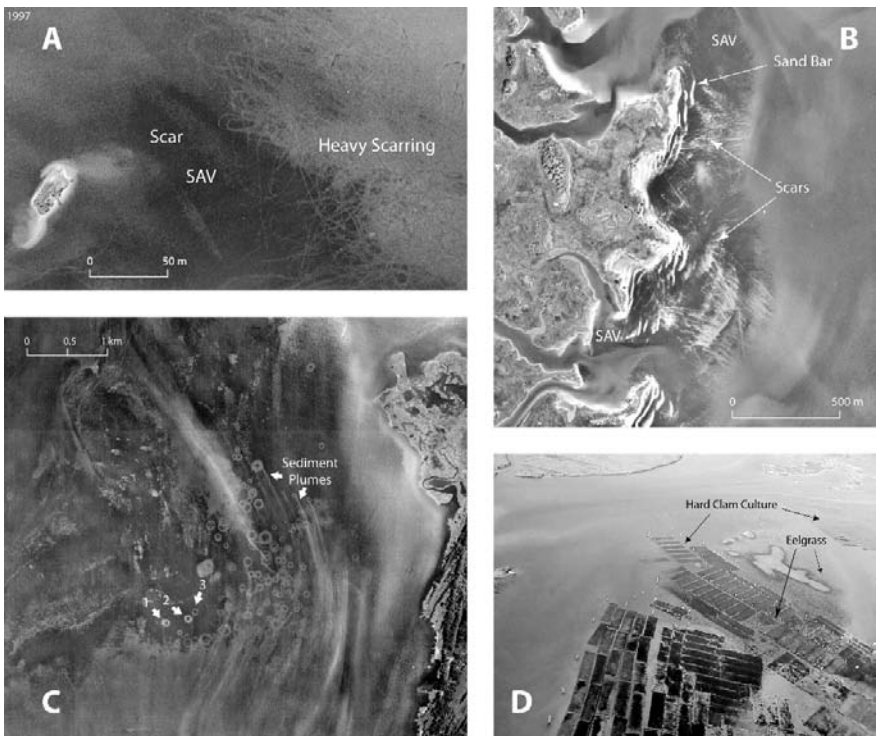


**Fig. 10.10** Cumulative frequency distribution (CFD) curves of water clarity exceedances for 13 monthly SAV growing season cruises in 2002 and 2003 within the Lower York River, Va (YRKPH) segment. Curves represent the 13 monthly measures of spatial extent of criteria exceedance over time for the current SAV, historical SAV or 0–1 m depth areas in that segment

the historical SAV area and the 0–1 m depth area are significantly different than the existing SAV reference area (K-S test,  $p < 0.05$ ). The increasing exceedances depicted by the curves (greater in the X and Y axes) progressing from existing SAV to historically vegetated SAV area to total bottom indicate that increasing water clarity exceedances of the standards are very likely limiting SAV regrowth in this region.

## 10.8 Direct Management Applications

The acquisition and analysis of annual photography for SAV distribution has had additional benefits for protecting SAV by identifying direct impacts or conflicts to SAV in this region and allowing for timely and efficient management to eliminate or minimize these direct impacts or conflicts (Orth et al. 2002a,b). Specific threats included: propeller scarring from fishing and recreational vessels traversing shallow water areas (Fig. 10.11A); the operation of large seines in shallow SAV beds (Fig. 10.11B);



**Fig. 10.11** Aerial photography showing (A) Scarring of SAV by boating and fishing activities in shallow areas of the lower Chesapeake Bay, (B) Scarring due to commercial haul seining fishing activity, (C) Scarring by commercial dredging for wild clam populations, (D) Hard clam aquaculture activities in SAV areas vegetated with eelgrass

and dredging for wild clams (*Mercenaria mercenaria*) using oyster and hydraulic dredges (Fig. 10.11C). In the case of dredging impacts, Virginia approved a regulation designating a SAV sanctuary prohibiting clam and crab dredging, while Maryland approved legislation protecting existing SAV based on a composite average of SAV coverage every three years (Orth et al. 2002a,b). In the case of propeller scarring, analysis of consecutive years of annual photography, coupled to a quantitative ground surveys revealed the extent of scarring baywide, but also the rates (generally three years or less) at which these three meter wide scars were recovering (Orth unpublished data). Management actions did not prohibit commercial fishing but rather attempted to direct fishing activity to times surrounding high tide to minimize propeller impacts (Orth unpublished data). Managers in Virginia now require annual reporting on the effectiveness of these new rules using the aerial photography to monitor areas for compliance.

Aquaculture activities involving growing hard clams (*Mercenaria mercenaria*) in shallow water sandy areas (Fig. 10.11D) have resulted in conflicts when permits were requested in areas of SAV. Regulatory bodies now incorporate the presence of SAV from the annual surveys into their permit processes and in 1998, passed regulations that prohibited any additional aquaculture permits in existing SAV beds (Orth et al. 2002a).

## 10.9 Conclusions

The assessment of the abundance of SAV communities in the Chesapeake Bay using high altitude aerial photography has been a successful and useful program for use in protecting, managing and restoring SAV in this system for the past 25 years (Orth et al. 2002a). Although new sensors and platforms have been developed over this time period, the combination of high utility, low cost, and flexibility of the aircraft-based black and white photography has proven superior overall to other approaches at this point. Future advances in direct-referencing using a combination of airborne GPS and an inertial measurement unit (IMU) may greatly simplify the orthorectification process. Digital airborne imaging systems can provide additional spectral data and bypass the physical processing and scanning steps associated with traditional aerial cameras. Satellite imagery at a resolution that might be sufficient to monitor SAV is becoming available. In addition, automated classification algorithms and analytic techniques for benthic mapping are being developed that might permit more rapid analysis of imagery. These areas of development are routinely evaluated for cost effectiveness, availability, and reliability. Appropriate new methods will be implemented carefully to prevent delays and ensure continuity and comparability with previous methods. Not only has the program provided imagery necessary for quantifying the SAV resource, but when combined with bathymetry and other information it has been used to develop and implement water quality criteria and standards necessary for the fundamental improvements in habitat conditions ultimately required for the recovery of this resource. SAV is an important resource and

designated use of shallow water regions throughout the bay that has habitat requirements similar to many other important species in the bay system: especially water quality that is low in nutrients and suspended sediments. Therefore SAV abundance has provided a good index of overall water quality that is desirable for bay restoration of many commercially important species. The annual assessments provide an important index of bay condition and trends that are used to assess the effectiveness of nutrient and sediment reduction strategies for the bay and its watershed. Because of the importance of the annual mapping of SAV distribution and abundance in providing a year-by-year index of the state of the bay and providing numerous applications for resolving use conflicts and direct impacts, the program has been an integral component of various agreements among by the various states and the federal government dating back to 1983 (Orth et al. 2002a) and will likely continue as such well in to the future.

**Acknowledgements** This is contribution no. 2927 for the Virginia Institute of Marine Science, School of Marine Science, College of William and Mary.

## References

- Batiuk RA, Bergstrom P, Kemp WM, Koch E, Murray L, Stevenson JC, Bartleson R, Carter V, Rybicki N, Landwehr J, Gallegos C, Karrh L, Naylor M, Wilcox D, Moore KA, Ailstock S, Teichberg M (2000) Chesapeake Bay submerged aquatic vegetation water quality and habitat-based requirements and restoration targets: a second technical synthesis. CBP/TRS 245/00. EPA 903-R-00-014, U.S. EPA, Chesapeake Bay Program, Annapolis, MD
- Batiuk RA, Orth RJ, Moore KA, Dennison WC, Stevenson JC, Staver LW, Carter V, Rybicki NB, Hickman RE, Kollar S, Heasley P (1992) Chesapeake Bay submerged aquatic vegetation habitat requirements and restoration targets: a technical synthesis. CBP/TRS83/92, U.S. EPA, Chesapeake Bay Program, Annapolis, MD
- Dennison WC, Orth RJ, Moore KA, Stevenson JC, Carter V, Kollar S, Bergstrom P, Batiuk R (1993) Assessing water quality with submersed aquatic vegetation. *BioScience* 43:86–94
- Dobson JE, Bright EA, Ferguson RL, Field DW, Wood LL, Haddad KD, Iredale III H, Jensen JR, Klemas VV, Orth RJ, Thomas JP (1995) NOAA coastal change analysis program (C-CAP): guidance for regional implementation. NOAA Tech Rep, NMFS 123
- Duarte CM (1991) Seagrass depth limits. *Aquat Bot* 40:363–377
- Kemp WM, Batiuk R, Bartleson R, Bergstrom P, Carter V, Gallegos C, Hunley W, Karrh L, Koch EW, Landwehr J, Moore K, Murray L, Naylor M, Rybicki N, Stevenson JC, Wilcox D (2004) Habitat requirements for submerged aquatic vegetation in Chesapeake Bay: Water quality, light regime, and physical-chemical factors. *Estuaries* 27:363–377
- Kemp WM, Boynton WR, Adolf JE, Boesch DF, Boicourt WC, Brush G, Cornwell JC, Fisher TR, Glibert PM, Hagy JD, Harding LW, Houde ED, Kimmel DG, Miller WD, Newell RIE, Roman MR, Smith EM, Stevenson JC (2005) Eutrophication of Chesapeake Bay: historical trends and ecological interactions. *Mar Ecol Prog Ser* 303:1–29
- Kemp WM, Boynton WR, Stevenson JC, Twilley RR, Means JC (1983) The decline of submerged vascular plants in upper Chesapeake Bay: summary of results concerning possible causes. *Mar Technol Soc J* 17:78–89
- Kirk JTO (1994) Light and photosynthesis in aquatic ecosystems. Cambridge University Press, Cambridge



- Koch EW (2001) Beyond light: physical, geological and geochemical parameters as possible submersed aquatic vegetation habitat requirements. *Estuaries* 24:1–17
- Leica Geosystems GIS & Mapping, LLC. (2005) ERDAS field guide. Atlanta, GA
- Moore KA, Anderson B, Wilcox D (2003a) Intensive water quality mapping of nearshore and mid-channel regions of the James River relative to SAV growth and survival using the DATAFLOW surface water quality mapping system. Spec Rep 385 App Mar Sci and Ocean Eng. VIMS, Gloucester Point, VA
- Moore KA, Neckles HA, Orth RJ (1996) *Zostera marina* (eelgrass) growth and survival along a gradient of nutrients and turbidity in the lower Chesapeake Bay. *Mar Ecol Prog Ser* 142: 247–259
- Moore KA, Wetzel RL, Orth RJ (1997) Seasonal pulses of turbidity and their relations to eelgrass (*Zostera marina* L.) survival in an estuary. *J Exp Mar Biol Ecol* 215:115–134
- Moore KA, Wilcox DL, Anderson B, Orth RJ (2001) Analysis of historical distribution of submersed aquatic vegetation (SAV) in the York and Rappahannock rivers as evidence of historical water quality. Spec Rep 375 App Mar Sci and Ocean Eng. VIMS, Gloucester Point, VA
- Moore KA, Wilcox DL, Anderson B, Orth RJ (2003b) Analysis of historical distribution of SAV in the Eastern Shore Coastal Basins and Mid-Bay Island Complexes as evidence of historical water quality conditions and a restored Bay ecosystem. Spec Rep 383 App Mar Sci and Ocean Eng. VIMS, Gloucester Point, VA
- Moore KA, Wilcox DJ, Anderson B, Parham TA, Naylor MD (2004) Historical analysis of submersed aquatic vegetation (SAV) in the Potomac river and analysis of Bay-wide SAV data to establish a new acreage goal. Final Report U.S. EPA Chesapeake Bay Program (CB983627-01), Annapolis, MD
- Moore KA, Wilcox DL, Orth RJ (2000) Analysis of abundance of submersed aquatic vegetation communities in the Chesapeake Bay. *Estuaries* 23:115–127
- Moore KA, Wilcox DL, Orth RJ, Bailey E (1999) Analysis of historical distribution of submersed aquatic vegetation (SAV) in the James River. Spec Rep 355 App Mar Sci and Ocean. VIMS, Gloucester Point, VA
- Mount RE (2003) The application of digital aerial photography to shallow water seabed mapping and monitoring – How deep can you see? Proceedings of coastal GIS 2003: an integrated approach to Australian coastal issues, 7–8 July 2003, Wollongong, University of Wollongong, Australia
- Naylor MD (2002) Historic distribution of submersed aquatic vegetation (SAV) in Chesapeake Bay, Md Sci Rep. Maryland Department of Natural Resources, Annapolis, MD
- Neckles HA, Wetzel RL, Orth RJ (1993) Relative effects of nutrient enrichment and grazing on epiphyte-macrophyte (*Z. marina* L.) dynamics. *Oecologia* 93:285–295
- Nielsen SL, Sand-Jensen K, Borum J, Geertz-Hansen O (2002) Depth colonization of eelgrass (*Zostera marina*) and macroalgae as determined by water transparency in Danish coastal waters. *Estuaries* 25:1025–1032
- Orth RJ, Batiuk RA, Bergstrom PW, Moore KA (2002a) A perspective on two decades of policies and regulations influencing the protection and restoration of submersed aquatic vegetation in Chesapeake Bay, USA. *B Mar Sci* 71:1391–1403
- Orth RJ, Carruthers TJB, Dennison, WD, Duarte CM, Fourqurean JW, Heck KL, Hughes AR, Kendrick GA, Short FT, Waycott M, Williams SL (2006a) A global crisis for Seagrass ecosystems. *BioScience* 56:987–996
- Orth RJ, Fishman JR, Wilcox DJ, Moore KA (2002b) Identification and management of fishing gear impacts in a recovering seagrass system in the coastal bays of the Delmarva Peninsula, USA. *J Coastal Res* SI:111–129
- Orth RJ, Moore KA (1983a) An unprecedented decline in submersed aquatic vegetation. *Science* 22:51–53
- Orth RJ, Moore KA (1983b) Submersed vascular plants: techniques for analyzing their distribution and abundance. *Mar Technol Soc J* 17:38–52
- Orth RJ, Moore KA (1984) Distribution and abundance of submersed aquatic vegetation in Chesapeake Bay: an historical perspective. *Estuaries* 7:531–540

- Orth RJ, Moore KA (1988) Distribution of *Zostera marina* and *Ruppia maritima* sensu lato along depth gradients in the lower Chesapeake Bay, USA. *Aquat Bot* 32:291–305
- Orth RJ, Wilcox DJ, Nagey LS, Owens AL, Whiting JR, Kenne AK (2006b) Distribution of SAV in the Chesapeake Bay. *Spec Sci Rep* 150. VIMS, Gloucester Point, VA
- Paine DP (1981) Aerial photography and image interpretation for resource management. John Wiley & Sons, New York
- Pasqualini V, Pergem-Martini C, Clabaut P, Marteel H, Pergent G (2001) Integration of aerial remote sensing, photogrammetry and GIS technologies in Seagrass mapping. *Photogramm Eng Rem S* 67:99–105
- Ralph P, Tomasko D, Moore K, Seddon S (2006) Human impacts on Seagrass: Eutrophication, Sedimentation and contamination. In: Larkum AWD, Orth RJ, Duarte CM (eds) *Seagrasses: biology, ecology and conservation*. Springer, The Netherlands, pp 567–593
- Rybicki NB, Landwehr JM (2007) Long-term changes in abundance and diversity of macrophyte and waterfowl populations in an estuary with exotic macrophytes and improving water quality. *Limnol Oceanogr* 52:1195–1207
- Twilley RR, Kemp WM, Staver KW, Stevenson JC and Boynton WR (1985) Nutrient enrichment of estuarine submersed vascular plant communities: I. Algal growth and effects on production of plants and associated communities. *Mar Ecol Prog Ser* 23:179–191
- US EPA (Environmental Protection Agency) (2003a) Ambient water quality criteria for dissolved oxygen, water clarity and Chlorophyll a for the Chesapeake Bay and its tidal tributaries. EPA 903-R-03-002. Region III Chesapeake Bay Program Office, Annapolis, MD
- US EPA (Environmental Protection Agency) (2003b) Technical support document for Chesapeake Bay designated uses and attainability. EPA 903-R-03-004. Region III Chesapeake Bay Program Office, Annapolis, MD
- US EPA (Environmental Protection Agency) (2004a) Chesapeake Bay program analytical segmentation scheme: revisions, decisions and rationales 1983–2003. EPA 903-R-04-008. CBP/TRS 268/04. Region III Chesapeake Bay Program Office, Annapolis, MD
- US EPA (Environmental Protection Agency) (2004b) Technical support document for Chesapeake Bay designated uses and attainability-2004 addendum. EPA 903-R-04-006. Region III Chesapeake Bay Program Office, Annapolis, MD
- US EPA (Environmental Protection Agency) (2005) Chesapeake Bay program analytical segmentation scheme: revisions, decisions and rationales 1983-2003-2005 addendum. EPA 903-R-05-004. CBP/TRS 278-06. Region III Chesapeake Bay Program Office, Annapolis, MD
- US EPA (Environmental Protection Agency) (2007) Ambient water quality criteria for dissolved oxygen, water clarity and Chlorophyll a for the Chesapeake Bay and its tidal tributaries 2007 addendum. Region III Chesapeake Bay Program Office, Annapolis, MD
- Zar JH (1996) *Biostatistical analysis*, 3rd edn. Prentice-Hall, Englewood Cliffs, NJ

## Chapter 11

# Distribution and Spatial Change of Hudson River Estuary Submerged Aquatic Vegetation: Implications for Coastal Management and Natural Resource Protection

William C. Nieder, Susan Hoskins, Stephen D. Smith and Stuart E.G. Findlay

The submerged aquatic vegetation (SAV) of the Hudson River estuary has been described as supporting an abundant and species-rich invertebrate community. Given the ecological significance of this aquatic habitat, understanding the spatial and temporal status and trends is critical to effectively manage and protect this important coastal resource. In this chapter we present the results from a change analysis between two inventories (1995/1997 and 2002). Total coverage of SAV and *Trapa natans* did not show a statistically significant change between the two inventory dates. However, change did occur with *T. natans* showing a net increase of 40 ha and SAV showing a net loss of more than 160 ha. Statistically significant loss occurred in areas where SAV beds were present during both inventories. These persistent SAV beds could serve as indicators of overall estuarine health and provide clues to the driving forces in the estuary responsible for the observed changes. The tidal fresh and oligohaline zones support the greatest abundance of SAV per unit area of available habitat with the mesohaline zone supporting the least. Over 95% of the shallow water area in the mesohaline zone lacked any vegetation. Salinity alone likely defines the southern limits of *T. natans* distribution in the Hudson River but other forces present in the brackish zone likely limit SAV distribution. It appears that light availability has a strong influence on the north-south distribution of SAV in the Hudson River estuary. Primary productivity of Hudson River SAV beds is inversely proportional to turbidity with the mesohaline zone experiencing the highest turbidity in the estuary with light extinction occurring approximately 0.2 m shallower than in the fresh tidal portion of the study area. An extremely high turbid summer in 2000 may have been a factor in the loss of SAV area mapped in 2002. Finally, we discuss how this information and data have been used to better protect SAV habitats in the Hudson River estuary.

---

W.C. Nieder (✉)

New York State Department of Environmental Conservation, Albany, NY 12233, USA  
e-mail: wcnieder@gw.dec.state.ny.us

## 11.1 Introduction

### 11.1.1 Ecology of Hudson River Estuary Submerged Aquatic Vegetation

Often referred to as *submerged aquatic vegetation* or *SAV*, the importance of this habitat to provide major ecosystem functions to aquatic systems is well documented and understood (Carpenter and Lodge 1986, Carter et al. 1991, Rybicki et al. 1997, Findlay et al. 2006a,b,c). The submerged aquatic vegetation (SAV) of the Hudson River estuary has been described as supporting more invertebrates per unit area than unvegetated sediments (Strayer and Malcom 2007), are known to support a high diversity of fish species, supports elevated levels of dissolved oxygen and contributes a significant portion of the Hudson River estuary's primary productivity (Strayer and Smith 2001, Findlay et al. 2006a,b,c). Given the ecological significance of this aquatic habitat, understanding the spatial and temporal status and trends is critical to determine causes and direction of change and management actions necessary to protect and encourage propagation of the habitat.

Results of research in Hudson River SAV habitat in the later part of the 20th century generally agreed with this understanding but much of what we knew prior to 1995 was drawn from intensive studies of a few SAV beds. Findlay et al. (2006c) synthesized the results of these studies, a necessary first step in identifying the gaps in our knowledge. Of the twenty-five species of macrophytes that are found in SAV beds on the Hudson River, water celery (*Vallisneria americana* Michx.) dominates the habitat, occurring in over 90% of benthic grabs containing plants. Water masses passing through SAV beds spent as much as 30% of the time supersaturated, with oxygen concentrations as high as 150% of saturation suggesting these plants are a significant source of in-river primary productivity. In fact, this production of oxygen is a large component of midsummer oxygen budgets (Cole and Caraco 2006).

Hudson River SAV support a high diversity and abundance of macroinvertebrates and the importance of this function increased after the zebra mussel (*Dreissena polymorpha*) invaded the Hudson River (Strayer and Smith 2001). This is largely due to the loss of planktonic food to zebra mussels which caused a large decline in the benthic animal community found in unvegetated deepwater habitats but not those found in shallow vegetated areas (Strayer 2006). The invertebrate community found in SAV beds is especially rich in species commonly fed upon by fish (for example chironomids, amphipods, mayflies, and caddisflies) (Findlay et al. 2006c).

The distribution and abundance of SAV can be directly and indirectly affected by a variety of natural and human factors. These include water quality (nutrients and suspended materials), nonindigenous species and infectious diseases (Orth and Moore 1983, Walker and McComb 1992, Carter et al. 1994, Madden and Kemp 1996, Short and Burdick 1996, Moore et al. 2003). The shallow water areas of the Hudson River also support the non-indigenous Eurasian water-chestnut (*Trapa natans* L.). This annual plant produces a rosette of floating leaves attached to the substrate by an underwater stem. This plant has been shown to cause a decline in

SAV in other systems (Orth and Moore 1983) and has likely replaced SAV in some areas on the Hudson River. Though this species of plant can provide some beneficial ecological functions to aquatic systems, large *T. natans* beds can cause conditions stressful to biota (i.e., hypoxia and anoxia) (Caraco and Cole 2002).

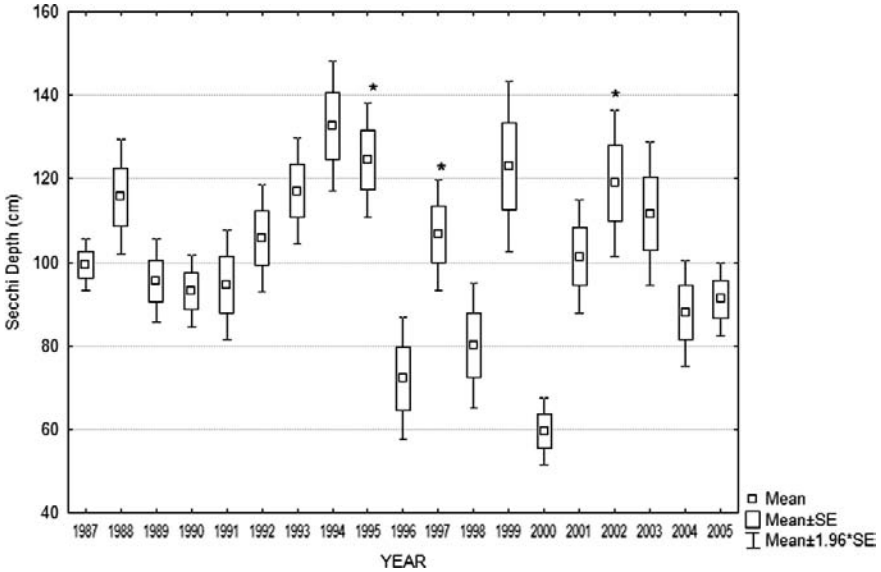
### ***11.1.2 The Hudson River Submerged Aquatic Vegetation Project***

The documented importance of the submersed macrophyte community in the Hudson River estuary led natural resource managers and scientists to gather and discuss the known distribution and ecological importance of SAV in the Hudson River estuary in 1993. Though it was determined that little was known, one important outcome of the workshop was a list of priority actions required to protect and manage this resource. These actions were to: (1) conduct an inventory of the distribution of SAV habitat; (2) conduct a trends analysis to determine the stability and dynamic nature of the SAV habitat; (3) determine the ecological functions SAV provide to the Hudson River estuary; (4) identify the primary anthropogenic and natural actions that threaten the habitat; and (5) develop regulatory guidance for the long-term protection of SAV habitat. A collaborative team was formed to address these five priority actions composed of ecologists, resource managers, remote sensing specialists and environmental educators.

### ***11.1.3 Spatial Distribution of Hudson River SAV and Eurasian Water-Chestnut***

The ability to reliably detect the presence of and change in the SAV habitat is critical to effectively manage and protect this important coastal resource. There was some uncertainty as to whether we would be able to acquire the imagery necessary to inventory the SAV. Flight windows were restricted to the morning hours on clear days between mid-July and early September. In addition to these restrictions, the Hudson River estuary is a moderately turbid system with an annual average secchi depth ranging from 60 to 130 cm (Fig. 11.1) further reducing the flight time to two hours on either side of spring low water. To further complicate the acquisition of the imagery, turbidity levels in the Hudson estuary are highly influenced by precipitation events.

In addition to providing knowledge of the distribution and abundance of SAV in the Hudson River estuary, a GIS based inventory was important for identifying field-sampling sites to conduct an ecology study of the SAV throughout its range along the estuary (Findlay et al. 2006b) and design a volunteer monitoring program to assess inter-annual variability. This inventory was also necessary to provide the base conditions to assess temporal and spatial change and for use by state and federal regulatory agencies staff to protect SAV from human development activities. In



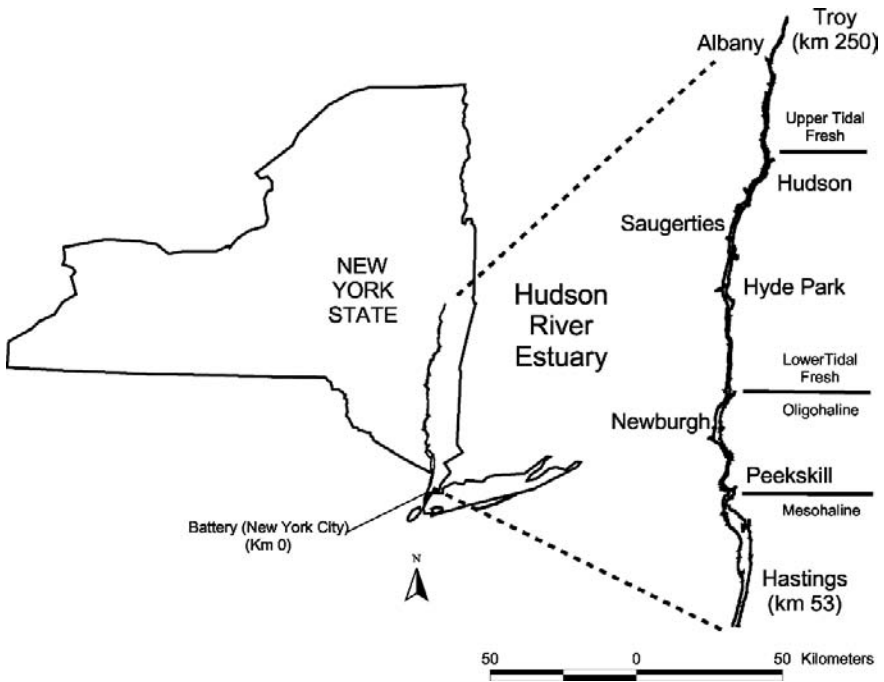
**Fig. 11.1** Box plot of the average summer secchi depths of the Hudson River estuary for the study area. The asterisk indicates the years aerial photographs were taken for this project (1995, 1997, and 2002)

this chapter we present the results from two inventories of SAV and *Trapa natans* (1995/1997 and 2002) and use these inventories to determine environmental factors that may limit the plants distribution.

## 11.2 Methods

### 11.2.1 Site Description

The Hudson River estuary from the federal dam at Troy south to Hasting-On-Hudson (200 km) was included in this study (Fig. 11.2). Tidal ranges along this reach are 1.4 m near Hastings, 0.8 m at West Point, and 1.4 m at Troy. Average depth is 11.0 m though approximately one third of the study area is shallower than 3.0 m. Three distinct estuarine zones based on degree of influence by ocean-derived salt exist along this reach (Limburg et al. 1986): (1) Tidal Fresh: combination of deep water and broad shallow areas (upper 130 km); (2) Oligohaline: salinity range 0.5–5 ppt (next 30 km); and (3) Mesohaline: salinity range 5.0–18.0 ppt (lower 40 km) (Limburg et al. 1986). Findlay et al. (2006b) argue that the tidal fresh estuarine zone can be further divided into two distinct zones based on channel morphology and aquatic organism assemblages: (1) Upper Tidal Fresh (upper 50 km); and (2) Lower Tidal Fresh (next 80 km).



**Fig. 11.2** Map of study area from Troy to Hastings-On-Hudson, New York indicating the four estuarine zones (modified from Nieder et al. 2004)

The Hudson River estuary along the study reach is moderately turbid with suspended sediment concentrations averaging 11.0 mg dry mass/L (Findlay et al. 1996) with an annual average secchi depth ranging from 60 to 130 cm (Fig. 11.1). Only about 1.0% of summertime light reaches a depth of 2.5 m (Harley and Findlay 1994). Nutrient concentrations are also moderate with an average DIN of 40.0  $\mu\text{M}$  and DIP of 1.0  $\mu\text{M}$  (Lampman et al. 1999).

## 11.2.2 Development and Assessment of the Digital Database

### 11.2.2.1 Aerial Photography Acquisition

Aerial photography specifications and methods are detailed in Nieder et al. (2004) and follow the protocol detailed by the National Oceanic and Atmospheric Administration (Dobson et al. 1995). Due to funding limitations and the initial pilot phase of the project, the initial inventory was created from aerial photographs acquired in two separate years: 1995 and 1997. The reach from Hyde Park to Castleton-On-Hudson was mapped from 1995 photography and the remainder of the study area was mapped from 1997 photography. Aerial photographs for the second inventory

were acquired for the entire study area in 2002. Aerial photographs were taken using Aerocolour 2445 Color Negative Film at a final scale of 1:14,400 with stereographic cover of 60% end lap, and 30% side lap.

### **11.2.2.2 Air-Photo Interpretation**

Interpretation of the aerial photography was carried out consistently among the years as described in Nieder et al. (2004). In brief, interpretation was carried-out using stereo pairs of photographs and an Abrams 2X or 4X stereoscope and a Delft Scanning stereoscope at 4.5X. SAV and *T. natans* were annotated on a 3-mil matte acetate overlay affixed to photographs. The minimum mapping unit was a 1.0 mm average diameter polygon that could be drawn with 0.5 mm pencil. At the scale of 1:14,400 this corresponds to a ground area of 0.016 ha (equivalent spherical diameter  $\sim 15$  m).

### **11.2.2.3 Digital Database Creation**

Good quality shoreline maps were not available for the study area; therefore, 25 base-maps for data transfer were created through photographic reproductions of the 1:24,000 USGS planimetric maps enlarged to 1:14,400 scale to match scale with the aerial photo contact prints. All vegetation was digitized with ArcInfo software from the mylar overlays using a CalComp Drawing Board II or an Altek 30 system for the 1995/1997 inventory. Details of the digitization can be found in Nieder et al. (2004). The digitizing board was replaced with a large format digital scanner for the 2002 inventory allowing us to scan the mylar overlays and create the final digital database by tracing the scan on screen. The final digital data products for both inventories were projected in UTM NAD27 and UTM NAD83.

### **11.2.2.4 Quality Assurance of Digital Spatial Database**

In 2004, we generated random points spanning the study area in areas with water depths less than 5 m but still contained within the shoreline (not including coves and tidal portions of tributaries). This resulted in 246 random points we intended to visit. When we conducted the field work, some points were inaccessible due to extreme shallow water, *T. natans* or commercial dock space resulting in a final collection of observations from 184 locations. At each location (within 5.0 m of target coordinates) we determined SAV cover as presence/absence along with water depth. These observations were compared to plant polygons mapped from the 2002 photographs. Field observation points that fell within 5.0 m of a polygon boundary were not included in data analysis ( $n = 14$ ) due to the accuracy limitation of the GPS units used.



### 11.2.2.5 Volunteer Monitoring Program

Data collection by volunteers was based on multiple transects that span beds of SAV identified in the GIS database. In general, there were three or four lateral transects, each of which included four or more observation points. Coordinates for observation points were obtained from the GIS coverage and intended to bracket the bed edges with one or two points in the bed interior. A rough map of the transects and a data sheet with coordinates of the observation points were provided to the volunteers but they did not know which points are expected to fall within the plant bed. To date, transect locations have not been random but are selected to cover east and west shores along the study reach. Volunteers may well report on bed expansion but they were not sent to areas where no plants had been mapped previously. For field work, volunteers are instructed to visit sites within two hours of low tide, place floating markers at the observation points along a transect and then visit each point to collect data. At an observation point they measure depth, record time of observation and determine water clarity using a secchi disc. Plant observations are scored as presence/absence and relative abundance in a 15 m diameter circle is scored from none to dense (greater than 50% cover).

Data sheets are checked for obvious errors of transcription or location then entered as points into the GIS database. Locations recorded by the handheld GPS units are presumed to have a 5.0 m uncertainty. Observations of SAV presence/absence are scored as either agreeing or not agreeing with mapped polygons derived from the photos.

### 11.2.3 Determining Spatial Patterns and Temporal Change

Overall change between the two inventories in the distribution of mapped vegetation within the study area was determined by making the following comparisons: (1) total and net gain and loss of area covered by SAV and *T. natans* across the entire study area; (2) total and net loss and/or gain of SAV and *T. natans* involving an interchange of the two mapped habitats; and (3) total and net loss and/or gain of SAV and *T. natans* that led to either gain or loss of unvegetated areas.

To determine if distribution and change in the mapped vegetation could be explained by the north-south position of the SAV along the study area, we divided the river into twenty 10-km blocks as measured along a UTM easting grid line beginning from the Troy dam to Hastings-On-Hudson. The area of each of the mapped habitats for each inventory and the area of change (gains and losses) was determined within each of the 20 blocks. The area of shallow habitat (defined as that less than 3.0 m deep below low water) was also determined within each block. Blocks were combined into estuarine zones (upper and lower fresh tidal, oligohaline, and mesohaline) with the blocks within each zone being treated as replicates.

To determine if distribution and change in the mapped vegetation was influenced by east-west positioning along the study area, the estuary was bisected

longitudinally following the center of the navigable channel as mapped on the digital raster graphics of USGS 7.5 min topographic maps. In areas where the channel was not clearly marked, the centerline between the lowest bathymetric contour was used as the east-west divide.

Spatial data were compared between years and estuarine zones using ArcGIS® 9.x spatial analyst tools, single sample and independent t-tests and analysis of variance tests followed by Tukey HSD test. All spatial data were log transformed before analysis. Statistica® 6.0 was used for all statistical tests.

## 11.3 Results

### 11.3.1 Assessment of the Digital Database

#### 11.3.1.1 Quality Assurance of Digital Database

There was overall good agreement between the observations from random points and the digital database coverage with 169 observations (92%) correctly classified (Table 11.1). Of the field observations, 41 (22%) had plants present and 28 of these fell in mapped polygons of SAV. Not surprisingly, the larger of the two error categories was errors of omission, 7% of the field-mapped plants did not fall in a mapped SAV polygon. There were only two instances where SAV were mapped but none were observed in the field observations.

**Table 11.1** Results of the quality assurance test of the mapped SAV in the 2002 digital database through the collection of random field data in 2004. Ninety-two percent of the samples were in agreement with the mapped SAV habitat

Mapping	Field observation	
	Vegetation absent	Vegetation present
<i>Vegetation absent</i>	141 (77%)	13 (7%)
<i>Vegetation present</i>	2 (1%)	28 (15%)

#### 11.3.1.2 Volunteer Monitoring Results (SF)

Over the course of three summers (2003 through 2005), volunteers visited 356 points. We compared their field observations with whether or not the locations fell within an SAV polygon mapped from the 2002 photos. In general, the proportion of field observations recording plant presence was very close to the proportions of points falling in a mapped SAV polygon (Table 11.2). Although these data clearly cannot be used as a quantitative error assessment (transects were set up based on mapped polygons) they do support the overall validity of the SAV inventories.

**Table 11.2** Results of the volunteer monitoring program. There is a close match between the percentage of the samples containing SAV and the percent of the sampling points that fell within an SAV polygon. This further supports the accuracy of the digital data by indicating it is a true representation of field conditions

Year	Percent of total		Mean (Max)	
	SAV observed in field	Samples falling within SAV polygon	Depth of pts in SAV polygon	Depth of pts outside SAV polygon
2003	46	49	1.07 (2.0)	1.26 (3.0)
2004	47	44	0.76 (1.5)	1.4 (6.0)
2005	54	51	0.98 (2.0)	1.23 (3.0)

The volunteers record water depth at the time of their observations and we can use these to describe mean water depths for points falling inside versus outside mapped SAV polygons. Not surprisingly, the points within polygons were shallower but the difference was small, ranging from 0.2 to 0.6 m across years.

### 11.3.2 Determining Patterns in the Spatial Distribution of Plants

Results of the first inventory (based on 1995 and 1997 aerial images) can be found in Nieder et al. (2004). In summary of that work, the SAV were wide spread in shallows (defined as less than 3.0 m deep at low water) along the study area from Troy south to Yonkers occupying 1,802 ha (4,453 ac) (Table 11.3).

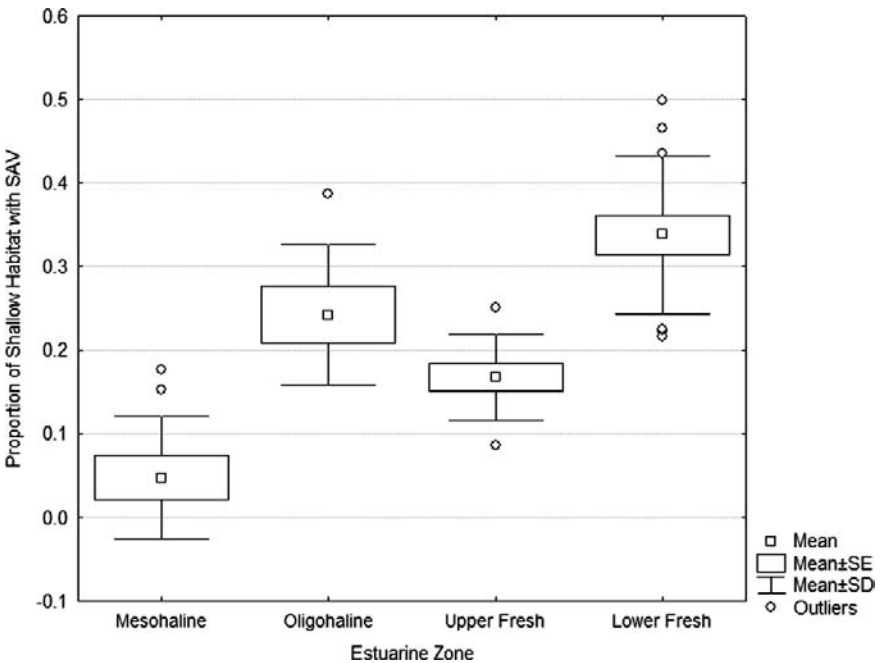
When we compare the spatial coverage of SAV among the twenty 10-km blocks, the coverage mapped in both the 1995/1997 and 2002 inventories was significantly higher in the upper half of the study area (blocks 1–10 vs. 11–20) (t-test;  $p < 0.05$ ). This is generally true for *T. natans* though not significant (t-test;  $p = 0.06$ ). To determine what factors may be responsible for this distributional difference with SAV, blocks were first grouped to represent two estuarine zones: fresh tidal (blocks 1–13) and brackish tidal (blocks 14–20). Here we find a significantly greater abundance of *T. natans* in the tidal fresh zone ( $p < 0.01$ ) but the SAV abundance was not significantly different between these two estuarine zones ( $p = 0.3$ ).

**Table 11.3** Area in hectares of SAV and *Trapa natans* occupying the mainstem of the Hudson River from Troy south to Hastings-on-Hudson (study area or SA). Also presented are the percent of the study area and percent change in both study area and target habitat (%TH)

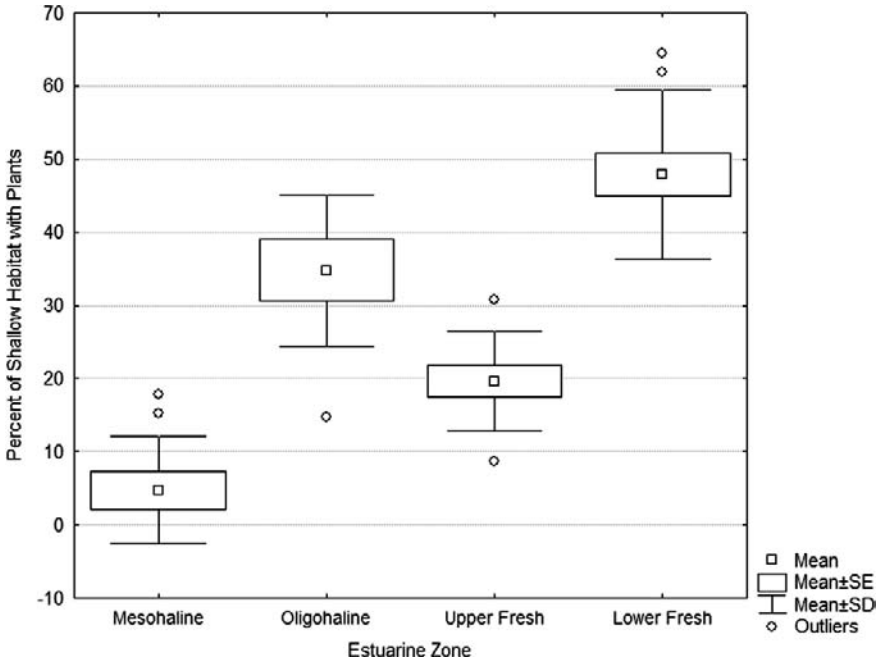
	1997		2002		Percent of change	
	Hectares	%SA	Hectares	%SA	%SA	%TH
<i>Trapa natans</i>	575	1.9	615	2.1	0.1	6.9
SAV	1,802	6.1	1,637	5.5	-0.6	-9.1

To further tease out the effect of estuarine zones, we then grouped the blocks into four estuarine zones based on physical and chemical characteristics: upper fresh tidal (blocks 1–5); lower fresh tidal (blocks 6–13); oligohaline (blocks 14–16); and mesohaline (blocks 17–20). Analysis of variance tests indicate that with the exception of the upper fresh tidal zone ( $p < 0.01$ ), SAV distribution could not be explained by estuarine zones alone. Furthermore, if the upper fresh tidal zone is ignored in the analyses, a significant difference exists in the abundance of SAV between the upper and lower portion of the study area (blocks 3–10 vs. 11–20;  $p < 0.01$ ) indicating that some other factor is responsible for the observed difference in distribution.

When we normalize the area of SAV and *T. natans* to the area of river bottom shallower than 3.0 m below mean low water (typical photic zone for Hudson River SAV; Nieder et al. 2004), significant differences in distribution of plants are found based on estuarine zone ( $p < 0.01$ ) (Fig. 11.3). The tidal fresh (both upper and lower) and oligohaline zones support the greatest abundance of SAV per unit area of available habitat with the mesohaline zone supporting the least. Over 95% of the shallow water area in the mesohaline zone lacked any vegetation. Normalizing the *T. natans* area to shallow water did not indicate a significant difference in the plant's distribution in the freshwater or oligohaline zones. No *T. natans* was mapped in the mesohaline zone.



**Fig. 11.3** Proportion of shallows (area shallower than 3 m below low water) with SAV present. The lower fresh tidal zone has significantly greater coverage of SAV than the mesohaline and upper fresh tidal zones ( $p < 0.01$ ); the oligohaline zone also had a significantly greater coverage of SAV than the mesohaline zone ( $p < 0.01$ )



**Fig. 11.4** Percent of shallows (area shallower than 3 m below low water) occupied by both SAV and *Trapa natans*

A significant difference also exists in the percent of the shallow water area supporting either SAV or *T. natans* across the four estuarine zones ( $p < 0.01$ ) (Fig. 11.4). The lower tidal fresh zone supported the greatest percentage, almost 50% of that available, followed by the oligohaline (34.8%), the upper fresh tidal (19.6%) and the mesohaline zones (4.7%).

### 11.3.3 Assessing Temporal Change in Plant Distribution

Coverage of SAV and *Trapa natans* did not show a statistically significant change between the two inventory dates (t-test;  $p > 0.05$ ). The actual area of change, however, was substantial with *T. natans* showing a net increase of 40 ha and SAV showing a net loss of more than 160 ha. These net changes in coverage can be viewed two ways: either as a percent of the entire study area, that is the total area of estuary included in the study; or as a percent of the two habitats mapped in 1995/1997. During the study period, SAV decreased by 0.6% of the study area but by almost 10% of the area that was mapped in 1995/1997.

Figure 11.5 displays the area of change for both SAV and *T. natans* along the study area with the bars representing the area of change within each of the twenty

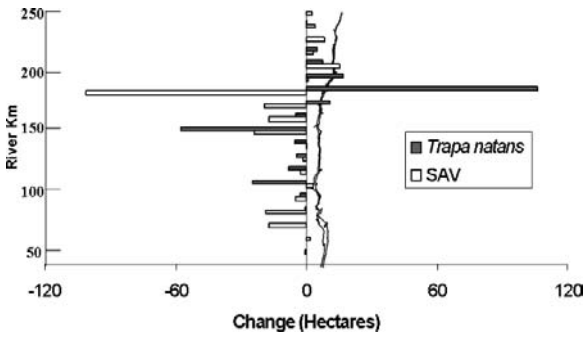


Fig. 11.5 The bar graph shows the change in both SAV and *Trapa natans* in twenty 10-km sections of the study area. The greatest change occurred at approximately river 175 km in Inbocht Bay where a large area of SAV was lost to the expansion of a *Trapa natans* bed. In general, SAV was lost throughout the lower two thirds of the study area. River distance is measured from the Battery in New York City

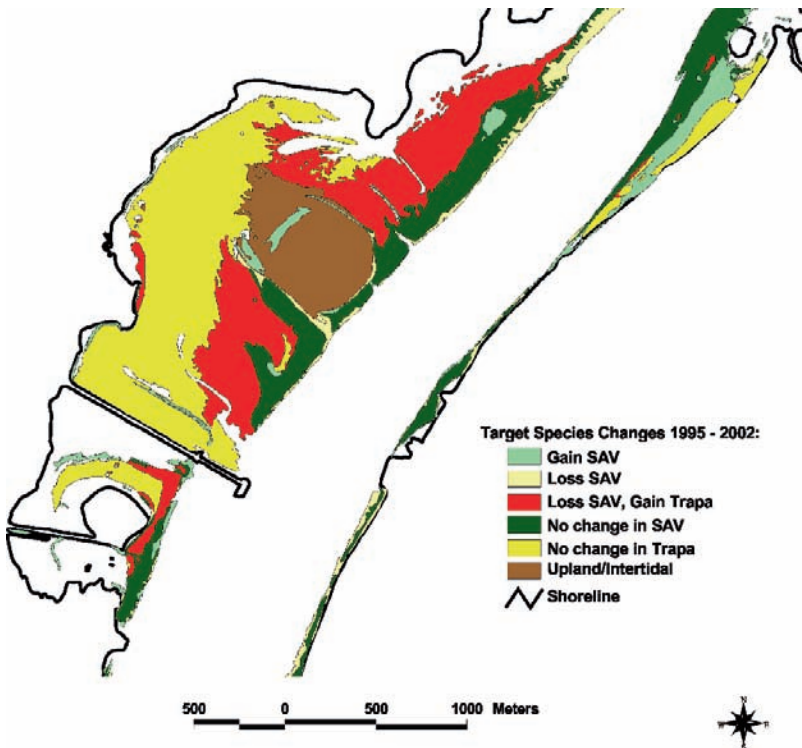
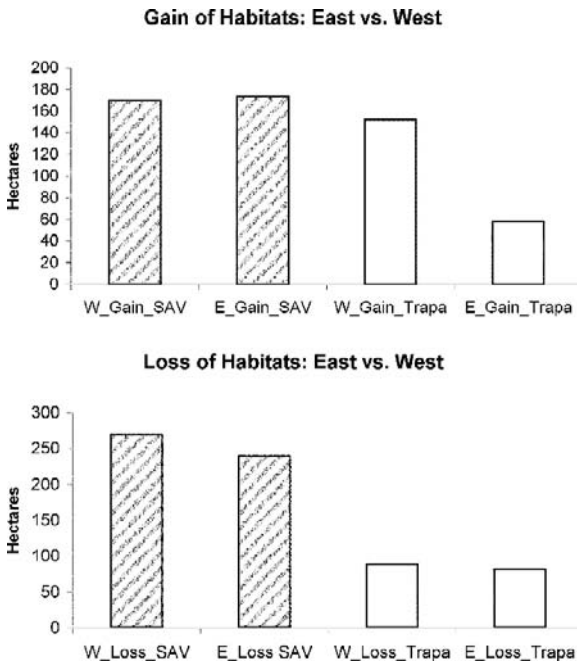


Fig. 11.6 Graphic representation of coverage exchange between SAV and *Trapa natans* in Inbocht Bay, Catskill, New York. The area in red was all SAV in 1995 but this area is now dominated by *Trapa natans*. This location experienced the greatest loss of SAV directly associated with the spread of *Trapa natans* during the study

10-km blocks. The greatest gains for both species occurred in the upper half of the study area with the greatest gain in SAV having occurred in the northern most sections. There was a large loss of SAV around river km 175 corresponding with a large gain of *T. natans*. Much of this change occurred in Inbocht Bay, a sheltered shallow water cove on the west shore of the Hudson in Catskill, New York (Fig. 11.6). Here we observed the highest area loss of SAV (almost 80 ha) as a direct result of the expansion of *T. natans*.

Gains and losses in SAV and *T. natans* could also be related to which bank of the Hudson River the habitat occurred (Fig. 11.7). Half of the SAV and *T. natans* occurs within 150 m of the shoreline (Nieder et al. 2004) and given the prevailing winds generally come from a westerly direction, the eastern shore may experience greater wave action leading to greater physical damage to plants and/or habitat. SAV show no difference in either gains or losses between the shorelines but *T. natans* increased coverage on the west shore two fold over the east shore gains.

Net changes in SAV coverage is due to: (1) beds completely disappearing or new beds appearing and; (2) changes in spatial coverage of SAV beds which occur in both inventories. These persistent beds could be a better indicator of directional changes due to longer-term stressors on the habitat than beds that appear or disappear in relatively short time periods. They could also help explain variables responsible for the observed north-south distribution of plants.



**Fig. 11.7** Gains and losses of SAV and *Trapa natans*. There was no apparent difference between the east and west shores with the exception of the large gain in *Trapa natans* on the west shore. This gain was mostly due to the spread of this species in Inbocht Bay, Catskill, New York

To determine if these persistent SAV beds are experiencing changes different from that detected by analyzing the entire dataset, we selected only the SAV polygons that overlapped between the two study periods. The spatial distribution of these beds was similar to that of the entire dataset but with a significantly greater abundance in the fresh tidal estuarine zones than the brackish zones when the coverage is normalized to area ( $p < 0.01$ ). The least abundance of persistent beds per unit area occurred in the mesohaline zone ( $p < 0.01$ ). One noticeable difference between the persistent SAV beds and the entire SAV dataset, is the significantly greater abundance of persistent beds in the lower fresh tidal than the upper fresh tidal zone ( $p < 0.01$ ). The magnitude and direction of loss in area coverage of these persistent beds was similar to that of the entire dataset, but now this loss proved statistically significant (180 ha loss, greater than 10%) ( $p < 0.01$ ). Though not significant, the greatest loss occurred in the lower fresh tidal reach of the study area. The reverse is seen with the SAV beds that were not mapped (therefore not persistent) during both study periods with almost a 15 ha (40%) net gain in coverage.

## 11.4 Discussion

### 11.4.1 Patterns of Plant Distribution in the Hudson River Estuary

Many environmental and physical features of an estuary including water depth, turbidity, and salinity regimes determine the distribution and abundance of submerged macrophytes. Human disturbances such as elevated turbidity levels, nutrient enrichment and prop-scarring also are known to limit and reduce distribution and abundance (Carter et al. 1994, Kennish et al. 2008). Determining which factor or factors contribute the most to limiting SAV habitat is important to guide resource management and protection. Understanding these influences can also help aid in restoring previously existing habitats.

Results of this study do show patterns in the distribution of both SAV and *Trapa natans* throughout the study area. *T. natans* was significantly more abundant in the fresh tidal compared to the brackish reaches. This would be expected since *T. natans* is a freshwater macrophyte intolerant of ocean-derived salt. SAV abundance was not significantly different between these two estuarine zones, which we would also expect since the plant species found on the Hudson are tolerant to the salinities that typically occur in the study area. However, much of the SAV mapped along the estuary occurs in the upper half of the study area (Nieder et al. 2004, this study), so some factor other than salinity must restrict macrophyte distribution in the lower portion of the estuary.

Since only about one third of the river area within the estuary is shallow enough to potentially support SAV (area less than 3.0 m below mean low water), the SAV coverage data were normalized to the amount of shallow water habitat present in the twenty 10-km blocks (abundance per unit area). This gives us some idea of how successful these macrophytes are at colonizing the available substrate at a given



location. By doing this, we find the SAV plants in the fresh tidal reach are more efficient at colonizing the shallow area than those in the brackish reach. This finding also holds true with the coverage of the persistent SAV beds. This indicates that there is some factor in the lower estuary other than salinity that reduces the ability of these macrophytes to occupy shallow water areas.

Primary productivity within SAV beds in the Hudson River is inversely related to turbidity levels (Findlay et al. 2006b). Light availability is a primary limiting factor in the distribution of SAV in many aquatic systems (for example Carter and Rybicki 1990) and likely has a strong influence on the reach-scale difference in distribution of SAV in the Hudson River estuary. Harley and Findlay (1994) showed that the summertime light availability of 1.0% at 2.5 m depth corresponds to the compensation point for *Vallisneria americana*, the dominant SAV found on the Hudson. When we compared the SAV distribution normalized by the amount of shallow water area available, we found the mesohaline reach of the brackish zone was significantly depauperate in SAV (Fig. 11.3). The mesohaline zone experiences the highest turbidity in the study area due to estuarine circulation and strong salinity gradients creating at least two turbidity maximums in this reach (Bokuniewicz 2006). It is estimated this lower portion of the Hudson River estuary receives between 1.14 million to 1.72 million MT/yr of silt-clay per year (Ellsworth 1986), which coupled with re-suspension limits light availability to plants in this reach. The relative lack of SAV occupying the shallows in the mesohaline zone supports this possibility with less than 5.0% of the shallows actually supporting SAV (Fig. 11.4).

Light extinction has been measured at both Castleton (tidal fresh) and Haverstraw (mesohaline) and this occurs approximately 0.2 m shallower in Haverstraw indicating a greater light limitation for plant growth in this area. The data collected by the volunteer monitoring team also illustrates the sensitivity of the SAV to light limitations. The relatively subtle depth difference for points falling inside versus outside mapped SAV polygons is further evidence of the strong light-limitation of these plants and suggests any attempt to determine lower depth limits or potential habitat availability will have to be capable of describing bathymetry at 10 cm resolution. Presently, the combination of individuals conducting field observations and large-scale remote sensing provides unique information about environmental controls on this habitat and confidence in our understanding.

### ***11.4.2 Assessing Temporal Change in Plant Distribution***

Since only two inventories have been conducted, we were not able to detect if statistically significant change in the mapped abundance of SAV or *T. natans* had taken place with the exception of the persistent SAV beds. However, measurable change did occur with losses and gains throughout the estuary resulting in a net loss of SAV of more than 160 ha or 9% between the two inventories. This loss could be due to natural processes or indicative of changing environmental stressors. There are many causes for SAV decline including nutrient enrichment, nonindigenous species

and increased suspended sediments (Walker and McComb 1992, Carter et al. 1994, Madden and Kemp 1996). Determining what might be at the root of the change is critical for successful management and protection of the habitat.

Throughout the study area, replacement of SAV by *T. natans* expansion accounted for 28% of the loss of SAV beds mapped in 1995/1997. The most dramatic interaction between these two mapped habitats occurred in Inbocht Bay (Catskill, New York) where almost 80 ha of SAV were lost to the spread of *T. natans* (Fig. 11.6). With most of its biomass floating on the surface of the water, *T. natans* is able to reduce the available light to submerged plants. Dramatic as this localized interaction was, most of the loss of SAV we observed throughout the study area was not caused by a direct interaction of *T. natans* and SAV but by some other mechanism. To understand what these mechanisms might be, it is important to understand the factors responsible for the observed distribution of both of these habitats.

The greatest net gain in SAV and *T. natans* occurred in the upper third of the study area with the greatest net loss of SAV occurring in the middle third (Fig. 11.5). However, statistically significant change did occur in SAV beds that were present during both inventories, resulting in a loss of 180 ha (greater than 10% loss). These persistent SAV beds could be functioning as indicators of overall estuarine health and provide clues to the driving forces in the estuary responsible for observed changes. Particular attention should be paid to these beds in future inventories to see if any significant trends occur.

### 11.4.3 Environmental Forces Driving Change

In 2000, the study area was extremely turbid with the lowest average secchi depth recorded in 13 years of measurements and the lowest recorded during this study period (Fig. 11.1). Average SAV productivity in persistent beds, as a function of the percent of time dissolved oxygen in SAV beds was over 8.0 mg/L, was less than half of the maximum measured in 2003 (Findlay et al. 2006b). This productivity did not increase much in 2001 (from approx. 20% of the 2003 maximum in 2000 to approx. 25% in 2001) even though the average secchi depth had increased to that which is more typical for the Hudson. It is possible that the high turbidity event in 2000 contributed to the decline in the persistent SAV beds, which as of 2002 had not yet recovered from this event.

To argue this point another way, the increased light availability in the fresh tidal zone caused by the invasion of the zebra mussel (*Dreissena polymorpha*) has increased the photosynthetic capacity of the SAV in this reach either by allowing them to spread to deeper water or by an increase in biomass (Caraco et al. 2000). Unfortunately, this invasion was well underway during the initial inventory but this too is indicative that Hudson River SAV are so light limited that a small change in light availability in either direction can lead to substantial changes in the SAV habitat.

#### ***11.4.4 Resource Protection and Management of Hudson River SAV***

The primary goal of this project has been to ensure proper management and protection of the SAV habitat on the Hudson River. To effectively do this, not only was it important to know the distribution, stability and ecological importance of the habitat, we also needed to identify the environmental laws that can be used to provide protection, and transfer the habitat information to the correct authorities. The Environmental Conservation Law of New York State (1994) provides protection to the water resources, freshwater wetlands and tidal wetlands of the state (Articles 15, 24, and 25 respectively). These three articles of law provide provisions to protect SAV if their protection results in the protection and propagation of fish and wildlife including birds, mammals and other terrestrial and aquatic life. Having made a strong connection between Hudson River aquatic life and the SAV (Findlay et al. 2006b), natural resource managers and environmental regulators of New York only need to know where the SAV beds are located and have access to the most recent digital database through New York's Master Habitat Database (or MHDB) maintained by the Department of Environmental Conservation (NYSDEC). The MHDB provides easy access to all natural resource data in a GIS environment necessary for environmental protection and management. NYSDEC also provides data and technical support to environmental consultants as they develop plans for in river and near shore projects.

These data are also being included in federal review of coastal projects. New York State's Coastal Zone Management Program (CZMP) includes the SAV coverage to determine the impact of any projects they review under the Federal Coastal Consistency Program (Coastal Zone Management Act, 15 CFR Part 930). These regulations establish the procedures to be followed in order to assure that federal agency activities are consistent with the enforceable policies of the New York State Coastal Management Program. The CZMP is currently incorporating the SAV areas into state designated Significant Coastal Habitats of the Hudson River to gain greater protection of the resource. NYSDEC has also provided the United States Army Corps of Engineers with the spatial data because they too consider the potential impacts any in-river and riverbank project may have on the SAV. Other federal agencies holding regulatory authority on the Hudson River with access to these data include the National Oceanic and Atmospheric Administration (National Marine Fisheries Service) and the Department of the Interior (Fish and Wildlife Service).

**Acknowledgements** We would like to acknowledge the following people for their assistance in conducting field and laboratory portions of this work: David Fischer, Geoffrey Eckerlin, Susan Dye, Pamela Templer, Erik Bedan, Cathy McGlynn, Wing Chan, and Danielle Ogurcak. We also wish to acknowledge the additional members of the Hudson River SAV Project team: Eugenia Barnaba, Elizabeth Blair, Nordica Holochuck, Jean McAvoy, Fran Dunwell, Mark Bain, and David Strayer. Funding for this work was provided by the following organizations: New York State Environmental Improvement Fund through the Hudson River Estuary Program, Coastal Change Analysis Program (C-CAP) of the National Oceanic and Atmospheric Administration, the Hudson River Foundation and the A.W. Mellon Foundation, and grants (DEB 0075265 and 0454001) from the National Science Foundation.

## References

- Bokuniewicz H (2006) Sedimentary processes in the Hudson River Estuary. In: Levinton JS, Waldman JR (eds) *The Hudson River Estuary*. Cambridge University Press, Cambridge, New York, pp 39–50
- Caraco NF, Cole JJ, Findlay SEG, Fischer DT, Lampman GG, Pace ML, Strayer DL (2000) Dissolved oxygen declines in the Hudson River associated with the invasion of the zebra mussel (*Dreissena polymorpha*). *Environ Sci Technol* 34:204–210
- Caraco NF, Cole JJ (2002) Contrasting impacts of a native and alien macrophyte on dissolved oxygen in a large river. *Ecol Appl* 12:1496–1509
- Carpenter SR, Lodge DM (1986) Effects of submerged macrophytes on water-quality in the Potomac River, Maryland. *J Freshwater Ecol* 4:493–501
- Carter V, Rybicki NB (1990) Light attenuation and submerged macrophyte distribution in the tidal Potomac River and estuary. *Estuaries* 13:441–452
- Carter V, Rybicki NB, Hammerschlag R (1991) Effects of submersed macrophytes on dissolved oxygen, pH, and temperature under different conditions of wind, tide, and bed structure. *J Freshwater Ecol* 6:121–133
- Carter V, Rybicki NB, Landwehr JM, Turtora M (1994) Role of weather and water quality in population dynamics of submersed macrophytes in the tidal Potomac River. *Estuaries* 17:417–426
- Cole JJ, Caraco NF (2006) Primary production and its regulation in the tidal-freshwater Hudson River. In: Levinton JS, Waldman JR (eds) *The Hudson River Estuary*. Cambridge University Press, Cambridge, New York, pp 107–120
- Dobson JE, Bright EA, Ferguson RL, Field DW, Wood LL, Haddad KD, Iredale H III, Jensen JR, Klemas VV, Orth RJ, Thomas JP (1995) NOAA coastal change analysis program (C-CAP): guidance for regional implementation. NOAA Technical Report NMFS 123, pp 35–44
- Ellsworth JM (1986) Sources and sinks for fine-grained sediment in the lower Hudson River. *North-east Geol* 8:141–155
- Environmental Conservation Law of New York Volume I (1994) Gould Publications 199/300 Street, Binghamton, New York, pp 13901–2782
- Findlay SEG, Nieder WC, Blair EA, Fischer DT (2006a) Multi-scale controls on water quality effects of submerged aquatic vegetation in the tidal freshwater Hudson River. *Ecosystems* 9:84–96
- Findlay SEG, Pace M, Fischer D (1996) Spatial and temporal variability in the lower food web of the Hudson River. *Estuaries* 19:866–873
- Findlay SEG, Strayer D, Bain M, Nieder WC (2006b) Ecology of Hudson River submerged aquatic vegetation. Final Report to the New York State Department of Environmental Conservation, Hudson River NERR, Staatsburg, New York, p 99
- Findlay SEG, Wigand C, Nieder WC (2006c) Submerged macrophyte distribution and function in the tidal freshwater Hudson River. In: Levinton JS, Waldman JR (eds) *The Hudson River Estuary*. Cambridge University Press, Cambridge, New York, pp 230–241
- Kennish MJ, Haag SM, Sakowicz GP (2008) Seagrass demographic and spatial habitat characterization in Little Egg Harbor, New Jersey, using fixed transects. *J Coastal Res*. SI55:171–179
- Lampman GG, Caraco NF, Cole JJ (1999) Spatial and temporal patterns of nutrient concentration and export in the tidal Hudson River. *Estuaries* 22:285–296
- Limburg K, Moran M, McDowell W (1986) *The Hudson River ecosystem*. Springer-Verlag, New York
- Harley MT, Findlay SEG (1994) Photosynthesis irradiance relationships for three species of submersed macrophytes in the tidal freshwater Hudson River. *Estuaries* 17:200–205
- Madden CJ, Kemp WM (1996) Ecosystem model of an estuarine submersed plant community: calibration and simulation of eutrophication responses. *Estuaries* 19:457–474
- Moore KA, Anderson BA, Wilcox DJ, Orth RT, Naylor M (2003) Changes in seagrass distribution as evidence of historical water quality conditions. *Gulf Mex Sci* 21:142–143

- Nieder WC, Barnaba E, Findlay SEG, Hoskins S, Holochuck N, Blair EA (2004) Distribution and abundance of submerged aquatic vegetation and *Trapa natans* in the Hudson River estuary. *J Coastal Res SI*:150–161
- Orth RJ, Moore KA (1983) Chesapeake Bay: an unprecedented decline in submerged aquatic vegetation. *Science* 222:51–53
- Rybicki NB, Jenter HL, Carter V, Baltzer RA (1997) Observations of tidal flux between a submerged aquatic plant stand and the adjacent channel in the Potomac River near Washington, DC. *Limnol Oceanogr* 42:307–317
- Short FT, Burdick DM (1996) Quantifying eelgrass habitat loss in relation to housing development and nitrogen loading in Waquoit Bay, Massachusetts. *Estuaries* 19:730–739
- Strayer DL (2006) The benthic animal communities of the tidal-freshwater Hudson River estuary. In: Levinton JS, Waldman JR (eds) *The Hudson River Estuary*. Cambridge University Press, Cambridge, New York, pp 266–279
- Strayer DL, Malcom HM (2007) Submersed vegetation as habitat for invertebrates in the Hudson River estuary. *Estuaries Coasts* 30:253–264
- Strayer DL, Smith LC (2001) The zoobenthos of the freshwater tidal Hudson River and its response to the zebra mussel invasion. *Arch Hydrobiol (Supplemental)* 139:1–52
- Walker DI, McComb AJ (1992) Seagrass degradation in Australian coastal waters. *Mar Pollut Bull* 25:191–195

# Chapter 12

## Mapping Marine Macrophytes along the Atlantic Coast of Tierra Del Fuego (Argentina) by Remote Sensing

Sandra E. Torrusio

A discontinuous series of rocky formations with variable dimensions exist along the intertidal zones in the eastern coast of Tierra del Fuego, Argentina, where an abundance of marine macrophytes grow, such as *Macrocystis pyrifera* forming sub-aquatic “forests”. This large amount of algae forms true fauna reservoirs and provide potential stocks for deriving industrial algae products. The purpose of this study is to map the undersea fauna resources by remote sensing and to evaluate the utilities of different remote sensors given the frequent cloud cover and the winter days with low sunlight. The data used include satellite imagery from Landsat, SAC-C, Aster, Radarsat and QuickBird, as well as aerial photographs and maps. We co-register them before actual mapping the algae distribution using different methods. The final maps illustrate the algae distribution and temporal change, which can be useful for managing the coastal environment and resources.

### 12.1 Introduction

The intertidal and subtidal environments with rocky bottom in temperate and sub-polar seas are dominated by brown algae associations (Dayton 1985). These marine macrophyte communities are constantly exposed to tidal changes. The algae communities are economically important due to its alginates contents; the phycocolloids found in algae are useful to different industries, such as textile, food, paper, dental and pharmaceutical, soldering, among others (Rees 1986). The fucales, laminariales and durvilleales are used to extract alginates all over the world. In South America the main exploited genus are *Lessonia spp* and *Macrocystis spp*, and both constitute the most extensive high-quality natural reserve of the world, located in the coasts of Chile and Argentina (Vasquez and Fonck 1993). The principal and most abundant alginate producing species in Argentina is *Macrocystis pyrifera*. Its popular name is “Cachiyuyo” in Spanish or “Kelp” in English. It forms subaquatic “forests” or

---

S.E. Torrusio (✉)

Faculty of Natural Sciences and Museum, National University of La Plata, and National Commission of Space Activities, Argentina  
e-mail: torrusio@mail.retina.ar

“prairies” along the coasts in the Patagonia region, which are considered as true fauna reservoirs and can provide potential stock for deriving industrial algae products. In Argentina, the algae extraction is concentrated in Chubut and Santa Cruz, between 42°S and 52°S, at the north of Tierra del Fuego (53°S–55°S).

Several works evaluated the average biomass and density (e.g. Alveal et al. 1973, Barrales and Lobban 1975, Santelices and Lopehandía 1981, Boraso de Zaixso et al. 1983, Werlinger and Alveal 1988), but most of them did not address the spatial and temporal distribution of algae. Another problem is that as the methods they used are not compatible so that a comparison among different sites is difficult. Therefore, it is urgent to evaluate the populations of macroalgae at appropriate temporal and spatial scales with standard and systematic methods.

Many studies were conducted in different regions of the world to identify aquatic macrophytes by using remote sensing (Lambert et al. 1987, Lavoie et al. 1987, Ritter and Lanzer 1997, Steeves et al. 1991, Veisze et al. 1999, Wittlinger and Zimmerman 2001, Dierssen et al. 2003, Fyfe 2003, Vahtmäe et al. 2006, Nezlin et al. 2007, Tignyt et al. 2007). Aerospace remote sensing can provide repetitive, multispectral and synoptic data, and thus can be quite useful for coastal studies (Lamaro et al. in press).

The aims of this project were to map the spatio-temporal distribution of algae using remotely sensed data and to evaluate the usefulness of the different types of data given the frequent cloud cover in our study site. On the average, there are only 15 sunny days per year; the winter days are very short with just between six and seven sunlight hours.

Another important consideration here is that Tierra del Fuego is rich in natural resources and contains the most extensive offshore oil-producing zone in Argentina and Chile; the knowledge of macrophyte distribution is critical for offshore oil-producing activities because it can be used to monitor oil spill. For this purpose, radar images can be very useful due to high temporal coverage, weather independence, and high sensitivity to oil slick (Catoe 1973, Bentz and Pellon De Miranda 2001, Ivanov et al. 2002, Brown and Fingas 2003, Tufte et al. 2004). However, black tones in radar images could confuse us since they could be either the area with oil spill or the area with slow wind and calm waters that produce low or null backscattering signals. In addition, coastal rocky formations, because of partially submerged with tidal waters, can form a calm water area like a pool resulting in low or null backscattering and hence dark tones in radar images. Moreover, dark tones could be caused by the existence of macrophytes floating on the open sea surface or fixed on the coastal rocky formations; both cases result in low or null backscattering signals. Therefore, understanding the algae distribution can also help improve the accuracy of oil spill monitoring in our study site.

## 12.2 Study Area

The Argentine Province of Tierra del Fuego is a large island shared with Chile, which is located between 52° 30'S and 55°S, and 64°W and 70°W, separated from the continent by the Magallanes Strait. The algae mapping was carried out along



**Fig. 12.1** Location of the study area: Magallanes Strait and the Atlantic coast of Province of Tierra del Fuego, Argentina. Note that the shoreline in the *lower right* insert extends approximately 315 km

the eastern coast extending 315 km in the island and the southeastern extreme of the Strait (Fig. 12.1). The zone has a typical glacial landscape with many channels, fiords and small islands, and its topography is irregular. Along the Atlantic coast, rocky formations are discontinuously distributed in shallow water areas. They can be submerged or not, depending on tidal dynamic.

The climate is quite cold, with strong winds during the whole year; the rainfall decreases from west with 3500 mm per year to east with 500 mm per year. The main plant community along the western and southern portions of the island is Andinean



Patagonic Forest, and different species of *nothofagus* and *peatbogs* (moss) are abundant. In the eastern and northern sectors, the steppa dominates with sparse grasses. In both the Atlantic and Pacific coasts, there are an abundance of marine mammals, such as dolphins, whales, sea lions, seals, and aquatic birds, such as fulmars, seagulls, penguins, among others.

### 12.3 Materials

It was necessary to combine data from several satellite sensors for mapping the algae along the eastern coast of Tierra del Fuego. The major characteristics of satellite data we used in this project are summarized in Table 12.1.

#### 12.3.1 SAC-C

These images were acquired by the Argentinean satellite SAC-C, with the Multi-spectral Medium Resolution Scanner (MMRS). SAC-C was launched in November 2000, providing data with spatial resolution of 175 m, scene swath of 360 km, five spectral bands in the visible and infrared portions of the spectrum, and temporal resolution of 16 days or less according to the latitude. In the study area it was possible to obtain images every three or six days, thus increasing the chances to obtain cloud-free data.

We were able to acquire ten cloud-free images covering the period of 2002–2004. The best band combination used for macroalgae identification was near infrared-NIR (4), shortwave infrared-SWIR (5), and red (3). The kelp forests are spectrally similar to land vegetation but with higher reflectance in the near infrared portion of the spectrum. The best band combination allows to identify and separate the kelp beds and other macrophytes from bare rocks, suspended sediments or phytoplankton components in the sea.

#### 12.3.2 Landsat

We used data from three Landsat sensors: Multispectral Scanner (MSS), Thematic Mapper (TM), and Enhanced Thematic Mapper Plus (ETM+). We acquired one 1981 MSS scene that was originally in film with the blue (4), green (5) and near infrared (7) band combination and at the scale of 1:1000000, and later digitized using a digital camera. We obtained nine cloud-free TM images from 1999 to 2004 covering Spring, Summer and Fall months. The band combination was NIR (4), SWIR (5), and red (3), identical to the one we used for the SAC-C images: We also composed a true color image using bands red (3), green (2), and blue (1), which allowed to distinguish suspended sediments from a coastal river. We also acquired 15

**Table 12.1** List of satellite images used in the study

Satellite/sensor	Path/row	Date	Spatial resolution (m)
SAC-C/(MMRS)	224	Jul. 28 2002	175
SAC-C/(MMRS)	225	Aug. 04 2002	175
SAC-C/(MMRS)	225	Sep. 05 2002	175
SAC-C/(MMRS)	225	Apr. 01 2003	175
SAC-C/(MMRS)	225	May 19 2003	175
SAC-C/(MMRS)	224	Nov. 04 2003	175
SAC-C/(MMRS)	224	Jan 23 2004	175
SAC-C/(MMRS)	224	Feb. 08 2004	175
SAC-C/(MMRS)	225	Feb 15 2004	175
SAC-C/(MMRS)	225	Mar. 18 2004	175
Landsat 5 TM	225/98	Mar. 13 1999	30
Landsat 5 TM	224/98	Oct. 27 2003	30
Landsat 5 TM	225/98	Nov. 03 2003	30
Landsat 5 TM	225/98	Dec. 05 2003	30
Landsat 5 TM	223/98	Jan. 24 2004	30
Landsat 5 TM	225/98	Feb 07 2004	30
Landsat 5 TM	223/98	Mar. 12 2004	30
Landsat 5 TM	224/98	Mar. 19 2004	30
Landsat 5 TM	224/98	Apr. 04 2004	30
Landsat 7 ETM+	226/97	Aug. 24 2001	30
Landsat 7 ETM+	226/97/98	Oct. 17 2003	30
Landsat 7 ETM+	224/98	Oct. 19 2003	30
Landsat 7 ETM+	224/97	Nov. 04 2003	30
Landsat 7 ETM+	224/97/98	Jan. 07 2004	30
Landsat 7 ETM+	224/97	Jan. 23 2004	30
Landsat 7 ETM+	225/97/98	Feb.15 2004	30
Landsat 7 ETM+	225/98	Mar. 02 2004	30
Landsat 7 ETM+	226/97	Mar. 09 2004	30
Landsat 7 ETM+	226/98	Mar. 25 2004	30
Landsat 7 ETM+	225/97	May. 05 2004	30
Landsat 7 ETM+	225/98	May. 05 2004	30
Terra/Aster-VNIR	226/98	Oct. 18 2006	15
Quick Bird	–	Feb. 06 2005	2.5
Quick Bird	–	Feb. 27 2004	2.5
Quick Bird	–	Dec. 25 2002	2.5
Radarsat/Beam Mode W1	Ascend. orbit	Apr. 06 2007	30
Radarsat/Beam Mode SNA	Descend. orbit	May. 23 2006	50

cloud-free ETM+ images from 2001 to 2004. The band combination more adequate to identify the algae was NIR (4), SWIR (5), and red (3).

### 12.3.3 ASTER

We acquired one image in Spring 2006 from the Advanced Spaceborne Thermal Emission and Reflection Radiometer (ASTER) on the Terra satellite, which covers a small portion of the coast. With a swath of 60 km, ASTER has 15 bands, including

three visible and near infrared bands with 15 m spatial resolution and 8-bit radiometric resolution, a second near infrared backward-scanning band used to create a stereo view, six SWIR bands with 30 m spatial resolution and 8-bit radiometric resolution, and five thermal bands (TIR) with 90 m spatial resolution and 16-bit radiometric resolution. The band combination we used was NIR (3), red (2), and green (1); these bands have 15 m spatial resolution, allowing to identify different macrophytes communities and determine the phenological state with textures and tones.

#### ***12.3.4 QuickBird***

We used three QuickBird multispectral images with very high spatial resolution, which cover part of the eastern coast of Tierra del Fuego and the Magallanes Strait for Spring 2002, Summer 2004 and Summer 2005. They allowed us to compare the current algae distribution with historical data.

#### ***12.3.5 Radarsat***

Radarsat's SAR (synthetic aperture radar) is an active sensor. It transmits a microwave energy pulse directly towards the Earth's surface. The SAR sensor measures the amount of energy which returns to the satellite after it interacts with the Earth's surface. Unlike optical sensors, the microwave energy penetrates clouds, rain, dust, or haze, and acquires images independent of the Sun and the weather conditions. Variations in the returned signal are the result of changes in the surface roughness and topography as well as physical properties such a moisture content and electrical properties (Radarsat User Guide 1995). There are several products with different spatial resolution according to the beam modes.

We acquired two Radarsat images: Scan Narrow A with 29° incidence angle, spatial resolution of 50 m, and 200 km swath for 23 May 2006; Wide 1 with 24° incidence angle, spatial resolution of 30 m, and 150 km swath for 6 April 2007. For oil spill detection, steep incidence angles are preferred. The SAR data were processed with the adaptative filters of Lee for the Scan Narrow A mode and Frost for the Wide 1 mode to suppress the image speckles for improving the visual interpretability.

The Radarsat images were used to analyze "black areas" and to separate the different features on or near the sea surface: area with low/null wind speed, inland waters, and emergent or floating kelps from real or potential oil spill. They also allow to view some offshore oil platforms that are hardly seen with medium-resolution optical data.

#### ***12.3.6 Other Data***

We also analyzed historical aerial photographs and bathymetric maps covering part of Tierra del Fuego. These materials were produced by the Naval Hydrographical

Survey. We considered four aerial photos from 1970 at the scale of 1:20000. The bathymetric map was from 1939 at the scale of 1:400000.

## 12.4 Methods

Mapping of the marine macrophyte communities in the entire study area was carried out by using the optical data from SAC-C and Landsat TM/ETM+. We clipped most of the images to focus on the coastal area of interest only; this could also help offset data processing burden. We georeferenced all the image subsets into geographic coordinates, WGS84 datum and ellipsoid. The resampling method used was cubic convolution and the average RMS was about one pixel for every image. For the SAC-C images the mean RMS was 98.4 m, and 35 ground control points (GCP) were used; for the Landsat images, the mean RMS was 17.8 m, and 23 GCPs were used; and for the ASTER images, the mean RMS was 10.4 m, and 18 GCPs were used.

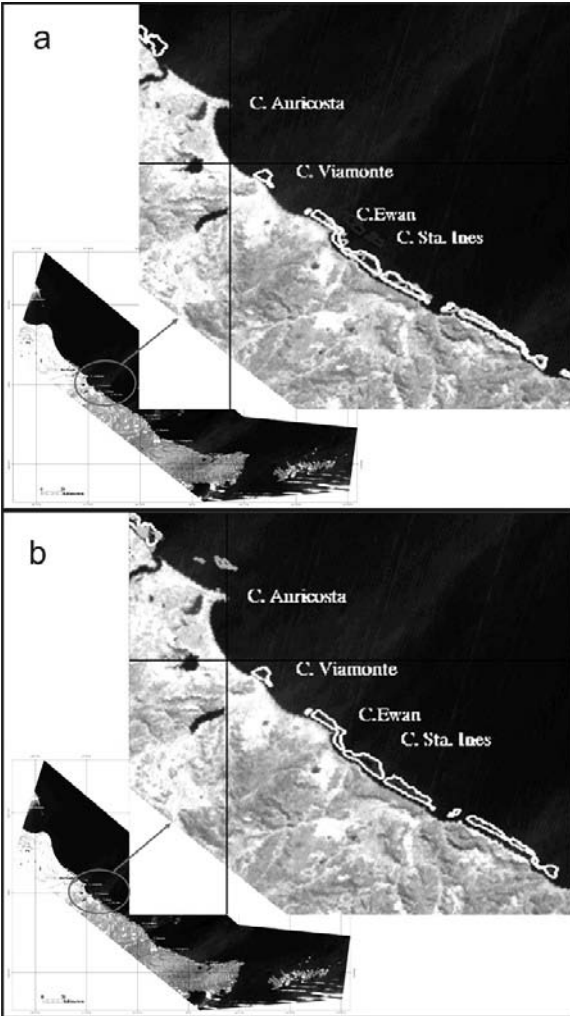
Both digital and visual analysis methods were combined to mutually maximize their capability for algae community identification. Because the weather and tidal conditions were various for each optical image, we tried different methods to distinguish the macrophytes. Firstly, we tested supervised and unsupervised classifiers, but the spectral confusion among some classes made difficult to obtain accurate results. Then, we conducted spectral enhancement to maximize the visual separability considering colors, tones, textures and shapes of the submerged vegetation along the coast. Specifically, we applied linear stretching, Gaussian, histogram equalization, standard deviations, interactive stretching, and band ratio to different images in order to improve the algae recognition. With the enhanced images, we further mapped the algae communities by using on-screen digitizing, and the derived maps were managed with a geographic information system.

The aerial photos were co-registered and mosaicked. The bathymetric map was co-registered too. A detailed visual analysis was done using the photos and the satellite images discussed in Sect. 12.3. This visual interpretation allowed us to analyze the temporal and spatial changes and to compare the contributions and/or disadvantages of each sensor.

All the above data processing tasks were conducted by using ERDAR Imagine 8.4, ENVI 3.5 and Arcview 3.1.

## 12.5 Results

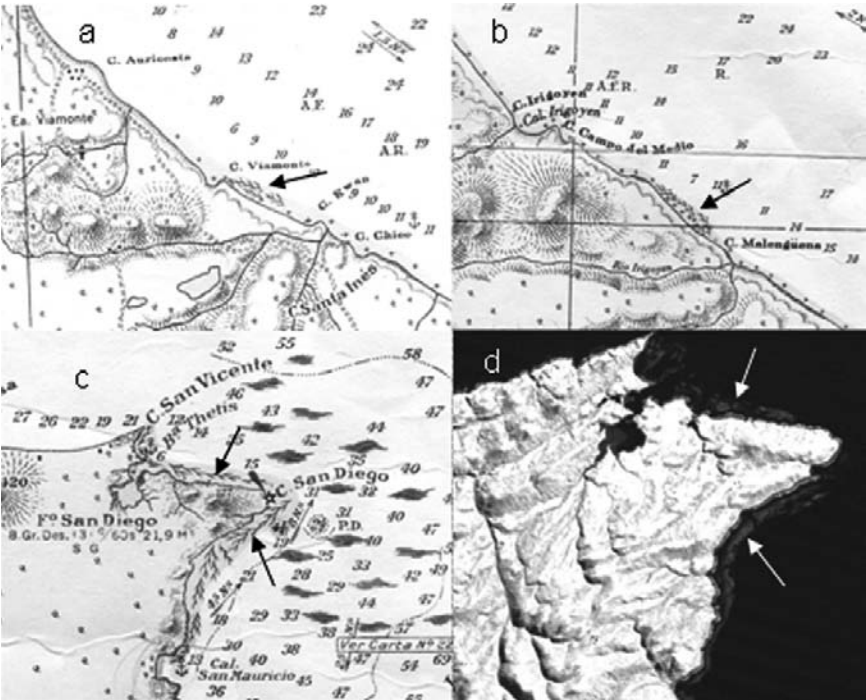
The final maps show that the marine macrophytes were discontinuously distributed along the eastern coast of Tierra del Fuego (Fig. 12.2a,b). This distribution pattern may be related to the tidal influence and the type of rocks where the plants can fix. As for the seasonal variation, we did not find any significant difference between



**Fig. 12.2** Seasonal algae distribution: (a) Interpretation from the Spring-Summer Landsat and SAC-C images overlaid on a SAC-C image. Note that the white polygons are the distribution of algae; (b) Interpretation from the Fall-Winter Landsat and SAC-C images overlaid on a SAC-C image. Note that the white polygons are the distribution of algae

Fall-Winter and Spring-Summer covers for the period of 1999–2004 (Fig. 12.2a,b). We believe that some field verifications by experts in algae and remote sensing around the year should help improve the mapping accuracy.

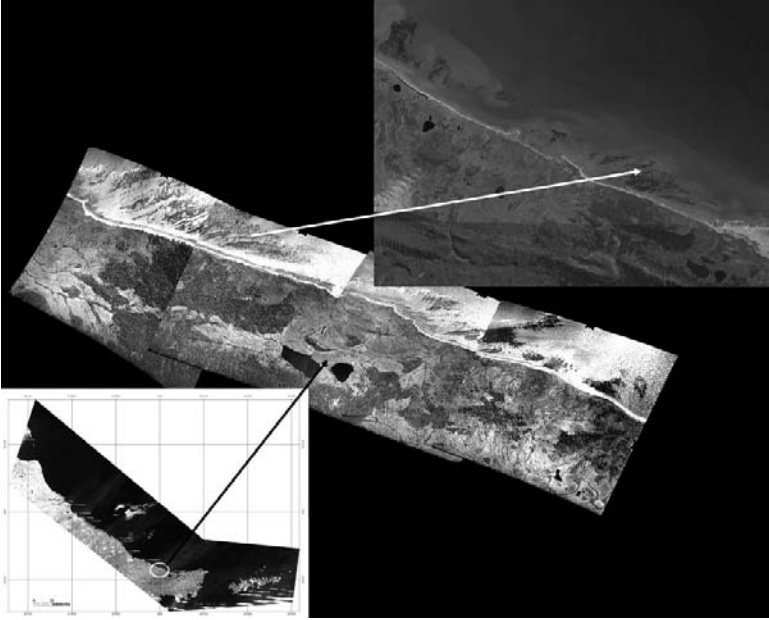
From Fig. 12.3, we can see three portions of the 1939 bathymetric map with the presence of algae in the same location where we can find them in recent satellite images, e.g. the Landsat 5 TM scene acquired on November 2003. In the same way we also compare the aerial photos mosaic (1970) versus Quick Bird (2002) (Fig. 12.4), and Landsat 2 MSS (1981) versus SAC-C (Fig. 12.5).



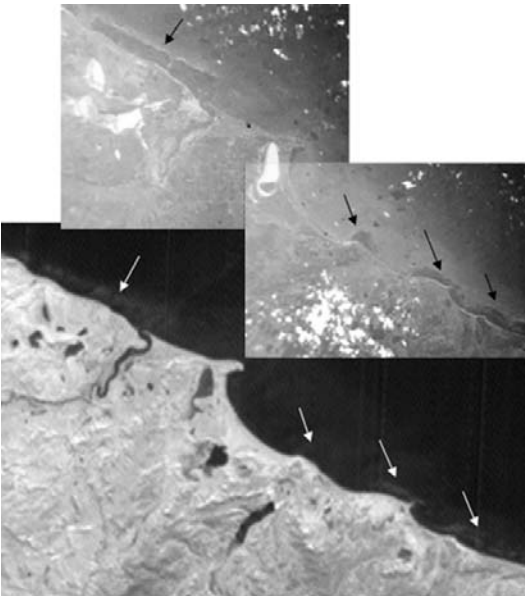
**Fig. 12.3** Bathymetric maps for the three sites (a, b, and c) along the eastern coast of Tierra del Fuego and the south extreme of the island. Note that (d) is part of the near infrared band of a Landsat 5 TM image acquired on November 2003, covering the same area as (c) does. The algae locations are indicated with arrows

Note that from the ASTER image (Fig. 12.6a) different marine macrophyte communities, such as *Macrocystis pyrifera* (Fig. 12.6b,c), can be observed with various reddish colors. Figure 12.6c,d are the outputs of different enhancements on a Landsat 5 TM image acquired on November 2003 with two different band combinations: (a) 3,2,1 (Fig. 12.6d) allowing to identify a sediments plume (in beige-yellowish color); and (b) 4,5,3 (Fig. 12.6e) permitting to identify macroalgae (in purplish color).

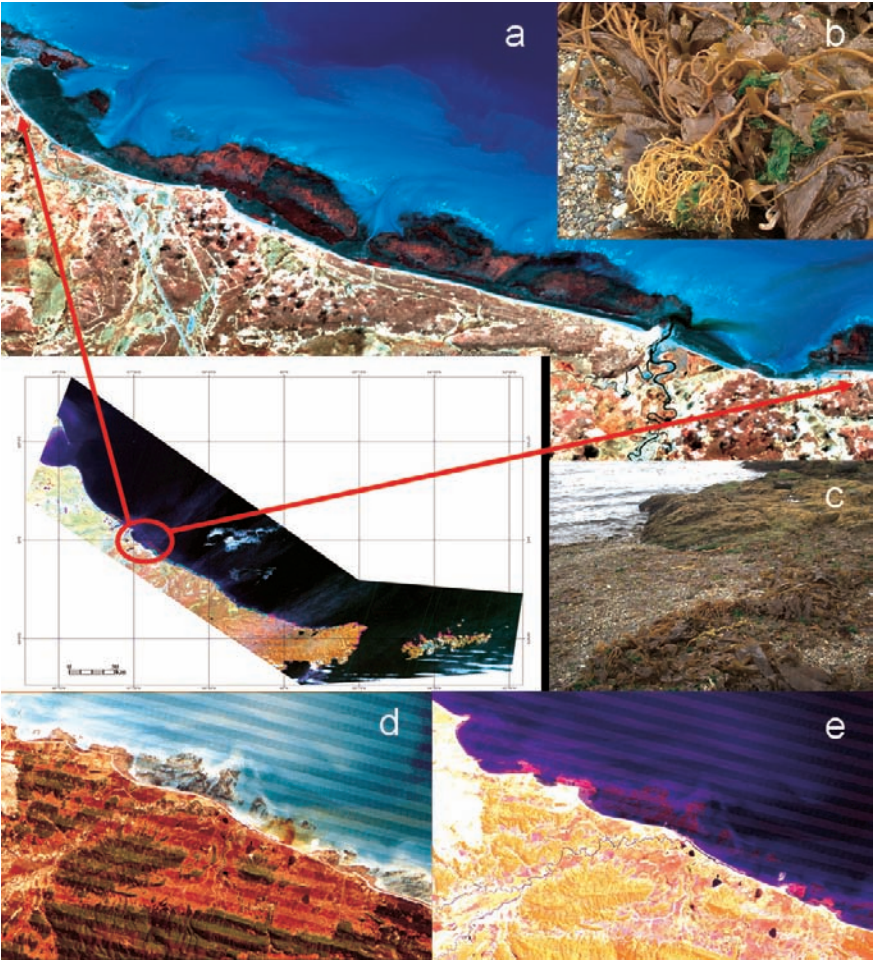
Several additional figures helped us to assess the contribution of radar images for algae identification and to explain how we separated and analyzed dark zones. Figure 12.7 is a 2004 Radarsat Scan Narrow A image on which we see some bright spots indicating offshore oil platforms in the Magallanes Strait and Northeast of Tierra del Fuego. In Fig. 12.8, we can see some black areas in the 2007 Radarsat image, which were with slow wind and calm water; we see some floating kelps (indicated with the white arrows) from the 2004 QuickBird image, which were over the same areas showing in black from the 2007 Radarsat image. In Fig. 12.9 we can see some partially submerged rocks in the 2004 Scan Narrow A Radarsat image (in dark tones) (Fig. 12.9a) and some offshore oil-platforms (Fig. 12.9b). Note from the



**Fig. 12.4** Comparison between a 1970 aerial photos mosaic (*centre*) and a 2002 QuickBird image (the *upper right* insert). The algae locations are indicated with the white arrow



**Fig. 12.5** Comparison between the images from Landsat 2 MSS (1981) (the *two upper* figures) and from SAC-C (September 2002)



**Fig. 12.6** (a) An ASTER image acquired on October 2006 showing algae in reddish tones on rocks. *Macrocystis pyrifera* on the rocks (b) and on the fixer disc (c). Color composites of the 2003 Landsat 5 TM image: (d) with bands 321; a sediments plume develops in the lower right portion; and (e) with bands 453; this sediment plume is not visible and algae are in purplish

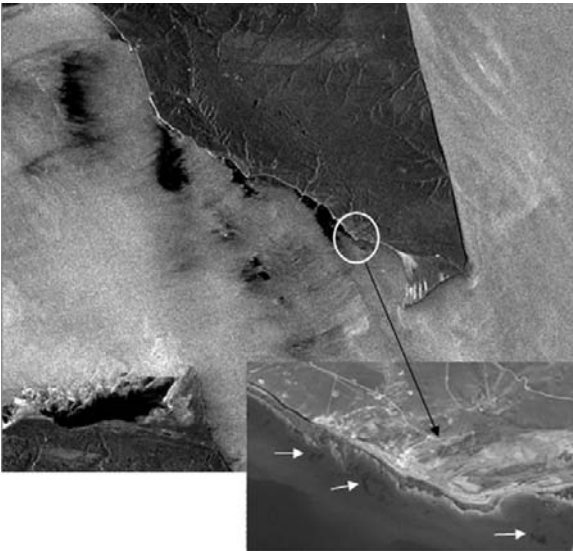
April 2006 Landsat 5 TM image, these areas emerged without plants (Fig. 12.9e). Similar comparison is shown in Fig. 12.9d between the 2007 radar and the 2004 QuickBird images (Fig. 12.9c) in the northern island; coastal areas with dark tones are calm water without fixed algae but with floating kelps near the shoreline.

In general we found that the macroalgal distribution did not change much over time considering the materials we used covered the period of 1939–2007. Moreover, the use of different sensors, both optical and active, helped improve the possibilities of obtaining cloud-free images, and thus promoting our inventory effort in this area where this type of information was sketchy and sometimes absent.

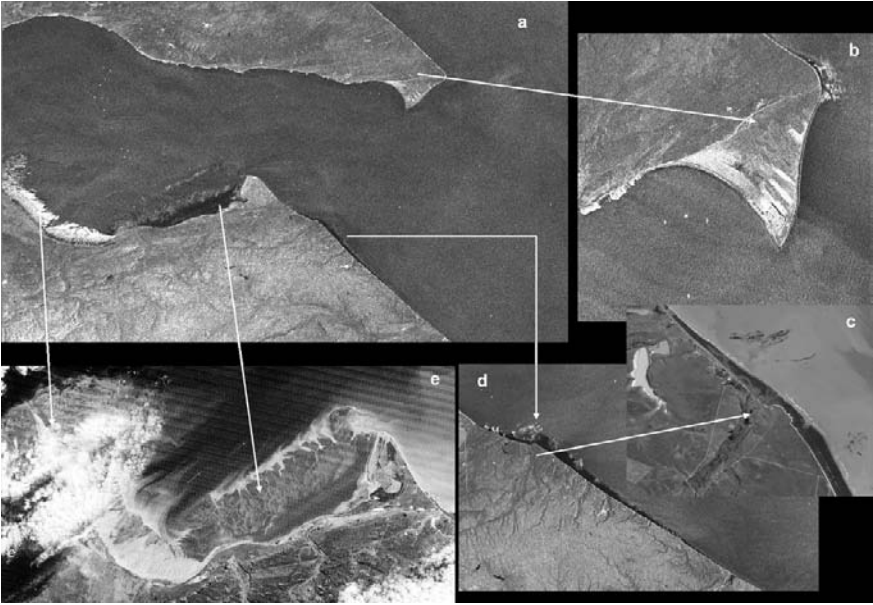




**Fig. 12.7** Part of the Radarsat image (Scan Narrow A, May 2004) covering the Magallanes Strait. Note that the bright spots indicate off-shore oil platforms



**Fig. 12.8** Part of the Radarsat image (Wide 1, Apr. 2007) covering the Magallanes Strait; dark areas are with slow wind and calm water. Part of the QuickBird image (the *lower right* insert) shows some floating seagrasses, which are indicated with three white *arrows*



**Fig. 12.9** Partially submerged rocks (in dark tones) on the radar image (Scan Narrow A 2004): (a) in the bay and (b) an enlargement to show some oil-platforms. (e) Part of the 2006 Landsat 5 TM image (original in color, displayed with bands 321) shows the same area that emerged without plants. Comparison between the 2007 radar (d) and the 2004 QuickBird (c) images shows that some floating algae rather than fixed ones are in the coastal areas with dark tones

## 12.6 Conclusions

Probably, the comparison among different satellite sensors and other sources of data was the most interesting aspect in this project. This study offers an insight concerning the advantages and combinations of several products for mapping natural resources, algae in this case. The use of these tools allows to obtain an integral perspective. We considered the advantages of using optical data with different spatial resolution to identify the current macroalgae distribution and to detect potential seasonal changes. On the other hand, the use of other data sources, such as historic bathymetric maps and aerial photographs, allowed us to map the spatial distribution of algae in the past. These have been very helpful to examine the temporal changes through several decades.

Considering the application of active remote sensor data in this study we should emphasize their advantage when there is frequent cloud cover during the year in our study area. Because of the existence of intensive offshore oil-producing activities, however, the radar images play a critical role in every segment of the environmental monitoring. Our results showed that it is not easy to separate among calm water areas, macroalgae communities, and oil spills by using active remote sensing alone. Thus, it would be very useful to construct a complete kelp bed data base for

Argentina's southern coast by combining both optical and radar data; we believe such database will help us to produce better results, and thus improving our oil spill monitoring plan.

Given the above considerations, we believe that the construction of the algae distribution base maps covering the 315 km coast is economically and environmentally important. We should incorporate this mapping effort into our coastal monitoring and management plans.

**Acknowledgements** I would like to thank National Commission of Space Activities (CONAE) for providing the valuable images used in this project. A very special acknowledgment to M.A. Geology Mr. J. Ulibarrena, to my advanced student Ms. J. Otero and to Mr. G. Weber, the computer operator, for their collaboration in the mapping of these algae. Besides, I thank Dr. C. Moyano, Dr. E. Baran, and several colleagues for the critical reading of the manuscript.

## References

- Alveal K, Romo H, Valenzuela J (1973) Consideraciones ecológicas de las regiones de Valparaíso y de Magallanes. *Rev Biol Mar* 15:1–29
- Barrales H, Lobban CS (1975) The comparative ecology of *Macrocystis pyrifera*, with emphasis in the forest of Chubut, Argentina. *J Ecol* 63:657–677
- Bentz CM, Pellon De Miranda F (2001) Application of remote sensing data for oil spill. Monitoring in the Guanabara Bay, Rio de Janeiro, Brazil. *Anais X SBSR, Foz do Iguaçu, April 21–26, INPE*, pp 747–752
- Boraso de Zaixso AL, Piriz ML, Romanello EE (1983) Posibilidades de desarrollo de la industria alguera en la Prov. de Santa Cruz (República Argentina). Informe Proyecto “Cinco Provincias Argentinas”, OEA
- Brown CE, Fingas MF (2003) Synthetic Aperture Radar Sensors: Viable for Marine Oil Spill Response? Emergencies Science and Technology Division Environment Canada. <http://www.ecy.wa.gov/programs/spills/response/taskforce/AMOP%202003%20SAR%20Oil%20Spills.pdf> (Last access on 16 June 2006)
- Catoo C (1973) Remote Sensing Techniques for Detecting Oil Slicks. *J Petrol Technol* 25:267–278
- Dayton PK (1985) The structure and regulation of some South American kelp communities. *Ecol Monogr* 55:447–468
- Dierssen HM, Zimmennan RC, Leathers RA, Downes TV, Davis CO (2003) Ocean color remote sensing of seagrass and bathymetry in the Bahamas Banks by high resolution airborne imagery. *Limnol Oceanogr* 48:444–455
- Fyfe SK (2003) Spatial and temporal variation in spectral reflectance: Are seagrass species spectrally distinct? *Limnol Oceanogr* 48:464–479
- Ivanov A, He M, Fang M (2002) Oil spill detection with the RADARSAT SAR in the waters of the Yellow and East China Sea: A case study. <http://www.gisdevelopment.net/aars/acrs/2002/sar/011.pdf> (Last access on 16 June 2006)
- Lamaro A, Torrusio S, Ulibarrena J, Mugni H, Bonetto C. Mapping of Coastal Changes Applying Maps, Satellite Images and GIS in Samborombón Bay, Argentina. *Int J Ecol Dev* (in press)
- Lambert E, Dubois JM, Lavoie A, Grenier M (1987) Remote sensing of marine macrophytes. *Photo Interprétation* 1:1–8
- Lavoie A, Lambert E, Dubois JM, Gendron L (1987) Sensing and mapping of *Laminaria* of the Coast of Quebec and biomass evaluation. *Photo Interprétation* 1:9–16
- MacDonald, Dettwiler and Associates Ltd (1995) Radarsat user guide p 113

- Nezlin NP, Kamer K, Stein ED (2007) Application of Color Infrared Aerial Photography to Assess Macroalgal Distribution in an Eutrophic Estuary, Upper Newport Bay, California. *Estuaries and Coasts* 30:855–868
- Rees WM (1986) Alginate marketing in the 1980's. *Monografías Biológicas (Chile)* 4:13–28
- Ritter R, Lanzer EL (1997) Remote Sensing of Nearshore Vegetation in Washington State's Puget Sound. *Proceedings of 1997 Geospatial Conference*, vol 3. Seattle, WA, pp 527–536
- Santelices B, Lopehandía J (1981) Chilean seaweeds resources: A quantitative review of potential and present utilization. *Int Seaweed Symp* 10:725–730
- Steeves P, Waldron MC, Finn JT (1991) Aquatic Macrophyte Mapping Using Thematic Mapper Imagery and a Geographic Information System. *ESRI Users Conference* in San Diego, California. [http://ma.water.usgs.gov/publications/ja/lakes\\_ponds\\_journal.htm](http://ma.water.usgs.gov/publications/ja/lakes_ponds_journal.htm) (Last access on 20 November 2007)
- Tignyt V, Ozer A, De Falcolt G, Baroli M, Djenidi S (2007) Relationship between the Evolution of the Shoreline and the *Posidonia oceanica* Meadow Limit in a Sardinian Coastal Zone. *J Coastal Res* 23:787–793
- Tufte L, Trieschmann O, Hunsänger T, Kranz S, Barjenbruch U (2004) Using air- and spaceborne remote sensing data for the operational oil spill monitoring of the german north sea and Baltic sea. <http://www.isprs.org/istanbul2004/comm7/papers/193.pdf> (last access on 16 June 2006)
- Vahtmäe E, Kutser T, Martin G, Kotta J (2006) Feasibility of hyperspectral remote sensing for mapping benthic macroalgal cover in turbid coastal waters: a Baltic Sea case study. *Remote Sens Environ* 101:342–351
- Vasquez JA, Fonck EA (1993) Estado actual y perspectivas de la explotación de algas alginofitas en Sudamerica. In: Zertuche Gonzalez JA (ed) *Situacion actual de la industria de macroalgas productoras de ficocoloides en América latina y el Caribe*, Project reports No.13, FAO Italy, p 66
- Veisze P, Kilgore A, Mark Lampinen M (1999) Building a California Kelp Database Using GIS. <http://www.imaging.geocomm.com/features/californiakelp> (Last access on 20 November 2007)
- Werlinger C, Alveal K (1988) Evaluación de algas en ambientes restringidos del Golfo de Arauco (Chile): Punta Fuerte Viejo a Río Tubul. *Guayana Bot* 45:461–474
- Wittlinger SK, Zimmerman RC (2001) Hyperspectral remote sensing of subtidal macrophytes in optically shallow water. *Aquatic Sciences Meeting*, Albuquerque. <http://www.aslo.org/albuquerque2001/507.html> (Last access on 25 March 2008)

**Part IV**  
**Shoreline Change, Coastal Wetland**  
**and Watershed Characterization**

# Chapter 13

## Shoreline Mapping and Coastal Change Studies Using Remote Sensing Imagery and LIDAR Data

Hongxing Liu

This chapter introduces algorithms and methods for numerically extracting shorelines from the remote sensing imagery and LIDAR elevation data. These methods aim to minimize human operator's intervention and editing efforts and to maximize the delineation accuracy. The shoreline extraction method designed for processing remote sensing imagery consists of three groups of algorithms: preprocessing, segmentation and classification, and post-processing. This method is applicable to both satellite images and digital aerial photographs, and the shoreline can be extracted from the imagery at a pixel level accuracy. Further, two methods are presented to process LIDAR data for automated shoreline delineation. The first method is composed of three processing steps: contouring, line selection with a length threshold, and line smoothing and generalization. The second one is based on the segmentation of the LIDAR DEM. These methods have been employed to process multi-temporal digital orthorectified aerial photographs, Landsat imagery, and airborne LIDAR data in the upper Texas Gulf coast. The shorelines delineated from the time series of remote sensing images and LIDAR DEMs are compared in GIS environment for coastal change studies.

### 13.1 Introduction

Shoreline information is important to navigation charting, marine boundary determination, and many coastal zone management activities, such as monitoring shoreline changes and delineating the inter-tidal zone, wetlands, and other coastal habitats. Land planners have relied on up-to-date shoreline information for establishing building setback lines, managing recreational resorts, inventorying the wetland and agricultural land resources, and delineating flood and hurricane hazard zones (Zeidler 1997). Engineers have employed shoreline and beach morphology information for designing coastal defense and shipping structures (Szmytkiewicz et al. 2000). Geomorphologists have long recognized the usefulness of shoreline information for

---

H. Liu (✉)

Department of Geography, Texas A&M University, TX 77843, USA  
e-mail: liu@geog.tamu.edu

studying coastal erosion and accretion and estimating sediment transport and budgets (Shepard and Wanless 1971, Leatherman and Douglas 2003). As pointed out by many coastal scientists (e.g. Morton 1991, Leatherman and Douglas 2003), tracking and investigating shoreline and coastal changes calls for rapid, highly accurate methods that minimize the mapping error and processing time and provide frequent and timely measurements.

Traditionally, shorelines on the nautical charts and topographic maps were compiled through ground surveys and visual interpretation of aerial photographs. In the ground surveys, the direction and distance of shoreline features were observed and determined in person on the beach with the plane table and rod, and the shorelines were drawn through the series of measured points on the shore. In the 1920s, the aerial photogrammetric survey method replaced the older plane table survey method and became the primary shoreline mapping technique. Using aerial photography mapping method, shoreline interpretation and compilation was brought from the field into the office, saving time and cost. At present, shorelines on the majority of maps are still determined through interpretation of the stereo-photogrammetric models of aerial photographs (Graham et al., 2003). In recent decades, new approaches have been developed for coastal and shoreline mapping. Those include the use of high-resolution satellite imagery (Li et al. 2003), all-terrain kinematic GPS vehicles (Morton 1997), and airborne LIDAR technology (Gibeaut et al. 2000, Robertson et al. 2004).

The fundamental problem in using remote sensing images for shoreline mapping is that the wet/dry beach (high-water) lines delineated from the imagery is affected by water level at the time the images were acquired. Remote sensing images are rarely taken at precise mean high water with no wave action throughout the survey. Therefore, the high water line derived from the remote sensing imagery is not exact intersection where a body of water at the precise desired tidal datum elevation and the shore meet. The seasonal tidal variation and storm surges often create different water levels. Water levels have their greater effects on the high water line for wide low-gradient beaches than for narrow, steep beaches. Some mapped shoreline changes could be merely a manifestation of the differences in water levels rather than actual coastal erosion or accretion. With the recorded tide stages, we can adjust and normalize the image derived shorelines to a common tidal elevation for comparison. However, the tide adjustment and normalization process is often difficult and inaccurate.

With the advent of airborne LIDAR technology, the coast zone and shoreline may be mapped more accurately and cost-effectively. Shorelines extracted from LIDAR data have unprecedented accuracy and can establish a baseline for change analysis. If the LIDAR data are collected at the time of low water level, it is possible to derive shoreline indicators using various tidal datums. Therefore, the airborne LIDAR data over coastal zones may offer a means to link and assimilate different shorelines obtained from divergent approaches such as the NOAA T-sheets, kinematic GPS, and aerial photographs, and satellite imagery.

While new remote sensing data have been increasingly becoming available, derivation of shorelines from remote sensing data still is challenging. Manual

tracing, digitizing, and delineating shorelines from an image is a tedious, subjective, and labor intensive process, resulting in long periods between successive maps. In previous studies, two different approaches have been proposed to derive shorelines from high resolution LIDAR Digital Elevation Model (DEM): the cross-shore profile method (Stockdon et al. 2002, Morton et al. 2005) and the contouring method (Robertson et al. 2004). Stockdon et al. (2002) used the cross-shore LIDAR DEM profiles to determine the shoreline position. A regression equation is fitted for the LIDAR points for the foreshore area along each profile, and then the selected water level is intersected with the regression line to identify the shoreline point for each cross-shore profile. The shoreline points determined from individual cross-shore profiles are linked to generate a shoreline representation. With this method, the spatial detail of the shoreline is controlled by the spacing between individual cross-shore profiles. To sample and analyze cross-shore profiles represent a tedious and time consuming process, particularly when a small spacing between profiles is chosen for a detailed shoreline. Many investigators used a contouring method to derive shorelines from the LIDAR DEMs (Parker 2003, Smyth et al. 2003, Robertson et al. 2004). By subtracting tidal datum (surface) from the LIDAR DEM, the zero contour lines can be derived from the difference grid as the tidal datum referenced shoreline indicator. Although the contouring routine is available in most GIS and mapping software packages, it is not optimized for the shoreline extraction. Consequently, the contouring process often tends to produce many noisy, broken shorelines (Parker 2003, Smyth et al. 2003, Robertson et al. 2004). A manual editing effort is required to clean and eliminate the erroneous shorelines, while enhancing the true shorelines.

This chapter introduces algorithms and methods for numerically extracting shorelines from the remote sensing imagery and LIDAR elevation data. These methods aim to minimize human operator's intervention and editing efforts and to maximize the delineation accuracy. The shoreline extraction method designed for processing remote sensing imagery consists of three groups of algorithms: preprocessing, segmentation and classification, and post-processing. This method is applicable to both satellite images and digital aerial photographs, and the shoreline can be extracted from the imagery at a pixel level accuracy. Further, two methods are presented to process LIDAR data for automated shoreline delineation. The first method is composed of three processing steps: contouring, line selection with a length threshold, and line smoothing and generalization. The second one is based on the segmentation of the LIDAR DEM. The LIDAR DEM is segmented into a binary image, consisting of land and water pixels, by intersecting it with the tidal datum surface. Then, a sequence of image processing algorithms, similar to those used in processing remote sensing imagery for shoreline extraction, are applied to extract vector shorelines of cartographical quality. These methods have been employed to process multi-temporal digital orthorectified aerial photographs, Landsat imagery, and airborne LIDAR data in the upper Texas Gulf coast. The shorelines delineated from the time series of remote sensing images and LIDAR DEMs are compared in GIS environment for coastal change studies.



## 13.2 Shoreline and Tide Datums

In coast survey usage, the shoreline is considered synonymous with coastline (Graham et al. 2003). Generally speaking, a shoreline refers to a spatially continuous line of contact between the land and a body of water (sea or lake). The horizontal position of the land-water interface is constantly changing with time as the water level moves up and down. Water level of the sea surface fluctuates due to short-term effects of tides as well as long-term relative sea level changes. It is also affected by wind, atmospheric pressure, river discharge, beach changes, and steric effects due to changing salinity and temperature of the water body. The more gentle the slope of the beach, the greater the change in the shoreline position with changing water level. The extreme storm surge from hurricanes can raise the water level several meters and temporarily cause the shoreline movement miles landward in an area with a gently sloping inter-tidal zone. Shorelines of different years are often compared to quantify the beach erosion and accretion. A consistent shoreline definition is critical to the reliable change analysis and erosion rate calculation. If the shorelines are delineated with different definitions, the detected changes might be merely a manifestation of inconsistencies of the chosen definition, rather than real shoreline changes due to the erosion or accretion.

The tide is the periodic rise and fall of the water resulting from gravitational interactions between Sun, Moon, and Earth. The high water is the maximum height reached by a rising tide, while low water is the minimum height reached by a falling tide. The higher high water is the highest of the high waters (or single high water) of any specific tidal day due to the declinational effects of the Moon and Sun. The lower low water is the lowest of the low waters (or single low water) of any specific tidal day due to the declinational effects of the Moon and Sun. Tidal datums at water level stations are elevation values that are determined by averaging the time series of observations. Tidal datums in the US are referenced to the National Tidal Datum Epoch (NTDE). The NTDE is the specific 19-year period adopted by the National Ocean Service as the official time segment over which tide observations are taken and reduced to obtain mean values for tidal datums. Mean Higher High Water (MHHW) for a particular gauging station is the average of the higher high water height of each tidal day observed over the National Tidal Datum Epoch, while Mean High Water (MHW) is the average of all of the high water heights of each tidal day observed over the NTDE. Mean Low Water (MLW) is the average of all the low water heights of each tidal day, and Mean Lower Low Water (MLLW) is the average of the lower low water height of each tidal day over the NTDE. Mean Sea Level (MSL) is the arithmetic mean of hourly heights observed over the NTDE.

Shorelines based on different water level indicators (vertical reference datum) may have significant shifts in horizontal placement due to beach slope characteristics. The mean high water line (MHWL), as published on the National Ocean Service (NOS) nautical charts, is treated as the legal shoreline by many US government agencies, including the United States Army Corps of Engineers, Federal Emergency Management Agency, and U.S. Census Bureau for the US (Parker 2003, Graham et al. 2003). A MHWL is the position of the land-water interface at a water

level elevation equal to a mean high water (MHW) datum. Although some coast scientists argued that the vegetation line, dune line, bluff top line or other morphologic features may be a better indicator for characterizing beach stability (Morton 1991), the MHWL line is widely accepted as the reference feature for mapping shorelines. Part of the reason is that identification of the MHWL is relatively easy in the field and on the remote sensing imagery (Morton 1997, Pajak and Leatherman 2002).

Tidal datums are local and vary from place to place over the region. The tidal datum variations are influenced by the gravitational attraction of water with the moon and sun, as well as non-astronomical factors such as the configuration of the coastline, local depth of the water, ocean floor topography, and other hydrographic and meteorological influences. Tidal datum values are only observed and calculated at tide gauge stations. The use of a numerical hydrodynamic model or spatial interpolation method like TCARI (Hess 2002, Hess 2003a,b) can compute the tidal datums between gauge stations, producing a two-dimensional tidal datum field.

The tidal datum information is essential for the pre-flight planning and post-flight data processing of remotely sensed data for shoreline extraction. The ground surveys, the mobile GPS vehicle traversing, and aerial photograph and satellite image acquisition should be scheduled at the time when the water level is close to the MWH datum value for the region being surveyed. The tide window defined by the NOS for collecting tide-coordinated or tide-predicted photographs is the time period when the water level is within 0.3 feet (0.0914 m) above or below the MWH datum (Graham et al. 2003). The tide window gives a guideline for the pre-flight planning of aerial photogrammetric surveys of the coast and shoreline. To obtain the MWH shoreline from the panchromatic or infrared color aerial photographs, the aircraft should be planned to fly over the section of coast being surveyed within the tide window. In the post-flight analysis of aerial photographs for shoreline interpretation and extraction, the water level and tidal datum should be carefully considered. For those images acquired at the time when the water level is close to the elevation of the desired MHW datum, the dry/wet line extracted from the images approximates the MHW shoreline. For those images acquired at the time when the actual water level is significantly above or below the MHW datum, the shorelines extracted from the images need to be corrected by compensating the difference between the actual water level elevation and the MHW datum. In other words, the image derived shorelines must be normalized to a common MHW tidal datum for comparison. Otherwise, the mapped shoreline changes could be merely the artifacts of differences in water levels rather than actual shoreline erosion or accretion.

The tide window requirement for airborne LIDAR surveys is different from that for aerial photography surveys. The optimal time for the airborne LIDAR surveys of the coast and shoreline is when the water level is significantly below MLLW so that the maximum extent of the inter-tidal zone is exposed. High tides, large waves, storm surge, and runoff at the time of survey may obscure the location of the vertical datum. If LIDAR data are collected during low tide and low wave energy, the tide coordinated shorelines can be derived by using different tidal datums as a reference, including MHW, MHHW, MSL, MLW, or MLLW.

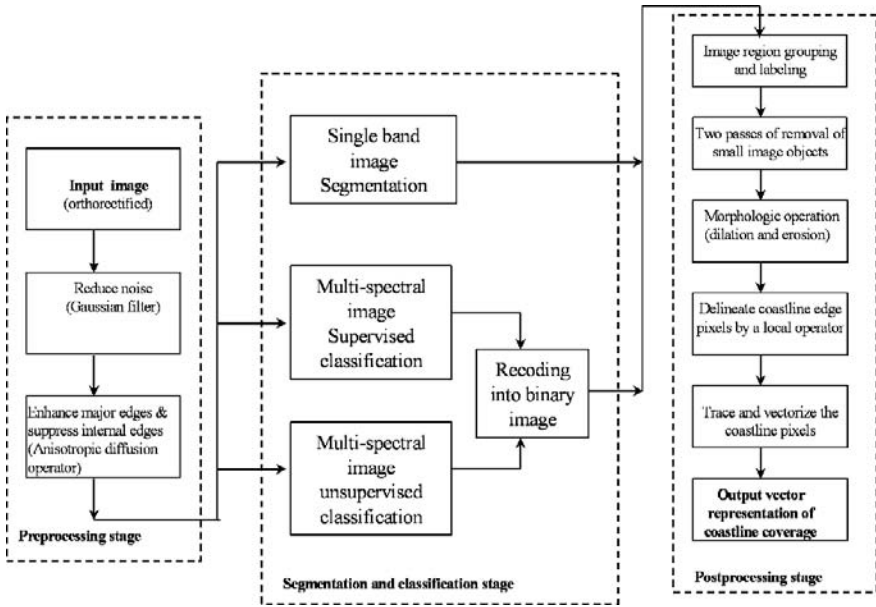
### 13.3 Shoreline Extraction from Remote Sensing Imagery

Aerial photographs and satellite images are the primary data sources for shoreline mapping. Conventionally, manual tracing and digitizing method was used to delineate shorelines onto a map from remote sensing images. The manual delineation of shoreline is a subjective, time-consuming, and labor intensive process. Errors were frequently introduced in the manual tracing and in the transfer of the traced shoreline features to the base topographical map. All these effects adversely influence the accuracy and precision of the resulting shorelines (Leatherman 1983, Crowell et al. 1991). Crowell et al. (1991) estimated the total combined error in shoreline position for 1:10,000 scale, non-tidal coordinated, aerial photography to be  $\sim 7.6$  m, not including errors associated with inaccurate interpretation of the location of the HWL. This section presents an automated method for numerically deriving shorelines from remote sensing imagery with a high precision.

On aerial photographs or high resolution satellite images, the visible high water line (HWL) is commonly interpreted and used as the MHW shoreline. The high water line is the intersection of land with the water surface at high tide, namely, the wet/dry sand boundary. It is created by the furthest landward extent of the rising water on a beach face. The wet/dry line can be recognized from the markings left on the beach by the last preceding high water, which manifests as distinct linear change and contrast in gray tone or color on images. In general, near infrared panchromatic or color image is the best for delineating the waterline, due to its sensitivity to moisture. To derive an accurate shoreline from a remote sensing image, the water level of the coast being surveyed should be close to the MHW datum when the image was acquired. In practice, the high water line from images taken in late summer following a neap high tide gives a good approximation to the MHW shoreline. Interpreting the high water shoreline indicator requires good quality imagery. Good visibility without the presence of clouds or cloud shadows is also important condition for collecting optical remote sensing images for shoreline extraction.

The automated method for shoreline delineation from remote sensing images consists of three phases of image processing: preprocessing, segmentation/classification, and post-processing as shown in Fig. 13.1. The input source remote sensing images need to be geocoded to assign precise geographic coordinates to image pixels and rectified to remove geometric and terrain distortions. The geographic coordinates of the derived shoreline are inherited from the source remote sensing imagery, accurate georeferencing and rigorous orthorectification of the source images are critical to ensure the derived shoreline with a precise geographic location and reliable geometric shape.

Figure 13.2 shows the processing results for an infrared color aerial photograph. The aerial photograph was orthorectified and projected to the UTM (zone 15) coordinate system, horizontally referenced to NAD83 datum. In the preprocessing phase, the orthorectified image is filtered to remove image noise and enhance the image edges along the shoreline (Fig. 13.2a). To preserve the precise position of the shoreline, an edge-preserving operator-Gaussian or median filter can be exploited to filter images without blurring the major edge features. In the preprocessing stage,

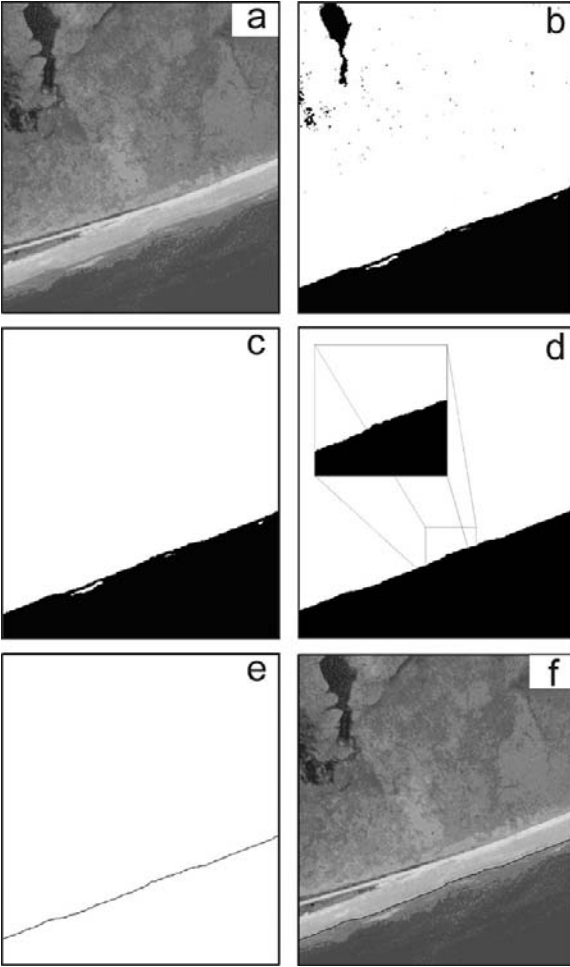


**Fig. 13.1** Data flow chart for shoreline extraction from a remote sensing image

we also utilize an anisotropic diffusion algorithm (Liu and Jezek 2004) to enhance strong edges along the shoreline and suppress the weak edges and interior variations inside the land or ocean masses.

In the segmentation/classification phase, the input image is partitioned into homogeneous land and water regions using a segmentation or classification algorithm. The border pixels between land/water regions (segments) are then delineated as the shorelines. For a panchromatic aerial photograph or a single band satellite image, a locally adaptive thresholding algorithm (Liu and Jezek 2004) is adopted for image segmentation. The thresholding method sets the threshold value dynamically according to the local characteristics to achieve a good separation between the land and ocean water. Digital image segmentation produces a binary image. For multi-spectral satellite imagery or color aerial photographs, supervised maximum likelihood algorithm, or unsupervised ISODATA algorithm can be used to classify the image into different land cover classes. The classified images can be further recoded into a binary image, showing land region and water region (Fig. 13.2b).

In the post-processing phase, the shoreline edges are differentiated from other object edges, and the shoreline edge pixels are traced into a vector representation. The segmentation or classification produces numerous connected water and land regions. A region grouping and labeling algorithm (Sonka et al. 1999) is implemented to group contiguous regions of land or water into a higher level of representation-image objects (or regions). Each object is labeled with a unique identification number, and its area is computed. Based on knowledge about the size and continuity of land and ocean masses, we can differentiate the true shoreline edge pixels from



**Fig. 13.2** Automated shoreline extraction algorithms. (a) Original infrared false color DOQQ image; (b) Recoding the classification results into binary images; (c) Removal of small, noisy water pixel regions. (d) Smoothed shoreline after morphology operation; (e) Extracted vector-based shoreline; (f) Overlay of extracted shoreline with original infrared color DOQQ image

other object edge segments. Image objects are scanned and corrected in two passes based on the knowledge about the size and continuity of land and ocean masses. In the first pass, the connected image pixels classified as water pixels are scanned, and those small water objects, which correspond to wetlands, lakes, stream, shadows, or image noise in the land area, are identified and removed by changing them into land objects (Fig. 13.2c). In the second pass, the land pixels are scanned. The small land objects scattered in the water are mainly due to whitewater foams, wave runups, small islands, or image noise. These isolated small land objects identified with a selected area threshold can be fused into the ocean water objects. After two passes

of removal of residual, isolated image objects, only two large continuous land and ocean water objects remain. This procedure effectively eliminates unwanted objects whose boundaries are not the shoreline, and therefore minimizes the editing work for cleaning up the final shoreline product. Next, the morphological operation, dilation immediately followed by erosion (Sonka et al. 1999), is used to generalize the jagged boundaries of land objects, making the shoreline morphologically smoother (Fig. 13.2d). Then, a line tracing and vectorization algorithm is employed to follow the border pixels between land and water objects and record their coordinates onto a list of vector line segments in ArcInfo Ungenerate format. Based on the Ungenerate file, an ArcInfo vector line coverage is created to represent the final MHW shoreline (Fig. 13.2e). The final product is a cartographic line coverage of the shoreline, which can be readily incorporated into a GIS database. Visual comparison between the extracted shorelines and the original digital aerial photograph shows that the position of the resulting shoreline is accurate to a pixel level (Fig. 13.2f). The degree of absolute accuracy of the shoreline varies with the spatial resolution of input digital aerial photographs and generalization level of morphology operations used in the post-processing stage.

### 13.4 Tidal Datum Referenced Shoreline from LIDAR Data

Airborne LIDAR promise an accurate and cost-effective approach to coast and shoreline mapping (Gibeaut et al. 2000, Robertson et al. 2004). The LIDAR system integrates three technology components: laser scanning system, differential GPS, and Inertial Measurement Unit (IMU). The onboard GPS receiver locates an X, Y, Z position for each laser pulse return. At the same time, an inertial navigation system (INS) monitors the attitude (pitch, roll, and yaw angles) of the laser sensor. The laser scanning system can record the range and backscatter intensity of the first and last laser returns of each laser reflection. By measuring the round trip travel time of the laser pulse from the aircraft to the ground, a highly accurate spot elevation can be calculated. LIDAR mapping of the coast and shoreline should be planned at the time when the water level of sea surface is close to a minimum elevation (e.g. neap tide), with a calm and low wave condition.

The airborne LIDAR data have been increasingly available for the coastal research community. The NOAA Coastal Services Center (CSC) has collected topographical LIDAR data along the United States coastline through a partnership program with the USGS Center for Coastal and Regional Marine Studies and the NASA Goddard Space Flight Center. LIDAR data have been acquired for a number of coastal states for several time periods. The data are available to the public through the CSC website (<http://www.csc.noaa.gov/crs/tcm/missions.html>). Airborne LIDAR data not merely provides an efficient approach to the shoreline mapping and change detection (Stockdon et al. 2002, Robertson et al. 2004), but also gives detailed, accurate near shore bathymetry and beach topography of coast areas over a broad region, allowing for analysis of micro-geomorphology of the beach and

sand dunes and quantifying sediment budget of the beach (White and Wang 2003, Zhang et al. 2005). The repeat LIDAR data of different years also render us the capability of conducting 3-D volumetric change analysis (White and Wang 2003, Finkl et al. 2005).

To derive tide coordinated shoreline, both the LIDAR DEM and the tidal datum (field) need to be converted to a common datum, for instance, the North American Vertical Datum of 1988 (NAVD88). The LIDAR data are often given in WGS84 ellipsoid height, and the tidal datum is commonly referenced to MLLW. The WGS84 ellipsoid heights of LIDAR data can be related to the NAVD88 orthometric heights (elevations) through the latest geoid model GEOID03 developed by the National Geodetic Survey (NGS) of the NOS (Parker 2003). To correlate the selected tidal datum to the LIDAR DEM, the tidal datum values also need to be converted to elevation values relative to the orthometric datum NAVD88. At a tidal gauge station, tidal datum elevations can be linked to NAVD88 datum through precise measurement of the horizontal and vertical positions of the benchmarks around the tide gauge stations. In addition, NGS developed a software tool, VDatum, to convert the height measurements between different datums. To make a connection between NAVD88 and MHW, this tool first transform the orthometric datum to local mean sea level (MSL). The difference, NAVD88-to-MSL field, is the sea surface topography, which is modeled by spatial interpolation of values at GPS-referenced tidal benchmarks. Then, the local MSL is linked to MLLW by hydrodynamic tidal model like TCARI (Hess 2003a,b).

This chapter presents two alternative methods for deriving shorelines from a LIDAR DEM. The first method is based on the combination of contouring, line selection with a length threshold, and line smoothing and generalization. Previous studies reported that the general-purpose contouring software routines often give broken, short, and noisy shoreline segments. A great deal of manual editing or re-digitizing work was involved in creating the final clean shoreline representation (Smyth et al. 2003, Parker 2003, Robertson et al. 2004). To achieve a continuous shoreline of cartographical quality, we combine a number of operations to optimize the shoreline extraction process as shown in Fig. 13.3. The data processing procedure can be summarized as the following steps:

- Filter the LIDAR DEM with a  $3 \times 3$  median. It can be realized by using ArcGIS grid focal function.
- Create a difference grid by subtracting the tidal datum surface from the LIDAR DEM after both are converted to the elevation values referenced to NAVD88.
- Contour zero values of the difference grid. In ArcGIS, contouring can be conducted only along a single specified value, instead of deriving a series of contour lines by specifying a base contour line and contour intervals in other software packages. This saves the computation time and avoids the manual editing work to eliminate non-zero contours.
- Select and delete short, noisy false shoreline segments with a specified length threshold.
- Smooth the shoreline using the Douglas-Peucker algorithm or a bend smoothing algorithm, which are available in ArcGIS as two options for line generalization.

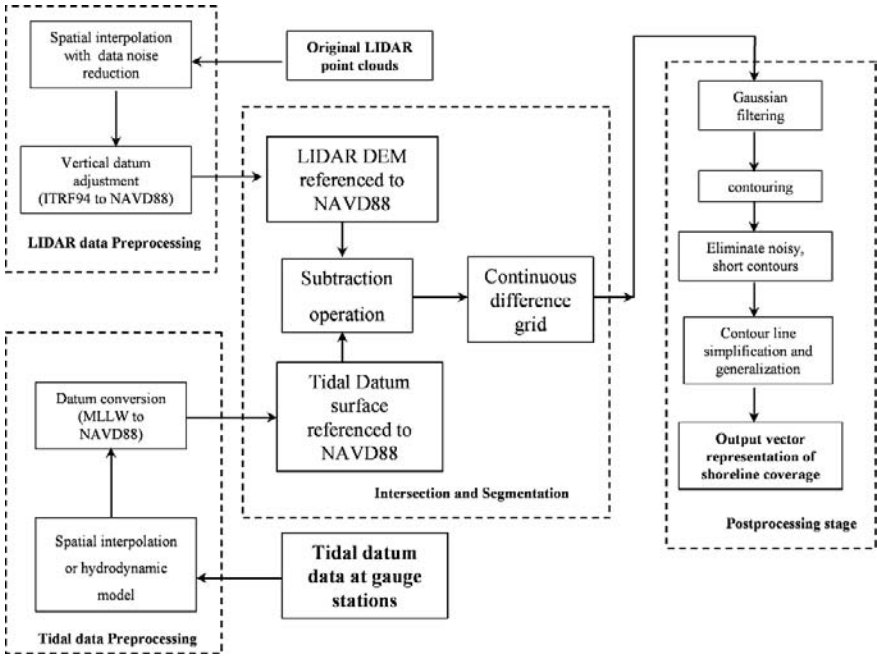
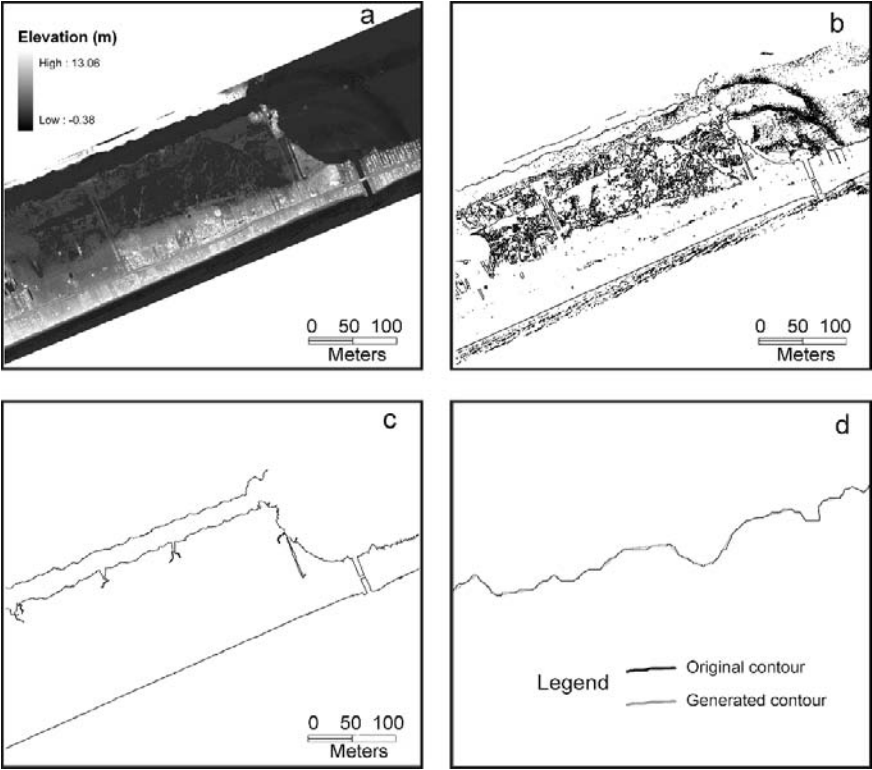


Fig. 13.3 Data flow chart of the contouring method for shoreline extraction

This method is demonstrated with a small area in the Galveston Bay, Texas. The coastal area in this example is characterized by relatively straight, sandy, barrier island beaches. All the processing steps are performed in ArcGIS environment, and the processing results are shown in Fig. 13.4. Before applying the shoreline extraction algorithms, the LIDAR measurements are projected to the UTM (zone 15) coordinate system, horizontally referenced to NAD83 datum. The LIDAR DEM is first converted to elevation values with reference to NAVD88. A  $3 \times 3$  median filter is applied to the LIDAR DEM to remove data noise (Fig. 13.4a). For this small study area, the tidal datum surface is assumed to be a level plane with a constant elevation. The constant tidal datum MHW is determined to be 0.36 m relative to NAVD88 through precise measurements of the horizontal and vertical positions of the benchmarks near tide gauge station-Galveston Pier 21. It should be pointed out that the use of a constant tidal datum value for a large region could lead to error in shoreline position determination. In the case of a large coastal region, a two-dimensional tidal datum surface should be modeled and computed using a numerical hydrodynamic model or spatial interpolation technique like TCARI (Hess 2003a,b).

Due to the contamination of the LIDAR measurements by waves and runups around the water line, thick debris deposits of sargassum, the very subtle topography variations of the sand berm crests and dunes, variations in vegetation height, erroneous MHW contours are created in the initial contouring step (Fig. 13.4b). These erroneous short MHW contours are eliminated by using a length threshold (Fig. 13.4c). Douglas-Peucker generalization method is applied to smooth the



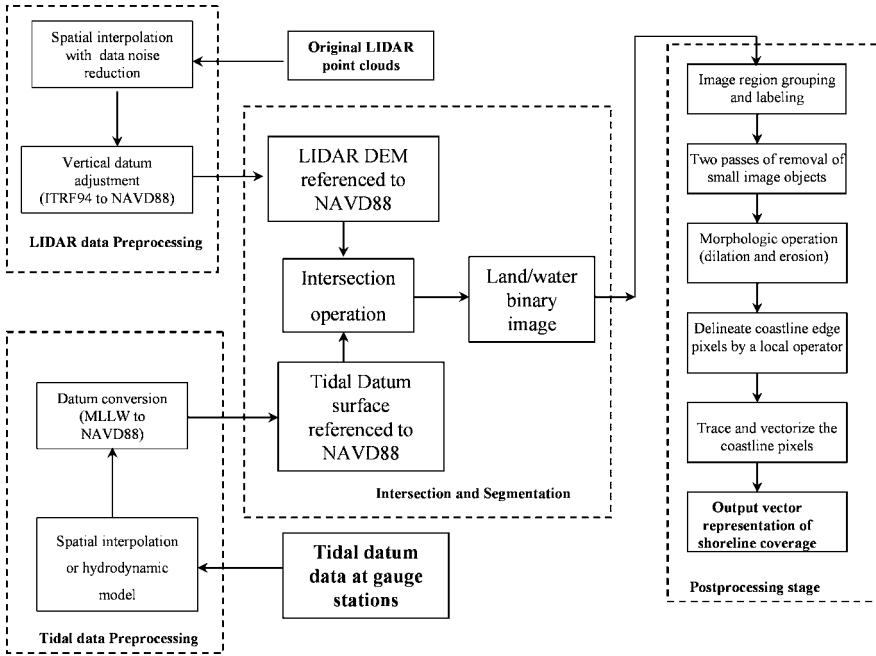


**Fig. 13.4** Contouring method for extracting shoreline from LIDAR DEM. (a) LIDAR DEM; (b) 36 cm contours derived from LIDAR DEM; (c) Shorelines selected from the contours with a length threshold; (d) shoreline after generalization, enlarged view for the small box indicated in (c)

contours with weeding tolerance of 0.25 m. Both the median filtering of the LIDAR DEM grid and the generalization of the resultant MHW shoreline (Fig. 13.4d) can enhance the visual smoothness for cartographic representation of the shoreline.

The second shoreline extraction method for processing LIDAR data is based on the segmentation of the LIDAR DEM. Similar to the shoreline extraction method for remote sensing imagery, this method consists of three processing phases: pre-processing, segmentation and post-processing (Fig. 13.5). The primary processing steps of this method include (Liu et al. 2007):

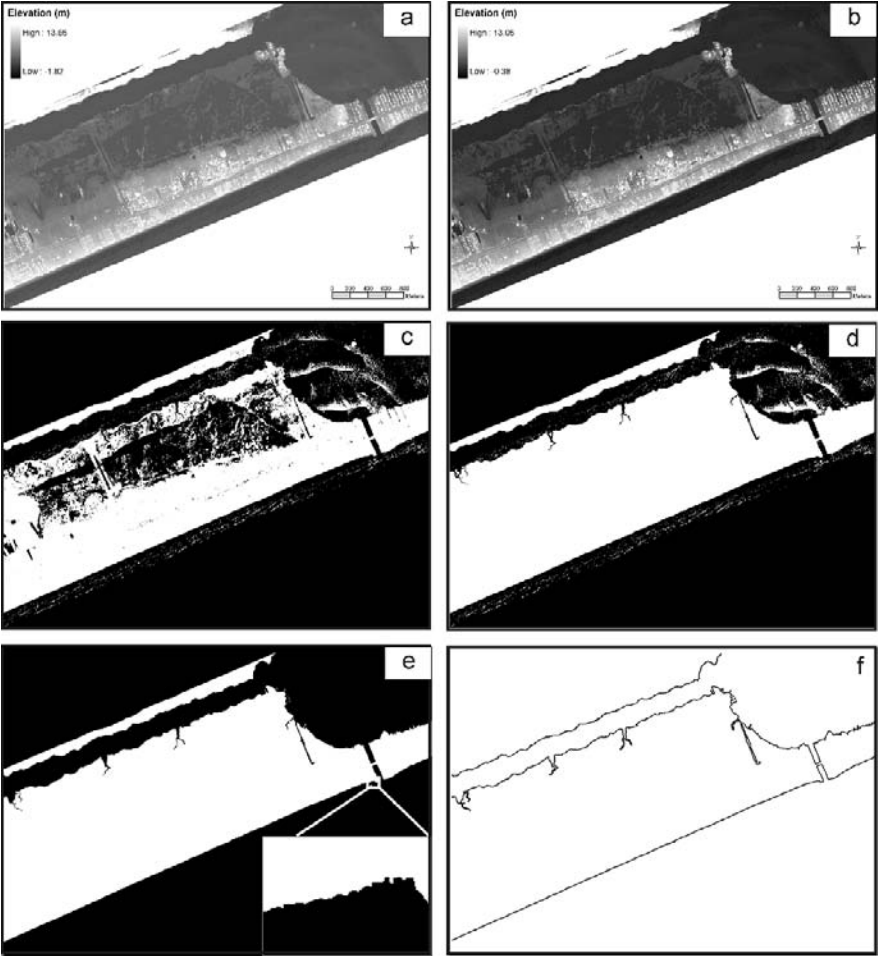
- Reduce the LIDAR DEM noise using an edge preserving filter, such as median filter (Sonka et al. 1999);
- Generate a binary grid consisting of water and land pixels, by intersecting the topographical surface of the LIDAR DEM with the reference tide datum surface;
- Group and label the binary image into water and land objects (regions) by identifying the connected water or land pixels, and calculate the area of each water or land object;



**Fig. 13.5** Data flow chart of the segmentation based method for processing LIDAR data for shoreline extraction

- Perform two passes of scans to remove small and noisy land and water objects. The first pass will identify and remove small land regions with a user specified areal threshold. The second pass will identify and remove small water regions with another areal threshold area;
- Perform mathematical morphologic operations (dilation followed by erosion) (Sonka et al. 1999) to smooth and generalize the land/water boundary; and
- Delineate the edge pixels of the land objects and trace the edge pixel into a continuous shoreline representation.

We have applied this method to extract a MHW shoreline for the upper Texas Gulf Coast. Figure 13.6 illustrates the processing steps with a 6 km stretch of the coast. In the preprocessing phase, the LIDAR DEM (Fig. 13.6a) is filtered by a  $3 \times 3$  median filter after the conversion to NAVD88 datum is completed. The purpose is to filter LIDAR measurement noise to prevent isolated and noisy shoreline segments. The median filter is an edge-preserving operator. It removes the data noise without blurring the position of the shorelines (Fig. 13.6b). In the segmentation phase, the LIDAR DEM is intersected with the tidal datum surface. We code a pixel as water, with a value of 0, if its LIDAR elevation is below the MHW tidal datum value of 0.36 m. Otherwise, the pixel is coded as land with a value of 255. This results in a binary image consisting of land and water pixels (Fig. 13.6c).

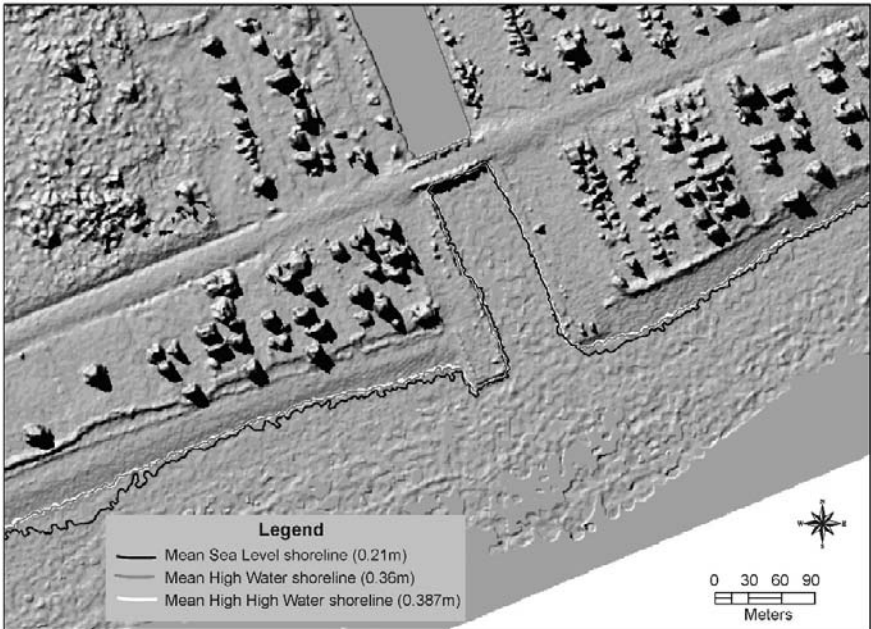


**Fig. 13.6** Segmentation based image processing method for extracting shoreline from LIDAR DEM. (a) LIDAR DEM; (b) Median filtered LIDAR DEM; (c) Binary image using the threshold value of MHW datum; (d) Grouping water objects and removing small and noisy water objects; (e) Applying morphology operation to smooth the shoreline; (f) shorelines traced and vectorized along the boundary of land objects

In the post-processing phase, the same sequence of operations as those used in processing remote sensing imagery for shoreline extraction are applied to extract vector shorelines from the binary image. The connected water or land regions in the binary image are grouped and labeled as image objects. Two passes of selective removals of small and noisy land and water objects with specified areal thresholds result in large and continuous land and water objects (Fig. 13.6d). The morphological operation smooths the shoreline (Fig. 13.6e). The final MHW shoreline product is in the format of ArcInfo vector line coverage (Fig. 13.6f). It should be

pointed out that the morphological operations will result in some level of shoreline generalization. For the purpose of cartographical representation, some degree of generalization is unavoidable although it might introduce additional uncertainty in the shoreline position. What level of error and uncertainty is acceptable depends on the application context and the required map scale of the final shoreline chart.

Shorelines based on different tidal datums may have significant shifts in horizontal placement due to beach slope characteristics. The tidal datum values (relative to NAVD88) for Galveston Pier 21 tide gauge station are: 0.36 m for MHW, 0.387 m for MHHW, 0.21 m for MSL, 0.048 m for MLW and  $-0.043$  m for MLLW. In addition to the MHW shoreline, the shoreline indicators for the MHHW and MSL datums have also derived. As shown in Fig. 13.7, the horizontal position of the LIDAR-derived shoreline varies with the selected tidal datum. The MHHW shoreline is located slightly landward of the MHW shoreline. In the most sections, the MHW shoreline and MHHW shoreline are overlapping and cannot be differentiated each other. This is because the spatial resolution (1 m) and the vertical accuracy (0.15 m) of the LIDAR data are not adequate to sense the small difference between MHW and MHHW datums. The MSL shoreline is obviously located seaward of the MHW shoreline. Also, it should be pointed out that the accuracy and reliability of the MSL shoreline is not as good as the MHW shoreline. The reasons are twofold. First, the beaches around the MSL line have a significantly lower



**Fig. 13.7** MHW, MHHW and MSL shorelines overlaid on the hill-shaded relief image of the LIDAR DEM

surface slope than the beaches around the MHW line. Second, the MSL datum is very close the water level at the time when the LIDAR data were acquired and easy to be contaminated by wave runups. For our LIDAR data set, the MLW (0.048 m) and MLLW ( $-0.043$  m) shorelines cannot be determined because the water level (0.134 m) on the LIDAR data acquisition day was higher than MLW and MLLW datums.

By using a Monte Carlo simulation technique (Openshaw 1989, Openshaw et al. 1991), the accuracy of the horizontal position of the LIDAR derived shoreline is evaluated. The shoreline error can be conceived of as a deviation of the derived horizontal position from the true position. The occurrence of the positional error is mainly related to inherent uncertainty in the vertical and horizontal measurements of the LIDAR data. Other potential sources of error include datum conversion, projection, and interpolation. Raw measurements of the LIDAR points used in this research have a horizontal accuracy of 0.8 m (RMSE) and a vertical accuracy of 0.15 m over the bare beach. It is a bulk error estimate representing all sources of error for the LIDAR system. The 0.8 m horizontal error in LIDAR points will be directly transferred to 0.8 m shoreline position error. The vertical error in LIDAR points would be propagated and inflated in the shoreline extraction process, causing the location of the shoreline to move landward or seaward. The error inflation factor is determined by the foreshore beach slope. For a beach with a gentle surface slope, a slight vertical measurement error would be amplified and translated to a large error in shoreline position. Overall, the error in the tidal datum determination and conversion is tiny. We used a constant value to represent the MHW datum for the study area, rather than a varying tidal datum field. The difference in MHW at the two gauge stations (Galveston Pier 21 and Sabine Pass) bracketing the study area is about 0.015 m, which can be regarded as the uncertainty level of the MHW datum for this region. Considering the high sampling density of the LIDAR points (about 1 m), the spatial interpolation and projection error is negligible. The surface slope around the MHW shoreline approximately ranges from 5 to 10% rise. A vertical error of 0.15 m for the LIDAR data combined with 0.015 m uncertainty in the MHW datum may cause the error in the shoreline's horizontal position of 1.65–3.3 m. Along with the horizontal error of 0.8 m for LIDAR points, the overall positional error of the MHW shoreline would be 2.45–4.1 m. The uncertainty and error of the shoreline horizontal position varies spatially, depending on the magnitude of surface slope. The beaches with a lower foreshore surface slope tend to have a larger uncertainty and error in the shoreline position. The effect of input data uncertainty and possible error propagation in the shoreline extraction process is simulated and quantified using the Monte Carlo simulation technique. Confidence intervals and summary error statistics are calculated for each section of the extracted shoreline (Liu et al. 2007). The analysis for the Upper Texas Gulf Coast suggests that the horizontal position of the LIDAR derived shoreline is accurate within 4.5 m at the 95% confidence level (Liu et al. 2007). It is superior to the shorelines obtainable from traditional aerial photography, which has a typical accuracy of about 6–7 m (Leatherman 1983, Crowell et al. 1991).

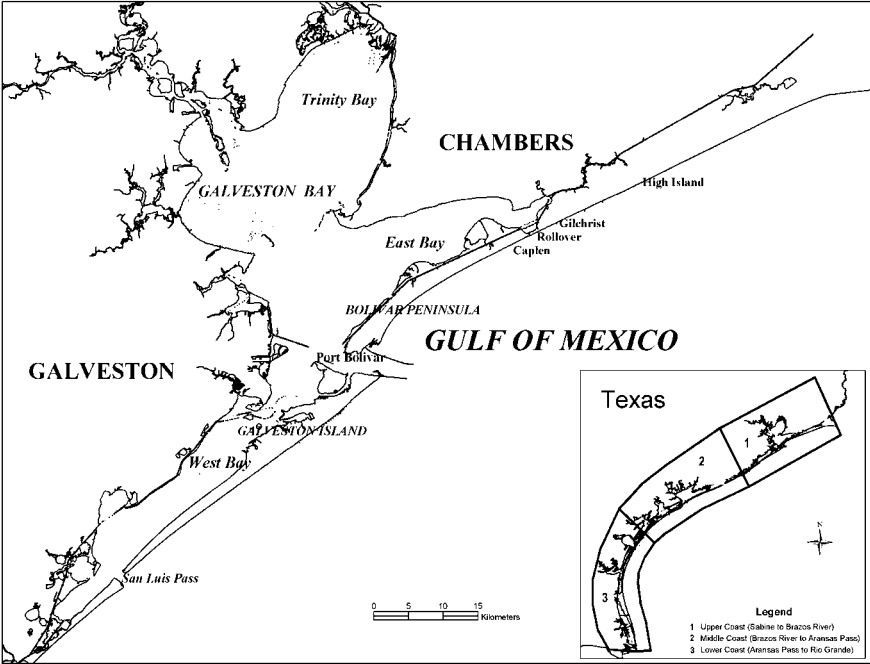
### 13.5 Applications in the Upper Texas Gulf Coast

Scientists have investigated the impacts of global climate changes and sea level rise on shoreline erosion (Leatherman and Douglas 2003). Global sea level has risen about 20 cm in the last century (Leatherman and Douglas 2003). Relative rates of rise have more than doubled this amount in Texas coast zone due to substantial land subsidence caused by excessive withdrawal of ground water and extraction of oil and natural gases (Paine and Morton 1993, Morton 1997). Average rates of beach erosion along the Texas Gulf coast were estimated to be above 2 m per year, much higher than in the US east coast (1 m per year). Future sea levels are projected to rise significantly faster than occurred in the 20th century, and acceleration of the present rate of shore recession is expected (Leatherman and Douglas 2003).

In terms of time scale, shoreline changes can be divided into three categories: long-term, short-term, and episodic changes. Long-term changes occur over tens to thousands of years; short-term change refers to movement occurring over several seasons to 5 or 10 years; and episodic changes occurs in response to a single storm. Pioneering work on the analysis of long-term shoreline changes in the Texas Gulf coast has been carried out by scientists at the Bureau of Economic Geology in University of Texas at Austin. By digitizing topographical maps and manually tracing aerial photographs, historical shorelines have been compiled for most parts of the Texas Gulf coast for 1937, 1956, 1965, 1974, and 1991 (Paine and Morton 1993). The digitized topographic sheets (T-sheets) of the National Ocean Service (NOS) provided the shoreline position of the Texas coast dating back to 1856. By using moderate resolution satellite data, high-resolution digital aerial photographs and airborne LIDAR, this research examines the shoreline change rates in recent decades for the upper Texas coast.

The upper Texas coast is the stretch from Sabine Pass in the border with Louisiana west to the Brazos River mouth, including the estuarine drainage area of Galveston Bay (Fig. 13.8). It is characterized by extensive western Louisiana-type marshes, coastal prairie, humid flat woods inland, and barrier islands. The shoreline in the upper Texas coast shoreline experienced a higher level of short-term and episodic fluctuations than the middle and lower Texas coasts, due to frequent hurricanes and tropical storms (Morton 1997).

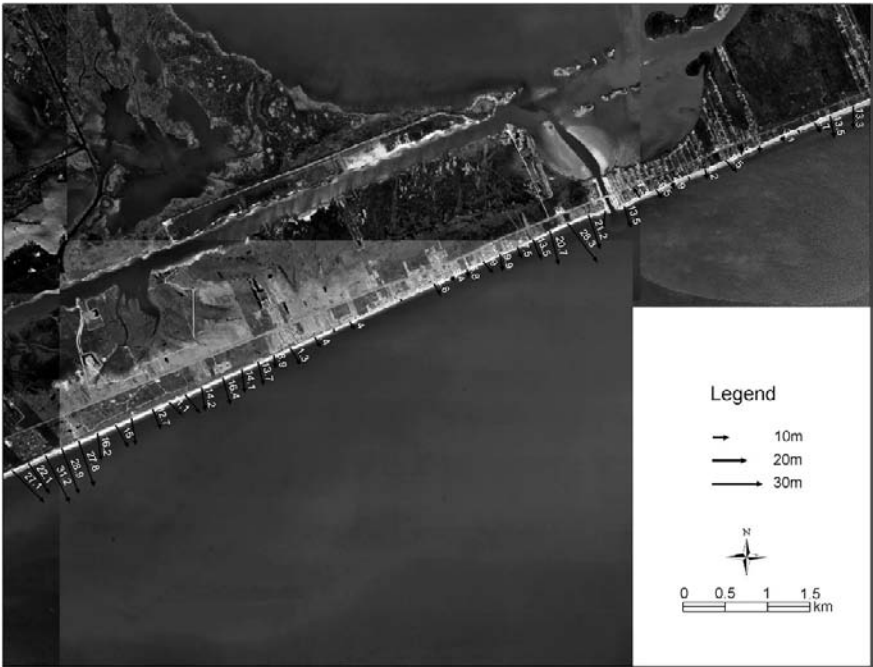
The airborne LIDAR data used in this research were acquired on October 16, 1999 by NASA's Airborne Topographic Mapper (ATM) laser instrument. The flights were timed to occur within a few hours of low tide, when the beach was most exposed. The shoreline LIDAR surveys cover a swath approximately 250 m wide, and the spacing between data points is between 1 and 2 m on the ground. The surveyed swath covers the beaches, fore dunes, and the a few rows of houses landward. In some parts of the coast, such as the Rollover Pass area on the Bolivar Peninsula, the data swath can extend a few kilometers inland, covering salt- and brackish-water marshes, tidal flats, and adjacent uplands. By applying the shoreline extraction method, a MHW datum referenced shoreline is derived from the 1999 LIDAR data. This MWH shoreline is compared with the 1977 NOS T-sheet shoreline to estimate shoreline change rates in the past two decades. The NOS T-sheet TP-00230



**Fig. 13.8** The upper Texas Gulf coast

was compiled at the scale 1:20,000 from tide-controlled aerial photographs flown on March 1, 1977. The HWL depicted on the NOAA T-sheets is a close approximation of the historical mean high water line (MHWL). Figure 13.9 shows the moving direction and distance of the oceanfront shoreline of the Bolivar Peninsula observed 22 years apart. Comparison of two sets of shorelines shows that most parts of the shoreline in this region are quite stable or experienced slight advancing. The average advancing rate is less than 1.5 m/year.

Landsat satellite image data are utilized to identify the erosion or accretion hotspots during 1990–2000. Each Landsat covers a ground area of 185 km by 185 km, and two image scenes are used to cover the entire upper Texas coast. Two Landsat 5 TM image scenes acquired on December 8, 1990 and two Landsat 7 ETM+ image scenes acquired on January 10, 2000 are used in the analysis. The Landsat 5 TM imagery has 7 multi-spectral bands with 30 m spatial resolution. The Landsat 7 ETM+ imagery has a panchromatic band and 7 multi-spectral bands. The panchromatic band has a spatial resolution of 15 m, and 6 non-thermal bands have a spatial resolution of 30 m. We acquired 41 ground control points (GCPs), and an affine transformation was applied to the two sets of Landsat images for refining geolocation. After georeferencing operation, the Root Mean Squares Error (RMSE) of the Landsat images has been reduced from 130 m to 9.77 m, reaching sub-pixel level accuracy. The images are projected into UTM (zone 15) coordinate system referenced to NAD83 datum. The locally adaptive thresholding algorithm

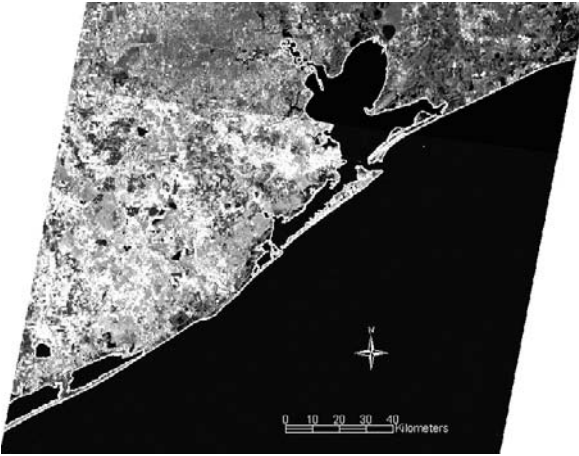


**Fig. 13.9** Shoreline variations during 1977–1999 by comparing the 1977 NOS T-sheet shoreline with the 1999 LIDAR derived MHW shoreline. Background images are 1995 infrared aerial photographs

was employed to segment the near infrared band (band 4) of the orthorectified Landsat images. Then, the image processing chain described above is applied, and two complete sets of shorelines for 1990 and 2000 have been derived (Figs. 13.10 and 13.11). The positional accuracy of shorelines extracted from the Landsat imagery is estimated to be about 50 m. The comparison of two sets of shorelines 10 years apart reveals the most rapidly changing sections of the coast (hot spots) (Fig. 13.12). The shorelines around the west Galveston Island, Atkinson Island, around Matagorda Bay, and near Bryan Beach State Park advanced or retreated as large as 1 km. The dramatic advances of the beaches and sand dunes in the west Galveston Island, around the Bryan Beach State Park, and the southwest Bolivar Peninsula are due to the sediment deposition or beach nourishment projects. Huge amount of sand have been carried west along the shore of Bolivar Peninsula and accumulated north of the Galveston Jetty at the Galveston Entrance Channel (Fig. 13.12). Due to the limitations of the spatial resolution and the positional accuracy of the derived shorelines, the Landsat imagery is not adequate for reliably resolving and detecting the shoreline variations less than 50 m. High resolution imagery is required to measure the short-term shoreline changes.

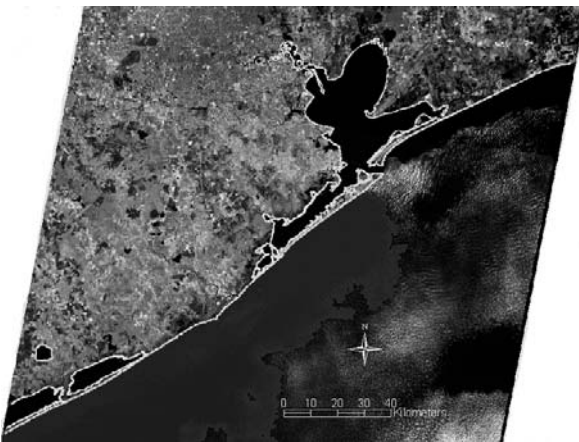
To resolve possible short-term shoreline variations, we collected high resolution digital aerial photographs for 1995 and 2000, covering the upper Texas coast.



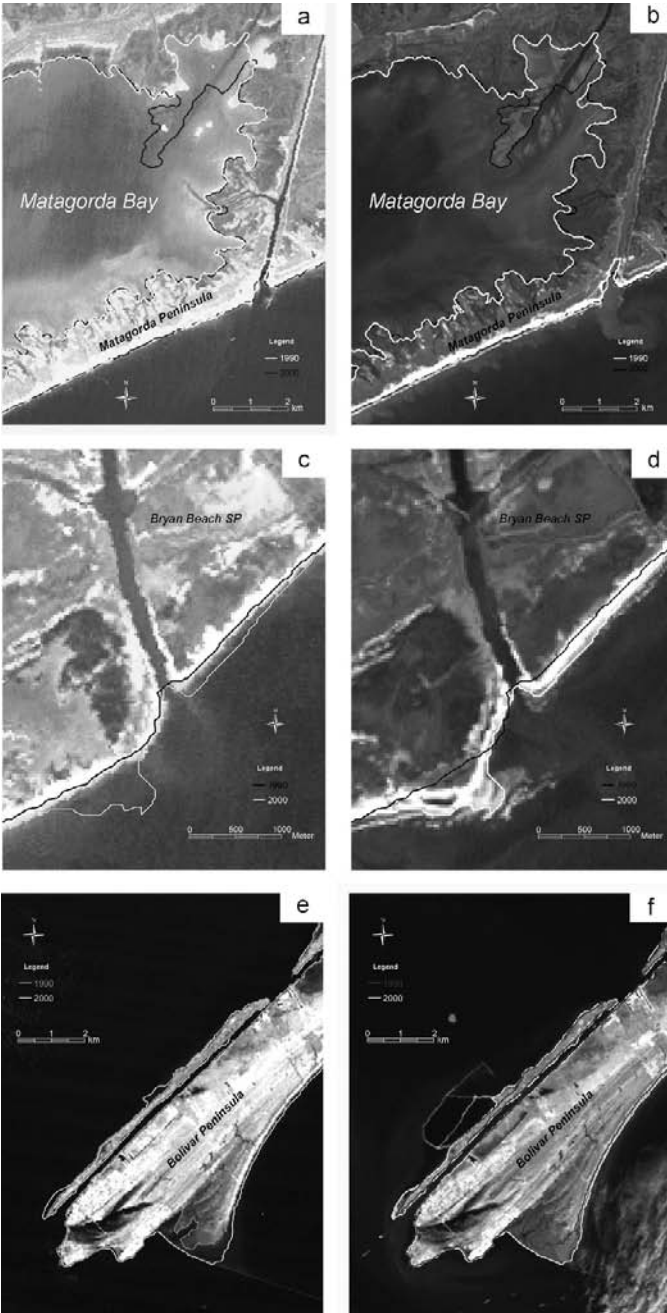


**Fig. 13.10** Shoreline derived from the 1990 Landsat 5 TM near infrared band

The 1995 digital aerial photographs are known as Digital Orthophoto Quarter Quadrangles (DOQQs) distributed by the Texas Natural Resource System data distribution web site. The distortions and displacement in the image due to sensor orientation and terrain relief have been removed during the orthorectification process by using digital elevation models, ground control points, and camera calibration data. The 1995 DOQQs have a 1 m spatial resolution, and each image covers quarter-quadrangle (about 7 km by 7.5 km). The images are in the UTM (zone 15) coordinate system with reference to NAD83 datum. The horizontal positional accuracy of the DOQQs is estimated to be about 4–5 m. The 1995 DOQQs are scanned from near infrared color film, producing three digital bands: near infrared, red, and green bands. The 2000 digital aerial photographs were acquired in January 2000 by the



**Fig. 13.11** Shoreline derived from the 2000 Landsat 7 ETM+ near infrared band



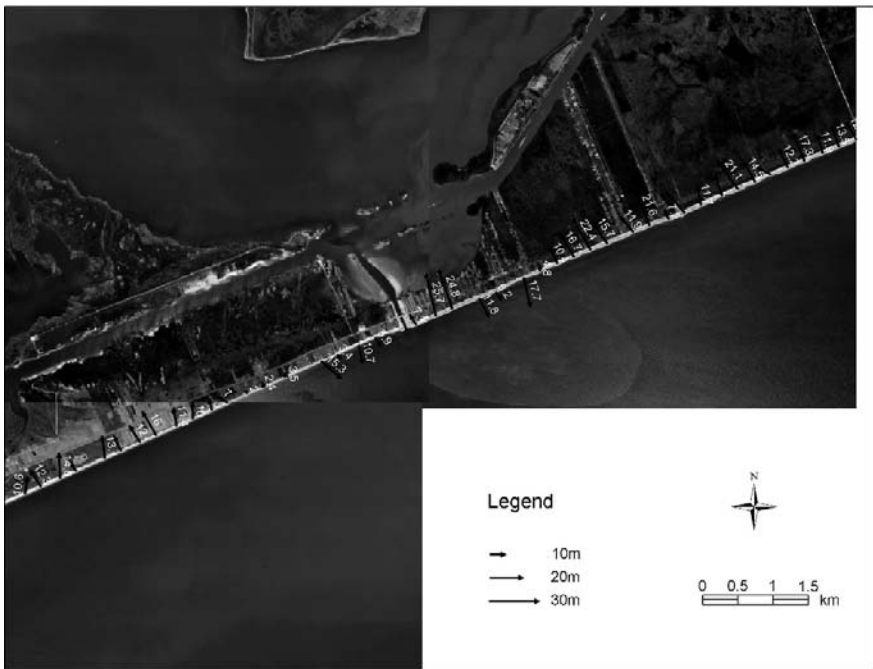
**Fig. 13.12** Shoreline changes around Matagorda Bay, Bryan Beach State Park, and the west end of Bolivar Peninsula. (a) 1990 Landsat image of Matagorda Bay; (b) 2000 Landsat image of Matagorda Bay; (c) 1990 Landsat image of Bryan Beach State Park; (d) 2000 Landsat image of Bryan Beach State Park. (e) 1990 Landsat image around Port Bolivar; (f) 2000 Landsat image around Port Bolivar

Houston-Galveston Area Council. The ground resolution of the 2000 orthophotos is 0.5 m, and each image covers about 2.5 km by 4 km ground area. The distortions and displacement of features in the image induced by terrain relief and camera orientation have been mathematically corrected during the orthorectification process. The horizontal positional accuracy is about 1.5 m. The digital images were scanned from true natural color film diapositives, resulting in three digital bands: red, green, and blue bands. The orthophotos are provided in State Plane coordinate System (Texas South Central Zone, fipscode 4204), referenced to NAD83 datum. The shorelines extracted from 2000 orthophotos are projected into the UTM (zone 15) coordinate system in order to compare with those derived from the 1990 DOQQs.



Fig. 13.13 Shoreline draped on the 1995 infrared color aerial photographs

We used the image processing chain described above to automatically derive the shorelines from the 1995 infrared false color DOQQs and the 2000 natural true color orthophotos. Maximum likelihood supervised classification method was used to first classify the digital aerial photograph images into a number of land cover categories. Then, these land cover types were recoded into binary images, consisting of land pixels and water pixels. The remaining processing steps are similar to those used to process the Landsat images. Figure 13.13 shows the comparison of shorelines respectively derived from the 1995 infrared color aerial photos and the 2000 natural color aerial photos. Within about 13 km stretch of the coast, the erosion area is 128052 m<sup>2</sup>, the accretion area is 25151 km<sup>2</sup>, and the net land loss is 102901 m<sup>2</sup>. Overall, the shoreline changes are dominated by a retreating process, and only a small stretch of the shoreline advanced seaward during 1995–2000 (Fig. 13.14). The maximum erosion rate is 5.1 m/year (25.7 m within 5 years), and most sections of the shoreline in this region experienced erosion at a rate of above 2 m/year. The accelerated short-term erosion during 1995–2000 was mainly caused by two significant tropical storms. Tropical storm Josephine in October 1996 and tropical storm Frances in September 1998 destroyed many beachfront structures, eroded the dunes and beaches, and caused as great as 25 m of scarp and vegetation line retreat. Large volumes of beach sand were swept inland through the Rollover Pass and permanently deposited in the east Galveston Bay and the GIWW (Gulf Intra-coastal Waterway) in the vicinity. Emergency erosion control efforts have been made to



**Fig. 13.14** Shoreline variations during 1995–2000 around the Rollover Pass

stem shoreline retreat brought to the forefront by tropical storms. Large round hay bales were placed after Josephine, and sand-filled geotextile tubes were installed along the oceanfront shoreline of Galveston Island and the Bolivar Peninsula in 2000 following tropical storm Frances. Small-scale beach nourishment projects have been also conducted, and muddy sand dredged behind Rollover pass was placed on the beach. The measured erosion rate represents a net effect of the storm induced erosion and beach nourishments.

## 13.6 Conclusions

This chapter has presented numerical algorithms and automated methods for automatically extracting shoreline features from remote sensing imagery and airborne LIDAR data. The methods are able to create continuous shorelines with the greatest amount of geometric details and high positional accuracy. The applications to the upper Texas Gulf Coast show that these methods are efficient, accurate, objective and replicable. Compared with conventional manual tracing and digitizing method, these methods represent a substantial technical improvement.

The dry/wet high water line on digital aerial photographs and satellite images can be automatically extracted at a pixel level as shoreline indicators. The absolute positional accuracy of shorelines extracted from remote sensing imagery depends on the image spatial resolution, the quality of image orthorectification and georeferencing, and the actual water level at the time of image acquisition. The primary challenge for the remote sensing imagery as the shoreline source is the difficulty in compensating the difference between the MHW datum and the actual water level when the imagery was acquired.

The airborne LIDAR technology represents an efficient and cost-effective approach to shoreline mapping. Our analysis results demonstrate that spatially detailed, tidal datum referenced shorelines can be automatically derived from the LIDAR data. The accuracy of the shoreline horizontal position attainable from the LIDAR data is estimated to be within 4.5 m at the 95% confidence level, which mainly associated with the vertical error of the LIDAR DEM and the surface slope of the foreshore beach. Our experiments show that the MHHW shoreline is virtually the same as the MHW shoreline in the case of the upper Texas coast, given the spatial resolution and vertical accuracy of the current topographical LIDAR technology. Although it is possible to derive the MSL shoreline from the LIDAR DEM, its accuracy and reliability is limited due to the very gentle surface slope in the inter-tidal zone and the contaminations of wave runups. In practice, it is difficult to derive the MLW and MLLW shorelines from the topographical LIDAR data. The actual water level is often higher than the MLW or MLLW datum when the LIDAR survey was conducted. The marine LIDAR system, the Scanning Hydrographic Operational Airborne LIDAR Survey (SHOALS), can measure the depth of water down to about 50 m in the moderately clear, non-turbulent, near shore coastal waters (Irish and Lillycrop 1999, Lillycrop et al. 2001). It may provide the capability of mapping the MLW and MLLW shorelines and the bathymetry of ocean bottom.

To investigate shoreline variations in the upper Texas Gulf Coast, the automated numerical methods have been employed to process multi-temporal remote sensing imagery and airborne LIDAR data. During 1990–2000, the large scale land accretions have been detected at a number of locations in the upper Texas coast by using the Landsat satellite imagery. By using two sets of high-resolution orthorectified digital aerial photographs, we also measured and quantified the short-term shoreline change rate for the Bolivar Peninsula during 1995–2000. The short-term shoreline change was dominated by the strong erosion process at a rate of 2–5 m/year. The 1999 MHW shoreline derived from airborne LIDAR is compared with the 1977 NOS T-sheet MHW shoreline. The comparison suggests that the oceanfront shoreline of the Bolivar Peninsula was relatively stable or experienced slight advancing with a rate of less than 1.5 m/year during the past two decades. This averaged change rate pattern in the past two decades is in strong contrast to the short-term erosion dominated change (2–5 m/year) during 1995–2000 detected from the orthorectified aerial photographs. To provide an accurate, timely prediction of shoreline change for disaster warning and resource management, further investigation on the magnitude and causes of short-term and episodic shoreline changes need to be conducted with high resolution remote sensing data in the future.

**Acknowledgement** This research is funded by the NOAA Sea Grant Program #NA16RG1078.

## References

- Crowell M, Leatherman SP, Buckley MK (1991) Historical shoreline change, error analysis and mapping accuracy. *J Coast Res* 7:839–852
- Finkl CW, Benedet L, Andrews JL (2005) Interpretation of seabed geomorphology based on spatial analysis of high-density airborne laser bathymetry. *J Coast Res* 21:501–514
- Gibeaut JC, White WA, Hepner T, Gutierrez R, Tremblay TA, Smyth R, Andrews J (2000) Texas Shoreline Change Project; Gulf of Mexico Shoreline Change from the Brazos River to Pass Cavallo. A report of the Texas Coastal Coordination Council pursuant to NOAA award NA870Z0251, Bureau of Economic Geology, The University of Texas at Austin, Austin
- Graham D, Sault M, Bailey C (2003) National ocean service shoreline: past, present, and future. *J Coast Res* SI:14–32
- Hess KW (2002) Spatial interpolation of tidal data in irregularly-shaped coastal regions by numerical solution of Laplace's equation. *Estuar Coast Shelf Sci* 54:175–192
- Hess KW (2003a) Tidal datums and tide coordination. *J Coast Res* SI:33–43
- Hess KW (2003b) Water level simulation in bays by spatial interpolation of tidal constituents, residual water levels, and datums. *Cont Shelf Res* 23:395–414
- Irish LJ, Lillycrop WJ (1999) Scanning laser mapping of the coastal zone: the SHOALS system. *ISPRS-J Photogramm Remote Sens* 54:123–129
- Leatherman S (1983) Shoreline mapping: comparison of techniques. *Shore Beach* 51:28–33
- Leatherman S, Douglas B (2003) Seal level and coastal erosion require large-scale monitoring. *EOS T Am Geophys Union* 84:13–16
- Li R, Di K, Ma R (2003) 3-D shoreline extraction from IKONOS satellite imagery. *Mar Geodesy* 26:107–115
- Lillycrop WJ, Johnson P, Lejdebrink U, Pope RW (2001) Airborne LIDAR hydrography: requirements for tomorrow. *Proc Oceanology International, Miami*, pp 5–7

- Liu H, Jezek K (2004) Automated extraction of coastline from satellite imagery by integrating Canny edge detection and locally adaptive thresholding methods. *Int J Remote Sens* 25: 937–958
- Liu H, Sherman D, Gu S (2007) Automated extraction of shorelines from airborne light detection and ranging data and accuracy assessment based on Monte Carlo simulation. *J Coast Res* 23:1359–1369
- Morton R (1991) Accurate shoreline mapping: past, present, and future. In: Nicholas K, Kathryn G, Kriebel D (eds) *Proceedings of a specialty conference on quantitative approaches to coastal sediment processes (coastal sediments 1991)*, vol 1. ASCE, New York, pp 997–1010
- Morton R (1997) Gulf shoreline movement between Sabine Pass and the Brazos River, Texas, 1974–1996. In: *Geological Circular 97-3*. The University of Texas at Austin, Austin
- Morton R, Miller T, Moore L (2005) Historical shoreline changes along the US Gulf of Mexico: a summary of recent shoreline comparisons and analyses. *J Coast Res* 21:704–709
- Openshaw S (1989) Learning to live with errors in spatial databases. In: Goodchild M, Gopal S (eds) *Accuracy of spatial databases*. Taylor & Francis, London, pp 79–104
- Openshaw S, Charlton M, Carver S (1991) Error propagation: a Monte Carlo simulation. In: Masser I, Blackemore M (eds) *Handling geographical information: methodology and potential applications*. John Wiley & Sons Inc, London, pp 78–101
- Paine J, Morton R (1993) Historical shoreline changes in Copano, Aransas, and Redfish Bays, Texas Gulf Coast. In: *Geological Circular 93-1*. The University of Texas at Austin, Austin
- Pajak MJ, Leatherman SP (2002) The high water line as shoreline indicator. *J Coast Res* 18: 329–337
- Parker BB (2003) The difficulties in measuring a consistently defined shoreline: the problem of vertical referencing. *J Coast Res* SI:44–56
- Robertson W, Whiteman D, Zhang K, Leatherman SP (2004) Mapping shoreline position using airborne laser altimetry. *J Coast Res* 20:884–892
- Shepard F, Wanless HR (1971) *Our changing coastline*. McGraw-Hill, New York
- Smyth R, Gibeau J, Andrews J, Hepner T, Gutierrez R (2003) *The Texas shoreline change project: coastal mapping of west and east bays in the Galveston bay system using airborne LIDAR*. Prepared for the Texas General Land Office, GLO contract number 02-520 C
- Sonka M, Hlavac V, Boyle R (1999) *Image processing, analysis, and machine vision*, 2nd edn. Brooks/Cole, Albany
- Stockdon HHF, Sallenger AH, List JH, Holman RA (2002) Estimation of shoreline position and change using airborne topographic LIDAR data. *J Coast Res* 18:502–513
- Szmytkiewicz M, Biegowski, Kaczmarek L (2000) Coastline changes nearby harbour structures: comparative analysis of one-line models versus field data. *Coast Eng* 40:119–139
- White SA, Wang Y (2003) Utilizing DEMs derived from LIDAR data to analyze morphologic change in the North Carolina coastline. *Remote Sens Environ* 85:39–47
- Zeidler RB (1997) Continental shorelines: climate change and integrated coastal management. *Ocean Coastal Manage* 37:41–62
- Zhang K, Whiteman D, Leatherman S, Robertson W (2005) Quantification of beach change caused by Hurricane Floyd along Florida's Atlantic coast using airborne laser surveys. *J Coast Res* 21:123–134

# Chapter 14

## Remote Sensing of Coastal Mangrove Forest

Le Wang and Wayne P. Sousa

Mangroves, once occupied 75% of the world's tropical and subtropical coastlines, are seriously threatened by coastal development projects and accelerated climate change, e.g. sea-level rise. In this study, we aim to attain three objectives: (1) to develop effective methods for discriminating mangrove species from IKONOS imagery; (2) to determine an optimal season for capturing the spectral and textural difference among mangrove species; (3) to investigate the capability of hyperspectral data for distinguishing mangrove species. Our study site is in Panama. Two scenes of IKONOS imagery respectively acquired during dry and wet seasons were employed. A Clustering-Based Neural Network (CBNN) classifier was developed and its performance was compared with two other conventional classifiers: Back-Propagation Neural Networks classifier (BPNN) and Maximum Likelihood Classifier (MLC). Results indicate that CBNN is superior to BPNN and MLC in employing textural information. Rainy season is better than dry season for mangrove species classification. To investigate the third objective, a one-way ANNOVA followed by linear discriminate analysis (LDA) method was devised for analyzing the leaf-level hyper-spectral reflectance. A kappa value of 0.9 was achieved in classifying leaves from three species. Four narrow-band indices were tested for detecting stress conditions associated with the three mangrove species.

### 14.1 Introduction

Mangrove forests are highly productive ecosystems that typically dominate the intertidal zone of low energy tropical and subtropical coastlines (Lugo and Snedaker 1974, Kathiresan and Bingham 2001). The constituent species in these forests are often differentially distributed with distance from the water's edge, forming zones of differing species composition perpendicular to the intertidal gradient. Mangrove habitats and the organisms they support are of significant ecological and economic value (Lugo and Snedaker 1974, Tomlinson 1986, Hutchings and Saenger 1987,

---

L. Wang (✉)

Department of Geography, State University of New York at Buffalo, Buffalo, NY 14261, USA  
e-mail: lewang@buffalo.edu



Hogarth 1999, Kathiresan and Bingham 2001). Among other values, mangroves (1) provide vital habitat for a wide variety of animal and plants species, many of them uniquely adapted to mangrove environments, and some of them rare and/or endangered, (2) function as nursery and feeding grounds for many species of commercially valuable fishes, crustaceans, and molluscs, (3) are an important source of carbon to detritus-based food webs in adjacent coastal waters, (4) stabilize deposited sediments, reducing shoreline erosion, (5) buffer the impact of storm waves and floods on inland areas, and (6) trap nutrients and sediments in runoff from upland areas, helping to maintain the quality of estuarine and nearshore waters.

However, mangrove forests' health and persistence are seriously threatened by coastal development projects and various forms of non-renewable exploitation (Saenger et al. 1983, Ellison and Farnsworth 1996, Farnsworth and Ellison 1997). In recent decades, mangrove habitats have suffered dramatic declines in area (Saenger et al. 1983, Farnsworth and Ellison 1997, Ellison and Farnsworth 2001, Alongi 2002) due to coastal development, non-renewable resource exploitation (e.g. clear cutting, mining, aquaculture), pollution, high rates of sedimentation, and alterations of hydrology. Alongi (2002) estimated that as much as a third of the world's mangrove forest have been lost in the past 50 years. In the Caribbean, the rate of mainland mangrove deforestation is estimated to be 1.4–1.7% annually (Ellison and Farnsworth 1996, FAO 2003), comparable to the rates documented for threatened tropical rainforests. Thus, there is an increasing need to monitor and assess mangrove forest structure and dynamics, both to gain a better understanding of their basic biology and to help guide conservation and restoration efforts. The ability to accurately map mangrove species with the tools of remote sensing would greatly assist in this effort.

Although remote sensing has been used to map many of the land cover types on earth, it has not been widely used for mapping mangrove forests due to the limited spectral and spatial resolution with conventional imagery. Using the conventional multispectral remote sensing imagery, study has been concentrated on distinguishing mangrove from non-mangrove habitats, without regard to species of mangrove. Among these studies, Venkataratnam and Thammappa (1993) used Landsat Multispectral Scanner (MSS) data to map mangroves along the coastline of Andhra Pradesh, India. Rasolofoharino et al. (1998) produced a detailed cartographic inventory of a mangrove ecosystem in Madagascar based on a classification from Satellite pour l'Observation de la Terre (SPOT) images (SPOT 1 and 2). Gao (1998) developed a two-tiered classification scheme based on a SPOT image and applied it to the mangrove mapping in the Waitemata Harbour of Auckland, New Zealand. This method was 81.4% accurate in classifying mangrove versus non-mangrove land cover. Green et al. (1998) compared the suitability of three types of data (SPOT XS, Landsat TM, CASI) in mapping mangrove species with five different classification approaches. Gao (1999) conducted a comparative study on mangrove mapping with SPOT XS and Landsat Thematic Mapper (TM) images at 10, 20, 30 m resolution.

Given the small patch size of some mangrove species, spatial resolution plays a more important role than spectral resolution in discriminating different mangrove species. The recent launching of so-called "Very High Resolution" (VHR) satellite sensors provides a new opportunity to map land cover types at a much higher

spatial resolution than with previously available sensors. In the VHR category, there are two major commercial sources of imagery: IKONOS images and QuickBird images. The IKONOS 2 satellite, launched in 1999, provided the first publically available VHR satellite images, while even higher resolution images became available from the QuickBird satellite in 2001. With this enhanced spatial resolution, a better classification of individual mangrove species has become possible. However, another challenge emerged, which is to develop analytical approaches that can realize the full potential of the acquired data when attempting to define and discriminate spatial entities. The development of methods for mapping mangrove forests using information collected by high resolution sensors, particularly at the species-level, is still at an early exploratory stage. Mumby and Edwards (2002) were able to improve thematic accuracy for a marine environment comprised of 13 habitat classes (including mangroves) by incorporating texture information in their analysis of an IKONOS image. Held et al. (2003) employed an integrated analysis of data from the high spatial/spectral resolution scanner CASI and the airborne AIRSAR (NASA's polarimetric radar) to map mangrove estuaries along the Daintree River in North Queensland, Australia. Higher classification accuracies of different habitats and mangrove forest types were achieved when hyperspectral and radar data were used in combination, and a slight improvement (around 3%) was achieved using a hierarchical neural network in place of MLC. Wang et al. (2004a) developed an integrated pixel-based and object-based method, and achieved a moderately accurate result when classifying the canopies of three mangrove species in an IKONOS image. Furthermore, Wang et al. (2004b) compared the ability to discriminate the canopies of different mangrove species using various combinations of spectral and textural information inherent to IKONOS and QuickBird imagery.

This chapter investigated effective methods that can be employed for monitoring and assessing the spatial and temporal pattern of mangrove forests with images acquired from VHR satellite sensors as well as hyperspectral sensors. Specifically, the following objectives are to be attained: (1) to investigate and develop suitable methods for discriminating mangrove species; (2) to determine an optimal season for capturing the spectral difference among mangrove species; (3) to investigate the capability of hyperspectral data for distinguishing mangrove species.

## 14.2 Study Sites

The study was conducted in mainland mangrove forests near the Smithsonian Tropical Research Institute's Galeta Marine Laboratory (9°24'18" N, 79°51'48.5" W) at Punta Galeta on the Caribbean coast of Panama, approximately 8 km northeast of the city of Colon.

Three tree species comprise the canopy of the study forests. They are: black mangrove (*Avicennia germinans*), white mangrove (*Laguncularia racemosa*), and red mangrove (*Rhizophora mangle*). Red mangrove forms a pure or nearly pure stand at the seaward fringe. About 10–20 m from the water's edge, white mangrove joins the canopy, forming a nearly even mixture with red mangrove in the low intertidal.

In these mixed-species stands, white mangroves reach average heights of 22 m, while red mangroves average 16 to 18 m in height (W. Sousa, unpublished data). So, the crowns of white mangroves tend to be emergent, and therefore more visible in the satellite image than those of red mangroves, which form a lower sub-canopy. Black mangrove joins the canopy in the mid-intertidal, creating a mixed canopy of the three species, and then gradually monopolizes most upper intertidal stands. White mangrove may disappear completely from the canopy in the upper intertidal, or occur only as scattered individuals or small stands (W. Sousa, unpublished data).

Over the past 31 years, Punta Galeta has received, on average, 2781 mm of rainfall per year (based on measurements made at the Galeta Marine Laboratory by the Smithsonian Tropical Research Institute's Environmental Science Program). There is marked seasonality in precipitation, with more than 90% of rainfall occurring between early May and late December (Cubit et al. 1988, 1989, Duke et al. 1997). Aspects of mangrove phenology exhibit a strong association with seasonal rainfall patterns. We regularly observe that new leaves are flushed primarily during the wet season, and this pattern was quantified for *Rhizophora mangle* on Punta Galeta by Duke and Pinzón (1993). They found that leaf production was lowest from December to February (dry season) and peaked in May to July (early wet season). Since the spectral properties of leaves change as they age (Carter et al. 1989), we would expect canopy reflectance to change seasonally with the shift in average leaf age.

## **14.3 Mangrove Species Classification with High Spatial Resolution Imagery**

### ***14.3.1 Data Collection and Preprocessing***

Two scenes of IKONOS Geo bundle images were employed in this study. They were acquired on 2 February 2004 at 16:04 pm local time and 8 May 2004 at 16:01 local time. Metadata for the two sets of images indicate that both were collected at a similar sensor elevation: 85.8° for the February images and 79.1° for the May images. The high elevation angle largely offsets the geometric distortion induced by variation in terrain elevation, which is very modest in mangrove habitats. An image to image registration was conducted using May imagery as the reference image and a registration error: root mean square (RMS) of 0.5 pixels was reported. A nearest neighbor resampling approach was adopted to rectify the February image.

### ***14.3.2 Methodology***

#### **14.3.2.1 Back-Propagation Neural Networks Classifier (BPNN)**

A BPNN is a multi-layered feed-forward network trained by the so-called back-propagation algorithm as first introduced by Rumelhart et al. (1986). This learning

algorithm, also called the generalized delta rule, is an iterative gradient descent training procedure. It is carried out in two stages. In the first stage, once the network weights have been randomly initialized, the input data are presented to the network and propagated forward to estimate the output value for each training pattern set. In the second stage, the difference (error) between known and estimated outputs is minimized. The whole process is repeated, with weights being recalculated at each iteration, until the error is minimal, or lower than a given threshold. For the classification problem a BPNN classifier recognizes spectral patterns by learning from training sets. After training, the neural network system fixes all the weights and maintains the original learning parameters. The classification process calculates the output of each pixel using the parameters learned from the training phase, and then decides the class assignment of the pixel.

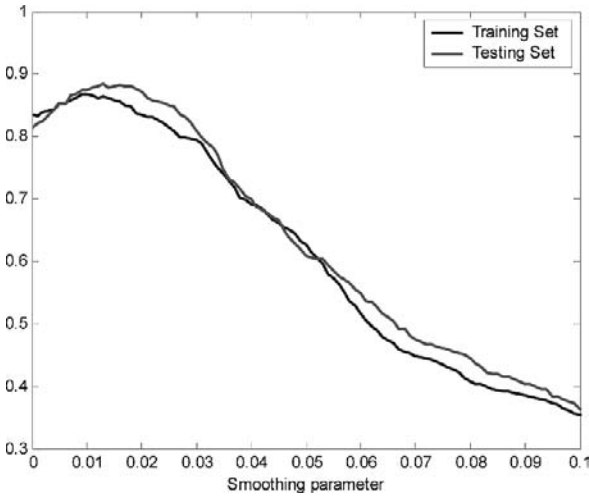
In this study, a BPNN with two hidden layers of 24 and 12 neurons respectively, hereafter referred to as BP:24:12, was trained using the MATLAB Neural Network Toolbox (V4.0.2-R13). One input node per band and one output neuron per class were employed with the output encoding convention of a high level (0.9) from the output neuron corresponding to a given class and simultaneously low output (0.1) from other output neurons. Each neuron computes a log-sigmoid function of the weighted sum of its input. The updates of the weights and activation level parameters were carried out using the Levenberg-Marquardt optimization method for 100 epochs.

#### 14.3.2.2 Clustering-Based Neural Network Classifier (CBNN)

Wang et al. (2008) developed a computationally efficient method based on neural network. This method is divided in two stages. In the first stage, the ISODATA algorithm is run on each training set to identify a number of clusters for each class. Each cluster center is labeled according to the class it belongs to and the entire set is used to build a Delaunay graph. In the second stage, a three-layered, feed-forward network is built as follows. For each pair of nodes belonging to different classes that are connected in the Delaunay graph, a neuron is created in the first hidden layer and its weight parameters are set to the coefficients of the hyperplane that separates the two clusters in question. A second layer of neurons is then added to perform the intersection of the half-spaces defined by the first layer to form the largest convex regions, each of which falls into a single class. Finally, the output layer joins the convex region into arbitrarily complex non-convex regions which define the decision region for each class.

It must be noted that the activation functions for all units are implicitly considered as hard limiters (or step functions) during the design stage. However, log-sigmoid functions may be used in the classification process. In the latter case a smoothing parameter is considered and the hard limiter results as a limiting process. More specifically, the sigmoid function is defined by

$$f(s) = \frac{1}{1 - e^{-s/\alpha}}$$



**Fig. 14.1** Plot of kappa values against the smoothing factor. Optimum smoothing parameter is 0.015

where  $\alpha$  is the smoothing parameter. As  $\alpha$  approach to zero the plot of  $f(s)$  tends to a hard limiter function.

Since different smoothing factors lead to different classification accuracies, a natural question to ask is how we can choose the best value for the smoothing parameter. In previous work, Silvan-Cárdenas (2003),  $\alpha$  was empirically set to 0.02. In this study, we developed a scheme to choose the optimal parameter  $\alpha$  with which the kappa value is at a maximum. The plot of the kappa value against  $\alpha$  obtained for the data set of May is shown in Fig. 14.1. In this case, the optimum smoothing factor falls around 0.01. After several trials it was observed that the optimum  $\alpha$  most likely lies at 0.015, which confirms that 0.02 is a good empirical choice. Another interesting observation is the fact that the optimum  $\alpha$  based on the testing set (and still using the same trained network) reports a similar value as the optimum  $\alpha$  based on the training set. This might indicate that (1) the training sample is representative of the classes under consideration and (2) the network can generalize very well the data that are not previously included in the training samples. Evidently, the second conclusion can be a consequence of the first one only if the training method succeeds.

This method was implemented in MATLAB software. The classifier is hereafter referred to as CBNN.

### 14.3.2.3 Maximum Likelihood Classifier (MLC)

For the purpose of evaluating the previous two types of neural network methods, we also adopted MLC as the third method. Equal *a priori* probability was assumed for all the classes in the implementation of MLC.

### **14.3.3 Results**

To compare classification performance of the two images, spatially consistent training and test samples were prepared with the aid of two field surveys carried out in January and July 2004, close to the times of image acquisition. During both field surveys, an extensive number of GPS points were measured by a high precision Trimble GPS (Pathfinder Pro XRS receiver). The species type, percentage of surrounding vegetation as well as other tree inventory information such as DBH, crown area were recorded as well. Given the patchy distribution of mangrove species, we used polygon tools to define training and test samples on the images. In reference to the field collected GPS points, small polygons, each encompassing no more than 10 pixels, were delineated across the study area to serve as training and test samples. Special caution was made to only choose polygons that fall in pure stands of a specific species in order to avoid including mixed pixels. Two experiments were designed to assess the accuracy of each classification method given two different combinations of input bands: spectral bands only, or spectral and textural bands. The results were reported in detail below.

#### **14.3.3.1 Classification Based on Spectral Information**

In the first experiment, the four multispectral bands were employed as input bands while the panchromatic band was not taken into account. For each classifier the overall kappa value was computed using both the training and test sample sets to analyze its generalization characteristic. Intuitively, one should expect lower kappa values for the test set than for the training set. A kappa value based on the training set represents the ability of the model to fit the training data, however a kappa based on the test set reveals the capability of the model to generalize (i.e. achieve the correct classification of data not previously encountered). Therefore, the ratio of the later with respect to the former is an index of the level of generalization achieved by a supervised classifier, provided that the number of samples in both sets is sufficiently large for rigorous statistical comparison. The corresponding kappa values and generalization ratio for the tested classifiers are shown in Table 14.1b. Three results are clearly discernable. First, in general the CBNN and MLC classifiers performed better with the May image than with the February image, while the BP:24:12 classifier displayed lower accuracy with the May than February image. Second, The CBNN and MLC classifier considerably outperformed the BP:24:12 for the May image in terms of both the kappa value and the generalization ratio. The three classifiers achieved comparable accuracy when applied to the February image. Third, MLC yielded the highest generalization ratios (0.99 and 1.05) for both images.

User accuracy was derived for each classifier and land cover type (Table 14.1a). For the individual mangrove species, user accuracy ranged from 35.6% (for black mangrove in the May image with the BP:24:12 classifier) to 96% (for white mangrove in the May image with the CBNN classifier). The CBNN and MLC classifiers

**Table 14.1** Accuracy of the three classification methods for the February and May IKONOS images using multispectral bands alone. (a) User accuracy for individual classes; (b) Kappa values from training and test samples, respectively, and ratios between two corresponding Kappa values

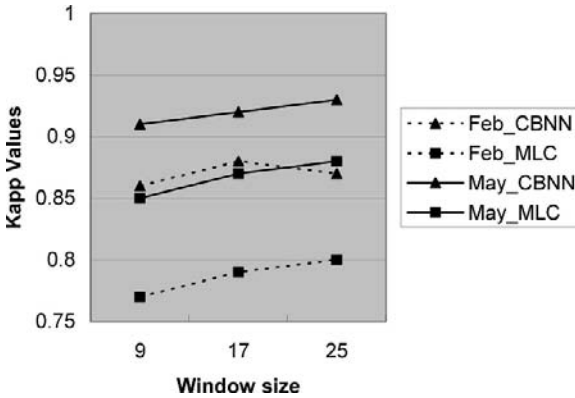
Land cover category	Feb-04			May-04		
	BP:24:12	CBNN	MLC	BP:24:12	CBNN	MLC
(a)	User's Accuracy (%)					
Red mangrove	88.8	81.6	86.6	44.3	94.3	92.6
White mangrove	56.8	65.6	73.3	82.1	96.0	92.4
Black mangrove	68.2	64.4	72.5	35.6	78.8	91.5
Gap	93.7	85.9	82.2	0.0	96.2	89.3
Lagoon	100.0	100.0	100.0	83.7	90.6	90.0
Rainforest	72.7	73.8	78.4	91.7	89.1	84.3
Road	94.6	100.0	89.9	90.4	98.0	71.8
(b)	Kappa Values					
Kappa (test samples)	0.74	0.73	0.78	0.49	0.87	0.86
Kappa (training samples)	0.79	0.78	0.79	0.6	0.87	0.83
Ratio	0.94	0.94	0.99	0.83	1.00	1.05

were noticeably more accurate than BP:24:12 when applied to either image, while in general, MLC gave consistently high user accuracy for the three mangroves in both images.

**14.3.3.2 Classification Based on Textural and Spectral Information**

As detailed above, the CBNN and MLC classifiers provided reasonably high overall classification accuracy when only spectral bands were considered. Given the high spatial detail associated with the panchromatic band of the IKONOS image, it was of interest to further investigate how well these two classifiers can utilize added textural information in assisting the classification process. In this experiment, the second order texture method, Grey Level Co-occurrence Matrix (GLCM), was adopted to extract the textural information from the panchromatic band of the IKONOS image. Displacement vectors at four directions (0, 45, 90, and 135 degrees), with a spatial distance of 1 pixel, were employed to compute three rotation invariant texture bands: Contrast (CON), Entropy (ENT), and Angular Second Moment (ASM) at three different window sizes: 9\*9, 17\*17, 25\*25. The quantization level was set to 16 in all cases. Then, each texture band was resampled to the same resolution as the multispectral bands (4 m), and stacked together with the four multispectral bands as the input bands for the CBNN and MLC classifier. For the CBNN method, the smoothing parameter was fixed to 0.015. The respective kappa values based on the test samples are presented in Fig. 14.2.

The addition of textural bands to the multispectral bands significantly improved the classification results for both CBNN and MLC (Fig. 14.2). For the February



**Fig. 14.2** Kappa values for the CBNN and MLC analyses of February and May images using both multispectral and textural bands. Feb\_CBNN and Feb\_MLC stand for CBNN and MLC methods applied to the February imagery. Similarly, May\_CBNN and May\_MLC stand for CBNN and MLC methods applied to the May imagery

image, the kappa values increased to 0.88 for CBNN and 0.8 for MLC, compared to 0.78 and 0.79, respectively when only multispectral bands are included. Likewise, for the May image, the kappa values when textural information was included were 0.93 for CBNN and 0.89 for MLC, compared to 0.87 and 0.83, respectively when textural information was not included. Furthermore, when textural information was included, analyses of the May image yielded consistently superior classification at all window sizes when compared to analyses of the February image. Finally, textural information extracted from a larger window size was more instructive than that from a smaller window size.

## 14.4 Spectral Discrimination Analysis of Mangrove Leaves with Lab Hyperspectral Remote Sensing

### 14.4.1 Data Collection and Preprocessing

Leaves of each species were sampled from trees growing in two different environmental settings: (1) areas supporting closed-canopy stands of large trees, some growing to more than 25 m, and (2) areas with a sparser cover of mostly short-stature (up to 3 m) trees that exhibited a wizened, shrub-like growth form. The former stands grow on organically rich soils of moderate salinity and relatively high nutrient availability, while the latter grow on sandy, coral reef-derived, soil that has lower nutrient concentrations, dries more rapidly between flood tides and rain storms, and is often higher in salinity (W. Sousa, unpublished data). A nutrient manipulation experiment conducted with *Rhizophora mangle* seedlings in this sandy



site demonstrated that their growth was nutrient-limited (L. Robinson, unpublished data). Leaves collected from the two sites differed in appearance and thickness: those from productive sites that support good growth tended to be larger, thinner, and more pliant than those collected from trees in the sandy site.

To determine whether the reflectance patterns of leaves from healthy individuals of the three mangrove species could be successfully discriminated, we selected 30 trees of each species for sampling from an array of productive stands across the study area. These ranged from fringe red mangrove stands growing at the water's edge to more inland stands dominated by white or black mangroves. Where possible, several trees of each species were sampled in each stand, so as to minimize the confounding influence of location on spectral measurements. Since leaves at different positions in the canopy might exhibit distinct spectral characteristics (due to differences in photosynthetic properties or water content), we stratified the leaf samples collected from each tree by height. From each tree, we collected one sample of 10 leaves from upper parts of the canopy surface and a second sample of 10 leaves from lower parts of the canopy surface. We were not able to sample leaves from the tops of taller trees at these productive sites, but the trees we sampled were growing in open areas, either at the water's edge or along a roadside, and therefore probably experienced similar levels of incident sunlight as the upper canopy of taller trees. Subsequent statistical analyses found that the reflectance patterns of leaves collected from upper versus lower heights in the canopy did not differ significantly for any of the three species (ANOVA,  $P > 0.05$ ). Therefore, we used the pooled sample of 20 leaves to calculate each tree's mean reflectance curve.

To examine the effect of physiological stress and/or nutrient limitation on foliar spectral properties, we collected leaves from stunted individuals of each species that were growing in an area of sandy soils located approximately 100 m behind fringe red mangrove stands that border the back reef adjacent to the Galeta Marine Laboratory. We sampled leaves from 20 trees of each species, haphazardly selected from across an approximately 1 ha area of this vegetation type; a sample of 10 leaves was collected from each tree. Since the crowns of these small trees were easily reached and contained relatively few leaves, we collected from the entire canopy of each tree; no effort was made to stratify these samples by height.

All leaves were collected on 16 July, 2004. They were immediately sealed in plastic bags, kept in a dark cooler, and transported back to the nearby laboratory for analysis. Leaf reflectance was measured with a Field Spec Pro FR (Analytical Spectral Devices, Boulder, CO, USA). The measurement procedure followed that employed by Pu et al. (2003). The light source consisted of two 500W halogen tungsten filament lamps. All spectra were measured in reflectance mode at the nadir direction of the radiometer with a 25° FOV. A white Spectralon panel was employed as the white reference and measured every five minutes to convert leaf radiance to percent reflectance. The spectrometer was configured to yield a spectra with 25 spectral averaging. Each sample of ten leaves was stacked in an overlapping pile on top of a calibrated black cloth and care was taken to make sure the field of view was fully occupied by leave stacks. The adaxial surfaces of a sample were measured five times, from which an average spectral reflectance curve was generated. Spectral

reflectance was originally measured over the ranges of 350–1000 nm at 1.4 nm intervals and 1000–2500 nm at 2.2 nm intervals. The entire spectral range (350–2500 nm) was automatically resampled to 1 nm when exported to the computer. To reduce system noise and redundancy between adjacent bands, we computed an average reflectance for each 10 nm interval, providing a total of 215 wavebands for analysis.

For band selection and classification of leaves from healthy trees, we had a sample size of 30 spectra for each tree species. We randomly split these 30 samples into a training group comprised of 20 samples and a test group of 10 samples; the latter were used to assess our classification accuracy. This procedure was repeated 10 times on randomly drawn sets of training and test samples.

#### ***14.4.2 Band Selection and Tree Species Classification***

Due to the high correlation inherent to adjacent wavebands, it was neither efficient nor reliable to include all 215 measured bands in the classification at one time. Instead, one must first choose a subset of bands that will maximize the likelihood of discrimination before proceeding with a conventional classification. A number of band or feature selection methods have been developed and documented in the remote sensing literature, including Principal Component Analysis (PCA), Fisher's Linear Discriminant Analysis (LDA), Penalized Discriminant Analysis (PDA), and wavelet-based feature selection (Yu et al. 1999, Pu and Gong 2004). Among them, LDA is the procedure that has been most widely adopted. However, a critical problem associated with LDA is that it will not provide a reliable solution when reflectance values for many highly correlated wavebands are included in the analysis and the number of available training samples is small. In this circumstance, estimates of within-class covariance matrices from the training samples are poor and unstable. In this study, we had 215 bands of reflectance values while only 20 samples for each species as training samples. The results of an LDA on such data would be highly questionable; the projection axis is likely to be misoriented, giving rise to over-fitting: i.e. a perfect performance on the training data, but a poor performance on the test data. Yu et al. (1999) provide a good graphical illustration of the problem.

To circumvent this problem, a method was developed by Wang and Sousa (2008) by first applying a series of one-way ANOVAs to filter out wavebands that did not differ significantly in mean reflectance among leaves of the three tree species. A one-way ANOVA, with species as the independent factor, was carried out for each of the 215 wavebands. The resultant probability provided an index of the importance of the tested band to the discrimination of the tree species. We considered  $P \leq 0.01$  as an indication that the mean reflectance of at least two of the three species differed in the tested band; all bands meeting this criterion were included in the LDA. One potential criticism of this band selection procedure is that the results of tests on adjacent bands are not statistically independent. However, our objective in applying ANOVA was not to test hypotheses about differences within specific bands; rather, we were seeking to eliminate bands from the analysis that provided no useful information

for discriminating species' reflectance patterns, and thereby reduce the number of analyzed bands to a level that would be operational for LDA. This band selection procedure was performed on all the training samples.

An LDA was then performed using the wavebands that ANOVA identified from the above procedure. The principle of LDA is to project the original redundant data to a new orthogonal space oriented along the axis that can maximize the ratio of between-class to within-class variance matrices of the training samples. The axis of the new space is aligned in the order of discrimination power among groups such that the first axis provides the greatest overall discrimination, the second provides second greatest, and so on. If we denote the total number of groups to be classified as  $NG$  and the total number of original bands as  $NB$ , then the number of dimensions for the new space is equal to either  $NG-1$  or  $NB$ , whichever is smaller. Since in practice,  $NB$  is usually larger than  $NG$ , LDA will typically yield a new data set with  $NG-1$  dimensions. In this way, the data dimensions are significantly reduced.

The significance of a specific wavelength to a discrimination function can be determined by examining the standardized coefficients for that band. The interpretation of the standardized coefficients resembles the logic of multiple regressions. The larger the absolute value of standardized coefficient, the larger is the respective variable's unique contribution to the discrimination as specified by the respective discriminant function. As such, by ordering the standardized coefficients the optimal wavebands were determined.

Given the fact that we have three species to classify, LDA generated two discriminant functions, with which the test samples were transformed. Then a Mahalanobis distance classifier was performed. A kappa value was calculated to assess the classification accuracy (Cohen 1960).

#### ***14.4.3 Discrimination Between Leaves from Healthy Versus Stressed Trees***

Previous studies have found that leaf spectral reflectance increases in portions of the visible and very-near infrared range (but not in the infrared) as a plant experiences physiological stress (Carter 1993, 1994, Carter and Knapp 2001). This response has been documented for numerous plant species when subjected to various agents of stress. We therefore focused on the 400–800 nm waveband in our comparison of healthy and stressed leaves. The sensitivity of reflectance to stress (i.e. relative change in reflectance) varies considerably within this spectral range. Sensitivity is greatest for wavelengths (e.g. 605, 695, and 710 nm) at which absorption by chlorophylls *a* and *b* is relatively weak. At these wavelengths, even a slight drop in leaf chlorophyll content caused by stress results in a large increase in leaf reflectance (Carter 1993).

As demonstrated by Carter (1994), reflectance sensitivity is best expressed as a ratio of reflectance in a stress-sensitive band to reflectance in a stress insensitive band. For our study, we calculated four narrow band leaf reflectance ratios

as indices of stress: R695/R420, R605/R760, R695/R760, and R710/R760. Carter (1994) found these ratios to be particularly sensitive indicators of stresses that affect chlorophyll content. We used ANOVA to compare the means of these ratios between leaf samples from trees growing in productive and stressful sites.

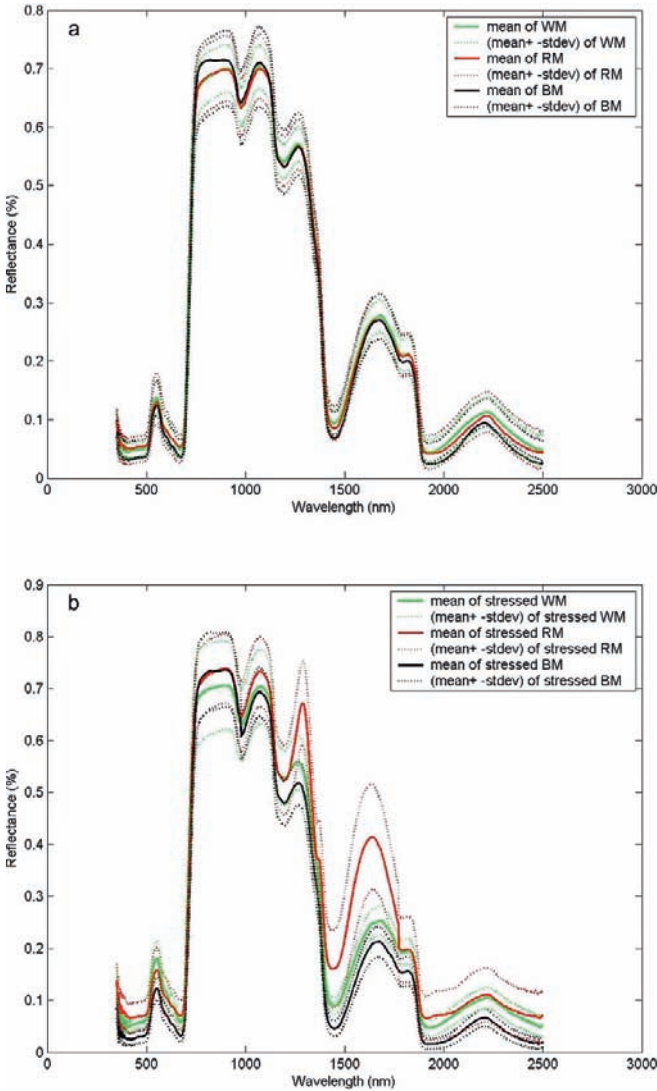
## 14.4.4 Results

### 14.4.4.1 Band Selection and Classification

Figure 14.3 presents the mean reflectance spectra of leaves from the three mangrove species; values for healthy and stressed trees are plotted separately (Fig. 14.3). We will first examine patterns of reflectance for leaves from healthy trees growing in productive sites. As expected, the general shapes of the species' curves are very similar, with considerable overlap.

However, one-way ANOVA tests revealed significant heterogeneity among the species in particular wavebands. Of the 215 10 nm-wide wavebands tested, 116 bands exhibited significant ( $P \leq 0.01$ ) interspecific variation in mean reflectance. These bands were clustered in five areas of the spectrum, i.e. 350–510 nm, 610–690 nm, 760–810 nm, 1370–1550 nm, and 1850–2500 nm. Bands within each of these areas are highly correlated and cannot be treated as independent estimates of species-level response. To reduce this correlation, we first regrouped the 116 significant bands into three regions as follows – region 1: VNIR (350–510 nm, 610–690 nm, and 760–810 nm); region 2: SWIR I (1370–1550 nm); and region 3: SWIR II (1850–2500 nm). An LDA was executed separately within each region and the standardized coefficients for two discrimination functions were respectively calculated and ranked. We concluded that a band was influential for its particular region if the absolute value of its LDA standardized coefficients were ranked among the top ten for both discrimination functions. Table 14.2 lists such influential bands for each region of wavelengths considered in the analysis.

The final classification of mangrove species was generated by LDA after pooling the influential bands from each region. In both the training and test samples, leaves of the three mangrove species were well separated in discriminant space. The average kappa value for the ten sets of test samples was 0.9, with a range of 0.85 to 1.00. This indicates that our method for extracting influential wavebands from the hyperspectral data, in combination with an LDA-based classification procedure, was very successful in discriminating the leaves of different mangrove species. Our results concur with several other researches that achieved good discrimination through use of the LDA method (Gong et al. 1997, Van Aardt and Wynne 2001, Clark et al. 2005). In addition, the LDA results show that the first discriminant function alone is sufficient to distinguish red from either black or white mangrove leaves. Examination of the standardized coefficients associated with the first discriminant function reveals that reflectance at the 780, 790, 800, 1480, 1530, and 1550 nm wavebands contribute most strongly to the first discriminant function. In other words, these



**Fig. 14.3** (a) mean and (mean  $\pm$  1 stdev) reflectance spectra for leaves from healthy leaves of the three mangrove species (WM: White Mangrove; RM: Red Mangrove; BM: Black Mangrove); (b) mean and (mean  $\pm$  1 stdev) reflectance spectra for leaves from physiologically stressed leaves of the three mangrove species

bands are critical to the discrimination of red from the other two types of mangrove. The second discriminant function best distinguishes white from black mangrove leaves; this function was most strongly influenced by wavebands at 770, 780, 790, 800, 1430, and 1480 nm.

**Table 14.2** Results of one-way ANOVA showing the potentially important wavelengths for discriminating leaf samples from healthy trees of the three mangrove species

Spectral region	Region 1: VNIR [350–510, 610–690, 760–810] (nm)	Region 2: SWIR I [1370–1550] (nm)	Region 3: SWIR II [1850–2500] (nm)
Influential wavelengths in each region	490, 500, 630, 770, 780, 790, 800	1400, 1430, 1480, 1530, 1550	1940, 1970, 1990

**14.4.4.2 Discrimination Between Leaves from Healthy Versus Stressed Trees**

One or more of the four reflectance ratio indices proved useful in detecting stress in each of the mangrove species (Table 14.3). R605/R760, R695/R760, and R710/R760 were effective in distinguishing stressed from non-stressed red mangrove leaves. In the case of white mangrove, R695/R420 was the only ratio that successfully detected the presence of stress. All four ratios were capable of detecting stress in black mangroves.

**Table 14.3** Results of ANOVA. Entries are *P* values by comparing the mean values of the four narrow band ratios between stressed and healthy leaves; bolded values are considered statistically significant (*P* value < 0.01)

Narrow Band Ratios	Mangrove species		
	Red	White	Black
R695/R420	0.371	< <b>0.001</b>	< <b>0.001</b>
R605/R760	<b>0.009</b>	0.799	< <b>0.001</b>
R695/R760	<b>0.008</b>	0.888	< <b>0.001</b>
R710/R760	0.013	0.613	< <b>0.001</b>

**14.5 Conclusion**

Multitemporal information can be very helpful in discriminating the canopies of different forest species (Jensen 2004). Our results confirmed that multiseasonal imagery can aid species-level classification of mangrove forests. Our study found that an IKONOS image acquired during the early rainy season more effectively captured the difference among mangrove species than one taken during the dry season. This difference is probably attributable to phenological and physiological changes that affect the reflectance of tree canopies. At our study sites, mangroves flush new leaves during the early wet season, while they experience stress from drought and high soil salinity during the dry season.

When only multispectral bands were included in the classification, MLC proved the best method for discriminating different mangrove species, consistent with the

findings of other studies, mentioned above. CBNN demonstrated a similar performance but at the cost of a considerable increment in computing time. However, when textual information was added to the classification, CBNN exhibited a strong advantage over MLC in characterizing the complex decision boundary associated with the combination of textural and spectral bands. The relative loss in MLC's power of discrimination when textural information was incorporated could have resulted from a violation of its central assumption of a multivariate Gaussian distribution model, as discussed earlier. Neural network-based analyses do not rest on this assumption, and thus gained discrimination power from the added textural information. Compared to the traditional back-propagation neural network method, the new CBNN method provides a computational simpler yet effective way in discriminating different mangrove species.

The high classification accuracy we obtained with the leave-level hyperspectral reflectance confirms the great potential of using hyperspectral data to distinguish mangrove species. We are confident that the use of narrow band hyperspectral data can effectively overcome the problem of overlap in spectral characteristics among species observed in our previous analyses of wide band multispectral imagery (Wang et al. 2004 a,b).

**Acknowledgement** Ms. Jose Silvan is thanked for his assistance in implementing CBNN method. This study was supported by grants to Le Wang from the National Science Foundation (DEB-0614040, DEB-0810933), from the Texas Remote Sensing Consortium and Texas State University research enhancement program, and financial support from University at Buffalo, and by grants to Wayne P. Sousa from the National Science Foundation (DEB-0108146) and the U.C. Berkeley Committee for Research.

## References

- Alongi DM (2002) Present state and future of the world's mangrove forests. *Environ Conserv* 29:331–349
- Carter GA (1993) Response of leaf spectral reflectance to plant stress. *Am J Bot* 80:239–243
- Carter GA (1994) Ratios of leaf reflectance in narrow wavebands as indicators of plant stress. *Int J Remote Sens* 3:697–703
- Carter GA, Knapp AK (2001) Leaf optical properties in higher plants: linking spectral characteristics to stress and Chlorophyll concentration. *Am J Bot* 4:677–684
- Carter GA, Paliwal K, Pathre U, Green TH, Mitchell RJ, Gjerstad DH (1989) Effect of competition and leaf age on visible and infrared reflectance in pine foliage. *Plant Cell Environ* 12:309–315
- Clark ML, Roberts DA, Clark DB (2005) Hyperspectral discrimination of tropical rain forest tree species at leaf to crown scales. *Remote Sens Environ* 3–4:375–398
- Cohen J (1960) A coefficient of agreement of nominal scales. *Educ Psychol Meas* 20:37–46
- Cubit JD, Thompson RC, Caffey HM, Windsor DM (1988) Hydrographic and meteorological studies of a Caribbean fringing reef at Punta Galeta, Panama: hourly and daily variations for 1977–1985. *Smithsonian Contributions in Marine. Science* 32:1–220
- Cubit JD, Caffey HM, Thompson RC, Windsor DM (1989) Meteorology and hydrography of a shoaling reef flat on the Caribbean coast of Panama. *Coral Reefs* 8:59–66
- Duke NC, Pinzón MZS (1993) Mangrove forests. In: Keller BD, Jackson JBC (eds) Long-term assessment of the oil spill at Bahía Las Minas, Panama, synthesis report, vol 2. Technical report.

- OCS Study MMS 93-0048. U.S. Department of the Interior, Minerals Management Service, Gulf of Mexico OCS Region, New Orleans, Louisiana, pp 447–533
- Duke NC, Pinzón MZS, Prada MC (1997) Large-scale damage to mangrove forests following two large oil spills in Panama. *Biotropica* 29:2–14
- Ellison AM, Farnsworth EJ (1996) Anthropogenic disturbance of Caribbean mangrove ecosystems: past impacts, present trends, and future predictions. *Biotropica* 4:549–565
- Ellison AM, Farnsworth EJ (2001) Mangrove communities. In: Bertness MD, Gaines SD, Hay ME (eds) *Marine Community Ecology*. Sinauer Associates, Sunderland, MA, pp 423–442
- Farnsworth EJ, Ellison AM (1997) The global conservation status of mangroves. *Ambio* 26: 328–334
- FAO (2003) State of the world's forests. Report of the Food and Agriculture Organization of the United Nations, Rome
- Gao J (1998) A hybrid method toward accurate mapping of mangroves in a marginal habitat from Spot multispectral data. *Int J Remote Sens* 10:1887–1899
- Gao J (1999) A comparative study on spatial and spectral resolutions of satellite data in mapping mangrove forests. *Int J Remote Sens* 14:2823–2833
- Gong P, Pu RL, Yu B (1997) Conifer species recognition: an exploratory analysis of in situ hyperspectral data. *Remote Sens Environ* 2:189–200
- Green EP, Clark CD, Mumby PJ, Edwards AJ, Ellis AC (1998) Remote sensing techniques for mangrove mapping. *Int J Remote Sens* 5:935–956
- Held A, Ticehurst C, Lymburner L, Williams N (2003) High resolution mapping of tropical mangrove ecosystems using hyperspectral and radar remote sensing. *Int J Remote Sens* 24: 2739–2759
- Hogarth PJ (1999) *The biology of mangroves*. Oxford University Press, Oxford, UK
- Hutchings P, Saenger P (1987) *The ecology of mangroves*. University of Queensland Press, St. Lucia, Australia
- Jensen JR (2004) *Introductory digital image processing: a remote sensing perspective*, 3rd edn. Prentice Hall, Upper Saddle River, NJ, USA
- Kathiresan K, Bingham BL (2001) Biology of mangroves and mangrove ecosystems. *Adv Mar Biol* 40:81–521
- Lugo AE, Snedaker SC (1974) The ecology of mangroves. *Annu Rev Ecol Syst* 5:39–64
- Mumby PJ, Edwards AJ (2002) Mapping marine environments with IKONOS imagery: enhanced spatial resolution can deliver greater thematic accuracy. *Remote Sens Environ* 2–3:248–257
- Pu R, Ge S, Kelly NM, Gong P (2003) Spectral absorption features as indicators of water status in coast live Oak (*Quercus agrifolia*) leaves. *Int J Remote Sens* 9:1799–1810
- Pu RL, Gong P (2004) Wavelet transform applied to EO-1 hyperspectral data for forest LAI and crown closure mapping. *Remote Sens Environ* 2:212–224
- Rasolofoharinoro M, Blasco F, Bellan MF, Aizpuru M, Gauquelin T, Denis J (1998) A remote sensing based methodology for mangrove studies in Madagascar. *Int J Remote Sens* 10: 1873–1886
- Rumelhart DE, Hinton GE, Williams RJ (1986) Learning representations by back-propagating errors. *Nature* 323:533–536
- Saenger P, Hegerl EJ, Davie JDS (1983) Global status of mangrove ecosystems. *Environmentalist* 3:1–88
- Silvan-Cárdenas JL (2003) Optimal design of neural networks for land-cover classification from multispectral imagery. In: Bruzzone L (ed) *Proc. SPIE (Image and Signal Processing for Remote Sensing IX)*, 5238, pp 420–431
- Tomlinson PB (1986) *The botany of mangroves*. Cambridge University Press, Cambridge, UK
- Van Aardt JAN, Wynne RH (2001) Spectral separability among six southern tree species. *Photogramm Eng Rem S* 12:1367–1375
- Venkataratnam L, Thammappa SS (1993) Mapping and monitoring areas under prawn farming. *Interface: A Bulletin from the NRSA Data Centre* 4:4–7
- Wang L, Silvan J, Sousa WP (2008) Neural network classification of mangrove species from multiseasonal IKONOS imagery. *Photogramm Eng Rem S*. (In press)



- Wang L, Sousa WP (2008) Distinguishing mangrove species with laboratory measurements of hyperspectral leaf reflectance. *Int J Remote Sens.* (In press)
- Wang L, Sousa WP, Gong P (2004a) Integration of object-based and pixel-based classification for mapping mangroves with IKONOS imagery. *Int J Remote Sens* 24:5655–5668
- Wang L, Sousa WP, Gong P, Biging GS (2004b) Comparison of IKONOS and Quickbird images for mapping mangrove species on the Caribbean Coast of Panama. *Remote Sens Environ* 91: 432–440
- Yu B, Ostland IM, Gong P, Pu RL (1999) Penalized discriminant analysis of in situ hyperspectral data for conifer species recognition. *IEEE T Geosci Remote* 5:2569–2577

# Chapter 15

## Remote Sensing Support for Tidal Wetland Vegetation Research and Management

Maggi Kelly and Karin Tuxen

Tidal marshes are ecotones that bridge estuary systems with upland areas and exhibit complex spatial patterning and ecological processes in response to multiple physical gradients. They are some of the most productive ecosystems on the earth and provide a range of valuable ecosystem services. Recent efforts to restore these systems only strengthen the need to accurately map and monitor tidal wetlands. While remote sensing has long been used to monitor wetlands, the recent availability of high spatial and spectral resolution remotely sensed imagery combined with new image processing and classification algorithms make mapping increasingly accurate and automated. This chapter discusses the complex spatial and temporal patterning of tidal wetland vegetation and the ecosystem services these systems provide and then examines how remotely sensed imagery has been used to map and monitor tidal wetlands in the past. Where appropriate, we demonstrate with examples from our work and from the published literature. Finally, this chapter discusses some of the remaining technical challenges facing wetland managers and scientists who wish to map tidal marshes using remote sensing. The discussion is grounded in recent work in the San Francisco Bay area, but lessons learned can be applied to other estuarine systems globally.

### 15.1 Introduction

Tidal wetland environments are among the world's most productive ecosystems (in plant, algal, and other communities) providing the basis for rich estuarine food webs. They provide habitat for large populations of migrating and local waterfowl; flood and erosion control, natural barriers against saltwater intrusion into freshwater aquifers; pollutant and sediment trapping; and critical fish and wildlife habitat; and space for recreational, scientific and educational activities (Fretwell et al. 1996, Mitsch and Gosselink 2000). In the San Francisco Bay estuary, tidal wetlands

---

M. Kelly (✉)

Department of Environmental Sciences, Policy and Management, University of California at Berkeley, Berkeley, CA 94720, USA  
e-mail: mkelly@nature.berkeley.edu

provide habitat for large populations of migrating waterfowl; every year, 15% of the Pacific Flyway waterfowl population uses the area's remaining wetlands as a stopover, wintering, or breeding habitat on their flight between Alaska and the southern tip of South America (Fretwell et al. 1996). Aside from the flood and erosion control, natural barriers against saltwater intrusion into freshwater aquifers, pollutant and sediment trapping, the estuary's tidelands provide critical habitat for a range of species, including the endangered and endemic salt marsh harvest mouse (*Reithrodontomys raviventris*), the California clapper rail (*Rallus longirostris obsoletus*), and the soft bird's beak (*Cordylanthus mollis* spp. *mollis*). And in the dense urban areas of the Bay Area, the tidal marshes also provide valuable land for recreational, educational, and scientific research activities, which together with the ecological functions, help our environment, economy, and quality of life in one of the nation's largest urban areas (Fretwell et al. 1996).

Tidal marshes are frequently or continually inundated wetlands containing emergent herbaceous vegetation adapted to saline and saturated soil conditions (Mitsch and Gosselink 2000). The physical stressors of salinity and inundation can be considered natural disturbances that cause spatial and temporal patterning in vegetation at multiple scales (Sousa 2001), including complex zonation and structure of plants (Mitsch and Gosselink 2000). While many salt marshes exhibit fairly simple vegetation community patterns in response to the strong physical gradients (Pennings and Bertness 2001), some salt marshes including more brackish marshes exhibit spatially complex and heterogeneous landscapes (Davy and Smith 1985, Phinn et al. 1996, Ramsey and Laine 1997). Saltier marshes have more obvious vegetation zones, although there is fine-scale mixing with fuzzy boundaries between vegetation patches. In Pacific Coast salt marshes for example, the lowest vegetation zone is usually made up of Pacific cordgrass (*Spartina foliosa*, except where invaded by Atlantic cordgrass [*S. alterniflora*]), the middle zone pickleweed (*Sarcocornia pacifica*), and the upper zone gumplant (*Grindelia* spp.) and other high marsh species (Cohen 2000). The zones are less distinct in more brackish Pacific coast marshes, where the lowest zone is made up mostly of tule; the middle zone alkali bulrush, cattail, and three-square bulrush; and the upper zone pickleweed, saltgrass, grindelia, and rush (Cohen 2000). In more freshwater tidal marsh systems, less salt-tolerant halophytes like pickleweed exist, and the high marsh plains contain more rush (*Juncus* spp.) and grass species like salt grass (*Distichlis spicata*) (Cohen 2000). Finally, tidal creeks within all types of tidal marshes cause microenvironments that have different vegetation zones along the creek banks (Mitsch and Gosselink 2000), and the level of inundation and salinity can affect plant height and size (Pennings and Bertness 2001).

The San Francisco Bay and Estuary's Mediterranean climate has strong effects on the structure and diversity of marsh vegetation (Callaway and Sabraw 1994, Sanderson et al. 2000). Rainfall is highly seasonal, and variations between years may lead to dominance by different annuals that have different salt tolerances during the wet months (Pennings and Bertness 2001). Also, primary productivity is higher than that of marshes in other climate regions due to the greater influx of solar energy, the longer growing season, and the nutrient-rich sediments carried from the

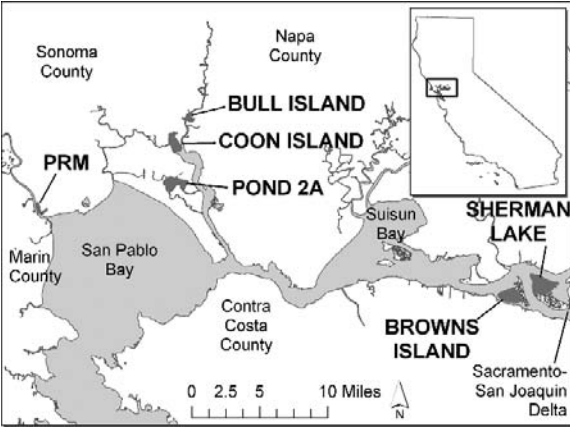
upstream Sacramento-San Joaquin River Delta. Vegetation distribution and abundance are strongly affected by the physical environment, inundation regime, nutrient availability, soil oxygen levels, salinity of water and soil. With a heterogeneous tidal channel network and micro-topography, and a variable Mediterranean climate, Pacific Coast tidal marshes exhibit particularly high spatial complexity in vegetation community patterns (Callaway and Sabraw 1994, Zedler et al. 1999).

These patterns can be stable in older marshes, but in newly restored marshes the patterning can be temporally dynamic. Patterns of vegetation colonization are influenced by plant reproductive strategy, competition, timing, and location in the marsh, and often long-term monitoring is needed to understand the emerging vegetation dynamics in a young marsh. In addition, disturbances (such as grazing, fire, sedimentation from upland watersheds, nutrient inputs from adjacent land use, and human use), climate and changes to hydrology can impact the patterning of older, more stable marshes. Changes in the salinity regime and inundation driven by global climate change will likely have ramification on tidal wetland vegetation patterning across scales in the world's estuaries.

While sea level rise is one of the more pressing threats facing tidal wetlands, there are others challenges facing wetlands. The pressure for development along the coast remains an active challenge: in California 77% of the population will live in coastal communities in 2000, which made up only 25% of the state; in the U.S., the areas of highest population growth are coastal areas and inland along coastal watersheds (California Resources Agency 2005). Newer threats from invasive species like Atlantic cordgrass (*Spartina alterniflora*), the hybridized native/non-native cordgrass (*Spartina alterniflora x foliosa*), and Perennial pepperweed (*Lepidium latifolia*) can invade recently-restored and natural wetlands (Cohen and Carlton 1998), causing ecological changes to the estuary. While the goals and methods for marsh restoration may differ between scientists and practitioners, there is increasing agreement that restoration of modified tidal marshes is important for the restoration and improvement of ecosystem services that they provide (Callaway and Sabraw 1994, Sanderson et al. 2000).

Mapping is critical to capture multi-scale dynamics of vegetation patterning in wetland sites and linking those patterns to ecological function, and has proved to be useful in wetland management and restoration: there is a recognized need to understand vegetation community dynamics and need to map through time (Pennings and Bertness 2001).

This chapter outlines current remote sensing applications in tidal wetland monitoring, management and science. The types of questions in a wetland context that can be answered using remote sensing are varied. For example, we might ask: How is wetland vegetation developing through time? Can we estimate biomass across a site? Can we map the growth of a particular species? Does vegetation patterning and diversity vary across sites? What controls vegetation patterning and diversity across sites? How does vegetation patterning and diversity support wetland function (e.g. birds, fish, macroinverts, primary productivity)? Is vegetation pattern and diversity related to wetland size, position in the bayscape, age, salinity or other gradients? And can we predict how a wetland's vegetation will restore through time, or



**Fig. 15.1** Our study areas in the SF Bay Estuary; these are part of the Integrated Regional Wetland Monitoring Program. These sites range from brackish to saline, from 48 acres to 972 acres in size, and range from very recently restored to mature marsh. See website (<http://www.irwm.org>) for more information

change in the face of rising sea level or threat from invasion by different species? These scientific and management questions can be organized into questions about (1) individual plants and plant community composition, (2) vegetation structure and patterning, and how that patterning is controlled, and (3) what kinds of ecosystem services such patterning supports. Remote sensing can help in all these areas. In addition to these questions, we also discuss the value of mapping technology for outreach and communication to a diverse public about the value of wetlands. We also discuss some of the technological trends and remaining challenges associated with remote sensing of wetland vegetation. Where possible, we illustrate concepts with examples from our work in the San Francisco Bay estuary (Fig. 15.1), and in other cases, with examples from the literature.

### 15.2 Remote Sensing of Tidal Wetlands

Remote sensing, or the capture and analysis of (most commonly) spectral information from a remote target organized in a image format is highly effective for analyzing estuaries and coastal systems (Phinn et al. 2000, Klemas 2001, Yang 2005a), and has been used to map, monitor, and detect and predict change in wetlands (Zhang et al. 1997, Jensen 2000). Remote sensing is ideal for monitoring wetlands because it is cost-effective, time-efficient, and non-invasive. It allows for a high intensity of measurements in relatively inaccessible and sensitive sites, without the potential invasiveness that traditional field methods present to delicate habitat conditions, bird nesting territories, or endangered species habitat (Shuman and Ambrose 2003). It also allows for broad-scale estimation of many parameters valuable to ecologists,

including land cover, vegetation structure, biophysical characteristics, and habitat areas (Wulder et al. 2004). In addition, many wetlands are inaccessible due to soft sediment or dense vegetation, restricting movement and causing traditional field data collection to be expensive and labor intensive.

### ***15.2.1 Early Efforts to Map Wetlands via Remote Sensing***

Mainly due to spatial, spectral, and temporal data limitations of coarse resolution satellite imagery, early (c. 1970–1985) use of remote sensing of wetland ecosystems primarily dealt with the mapping, monitoring, and change detection of very general wetland types, e.g., palustrine emergent wetland, estuarine emergent wetland (Scarpace et al. 1981, Jensen et al. 1984, Henderson et al. 1999), and very large spatial extents (e.g. Kelly 2001). There are several early examples of the use of Landsat TM and other coarse-scale imagery for mapping tidal wetlands (Gross et al. 1987, Browder et al. 1989, Kelly 2001). For example, Browder et al. (1989) used Landsat TM imagery to examine large-scale trends in wetland loss along the Louisiana coast, and infer a relationship between shrimp production and trends in wetland loss. Gross et al. (1987) quantified biomass for the tidal marsh species *Spartina alterniflora* Loisel in Delaware. The Coastal Change Analysis Project (C-CAP), detailed elsewhere in this volume is another notable example of broad scale wetland mapping (Dobson et al. 1992, 1995, Klemas et al. 1993, Dobson and Bright 1993).

Concurrent with these advancements was more research with spectral radiometry of wetland plants (Bartlett and Klemas 1981, Best et al. 1981, Ernst-Dottavio et al. 1981). In more homogeneous tidal wetlands, early research linked spectral reflectance to plant biomass and productivity, and vegetation indices such as NDVI were found to be correlated with biomass, salinity, and moisture (Hardisky et al. 1983a,b,c, Hardisky et al. 1984, Gross et al. 1990, Cohen 1991, Gross et al. 1993). Airborne imagery and digital photography were also utilized for more detailed mapping of wetlands. For example, Jensen et al. (1986) used airborne multi-spectral scanner data with a 3 m resolution to achieve greater spectral resolution, and were therefore able to map general wetland classes (e.g., emergent marsh, algal map, mixed deciduous swamp).

### ***15.2.2 Species to Community Level Mapping***

These advances in biophysical remote sensing, when coupled with recent increases in spatial, spectral, and temporal resolutions, as well as reduced price and increased cost-effectiveness, have enabled more detailed classification and mapping of vegetation cover types (Byrd et al. 2004, Hinkle and Mitsch 2005, Rosso et al. 2005a). Wetland plant species classification can be challenging because of the high level of spectral confusion between different wetland species and within assemblages

(Andresen et al. 2002, Ozesmi and Bauer 2002, Schmidt and Skidmore 2003). High spatial resolution imagery is especially needed to map and monitor changes to vegetation types or individual species within a marsh, due to the small patch sizes of wetland vegetation. High spectral resolution, or hyperspectral data allows for very specific narrow spectral bands to be targeted helping distinguish between marsh plant species (Schmidt and Skidmore 2003, Rosso et al. 2005b, Yang 2005a). Hyperspectral imagery has been used successfully to map vegetation in a range of ecosystems (Kokaly et al. 2003, Schmid et al. 2004) and its use for species-level wetland vegetation mapping shows great potential (Schmidt and Skidmore 2003). However, there is still much need for research on both the technical and applied aspects using hyperspectral data for monitoring and modeling coastal ecosystems (Cochrane 2000, Phinn et al. 2000, Hirano et al. 2003, Marani et al. 2003, Underwood et al. 2003, Artigas and Yang 2005).

In the past few years, there has been an increase in the number of studies or projects classifying wetlands to a community or individual species level. This has mainly been due to the increase in the availability and acquisition of remotely sensed imagery with high spatial and spectral resolutions (Hirano et al. 2003, Schmidt and Skidmore 2003, Rosso et al. 2005a). However, few studies have been successful at mapping wetland vegetation to the genus or species level. Mapping vegetation types within a wetland is particularly difficult for two reasons. First, herbaceous wetland vegetation exhibits high spectral and spatial variability (Töyrä and Pietroniro 2005). Second, wetland plant species are often very similar spectrally (Yang 2005b). Many studies have cited the benefit of multi-temporal and multi-source data in increasing the accuracy of wetland vegetation classification (Ozesmi and Bauer 2002). Non-optical data sources, such as radar data (e.g. SAR, RADAR) and laser altimetry (e.g. LiDAR) have been shown to add value when combined with optical remote sensing data. Rosso et al. (2005b) used LiDAR data to map invasive cordgrass (*Spartina alterniflora* and *Spartina alterniflora x foliosa*) affecting the San Francisco Bay. They used LiDAR data to map cordgrass structure and marsh topography and showed that the species was having an impact on the accretion and erosion processes of the marsh banks.

It is often difficult to identify boundaries where one community type stops and another begins, especially in diverse systems such as salt marshes, which exhibit mixed vegetation types blending into one another. However, the grouping of species into classes that are represented by the one or two most abundant species is useful (Mueller-Dombois and Ellenberg 1974) and necessary for mapping land cover and understanding change, not to mention fundamental to image classification. Certain species commonly reoccur with certain dominants or co-dominants, forming associations (Mueller-Dombois and Ellenberg 1974). However, it is necessary to provide clear definition of the limits between vegetation types (Adams 1999). The selection of the classes prior to community analysis, with the assumption that some are more important than others can lead to biased results in both the formation of vegetation classes (Mueller-Dombois and Ellenberg 1974) and in the image classification.

### ***15.2.3 Spatial Patterning of Vegetation***

Wetland scientists, restoration ecologists and resource managers are concerned with wetland ecosystem functions and ecological processes. Processes, such as productivity, nutrient cycling, habitat provision and population dynamics can influence and be influenced by landscape pattern which can be measured from remotely sensed imagery (Turner et al. 2001, Yang and Liu 2005a). Remotely sensed imagery taken on a regular basis can provide the opportunity to detect change in wetland vegetation cover and patterning by measuring relationships in the spectral and spatial responses over time (Töyrä and Pietroniro 2005). Ecological processes, such as vegetation colonization and succession of recently restored marshes can progress very quickly (Tuxen et al. 2008), altering landscape diversity, patch connectivity, and habitat quality. For this reason, restoring marshes should be monitored frequently with tools and methods that are objective, cost-effective, and highly automated (Andresen et al. 2002) to produce timely and accurate results. Remote sensing has been used to map and detect change in flood-tide deltaic wetlands (Guo and Psuty 1997) forested wetlands (Michener and Houhoulis 1997), mangroves (Wang et al. 2004a,b), and inland freshwater wetlands (Jensen et al. 1995).

Vegetation patterning in wetland sites is controlled by the interplay of a number of local-scale controls like salinity and inundation, but also responds to larger-scale processes and patterns (including management decisions), and remote sensing can be valuable tools to understand the linkages between vegetation patterning through time and such factors as adjacency and large-scale site context. One early broad-scale example is provided by Kelly (2001), who looked at the large-scale spatial patterning of tidal wetland vegetation in and adjacent to permitted wetland alterations under Section 404 of the Clean Water Act. She found that in many of the cases, more wetland loss than was permitted was found immediately adjacent to wetland permit sites. In another example, Byrd et al. (2004) used historic remote sensing through time to map vegetation succession and edaphic conditions in tidal marshes located in an agricultural drainage. They showed that controls on site-scale vegetation patterning were largely external in nature (the vegetation patterning was driven by upland sedimentation); these results were useful in planning restoration and managing the sites. We highlight a case study later in the chapter describing our effort to map the vegetation patterning associated with salt marsh harvest mouse and marsh song sparrow (Tuxen and Kelly, 2008).

### ***15.2.4 Examining Tidal Wetland Change***

There has been a recent increase in the number of tidal marsh restoration projects, particularly in the United States. In the San Francisco Bay in particular there have been some significant accomplishments in recent years: 9,000 acres of North Bay salt ponds (now known as the Napa-Sonoma Marsh State Wildlife Area) on the



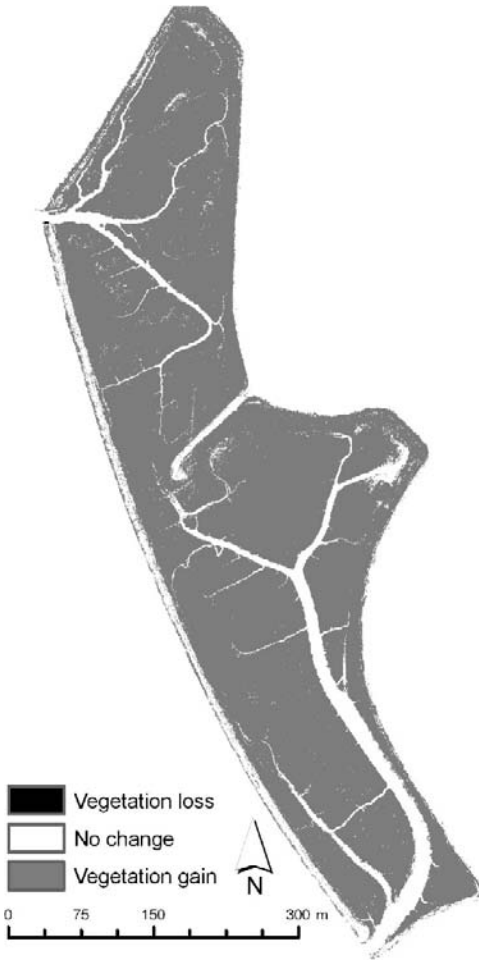
west side of the Napa River were restored after the Department of Fish and Game acquired the land in 1994; and the State and other agencies purchased 16,500 acres from Cargill Inc. in 2002 for future restoration (San Francisco Estuary Institute (SFEI) 2005). Remote sensing technologies can support monitoring in these projects, and has been shown to aid restoration efforts in the past (Phinn 1998), although its use on restoring wetlands has been limited (Phinn et al. 1999). This is changing, and a recent study of ours examined the feasibility of mapping a restored tidal wetland site through 10 years using high-spatial resolution digital photography. We examined Petaluma River Marsh (PRM) – a restored tidal marsh on the Petaluma River in the San Francisco Bay CA from 1994 to 2004. Aerial photography was acquired for a range of different purposes, but with precise geometric and spectral control, we were able to map vegetation/non-vegetation over the site through 10 years using simple NDVI thresholding based on field reconnaissance (Fig. 15.2). This work was simple to implement, but rich in results; clearly showing the need for long term monitoring of restoration success to compensate for small temporal scale changes in water availability (Fig. 15.3).



**Fig. 15.2** Example of the NDVI thresholding method for mapping wetland vegetation growth after marsh restoration: (A) original imagery, (B) NDVI transform, and (C) the thresholded result; grey = vegetation and white = mud

### 15.2.5 Remote Sensing and Geospatial Technologies for Outreach

Finally, remote sensing allows for enhanced visualization and increased participation of all stakeholders involved; and aid in legislation and decision-making (Skidmore et al. 1997). Maps, imagery and associated spatial data can be powerful communicators of place, environment, and personal context. The ability and readiness of the Internet to distribute such information without expensive and complicated software requirements have led to a proliferation of Internet-based GIS sites (also called webGIS) that have the potential to profoundly change the way the public interacts with local land use decision making. Examples like the SFEI Wetland Tracker (San Francisco Estuary Institute (SFEI) 2005), the interactive map for the South Bay Restoration Project, and other web-based GIS systems (Kearns et al. 2003) demonstrate show that public availability of spatial information, including remotely sensed imagery, when linked to specific data on wetland restoration or

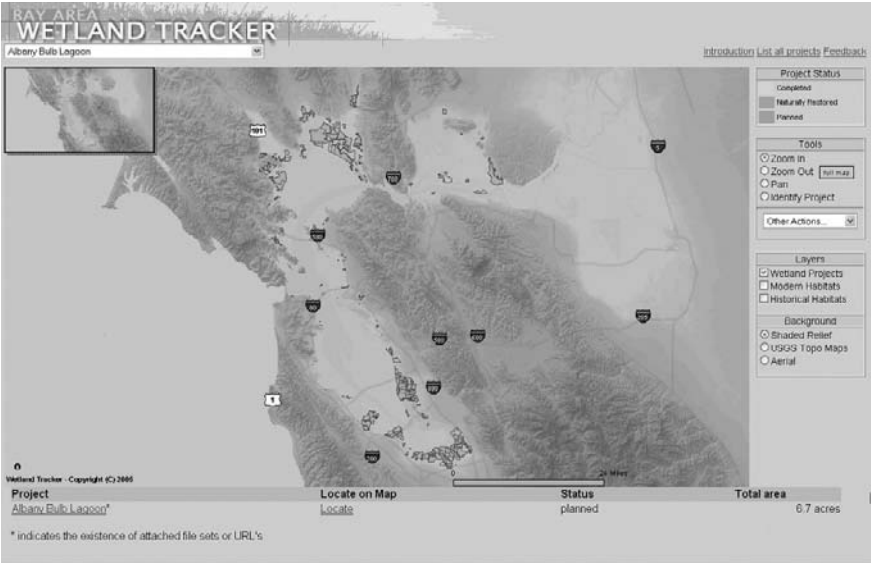


**Fig. 15.3** Carl's marsh, a restoring tidal marsh on the Petaluma River in the San Francisco Bay Estuary, showing 10 years of vegetation growth

planning goals can be an effective way of including the public in wetland management scenarios (Fig. 15.4).

### 15.3 Technological Trends and Remaining Challenges

The review above clarifies some of the research and management questions that can be addressed using remote sensing in tidal wetland communities. Our experience in the San Francisco Bay area wetland imaging has further highlighted several remaining questions, and we provide guidance from our experience on: (1) the use



a



b

**Fig. 15.4** Screen capture from the Wetland Tracker, an Internet-based Geographic Information System designed to allow public to view data, photographs, videos and remotely sensed data about wetland sites in the San Francisco Bay Estuary created by the San Francisco Estuary Institute: (A) project interface for the bay, (B) imagery from the south bay

of satellite vs. airborne imagery, (2) manual delimitation vs. automated classifiers, and (3) new methods for automated classification of tidal wetland plant species, communities and patterning.

### *15.3.1 Satellite vs. Airborne Imagery*

With the launch of the first Landsat satellite in 1972, scientists working in wetlands and other ecosystems employed more satellite imagery in their remote sensing work. However, depending on a project's particular wetland mapping goals, much of wetland science still required the finer scales and flexible flight times offered by aircraft-borne sensors. For these same reasons, some organizations still choose aerial photography over satellite imagery for their wetland monitoring projects. One example of this is the National Wetland Inventory (NWI), managed by the United States Fish & Wildlife Service, which maps the characteristics, extent, and status of U.S. wetlands and deepwater habitats (<http://www.fws.gov/nwi/>. Last access on 31 March 2008). Furthermore, the use of historical imagery is often required in long-term studies (Byrd et al. 2004, Van Dyke and Wasson 2005), and researchers are therefore restricted in the imagery that is available.

While the spatial and spectral resolutions of satellite imagery are increasing and are expected to increase in the future, currently there are certain circumstances where one would choose aerial photography over satellite imagery for wetland mapping. Aerial photography is useful for small, shallow, and spatially complex wetlands where high spatial resolution imagery is needed (Yang and Liu 2005b). Aerial photography is more commonly used for marsh studies and projects due to the higher resolution and flexibility it offers. Flights can be planned in order to acquire imagery during certain tide levels or vegetation states. It also allows for specification of the spatial resolution, or pixel size, of the imagery, which can result in a very small pixel size to map heterogeneous patches that exist in marshes. Aerial photography, however, has inherent challenges such as individual image differences from airplane tilt and variable brightness gradients within tile(s), and other radiometric and geometric inconsistencies (Devereux et al. 1990). The identification and understanding of these issues with aerial imagery is crucial so that efforts can be made to reduce confounding problems.

Some aerial photography, such as color infrared (CIR) photography, is relatively inexpensive when compared with other imagery options, an important consideration for monitoring projects with limited funds. CIR photographs are multispectral and typically have three bands in the green, red, and near-infrared (NIR) spectral regions. Multispectral imagery is divided into multiple spectral bands (usually three to seven), each spanning a certain part of the electromagnetic spectrum (e.g. red, blue, green, NIR, middle infrared, etc.). The three bands of CIR photographs span the portion of the electromagnetic spectrum necessary to calculate many vegetation indices, but do not contain any spectral information in the middle infrared, which can be useful for plant water content.

High-resolution multispectral satellite imagery offers some advantages over aerial photography, in terms of geometric control, radiometric precision, spectral range and image processing, and possesses the same ability as aerial photography to map vegetation composition, structure, and condition. The high-spatial resolution satellite platforms available on the commercial market today that compare with the high spatial resolution of aerial photography include IKONOS, OrbView-3, and Quickbird. IKONOS and OrbView-3 have a spatial resolution of 4 m for each multispectral band (blue, green, red, and near infrared), and have a spatial resolution of 1 m for the panchromatic (visible spectrum) band. Quickbird has a spatial resolution of 2.4 m for each multispectral band and 0.6 m for the panchromatic band. While 2.4–4 m is too large to map the fine-scaled heterogeneous marsh patterns, the imagery can be pan-sharpened using the higher-resolution panchromatic band combination, to render a higher-resolution multispectral image. While this is highly desired for studies that use satellite imagery, it does not substitute the frequent need for even finer resolutions, in the realm of 0.20–1.0 m, as is used in this study.

Past work has shown that aerial and satellite imagery offer different, but complementary, information (Ozesmi and Bauer 2002). Much work was done by Jensen and others in the 1980s (Jensen et al. 1984, 1986) with Airborne Multispectral Scanner (MSS) data, as well as Landsat MSS and Thematic Mapper (TM) satellite data. The two platforms were thought to complement each other well, as aerial imagery possessed high spatial resolution required for small minimum mapping units (MMUs), while the satellite data possessed high spectral resolution useful for spectral discrimination of large-scale wetland areas at the watershed level (Jensen et al. 1986). Many others have described the combination of aerial photography and satellite imagery used to reap the benefits of both (Ramsey and Laine 1997, Ozesmi and Bauer 2002, Palandro et al. 2003); however, the very high resolutions and flexible flight times offered by aerial photography are still required for most wetland monitoring projects.

Typically, coastal wetland classification maps are produced every five to ten years (Jensen et al. 1995). While this work is helpful at detecting long-term changes in composition and health, this time scale does not allow for a timely response and may not effectively depict short-term changes so that action can be taken (Jensen et al. 1995). However, space-borne imagery is anticipated to surpass airborne imagery in efficiency and effectiveness for short- or long-term wetland monitoring projects in the coming decades, due to (1) increasing spatial resolutions, (2) better temporal resolutions, and (3) decreasing costs (Ozesmi and Bauer 2002). Furthermore, with increased access to software that allows object-based image analysis and modeling, the monitoring of disturbed and restored wetlands will be improved (Phinn 1998, Klemas 2001).

We have some experience with the choice between aerial and satellite imagery. For our recent Integrated Regional Management Program (IRWM) that focused on mapping six sites (Fig. 15.1) in the San Francisco Bay Estuary, satellite imagery was not possible for our study areas as we required both extremely high spatial resolution imagery as well as particular flight times that were timed for proper sun angle and tidal stage. We used color infrared aerial photography that was acquired for the

IRWM Project (<http://www.irwm.org>. Last access on 31 March 2008). Imagery was taken at the lowest possible tide in 2003 to aid in vegetation mapping, whereas in 2004, imagery was taken at mid-tide to aid in channel delineation. Images had three bands: near infrared, red, and green. All sites were flown at a scale of 1:9,600 and scanned at a resolution of 1,200 dpi, resulting in a pixel size of 0.2 m for all sites. The overall goal was to achieve the same scale and pixel resolution for all sites, regardless of site size, in order to achieve uniform data for subsequent analyses. The aerial images were used primarily for vegetation classification and map production, as well as channel delineation. Imagery is freely-available at <http://www.irwm.org/>. The imagery was used to classify vegetation community patterning for six sites (Fig. 15.1) over two years.

### ***15.3.2 Automated Mapping vs. Manual Delimitation***

Even with these advancements in remote sensing image acquisition technology, there still exist some obstacles to effectively mapping tidal marsh vegetation. While the benefit of remote sensing for mapping vegetation in diverse, inaccessible, and sensitive marsh environments was recognized over 30 years ago, obstacles to accurate mapping arose regularly. At that time, scientists used visual photo interpretation of color-infrared aerial photography to recognize size, shape, photographic tone, color, pattern, shadow, and texture to distinguish between vegetation types (Reimold et al. 1973, Seher and Tueller 1973, Shima et al. 1976, Howland 1980). General boundaries of vegetation patches could be discerned, and studies were able to map wetlands as small as 6 m in diameter (Cowardin and Myers 1974). However, high color variation from varied species diversity or plant densities, conflicting color (or spectral) variation for two different species, and the same species producing different color (or spectral) properties under different conditions within the same site (Shima et al. 1976). Timing of flights and knowledge of the ecology of each site were identified as important criteria for accurate mapping (Cowardin and Myers 1974). The same obstacles still exist today; however, advances made since the 1980's have provided image analysts with much technological assistance.

Despite the advancements in remote sensing, numerous analysts prefer less automated tools, and concentrate on visual interpretation and manual digitization to outline wetland habitats on photography or imagery. On-screen digitizing is very common in wetland mapping (Harvey and Hill 2001, Higinbotham et al. 2004, Hinkle and Mitsch 2005), largely because of the importance of capturing discrete wetland vegetation patch boundaries, and also due to the spectral confusion between species which can make automated classifiers more challenging. These manual methods are still appropriate for some projects but such manual tools are not ideal in many cases, as analyst subjectivity can be a factor. More automated approaches allow for more objective, consistent, and repeatable results, making them able to scientifically defended.

Automated pixel-based classifiers have been gaining in popularity over the past decade because computational power has made them more operational. The use

of automated (computer-assisted) image classification reduces inconsistencies and error introduced through visual photo-interpretation of imagery. Therefore, classifications between sites and between time periods are more consistent with automated methods. In addition, automated methods have been found to be more cost-effective than visual delineation and classification (Thomson et al. 2003). Remotely sensed imagery has long been interpreted either by human or machine to achieve a landscape view of land use land cover (LULC) types for wetlands, as well as other ecosystems. Visual interpretation of remotely sensed imagery is still a common method in wetland mapping (Andresen et al. 2002), and there has been numerous studies demonstrating this (Field and Philipp 2000, Harvey and Hill 2001, Higinbotham et al. 2004, Hinkle and Mitsch 2005). This includes digitizing either on-screen or using a digitizing tablet. There are many reasons why visual interpretation has commonly been used in the past, including the desire to delineate accurate boundaries around objects and to produce a map that is visually appealing. While effective for some, it can be expensive and time-intensive to achieve detailed classification results as these manual methods are not automated; and maps by different interpreters or at different time periods can produce very different results that are not comparable across space or time (Blaschke and Strobl 2001).

Our efforts at repeatable, defensible mapping of sites necessitated we use more automated approaches to mapping tidal wetland vegetation, and we investigated both pixel-based and object-based procedures for analyzing remotely sensed imagery, both in a fully automated and semi-automated (with some human decision input) fashion. The results from pixel-based methods (e.g. ISODATA and Maximum Likelihood Classifier) used on our high spatial resolution imagery in extremely complex vegetation patterns were poor (Tuxen and Kelly, 2008), and necessitated the use of object-based image analysis methods.

### ***15.3.3 Pixel-Based vs. Object-Based Methods in Remote Sensing***

The recent proliferation in high spatial resolution imagery (<1 m pixel size) from new satellites and airborne platforms has catalyzed the refinement and development of image processing routines and algorithms that better deal with the local detail and heterogeneous spectral values found in high spatial resolution imagery. At the forefront of this trend are techniques for image segmentation and classification often grouped under the term “object based image analysis” or OBIA (Blaschke and Hay 2001, Andresen et al. 2002, Burnett et al. 2003, Hay et al. 2003, Blaschke 2005, Blaschke et al. 2005, Guo et al. 2007, Laliberte et al. 2006, Yu et al. 2006), which can be directly compared to more traditional “pixel-based” image processing methods that classify pixels individually, ignoring local context and spatial information content.

Object-based image analysis (OBIA) describes the process of segmenting remotely sensed imagery into meaningful objects and the analysis and classification of the objects across spatial, spectral, and temporal scales (Hay et al. 2001, Guo

et al. 2007). Homogeneous patches are created (by image segmentation) first, and those patches, or objects, are classified into land cover classes. The image segmentation applies a homogeneity threshold to allow some heterogeneity within objects. Because objects are used instead of individual pixels, results do not have spurious erroneously classified pixels (termed the “speckle” or “salt-and-pepper” effect) that are common in pixel-based classifications (Blaschke et al. 2000) so no post-classification filtering or smoothing is needed. OBIA allows for the segmentation of one image into segments at multiple scales (Schiewe et al. 2001), allowing scales to be linked to each other, to model the hierarchical nature of complex systems, such as salt marshes (Burnett and Blaschke 2003).

We see three reasons why OBIA holds promise as a method for classifying tidal marsh vegetation with high spatial resolution imagery. First, in contrast to traditional pixel-based methods, in OBIA, homogeneous objects are extracted at multiple scales from a single image, linked across scales with rules of inheritance, enabling multi-scale analyses that utilize hierarchical relationships between the different scales. Pixels, on the other hand, are uni-scale and represent a fixed area on the ground (Benz et al. 2004), and while pixel-based classification methods essentially cluster these pixels into “objects,” they are non-hierarchical, single-valued, and are not part of a multi-scalar framework. Manual delineation methods also “segment” an image, but can depict only the one scale perceived by the image interpreter (Burnett and Blaschke 2003).

A second reason why OBIA holds promise for tidal marsh mapping is because objects are segmented based on a certain level of local homogeneity. For this reason, object-based approaches are especially good for high spatial resolution data, because neighboring pixels more likely belong to same class (Blaschke and Hay 2001, Schiewe et al. 2001). Variability between pixels becomes advantageous information because it now defines the internal heterogeneity, or texture, of an object, thus expressing texture more explicitly than with pixel-based approaches (Blaschke and Hay 2001). Moving from pixels to objects causes the local pixel variability to decrease (Schiewe et al. 2001), which produces more accurate mapped products. At the same time, the variability within classes increases because now classes can include some heterogeneity within objects, which actually better represents reality in which certain patches belonging to the same vegetation type can possess different levels of internal heterogeneity. The process also reduces the spurious pixel problem that is a typical result of pixel-based classifiers, which cannot recognize the local spatial variability found in high spatial resolution imagery (Yu et al. 2006, Guo et al. 2007).

In addition to the accuracy benefits of OBIA, we propose that ecosystem mapping is more ecologically sound with OBIA because principles of landscape ecology are maintained, with patches based on homogeneous objects rather than pixels (Andresen et al. 2002), making up classes that incorporate the inter-patch variability, which in turn make up the entire landscape in all its heterogeneity. Thus, object-based methods follow ecological phenomenon more closely than traditional pixel-based methods (Blaschke and Strobl 2001), which analyze each pixel independently, without taking into account spatial concepts like neighborhood, proximity,



and homogeneity (Burnett and Blaschke 2003). Likewise, the hierarchical relationships between objects at multiple scales represent the multi-scale nature of complex ecosystems such as salt marshes, with patterns and processes interacting across multiple scales. Therefore, a major goal with OBIA is to segment out patches that represent meaningful objects based on a specific level of homogeneity.

A third reason why OBIA has mapping potential is because it allows for the integration of Hierarchical Patch Dynamics (HPD) (Burnett and Blaschke 2003, Blaschke et al. 2005). HPD is the representation of a landscape in spatially nested patch hierarchies, with larger patches being made up of smaller patches. Landscape dynamics are linked between adjacent hierarchical scales, or levels. In this past, it was difficult to represent pattern and processes in this multi-scale manner because hierarchical linking of scales was not well defined (Hay et al. 2003). Geographic Information Science (GIS) was often considered the closest thing to multi-scale mapping because different scales could be analyzed separately, but GIS had some problems representing more than one scale at a time. OBIA has the potential to model landscapes in a multi-scale manner because a single image represents a variety of scales and levels of abstraction (Hay et al. 2003). Object segmentation uses the same object boundaries across scales (Hay et al. 2003), so topological relationships can be utilized. In this way, OBIA can integrate GIS analyses while representing the hierarchical scaling of real-world ecosystems which humans can mentally move between easily, but previously could not adequately model in a GIS (Blaschke and Strobl 2001).

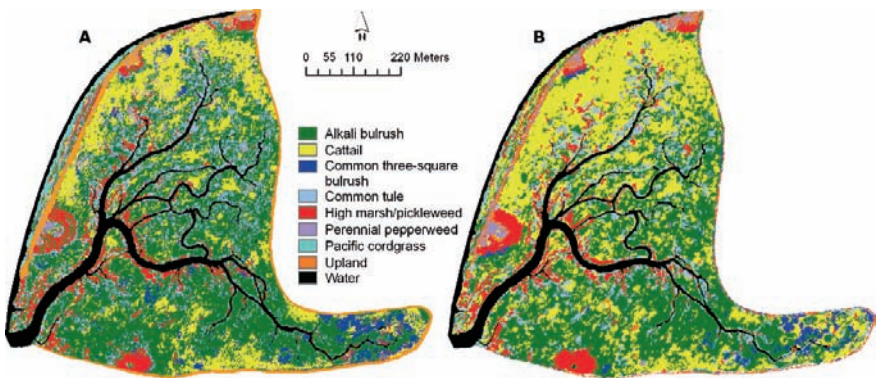
In summary, OBIA combines the advantages of visual interpretation and pixel-based methods in that patches are delineated into homogeneous areas that are both accurate and visually appealing, and the methods are objective, automated, and repeatable. OBIA allows for more semantic, real-world, and intuitive and human-conceived object shapes (Blaschke and Strobl 2001, Schiewe et al. 2001) based on user knowledge (Hay et al. 2003). Shape and context are taken into account as well as color or spectral quality of the patch (Schiewe et al. 2001). In addition, soft classifications, or fuzzy modeling, that are based on user knowledge can be integrated into the analyses, where an object is assigned to multiple classes at varying degrees of membership, in order to reflect the ecotonal nature of many systems.

Wetland ecosystems often consist of small isolated wetland patches, with complex pattern. The use of high spatial resolution imagery is necessary to capture detail. There are several studies published using object-based techniques for mapping wetlands. Some have used OBIA with coarse-scale Landsat imagery (Bock 2003, Stankiewicz et al. 2003, Yoon et al. 2003), while others have used it with high spatial resolution images, such as CIR aerial photography (0.2–1 m) (Ivits et al. 2002, Burnett et al. 2003), Quickbird satellite imagery (60 cm–2.4 m) (Wang et al. 2004a,b, Hurd et al. 2005), and IKONOS satellite imagery (Blaschke and Hay 2001, Hall et al. 2004, Wang et al. 2004a).

Andresen et al. (2002) applied OBIA to IKONOS satellite imagery to map aquatic vegetation, and found that they could successfully map vegetation both for inventory purposes using hierarchical segmentation and classification, and for monitoring purposes by measuring incremental patch change. Stankiewicz et al. (2003)

found that while shrub classes could be successfully delineated, many wetland patches could not be identified with coarse-scale Landsat imagery. Multiple studies have compared OBIA with pixel-based methods. Wang et al. (2004b) compared the two methods together and found that while object-based methods were more efficient at differentiating spectrally mixed vegetation classes, but over-generalized species diversity in areas where spectral differentiation was clear. Therefore, they integrated both methods by applying object-based methods only to those classes that were spectrally similar, and pixel-based methods to all other classes (Wang et al. 2004a,b). Hurd et al. (2005) who found that results from the object-based multi-scale methods on Quickbird imagery were smoother and reduced errors of commission and omission. Harken and Sugumaran (2005) found object-based results from eCognition software to be nearly 30% more accurate overall than pixel-based results from Spectral Angle Mapper (SAM). The majority of applied OBIA studies found used the commercially available software Definiens Professional (formerly known as “eCognition”) made by Definiens, Inc. (1995–2006). Using this software, studies have implemented multi-scale object-based segmentation and classification of mires (Burnett et al. 2003). Others have integrated multiple data sources (Stankiewicz et al. 2003, Li and Chen 2005), such as elevation data, to help further discriminate classes. Some have experimented with hyperspectral data, such as Greiwe and Ehlers (2005), who found an almost 20% accuracy improvement when they used hyperspectral information rather than just high spatial resolution data. All of these studies demonstrated an increase in accuracy over pixel-based image analysis, but none discuss the multi-scale mapping of ecosystem function (Sugumaran et al. 2000, Greiwe and Ehlers 2005). OBIA has the ability for powerful mapping, modeling, and visualization across multiple scales for many future applications, including restoration.

We used OBIA methods to map vegetation in a restored tidal marsh (Bull Island on the Napa River in the San Francisco Bay estuary (see Fig. 15.1 for location map)). Our objective was to accurately map vegetation communities using high spatial resolution imagery, but also to map the spatial pattern of certain vegetation communities



**Fig. 15.5** A comparison between (A) pixel-based classification approach and (B) object-based image analysis for Bull Island a restored marsh in the San Francisco Bay estuary

that comprise habitat for two species: the salt marsh harvest mouse (*Reithrodontomys raviventris*) and song sparrow (*Melospiza melodia*). Each uses different wetland plants as habitat, but requires certain spatial configuration of habitat to be successful. For example, the song sparrow prefers to nest in shrub cover away from upland areas to limit predation. The mouse is cover dependent on pickleweed (*Sarcocornia pacifica*), and prefers dense continuous cover of the plant with nearby areas of higher elevation which can serve as refugia in high tides. The OBIA method not only increased classification accuracy by reducing spurious pixels and mis-classification, we were also able to maintain the spatial cohesion of habitat patches, providing a better “functional” map of habitat (Fig. 15.5) (Tuxen and Kelly, 2008).

## 15.4 Conclusions

Tidal wetlands are critical linkages between water and land, and are increasingly facing pressure from coastal development, sea level rise, and other threats. Encouragingly, at least in the US, wetland restoration is also taking place in some areas. Remote sensing can provide research and management support for those working in these important ecosystems. The implementation of large-scale restoration projects will necessitate accurate, precise, multi-scale mapping of wetland sites to integrate into regional and global planning for climate change. This chapter discussed several trends in the mapping of tidal marshes: increases in the spatial and spectral resolution of sensors, increase in temporal resolution and control, and the general increase in availability of spatial data and imagery. We also discuss the integration across numerous spatial technologies like GIS and landscape ecology that lend support to wetland science and management. Despite the abundance of tools and data, mapping the complex and dynamic pattern of vegetation in coastal tidal marshes still faces challenges, and scientists and managers must consider numerous trade-offs in cost, accuracy, speed in choosing a monitoring method. The choice between satellite imagery (with its better spatial fidelity and cost savings) and airborne imagery (providing better temporal control and spatial resolution) remains. In addition, despite numerous research examples of operational accuracies in wetland classification using automated methods, manual delimitation remains as an important wetland management tool. New approaches that better deal with large volumes of high-spatial resolution imagery through object-based techniques are the impetus for studies comparing accuracies and labor costs between manual and automated approaches.

**Acknowledgement** We would like to acknowledge other current and past members of the Kelly-Lab Research and Outreach Team who are also actively involved in tidal wetland mapping, including Lisa Schile and Kristin Byrd; The Integrated Regional Wetland Monitoring Project Personnel, including Stuart Siegel, Tom Parker, John Calloway, and many others; Funding for some of our work presented here was provided by CalFed, the University of California Water Resources Center, North Carolina Sea Grant, and the Renewable Resources Extension Act (RREA).

## References

- Adams JA (1999) A suggestion for an improved vegetation scheme for local and global mapping and monitoring. *Environ Manage* 23:1–13
- Andresen T, Mott C, Zimmermann S, Schneider T, Melzer A (2002) Object-oriented information extraction for the monitoring of sensitive aquatic environments. *IEEE International* 5: 3083–3085
- Artigas FJ, Yang JS (2005) Hyperspectral remote sensing of marsh species and plant vigour gradient in the New Jersey Meadowlands. *Int J Remote Sens* 26:5209–5220
- Bartlett DS, Klemas V (1981) In situ spectral reflectance studies of tidal wetland grasses. *Photogramm Eng Rem S* 47:1695–1703
- Benz UC, Hofmann P, Willhauck G, Lingenfelder I, Heynen M (2004) Multi-resolution, object-oriented fuzzy analysis of remote sensing data for GIS-ready information. *ISPRS J Photogramm* 58:239–258
- Best RG, Wehde ME, Linder RL (1981) Spectral reflectance of hydrophytes. *Remote Sens Environ* 11:27–35
- Blaschke T (2005) Towards a framework for change detection based on image objects. *Göttinger Geographische Abhandlungen* 113:1–9
- Blaschke T, Hay G (2001) Object-oriented image analysis and scale-space: theory and methods for modeling and evaluating multi-scale landscape structure. *Int Arch Photogram Rem Sens* 34:22–29
- Blaschke T, Lang S, Lorup E, Strobl J, Zeil P (2000) Object-oriented image processing in an integrated GIS/remote sensing environment and perspectives for environmental applications. In: Cremers A, Greve K (eds) *Environmental information for planning, politics and the public*. Metropolis Verlag, Marburg, pp 555–570
- Blaschke T, Lang S, Möller M (2005) Object-based analysis of remote sensing data for landscape monitoring: recent developments. *Anais XII Simpósio Brasileiro de Sensoriamento Remoto*, Goiânia, Brasil, pp 2879–2885
- Blaschke T, Strobl J (2001) What's wrong with pixels? Some recent developments interfacing remote sensing and GIS. *GIS* 6:12–17
- Bock M (2003) Remote sensing and GIS-based techniques for the classification and monitoring of biotopes. *J Nat Conserv* 11:145–155
- Browder JA, May LN, Rosenthal A, Gosselink JG, Baumann RH (1989) Modeling future trends in wetland loss and brown shrimp production in Louisiana using Landsat Thematic Mapper imagery. *Remote Sens Environ* 28:45–59
- Burnett C, Aaviksoo K, Lang S, Langanke T, Blaschke T (2003) An object-based methodology for mapping mires using high resolution imagery, *Ecological Processes in Northern Wetlands*, Tallinn
- Burnett C, Blaschke T (2003) A multi-scale segmentation/object relationship modelling methodology for landscape analysis. *Ecol Model* 168:233–249
- Byrd K, Kelly M, Dyke EV (2004) Decadal changes in a Pacific estuary: a multi-source remote sensing approach for historical ecology. *GISci Remote Sens* 41:347–370
- California Resources Agency (2005) *California's Ocean Economy*. The National Ocean Economics Program [Online] Available: <http://www.resources.ca.gov/> (Last access on 31 March 2008)
- Callaway RM, Sabraw CS (1994) Effects of variable precipitation on the structure and diversity of a California salt marsh community. *J Veg Sci* 5:433–438
- Cochrane MA (2000) Using vegetation reflectance variability for species level classification of hyperspectral data. *Int J Remote Sens* 21: 2075–2087
- Cohen AN (2000) Introduction to the San Francisco estuary. *Save the Bay*, San Francisco Estuary Project, and San Francisco Estuary Institute
- Cohen AN, Carlton JT (1998) Accelerating invasion rate in a highly invaded estuary. *Science* 279:555–558
- Cohen WB (1991) Response of vegetation indexes to changes in 3 measures of leaf water-stress. *Photogramm Eng Rem S* 57:195–202

- Cowardin LM, Myers VI (1974) Remote sensing for identification and classification of wetland vegetation. *J Wildlife Manage* 38:308–314
- Davy AJ, Smith H (1985) Population differentiation in the life-history characteristics of salt-marsh annuals. *Vegetation* 61:117–125
- Devereux BJ, Fuller RM, Carter L, Parsell RJ (1990) Geometric correction of airborne scanner imagery by matching Delaunay triangles. *Int J Remote Sens* 11:2237–2251
- Dobson J, Bright EA (1993) Large area change analysis: the coastwatch change analysis project (C-CAP). Proceedings of the pecora 12 conference
- Dobson JE, Bright EA, Ferguson RL, Field DW, Wood LL, Haddad KD, Iredale H, Jensen JR, Klemas VV, Orth RJ, Thomas JP (1995) NOAA coastal change analysis program (C-CAP): guidance for regional implementation. NOAA Technical Report NMFS 123, Coastwatch Change Analysis Project, Coastal Ocean Program, NOAA, U.S. Department of Commerce
- Dobson JE, Ferguson RL, Field DW, Wood LL, Haddad KD, Iredale H, Klemas VV, Orth RJ, Thomas JP (1992) NOAA coastwatch analysis project guidance for regional implementation. NOAA, U. S. Department of Commerce
- Ernst-Dottavio CL, Hoffer RM, Mroczynski RP (1981) Spectral characteristics of wetland habitats. *Photogramm Eng Rem S* 47:223–227
- Field RT, Philipp KR (2000) Vegetation changes in the freshwater tidal marsh of the Delaware estuary. *Wetl Ecol Manage* 8:79–88
- Fretwell JD, Williams JS, Redman PJ (eds) (1996) National water summary on wetland resources. Water-Supply Paper 2425, U.S. Geological Survey, Washington, DC, USA
- Greiwe A, Ehlers M (2005) Combined analysis of hyperspectral and high resolution image data in an object oriented classification approach. American Society for Photogrammetry and Remote Sensing (ASPRS), Baltimore, MD, USA
- Gross MF, Hardisky MA, Klemas V (1990) Inter-annual spatial variability in the response of *Spartina alterniflora* biomass to amount of precipitation. *J Coastal Res* 6:949–960
- Gross MF, Hardisky MA, Klemas V, Wolf PL (1987) Quantification of biomass of the marsh grass *Spartina alterniflora* loisel using Landsat Thematic Mapper imagery. *Photogramm Eng Rem S* 53:1577–1583
- Gross MF, Hardisky MA, Wolf PL, Klemas V (1993) Relationships among *Typha* biomass, pore water methane, and reflectance in a Delaware (U.S.A.) brackish marsh. *J Coastal Res* 9: 339–355
- Guo Q, Kelly M, Gong P, Liu D (2007) An object-based classification approach in mapping tree mortality using high spatial resolution imagery. *GISci Remote Sens* 44:24–47
- Guo Q, Psuty NP (1997) Flood-tide deltaic wetlands: detection of their sequential spatial evolution. *Photogramm Eng Rem S* 63:273–280
- Hall O, Hay GJ, Bouchard A, Marceau DJ (2004) Detecting dominant landscape objects through multiple scales: an integration of object-specific methods and watershed segmentation. *Landscape Ecol* 19:59–76
- Hardisky MA, Daiber FC, Roman CT, Klemas V (1984) Remote sensing of biomass and annual net aerial primary productivity of a salt marsh. *Remote Sens Environ* 16:91–106
- Hardisky MA, Klemas V, Smart RM (1983a) The influence of soil salinity, growth form, and leaf moisture on the spectral radiance of *Spartina alterniflora* canopies. *Photogramm Eng Rem S* 49:77–83
- Hardisky MA, Smart RM, Klemas V (1983b) Growth response and spectral characteristics of a short *Spartina Alterniflora* salt marsh irrigated with freshwater and sewage effluent. *Remote Sens Environ* 13:57–67
- Hardisky MA, Smart RM, Klemas V (1983c) Seasonal spectral characteristics and aboveground biomass of the tidal marsh plant, *Spartina alterniflora*. *Photogramm Eng Rem S* 49:85–92
- Harken J, Sugumaran R (2005) Classification of Iowa wetlands using an airborne hyperspectral image: a comparison of the spectral angle mapper classifier and an object-oriented approach. *Canadian J Remote Sens* 31:167–174
- Harvey KR, Hill GJE (2001) Vegetation mapping of a tropical freshwater swamp in the Northern Territory, Australia: a comparison of aerial photography, Landsat TM and SPOT satellite imagery. *Int J Remote Sens* 22:2911–2925

- Hay GJ, Blaschke T, Marceau DJ, Bouchard A (2003) A comparison of three image-object methods for the multiscale analysis of landscape structure. *ISPRS J Photogramm* 57:327–345
- Hay GJ, Marceau DJ, Dube P, Bouchard A (2001) A multiscale framework for landscape analysis: object-specific analysis and upscaling. *Landscape Ecol* 16:471–490
- Henderson FM, Hart TF, Heaton BP, Portolese JE (1999) Mapping coastal ecosystems over a steep development gradient using C-CAP protocols. *Int J Remote Sens* 20:727–744
- Higinbotham CB, Alber M, Chalmers AG (2004) Analysis of tidal marsh vegetation patterns in two Georgia estuaries using aerial photography and GIS. *Estuaries* 27:670–683
- Hinkle RL, Mitsch WJ (2005) Salt marsh vegetation recovery at salt hay farm wetland restoration sites on Delaware Bay. *Ecol Eng* 25:240–251
- Hirano A, Madden M, Welch R (2003) Hyperspectral image data for mapping wetland vegetation. *Wetlands* 23:436–448
- Howland WG (1980) Multispectral aerial photography for wetland vegetation mapping. *Photogramm Eng Rem S* 46:87–99
- Hurd JD, Civco DL, Gilmore MS, Prisloe S, Wilson EH (2005) Coastal marsh characterization using satellite remote sensing and in situ radiometry data: preliminary results. American Society of Photogrammetry and Remote Sensing, Baltimore, MD, USA
- Ivits E, Koch B, Blaschke T, Waser L (2002) Landscape connectivity studies on segmentation based classification and manual interpretation of remote sensing data. The Third International eCognition User Meeting, München, Germany, pp 1–10
- Jensen JR (2000) Remote sensing of the environment: an earth resource perspective (2nd edn). Prentice Hall, Upper Saddle River, New Jersey
- Jensen JR, Christensen EJ, Sharitz R (1984) Nontidal wetland mapping in South Carolina using airborne multispectral scanner data. *Remote Sens Environ* 16: 1–12
- Jensen JR, Hodgson ME, Christensen E, Halkard E, Mackey J, Tinney LR, Shartz R (1986) Remote sensing inland wetlands: a multispectral approach. *Photogramm Eng Rem S* 52:87–100
- Jensen JR, Rutchey K, Koch MS, Narumalani S (1995) Inland wetland change detection in the Everglades Water Conservation Area 2A using a time series of normalized remotely sensed data. *Photogramm Eng Rem S* 61:199–209
- Kearns FR, Kelly M, Tuxen K (2003) Everything happens somewhere: using webGIS as a tool for sustainable natural resource management. *Front Ecol Environ* 1:541–548
- Kelly NM (2001) Changes to the landscape pattern of coastal North Carolina wetlands under the Clean Water Act, 1984–1992. *Landscape Ecol* 16:3–16
- Klemas VV (2001) Remote sensing of landscape-level coastal environmental indicators. *Environ Manage* 27:47–57
- Klemas VV, Dobson JE, Ferguson RL, Haddad KD (1993) A coastal land cover classification system for the NOAA Coastwatch Change Analysis Project. *J Coastal Res* 9:862–872
- Kokaly RF, Despain DG, Clark RN, Livo KE (2003) Mapping vegetation in Yellowstone National Park using spectral feature analysis of AVIRIS data. *Remote Sens Environ* 84:437–456
- Laliberte AS, Rango A, Fredrickson EL (2006) Separating green and senescent vegetation in very high resolution photography using an intensity-hue-saturation transformation and object based classification. American Society for Photogrammetry and Remote Sensing, Reno, NV, USA
- Li J, Chen W (2005) A rule-based method for mapping Canada's wetlands using optical, radar and DEM data. *Int J Remote Sens* 26:5051–5069
- Marani M, Silvestri S, Belluco E, Camuffo M, D'Alpaos A, Lanzoni S, Marani A, Rinaldo A (2003) Patterns in tidal environments: salt-marsh channel networks, vegetation, AGU, San Francisco, CA, USA
- Michener WK, Houhoulis PF (1997) Detection of vegetation changes associated with extensive flooding in a forested ecosystem. *Photogramm Eng Rem S* 63:1363–1374
- Mitsch W, Gosselink J (2000) *Wetlands*. John Wiley & Sons, New York
- Mueller-Dombois D, Ellenberg H (1974) *Aims and methods of vegetation ecology*. John Wiley & Sons, New York
- Ozesmi SL, Bauer ME (2002) Satellite remote sensing of wetlands. *Wetl Ecol Manage* 10:381–402

- Palandro D, Andréfouët S, Dustan P, Muller-Karger FE (2003) Change detection in coral reef communities using Ikonos satellite sensor imagery and historic aerial photographs. *Int J Remote Sens* 24:873–878
- Pennings SC, Bertness MD (2001) Salt marsh communities. In: Bertness SDGMD, Hay ME (eds) *Marine community ecology*. Sinauer, Sunderland, Massachusetts, USA, pp 289–316
- Phinn SR (1998) A framework for selecting appropriate remotely sensed data dimensions for environmental monitoring and management. *Int J Remote Sens* 19:3457–3463
- Phinn SR, Menges C, Hill GJE, Stanford M (2000) Optimizing remotely sensed solutions for monitoring, modeling, and managing coastal environments. *Remote Sens Environ* 73:117–132
- Phinn SR, Stow DA, Mouwerik DV (1999) Remotely sensed estimates of vegetation structural characteristics in restored wetlands, Southern California. *Photogramm Eng Rem S* 65:485–493
- Phinn SR, Stow DA, Zedler JB (1996) Monitoring wetland habitat restoration in southern California using airborne multispectral video data. *Restoration Ecol* 4:412–422
- Ramsey EW, Laine S (1997) Comparison of Landsat Thematic Mapper and high resolution photography to identify change in complex coastal wetlands. *J Coastal Res* 13:281–292
- Reimold RJ, Gallagher JL, Thompson DE (1973) Remote sensing of tidal marsh. *Photogramm Eng Rem S* 39:477–488
- Rosso PH, Ustin SL, Hastings A (2005a) Mapping marshland vegetation of San Francisco Bay, California, using hyperspectral data. *Int J Remote Sens* 26:5169–5191
- Rosso PH, Ustin SL, Hastings A (2005b) Use of lidar to study changes associated with *Spartina* invasion in San Francisco Bay marshes. *Remote Sens Environ* 100:295–306
- San Francisco Estuary Institute (SFEI) 2005. *Wetland Tracker*. San Francisco Estuary Institute [Online] Available: <http://www.wetlandtracker.org/> (Last access on 1 June 2008)
- Sanderson EW, Ustin SL, Foin TC (2000) The influence of tidal channels on the distribution of salt marsh plant species in Petaluma Marsh, CA, USA. *Plant Ecol* 146:29–41
- Scarpace FL, Quirk BK, Kiefer RW, Wynn SL (1981) Wetland mapping from digitized aerial photography. *Photogramm Eng Rem S* 47:829–838
- Schiewe J, Tufte L, Ehlers M (2001) Potential and problems of multi-scale segmentation methods in remote sensing. *GIS* 14: 34–39
- Schmid T, Koch M, Gumuzzio J, Mather PM (2004) A spectral library for a semi-arid wetland and its application to studies of wetland degradation using hyperspectral and multispectral data. *Int J Remote Sens* 25:2485–2496
- Schmidt KS, Skidmore AK (2003) Spectral discrimination of vegetation types in a coastal wetland. *Remote Sens Environ* 85:92–108
- Seher JS, Tueller PT (1973) Color aerial photos for marshland. *Photogramm Eng Rem S* 39: 489–499
- Shima LJ, Anderson RR, Carter VP (1976) The use of aerial color infrared photography in mapping the vegetation of a freshwater marsh. *Chesapeake Sci* 17:74–85
- Shuman CS, Ambrose RF (2003) A comparison of remote sensing and ground-based methods for monitoring wetland restoration success. *Restoration Ecol* 11:325–333
- Skidmore AK, Bijker W, Schmidt KS, Kumar L (1997) Use of remote sensing and GIS for sustainable land management. *ITC J* 3/4:302–315
- Sousa WP (2001) Natural disturbance and the dynamics of marine benthic communities. In: Bertness SDGMD, Hay ME (eds) *Marine community ecology*. Sinauer, Sunderland, Massachusetts, USA, pp 85–130
- Stankiewicz K, Dąbrowska-Zielińska K, Gruszczyńska M, Hościło A (2003) Mapping vegetation of a wetland ecosystem by fuzzy classification of optical and microwave satellite images supported by various ancillary data. In: Owe M, D'Urso G, Toullos L (eds) *SPIE. Remote Sensing for Agriculture, Ecosystems, and Hydrology IV*
- Sugumaran R, Davis C, Meyer J, Prato T, Fulcher C (2000) Web-based decision support tool for floodplain management using high-resolution DEM. *Photogramm Eng Rem S* 66:1261–1265
- Thomson AG, Fuller RM, Yates MG, Brown SL, Cox R, Wadsworth RA (2003) The use of airborne remote sensing for extensive mapping of intertidal sediments and saltmarshes in eastern England. *Int J Remote Sens* 24:2717–2737

- Töyrä J, Pietroniro A (2005) Towards operational monitoring of a northern wetland using geomatics-based techniques. *Remote Sens Environ* 97:174–191
- Turner MG, Gardner RH, O'Neill RV (2001) *Landscape ecology in theory and practice: pattern and process*. Springer-Verlag, New York
- Tuxen K, Kelly M (2008) Multi-scale functional mapping of tidal marsh vegetation using object-based image analysis. In: Blaschke T, Lang S, Hay G (eds.). *Object-based image analysis: spatial concepts for knowledge-driven remote sensing applications*. Series: Lecture notes in Geoinformation and Cartography. Springer. pp. 415–442
- Tuxen, KA, Schile LM, Kelly M, Siegel SW (2008) Vegetation Colonization in a restoring tidal marsh: a remote sensing approach. *Restoration Ecology* 16(2):313–323
- Underwood E, Ustin S, DiPietro D (2003) Mapping nonnative plants using hyperspectral imagery. *Remote Sens Environ* 86:150–161
- Van Dyke E, Wasson K (2005) Historical ecology of a Central California Estuary: 150 years of habitat change. *Estuaries* 28:173–189
- Wang L, Sousa WP, Gong P (2004a) Integration of object-based and pixel-based classification for mapping mangroves with IKONOS imagery. *Int J Remote Sens* 25:5655–5668
- Wang L, Sousa WP, Gong P, Biging GS (2004b) Comparison of IKONOS and QuickBird images for mapping mangrove species on the Caribbean coast of Panama. *Remote Sens Environ* 91:432–440
- Wulder MA, Hall RJ, Coops NC, Franklin SE (2004) High spatial resolution remotely sensed data for ecosystems characterization. *BioScience* 54:511–521
- Yang X (2005a) Remote sensing and GIS applications for estuarine ecosystem analysis: an overview. *Int J Remote Sens* 26:5347–5356
- Yang X (2005b) Use of LIDAR elevation data to construct a high-resolution digital terrain model for an estuarine marsh area. *Int J Remote Sens* 26:5163–5166
- Yang X, Liu Z (2005a) Quantifying landscape pattern and its change in an estuarine watershed using satellite imagery and landscape metrics. *Int J Remote Sens* 26:5297–5323
- Yang X, Liu Z (2005b) Using satellite imagery and GIS for land-use and land-cover change mapping in an estuarine watershed. *Int J Remote Sens* 26:5275–5296
- Yoon G-W, Cho SI, Jeong S, Park J-H (2003) Object oriented classification using Landsat images, American Society for Photogrammetry and Remote Sensing (ASPRS), Anchorage, Alaska
- Yu Q, Gong P, Clinton N, Kelly M, Shirokauer D (2006) Object-based detailed vegetation classification with airborne high resolution remote sensing imagery. *Photogramm Eng Rem S* 72: 799–811
- Zedler JB, Callaway JC, Desmond JS, Vivian-Smith G, Williams GD, Sullivan G, Brewster AE, Bradshaw BK (1999) California salt marsh vegetation: an improved model of spatial pattern. *Ecosystems* 2:19–35
- Zhang M, Ustin SL, Rejmankova E, Sanderson EW (1997) Monitoring Pacific coast salt marshes using remote sensing. *Ecol Appl* 7:1039–1053



## Chapter 16

# Assessment of Coastal-Vegetation Habitats Using Airborne Laser Remote Sensing

Amar Nayegandhi and John C. Brock

Airborne light detection and ranging (LIDAR) technology has broad applications in vegetation-structure mapping within coastal communities. This chapter provides an overview of airborne LIDAR technology and assesses the capabilities and limitations of LIDAR instruments available from research and commercial sources. Previous studies on the extraction of vegetation metrics such as height and density of vegetation in coastal forests are reviewed, with special emphasis on canopy height of short shrubs, marsh, grass, and other vegetation found in the littoral zone. The studies reviewed in this chapter report accurate measurements of canopy height and ground topography in most forested environments. The accuracy in determining the height of low vegetation is considerably improved when using a small-footprint, waveform-resolving LIDAR system. The integration of spectral imagery and LIDAR has the potential of significantly improving the classification and structural mapping of coastal-plant communities. Technical challenges facing the airborne LIDAR remote sensing industry include: (i) the estimation of vegetation height and density for submarine vegetation, (ii) better understanding of the relations that exist between forest structure and LIDAR backscatter return, and (iii) improvements in standardized software to glean structural information from waveform data. In total, the studies reported in this chapter demonstrate that laser remote sensing is a cost-effective and reliable tool for the quantitative assessment of vegetation habitats on barrier islands, wetlands, and other coastal-plant communities.

### 16.1 Introduction

Coastal forests provide a protective barrier between terrestrial ecosystems and nearshore water bodies. The plant species native to this habitat are specially adapted to withstand salinity, soil type, and other stressors such as high tides and winds. Coastal geomorphology, and consequently coastal forest characteristics, have been

---

A. Nayegandhi (✉)

Jacobs Technology, U.S. Geological Survey, Florida Integrated Science Center,  
St. Petersburg, FL 33701, USA  
e-mail: anayegandhi@usgs.gov

shaped over geologic time by changing sea levels and variation in sediment supply (Williams et al. 1999). In the littoral zone, intertidal salt marshes occupy a broad, flat expanse of landscape often referred to as the marsh platform at an elevation that approximates that of mean high water. The elevation of this platform relative to sea level determines total wetland area, inundation frequency, and wetland productivity (Morris et al. 2005). Vegetation change in coastal communities is also a potentially valuable integrative measure of sea-level rise. Moreover, forest structure is a key to the functioning of an ecosystem (Spies 1998), and accordingly techniques to distinguish organizational patterns are quite useful in understanding processes related to coastal-forest habitat, physiology, and dynamics.

Remote sensing represents an important tool for understanding coastal-ecosystem diversity across several different spatial scales and is also critical for assessments of changes in ecosystem patterns over time. Remote sensing provides the most efficient tool available for determining landscape-scale elements of forest biodiversity, such as the physical arrangement of patches of vegetated communities (Innes and Koch 1998), and as a hydrologic monitoring tool (Kite and Pietroniro 1996). Passive remote sensing techniques, based on reflected or emitted light energy from natural sources within the electromagnetic spectrum, have been widely used in forestry applications since the advent of airborne and spaceborne sensors. Several different types of spaceborne spectral remote sensing tools exist, ranging from high-resolution sensors capable of providing 2 to 4 m resolution multi-spectral imagery at swath widths of 10–16 km, to medium- (4–30 m) or low- (30–>1000 m) resolution imagery with increased spectral resolution (3–15 bands) and 100–1000 km image swath widths (Cracknell and Hayes 2006). In contrast, airborne instruments provide higher spatial resolution than satellite sensors do, but with typically much smaller sampling swath or area, because of the much lower altitude at which they operate. Remote sensing is thus capable of providing a range of spectral data for coastal-biodiversity studies.

The recent emergence of remote sensing based on airborne **Light Detection and Ranging (LIDAR)** as a coastal-forest management tool promises to increase the efficiency of forest inventory programs dramatically. LIDAR is an active remote sensing technique that determines the distance between the sensor and the target by accurately measuring the round-trip time of a pulse of laser energy (Wehr and Lohr 1999). LIDAR altimeters have demonstrated the capability to provide greatly improved remotely sensed estimates of important aspects of canopy structure (Lefsky et al. 1999).

Airborne LIDAR technology has been commonly used in mapping barrier island vegetation communities. These communities are strongly influenced by littoral geomorphic processes. Subjected to frequent and major storm events, coastal-vegetation communities undergo more frequent and stochastic changes than do their upland counterparts. The relative abundance and spatial distribution of vegetation-community types on a barrier island can also serve as an indicator and a measure of change due to littoral processes (Nayegandhi et al. 2006). Detailed and accurate topography from LIDAR surveys provides relevant information for understanding the dynamics of habitat distribution on low-lying barrier islands. LIDAR digital elevation models (DEMs) have been used to model changes in marsh distribution

and as additional and independent data layers for mapping barrier island habitats in conjunction with other remote sensing imagery (Gibeaut et al. 2003).

LIDAR has routinely been used to determine precise digital canopy height and terrain models for surface hydrologic studies. Hydrodynamic vegetation roughness refers to the resistance force exerted by vegetation on water flowing over or through it (Straatsma and Middlekoop 2006). High vegetation roughness reduces the velocity of flowing water, which leads to higher water levels, thereby increasing flood risks (Straatsma and Middlekoop 2006). Roughness coefficients can be derived using topographic information acquired by airborne laser scanning for modeling hydrologic processes and hydraulic surface-flow models in stream channels and the surrounding floodplain (Cobby et al. 2001, Mason et al. 2003, Hollaus et al. 2007).

However, several challenges still exist in mapping wetland topography in coastal areas, where the elevation changes are slight, except for levees and outcrops, and the vegetation cover varies from short shrubs to dense maritime forests. In an evaluation study of LIDAR technology in a deltaic wetland environment, Toyra et al. (2003) demonstrated that LIDAR pulses had difficulties penetrating thick willow cover and dense thatch layers beneath grasses and sedges. However, recent advances in LIDAR technology have resulted in the potential to produce detailed vertical structure of coastal vegetation canopies (Lefsky et al. 1999), and derive accurate digital terrain models under dense coastal marshes and short shrubs (Andersen et al. 2006). The primary objective of this chapter is to review the capabilities and potential of airborne laser remote sensing as a tool for quantitative assessment of vegetation habitats on barrier islands, wetlands, and other coastal zones.

## 16.2 Airborne LIDAR Technology Overview

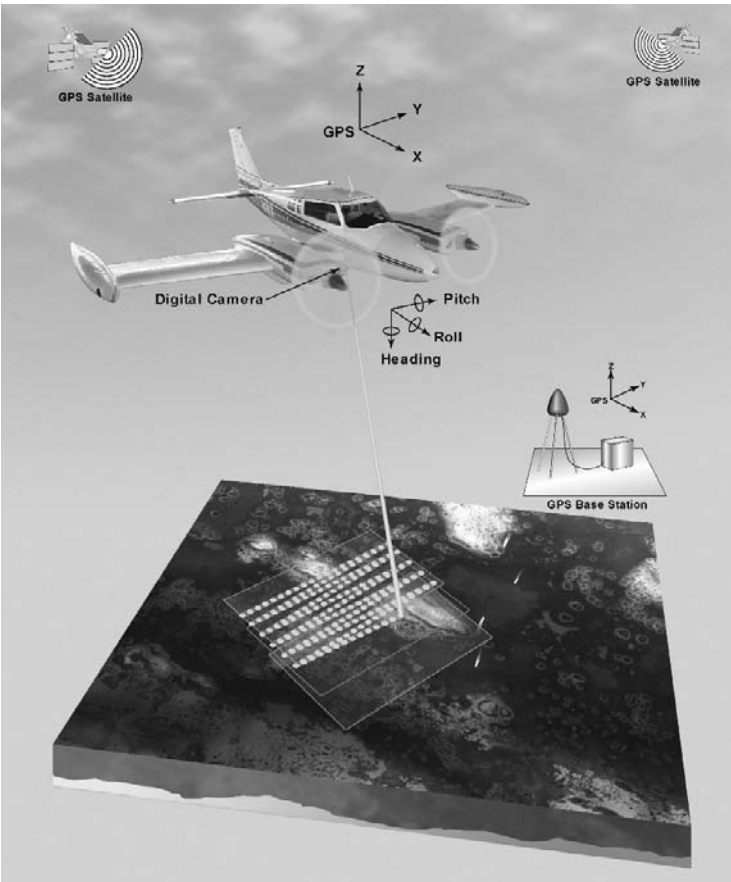
Most airborne LIDAR systems consist of the following components:

- Laser ranging device to determine the distance between the aircraft and the target object below,
- Differential Global Positioning System (DGPS) to determine the location of the aircraft,
- Inertial Navigation System (INS) to determine the orientation of the aircraft, and
- Digital red-green-blue (RGB) or color-infrared (CIR) camera, to provide a visual representation of the mapped area.

The laser ranging device typically includes a pulsed laser transmitter emitting highly collimated laser pulses directed to a scanning mirror. Laser system characteristics that help differentiate between current airborne LIDAR instruments include: (i) pulse repetition frequency (PRF) ranging from 1 kHz to 170 kHz, (ii) the total energy content of the laser pulse – varying from 50  $\mu$ J for low power, high-PRF systems to 5 mJ for high-power, low-PRF systems, (iii) pulse duration, which is the time during which the laser output-pulse power remains continuously above half its maximum value – varying from 1.5 ns for short-temporal-pulse systems that provide increased measurement accuracy and enhanced multiple-return pulse resolution, to

10 ns for traditional discrete-return systems, and (iv) wavelength of the outgoing pulse, which is typically near-infrared (1064 nm) for subaerial topographic mapping and green (532 nm) for submerged topographic mapping.

The scanning device steers the laser transmitted beam to create a scanning pattern based on the opto-mechanics and electro-optical properties of the scanner. Several types of scanning mechanisms have been used on airborne LIDAR systems (Wehr and Lohr 1999). The most common scanning device is the oscillating mirror that produces a zigzag line (bidirectional scan) on the surface of the target area as the mirror rotates back and forth within its pre-defined field of view (Fig. 16.1).



**Fig. 16.1** Principles of airborne laser scanning using the Experimental Advanced Airborne Research LIDAR (EAARL). This laser instrument uses a green wavelength laser and a raster scanning mechanism to acquire LIDAR data. GPS receivers on the aircraft are combined with data acquired by a base station set up at a nearby location to locate position of the aircraft precisely. Aircraft orientation parameters (pitch, roll, and heading) are obtained by an Inertial Measurement Unit (IMU) onboard the aircraft. A digital camera provides coincident high-resolution imagery of the mapped area

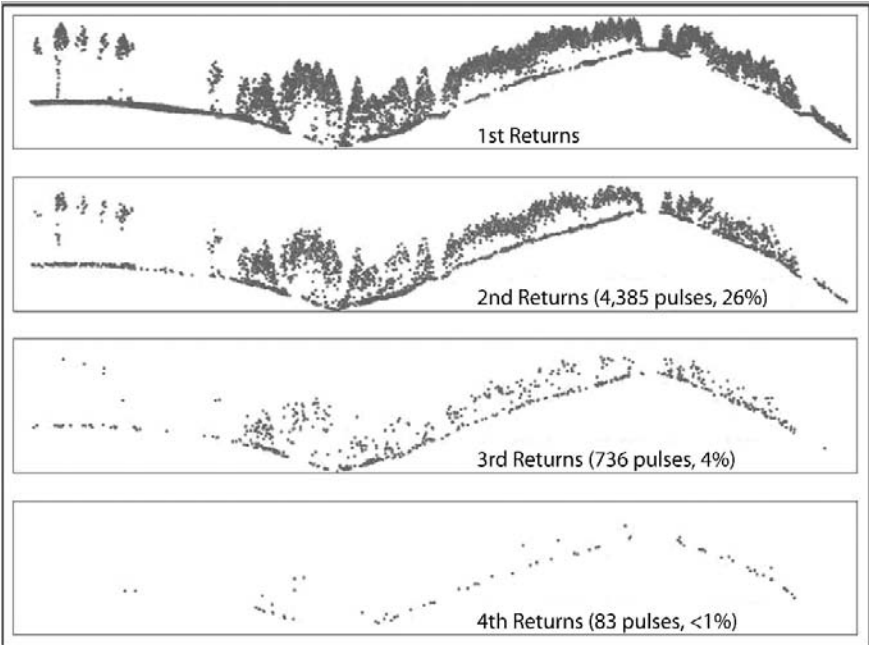
Data acquired by an onboard GPS receiver are differentially corrected using one or more nearby GPS base stations to provide the absolute aircraft trajectory. The base-station antenna is mounted on a known location and remains stationary during the survey, thereby enabling the post-flight differential correction of the trajectory of the aircraft. The Inertial Measurement Unit (IMU) comprises three accelerometers and three gyroscopes arranged in an orthogonal triad to measure the local gravity vector, acceleration vector, and angular rate vector experienced by the IMU at a typical sampling rate of 200 Hz. Post-flight processing GPS-IMU software is generally used to convert the measured accelerations and angular rates along with differential GPS positioning to determine pitch, roll, and heading of the aircraft. The aircraft trajectory, IMU-derived orientation data, and the laser range measurements are combined with calibration data and instrument mounting parameters in post-flight processing software to determine the three-dimensional location of the target.

Two of the major characteristics that distinguish among LIDAR instruments are the footprint size of the laser pulse and the way in which the intensity of the return is recorded. Accordingly, airborne LIDAR systems used in coastal vegetation applications can be categorized as large footprint or small footprint, and discrete-return or waveform-resolving as explained in the following sections.

### ***16.2.1 Small-Footprint, Discrete-Return LIDAR***

Discrete-return systems are currently the most common type of LIDAR systems available in commercial industry. They typically record one (e.g., first *or* last), two (e.g., first *and* last), or several (i.e., up to five) returns for each laser pulse. All discrete-return LIDAR systems have a relatively small footprint (0.2–0.9 m), the precise size of which depends on the beam divergence, receiver field-of-view, and flight altitude. Recent studies have suggested that the optimal experimental design for discrete-return systems is to capture three echoes per pulse, since less than 1% of pulses return a fourth echo, and only about 0.1% of pulses return a fifth echo (Lim et al. 2003; Fig. 16.2). The basic principles and design constraints of discrete-return LIDAR systems are well documented in literature (Wehr and Lohr 1999, Baltsavias 1999, Fowler et al. 2007). System characteristics of two small-footprint discrete-return LIDAR systems currently available in commercial industry reveal a push toward higher sampling resolution and greater operating altitude, with increased horizontal and vertical accuracy (Table 16.1).

Obtaining forest measurements such as canopy height and volume using discrete-return, small-footprint LIDAR systems has yielded useful results (Næsset 2002, Lim et al. 2003, Popescu et al. 2003, Bortolot and Wynne 2005). However, a number of factors limits the capability of discrete-return small-footprint sensors in deriving forest measurements: (1) the inability of a small-footprint laser pulse to strike the *tops* of trees consistently, especially in conifer stands; (2) the small-footprint laser pulse may penetrate through gaps all the way through to the ground without intercepting the canopy, thereby indicating the absence of a canopy; (3) conversely, the laser



**Fig. 16.2** Data acquired by a discrete-return LIDAR system in a forested area showing the percentage of returns resolved from successive reflections from a laser pulse. Returns from all laser pulses resulted in 16,864 returns. The 3rd and 4th returns account for less than 5% of the total returns. *Image courtesy of Robert J. McGaughey, USDA Forest Service*

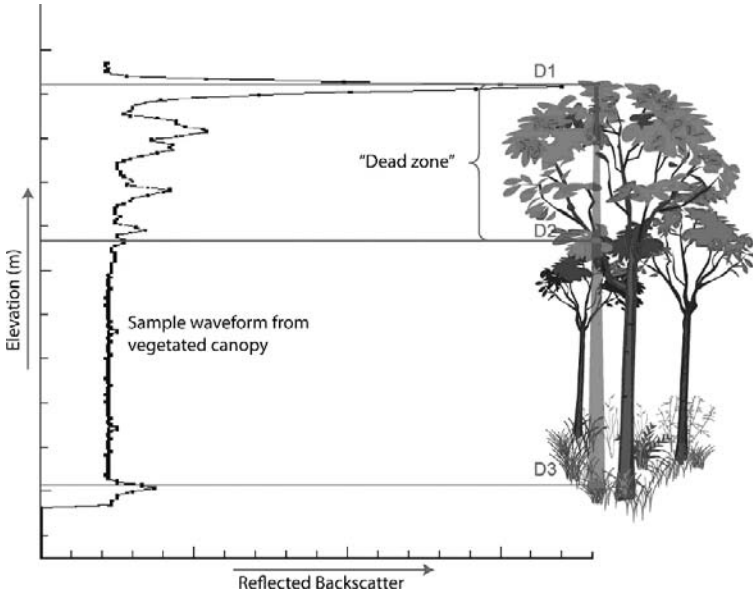
pulse may be entirely blocked by dense canopy materials (leaves and branches), thereby not reaching the ground; (4) low-altitude surveys with narrow swaths require extensive flying to obtain adequate data coverage over large areas; and (5) most discrete-return systems require a minimum vertical object separation to register consecutive returns from the pulse separately, thereby being blind to canopy material within this “dead zone” (Fig. 16.3). The dead zone, which typically ranges from 1.5 m to greater than 7 m in vertical height (Nayegandhi et al. 2006), is usually caused by hardware limitations in the sensor design. Figure 16.3 is a schematic illustrating the effect of the dead zone between successive discrete returns D1 and D2, wherein reflected laser backscatter from canopy materials between these reflections are not distinguishable by the sensor unless the backscatter is digitized to represent a waveform as explained in the next section.

### 16.2.2 Small-Footprint, Waveform-Resolving LIDAR

Discrete-return LIDAR systems output the three-dimensional coordinates of the surface locations hit by the laser pulse. However, it is not always clear how to interpret

**Table 16.1** Airborne lidar system characteristics of sample commercial and research sensors

	Small-footprint, discrete-return		Small-footprint, waveform-resolving		Large-footprint, waveform-resolving	
Sensor	ALTM	ALS50	EAARL	LMS-Q560	SLICER	LVIS
Type of Operation	Commercial	Commercial	Research	Commercial	Research	Research
Max. Operating Altitude (AGL)	4000 m	6000 m	1000 m	1500 m	10 km	10 km
Wavelength (nm)	1064	1064	532	1500	1064	1064
Pulse energy	< 200 $\mu$ J	?	< 70 $\mu$ J	< 8 $\mu$ J	0.7 mJ	5 mJ
Max. Pulse Repetition Frequency	167 KHz	150 KHz	10 KHz	100 KHz	80 Hz	500 Hz
Pulse width at half maximum	8 ns	11.8 ns	2 ns	4 ns	4 ns	10 ns
Scan angle range	$\pm 25^\circ$	$\pm 75^\circ$	$\pm 22.5^\circ$	$\pm 22.5^\circ$	?	$\pm 7^\circ$
Footprint size@nominal operating altitude	0.3–0.8 m@1km	0.15–0.22 m@1km	0.18 m@300 m	0.5 m@1 km	10 m@5 km	40 m@5 km
Digitizer interval	N/A	N/A	1 ns	1 ns	1 ns	2 ns
Max. number of returns	4	4	N/A	N/A	N/A	N/A



**Fig. 16.3** Schematic showing the dead-zone effect in discrete return LIDAR systems. “D1”, “D2”, and “D3” are successive reflections from a discrete return laser pulse. The laser pulse is effectively blind to canopy material between “D1” and “D2”. The vertical structure information is, however, captured in the sample waveform from a vegetated canopy acquired by a small-footprint waveform-resolving system

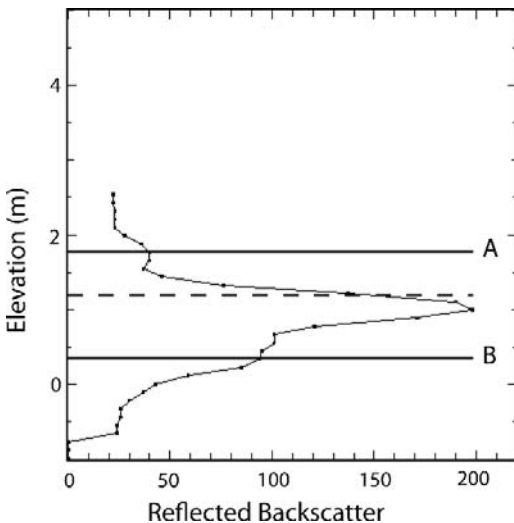
these discrete measurements for different targets, particularly since commercial vendors rarely disclose the detection methods for the determination of the trigger pulses (Wagner et al. 2004). Further, the choice of pulse detection methods has significant impact on accuracy and may affect the quality of measurements (Hug et al. 2004).

A full-temporal waveform-digitizing LIDAR system senses and records LIDAR backscatter returned to the sensor in a series of equal time intervals, usually in 1- to 3- nanosecond increments. The high sensitivity of the receiver optics and electronics results in the characterization of small volume changes of vegetation and a detailed description of vertical canopy volume distribution, which are not separated by discrete-return LIDAR systems (Fig. 16.3). Digitized return waveforms can give detailed insights into the vertical structure of surface objects, surface slope, roughness, and reflectivity (Hug et al. 2004). Recent advances in digital electronics and storage capacities have made it feasible to construct waveform-resolving LIDAR systems that are self-contained and small enough for operational and commercial use (Hug et al. 2004, Fowler et al. 2007). The Riegl waveform-processing airborne laser scanner LMS-Q560 is one of the first commercial airborne LIDAR terrain mapping systems to use waveform digitization (Wagner et al. 2006). The Experimental Advanced Airborne Research LIDAR (EAARL) is a non-commercial, green-wavelength, waveform-resolving system capable of mapping submarine and sub-aerial topography simultaneously (Wright and



Brock 2002, Nayegandhi et al. 2006). Both systems digitize the return waveform at a 1-nanosecond interval over a wide dynamic range, giving a temporal resolution of 14.9 cm in air (Table 16.1). In coastal forestry applications, vertical information from waveform-resolving LIDAR gives details on canopy and sub-canopy structures and the potential to derive accurate ground information under short herbaceous vegetation (Persson et al. 2005, Nayegandhi et al. 2006).

Full waveform digitization of a laser pulse creates a pulse-by-pulse reflection record that is highly sensitive to even minor changes in vegetation structure. This technique enables many multiple returns with short separation to be collected from a single laser shot (Fig. 16.3). This is especially true for a short-temporal-pulse-width laser pulse. Small variations in the vertical structure can be detected by processing the resulting waveforms using a variety of pulse detection methods. Wagner et al. (2004) report a number of detection methods that can be applied on the backscatter waveform: threshold, center of gravity, maximum, zero crossing of the second derivative, and constant fraction. Determining the range in post-flight processing software has the advantage of selecting one or more pulse detection algorithms based on the application, analyzing the intermediate results, and considering neighborhood relations of pulses. For example, canopy-height estimation may be improved by detecting small inflections or “sub-peaks” in the waveform. Figure 16.4 illustrates the result of using different pulse detection methods to derive the range to the first and last return from short vegetation. LIDAR reflections from short shrubs, grass, or other herbaceous vegetation cause the return pulse to widen. The early inflection in the waveform at height A is detected by determining the zero crossing



**Fig. 16.4** Sample waveform illustrating the widening of the return pulse from low, coastal, herbaceous vegetation. The horizontal lines “A” and “B” denote the range to the top and bottom of the vegetation structure, respectively. The dotted line indicates the range determined by a discrete-return LIDAR system using leading-edge threshold detection method

of the second derivative at a low backscatter threshold. Similarly, the range to the last return can be determined by analyzing the waveform starting from the trailing edge, thereby selecting the small inflection at height B from the convolved waveform (Fig. 16.4). The first return represents the height of the canopy surface, and the last return represents ground topography. If this area were mapped by a traditional discrete-return LIDAR sensor using real-time leading-edge threshold detection to determine the range, it would have resolved the range to only one significant return (dashed line in Fig. 16.4).

Small-footprint, waveform-resolving LIDAR systems thus have tremendous potential for mapping forested environments. Many of the limiting factors of discrete-return LIDAR systems are addressed by waveform-resolving systems. The pulse detection method can be modified for determining canopy heights in conifer stands, such that the canopy-top elevation can be determined by small and often convolved inflections in the leading edge of the waveform. The small-footprint LIDAR pulse may still reflect directly off the ground through gaps in the canopy or be entirely blocked by canopy materials in the upper story. In order to minimize these effects and better describe the vertical structure of a vegetation canopy, several individual small-footprint laser pulses can be combined to make a composite “large-footprint” waveform that defines a larger horizontal area (Nayegandhi et al. 2006). The size of the synthesized large footprint can be varied depending on the point sampling density and nature of the vegetated terrain. Further, the short temporal pulse width combined with the ability to determine the pulse detection method in post-processing software can significantly reduce the effect of the “dead zone.”

### ***16.2.3 Waveform-Resolving Large-Footprint LIDAR***

Large-footprint systems collect the complete waveform of reflected energy in a single pulse over a large horizontal footprint (>10m), which generally includes returns from the top of the canopy, and from the ground visible through gaps in the canopy. These systems have been widely used in forestry research over the past decade to determine the vertical distribution of canopy characteristics (Means et al. 1999, Lefsky et al. 1999, Dubayah and Drake 2000, Harding et al. 2001, Lim et al. 2003, Anderson et al. 2006). Metrics derived from large-footprint LIDAR systems have proven useful for predicting a range of ecological variables such as canopy height and structure, the density of forest cover, and aboveground biomass (Means et al. 1999, Dubayah and Drake 2000, Harding et al. 2001, Anderson et al. 2006). Other studies have reliably inferred a Leaf Area Index (LAI) using methods to characterize canopy volume, spatial organization of vegetative material, and empty space within the forest canopy (Lefsky et al. 1999). The Scanning LIDAR Imager of Canopies by Echo Recovery (SLICER) (Harding et al. 2001) and the Laser Vegetation Imaging Sensor (LVIS) (Blair et al. 1999) are large-footprint waveform-resolving LIDAR systems developed for research purposes at NASA's Goddard Space Flight Center (Table 16.1). The instruments have been evaluated by comparing simulated

waveforms from various types of vegetation canopies contained within the laser footprint (Blair et al. 1999). These prototype instruments were originally planned as part of the pre-launch calibration/validation of a spaceborne laser altimeter, the Vegetation Canopy LIDAR (VCL).

Large-footprint systems are optimal for mapping forest structure at the plot level (Dubayah and Drake 2000) for several reasons, including: (1) large footprint size that illuminates the average crown diameter of a tree (10–25 m), thereby providing consistent canopy top and ground returns, (2) high operating altitude and wide image swath, allowing the inexpensive mapping of large forested areas, and (3) digitization of the entire return signal, providing the vertical distribution of intercepted surfaces through the canopy. Waveform data from these instruments have been evaluated using regression techniques to estimate forest stand characteristics in conifer forests (Means et al. 1999), deciduous forests (Lefsky et al. 1999), tropical forests (Drake et al. 2002), and mixed northern temperate forests (Anderson et al. 2006). However, no studies have reported the use of these systems in maritime forests. In coastal environments with low-lying, dynamic and dense vegetation, high-altitude, large-footprint LIDAR systems are cost-prohibitive and inefficient to operate on a regular basis. However, a spaceborne laser altimeter will provide the vertical distribution of intercepted surfaces at very large spatial scales, thereby providing a global reference dataset for terrestrial ecosystem modeling, monitoring, and prediction.

## 16.3 Vegetation Metrics

Current ecological applications of LIDAR remote sensing tend to fall within four categories: (i) deriving canopy heights at the individual tree, plot, and stand level, (ii) deriving ground topography, (iii) measuring the three-dimensional structure and function of vegetation canopies, and (iv) predicting forest stand structure attributes. The first three categories are metrics derived from data acquired by LIDAR systems. These metrics can be evaluated by comparing with ground-based measurements using statistical methods. The fourth category includes predicted measures such as basal area and aboveground biomass, which are derived and evaluated using regression techniques by comparing LIDAR-derived metrics from the first three categories to allometric equations based on field measurements (e.g., DBH). The following sections discuss the metrics derived for the first three categories by reviewing studies conducted using discrete-return and waveform-resolving LIDAR systems and how these metrics may be used to predict forest structure attributes.

### 16.3.1 Canopy Height

Canopy height is determined by calculating the distance between the first return and the ground. An accurate bare-Earth or digital terrain model (DTM) is required to

determine a digital canopy height model. Canopy height is one of the more fundamental measurements in coastal forest inventory and is a critical variable in the quantitative assessment of forest biomass, carbon stocks, growth, and site productivity (Andersen et al. 2006). The height of a forest patch can be expressed as the mean tree height or the maximum tree height in a limited-size plot. Canopy heights are also estimated from percentiles of the laser data by assuming that the vertical leaf area distribution of canopy-forming trees is the same as the vertical distribution of laser points (Magnussen and Boudewyn 1998). Straatsma and Middlekoop (2006) provide a tabulated summary of explained variances based on regression analyses from research on forest height prediction. Several studies have demonstrated that the overall quality of laser scanning prediction of canopy height is better than conventional methods, such as the manual interpretation of aerial stereo photos (Næsset 2002, Popescu et al. 2003). However, most LIDAR canopy height studies demonstrate accuracy within a limited sample environment. Hopkinson et al. (2006) present a method that shows some promise in the search for a more universal canopy height model across a wide range of canopy height, canopy openness, vegetation type, and data collection configurations for small-footprint discrete-return LIDAR.

With the advent of very high-density, discrete-return LIDAR, determination of individual tree and stand heights has become feasible. High-density, small-footprint LIDAR data have been used for estimating plot-level tree height by measuring individual trees identifiable on the three-dimensional LIDAR surface (Popescu et al. 2003). In a rigorous assessment of tree height measurements obtained using LIDAR and conventional field methods, Andersen et al. (2006) determined that LIDAR-derived height measurements were more accurate for ponderosa pine forest ( $-0.43 \pm 0.13$  m) than for Douglas-fir forest ( $-1.05 \pm 0.41$  m), and although tree heights using conventional field techniques ( $-0.27 \pm 0.27$  m) were more accurate than LIDAR ( $-0.73 \pm 0.43$  m), this difference was insignificant compared to the wider coverage and cost efficiencies afforded by a LIDAR-based survey. Small-footprint, waveform-resolving LIDAR data with high sampling density may also be used to determine the height of individual trees, though studies using LIDAR waveforms have only been conducted at the plot level (Nayegandhi et al. 2006). However, large-footprint LIDAR systems cannot be used for characterizing individual trees since the footprint is usually wider than the diameter of the canopy-forming tree.

The effect of beam angle plays a significant role in the determination of canopy height, which may influence the ability of the low power discrete-return LIDAR systems to measure canopy height accurately. The power of the wide-beam LIDAR pulse is spread out over a larger area, leading to a lower signal-to-noise ratio for the returning LIDAR signal, which is sometimes below the threshold detection value of discrete-return LIDAR. Andersen et al. (2006) indicated that high-density ( $6 \text{ points/m}^2$ ), discrete-return, narrow-beam ( $0.3 \text{ mrad}$ ) LIDAR is significantly more accurate than a wide-beam ( $0.8 \text{ mrad}$ ) LIDAR for measuring individual tree heights. However, individual tree height estimates are more influenced by pulse density than by beam divergence (Yu et al. 2004), which indicates that airborne surveys can be conducted at higher flight altitudes if the pulse density and transmit power are sufficient to penetrate through gaps in the canopy.

Few studies have investigated the estimation of short vegetation height from discrete-return LIDAR. In a hydrologic study to understand the effects of landscape roughness on evaporation, soil moisture, runoff, and soil erosion, Cobby et al. (2001) used different algorithms to extract topographic and vegetation heights from discrete-return LIDAR data depending on land cover. Short vegetation heights are calculated using a logarithmic regression relation that predicts the vegetation height from the standard deviations of detrended LIDAR heights in a smaller surrounding area. In a boreal wetland environment, Hopkinson et al. (2005) found the vertical bias of discrete-return LIDAR data to vary with vegetation cover, with no significant vertical bias for grass and herbs. The error in canopy heights was also found to vary with vegetation class, ranging from 0.10 to 0.84 m. The study also determined that low shrubs displayed the highest proportion of vegetation surface underestimation with average laser pulse penetration of 63%. Hollaus et al. (2007) suggest that some inaccuracies of the vegetation height model arose in areas covered by homogeneous meadows with high-grass or scrubs due to technical limitations of the current discrete-return laser systems. When measuring senescent herbaceous vegetation, Straatsma and Middlekoop (2006) note that the minimum detectable object size is of specific importance. The minimum object size is generally influenced by flying altitude, reflectivity, laser power, detector sensitivity, and laser wavelength (Baltsavias 1999).

A short-pulse-width, waveform-resolving LIDAR system is more likely to be able to discriminate between first and last returns from short shrubs (Fig. 16.4), thereby enabling canopy height estimation. High sampling density in small-footprint LIDAR systems also increases the probability that laser pulses will proceed down through gaps in the canopy. As noted earlier, canopy height estimations may be improved by detecting sub-peaks in the waveform, which are too weak to be detected in real time by discrete-return LIDAR (Hug et al. 2004). High-resolution, small-footprint, short-pulse-width, waveform-resolving LIDAR systems thus have the greatest potential in mapping short vegetation communities.

### ***16.3.2 Ground Topography***

Reliable bare Earth information in coastal areas is useful in a wide range of applications, including flood-risk analysis, change detection, and hydrographic numerical modeling. Ground topography is needed in modeling the hydrology of areas, and hence aid in predicting vegetation assemblages likely to occur across specific topographies (Straatsma and Middlekoop 2006). For example, knowing the elevation of the land surface above sea level on barrier islands gives an estimate of relative depths to water tables, which can aid in predicting water availability to vegetation on sandy substrates. Further, the relative elevation of the sediment surface within salt-marsh landscapes is a critically important variable that determines the duration and frequency that these habitats are submerged by the tides. The productivity of the salt marsh plant community is thus dependent on the elevation of the sediment surface (Morris et al. 2005).

Detecting ground topography under vegetation using airborne LIDAR is influenced by the ability of the transmitted laser pulse to “see” the ground. In vegetated terrains, the transmitted laser pulse is intercepted by canopy elements within the path of the laser illumination. The non-intercepted component of the pulse proceeds through the canopy, with any remaining energy being backscattered, reflected, or absorbed at the ground surface. In many situations, the laser pulse is not able to penetrate dense vegetation surfaces completely. Various methods have been developed to extract and identify ground elevations from a point cloud of last returns. The majority of these methods uses spatial filtering techniques that calculate a measure of discontinuity based on a local neighborhood. In dense vegetation, the filtering methods will fail if there are only a few or no ground points in the analyzed area. Sithole and Vosselman (2004) provide an excellent overview and analysis of eight different bare-Earth-extraction algorithms implemented in a variety of land cover types. Almost all bare-Earth algorithms perform better in flat or sparsely vegetated areas. Accuracy usually deteriorates with an increase in vegetation cover or terrain slope. Further, it is difficult to detect ground topography under low vegetation that is not significantly higher than the surrounding bare ground. In addition to errors caused by laser systems and errors caused by applied methodology and algorithms, the quality of the DTM is influenced by data-acquisition characteristics (e.g., point density, flight altitude, and scan angle) as well as errors due to characteristics of the complexity of the terrain (e.g., type, flatness, density of canopy above).

Traditional discrete-return small-footprint LIDAR systems tend to overestimate ground elevation due to (i) minimal pulse penetration through dense vegetation, and (ii) the inability to detect small vertical variations in short vegetation due to the significant “dead zone” between successive reflections. High point-sampling density improves the probability of the laser pulses to find gaps in the canopy. In vegetated coastal areas, ground elevation is highly correlated with vegetation type. Therefore, parallel knowledge of the distribution of vegetation greatly improves the ability to determine an accurate DTM (Göpfert and Heipke 2006). In a deltaic wetland environment, Toyra et al. (2003) computed vertical bias ranging from +0.07 m ( $\pm 0.15$  m) to +0.15 m ( $\pm 0.26$  m) for determining bare Earth elevations under graminoid and willow scrub, respectively. Hopkinson et al. (2005) reported similar results in a boreal wetland environment but noted that the LIDAR system used in estimating ground elevation was unable to distinguish between first and last returns less than 4.6 m apart, thereby recording only one return in canopies lower than this height. The single return usually represented a canopy element in short vegetation, which greatly affected the ability to measure ground topography accurately.

Small-footprint, short-pulse-width, waveform-resolving systems provide the greatest potential to map bare Earth accurately, due to (i) low minimum object separation for each laser-pulse return backscatter, and (ii) the ability to determine ground elevations under short vegetation by analyzing the waveforms using different detection methods in post-processing software (Fig. 16.4). Prior knowledge of land cover type is extremely useful in such cases, since the detection methods can be applied based

on the type of land cover. Nayegandhi et al. (in press) report bare Earth measurement accuracies of 0.16–0.2 m using the EAARL system in a variety of coastal vegetation communities dominated by invasive species such as Australian pine, Brazilian pepper, needle grass, as well as native species such as mangroves.

All small-footprint laser pulses suffer from sampling bias inherent to spaced data points. In contrast, a large-footprint laser pulse will fully illuminate the canopy, thereby penetrating any gaps in the canopy to reach the ground. Large-footprint LIDAR systems are most effective on relatively flat surfaces; however, on steep slopes the spreading of the ground return limits the ability to distinguish between the ground and short shrubs (Harding et al. 2001). An accuracy analysis study conducted in a dense tropical forest to determine sub-canopy topography using the LVIS sensor revealed that the measurements were within  $\sim 1.5$  m of each other on less than  $3^\circ$  slopes, and  $\sim 5$  m on slopes up to  $30^\circ$  (Hofton et al. 2002). Further, in some dense forest canopies, or areas of high canopy cover, the portion of the LIDAR signals being reflected from the ground was weak, making ground determination ambiguous at best, and sometimes completely indeterminable. Measurements made from waveforms containing less than 20% of the total return energy within their lowest reflection caused the largest number of outliers and the largest error (5.22 m), compared to reflections with greater than 50% of the total energy (0.98 m). In general, studies suggest that the accuracy of sub-canopy topography using large-footprint LIDAR systems is worse than those reported using small-footprint LIDAR systems, where accuracies are typically 0.1–0.2 m in flat areas, and  $\sim 1$  m on high slopes (Andersen et al. 2006).

Vegetation-removal algorithms are often used to produce a bare-Earth model at a nominal posting density that is lower than the PRF at data acquisition for very dense vegetation (Morris et al. 2005). The accuracy of the less dense dataset is more likely to improve if one ground return can be selected reliably from a large neighborhood of last returns. Typically, LIDAR vendors will provide a DTM at 5 m resolution in dense vegetation communities even though the data were acquired at 1 m or better spatial resolution.

Very few studies have attempted to determine the ground topography in aquatic vegetation, and the results from these studies are not very encouraging (Hopkinson et al. 2005). Near-infrared-wavelength laser pulse is usually absorbed at the water surface, thereby leading to unpredictable height measurement of vegetation emerging above a water body. Dense patches of mangrove forests, prevailing around the many brackish lakes in coastal regions, are particularly difficult to map using near-infrared LIDAR systems. Water-surface specular reflection from a green-wavelength LIDAR system generally occurs at or near nadir, which results in a strong backscatter signal (Nayegandhi et al. in press). The green-wavelength LIDAR system, capable of mapping subaerial and submarine topography, may also be able to penetrate through the water surface to provide submarine bottom topography. The only known study to map sub-canopy topography under mangroves indicated a 0.2 m RMS error and a very low spatial data density due to the inability to extract sufficient and accurate ground returns from under the dense thickets (Nayegandhi et al. in press).

### 16.3.3 *Canopy Structure*

The accurate and detailed representation of the horizontal and vertical structure of plant communities, also called canopy structure, is a critical metric for a variety of coastal processes. Structural characteristics of canopies have manifold effects on ecosystem composition and function by controlling growth and production, affecting microclimates at various scales, and providing habitat for a diversity of organisms (Parker et al. 2004). The basis for detailed canopy structure information is a set of spatially referenced distance measurements, which are provided by waveform-resolving and discrete-return LIDAR.

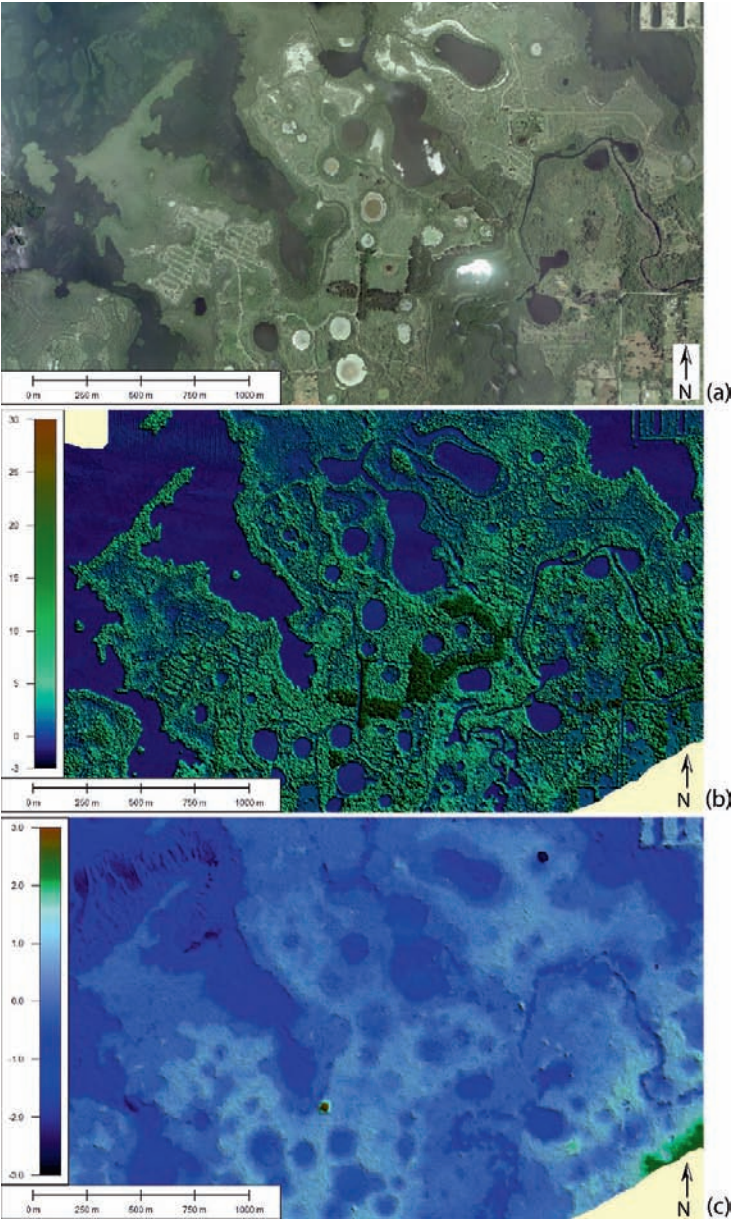
Forest stand characteristics derived from large-footprint LIDAR systems have been successfully extracted over a wide range of forest types and climate zones; from the tropics (Drake et al. 2002) to northern temperate conifer (Means et al. 1999), deciduous (Lefsky et al. 1999), and mixed forests (Anderson et al. 2006). The most common field-derived metric for characterizing canopy structure is foliage height profile (FHP), in which the observer determines the height to the nearest leaf overhead at many locations in the stand. This is done by focusing an upward-viewing telephoto lens calibrated to measure distance (Parker et al. 2004). Since LIDAR systems do not easily distinguish leaves from other surfaces (Lefsky et al. 1999), the derived vertical profile is the surface area of all canopy material, foliar and woody, as a function of height, and is known as the canopy height profile (CHP). CHP is adjusted for occlusion (i.e., the amount of transmit energy seen by lower-canopy elements is less than that seen by the upper-canopy elements) using the same principles as field-derived FHP. Results from Harding et al. (2001) and Lefsky et al. (1999) showed that the large-footprint waveform-based CHPs were highly reproducible and reliably provided a measure of canopy structure that reveals ecologically interesting structural variations in a variety of forest stands. The quadratic mean canopy height metric, derived from CHP as the mean canopy height weighted by the square of the distance from the ground, was found to be highly correlated to both basal area and aboveground biomass in deciduous forests (Lefsky et al. 1999). Several other metrics derived from large-footprint LIDAR returns were found to be significantly correlated with forest structural characteristics at both footprint and plot levels (Means et al. 1999, Drake et al. 2002, Anderson et al. 2006). Canopy reflection ratio (CRR), which is the sum of the portion of the waveform return reflected from the canopy divided by the sum of the portion of the waveform return reflected from the canopy and the ground, is a relative measure of canopy cover (Harding et al. 2001). Independent knowledge of the vertical distribution of canopy reflectance and the reflectance of the ground at the laser wavelength are required to convert CRR into an absolute measure of canopy cover. Nevertheless, CRR was found to correlate with ground-based canopy cover and forest biomass in coniferous forest (Means et al. 1999). The height of median energy (HOME), which is the median height of the entire signal from the waveform, was found to be a good predictor of biomass in tropical forests, and sensitive to changes in both the vertical arrangements of the canopy and the degree of canopy openness (Drake et al. 2002).



Although structural metrics derived from large-footprint LIDAR systems were not tested in coastal forests, similar metrics derived from small-footprint waveforms acquired by the EAARL system yielded promising results in coastal vegetated environments on a barrier island and within a wetland (Nayegandhi et al. 2006). The composite waveforms, derived from a collection of individual small-footprint waveforms within a 10-m-diameter footprint, showed high correlation when tested for reproducibility from overlapping surveys for CRR and HOME metrics. The effect of occlusion in small footprint waveforms is minimal, since the individual waveforms within the composite footprint attenuate only within the small footprint but originate from various vertical layers in the canopy as they travel through gaps within the canopy. Further, the spatial distribution of energy within each small footprint minimally affects the horizontal organization of reflecting surfaces. In contrast, the large-footprint LIDAR is greatly affected by the Gaussian distribution of laser energy within the footprint (Harding et al. 2001).

Research conducted to determine canopy structural attributes using discrete-return LIDAR systems has focused on an individual tree-based approach (Maltamo et al. 2004, Bortolot and Wynne 2005). High sampling density provides the possibility to recognize individual trees and attributes such as crown area, tree height, stem diameter, and stem number. While much research using large-footprint LIDAR systems has been to derive structural canopy information using statistical methods, in which features and predictors are assessed using regression and discriminant analysis (Means et al. 1999, Lefsky et al. 1999, Dubayah and Drake 2000, Harding et al. 2001, Anderson et al. 2006), the small-footprint, high-density LIDAR data have been analyzed with image processing methods, which utilize computer-vision techniques to locate and measure the properties of individual trees (Popescu et al. 2003, Maltamo et al. 2004, Bortolot and Wynne 2005, Andersen et al. 2006). Characteristics of forest stands derived from discrete-return LIDAR systems have been found to be correlated strongly to vegetation density, biomass, and timber volume using image processing based retrieval methods (Maltamo et al. 2004, Bortolot and Wynne 2005). Næsset (2002) estimated several forest attributes with regression methods using canopy density metrics which were computed as the proportions of both first- and last-pulse laser hits above the 0, 10, . . . , 90 quantiles of the height distributions to the total number of pulses. However, individual stems in under-story vegetation in dense canopies were difficult to detect using these methods (Maltamo et al. 2004).

Compared to forestry research, few studies have been reported on the extraction of vegetation structure of low vegetation, such as reed, natural grassland, herbaceous vegetation, or low shrubs. Straatsma and Middlekoop (2006) report one study that found only very poor relations between height distributions of laser scan data and the vegetation density of low floodplain vegetation. A look-up table was established to assign vegetation density values to areas with a specific vegetation height range to enable roughness computation. Vegetation density determination from laser scanning data thus remains a challenge. A detailed structural characterization of intertidal marshes is particularly challenging, because sites typically have a complex net of small channels and creeks among uniform and dense vegetation with low-elevation relief. Accurate mapping of channels hidden by vegetation, areas of



**Fig. 16.5** Coastal-vegetation topography acquired by the EAARL system on March 5, 2004, in Terra Ceia Aquatic and Buffer Preserve, located in the southeast coast of Tampa Bay, FL, USA. (a) High-resolution digital georeferenced imagery of a section of the Preserve shows patches of vegetated communities dominated by invasive species such as Australian pine, Brazilian pepper, and needle grass. Native mangroves surround the many fresh and saltwater ponds in the region. The submerged vegetation is primarily composed of seagrass on sandy substrates. *Image courtesy of TerraServer-USA, obtained using Global Mapper software.* (b) Canopy height sub-aerial topography derived from data acquired by the EAARL system. (c) Seamless bare-Earth and submerged topography acquired by the EAARL system

flooding, or the elevation of small mounds are of great importance to the functioning of intertidal marshlands.

### ***16.3.4 Submerged Topography***

Airborne laser remote sensing has been successfully used in characterizing emergent coastal vegetation communities. However, the challenge still remains to estimate vegetation height and density for submerged vegetation from laser scanning data. Airborne LIDAR Bathymetry (ALB) is a technique for measuring the depths of moderately clear, nearshore coastal waters and lakes from a low-altitude aircraft using a scanning pulse laser beam (Guenther 2007). Instruments that use a green-wavelength laser, such as the EAARL system, can penetrate through relatively clear water, but very little research has been conducted to determine the height of submarine vegetation using ALB. Mapping submerged topography using LIDAR presents several challenges and requires thorough understanding of the effect of the air/water interface on the laser pulse and its scattering through the water column. The laser transmit power is regulated in some ALB systems to allow eye-safe operation with sufficient pulse energy for high signal-to-noise ratios by expanding the beam to illuminate a diameter of at least several meters at the water surface (Guenther 2007). Another generic problem that must be solved is the handling of the several orders of magnitude of amplitude dynamic range between strong water-interface returns and the weak bottom returns. ALB is often optimal in shallow areas where boat-based acoustic surveying is inefficient, dangerous, or impossible to undertake. Further, the ability of an airborne LIDAR system to map submerged and sub-aerial topography simultaneously in a single overflight allows for detailed and seamless mapping of vegetation communities in coastal areas (Fig. 16.5). Recent advances in laser hardware, in-flight LIDAR operation, and post-processing of waveform data from the EAARL system present a viable solution to mapping submarine and terrestrial topography using a short-pulse, green-wavelength LIDAR system.

## **16.4 Comparison with Other Technologies**

Photogrammetry and Interferometric Synthetic Aperture Radar (IFSAR) are the other remote sensing technologies capable of making topographic measurements. A large variety of IFSAR, LIDAR, and photogrammetric sensors exist, and the technology and performance for all three types of sensors are continuously improving. Hence, only very general comparisons of the sensor characteristics are presented. Photogrammetric sensors generate geo-referenced spectral and topographic data when operated with enabling technologies (GPS, IMU) and supporting ground control information. Airborne photogrammetric surveys are conducted to produce significant image overlap along each flight segment to allow stereo viewing for orthoimage production. An aerotriangulation process is generally required

to combine the ground coordinates, image measurements, and exterior orientation data to create orthoimage DEMs. IFSAR systems operate at microwave frequencies (3–40,000 MHz) and determine the parallax of stereoscopic observations by measuring the phase difference between signals received by two antennas spatially separated in the cross-track plane (Hensley et al. 2007).

IFSAR and LIDAR are active sensors that can be flown in the day or night, while photogrammetry requires daylight and optimum sun angle during the survey. LIDAR and IFSAR missions can be conducted in coastal regions during overcast weather conditions. Planning considerations required when using IFSAR and LIDAR are primarily driven by tides and GPS satellite configuration, i.e., the effect of sun angle is given lower priority as compared to photogrammetric surveys. IFSAR has the additional advantage of not being affected by inclement weather and low-level cloud cover, as long as conditions do not degrade the image formation process. IFSAR systems are typically flown at higher altitudes allowing efficient mapping of broad spatial areas.

In forested areas, the ability of LIDAR to obtain ground topography is far superior to IFSAR or photogrammetric methods. Both IFSAR and photogrammetric methods require the same surface to be “seen” by at least two independent images, to allow stereoscopic viewing. In dense vegetation canopies, the same spot on the ground is rarely seen from two different viewing angles, thereby making it nearly impossible for the two independent images to “see” the same spot on the ground beneath the canopy. In photogrammetry, true ground surface is usually determined by manually selecting the ground surface heights and then extrapolating to other portions of the canopied area. Heights measured by IFSAR systems are reflective surface heights that may lie anywhere within the canopy, and although longer wavelength systems penetrate deeper into the canopy, the precise location within the canopy corresponding to the height measurement is not easily determined (Hensley et al. 2007).

The integration of spectral imagery and LIDAR has the potential to improve the extraction of forest information significantly. Laser data provide vertical information on various layers through the canopy, including accurate ground topography, whereas optical imagery provides more details about the spatial geometry and spectral information usable for classification of tree species and health. In coastal forests, simultaneous acquisition of aerial imagery and LIDAR can provide the necessary spectral and three-dimensional canopy information to resource managers, especially after major storm events. Even though most LIDAR surveys include a digital camera for spectral image acquisition, these images are only used for visual inspection during processing and quality control of topography products generated from LIDAR. The mission planning considerations and optimal flight operations for airborne LIDAR and digital imagery surveys are considered different enough by commercial vendors to fly these surveys independently. Nevertheless, the integration of multi-spectral and LIDAR elevation data can provide canopy, sub-canopy, and habitat classification in coastal regions ranging from marsh characterization in the littoral zone (Morris et al. 2005) to dense and tall vegetation canopy structure information on watersheds (Straatsma and Middlekoop 2006).

## 16.5 Outlook

Recent advances in acquisition, processing, and visualization of remotely sensed data have led to the availability of a broad range of techniques for the management of coastal resources. Over the past decade, significant advances have been made in using laser ranging to determine ground topography and vegetation structure. Several studies reviewed in this paper show that vegetation heights of coastal forests and bare Earth under different types of vegetation can be measured reliably. The laser pulse must be able to proceed through gaps in the canopy for accurate estimation of ground topography. As a rule of thumb, if on a bright sunny day, some amount of sunlight can be seen on the ground beneath the canopy, then there is a very good possibility that some laser pulses will reach the ground. If the density of vegetation precludes any sunlight from reaching the ground, the laser pulse will not be able to penetrate through the canopy. High pulse density increases the probability to find any gaps in the canopy. Advances in computer storage hardware and electronics are pushing commercial sensors toward higher sampling density, which also enables the sensor to be operated at higher altitudes for increased swath width.

The time duration of the laser pulse affects the ability to distinguish between successive reflections from different objects within the path of the laser illumination – short temporal-width laser pulses provide increased measurement accuracy and enhanced multiple-return pulse resolution (Nayegandhi et al. 2006). Determining heights of short vegetation canopies is a more difficult problem due to the lack of separation between the top of the vegetation and the ground. Small-footprint, discrete-return LIDAR systems tend to overestimate the height of bare Earth due to the inability to detect ground below herbaceous vegetation. The waveform resolving systems have a greater ability to detect bare Earth by analyzing the waveform in post-processing software and detecting small inflections in the waveforms that are not detected by discrete-return systems in real-time hardware. The software techniques to detect these inflections in small-footprint systems have only been developed and applied to sample environments (Nayegandhi et al. 2006, Wagner et al. 2006). The analysis of large-footprint waveforms has also been conducted for research purposes only and applied to specific target locations where the study was conducted (Dubayah and Drake 2000). There is no commercial software package that analyzes waveforms acquired by LIDAR systems. With the advent of commercial small-footprint LIDAR systems (Wagner et al. 2006) and several other airborne LIDAR manufacturing companies including a “waveform” mode to their product, there will be an incentive for commercial software to be developed to glean more information from waveform data.

The theoretical understanding of the relations that exist between forest structure and the LIDAR backscatter return is still incomplete. LIDAR backscatter, whether resolved as discrete return or waveform, is dependent on the reflectivity and orientation of the target object. The canopy elements (i.e., branches, trunks, leaves) and the ground each have different reflectance measures at the laser wavelength. Further, the transmit pulse is uncalibrated, and the transmit energy often varies from pulse to pulse. The effects of varied transmit energy and canopy reflectances minimally

affect the ranging capability of the laser system. However, when laser intensity is used in the computation of LIDAR-derived metrics, it is necessary to have better understanding of these attributes. If the canopy and ground reflectance values were known and the laser pulse were calibrated, waveform-resolving LIDAR systems would be able to provide an absolute measure of canopy cover (Harding et al. 2001). Currently, small- and large-footprint waveforms have only been used to derive a relative measure of canopy cover (Drake et al. 2002, Nayegandhi et al. 2006). The intensity component of the laser return signal, if properly calibrated and radiometrically corrected, could serve as an excellent tool to discriminate between different types of vegetation cover.

While the absolute and calibrated measure of laser intensity to conduct land cover classification is still being researched, the fusion of LIDAR data and other image sources provides the necessary three-dimensional and spectral synoptic data at multiple scales to address key coastal vegetation issues. Several studies discussed in this paper reveal the strong potential of using a combination of spectral and LIDAR data for marsh characterization, wetland delineation, and floodplain management. Boundaries between vegetation types can be generated from object-based classification techniques using spectral data and metrics derived from LIDAR data.

Large-footprint, waveform-sampling LIDAR can characterize the structural complexity and associated functional properties of natural landscapes relevant to ecological investigations by providing vertical and volumetric profiles of forest vegetation (Anderson et al. 2006). The reported accuracies for canopy height and ground topography using large-footprint systems compare favorably to those reported by small-footprint systems in most forested environments, except on slopes and under short vegetation. Research using large-footprint LIDAR systems to predict forest stand structure attributes such as basal area and aboveground biomass has yielded potentially significant results in assessing coastal vegetation communities; however, no specific study has been conducted in coastal communities using a large-footprint LIDAR system. Nevertheless, the results obtained from small-footprint, waveform-resolving LIDAR systems that combine several small-footprint laser pulses to create a synthesized large footprint reveal significant potential in characterizing vegetation structure in coastal communities. It is expected that full waveform digitizing of the return pulse is the future of airborne laser remote sensing for vegetation structure mapping, as it provides a more detailed structure of plant communities, more accurate range measurements, and extraction of more detailed information from the data using custom post-processing methods. Further, research sensors such as the EAARL system have illustrated the use of a short-pulse, green-wavelength laser to map submerged and emergent vegetation structure simultaneously and create seamless topography products for the effective management of coastal resources.

**Acknowledgement** The U.S. Geological Survey's Coastal and Marine Geology Program funded this investigation. The authors thank Monica Palaseanu-Lovejoy (Jacobs – USGS), Robert Woodman (NPS), Barbara Lidz (USGS) and the anonymous referees for their comments and careful review of this manuscript. Any use of trade names is for descriptive purposes only and does not imply endorsement by the U.S. Government.

## References

- Andersen H, Reutebuch SE, McGaughey RJ (2006) A rigorous assessment of tree height measurements obtained using airborne LIDAR and conventional field methods. *Can J Rem Sens* 32:355–366
- Anderson J, Martin ME, Smith ML, Dubayah RO, Hofton MA, Hyde P, Peterson BE, Blair JB, Knox RG (2006) The use of waveform LIDAR to measure northern temperate mixed conifer and deciduous forest structure in New Hampshire. *Remote Sens Environ* 105:248–261
- Baltsavias E (1999) Airborne laser scanning: basic relations and formulas. *ISPRS J Photogramm* 54:199–214
- Blair JB, Rabine DL, Hofton MA (1999) The laser vegetation imaging sensor: a medium-altitude, digitization-only, airborne laser altimeter for mapping vegetation and topography. *ISPRS J Photogramm* 54:115–122
- Bortolot Z, Wynne R (2005) Estimating forest biomass using small footprint LIDAR data: an individual tree-based approach that incorporates training data. *ISPRS J Photogramm* 59:342–360
- Cobby DM, Mason DC, Davenport IJ (2001) Image processing of airborne scanning laser altimetry data for improved river flood modeling. *ISPRS J Photogramm* 56:121–138
- Cracknell AP, Hayes L (2006) Introduction to remote sensing, 2nd edn. Taylor and Francis, UK
- Drake JB, Dubayah RO, Clark DB, Knox RG, Blair JB, Hofton MA, Chazdon RL, Weishampel JF, Prince S (2002) Estimation of tropical forest structural characteristics, using large-footprint LIDAR. *Remote Sens Environ* 79:305–319
- Dubayah RO, Drake JB (2000) LIDAR remote sensing for forestry. *J Forest* 98:44–46
- Fowler R, Samberg A, Flood MJ, Greaves TJ (2007) Topographic and terrestrial LIDAR. In: Maune DF (ed) Digital elevation model technologies and applications: the DEM users manual. American Society for Photogrammetry and Remote Sensing, Bethesda, pp 199–248
- Gibeaut JC, White WA, Smyth RC, Andrews JR, Tremblay TA, Gutiérrez R, Hepner TL, Neuenschwander A (2003) Topographic variation of barrier island subenvironments and associated habitats. Coastal sediments '03: proceedings of the fifth international symposium on coastal engineering and science of coastal sediment processes, American Society of Civil Engineers, CD-ROM
- Göpfert J, Heipke C (2006) Assessment of LIDAR DTM accuracy in coastal vegetated areas. *Int Arch Photogram Rem Sens Spatial Inform Sci* 36:79–85
- Guenther G (2007) Airborne LIDAR bathymetry. In: Maune DF (ed) Digital elevation model technologies and applications: the DEM users manual. American Society for Photogrammetry and Remote Sensing, Bethesda, pp 253–320
- Harding DJ, Lefsky MA, Parker GG, Blair JB (2001) Laser altimeter canopy height profiles: methods and validation for closed-canopy, broadleaf forests. *Remote Sens Environ* 76:283–297
- Hensley S, Munjy R, Rosen P (2007) Interferometric Synthetic Aperture Radar (IFSAR). In: Maune DF (ed) Digital elevation model technologies and applications: the DEM users manual. American Society for Photogrammetry and Remote Sensing, Bethesda, pp 141–198
- Hofton MA, Rocchio LE, Blair JB, Dubayah R (2002) Validation of vegetation canopy LIDAR sub-canopy topography measurements for a dense tropical forest. *J Geodyn* 34:491–502
- Hollaus M, Wagner W, Maier B, Schadauer K (2007) Airborne laser scanning of forest stem volume in mountainous environments. *Sensors* 7:1559–1577
- Hopkinson C, Chasmer LE, Lim K, Treitz P, Creed I (2006) Towards a universal LIDAR canopy height indicator. *Can J Rem Sens* 32:139–152
- Hopkinson C, Chasmer LE, Sass G, Creed I, Sitar M, Kalbfleisch W, Treitz P (2005) Vegetation class dependent errors in LIDAR ground elevation and canopy height estimates in a boreal wetland environment. *Can J Rem Sens* 31:191–206
- Hug C, Ullrich A, Grimm A (2004) Litemapper-5600: a waveform-digitizing LIDAR terrain and vegetation mapping system. *Int Arch Photogram Rem Sens Spatial Inform Sci* 36:24–49
- Innes JL, Koch B (1998) Forest biodiversity and its assessment by remote sensing. *Global Ecol Biogeogr* 7:397–419

- Kite GW, Pietroniro A (1996) Remote sensing applications in hydrological modeling. *Hydrolog Sci J* 41:563–591
- Lefsky MA, Harding D, Cohen WB, Parker G, Shugart HH (1999) Surface LIDAR remote sensing of basal area and biomass in deciduous forest of eastern Maryland, USA. *Remote Sens Environ* 67: 83–98
- Lim K, Trietz P, Wulder M, St.-Onge B, Flood M (2003) LIDAR remote sensing of forest structure. *Prog Phys Geog* 27:88–106
- Magnussen S, Boudewyn P (1998) Derivations of stand height from airborne laser scanner data with canopy-based quantile estimators. *Can J Forest R* 28:1016–1031
- Maltamo M, Eerikainen K, Pitkanen J, Hyyppa J, Vehmas M (2004) Estimation of timber volume and stem density based on scanning laser altimetry and expected tree size distribution functions. *Remote Sens Environ* 90:319–330
- Mason DC, Cobby DM, Horritt MS, Bates PD (2003) Floodplain friction parameterisation in two-dimensional river flood models using vegetation heights derived from airborne laser altimetry. *Hydro Processes* 17:1711–1732
- Means JE, Acher SA, Harding DJ, Blair JB, Lefsky MJ, Cohen WB, Harmon ME, Mckee WA (1999) Use of large-footprint scanning airborne LIDAR to estimate forest stand characteristics in the western Cascades of Oregon. *Remote Sens Environ* 67: 298–308
- Morris JT, Porter D, Neet M, Noble PA, Schmidt L, Lapine LA, Jensen JR (2005) Integrating LIDAR elevation data, multi-spectral imagery and neural network modelling for marsh characterization. *Int J Remote Sens* 26:5221–5234
- Næsset E (2002) Predicting forest stand characteristics with airborne scanning laser using a practical two-stage procedure and field data. *Remote Sens Environ* 80:88–99
- Nayegandhi A, Brock JC, Wright CW, O'Connell MO (2006) Evaluating a small-footprint, waveform-resolving LIDAR over coastal vegetation communities. *Photogramm Eng Rem S* 12:1408–1417
- Nayegandhi A, Brock JC, Wright CW. Small-footprint, waveform-resolving LIDAR estimation of submerged and sub-canopy topography in coastal environments. *Int J Remote Sens.* (In press)
- Parker GG, Harding DJ, Berger ML (2004) A portable LIDAR system for rapid determination of forest canopy structure. *J Appl Ecol* 41:755–767
- Persson A, Soderman U, Topel J, Ahlberg S (2005) Visualization and analysis of full-waveform airborne laser scanner data. Proceedings of the ISPRS WG III/3, III/4, V/3 workshop “laser scanning 2005”, Enschede, the Netherlands, pp 103–108
- Popescu SC, Wynne RH, Nelson RF (2003) Measuring individual tree crown diameter with LIDAR and assessing its influence on estimating forest volume and biomass. *Can J Rem Sens* 29: 564–577
- Sithole G, Vosselman G (2004) Experimental comparison of filter algorithms for bare-earth extraction from airborne scanning point clouds. *ISPRS J Photogramm* 59:85–101
- Spies TA (1998) Forest structure: a key to the ecosystem. *Northwest Sci* 72:34–39
- Straatsma MW, Middlekoop H (2006) Airborne laser scanning as a tool for lowland floodplain vegetation monitoring. *Hydrobiologia* 565:87–103
- Toyra J, Pietroniro A, Hopkinson C, Kalbfleisch W (2003) Assessment of airborne scanning laser altimetry (LIDAR) in a deltaic wetland environment. *Can J Rem Sens* 29:718–728
- Wagner W, Ullrich A, Ducic V, Melzer T, Studnicka N (2006) Gaussian decomposition and calibration of a novel small-footprint full-waveform digitising airborne laser scanner. *ISPRS J Photogramm* 60:100–112
- Wagner W, Ullrich A, Melzer T, Briese C, Kraus K (2004) From single-pulse to full-waveform airborne laser scanners: potential and practical challenges. *Int Arch Photogram Rem Sens* 35B: 201–206
- Wehr A, Lohr U (1999) Airborne laser scanning - an introduction and overview. *ISPRS J Photogramm* 54:68–82
- Williams K, Pinzon ZS, Stumpf RP, Raabe EA (1999) Sea-level rise and coastal forests on the Gulf of Mexico. U.S. Geological Survey Open-File Report 99–441



- Wright CW, Brock JC (2002) EAARL: a LIDAR for mapping shallow coral reefs and other coastal environments. Proceedings of the seventh international conference on remote sensing for marine and coastal environments, Miami, FL, CD-ROM
- Yu X, Hyypä J, Hyypä H, Maltamo M (2004) Effects of flight altitude on tree height estimation using airborne laser scanning. *Int Arch Photogram Rem Sens* 36:96–101

# Chapter 17

## Measuring Habitat Changes in Barrier Island Marshes: An Example from Southeastern North Carolina, USA

Joanne N. Halls

The rate of change of back-barrier land cover types was computed by gathering, rectifying, interpreting, and digitizing historical aerial photography (from 1938 to 1998) at Topsail Island in southeastern North Carolina. Marsh area has steadily decreased from 1938 to 1998. To quantify the significance of the spatial changes, cross-tabulation matrices were analyzed to create observed versus expected changes. Results indicate that when upland gains, it replaces marsh; when upland loses, marsh replaces it; when marsh gains, it replaces upland; when water loses, marsh replaces it; and there was no clear pattern for what transitions when marsh is lost. A series of tests were conducted to test the accuracy of the rectified photographs, the digitized polygons, and the change detection results. The accuracy of the photointerpretation and digitizing was greater than 80%. The digitized polygons were tested for degree of crenulation, or curviness, and also line generalization tests were conducted which indicated that the interpretation of the photographs was not a factor in the results. Third, a fuzziness test (using derived epsilon bands) was used to identify true changes in the marsh habitats versus positional changes, or sliver polygons. Results indicated that rectification of aerial photography (with an RMS error of less than 1), interpretation, and digitizing did not result in erroneous results. These accuracy assessment techniques are useful for testing the validity of change detection and spatial landscape indices.

### 17.1 Introduction

Traditionally the disciplines of demography, ecology, and environmental science have performed research independently. However, recently there has been more interdisciplinary research where these disciplines have collaborated using GIS and remote sensing technologies. In coastal environments, GIS and remote sensing have been utilized to address the relationship between population growth and health of

---

J.N. Halls (✉)

Department of Geography and Geology, University of North Carolina Wilmington, Wilmington, NC 28403, USA

e-mail: hallsj@uncw.edu

coastal ecosystems (Benfield et al. 2005, Conway 2005, Phinn and Stanford 2001, Ramessur 2002). The purpose for this chapter is to describe methods for mapping and analyzing barrier island salt marshes.

### 17.1.1 Population Growth in Coastal North Carolina

Population growth and decline varies throughout the United States. One popular method for analyzing the changing population is the national Census of Population which occurs every 10 years. From 1980 to 1990, the urban areas of the South, West, and coastal Northeast gained population while large Midwestern cities and rural areas substantially declined. From 1990 to 2000, population change was still largest along the coasts, but the non-coastal cities of Las Vegas, Phoenix, Dallas, and Chicago also grew substantially.

In North Carolina, population growth has been steady, as reflected throughout the southern United States. However, across the state there are spatial patterns of population decline in the rural areas, large population growth in the largest urban centers of Charlotte and Raleigh, and population growth along the southeastern coast (Fig. 17.1). Along the southeastern coast, Wilmington has experienced rapid growth in the city, bedroom communities, and surrounding beaches (Fig. 17.2). The urban area has spread from the City of Wilmington to include a majority of the surrounding counties spreading along major transportation routes and the coastal retirement destinations. The study area chosen for investigation is a typical developed barrier

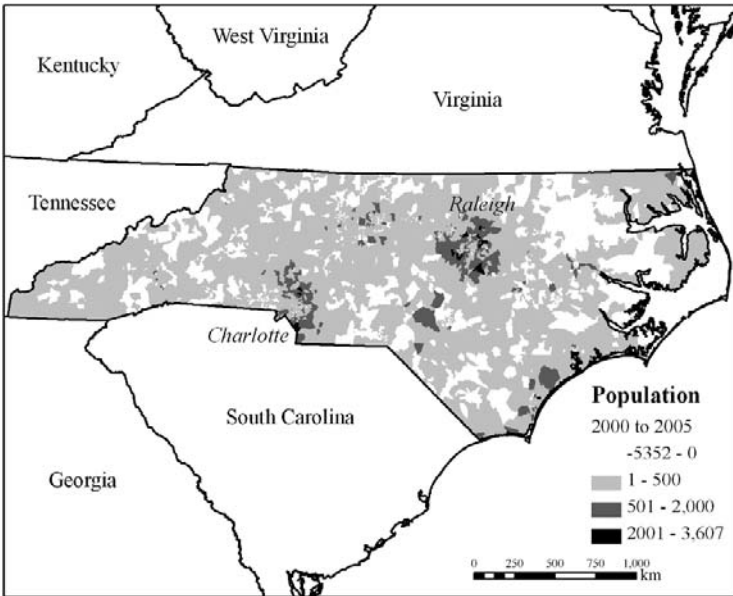
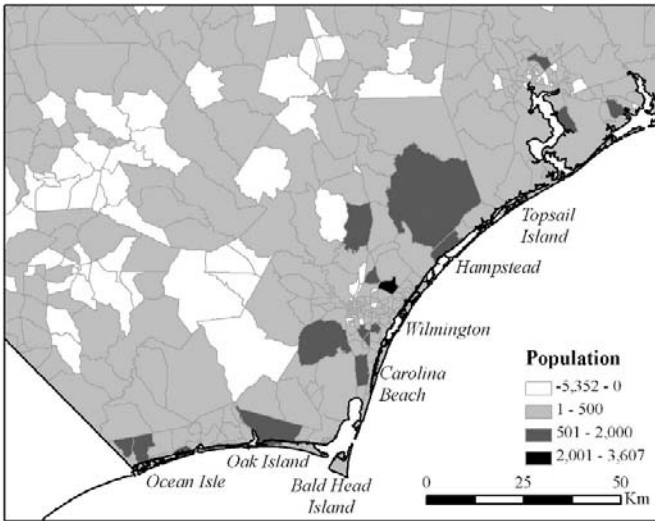
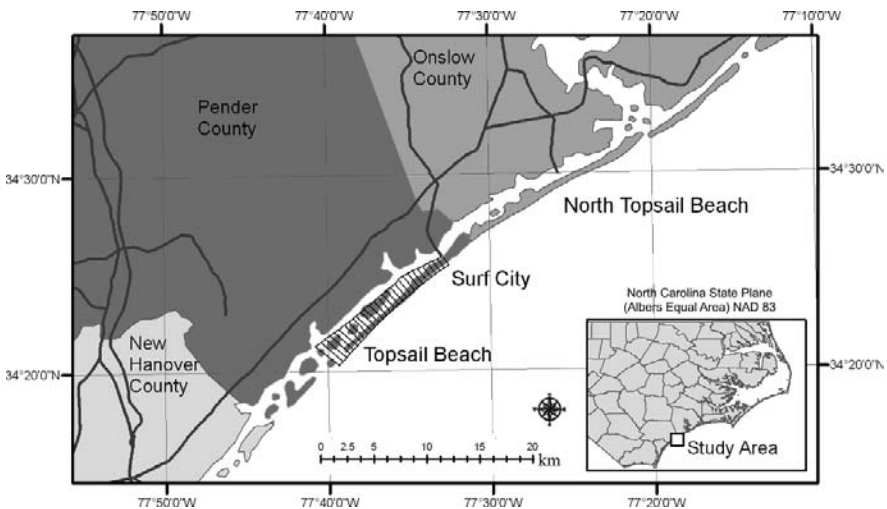


Fig. 17.1 North Carolina change in population, by Census Block Group, from 2000 to 2005



**Fig. 17.2** Southeastern North Carolina change in population, by Census Block Group, from 2000 to 2005

island located in southeastern North Carolina. Topsail Island was first developed primarily with vacation homes with few year-round residents. However, the population has steadily increased over time and currently has a much larger resident population comprised of retirees and working professionals (Fig. 17.3).



**Fig. 17.3** Location of Topsail Island, North Carolina. The island straddles two counties, Onslow and Pender, which can lead to difficulties in locating comprehensive aerial photography. The portion of the island that was studied is highlighted in a series of 0.5 km width boxes from the Surf City bridge south to New Topsail Inlet

### ***17.1.2 Coastal GIS and Remote Sensing***

Each local planning agency is GIS savvy and has developed several data layers for monitoring growth and mapping infrastructure. For example, the City of Wilmington and New Hanover County have an Internet mapping website for people to visualize a variety of data and also a link to download data for use by other GIS users. Both Brunswick and Pender counties also have a planning and GIS department where they report to the county commissioners on growth, zoning, infrastructure and other mandated activities.

Other than local government GIS data, remote sensing imagery is another possible data source for investigating land use/land cover change. For example, one popular satellite system is Landsat (the older Multispectral Scanner and the more recent Thematic Mapper and enhanced Thematic Mapper) which is useful for mapping both urban and natural areas. There are many types of commercial satellite and airborne imaging sensors, but the most popular in the United States are Landsat and SPOT. SPOT, a French satellite, is most appropriate for mapping urban areas because it has a relatively high spatial resolution (color is 20 m by 20 m cell size and black and white is 10 m by 10 m cell size) which is needed when discerning urban objects such as small buildings, roads, etc. Landsat (such as Landsat 5 and 7) is better for identifying natural habitats because of its ability to discriminate various types of vegetation, although the spatial resolution is coarser (30 m by 30 m cell size) (Alphan and Yilmaz 2005, Donoghue and Mironnet 2002, Phinn and Stanford 2001, Shi et al. 2002, Ucuncuoglu et al. 2006, Vanderstraete et al. 2006). There is also aerial photography which is an excellent source of data that enables more detailed mapping and can provide a longer historical record than satellite imagery (Al-Bakri et al. 2001, Higginbotham et al. 2004, Jones 2006, Zharikov et al. 2005). However, with the large scale of aerial photography this translates to small cell size and consequently much more data. So, aerial photography is usually analyzed when the study area is relatively small.

To investigate how satellite imagery and aerial photography can be utilized for mapping land cover change, two studies were conducted where Landsat 5 imagery was used to investigate change in New Hanover County and aerial photography was used to map changes in marsh habitats at Topsail Island.

## **17.2 Physical Geography of Barrier Islands**

Barrier islands and coastal salt marshes are complex ecosystems that move and change through time in response to many factors. For example, hurricanes bring strong winds, rain, and storm surge which can greatly change the distribution of surficial deposits (Nordstrom et al. 2006). Through time the islands can migrate and inlets change their positions.

There are many reasons for investigating how back-barrier marsh systems change through time. For example, they provide protection for the mainland during storms

by absorbing the tidal surge and providing a stabilizing environment for storm overwash. These environments are also economically and environmentally important ecosystems because they provide fish nursery habitats, bird nesting and foraging sites, and act as a filter for chemicals entering the ecosystem. In the southeastern United States salt marshes are typically found in tandem with barrier islands. This ecosystem includes the beach, dunes, vegetated zones, maritime forest, swampy terrains, tidal flats, and low-lying salt marshes (Bates and Jackson 1984). Researchers have identified several factors related to marsh stability: geomorphology, elevation, vegetation, hydrologic conditions, frequency of tropical storms, tidal range, and sediment supply (Goodbred and Hine 1995, Davidson-Arnott et al. 2002). If estimates are correct and sea level rise is increasing at 1.9 cm/year (Davis 1994), then the salt marshes in this region require a substantial amount of sediment, either from overwash or other transport mechanisms, to sustain their existing size.

In addition to the geologic and geomorphic processes of marsh formation, there has been a steady increase in coastal development along all coasts of the United States (Titus 1990) and it is yet to be determined what impact this urbanization has on back barrier marshes (Bertness et al. 2004). Therefore, a study was undertaken to map back barrier marshes in order to quantify change as well as compute various spatial measures to identify patterns in how these marshes have changed through time. To understand how barrier island marsh habitats change through time Topsail Island, located in southeastern North Carolina, was investigated. The island is part of a chain of barrier islands in the geologic system known as the Georgia Bight. Topsail Island is a 30km barrier island that was initially used as a military rocket testing site in the 1940s and is now primarily single-family vacation homes but has an increasing population of year-round residents.

### 17.3 GIS Database Development

It has become quite common to utilize the tools available in remote sensing and GIS software for mapping coastal habitats such as salt marshes (Zharikov et al. 2005, Dech et al. 2005, Jupiter et al. 2007). For Topsail Island, the GIS development began with a detailed survey of all local, regional, state, and federal agencies that commonly acquire aerial photography. Many dates of photography were identified, however only those dates where photography covered all of the back barrier marshes, were of similar scale (1:12,000 and 1:20,000), were at similar tidal stages, and same time of year were used in the study. The most recent photography was 1998, it was already rectified into orthophotography, and was near-infrared. All other years (1938, 1949, 1956, 1971, and 1986) were in analog format which required scanning and rectifying. After several tests at varying resolutions, it was determined that scanning the aerial photographs at 400 dpi was sufficient for the scale, interpretation and digitization of the marshes.

### ***17.3.1 Interpretation and Digitizing***

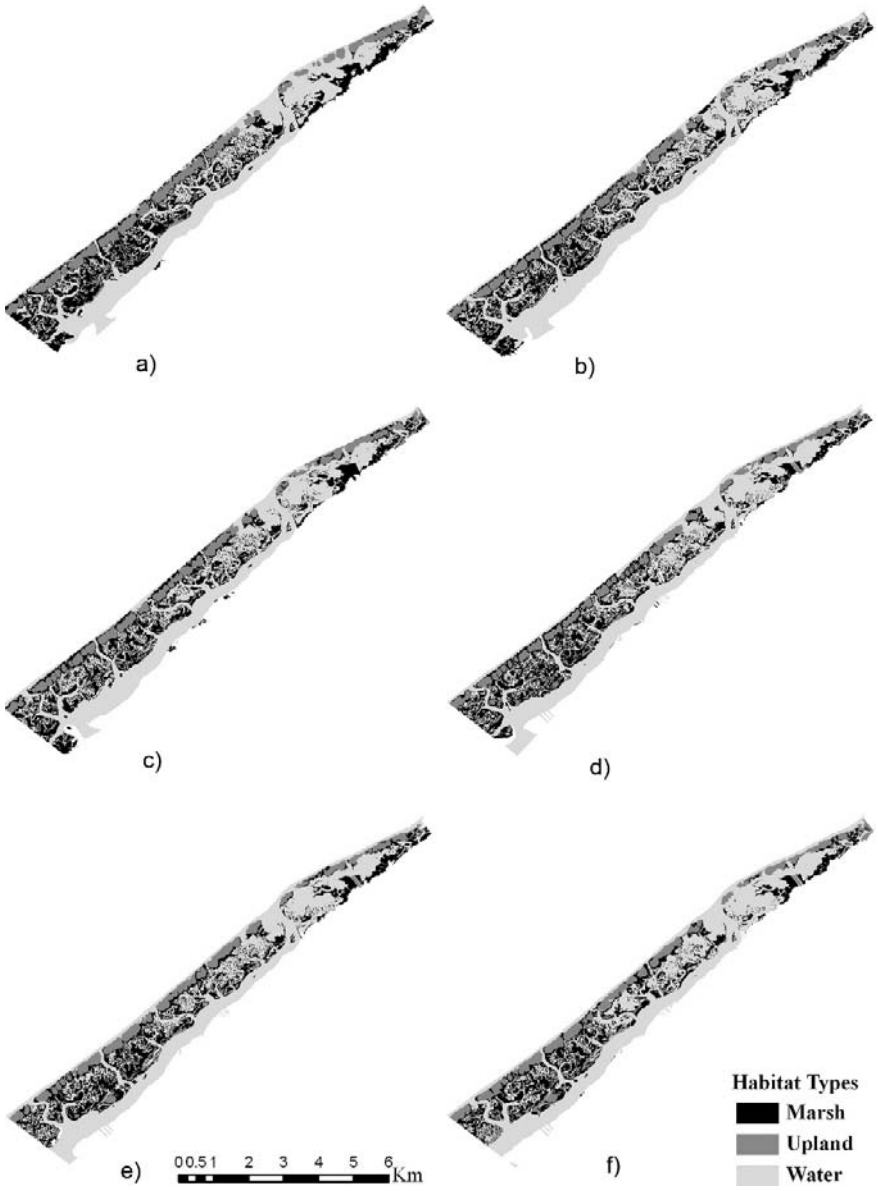
Once in a GIS, each of the photographs were interpreted, digitized and then compared. Although the scanning produced pixels with 1 m spatial resolution, the scale of the photography dictated the minimum mapping unit based on standards developed by the US Geological Survey. Therefore, the aerial photography was precisely mapped where the smallest marsh polygon interpreted and digitized was less than 0.1 hectare. The land cover classification scheme was: marsh, upland, water, and barrier island (Fig. 17.4). To aid in the interpretation process, field work was conducted where hundreds of sites were visited and a comparison was made between the real land cover types (predominantly wetlands) and the photography. The field work was imperative for becoming comfortable interpreting the imagery. Although photointerpretation and digitizing are labor intensive and time consuming, several image processing classification techniques were tested but did not produce acceptable results. For example, unsupervised and supervised analyses were tested using a variety of cluster algorithms and training site selection trials. Unfortunately, the image processing algorithms were not able to distinguish marshes from water with any consistency because the photography had little spectral variety. Perhaps future tests using object-oriented classification rather than pixel spectral analysis will yield improved habitat mapping (Laliberte et al. 2004, Lathrop et al. 2006).

### ***17.3.2 Accuracy Assessment of Photointerpretation and Digitizing***

Performing an accuracy assessment is an important part of any change detection analysis or other type of temporal spatial analysis (Couto 2003; Hughes et al. 2006). After all of the photographs for the 6 years were digitized and checked for logical consistency and topological correctness an accuracy assessment was conducted where 140 points were randomly located in the study area and the digitized land cover classes were compared to the aerial photography. Using an error matrix, an overall accuracy greater than 80% was computed for each year which was acceptable.

## **17.4 Change Detection**

The back barrier marsh habitats of Topsail Island changed from 1938 to 1998, but the changes were not systematic across the study area (Fig. 17.4). When summarizing the total area of marsh, it steadily decreased from 1938 to 1998 (Fig. 17.5). In fact, by simply calculating regression statistics between marsh area and time, there was a strong negative linear relationship between the area of marsh and time ( $y = -2.112x + 4739$ ,  $R^2 = 0.961$ ). However, these summary results do not fully describe how the marsh has changed through time. There are several analytical



**Fig. 17.4** Topsail Island interpreted and digitized habitat maps in (a) 1938, (b) 1949, (c) 1956, (d) 1971, (e) 1986, and (f) 1998



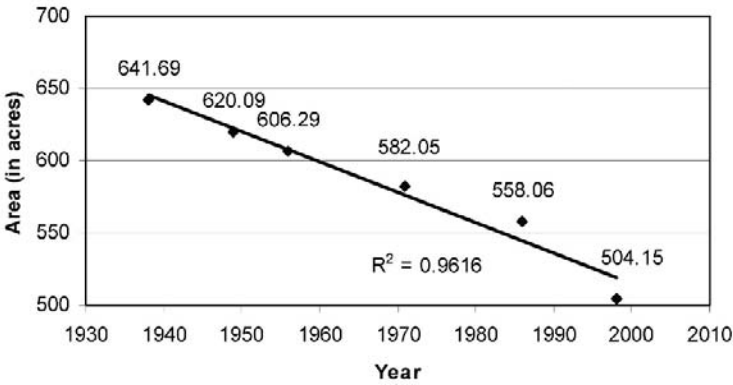


Fig. 17.5 Area of marsh from 1938 to 1998

techniques that were employed to further investigate how the Topsail marshes have changed including change detection analyses and landscape fragmentation.

To compare how the land cover changed from one time period to the next transition matrices, also referred to as cross-tabulation matrices, were created. The technique used in this study is known as the post-classification comparison where the input data layers have been independently classified/interpreted and then the results are compared, or overlaid (Jensen 1996). Using this approach, classification matrices document how each land cover class changed from one time period to the next (Table 17.1). The diagonal cells (shown in grey) contain the area (in hectares) that did not change from time 1 to time 2 and conversely, the off-diagonal cells document the area that changed from time one to time two and how the area changed. So, the diagonal values can be considered persistent whereas the off-diagonal values document the areas that have transitioned from one class to another. Although documenting the area of change is useful, it is best to represent this change in percentages so that further statistical analyses can be computed (Table 17.2). The total percentage column is the summation of each habitat row in time 1 and likewise the total percentage row is the summation of each habitat column in time 2. The percentage of habitat lost is the summation of the off-diagonal row values and the percentage of habitat gained is the summation of off-diagonal column values. The total net change is the difference between the total in time 1 and total in time 2. However, the net change does not describe how the habitats have persisted versus changed, or transitioned, to another habitat type.

The change detection cross-tabulation matrices revealed that 71% (22.47/31.75) of the marsh in 1938 remained marsh in 1949; this dropped to 65% in 1956, 58% in 1971, 65% in 1986 and 73% in 1998. To visualize how the marshes have changed through time, we can track the persistent marsh (marsh that remained from time 1 to time 2), the marsh that didn't remain (lost marsh) and new marsh (marsh that was gained) (Fig. 17.6). Although it is interesting to map the persistent, gained, and lost marsh there isn't a clear spatial pattern. From a vulnerability standpoint, it would be best if we could clearly decipher a pattern of marsh loss versus gain (Fig. 17.7).

**Table 17.1** Cross-tabulation matrices for each date of aerial photography (in hectares)

		1949		
		marsh	upland	water
1938	marsh	449.2	28.6	156.8
	upland	45	215.7	20.7
	water	118.1	17.6	947
		1956		
		marsh	upland	water
1949	marsh	402.6	36.5	176.7
	upland	42.6	202.9	13.5
	water	143.9	24.3	961.6
		1971		
		marsh	upland	water
1956	marsh	338.8	53.9	192.2
	upland	47.6	180.2	33.5
	water	192.9	28.7	922.9
		1986		
		marsh	upland	water
1971	marsh	378.3	49.7	151.8
	upland	38.3	205.1	17.3
	water	134.8	17.1	1,003.70
		1998		
		marsh	upland	water
1986	marsh	405.6	34.4	114.1
	upland	17.4	239.9	14.6
	water	80.6	10	1,087.20

However, there clearly isn't a consistent spatial pattern to marsh loss other than that there is more loss than gain. So, further analysis into how the habitats are changing is necessary in order to more clearly understand the changing landscape.

As can be seen in the cross-tabulation matrices (Table 17.2), the amount of persistence in each habitat class far exceeds the amount of change from one habitat class to another (the diagonals are larger than the off-diagonals), but this is to be expected in change detection studies. So, although the percentage of persistence is greater than the percentages that have transitioned to other classes, it is important that we investigate these transitions in order to determine which transitions are creating the greatest impact to the landscape. In Table 17.2, the conversion of marsh to water was an average of 7.9% over the entire study area. The next largest transition was water converting to marsh (averaging 6.71%), but the largest transitions don't necessarily mean these are the most important, or indicative, of how the landscape has changed. To investigate the habitat change further, there is another technique that can measure how the landscape has changed by quantifying the amount of habitat that has changed to another class, also known as the amount of class swapping (Pontius et al. 2004). The equation to calculate the amount of swapping is:

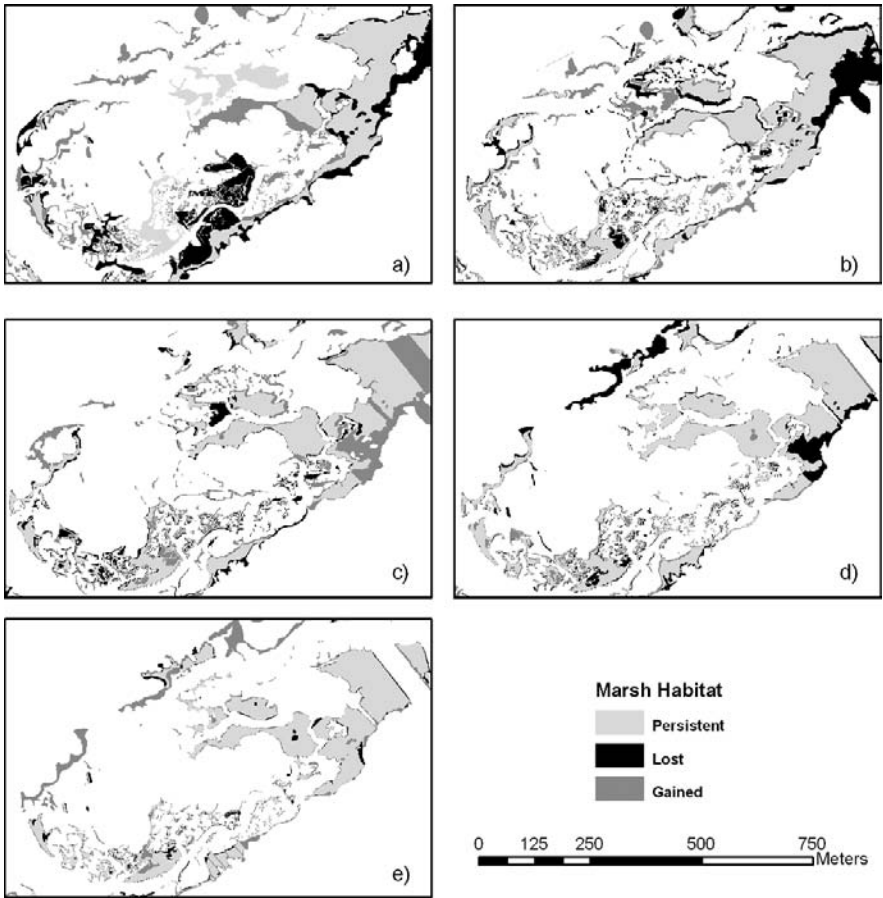
$$S_j = 2 * \min(\text{gain}, \text{loss}) \tag{17.1}$$

**Table 17.2** Cross-tabulation matrices for each date of photography (in percent)

		1949			total 1938	Loss
		marsh	upland	water		
1938	marsh	22.47	1.43	7.85	31.75	9.28
	upland	2.25	10.79	1.04	14.08	3.29
	water	5.91	0.88	47.38	54.17	6.79
total 1949		30.63	13.10	56.26	100.00	
Gain		8.16	2.31	8.88		
		1956			total 1949	Loss
		marsh	upland	water		
1949	marsh	20.08	1.82	8.81	30.72	10.64
	upland	2.13	10.12	0.67	12.92	2.80
	water	7.18	1.21	47.97	56.36	8.39
total 1956		29.39	13.15	57.46	100.00	
Gain		9.30	3.03	9.49		
		1971			total 1956	Loss
		marsh	upland	water		
1956	marsh	17.02	2.71	9.65	29.38	12.36
	upland	2.39	9.05	1.68	13.13	4.07
	water	9.69	1.44	46.36	57.49	11.13
total 1971		29.10	13.20	57.70	100.00	
Gain		12.08	4.15	11.34		
		1986			total 1971	Loss
		marsh	upland	water		
1971	marsh	18.95	2.49	7.60	29.05	10.09
	upland	1.92	10.28	0.87	13.06	2.79
	water	6.75	0.86	50.28	57.89	7.61
total 1986		27.62	13.62	58.75	100.00	
Gain		8.67	3.35	8.47		
		1998			total 1986	Loss
		marsh	upland	water		
1986	marsh	20.24	1.72	5.69	27.65	7.41
	upland	0.87	11.97	0.73	13.57	1.60
	water	4.02	0.50	54.26	58.78	4.52
total 1998		25.13	14.19	60.68	100.00	
Gain		4.89	2.22	6.42		

where,  $S_j$  is the amount of swapping of class  $j$  and gain and loss are the percentages of greatest gain and largest loss from class  $j$  to all other classes. Table 17.3 contains the overall percentage change, the percentage of gain and loss, the total change (gain plus loss) and the amount of swapping among classes. The following conclusions can be drawn from this table:

- The net change reveals the overall loss of marsh habitat in all time periods.
- Water and marsh change more than upland.

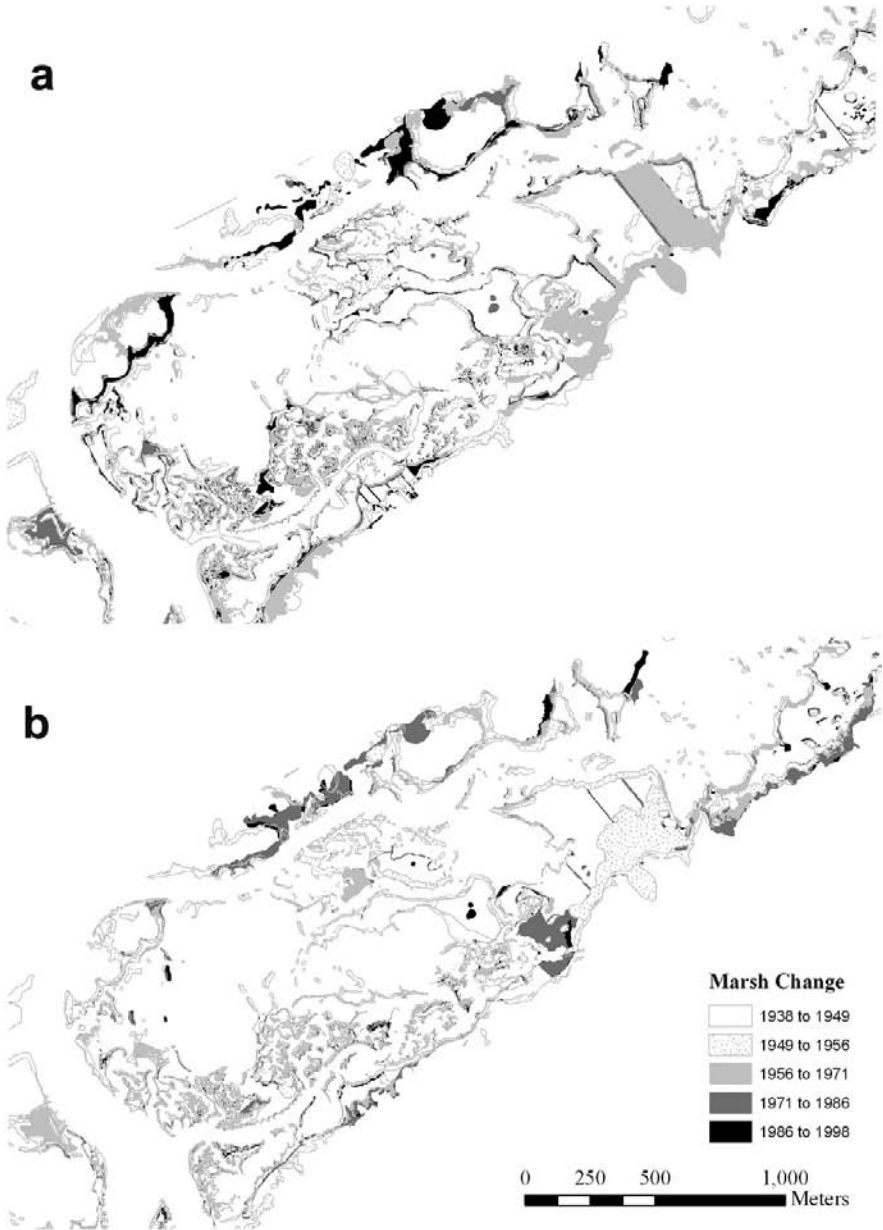


**Fig. 17.6** A subset of the Topsail study area showing marsh that has persisted, gained, and lost for (a) 1938 to 1949, (b) 1949 to 1956, (c) 1956 to 1971, (d) 1971 to 1986, and (e) 1986 to 1998

- Although the overall percentage of marsh area has decreased through time (Fig. 17.5) there has been a much greater percentage of marsh swapping (gain and loss) across the study area.

### 17.4.1 Observed Versus Expected Change

Although it is customary to describe how much change has taken place between time periods, a further investigation into how much change is significant can be accomplished by calculating the difference between expected and observed change (Pontius et al. 2004). To determine the importance of the off-diagonals (or



**Fig. 17.7** A portion of the study area showing (a) all marsh areas lost over each time period and (b) marsh areas that were gained in each time period. Although there was more marsh lost than gained, there is no clear spatial pattern to the gains and losses

**Table 17.3** Percent net change, gains/losses, and amount of swapping between land cover habitats for each date of aerial photography

		Net Change	Gain	Loss	Total Change	Swap
1938 to 1949	Marsh	-1.12	8.16	9.28	17.44	16.32
	Upland	-0.98	2.31	3.29	5.60	4.62
	Water	2.09	8.88	6.79	15.67	13.58
1949 to 1956	Marsh	-1.33	9.30	10.64	19.94	18.61
	Upland	0.23	3.03	2.80	5.83	5.60
	Water	1.10	9.49	8.39	17.88	16.78
1956 to 1971	Marsh	-0.28	12.08	12.36	24.44	24.16
	Upland	0.08	4.15	4.07	8.22	8.15
	Water	0.21	11.34	11.13	22.47	22.26
1971 to 1986	Marsh	-1.42	8.67	10.09	18.77	17.34
	Upland	0.56	3.35	2.79	6.13	5.57
	Water	0.86	8.47	7.61	16.08	15.22
1986 to 1998	Marsh	-2.52	4.89	7.41	12.30	9.78
	Upland	0.62	2.22	1.60	3.81	3.19
	Water	1.90	6.42	4.52	10.94	9.04

transitions), we need to calculate the expected transition percentages and compare these to the observed to identify transitioning trends. To calculate the expected gains, the percentage of gain is distributed across the habitat types according to the overall percentages of these categories in time 1. Likewise, the expected losses were calculated using the overall distribution of losses in time 1. The equations to calculate expected gains and losses were:

$$g_{ij} = (c + j - c_{jj}) (c_{i+} / 100 - c_{ji}) \tag{17.2}$$

$$l_{ij} = (c_{i+} - c_{ii}) (c + j / 100 - c + i) \tag{17.3}$$

where the expected gain in class *i* from class *j* ( $c_{ij}$ ) is the expected amount of gain of class *j* in proportion to the amount of the losing class *i*. The expected loss in class *i* from class *j* ( $l_{ij}$ ) is in proportion to the amount of the gaining class *i*.

Using the cross-tabulation matrices, the observed and expected percentages were computed to identify which observed gains were greater or less than expected (Table 17.4) and which losses were also greater or less than expected (Table 17.5). In Table 17.4, if the difference between the observed and expected gains was positive, then there was more gain in the new transition class than was expected. Conversely, if the difference was negative, then there was less gain than expected. In Table 17.5, if the difference between the observed and expected losses was positive then there was more loss than expected. Conversely, if the difference was negative then there was less loss than expected.

To identify which expected and observed habitat transitions clearly illustrated a systematic pattern we divided the difference between observed minus expected (deviation) by the expected (this is analogous to computing a chi square statistic).

**Table 17.4** Cross-tabulation matrices for each date of photography with calculations for the expected gains in each land cover class. The column headings correspond to: Obs is the percent observed, Exp is the expected gain (in percent), Dev is the deviation (or absolute value) of the difference between expected and observed, and Dev/Exp is the ratio of the deviation to percent expected for each habitat type and time period

		1949											
		Marsh				Upland				Water			
1938		Obs	Exp	Dev	Dev/Exp	Obs	Exp	Dev	Dev/Exp	Obs	Exp	Dev	Dev/Exp
	Marsh	22.47	22.47	0.00	0.00	1.43	0.85	0.58	0.68	7.85	12.82	-4.97	-0.39
	Upland	2.25	1.68	0.57	0.34	10.79	10.79	0.00	0.00	1.04	2.73	-1.69	-0.62
	Water	5.91	6.48	-0.57	-0.09	0.88	2.51	-1.63	-0.65	47.38	47.38	0.00	0.00
		1956											
		Marsh				Upland				Water			
1949	Marsh	20.08	20.08	0.00	0.00	1.82	0.81	1.01	1.23	8.81	13.48	-4.66	-0.35
	Upland	2.13	1.74	0.39	0.22	10.12	10.12	0.00	0.00	0.67	2.81	-2.14	-0.76
	Water	7.18	7.57	-0.39	-0.05	1.21	2.75	-1.54	-0.56	47.97	47.97	0.00	0.00
		1971											
		Marsh				Upland				Water			
1956	Marsh	17.02	17.02	0.00	0.00	2.71	0.78	1.93	2.47	9.65	16.40	-6.75	-0.41
	Upland	2.39	2.25	0.15	0.06	9.05	9.05	0.00	0.00	1.68	3.50	-1.82	-0.52
	Water	9.69	9.84	-0.15	-0.01	1.44	3.73	-2.29	-0.61	46.36	46.36	0.00	0.00
		1986											
		Marsh				Upland				Water			
1971	Marsh	18.95	18.95	0.00	0.00	2.49	0.77	1.72	2.23	7.60	12.28	-4.68	-0.38
	Upland	1.92	1.60	0.32	0.20	10.28	10.28	0.00	0.00	0.87	2.63	-1.76	-0.67
	Water	6.75	7.08	-0.32	-0.05	0.86	2.69	-1.83	-0.68	50.28	50.28	0.00	0.00
		1998											
		Marsh				Upland				Water			
1986	Marsh	20.24	20.24	0.00	0.00	1.72	0.74	0.98	1.32	5.69	9.57	-3.88	-0.41
	Upland	0.87	0.92	-0.05	-0.05	11.97	11.97	0.00	0.00	0.73	2.11	-1.39	-0.66
	Water	4.02	3.97	0.05	0.01	0.50	1.61	-1.11	-0.69	54.26	54.26	0.00	0.00

**Table 17.5** Cross-tabulation matrices for each date of photography with calculations for the expected losses in each land cover class. The column headings correspond to: Obs is the percent observed, Exp is the expected loss (in percent), Dev is the deviation (or absolute value) of the difference between expected and observed, and Dev/Exp is the ratio of the deviation to percent expected for each habitat type and time period

		1949											
		Marsh				Upland				Water			
1938		Obs	Exp	Dev	Dev/Exp	Obs	Exp	Dev	Dev/Exp	Obs	Exp	Dev	Dev/Exp
Marsh		22.47	22.47	0.00	0.00	1.43	1.75	-0.32	-0.18	7.85	11.44	-3.59	-0.31
Upland		2.25	1.16	1.09	0.94	10.79	10.79	0.00	0.00	1.04	2.13	-1.09	-0.51
Water		5.91	4.76	1.15	0.24	0.88	2.03	-1.15	-0.57	47.38	47.38	0.00	0.00
		1956											
		Marsh				Upland				Water			
1949	Marsh	22.47	22.47	0.00	0.00	1.43	1.98	-0.55	-0.28	7.85	13.07	-5.23	-0.40
	Upland	2.13	0.95	1.18	1.24	10.12	10.12	0.00	0.00	0.67	1.85	-1.18	-0.64
	Water	7.18	5.80	1.38	0.24	1.21	2.59	-1.38	-0.53	47.97	47.97	0.00	0.00
		1971											
		Marsh				Upland				Water			
1956	Marsh	22.47	22.47	0.00	0.00	1.43	2.30	-0.87	-0.38	7.85	15.19	-7.35	-0.48
	Upland	2.39	1.37	1.03	0.75	9.05	9.05	0.00	0.00	1.68	2.71	-1.03	-0.38
	Water	9.69	7.66	2.03	0.27	1.44	3.47	-2.03	-0.58	46.36	46.36	0.00	0.00
		1986											
		Marsh				Upland				Water			
1971	Marsh	22.47	22.47	0.00	0.00	1.43	1.90	-0.47	-0.25	7.85	12.44	-4.59	-0.37
	Upland	1.92	0.89	1.03	1.15	10.28	10.28	0.00	0.00	0.87	1.89	-1.03	-0.54
	Water	6.75	5.10	1.66	0.33	0.86	2.51	-1.66	-0.66	50.28	50.28	0.00	0.00
		1998											
		Marsh				Upland				Water			
1986	Marsh	22.47	22.47	0.00	0.00	1.43	1.40	0.03	0.02	7.85	9.14	-1.30	-0.14
	Upland	0.87	0.47	0.40	0.86	11.97	11.97	0.00	0.00	0.73	1.13	-0.40	-0.35
	Water	4.02	2.89	1.13	0.39	0.50	1.63	-1.13	-0.69	54.26	54.26	0.00	0.00



By comparing the expected to the observed, for both gains and losses the following statistics clearly stand out:

- When upland gains, it replaces marsh.
- When upland loses, marsh replaces it.
- For almost all of the time periods, when marsh gains, it replaces upland.
- When water loses, marsh replaces it.
- There was no clear pattern for what transitions when marsh is lost.

Interestingly, of the marshes that did not remain as marsh in the next time period, most of this area became water, not upland. In the areas that were upland, some converted to marsh (e.g. 16% in 1938 and 1956) and to a lesser extent, some converted to water. Lastly, water generally stayed the same from one time period to the next, but when the water did change it mostly became marsh, not upland.

This change detection analysis demonstrated the usefulness of gathering this information in order to understand where the barrier island environment has changed through time. The marsh habitats at Topsail Island have generally decreased since the 1930s, but there have also been some areas where the marsh has increased (Fig. 17.7).

## 17.5 Predicted Marsh Change

There are additional techniques, known as landscape metrics, which can be employed to attempt to predict future landscapes. Three of these (Area, Area/Perimeter, and Fractal Dimension) were tested in this study (Lovejoy 1982). Although future research may investigate additional spatial indices, these three techniques were tested and compared. The first two indices, Area and Area/Perimeter, are simple calculations where Area ranks the total area, or size, of the marsh polygons and Area/Perimeter is a ranking of the division of Area by the Perimeter of the polygon (Lovejoy 1982). The hypothesis is that the larger the polygon the more likely it will be present in the future and likewise the larger the ratio of area to perimeter will be more likely to be present in the future (a circle has the largest Area to Perimeter ratio). The fractal dimension index uses fractal geometry to measure the degree of edginess so the higher the score the more convoluted the polygon (Mandelbrot 1982, Olsen et al. 1993). Conversely, the lower the score the more round the polygon and so with regards to marshes, the rounder a polygon the less likely it is to erode. The equation to compute the fractal dimension index was:

$$S = \frac{2 \ln(Pr/4)}{\ln(A)} \quad (17.4)$$

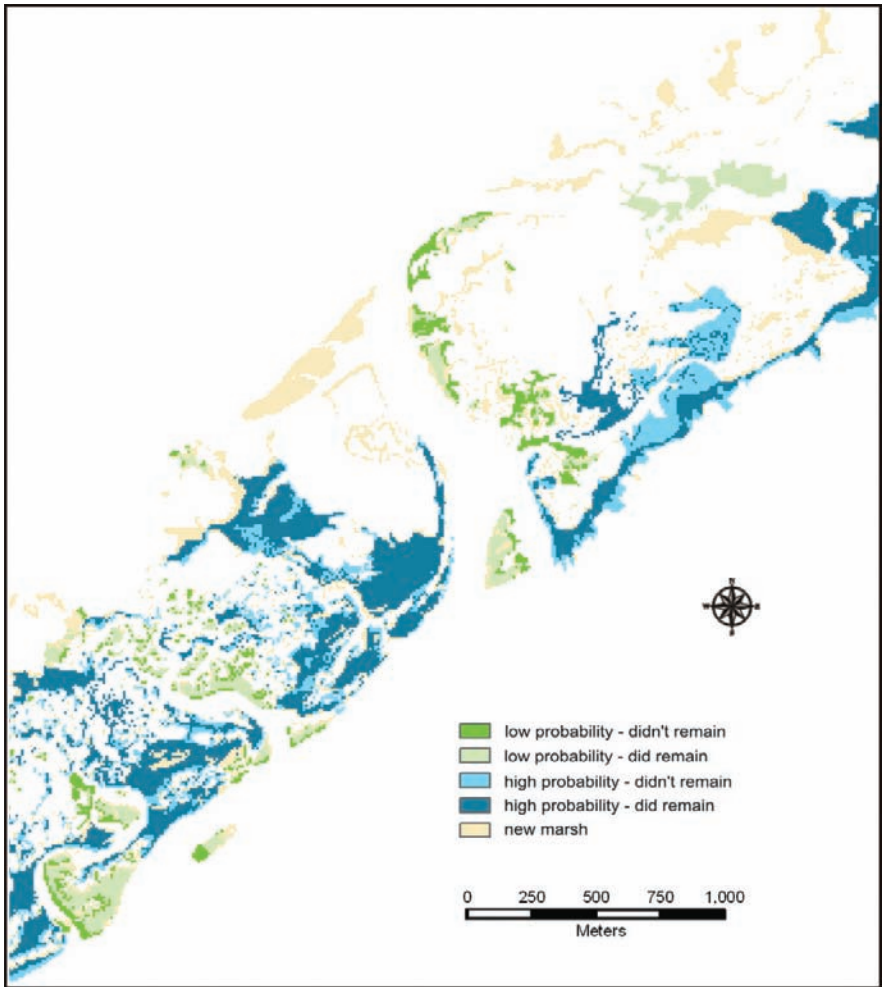
where:  $S$  = fractal dimension,  $Pr$  = perimeter, and  $A$  = area.

The three techniques were computed for each year and compared with the subsequent time period to see how well the techniques predicted the future gain and loss

in marshes. Each spatial index was ranked into 5 classes to statistically compare with the change detection results.

An example of the Fractal Dimension Index is given in Fig. 17.8. Note that in this figure, the green polygons are marshes that were predicted to have a low probability of remaining and in fact were not present in the next time period. The dark blue marshes were predicted to remain and they did. This type of predictive measure isn't perfect, but it is useful to gain an understanding of how areas have changed and where the fractal dimension index can be used as a predictive tool.

The spatial indices were applied to each year and statistical analysis concluded there was no difference in the Area versus Area/Perimeter indices and these indices



**Fig. 17.8** An example of the Fractal Dimension Index for predicting future marsh changes from 1938 to 1949

**Table 17.6** Probability of each spatial index predicting presence or absence of marshes in the next time period. A/P is the Area/Perimeter index and FD is the Fractal Dimension index. Rankings are: (1) low probability of marsh remaining but they did, (2) low probability of remaining and they did not, (3) high probability of remaining but they didn't, and (4) high probability of remaining and they did

Rank	A/P	Area	FD
1938 to 1949			
1	0.5	0.8	11.9
2	0.2	0.6	25.4
3	29.4	29.0	18.0
4	69.9	69.5	44.7
1949 to 1956			
1	2.0	2.2	11.2
2	1.1	0.9	18.4
3	33.1	32.9	23.9
4	63.8	64.0	46.5
1956 to 1971			
1	1.6	1.6	18.2
2	0.6	0.7	21.6
3	42.6	42.6	26.0
4	55.2	55.1	34.2
1971 to 1986			
1	2.0	2.1	10.8
2	0.9	1.0	23.0
3	33.0	32.9	24.2
4	64.1	64.0	42.0
1986 to 1998			
1	1.8	1.7	9.3
2	0.9	1.0	24.1
3	25.5	25.6	18.0
4	71.8	71.8	48.6

predicted marsh survival that ranged from 55 to 72% (Table 17.6). Interestingly, although the Fractal Dimension index had a lower probability of predicting marshes that remained through time (ranging from 34 to 50%), this index outperformed the others by more correctly predicting which marshes would not remain through time. Future research will expand on these results by incorporating other landscape measures into the predictive tools.

## 17.6 Sensitivity Assessment

The habitat change detection and marsh spatial indices have provided useful information about the changing barrier island environment, but what confidence can we place on these results? Even though we have an overall photointerpretation accuracy greater than 80%, does the level of detail, or number of vertices in the polygons,

influence the quantification of change? To answer these questions, several smoothing functions were applied to a subsection of the study area, computed the curviness, or degree of crenulation, and compared these data with the original polygons to see if these new data would derive statistically different results. A smoothing algorithm was applied to the polygons for each year using increasing distances beginning with 5 m and ending with 70 m. With each new data set the three indices of Area, Area/Perimeter, and Fractal Dimension were calculated. Statistical analyses using chi square determined that there were no significant differences between the original polygons and the smoothed data; therefore, it was concluded that the level of detail did not influence the spatial indices.

To test whether or not the precision of interpretation and digitization impacted the change detection results, epsilon bands were created which were then used to remove polygons from the change detection results (Mas 2005). The sizes of the epsilon bands were the average and standard deviation widths of the sliver polygons which were then used to remove polygons. In the Mas (2005) study it was determined that this method increased the accuracy of the change detection matrix. In the Topsail data, the change from 1938 to 1949 was used to test the amount of change to see if sliver polygons statistically impacted the change detection results. The average width (1.44m) and standard deviation (0.4) of the sliver polygons was calculated by dividing the area by half the perimeter (Mas 2005, p. 621). Therefore, a buffer distance of 1.84m was applied to the 1938–1949 change dataset to create the epsilon bands. The polygons within the buffer were deleted by merging them with the adjacent polygons that had the longest shared boundary. The process was then repeated using a distance of 2 standard deviations (2.24 m). Two new classification matrices were created and compared to the original change matrix. Unlike the Mas (2005) study, the epsilon band matrices were not statistically different from each other or the original matrix. Therefore, it was concluded that creating epsilon bands for removal of sliver polygons did not alter the change detection results. However, it is prudent for all change detection studies to perform this analysis to verify the accuracy of the interpretation and digitization process.

## 17.7 Conclusions and Further Research

Traditional land use/land cover change models have relied on urban growth models, such as cellular automata, to predict future landscape scenarios. However, in many coastal areas the increase in population is not due to economics (such as employment opportunities) but rather the climate, natural resource amenities, recreation, cultural opportunities, and retirement lifestyle, provide ample reasons to migrate to the coasts.

Remote sensing and GIS techniques can be used to measure land cover change, model the future, and disseminate information. Several scales, from continental to local, and several types of data, from the Census to aerial photography, have been analyzed to illustrate a variety of GIS techniques and provide some insight into one

coastal location. It is clear from these analyses that population growth and urbanization has occurred in southeastern North Carolina where natural, undeveloped, areas have been converted to urban (including transportation, residential, commercial, and industrial uses). Where there was growth in urban land, it generally replaced agriculture which has been found in similar coastal environments (Alphan and Yilmaz 2005, Chen et al. 2005).

This study has computed land use/land cover change and has determined that the change is real and not an artifact of either the data collection or processing methodologies. Other researchers have conducted similar change detection analyses of coastal environments, including using aerial photography (Lu et al. 2004, Frederiksen et al. 2004, Field and Philipp 2000, Higginbotham et al. 2004, Feist and Simenstad 2000). So, it can be concluded that the techniques used here are widely supported in the research community. In fact, the success of mapping emergent vegetation has led to an increase in the number of studies mapping submersed vegetation (seagrasses) (Meehan et al. 2005, Lathrop et al. 2001, Pasqualini et al. 2001). In addition, several indices have been implemented, tested, and appear to be able to provide some insight into the changing morphology of back-barrier marshes; however a robust model of the spatial dynamics of marshes in the Topsail Island study area has yet to be created. One step in that direction would be the calculation of Relative Errors of Area which is a tool for assessing the accuracy of landscape indices (Shao and Wu 2004).

Although we determined that traditional interpretation and on-screen digitizing was the most appropriate technique for this study, there are several image processing techniques that may be tested in future research. For example, cross-correlation analysis, neural networks, and object-oriented classification have been found to be useful methods in land use change analyses (Calvo et al. 2003). These techniques may provide good mapping results, would be repeatable, and less time consuming in comparison to photointerpretation and digitizing.

There are several additional research projects being developed to further understand the marsh environment. First is the development of a predictive landscape model. Although there are numerous types of models, essentially spatially explicit models can be grouped into process-based models and spatial pattern models (Castella and Verburg 2007, Schroder and Seppelt 2006, Perry and Enright 2006). One method of spatial pattern modeling uses the historical probability of change and this would be useful to implement in this type of environment since there are no clearly defined rules for land cover change (Pontius and Batchu 2003).

Dissemination of these data is being developed at an Internet GIS website ([www.uncw.edu/gis](http://www.uncw.edu/gis)) where users can view all of the years of data. While this project demonstrated the techniques for quantifying spatial changes through time, there are certainly other data sources that could be gathered and tested (Phinn et al. 2000). Lastly, multi and hyper spectral imagery will be analyzed at several study areas in North Carolina where marsh habitats will be mapped by species. Using the enhanced capabilities of these types of imagery may provide more information about the species health and spatial characteristics that we have not previously mapped using aerial photography (Filippi and Jensen 2006, Li et al. 2005, Pengra et al.

2007). One drawback, of course, is the spatial resolution of satellite imagery can lead to mixed pixels which can be difficult to classify (Donoghue and Mironnet 2002). However, using the existing aerial photography with the satellite imagery may yield improved mapping results.

**Acknowledgement** The study would not be possible without the cooperation of several government agencies who provided access to their archives of aerial photography. In particular, Mr. Lynn Jack of the U.S. Army Corps of Engineers, Wilmington office was particularly helpful. The author would also like to thank Ms. Lindsey Kraatz, Mr. Jason Eversole and Mr. Jimmy Sharp who helped with photointerpretation and digitization of the aerial photography. Partial funding for this research was provided by a grant from the North Carolina SeaGrant.

## References

- Al-Bakri JT, Taylor JC, Brewer TR (2001) Monitoring land use change in the Badia transition zone in Jordan using aerial photography and satellite imagery. *Geogr J* 167:248–262
- Alphan H, Yilmaz KT (2005) Monitoring environmental changes in the Mediterranean coastal landscape: the case of Cukurova, Turkey. *Environ Manage* 35:607–619
- Bates RL, Jackson J (1984) Dictionary of geological terms. Doubleday, New York
- Benfield SL, Guzman HM, Mair JM (2005) Temporal mangrove dynamics in relation to coastal development in Pacific Panama. *Environ Manage* 76:263–276
- Bertness M, Silliman BR, Jefferies R (2004) Salt marshes under siege: agricultural practices, land development and overharvesting of the seas explain complex ecological cascades that threaten our shorelines. *Am Sci* 92:54–61
- Calvo S, Ciraolo G, La Loggia G (2003) Monitoring *Posidonia oceanica* meadows in a Mediterranean coastal lagoon (Stagnone, Italy) by means of neural network and ISODATA classification methods. *Int J Remote Sens* 24:2703–2716
- Castella JC, Verburg PH (2007) Combination of process-oriented and pattern-oriented models of land-use change in a mountain area of Vietnam. *Ecol Model* 202:410–420
- Chen SS, Chen LF, Liu QH, Li X, Tan Q (2005) Remote sensing and GIS-based integrated analysis of coastal changes and their environmental impacts in Lingding Bay, Pearl River Estuary, South China. *Ocean Coast Manage* 48:65–83
- Conway TM (2005) Current and future patterns of land-use change in the coastal zone of New Jersey. *Environ Plann B* 32:877–893
- Couto P (2003) Assessing the accuracy of spatial simulation models. *Ecol Model* 167:181–198
- Davidson-Arnott RGD, van Proosdij D, Ollerhead J, Schostak L (2002) Hydrodynamics and sedimentation in salt marshes: examples from a macrotidal marsh, Bay of Fundy. *Geomorphology* 48:209–231
- Davis RA (1994) The evolving coast. In: Scientific American library series, vol 231. Scientific American Library
- Dech JP, Maun MA, Pazner MI (2005) Blowout dynamics on Lake Huron sand dunes: analysis of digital multispectral data from colour air photos. *Catena* 60:165–180
- Donoghue DNM, Mironnet N (2002) Development of an integrated geographical information system prototype for coastal habitat monitoring. *Comput Geosci* 28:129–141
- Feist BE, Simenstad CA (2000) Expansion rates and recruitment frequency of exotic smooth cordgrass, *Spartina alterniflora* (Loisel), colonizing unvegetated littoral flats in Willapa Bay, Washington. *Estuaries* 23:267–274
- Field RT, Philipp KR (2000) Vegetation changes in the freshwater tidal marsh of the Delaware estuary. *Wetl Ecol Manage* 8:79–88

- Filippi AM, Jensen JR (2006) Fuzzy learning vector quantization for hyperspectral coastal vegetation classification. *Remote Sens Environ* 100:512–530
- Frederiksen M, Krause-Jensen D, Holmer M, Laursen JS (2004) Long-term changes in area distribution of eelgrass (*Zostera marina*) in Danish coastal waters. *Aquat Bot* 78:167–181
- Goodbred SL, Hine AC (1995) Coastal storm deposition: salt-marsh response to a severe extratropical storm, March 1993, west-central Florida. *Geology* 23:679–682
- Higginbotham CB, Alber M, Chalmers AG (2004) Analysis of tidal marsh vegetation patterns in two Georgia estuaries using aerial photography and GIS. *Estuaries* 27:670–683
- Hughes MI, McDowell PF, Marcus WA (2006) Accuracy assessment of georectified aerial photographs: implications for measuring lateral channel movement in a GIS. *Geomorphology* 74:1–16
- Jensen JR (1996) *Introductory digital image processing: a remote sensing perspective*. Prentice Hall series in geographic information science. Prentice Hall, Upper Saddle River, New Jersey
- Jones JL (2006) Side channel mapping and fish habitat suitability analysis using Lidar topography and orthophotography. *Photogramm Eng Rem S* 72:1202–1207
- Jupiter S, Potts D, Phinn S, Duke N (2007) Natural and anthropogenic changes to mangrove distributions in the Pioneer River Estuary (QLD, Australia). *Wetl Ecol Manage* 15:51–62
- Laliberte AS, Rango A, Havstad KM, Paris JF, Beck RF, McNeely R, Gonzalez AL (2004) Object-oriented image analysis for mapping shrub encroachment from 1937 to 2003 in southern New Mexico. *Remote Sens Environ* 93:198–210
- Lathrop RG, Montesano P, Haag S (2006) A multi-scale segmentation approach to mapping seagrass habitats using airborne digital camera imagery. *Photogramm Eng Rem S* 72:665–675
- Lathrop RG, Styles RM, Seitzinger SP, Bognar JA (2001) Use of GIS mapping and modeling approaches to examine the spatial distribution of Seagrasses in Barnegat Bay, New Jersey. *Estuaries* 24:904–916
- Li L, Ustin SL, Lay M (2005) Application of multiple endmember spectral mixture analysis (MESMA) to AVIRIS imagery for coastal salt marsh mapping: a case study in China Camp, CA, USA. *Int J Remote Sens* 26:5193–5207
- Lovejoy S (1982) Area-perimeter relation for rain and cloud data. *Science* 216:185–187
- Lu D, Mausel P, Brondizio E, Moran E (2004) Change detection techniques. *Int J Remote Sens* 25:2365–2407
- Mandelbrot BB (1982) *The Fractal Geometry of Nature*. WH Freeman, San Francisco, USA
- Mas JF (2005) Change estimates by map comparison: a method to reduce erroneous changes due to positional error. *Trans GIS* 9:619–629
- Meehan AJ, Williams RJ, Watford FA (2005) Detecting trends in Seagrass abundance using aerial photograph interpretation: problems arising with the evolution of mapping methods. *Estuaries* 28:462–472
- Nordstrom KF, Jackson NL, Klein AHF, Sherman DJ, Hesp PA (2006) Offshore aeolian transport across a low foredune on a developed barrier island. *J Coastal Res* 22:1260–1267
- Olsen ER, Ramsey RD, Winn DS (1993) A modified fractal dimension as a measure of landscape diversity. *Photogramm Eng Rem S* 59:1517–1520
- Pasqualini V, Pergent-Martini C, Clabaut P, Marteel H, Pergent G (2001) Integration of aerial remote sensing, photogrammetry, and GIS technologies in seagrass mapping. *Photogramm Eng Rem S* 67:99–105
- Pengra BW, Johnston CA, Loveland TR (2007) Mapping an invasive plant, *Phragmites australis*, in coastal wetlands using the EO-1 Hyperion hyperspectral sensor. *Remote Sens Environ* 108:74–81
- Perry GLW, Enright NJ (2006) Spatial modelling of vegetation change in dynamic landscapes: a review of methods and applications. *Prog Phys Geog* 30:47–72
- Phinn SR, Menges C, Hill GJE, Stanford M (2000) Optimizing remotely sensed solutions for monitoring, modeling, and managing coastal environments. *Remote Sens Environ* 73:117–132
- Phinn SR, Stanford M (2001) Monitoring land-cover and land-use change in a rapidly urbanising coastal environment: the Maroochy and Mooloolah Rivers catchments, Southeast Queensland, 1988–1997. *Aust Geogr Stud* 39:217–232

- Pontius RG, Batchu K (2003) Using the relative operating characteristic to quantify certainty in prediction of location of land cover change in India. *Trans GIS* 7:467–484
- Pontius RG, Shusas E, McEachern M (2004) Detecting important categorical land changes while accounting for persistence. *Agr Ecosyst Environ* 101:251–268
- Ramessur RT (2002) Anthropenic-driven changes with focus on the coastal zone of Mauritius, south-western Indian Ocean. *Reg Environ Change* 3:99–106
- Schroder B, Seppelt R (2006) Analysis of pattern-process interactions based on landscape models: overview, general concepts, and methodological issues. *Ecol Model* 199:505–516
- Shao G, Wu W (2004) The effects of classification accuracy on landscape indices. In: Lunetta RS, Lyon JG (eds) *Remote sensing and GIS accuracy assessment*. CRC Press, Boca Raton, Florida
- Shi Z, Wang RC, Huang MX, Landgraf D (2002) Detection of coastal saline land uses with multi-temporal landsat images in Shangyu City, China. *Environ Manage* 30:142–150
- Titus JG (1990) Greenhouse effect, sea level rise, and barrier islands: Case study of Long Beach, New Jersey. *Coastal Manage*, 18:65–90
- Ucuncuoglu E, Arli O, Eronat AH (2006) Evaluating the impact of coastal land uses on water clarity conditions from Landsat TM/ETM+ imagery: Candarli Bay, Aegean Sea. *Int J Remote Sens*, 27(17):3627–3643
- Vanderstraete T, Goossens R, Ghabour TK (2006) The use of multitemporal Landsat images for the change detection of the coastal zone near Hurghada, Egypt. *Int J Remote Sens*, 27(17):3645–3655
- Zharikov Y, Skilleter GA, Loneragan NR, Taranto T, Cameron BE (2005) Mapping and characterising subtropical estuarine landscapes using aerial photography and GIS for potential application in wildlife conservation and management. *Biol Conserv*, 125(1):87–100



# Chapter 18

## Mapping Fire Scars and Marsh Recovery with Remote Sensing Data

Elijah Ramsey III, Amina Rangoonwala, Frank Baarnes and Ruth Spell

Two coastal marshes exhibiting dramatically different patterns of seasonal biomass turnover were monitored with satellite and aircraft-based sensors and ground and helicopter-based site-specific measures that portrayed the canopy structure and optical reflectance. The seasonal maidencane fresh marsh completely recycled annually, producing a very different temporal response to burning than did the seasonally stable black needlerush saline marsh. For the black needlerush marsh, we used atmospherically corrected, normalized optical image data transformed to a vegetation indicator. When optical data were limited, time-since-burn prediction was constrained to the first year since burn, but single frequency (C band) and polarization (VV) Synthetic Aperture Radar image data showed good correspondence, extending the time-since-burn prediction to  $\sim 900$  days. For the maidencane marsh, we focused on multiple date Landsat Thematic Mapper (TM) image data and nearly concurrent site-specific canopy reflectance and structural measurements. In spring, these measures of nonburnt, winter burnt, and spring burnt marshes indicated that form and magnitude could differentiate variations in marsh burn history, but by summer, nonburnt and burnt marshes were inseparable. To overcome these inseparabilities and provide a full marsh burn history, we overlaid TM winter, spring, and summer classifications. The produced map successfully depicted complex changes in the maidencane marsh that resulted from late fall to spring wildfires.

### 18.1 Introduction

Each year over a million acres of Department of the Interior lands (Bureau of Land Management, National Park Service, Bureau of Indian Affairs, and U.S. Fish and Wildlife Service) are burnt by prescribed and wildfires. Although public awareness is normally focused on fires occurring in forests or shrublands surrounding densely populated urban centers, coastal and inland marsh fires can risk lives and property and destroy critical wildlife habitat and ground cover necessary for erosion control,

---

E. Ramsey (✉)

National Wetlands Research Center, U.S. Geological Survey, Lafayette, LA 70506, USA  
e-mail: elijah\_ramsey@usgs.gov



**Fig. 18.1** More than 100 firefighters battled a brush fire that swept through a salt marsh in the Cleveland suburb of Mentor before it reached nearby homes. “If you were standing here when the flames were 50 feet in the air and they were coming to the road where the firefighters were making their stand, that’s pretty dramatic,” said Mentor Fire Chief Rich Harvey. Mentor Marsh was once a freshwater marsh, but salt contamination starting in the 1950s resulted in the saline-tolerant reed grass, phragmites, proliferating there permission requested (<http://www.cnn.com/2003/US/Midwest/04/28/ohio.brush.fire/>)

and unique to coastal marshes, suppression of devastating storm surges. The marsh fire in suburban Cleveland in 2003 dramatically illustrated the threat to human populations that are increasing abutting marshes (Fig. 18.1). As the responding Fire Chief said, “It’s a beautiful place to live until it’s on fire.” Fueled by a salt-tolerant reed grass (*Phragmites*) containing an oily hydrocarbon, the fire reached 50 feet high and sent thick black clouds hundreds of feet into the air. Once a freshwater marsh in the 1950s, salt contamination allowed the invasion and proliferation of the highly flammable *Phragmites*.

Replacement of the freshmarsh with *Phragmites* illustrates how different management options (Beukema et al. 1999) can substantially influence fire risk and destruction. Build-up of fuel or replacement with more flammable materials and the lack of moisture in these marsh environments can dramatically increase fire danger (flammability) and smoke emissions and result in high risk to human populations. In May of 2007, southern Georgia and northern Florida, specifically the Big Bend area of Florida, experienced numerous life threatening grassland fires causing substantial loss in property and habitat, escalating pulmonary complications, and raising visibility concerns along transportation corridors. Similar fire events have occurred throughout Florida to North Carolina over the past 40 years.

As the suburban Cleveland marsh fire and recent devastating grassland fires in the Southeastern United States demonstrate, there is a critical need to develop monitoring methods that will decrease the risk to humans and facilities in these densely populated environments. At the same time that improved monitoring methods are needed to assess the spatial variability of marsh and grassland fire danger and fuel distribution (related to fire behavior), the ecological impact of these fires

and fire abatement practices and the part these fires play in influencing fire risk and destruction must be better understood (e.g., Angeler et al. 2006). Grassland fires are a major component of managed and nonmanaged (wildfire) burning practices occurring from the open prairie to the coastal wetlands (marshes) (Johnson and Knapp 1993). Each year immense but unknown acreages of fresh to saline Gulf of Mexico coast marshes are burnt (Hoffpauer 1968, Wilson 1968, Ramsey et al. 1992a, 1993, 1994a). These fires range widely in spatial extent and intensity with multiple burns occurring over time causing interspersion and juxtaposition of burn histories.

Little information exists concerning the effect of fire on wetland grasses (marsh) (Johnson and Knapp 1993, Taylor et al. 1994), and little, if any information on the number, extent, and intensity of marsh burns in the Gulf region. Further, marsh management practices that include fire management may not produce intended results and could be detrimental to sustaining the desired marsh function (Whigham 1999, Gabrey and Afton 2001, Gabrey et al. 2001, Smith et al. 2001). To properly manage wetland resources as related to fire danger, fire risk, and ecological impact, it is important that we fully understand how the grassland responds to common fire management practices. However, even though direct assessment techniques can be used to monitor local effects, these surveys to assess the extent and spatial variability of a burn are constrained by time, personnel, costs, and site accessibility. Further, unless field observations are performed strictly adherent to accepted standard procedures, quantitative and repeatable measurements are not obtained (Belluco et al. 2006). To circumvent these limitations in temporal and spatial measurements, we continue to develop remote sensing tools to detect, inventory, and monitor areas of burnt marsh. The development and implementation of these tools provide critical inputs to fire behavior and ecological models that could be used to understand the effects of fires on grassland development and how these developments influence fire danger and risk.

### ***18.1.1 Data Sources***

For more than 15 years, we have collected ground-based, aircraft, and satellite measurements at numerous sites throughout coastal Louisiana and the Big Bend area of Florida (e.g., Ramsey et al. 2006). Objectives of these collections were not designed or funded for burn detection and monitoring; however, ground-based and image data collections encompassed marsh burns and recovery at numerous field sites that included at least four dominate marsh types throughout the Big Bend region of Florida and coastal Louisiana. Ground-based measurements included time-sequences of canopy structure and biomass estimators and canopy reflectance from a helicopter platform of burnt and nonburnt marsh sites. Within the same time period, passive visible and near infrared (VNIR), shortwave infrared (SWIR), and active microwave at multiple frequencies and polarizations (e.g., X, C, and L bands: HH

and VV “like” polarizations and the HV or VH “cross” polarization pairs) image data were collected from sensors that are currently available to the public. Pertinent image data sources included satellite (e.g., Landsat Thematic Mapper (TM), ERS Synthetic Aperture Radar (SAR), Shuttle Imaging Radar-C (SIR-C) SAR, and aircraft image data (NAVY P3 Orion and USGS STAR-1 SAR’s, and NASA Thematic Mapper Simulator (TMS)). Unless specified otherwise, the passive visible and near infrared (VNIR) to shortwave infrared (SWIR) image data (0.40 $\mu\text{m}$  to 2.5 $\mu\text{m}$ , for example Landsat TM or ETM+) were calibrated to radiance, corrected for atmospheric influences and changes, and normalized to ground reflectance. ERS-1 (CVV) and SIR-C (L and C multiple polarization) SAR image data were calibrated with software provided by the Canadian Center of Remote Sensing (Ramsey et al. 1994b, Ramsey 1995) and NASA Jet Propulsion Laboratory (JPL), respectively. The NAVY P3 Orion (L multiple polarization) and USGS STAR-1 (XHH) SAR image data were converted from slant to ground range and a relative calibration applied to the P3 Orion SAR image data (Ramsey et al. 1999). Calibrated radar images also explicitly contained differences related to spatial resolutions (1 m, 12 m, and 25 m) and incident and look angles. Incident angles ranged from steep (for example about 22° in the case of ERS-1 SAR) to mid range angle around 40° in the case of P3 Orion SAR (mid range included the St. Marks National Wildlife Refuge coverage). Azimuth was primarily shore-parallel and look angles were toward the east or toward the west in all SAR collections.

### ***18.1.2 Monitoring Marsh Burn Recovery with Optical Satellite Sensor Image Data***

Remote sensing can economically monitor biophysical characteristics over large areas, and generate data on various spatial and temporal scales by using a wide variety of sensors and sensor platforms (Lulla and Mausel 1983). It is the repetitive ability; however, that has the greatest potential in fire management. The repetitive ability, or temporal monitoring, allows patterns to be revealed in the data that may be transformed into quantitative determinations of fuel quantity and fire danger and provides a means for monitoring the recovery of marsh (or grasslands) from fire. From a remote sensing point of view, monitoring vegetation canopy recovery involves detecting and separating normal change and variability from abnormal changes and variabilities (e.g., Ramsey and Rangoonwala 2005, 2006). Although the definition varies about what marsh canopy changes and variabilities are both pertinent to estimating the vegetation canopy recovery and amenable to remote sensing, when the monitoring period extends over seasons, the seasonal variability must be considered. In these cases, the obvious question is whether or not the canopy vegetation seasonal changes and variabilities can mask those that are a consequence of the impact agent. For this reason, we will describe one situation where the marsh changes little with season and another where the marsh totally recycles yearly.

### ***18.1.3 Monitoring Marsh Burn Recovery with Site-Specific Canopy Reflectance and Backscatter***

The canopy reflectance or backscatter is that portion of the remotely sensed signal most directly related to the vegetation canopy properties. Broadly and in aggregate, the vegetation canopy includes the plant canopy and background (Lorenzen and Jensen 1988, Spanglet et al. 1998, Penuelas and Filella 1998). Dominantly, the plant canopy comprises the plant leaf spectral properties and the canopy structure (e.g., height, orientation), intimately coupling the leaf reflectance (or backscatter) and canopy structure in the remote sensing signal. Variability in plant leaf optical properties or canopy structure can reflect changing biophysical forces defining the natural landscape (Ramsey et al. 1992b,c, 1999, 2001). In the later stage of marsh recovery, it is likely that changes in the leaf optical properties will primarily control VNIR to SWIR canopy reflectance variabilities (e.g., Ramsey and Rangoonwala 2004, 2005, 2006), while canopy structural changes will more likely be measurable with radar data (e.g., Ramsey 1998, Ramsey et al. 1999, Ramsey 2005). From a remote sensing perspective, to provide the subtle marsh discrimination necessary for mapping and monitoring burn impact and recovery above natural variability, the separate influences of plant leaf spectral, canopy structural, and background variability on the remote sensing signal must be estimated. Reliance on visual appearance does not provide an acceptable means to detect subtle changes related to recovery or a metric to measure the recovery progression against (Ramsey and Rangoonwala 2005, 2006).

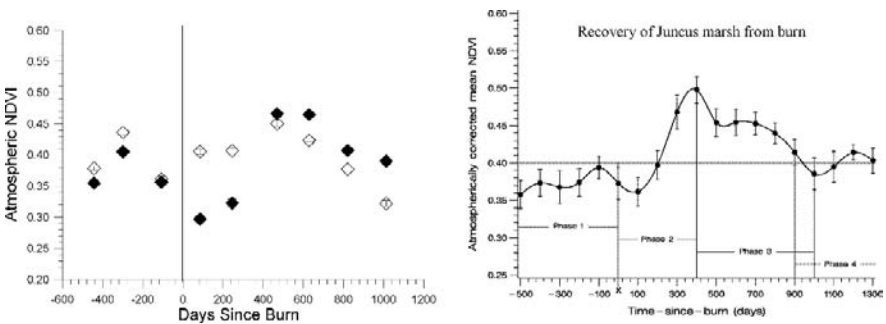
To minimize these complications and to fully control target location complications in linking canopy spectral properties to image data (e.g., Vanderbilt and Grant 1985, Ranson et al. 1985, Deering and Eck 1987, Gross et al. 1988, Huete and Jackson 1988), we used ground-based and helicopter-based field radiometers for collecting data (Hobbs and Shennan 1986, Ramsey et al. 1992a,b,c, 1993, Spell and Ramsey 1991, 1993). Further, our helicopter-based recordings were at near nadir during clear skies and at times of higher sun elevations to simulate most satellite operations and minimize sun-view influences (Kimes 1983). Generation of canopy reflectance spectra in this way was analogous to moving the satellite sensor a few hundred meters above the canopy and controlling for sunlight illumination and atmospheric variability (e.g., Ramsey and Nelson 2005, Ramsey and Rangoonwala 2006). Even with controlled measurements, multiple vegetation canopy contributors (Colwell 1974, Myneni et al. 1995) each with a varied relationship and importance to burn occurrence complicate linking the marsh burn recovery to canopy reflectance or backscatter. Even if the image pixel contains only a single plant species (similar leaf spectral properties), variability in the background and at least one component of the canopy structure, the plant structure, will be combined into the remote sensing signal (Allen and Richardson 1968, Ranson et al. 1985, Huete and Jackson 1988, Peterson et al. 1988, McCloy et al. 1993, Spanglet et al. 1998). Changes in canopy structure and background (e.g., surface water and soil water content) occur naturally in these marshes, mainly reflecting inundation gradients (Hardisky et al. 1986),

and are more visually apparent in the earlier stages of burn recovery progression (e.g., Ramsey 1995, Ramsey et al. 1999).

### 18.2 Monitoring Burn Recovery in a Seasonally Stable Marsh

Our seasonally stable marsh example includes a *Juncus romerianus* (black needlerush) saline marsh in the Big Bend area of coastal Florida. In our studies and those of others (William and Murdoch 1972, Hopkinson et al. 1978, Stout 1984), black needlerush marshes of the Gulf coast wetlands tend to have little and varied change in canopy live and dead biomass or structure related to seasons. In a study monitoring the burn recovery of a *Juncus romerianus* (black needlerush) (Ramsey et al. 2002), we observed a depressed vegetation index (VI) within the first year following the burn and after that a higher than normal VI for at least two years (Fig. 18.2 left) (see Tucker 1979 for the relevance of the VI transform to vegetation condition). At 13 sites throughout the marsh, the time-since-burn extracted from the St. Marks National Wildlife Refuge (NWR) burn records and personal observations was related to corresponding image data (PCI 1998, Ramsey et al. 1999, Ramsey et al. 2002).

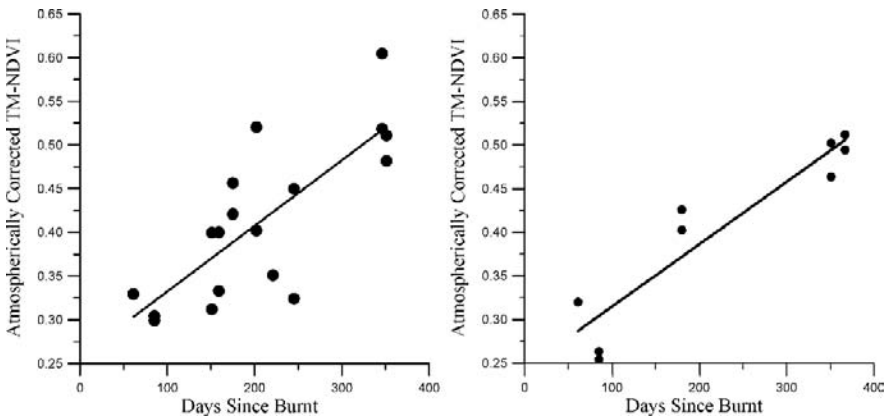
The VI was based on the atmospherically corrected and normalized TM image data and the Normalized Difference Vegetation Index (NDVI) transform. Heute et al. (1985) and Heute and Jackson (1988) showed that NDVI based on reflectance data (atmospherically corrected and normalized) performed as well or better than all other VI's transforms in portraying vegetation canopy differences and changes. The VI transform of the TM responses from a single burn site showed a response pattern was observable with the VNIR-SWIR sensor (Fig. 18.2 left). Combining all burn sites and corrected and transformed NDVI data from the nine TM image dates, we observed marsh recovery was divided into four general regions; preburn (phase 1), immediate postburn (0 to ~360 days, phase 2), rapidly increasing biomass (1–3 years, phase 3), and asymptotic plateau (> 3 yrs, phase 4) (Fig. 18.2 right). As in the



**Fig. 18.2** Data from nine Landsat Thematic Mapper images collected on 09/18/90, 02/09/91, 08/20/91, 02/28/92, 08/06/92, 03/18/93, 08/25/93, 03/05/94, and 09/13/94 were transformed to NDVI. (left) The NDVI trend at one marsh burn site (solid symbol) and its associated non burnt control (open symbol). (right) The NDVI temporal trend extracted from all 13 burnt marsh sites (Ramsey et al. 2002, Fig. 18.3, p. 90 with kind permission of Springer Science and Business Media)

single site comparison to its associated non burnt control (Fig. 18.2 left), the NDVI in phase 2 was lower and phase 3 was higher as related to the average NDVI (0.40) of non burnt controls. These NDVI temporal trends in response to marsh burns was apparent even though canopy spectral reflectances differences between burnt and non burnt marshes were low (i.e., <2–5%) throughout the VNIR spectral range.

In a following comparison with TM image data, we combined the calculated VI data into a single regression predictor of the time-since-burn. First, we regressed the combined TM-NDVI data from the suite of nine TM dates with the time-since-burn from all 13 sites up to 365 days since burn ( $n = 18$ ,  $p < 0.01$ ,  $R^2 = 0.60$ ) (Fig. 18.3 left). Second, we regressed TM-NDVI data from a single TM date with time-since-burn restricted to one year since burn ( $n = 9$ ,  $p < 0.05$ ,  $R^2 = 0.88$ ) (Fig. 18.3 right).



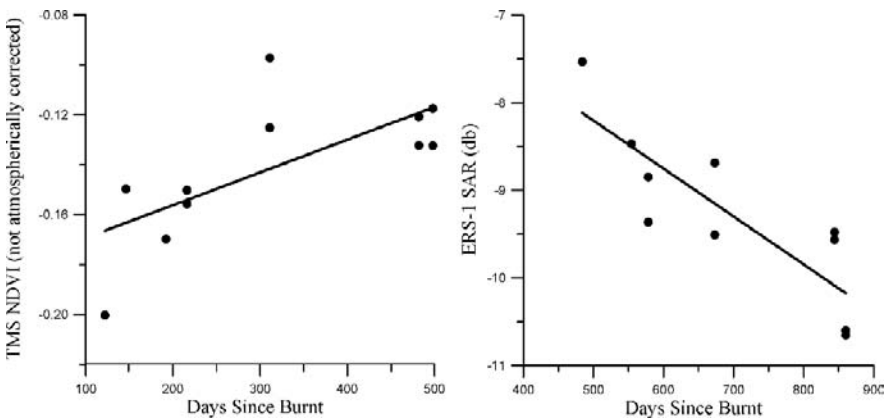
**Fig. 18.3** (left) All nine TM-NDVI image dates (listed in Fig. 18.2). (right) A single TM-NDVI image collected on 28 February 1992

### 18.2.1 Single-Date Monitoring of Marsh Burn Recovery

As illustrated in the mapping of burn recovery (Fig. 18.2), repeatability of satellite and aircraft remote sensing measurements is critical in determining patterns in the image data that can be quantifiably linked to landscape process. However, orbital characteristics (Landsat collects image data over the same area every 16 days) combined with prevalent cloud cover or extreme atmospheric turbidity in the subtropical to tropical regions results in the collection of very few useful images per year (Ramsey and Laine 1997). This inability to provide consistent monitoring fundamentally restricts passive VNIR to SWIR remote sensing systems' ability to determine and monitor wetland condition and change. A second restriction of these passive sensor systems is the very limited penetration of fully developed vegetation canopies. This lack of penetration results in the collection of little or no information from beneath the top of the canopy (Ramsey et al. 1998b, Ramsey 1998, 2005). To minimize weather restrictions and maximize recovery monitoring, we examined single-date image collections as burn recovery predictors. In conjunction with

minimizing our reliance on multiple passive VNIR to SWIR collections of acceptable quality, we examined the ability of different SAR satellite systems to provide the burn history. SAR sensor systems nearly eliminate collection restrictions due to weather, allow nighttime reconnaissance, and most often increases canopy penetration compared to passive VNIR to SWIR sensor systems. In both passive VNIR to SWIR and SAR single-date image analyses, we used the same coastal *Juncus roemerianus* burn sites as used in the suite of nine TM images (Fig. 18.2, Ramsey et al. 2002). Instead of the time-since-burn of each burn site varying with-respect-to the suite of temporal TM image dates, the single-date image analyses used the time-since-burn to the sensor response correlation strength (goodness of fit,  $R^2$ ) as an indicator of sensor type usefulness in monitoring burn recovery.

Continuing with the seasonally stable marsh, a single-date NASA TMS image was collected on 8 July 1992 and calibrated with coefficients supplied by NASA (Fig. 18.4 left). The TMS image was neither atmospherically corrected nor normalized to reflectance. Even though not corrected or transformed, the NDVI image data from a single date NASA TMS image were significantly related to time-since-burn with a goodness of fit of  $R^2 = 0.48$  ( $n = 9$ ,  $p < 0.02$ ); although the tendency toward an exponential trend suggests saturation of the TMS-NDVI response with time. With the same set of burn sites and the set prediction level we obtained with operational optical data, we produced similar prediction simulations with available and operational SAR image data. The single date (X band HH polarization) USGS STAR-1 SAR was not significantly related to time-since-burn ( $p < 0.05$ ), with or without normalization by the relevant per site control (Ramsey 1998). Of the six ERS-1 SAR images collected and processed of the St Marks NWR, Florida, the July, August, October, and November SAR responses were significantly related to time-since-burn ( $p < 0.1$ ). Estimated from the explained variance statistic, the best relationship was between the July ERS-1 SAR image data and the time- since-burn



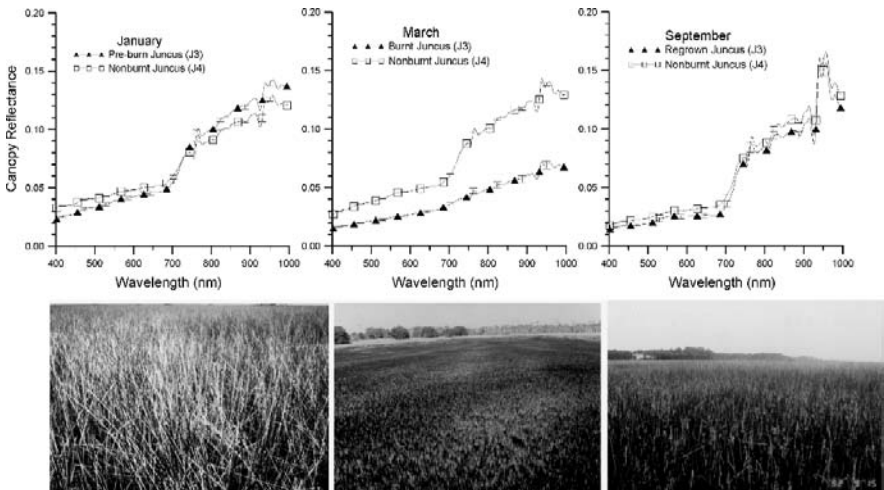
**Fig. 18.4** (left) NASA TMS collected on 8 July 1992. Not atmospherically corrected or normalized to reflectance. (right) A single date ERS-1 SAR image collected in July 1993 (dB refers to decibel units)



( $R^2 = 0.71$ ,  $n = 10$ ,  $p < 0.01$ ) (Fig. 18.4 right). Normalization of the July data by site-specific control decreased the correspondence in July, increased correspondence in October, and left the relationships unchanged in August and November regression analyses. The SIR-C C band and HH polarization normalized by the CHH control ( $n = 10$ ,  $p < 0.05$ ,  $R^2 = 0.42$ ) and the L and C band cross polarization (HV) difference (LHV-CHV) ( $n = 10$ ,  $p < 0.1$ ,  $R^2 = 0.32$ ) exhibited significant relationships with time-since-burn (graphs not shown). Excluding one site from the LHV-CHV and time-since-burn regression increased the explained variance from 32% to 71% and changed the significance from  $p < 0.10$  to  $p < 0.05$ .

### 18.2.2 Site-Specific Canopy Reflectance and Structure Related to Burn Recovery

As an example of canopy reflectance related to burn recovery, canopy spectra collected over a non burnt and a burnt black needlerush marsh sites were compared (see Ramsey and Nelson (2005) and Ramsey and Rangoonwala (2006) for details concerning canopy reflectance generation) (Fig. 18.5). The non burnt and burnt marsh sites portrayed in Fig. 18.5 were within similar marsh zones (Ramsey et al. 1998a) in order to minimize differences related to normal and hydrologic variabilites. As illustrated in the pictures in Fig. 18.5, the mature marsh contains more dead material than the recovering marsh. The more flattened spectral response across the VNIR



**Fig. 18.5** (top) Representative ground pictures of a black needlerush marsh site that was burnt and (bottom) a series of canopy reflectance spectra of a non burnt (J4) and burnt (J3) black needlerush marsh sites. In both top and bottom series the leftmost picture and graphic portrays before burn, the center – just after burnt, and the rightmost – within 1 year after burnt. Canopy reflectances were derived from light measurements from a helicopter platform and on the ground (ground resolution about 20 m) (Ramsey et al. 1992a, 1993; Spell and Ramsey 1993)

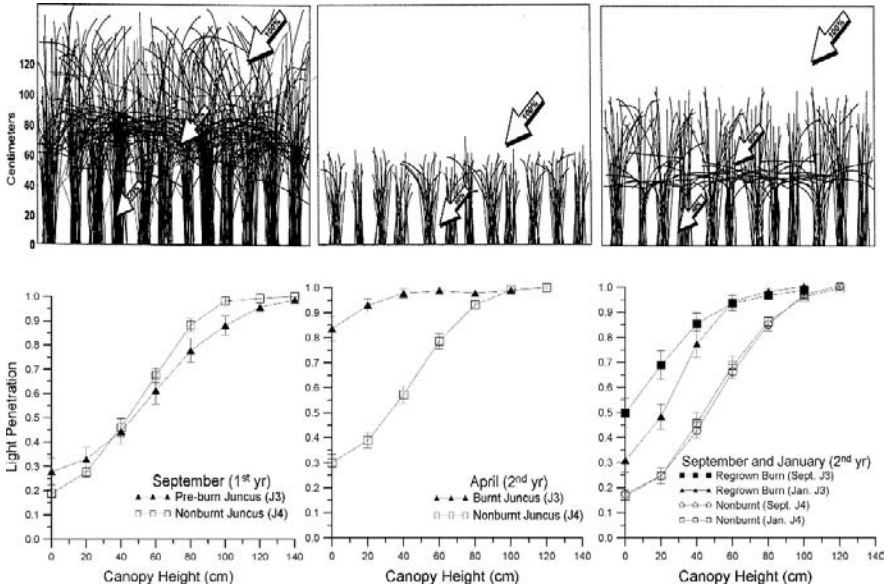
as exhibited in the before versus one year after burn spectra is also indicative of a higher concentration of dead material in the vegetation canopy. Excluding these differences between the before and one year after spectral pairs related to biomass composition, burnt and non burnt spectral differences were similar for both spectral pairs.

Noted earlier, this close correspondence from about 2% to 5% of the burnt and non burnt spectra across the VNIR reflectance complicates the burn recovery monitoring in these black needlerush marshes. As illustrated in Fig. 18.2, however, marsh burn monitoring until full recovery in this fairly stable marsh is possible by employing multiple image dates containing high fidelity data. In addition, Figs. 18.3 and 18.4 indicate that if restricted to the first year since burn, single date recovery estimation is possible with high fidelity satellite optical data and somewhat possible with non corrected aircraft optical image data. However, a saturation of the TMS-NDVI response with time-since-burn was indicated (Fig. 18.4 left). Importantly, single date satellite radar image data collected outside of flooding periods was also highly predicted of the time-since-burn (Fig. 18.4 right). This variable radar response most likely indicated a change in canopy structure that occurred with burn recovery. To more directly evaluate the changes in canopy structure accompanying marsh burn recovery, we isolated and plotted changes in light-canopy attenuation with recovery as an indicator of marsh structural changes (Fig. 18.6) (Ramsey et al. 2004).

Light penetration curves parallel canopy spectral changes (Figs. 18.5 and 18.6). The marsh canopies were very similar before the burn and highly different directly following the burn occurrence; however, the parallel similarity ends there. The penetration curves shown after one year and 16 months after burn (Fig. 18.6 rightmost) still portray differences in the non burnt and burnt canopy structure. This longer term canopy structure response is in stark contrast to the high similarity and low magnitude differences obtained in the canopy reflectance progression of marsh burn recovery. As illustrated in the cartoon series of Fig. 18.6 (top), the canopy gains both density and height with time-since-burn. This is clearly portrayed in the light penetration series (Fig. 18.6 bottom). The relatively high differences in light penetration after one year-since-burn indicated that radar, as a more direct indicator of marsh canopy structure, would be more responsive to documenting canopy changes that accompany marsh burn recovery. Another feature illustrated in the cartoon series (Fig. 18.6 top) is the canopy overall orientation change from primarily a vertical to a more mixed vertical and horizontal orientation as the marsh recovers. The change in dominate canopy orientation with recovery was based on St. Marks NWR field observations (Ramsey et al. 1999).

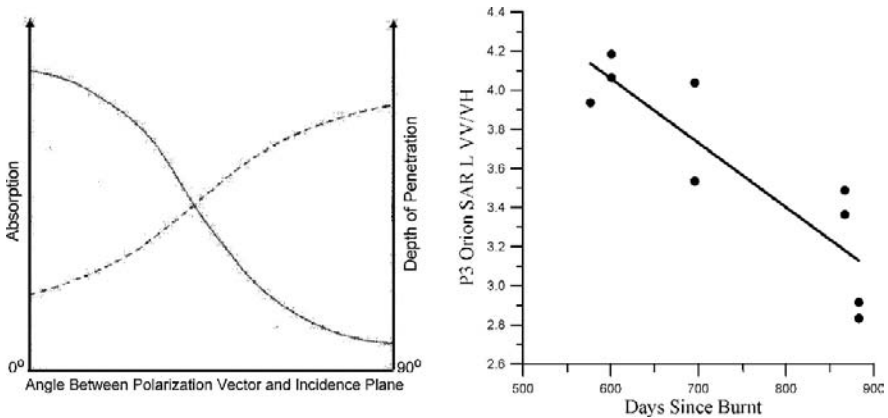
### ***18.2.3 Marsh Burn Recovery Related to Polarimetric Radar***

We tested the ability to capture this canopy orientation change with recovery by applying polarimetric radar image data (Ramsey et al. 1999). Following Elachi (1987),



**Fig. 18.6** (top) An illustration of regrowing black needlerush marsh recovering from a burn. The arrows represent percent light penetration from the top-of-canopy (TOC) to the marsh surface. The leftmost cartoon portrays recent regrowth, the center within 1 year, and the rightmost within 2 to 3 years after burn. (bottom) A series of canopy-light attenuation curves representing light penetration with depth. These graphics depict measurements collected from the same non burnt (J4) and burnt (J3) black needlerush marsh sites depicted in Fig. 18.5. The leftmost graphic portrays before burn, the center just after burn, and the rightmost within 1 year after burn. Light penetration profiles were generated from 22 measurements at each height along 30 m transects

we predicted that changes in the preferred orientation of the canopy with recovery would be observable as changes in the strength of interaction, and thereby in the amplitudes, of vertical and horizontal polarimetric send and return combinations from the recovering burnt marsh (e.g., Fig. 18.7 right). As shown in Fig. 18.7(left), absorption increases as the wave polarization is more aligned with the target orientation, and conversely absorption decrease as the wave and target orientations become more orthogonal. Another way to look at this absorption trend is that interaction of the wave and target increases as alignment increases. In general, this interaction can take on various forms primarily partitioned following Kirchoff's law into whether the plant material absorbs, transmits, or reflects the impinging radiation. From this diagram (Fig. 18.7 left) and our field observations, we expected that in the earlier stages of regrowth, a vertical send and receive (VV) would most interact and HH would least interact with the mostly vertical canopy, and VH interactions would be most related to the amount of canopy biomass (Ramsey 1998, 2005). At later stages of regrowth recovery, VV interactions would decrease while HH and VH interactions would increase as the upper canopy included a greater mixture of orientations and plant material. The upper canopy biomass increase would effectively block penetration of the radar into the lower canopy more dominated by vertical components.



**Fig. 18.7** (left) After Elachi (1987, Fig. 6-5, p. 170, with permission of John Wiley & Sons, Inc.) (Absorption —; Depth of Penetration- - -). (right) NAVY P3 Orion SAR image data collected and normalized over nine black needlerush marsh burn sites (Ramsey et al. 1999). The ordinate depicts the VV return normalized by the VH return. In this case, VH is used to indicate the change in canopy biomass. VH increased with burn recovery (Ramsey et al. 1999)

As shown in Fig. 18.7(right), VV return amplitudes did decrease with black needlerush canopy regrowth and recovery (Ramsey et al. 1999). Not shown but also documented in Ramsey et al. (1999), HH and VH return amplitudes increased with time-since-burn. To obtain the high correspondences, the mean radar polarimetric amplitude of each site was first normalized by a nearby non burnt marsh site. Ratios of the normalized polarimetric amplitudes were used to diminish surface returns most prominent in the earliest stages of recovery and additionally to decrease the influence of biomass increase accompanying the marsh recovery (e.g., Fig. 18.7 right). With normalizations, the P3 Orion polarimetric SAR provided a time-since-burn prediction of black needlerush marsh recovery of around 1000 days (Ramsey et al. 1999). This time interval matched that predicted by the multiple TM burn marsh series obtained by Ramsey et al. (2002) and shown in Fig. 18.2 (left). As previously stated, this long-term recovery of Gulf coast black needlerush marsh was suggested but not documented by earlier field researchers (Hopkinson et al. 1978).

### 18.3 Monitoring Burn Recovery in a Yearly Turnover Marsh

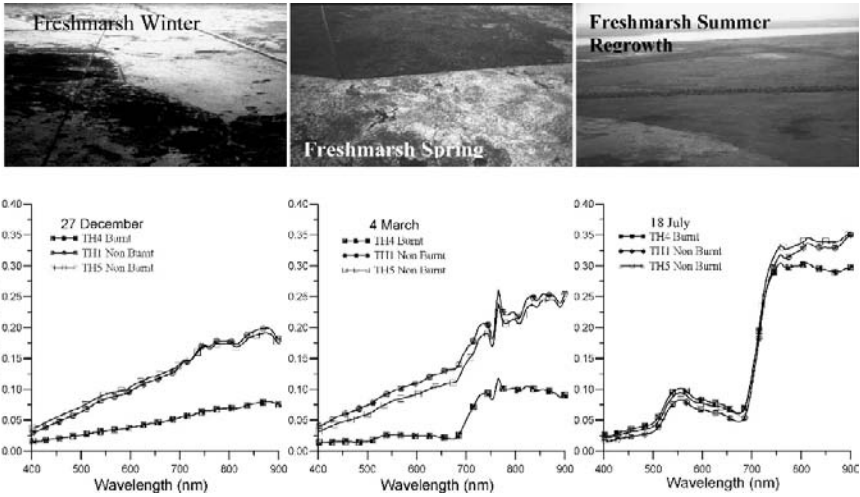
Our annual marsh example includes a *Panicum hemitomon* (maidencane) fresh marsh in the coastal zone of Louisiana. As shown in our studies (e.g., Ramsey et al. 1992b,c, 2004), maidencane marshes in coastal Louisiana completely recycle from one year to the next. Canopy green-up begins in March to April and obtains full canopy regrowth by June. Senescence starts in late September to late October leading to a complete lack of live canopy plant material by January to February. During the latter period of canopy senescence and into the spring green-up much

of the accumulating dead material can be carried away by freshwater flushing and some possibly lost to in-situ decomposition. By mid summer, the regrown canopy is most often nearly devoid of dead or dying plant material. This phenological development contrasts sharply with the more perennial black needlerush marshes of the Gulf coast wetlands that we have shown have little and varied change in canopy live and dead biomass or structure related to seasonal changes. As a comparison to the more seasonally stable black needlerush marshes, we describe the response of a maidencane marsh situated well within the fresh marsh zone of coastal Louisiana and outside of Gulf of Mexico salinity influences (Chabreck 1970). From the set of Louisiana freshmarsh data, the sites and data acquisition times were chosen to best illustrate the spectral and structural response of the marsh to being burnt. The discussions are limited to three sites (TH1=burnt between the start and end of the study; TH4=burnt pre-study; TH5=unburnt throughout the study), and partitioned between different methods used to monitor the marsh status: satellite (thematic mapper imagery-TM), and ground-based measurements (canopy reflectance and light attenuation). Canopy reflectance spectra were chosen to best correlate with times of available TM imagery; however, light penetration data were acquired about a year later in sites of similar burn histories.

### ***18.3.1 Site-Specific Canopy Reflectance and Structure Related to Burn Recovery***

Canopy reflectance spectra of three maidencane marsh sites were calculated from upwelling radiance collected from a helicopter platform and downwelling irradiance measurements measured at the ground surface in December 1990, March 1991, and July 1991 (Fig. 18.8). December and July upwelling radiance spectra were normalized by using pre-flight downwelling irradiance spectra, while March spectra were normalized by using simultaneously recorded downwelling irradiance spectra. Thus, in interpreting the canopy reflectance data, the March data are more credible; however, the form and magnitude of the December and July spectra follow field observations of canopy changes and changes in the uncorrected (atmospheric) TM imagery obtained near these dates. Additionally, similar grass canopies exhibited similar canopy reflectance spectra, and spectra acquired on March 9 and 18, but normalized with preflight data, closely followed March 4 canopy spectra. Finally, site markers were not in place during the December and March helicopter collections; thus, reoccupation locations were not exact, especially at site TH5.

Canopy reflectance spectra acquired in December are spectrally nondistinct. Spectra associated with sites TH1 and TH5 depicted dead, non burnt maidencane, whereas the burnt marsh at site TH4 was in the very early stages of recovery (green shoots just beginning to appear). Marsh at site TH4 was burnt after the November TM collection but before the December helicopter site-specific collections. Spectra in March showed the early appearance of a near-infrared (NIR) plateau and abrupt red to NIR amplitude shift (red-edge) at sites TH1 and TH5 and a more defined

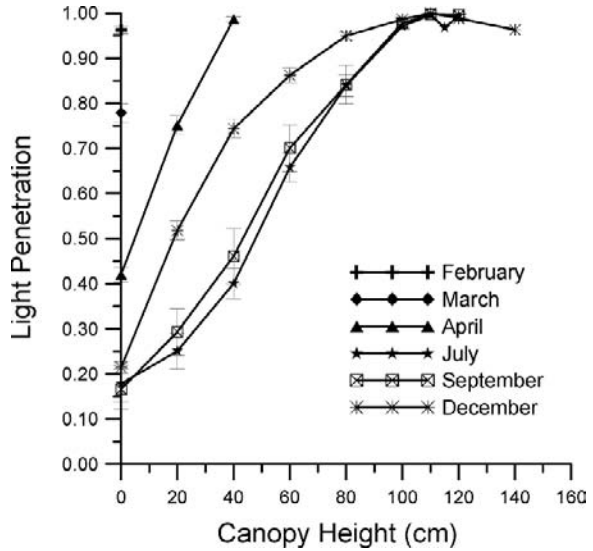


**Fig. 18.8** (top) A typical progression of burnt (winter—black, spring—green) and non burnt (winter—brown [no live material], spring—green-up [mixture of dead and live material]) *Panicum hemitomon* (maidencane) fresh marsh in the coastal zone of Louisiana. (bottom) A similar progression as shown in the top pictures illustrated in the canopy reflectance spectra progression (the locations of TH4, TH1, and TH5 are shown in Fig. 18.10)

NIR plateau and red-edge associated with site TH4 as new growth appeared in the marsh. Physically, the difference between non burnt marsh at sites TH1 and TH5 and recently burnt maidencane at site TH4 was the addition of dead material (light brown stalks) at the non burnt sites, while only black stubble remained as background at the burnt site. By July, the spectra associated with the three sites were generally similar, small differences remain in the amplitude that may or may not have been significant. However, the concurrence of the spectra in July was deceiving. A site occupation on March 18 revealed the marsh at site TH1 had been burnt sometime after March 9 (the previous field occupation). On March 18 the canopy reflectance spectrum associated with site TH1 almost exactly overlaid the spectrum related to marsh canopy at site TH4 during the December helicopter collection. By July, only small differences existed between canopy reflectance spectra associated with sites TH1 and TH5, while spectra associated with TH4 exhibited slightly lower amplitudes, especially in the NIR wavelengths.

Typical progression of light penetration curves beginning at the time of burn and extending until the canopy reached maturity less than one year later is illustrated in Fig. 18.9. As in the stable marsh discussion, the light penetration curves depict the change in marsh structure. In the case of this turnover marsh, however, the entire canopy biomass from previous year disappears as the marsh reaches maturity normally by mid to late summer (Spell and Ramsey 1991, Ramsey et al. 1993). In general, the regrowth of a maidencane marsh begins in late March to early April. Nearly vertical green shoots of maidencane begin to emerge from the black background in the burn, whereas taller dead and the shorter new growth are mixed at

**Fig. 18.9** A typical progression in light attenuation profiles for a *Panicum hemitomon* (maidencane) fresh marsh in the coastal zone of Louisiana (Ramsey et al. 1992a, 2004). Note February and March measurements were at zero canopy depth (soon after burnt). Light attenuation increases through July then begins to decrease from September onto December. Site TH4 is depicted (canopy reflectance is illustrated in Fig. 18.8 and the site is located on Fig. 18.10). Error bars associated with each data point depict plus/minus two standard errors (95%)

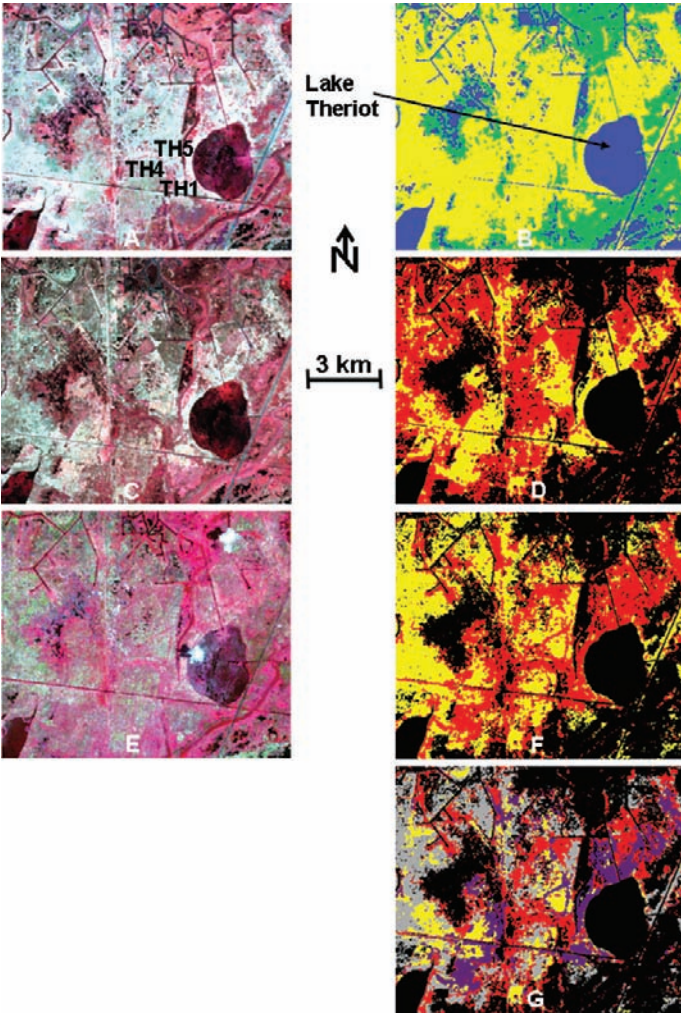


the non burnt sites (Fig. 18.8). In general by mid summer, winter burnt and non burnt marsh canopies have obtained similar heights and light attenuation profiles; the burnt canopy structure has fully recovered. At marsh sites burnt after winter, summer canopy light attenuation profiles can be steeper than in non burnt marshes indicating a less dense canopy or possibly a more vertical canopy structure in marsh canopies impacted by seasonally later burns (Ramsey et al. 1993, 2004).

### 18.3.2 Satellite Optical Image Data and Site-Specific Burn Recovery Monitoring

Classified maps were generated from November 1, 1990, March 9, 1991, and July 31, 1991 TM scenes (Fig. 18.10a). The area is centered at latitude 90.861° and longitude 29.478° and covers about 11.6 km (east/west) and 9.9 km (north/south). The March and July scenes were coregistered to the rectified November scene. Classifications were accomplished by first using a simple spectral algorithm to cluster the brightness values related to the six reflectance bands, and subsequently attaching the cluster signatures to assumed landcovers by using knowledge based on field occupations of the area. On the maps, the areas immediately to the west, south, and southwest of Lake Theriot encompassed sites occupied on the ground. Figure 18.10a depicts approximate locations for sites TH1, TH4, and TH5.

No burnt maidencane marsh areas were visible on the November TM imagery (Fig. 18.10a). Classes were limited to those easily definable: maidencane marsh, open water, and shrub or upland (Fig. 18.10b). In the March image, marsh areas (burnt and non burnt) were not always separable from shrub or upland areas



**Fig. 18.10** A and B—November, C and D—March, and E and F—July. A, C, and E are non classified color composites of TM bands 4, 3, 2. B is the November classified TM image; blue is water, green non marsh, and yellow non burnt maidencane marsh. In classified images B, D, and F, yellow is non burnt and red burnt is marsh and black is non marsh. G composites B, D, and F. Yellow is non burnt marsh November to July, grey is burnt in March not July, purple July not March, and red is burnt in March and July

(Fig. 18.10c and d). Thus, in order to facilitate differentiation between burnt and non burnt marsh in the March and July TM images, the classified November image was used to mask-out all non-maidencane marsh in these images before classification. Thus, only brightness values of the six TM reflectance bands associated with maidencane marsh areas – determined from the November classification – were entered into the classification algorithm. This procedure was valuable in separating



classes of landcovers found to be spectrally similar relative to the variance of the entire data set (Jensen et al. 1987, Ramsey and Laine 1997).

The March classified image showed burnt and non burnt maidencane marsh areas (Fig. 18.10d). Mixed within the marsh burnt class were older (already regrowing) and more recent burns (both since November 1990). Within the maidencane marsh, recent burnt marshes (typified by TH4—Fig. 18.8 [December]) were associated with low returns (brightness values), and older burnt marshes (TH4—Fig. 18.8 [March]) with higher returns in the NIR wavelengths. Non burnt marshes (typified by sites TH1 and TH5—Fig. 18.8 [March]) were associated with higher returns throughout the wavelength range compared to those associated with burnt marshes. Additional burning continued following the 9 March TM collection as is illustrated in the July classified image (Fig. 18.10f). The July burn map (and field spectra) revealed that new burning—since the March 9 image—had occurred primarily adjacent to Lake Theriot (typified by TH1—Fig. 18.8 [December and March]) and in the southwest corner of the marsh study area. Canopy reflectance spectra (Fig. 18.8) related to these new burnt marshes (TH1) and to non burnt marshes (TH5) suggest little spectral difference existed between marsh at the two sites in July, at least between 400 nm to 900 nm. Incorporated within this burnt class are marshes burnt before March (classified March image) that still could be separated from non burnt maidencane marsh. Further, incorporated in the July non burnt class are maidencane marshes that were burnt in March but were not spectrally separable by using simple classification techniques.

In order to properly map the development history of the maidencane marsh, the November, March, and July TM classifications were spatially overlain and the burn history of each image pixel calculated (Fig. 18.10g). Four classes of maidencane marsh related to burn history between November 1990 and July 1991 were (1) those areas of marsh that remained unburned throughout this time period, (2) those areas burned by March that could be distinguished as burns in July, (3) those areas burned by March that could not be distinguished as burns in July, and (4) marsh areas burned after March 9.

## 18.4 Summary

Two coastal marshes exhibiting dramatically different patterns of seasonal biomass turnover were monitored with satellite and aircraft based sensors and site-specific canopy measurements. The biomass turnover trends of the two marshes were used to illustrate how monitoring might differ dependent on its seasonal covariance. The black needlerush saline marsh in coastal Florida had minimal covariance with season while that maidencane fresh marsh in coastal Louisiana completely covaried with changing seasons under normal circumstances. In neither marsh-burn study were the burn locations or extents detected without *a priori* information or ground-based observations. Instead, the studies examined the ability to monitor marsh recovery with satellite and aircraft image-based data and relate those data to

ground-based site-specific measures that portrayed the canopy structure and optical reflectance without interferences from atmospheric contributions and illumination changes.

### ***18.4.1 Non Seasonal Marsh***

In the black needlerush saline marsh, trends in burn recovery were possible with atmospherically corrected and normalized optical image data transformed to a vegetation indicator (VI). As shown in that study based on a time series of temporal TM image data, the lower than normal VI following the canopy burn transformed into a higher than normal VI period as the canopy responded with new growth. As dead plant material was gradually added, the canopy VI lowered once again to preburn spectral condition. The periods of depressed, then elevated, and finally a return to before burnt VI ranged from three to four years on average. Although a series of well-conditioned TM data transformed into an optical recovery indicator (VI) could monitor the trends in black needlerush marsh recovery, the non monotonic trend proved optical sensor data were incapable in providing a clear indication of time-since-burn of the full burn-recovery record based on a single or even multiple data collection dates. The time-since-burn prediction was possible, however, with optical image data when constrained to the first year since burn when based on multiple dates or a single date of TM image data. A closer examination of the spectral recovery was obtained in a comparison of site-specific canopy reflectance collected of burnt and non burnt black needlerush marshes over time. A similar trend shown in the temporal TM study was observed; however, the site-specific spectral differences were even less than expected from the TM-VI study. The VI transform of the well-conditioned TM image data seemed to accentuate the burnt and non burnt canopy green biomass differences. In either case, even though recovery trends were obtainable when VI indicators were available at least twice yearly, and time-since-burn was obtainable when restricted to the first year of recovery, an indicator based on a single remote sensing image date was preferred that could predict the time-since-burn over the entire three to four year range of recovery.

ERS-1 SAR image data collected within the same time period as the optical images showed good correspondence with the time-since-burn extending nearly 900 days since burn. The ERS-1 SAR C band VV polarization sensor decreased throughout the marsh canopy recovery time-range. The decrease in VV returns was expected from site-specific measurements that documented the change in marsh density and orientation through the recovery period. As the black needlerush canopy reemerged, the mostly vertical marsh transformed with time into a more dense marsh containing a mixture of vertical and horizontal component orientations. The increasingly thicker and mixed orientation upper marsh canopy tended to obstruct the radar penetration to the lower more vertical marsh canopy resulting in a decreasing VV return. From our ERS-1 SAR results and site-specific canopy structure measurements, we further expected that HH polarization returns would increase as the

horizontal components increased and that VH polarization returns would increase as the canopy density increased. To test this idea, we collected a full polarization SAR image of the coastal Florida black needlerush marsh.

The multiple polarization SAR returns were as expected. The VV returns decreased and the HH and VH returns increased with time-since-burn. These results, however, depended on normalization of the burnt marsh returns either by a suitable non burnt marsh control near to or within the same marsh zone as the burnt marsh site or by another polarization return (e.g., VV/VH). In either case, once normalized the polarimetric returns provided a good predictor of time-since-burn. In addition, the relative variation in polarimetric returns provided canopy structural information independent of weather or illumination conditions. The single date polarimetric SAR, and to a lesser extent, the single date single polarimetric SAR provided an adequate predictor of time-since-burn in a black needlerush marsh. Including only canopy changes due to burn recovery (excluding flooding, herbivory, etc.), these results indicate that radar would provide an appropriate source of consistent image data for monitoring burn recovery, and as likely, the overall status of a black needlerush or similar herbaceous canopy over an extended time period.

### ***18.4.2 Seasonal Marsh***

Burn recovery monitoring of a seasonally changing maidencane marsh in coastal Louisiana was also studied with satellite optical and site-specific canopy reflectance and structure measurements. In contrast to the black needlerush marsh of coastal Florida, the maidencane marsh biomass completely recycled from year-to-year producing a very different temporal marsh response to burning than the mostly or entirely non seasonally connected black needlerush marsh. Our results in the maidencane marsh, however, were similar to those in the black needlerush marsh. We focused primarily on documenting what remote sensing methods could provide adequate indicators of burn recovery and which of these tools were sensitive to long-term changes (over a year). Radar image collections were not part of the coastal Louisiana study; thus, the documentation was limited to passive optical methods. Multiple TM image dates as well as nearly concurrent site-specific canopy reflectance spectra and limited canopy structural measurements were available for the maidencane marsh burn recovery study.

Site-specific canopy reflectance spectra obtained at non burnt, winter burnt, and spring burnt marsh sites indicated that changes in spectra form and magnitude could be used to differentiate burnt and non burnt maidencane marsh in the spring. Visual interpretation further implied that some information could be extracted from the reflectance spectra that defined the burn age, at least in general for that season. By summer, however, non burnt and burnt marshes in different stages of recovery were not separable by using canopy reflectance as in the set of spring spectra. The set of light penetration curves (canopy structure) typifying two maidencane marsh sites – one that was burnt and recovered and the other unburned throughout the same time

periods – indicated the same trend. Maidencane marsh recovery to non burnt marsh condition was nearly complete by midsummer, judging by the similar form of the canopy reflectance spectra and light penetration curves. Finally, TM images obtained close to the same dates as the site-specific canopy reflectance spectra were analyzed as a simple means of monitoring burn extent and recovery. The winter image contained no burnt marsh, but the spring and summer images contained various stages of marsh burn and recovery.

Along with the winter image to define areas of maidencane marsh versus all other landcovers in the study area, a simple clustering algorithm and a masking technique were used to restrict and improve the classification of the spring and summer images into burnt and non burnt marsh. With the marsh isolation technique, winter-early-spring burns were identifiable on the spring image, while spring burns (post-spring image) and some winter-early-spring burns were detectable on the summer image; however, they were not spectrally separable from each other. For example, winter-early spring burns were not commonly identifiable in summer by using this method; in the summer map, these were classified as non burnt maidencane marsh. Because of the spectral inseparability of the winter-early-spring burns from the post-spring burns, we devised a multiple TM-classification approach in order to account for the various burn histories throughout the maidencane marsh.

Our approach entailed spatially overlaying the winter, spring and summer classification and identifying the burn history of each image pixel area (about 25 m by 25 m). A burn-history map was produced that depicted changes in the maidencane marsh due to burns the covering winter-spring-summer time period. The map portrays a complex marsh landscape that resulted from the wildfires that occurred from November to July. The produced burn-history map encompassed non burnt marsh from November to July, burnt marsh that was identifiable in March but not in July, burnt marsh that was identifiable in July but not in March, and marsh that was burnt in March and burnt again by July. Of note is the spatial extent of wildfires and the very little non burnt marsh that remained in the study area in just nine months. As indicated by the site-specific measurements, the high frequency collection of images throughout the winter to summer regrowth period is most likely the only method to properly document the extensive and non managed (wildfire) burns within these fresh marshes of coastal Louisiana. However, the ability to consistently collect high temporal frequency optical data is questionable in these sub tropical regions. As shown in the black needlerush marsh burn study, radar can provide similar monitoring results even with a single image date. With this in mind, we are currently pursuing the application of radar in these marshes and other marshes occurring within the brackish and saline environments as well as detecting burn locations and extents solely with image data.

As we have discussed, each year extensive marshes are burnt by fires that range widely in spatial extent and intensity and that can occur interspersed and in juxtaposition resulting in a complexity of marsh burn histories. Our work has shown that it is possible to monitor marsh recovery and predict burn history (time-since-burn) with optical as well as radar image data when burn locations have been identified. We expect the ability to monitor these burns and estimate the time-since-burn and the

extent of burn recovery will aid resource managers by providing (1) improved tools for the spatial assessment of marsh and grassland fire danger and fuel distribution, and (2) improved data relating to ecological impact of these fires as, for example, the function of these marshes as habitat and natural barriers to storm impacts, flooding, and contaminants.

**Acknowledgement** The authors are indebted to the U.S. Coast Guard at the Naval Air Station, Belle Chase, LA, for providing flight time and personnel for helicopter flights within Louisiana. Special thanks are extended to LCDR Randy Perrin, LT Jonathan Flanner, and LT John Fagan. We thank the Fina Laterre, Inc., and the Louisiana Land and Exploration Company for allowing access to study sites in Louisiana. We thank Allison Smith, Kevin McRae, Steve Laine, and Troy Stoute for field support, and Diane Baker, Miles Roberts, Bob Capezza, and Rick Lester for volunteering indispensable help in data collection. Finally, the authors are thankful to Victoria Jenkins (IAP World Services Inc.) for editing the chapter. Funding for studies that supported works described in this chapter was granted through the U.S. Geological Survey's National Wetlands Research Center, the Global Climate Change Program, and the Venture Capital Funds Program.

## References

- Allen W, Richardson A (1968) Interaction of light with a plant canopy. *J Opt Soc Am* 58: 1023–1028
- Angeler D, Sanchez B, Garcia G, Moreno J (2006) Community ecotoxicology: invertebrate from Fire Trol 934 contaminated vernal pool and salt marsh sediments under contrasting photoperiod and temperature regimes. *Aquat Toxicol* 78:167–175
- Belluco E, Camuffo M, Fererari S, Modenese L, Silvestri S, Marani A, Marani M (2006) Mapping salt-marsh vegetation by multispectral and hyperspectral remote sensing. *Remote Sens Environ* 105(1):54–67
- Beukema S, Reinhardt E, Greenough J, Kurz W, Crookston N, Robinson D (1999) Fire and fuels extension to the forest vegetation simulator: model description. Working draft. ESSA Technologies Ltd., Vancouver BC, 58pp
- Chabreck R (1970) Marsh zones and vegetative types in the Louisiana coastal marshes. Louisiana State University, Baton Rouge, dissertation, 112pp
- Colwell J (1974) Vegetation canopy reflectance. *Remote Sens Environ* 3:175–183
- Deering D, Eck T (1987) Atmospheric optical depth effects on angular anisotropy of plant canopy reflectance. *Int J Remote Sens* 8(6):893–916
- Elachi C (1987) Introduction to the physics and techniques of remote sensing. John Wiley & Sons, New York
- Gabrey S, Afton A (2001) Plant community composition and biomass in Gulf Coast Chenier Plain marshes: responses to winter burning and structural marsh management. *Environ Manag* 27(2):381–293
- Gabrey S, Afton A, Wilson B (2001) Effects of structural marsh management and winter burning on plant and bird communities during summer in the Gulf Coast Chenier Plain. *Wildl Soc Bull* 29(1):218–231
- Gross M, Hardisky M, Klemas V (1988) Effects of solar angle on reflectance from wetland vegetation. *Remote Sens Environ* 26:195–212
- Hardisky M, Gross M, Klemas V (1986) Remote sensing of coastal wetlands. *BioScience* 36: 453–460
- Hobbs A, Shennan I (1986) Remote sensing of salt marsh reclamation in the Wash, England. *J Coastal Res* 2(2):181–198

- Hoffpauer C (1968) Burning for coastal marsh management. Proceedings of the Marsh and Estuary Management Symposium held in Baton Rouge, LA, pp 134–139
- Hopkinson C, Gosselink J, Parrondo R (1978) Aboveground production of seven marsh plant species in coastal Louisiana. *Ecology* 59:760–769
- Huete A, Jackson R (1988) Soil and atmosphere influences on the spectra of partial canopies. *Remote Sens Environ* 25:89–105
- Huete A, Jackson R, Post D (1985) Spectral response of a plant canopy with different soil backgrounds. *Remote Sens Environ* 17:37–53
- Jensen J, Ramsey E III, Mackey H, Christensen E, Sharitz R (1987) Inland wetland change detection using aircraft MSS data. *Photogram Eng Remote Sens* 53(5):521–529
- Johnson S, Knapp A (1993) The effect of fire on gas exchange and aboveground biomass production in annually versus biennially burned *Spartina pectinate* wetlands. *Wetlands* 13:299–303
- Kimes D (1983) Dynamics of directional reflectance factor distributions for vegetation canopies. *Appl Optics* 22:1364–1372
- Lorenzen B, Jensen A (1988) Reflectance of blue, green, red and near infrared radiation from wetland vegetation used in a model discriminating live and dead above ground biomass. *New Phytol* 108:345–355
- Lulla K, Mausel P (1983) Ecological applications of remotely sensed multispectral data. In: Richasen BF Jr (ed) Introduction to remote sensing of environment. Kendall/Hall Publishing, Dubuque, IA, pp 354–377
- McCloy K, Schoneveld R, Kemp D (1993) Measurement of pasture parameters from reflectance data. *Int J Remote Sens* 14:1107–1118
- Myneni R, Maggion S, Jaquinta J, Privette J, Gobron N, Pinty B, Kimes D, Verstraete M, Williams D (1995) Optical remote sensing of vegetation: modeling, caveats, and algorithms. *Remote Sens Environ* 51:169–188
- PCI Geomatics (1998) Using PCI software, version 6.3 EASI/PACE. PCI Geomatics, Richmond Hill, Ontario, Canada
- Penuelas J, Filella I (1998) Visible and near-infrared reflectance techniques for diagnosing plant physiological status. *Trends Plant Sci* 3:151–156
- Peterson D, Aber J, Matson P, Card D, Swanberg N, Wessman C, Spanner M (1988) Remote sensing of forest canopy and leaf biochemical contents. *Remote Sens Environ* 24:85–108
- Ramsey E III (1995) Monitoring flooding in coastal wetlands by using radar imagery and ground-based measurements. *Int J Remote Sens* 16:2495–2502
- Ramsey E III (1998) Radar remote sensing of wetlands. In: Lunetta R, Elvidge C (eds) Remote sensing change detection: environmental monitoring methods and applications. Ann Arbor Press Inc, MI, pp 211–243
- Ramsey E III (2005) Remote sensing of coastal environments. In: Schwartz ML (ed) Encyclopedia of coastal science. Encyclopedia of earth sciences series. Kluwer Academic Publishers, The Netherlands, pp 797–803
- Ramsey E III, Laine S (1997) Comparison of Landsat Thematic Mapper and high resolution photography to identify change in complex coastal marshes. *J Coastal Res* 13(2):281–292
- Ramsey E III, Nelson G (2005) A whole image approach for transforming EO1 Hyperion hyperspectral data into highly accurate reflectance data with site-specific measurements. *Int J Remote Sens* 26(8):1589–1610
- Ramsey E III, Ragoonwala A (2004) Determining the optical properties of the narrow, cylindrical leaves of *Juncus roemerianus*. *IEEE Geosci Remote Sens* 42(5):1064–1075
- Ramsey E III, Ragoonwala A (2005) Leaf optical property changes associated with the occurrence of *Spartina alterniflora* dieback in coastal Louisiana related to remote sensing mapping. *Photogram Eng Remote Sens* 71(3):299–311
- Ramsey E III, Ragoonwala A (2006) Site-specific canopy reflectance related to marsh dieback onset and progression in coastal Louisiana. *Photogram Eng Remote Sens* 72(6):641–652
- Ramsey E III, Spell R, Day R (1992a) Monitoring recovery of coastal wetlands from acute stress by using high spectral resolution remote sensing data. First thematic conference on remote sensing for marine and coastal environments: summaries. Environmental Research Institute of Michigan, Ann Arbor

- Ramsey E III, Spell R, and Day R (1992b) Light attenuation and canopy reflectance as discriminators of gulf coast wetland types, vol. II. In: Proceedings of the international symposium on spectral sensing research, 15–20 November 1992, Maui, HI, pp 1176–1189
- Ramsey E III, Spell R, Johnston J (1992c) Preliminary analysis of spectral data collected for the purpose of wetland discrimination, vol. 1. In: ASPRS (American Society for Photogrammetry and Remote Sensing) technical papers, 1992 ASPRS-ACSM (American Congress on Surveying and Mapping) annual convention, Albuquerque, NM, pp 386–394
- Ramsey E III, Spell R, Day R (1993) Measuring and monitoring wetland response to acute stress by using remote sensing techniques, vol. 2. In: Proceedings of the 25th international symposium on remote sensing and global environmental change: tools for sustainable development, 4–8 April 1993, Graz, Austria. Environmental Research Institute of Michigan, Ann Arbor, pp 43–54
- Ramsey E III, Spell R, Day R (1994a) GIS and remote sensing as wetland resource management tools: the fire monitoring example. In: Ehlers M, Steiner D, Johnston J (eds) Proceedings of an international workshop on requirements for integrated geographic information systems, 2–3 February 1994, New Orleans, LA. Environmental Research Institute of Michigan, Ann Arbor, pp 133–145
- Ramsey E III, Laine S, Werle D, Tittley B, Lapp D (1994b) Monitoring Hurricane Andrew damage and recovery of the coastal Louisiana marsh using satellite remote sensing data. In: Wells P, Ricketts P (eds) Proceedings of the Coastal Zone Canada '94, pp 1841–1852
- Ramsey E III, Nelson G, Sapkota S (1998a) Classifying coastal resources by integrating optical and radar imagery and color infrared photography. *Mangroves and Salt Marshes* 2(2) 109–119
- Ramsey E III, Nelson G, Laine S, Topham W, Kirkman R (1998b) Generation of coastal marsh topography with radar and ground-based measurements. *J Coastal Res* 14(3):1158–1164
- Ramsey E III, Nelson G, Sapkota S, Laine S, Verdi J, Krasznay S (1999) Using multiple polarization L band radar to monitor marsh burn recovery. *IEEE Trans Geosci Remote Sens* 37(1): 635–639
- Ramsey E III, Nelson G, Sapkota S (2001) Coastal Change Analysis Program implemented in Louisiana. *J Coastal Res* 17(1):55–71
- Ramsey E III, Sapkota S, Baarnes F, Nelson G (2002) Monitoring the recovery of *Juncus roemerianus* marsh burns with the normalized vegetation index and Landsat Thematic Mapper data. *Wetlands Ecol Manag* 10(1):85–96
- Ramsey E III, Nelson G, Baarnes F, Spell R (2004) Light attenuation profiling as an indicator of structural changes in coastal marshes. In: Lunetta R, Lyon J (eds) Remote sensing and GIS accuracy assessment. CRC Press, New York, pp 59–73
- Ramsey E III, Lu Z, Rangoonwala A, Rykhuis R (2006) Multiple baseline radar interferometry applied to coastal landscape classification and change analyses. *GIS Sci Remote Sens* 43(4): 283–309
- Ranson K, Daughtry C, Biehl L, Bauer M (1985) Sun-view angle effects on reflectance factors of corn canopies. *Remote Sens Environ* 18:147–161
- Smith S, Newman S, Garrett P, Leeds J (2001) Differential effects of surface and peat fire on soil constituents in a degraded wetland of the northern Florida Everglades. *J Environ Qual* 30: 1998–2005
- Spanglet H, Ustin S, Rejmankova E (1998) Spectral reflectance characteristics of California sub-alpine marsh plant communities. *Wetlands* 18:307–319
- Spell R, Ramsey E III (1991) Monitoring marsh burns using remote sensing technology. In: Proceedings of the second national U.S. Fish and Wildlife Service geographic information systems workshop. National Ecology Research Center, Fort Collins, CO, pp 51–55
- Spell R, Ramsey E III (1993) Spectral reflectance and canopy structure characteristics of gulf coast wetland vegetation types. In: Technical papers of the 1993 CSM-ASPRS annual convention and exposition, 15–18 February 1993, New Orleans, LA, pp 353–363
- Stout J (1984) The ecology of irregularly flooded salt marshes of the northeastern Gulf of Mexico: a community profile. U.S. Fish and Wildlife Service Biological Report 85 (7.1), 98pp
- Taylor K, Grace J, Guntenspergen G, Foote A (1994) The interactive effects of herbivory and fire on an oligohaline marsh, Little Lake, Louisiana, USA. *Wetlands* 14:82–87

- Tucker C (1979) Red and photographic infrared linear combinations for monitoring vegetation. *Remote Sens Environ* 8:127–150
- Vanderbilt V, Grant L (1985) Plant canopy specular reflectance model. *IEEE Trans Geosci Remote Sens* GE-23:722–730
- Whigham D (1999) Ecological issues related to wetland preservation, restoration, creation and assessment. *Sci Total Environ* 240:31–40
- Williams R, Murdoch M (1972) Compartmental analysis of the production of *Juncus roemerianus* in a North Carolina salt marsh. *Chesapeake Sci* 13:69–79
- Wilson E (1968) Fur production on southeastern coastal marshes. Proceedings of the marsh and estuary management symposium held Baton Rouge, LA, pp 149–162



## Chapter 19

# Response of Reed Mudflats in the Caspian Coastal Zone to Sea Level Fluctuations

Valentina I. Kravtsova

We investigate the response of the low-lying northwestern Caspian coasts and the main Caspian deltas to sea level fluctuations by using multi-temporal optical and radar images. We compile a time series of maps illustrating the coastal ecosystems dynamics during 1977–2001 for the Kalmykian coastal zone and the Ural River delta. These maps suggest an important role of the reed mudflats in relation to the coastal zone dynamics. When the Caspian Sea level rose, the shoreline began to change not from the front reed-belt bound but from the rear bound; when the sea level declined, the rear bound moved seaward faster than the front bound. This trend revealed from the optical image interpretation can also be observable in the color composite of the multi-date radar images by using an interpretation key. In order to answer the question “at what depth the reed can survive when the sea level rise”, we constructed a series of profiles along the Ural River delta; the profiles show at what depths the reed belt grew or withered. We found that the ecological niche for reed growth was around the 2 m water depth. Overall, this study demonstrates the usefulness of satellite imagery for the study of coastal zone dynamics in the context of global changes.

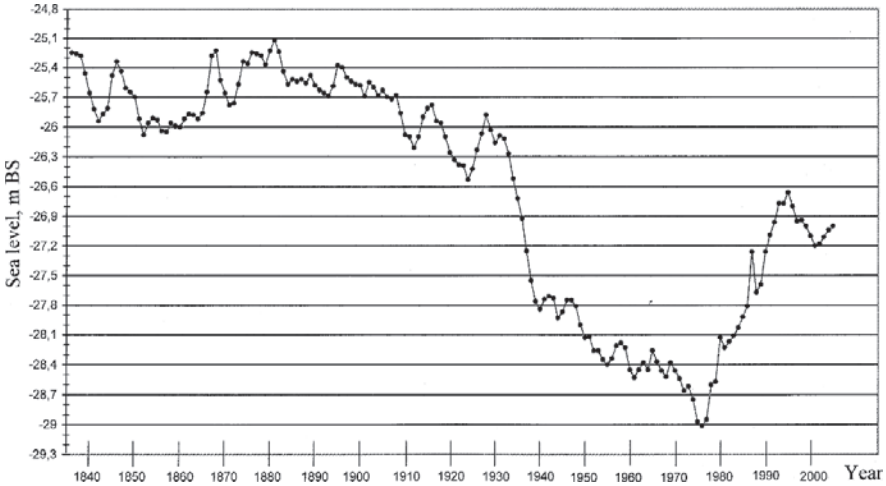
### 19.1 Introduction

The Caspian Sea level had risen rapidly during 1977–1995, from  $-29.01$  m ASL in 1977 to  $-26.66$  m ASL in 1995, with approximately 130 mm per year (Mikhailov 1997). Afterwards, the sea level fluctuated around  $-27$  m ASL, declined to  $-27.20$  m ASL in 2002, and then rose to  $-27.0$  m ASL in 2005 (Kravtsova and Baldina 2006) (Fig. 19.1). Due to global warming, the World ocean coasts could experience rapid sea-level rise in the 21st century. Therefore, the Caspian Sea is considered as an ideal site for the study of coastal zone and river mouths response to sea-level change.

---

V.I. Kravtsova (✉)

Faculty of Geography, Moscow State University, Moscow 119991, Russia  
e-mail: vik@lakm.geogr.msu.su



**Fig. 19.1** Changes of the Caspian Sea level in 1837–2005 (mean annual sea levels)

The Laboratory of Aerospace Methods, the Department of Cartography and Geoinformatics, and the Department of Hydrology, Moscow State University established a research initiative aiming to investigate the response of low-lying northwestern Caspian coasts and the main Caspian deltas to sea-level change. The major research activities included multi-date satellite image interpretation and map compilation to illustrate the coastal and deltaic ecosystems dynamics.

This research effort uncovered a very important role of the reed mudflats in relation to the coastal zone dynamics. Interaction between vegetation and tidal inundation was studied by Beeftink (1987) and De Leeuw et al. (1994). The reed mudflats along the low-lying Caspian coasts are found to be somewhat similar to the salt marshes along the North American coasts. However, there is a significant difference. In the Caspian coastal zone, reed mudflat formation is mainly due to the wind-induced surges rather than the tidal-level fluctuations since the later are very weak. The role of reed mudflat ecosystems has been widely examined. For example, Halls and Kraatz (2006) noted that reed mudflat ecosystems can serve as ‘buffers’ to protect the highland by softening tidal surges during storms. Goodbred and Hine (1995) studied the response of salt marshes to a severe tropical storm. In 2005, when Hurricane Katrina hit the Gulf of Mexico, the salt marshes in the Mississippi delta protected the city of New Orleans from flooding; waters from Lake Pontchartrain flooded the City from the north, where reed thickets did not exist. In addition, reed mudflats are also economically and environmentally important because they provide fish nursery habitats, bird nesting and foraging sites, and act as a filter for chemicals entering the ecosystem (Halls and Kraatz 2006).

This chapter presents our reed mudflats research for two test sites at the Caspian Sea coasts: the Kalmykian coastal zone and the Ural River delta (Fig. 19.2).



**Fig. 19.2** Location of the study sites: 1– Kalmykian coastal zone; 2 – the Ural River delta

## 19.2 Materials and Methods

Compiling maps to illustrate the status and dynamics of the coastal and deltaic ecosystems requires the use of images with a sufficient spatial resolution. Image types we used varied over time. For example, we used photos taken from orbital stations for the sea-level decline period in 1970s (see Fig. 19.1), photos from Resurs-F and images from Resurs-O for the sea-level rise period in late 1970s–mid 1990s, and optical and radar images from Landsat-7 and Meteor-3M for the stable sea-level period and afterwards since late 1990s (Table 19.1).

We used satellite images to compile a time series of maps for the low-lying Kalmykian coast and the Ural River delta. By using visual interpretation and computer processing of multi-date satellite images, we compiled several maps to illustrate the coastal and deltaic ecosystems statuses in 1977–1978, 1991–1992, 1997–1998, and 2000–2001, the transgressive changes in the coastal zone for the periods of 1978–1991 and 1991–1997, and the post-transgressive changes for 1997–2001. The map scale is at 1:200 000, with approximately 90 percent accuracy.

The coastal ecosystem types shown in the coastal zone status maps for various years are listed in Table 19.2, and the change types illustrated in the coastal zone dynamics maps are summarized in Table 19.3.

We also used radar images to study the coastal zone changes with a multi-date color composite and a tailored interpretation key to define the changes. The results of the coastal and delta change mapping are presented in the next three sections.

**Table 19.1** List of satellite images used for mapping coastal ecosystems dynamics

		Date	Satellite	Surveying system	Image resolution (m)
The Kalmykian coastal zone	<i>Optical</i>	July 1978	Salut-6	MKF-6	20
		23 May 1983	Resurs-F	KFA-1000	10
		19 June 1991	Resurs-F	MK-4	10
		28 August 1997	Resurs-O	MSU-E	35
		25 August 2001	Landsat-7	ETM+	30,15
	<i>Radar</i>	26 June 1995	ERS-1	SAR	30
		16 June 1999	ERS-2	SAR	30
		9 June 2004	Envisat	ASAR	30
The Ural River delta	<i>optical</i>	June 1975	Salut-4	KATE-140	60
		5 October 1992	Landsat-5	TM	30
		April 1996	Mir	Photo	20
		5 August 2000	Resurs-O	MSU-E	35
		30 August 2003	Meteor-3M	MSU-E	35

**Table 19.2** List of geographic features shown in the maps of Kalmykian coastal zone status in various years (1978, 1991, 1997). Note the numbers here do not correspond to the numbers in Figs. 19.3, 19.4, and 19.6

No	Features
1	Shoreline (defined with the outer limit of reed mudflats)
2	Offshore depositional features
3	Beach ridges
4	Sand flat
5	Reed mudflat
6	Mudflat saturated with water
7	Lagoons behind reed mudflats
8	Lagoon relicts behind the reed mudflats
9	Narrow strips of water along beach ridges within the reed mudflat
10	Waterlogged area behind mudflat and along the lagoons and canals
11	Meadow-solonchak depressions, solonchak meadows in the troughs between Baer's mounds
12	Semi-desert plain
13	Inner water bodies (lakes, man-made reservoirs)
14	Canals
15	Urban area
16	Sea
17	Sea zone with exposed aquatic vegetation
18	Sea zone with submerged reeds

**Table 19.3** Features shown at maps of Kalmykian coastal zone dynamics for various periods (1978–1991 and 1991–1997), Note the numbers here do not correspond to the numbers in Figs. 19.5 and 19.7

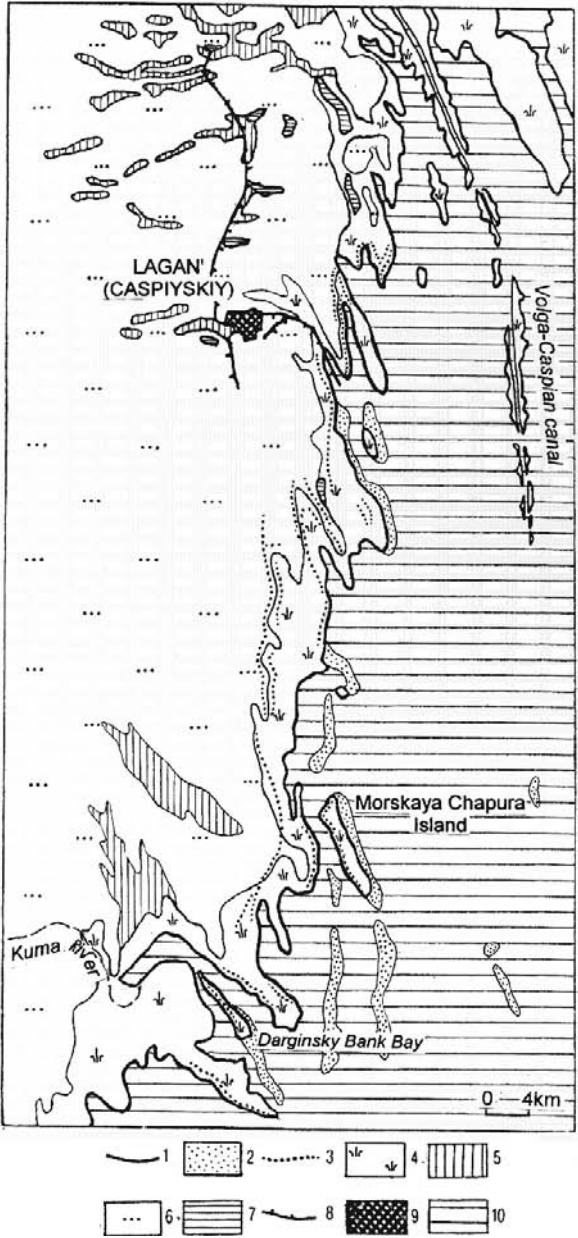
No	Type of changes
1	Shoreline (defined with the outer limit of the reed-covered mudflats): a – in 1978, b – in 1991, c – in 1997
2	Offshore depositional features eroded
3	Submerged reed mudflat (zone of the coast retreat)
4	Sand flat formed (zone of the coast accretion)
5	Beach ridges
6	Reed mudflat retained
7	Reed mudflat newly appeared (zone of the landward shift of the reed mudflat) in place of: a – lagoon behind the reed mudflat, b – waterlogged area along the lagoon, c – semi-desert plain
8	Lagoons formed behind the reed mudflat
9	Retained segments of the lagoon behind of the reed mudflat
10	Narrow strips of water formed along beach ridges within the reed mudflat
11	Waterlogged area along lagoons and the reed mudflat: a – retained, b – newly appeared in place of semi-desert plain
12	Solonchak meadows in the troughs between Baer’s mounds and in erosion basins: a - retained, b - newly formed
13	Semi-desert plain
14	Inner water bodies (lakes, man-made reservoirs): a – retained, b – newly formed
15	Canals
16	Urban area
17	Sea
18	Boundaries of objects which: a – retained and newly formed, b – disappeared

## 19.3 Coastal Dynamics and Sea Level Fluctuations: The Kalmykian Coast

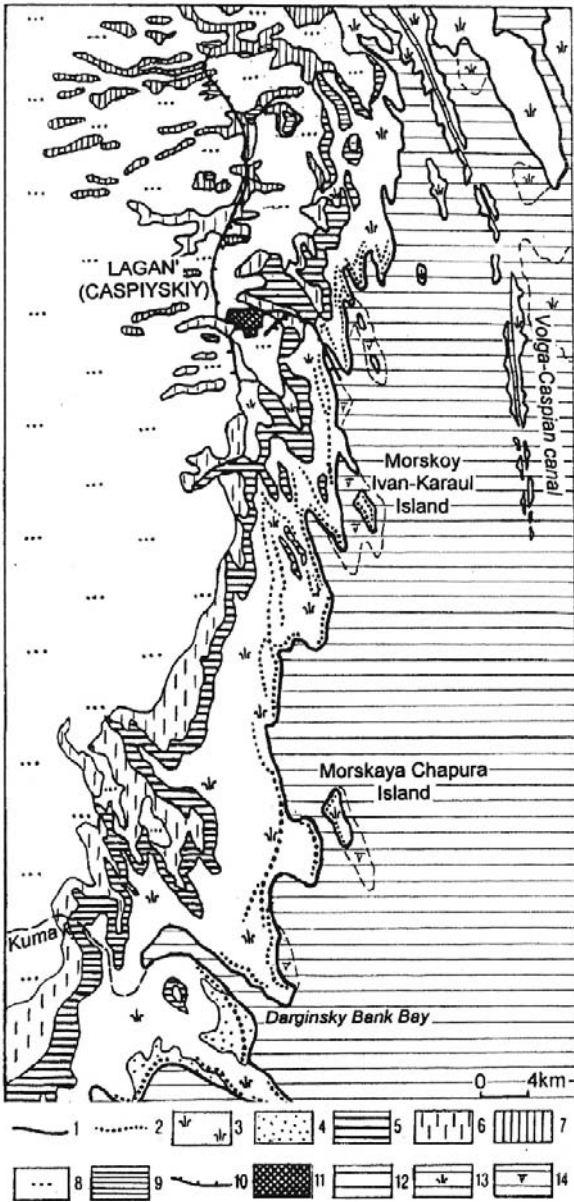
### 19.3.1 Optical Image Analysis

The Kalmykian coast extends 120 km from north to south, along the northwestern Caspian Sea. It is a low-lying coast affected by wind-induced surges. An extensive mudflat belt covered with dense reeds has been formed there. The mudflats are adjacent to dry land, which comprises plains at the top of the Caspian Sea terraces covering with dry steppe in the north and semi-desert vegetation in the south. In the north, a specific relief of the Baer’s mounds exists near the Volga River delta. It is a repetitive succession of dry steppe hills and wet swamp hollows, which extends toward the west-east direction. Our satellite image interpretation indicates that the sea-level transgressive changes along this coast increased with distance from the Volga River delta, suggesting that the delta serving as ‘buffer’ due to its steep coasts (Kravtsova and Lukyanova 1999).

During 1978–1991, the sea-level rose by 1.75 m, but the northern shoreline changed very little (see Figs. 19.3, 19.4, and 19.5). This weak response can be

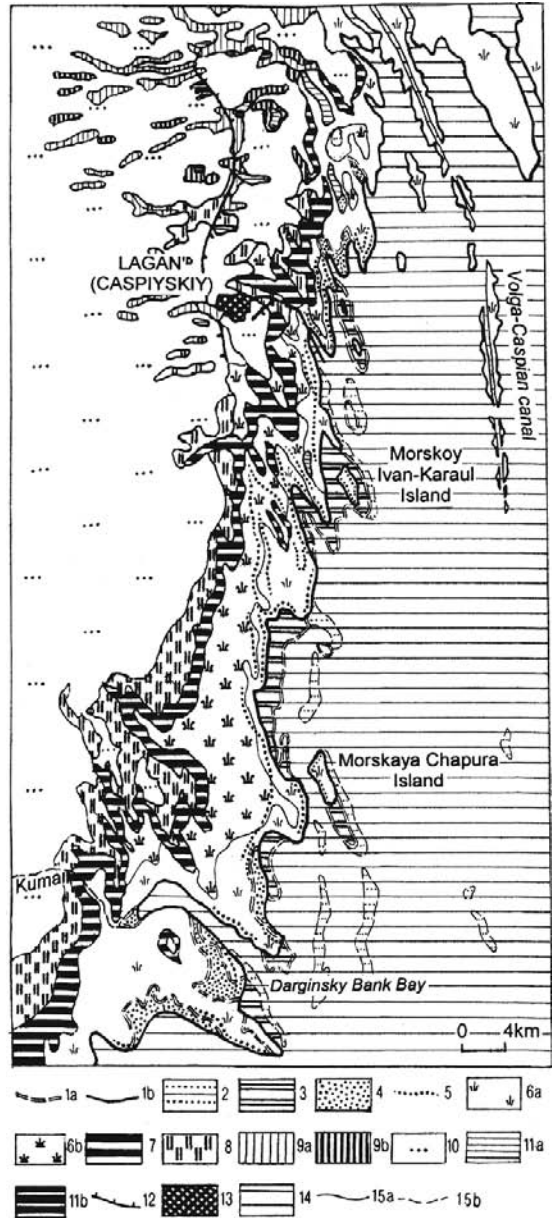


**Fig. 19.3** Status of the Kalmykian coastal zone in 1978: 1 – shoreline; 2 –offshore depositional features; 3 – beach ridges; 4 – reed mudflat; 5 – meadow-solonchak depressions; 6 – semi-desert plain; 7 – inner water bodies; 8 – canals; 9 – urban area; 10 – sea



**Fig. 19.4** Status of the Kalmykian coastal zone in 1991: 1 – shoreline; 2 – beach ridges; 3 – reed mud flat; 4 – sand flat; 5 – lagoons behind reed mudflats; 6 – waterlogged area along the lagoons and canals; 7 – meadow-solonchak depressions; 8 – semi-desert plain; 9 – inner water bodies; 10 – canals; 11 – urban area; 12 – sea; 13 – sea zone with aquatic vegetation; 14 – sea zone with submerged reeds

**Fig. 19.5** Dynamics of the Kalmykian coastal zone in 1978–1991: 1 – shoreline: 1a – in 1978, 1b – in 1991; 2 – offshore depositional features eroded; 3 – submerged reed mudflat (zone of the coast retreat); 4 – sand flat (zone of the coast accretion); 5 – beach ridges; 6 – reed mudflat: 6a – retained, 6b – newly formed; 7 – lagoons behind the reed mudflat; 8 – waterlogged area along lagoons; 9 – solonchak meadows in the troughs between Baer’s mounds and in erosional basins: 9a – retained, 9b – newly formed; 10 – semi-desert plain; 11 – inner water bodies: 11a – retained, 11b – newly formed; 12 – canals; 13 – urban area; 14 – sea; 15 – boundaries of objects which: 15a – retained and newly formed, 15b – disappeared



attributed to the ‘buffer effect’ due to the existence of extensive shallow-water area in front of the Volga River delta. On the other hand, the sea-level rise significantly affected the southern coast, which is far away from the Volga River delta. From the satellite images, we can see that the mudflat’s front edge was submerged with sea waters and the shoreline retreated 1–3 km; by constructing a coastal zone profile,



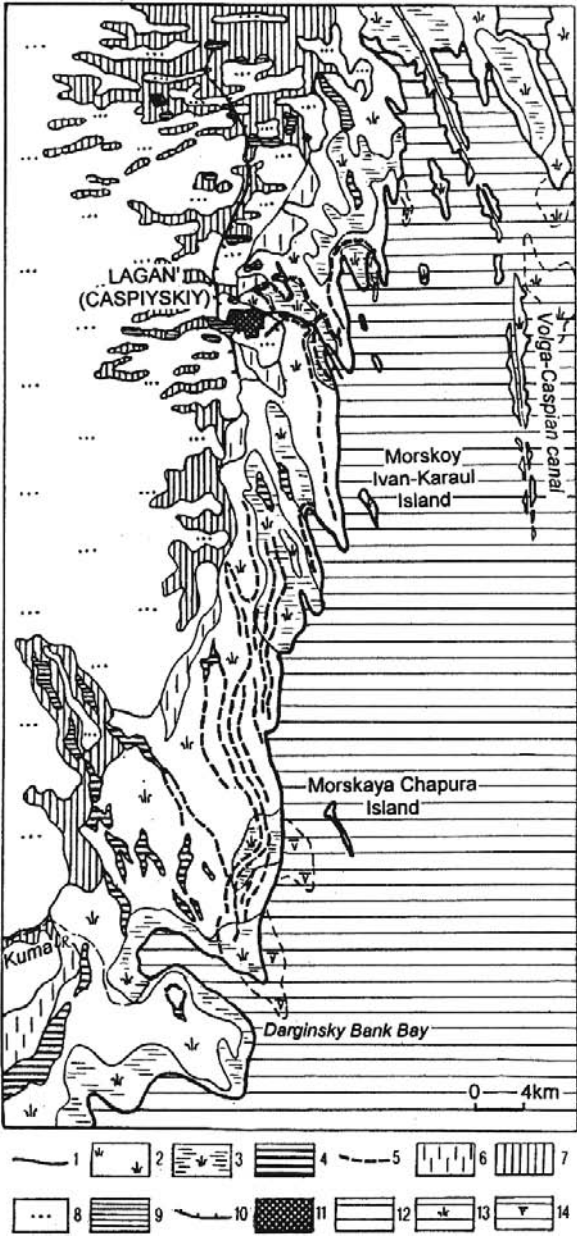
we see that new beach ridges formed along the water line due to the wave activities. The development of beach ridges and lagoons behind the ridges was quite common along the Caspian coastal zone under the sea-level rise condition (Ignatov et al. 1993, Kravtsova and Lukyanova 2000). Mudflat widened landward from 1–2 to 6–10 km. With the beginning of sea-level rise, a large lagoon was formed behind the mudflats due to the wave activities and the groundwater level rise. During the 1990s this lagoon belt was clearly seen with 1–2 km in width along the northwestern Caspian coast. The coastal plain behind the mudflats was influenced by groundwater; a waterlogged zone can be observed with several kilometres in width at the back of the lagoon.

During 1991–1997, the sea-level continued to rise till 1995 when it remained at  $-26.6$  m ASL, and then it began to decline; the shoreline in the northern Kalmykian coast and near the Volga River delta changed very little, which was consistent to the preceding period (Figs. 19.6 and 19.7). However, the coastal plain became more humid, particularly along the troughs between Baer's mounds. In the southern Kalmykian coast, the shoreline retreated by 4–5 km in some places. As a result, the reed mudflat changed considerably with less dense vegetation cover and more open water areas, particularly along the narrow, prolonged troughs between beach ridges. The reed thickets became more fragmented, and the landward side of the mudflat changed significantly. The large lagoon began to disintegrate into separate segments and then disappeared from most of the coast. The mudflat continued to grow landward and reached beyond 2–4 km in width. However, the mudflat belt only shifted landward and did not change its width noticeably after 1991.

During 1997–2001, the sea-level fell to  $-27.2$  m ASL, representing 0.3 m of decline; the shoreline change was marginal. The shoreline near the Volga River delta virtually did not change, which was consistent to the previous periods (Fig. 19.8). But the shoreline in the northern part, which was more than 30 km from the Volga delta, changed at two opposite directions: retrogression and progression. During this period, the mudflat became less humid, largely due to the less progressive sea-level change. Interestingly, the lagoon behind the mudflat completely withered, with only some narrow water strips remained. Reed mudflats shrank and dry steppe vegetation expanded along the mudflat's landward bound; this trend was well observed from the satellite images.

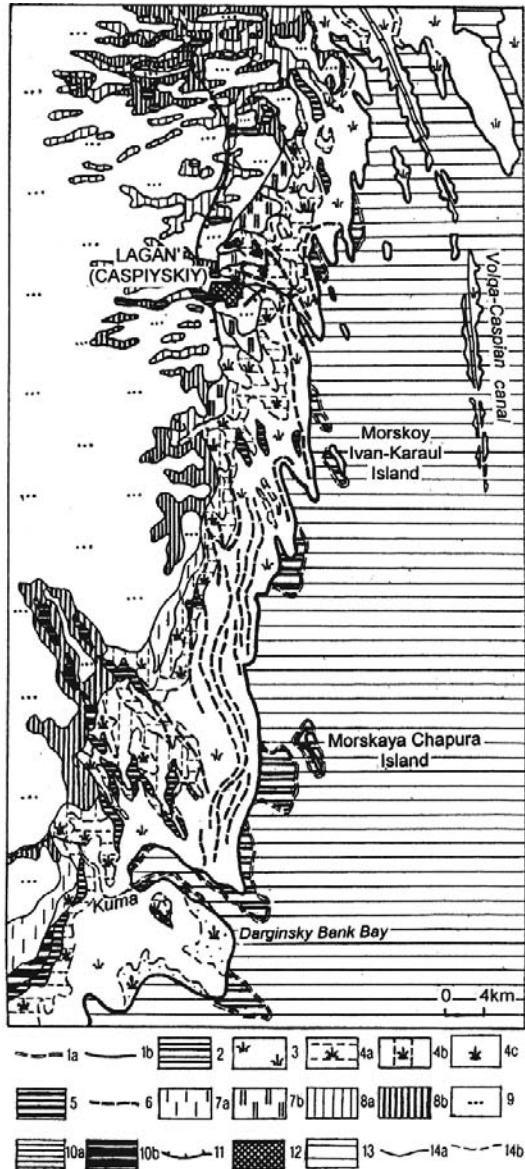
Based on the multi-date image mapping and the subsequent analysis of the coastal and delta dynamics, we can draw the following observations:

- Coasts with reed mudflat have two critical bounds: one between reed thickets and the open sea and the other between reed thickets and land. We found that the first bound tended to be less mobile, largely due to the 'buffer' effect from the reeds. The second was more sensitive to the sea-level changes; it tended to move landwards when the sea-level rose and seawards when the sea-level declined.
- The status of reed thickets had something to do with water depth and hence the magnitude of the sea-level rise. During 1978–1991, the sea-level rose by 1.75 m, the reed thickets were intact, with the increase in both area and width, indicating a good ecological condition. During 1991–1997, the sea-level rose 2.35 m by 1995, and then began to decline; the reed thickets became more fragmented.



**Fig. 19.6** Status of the Kalmykian coastal zone in 1997; 1 – shoreline; 2 – reed mudflat; 3 – mudflat saturated with water; 4 – lagoon relicts behind the reed mudflats; 5 – narrow strips of water along beach ridges within the reed mudflat; 6 – waterlogged area behind mudflat; 7 – solonchak meadows in the troughs between Baer’s mounds; 8 – semi-desert plain; 9 – inner water bodies; 10 – canals; 11 – urban area; 12 – sea; 13 – sea zone with aquatic vegetation; 14 – sea zone with submerged reeds

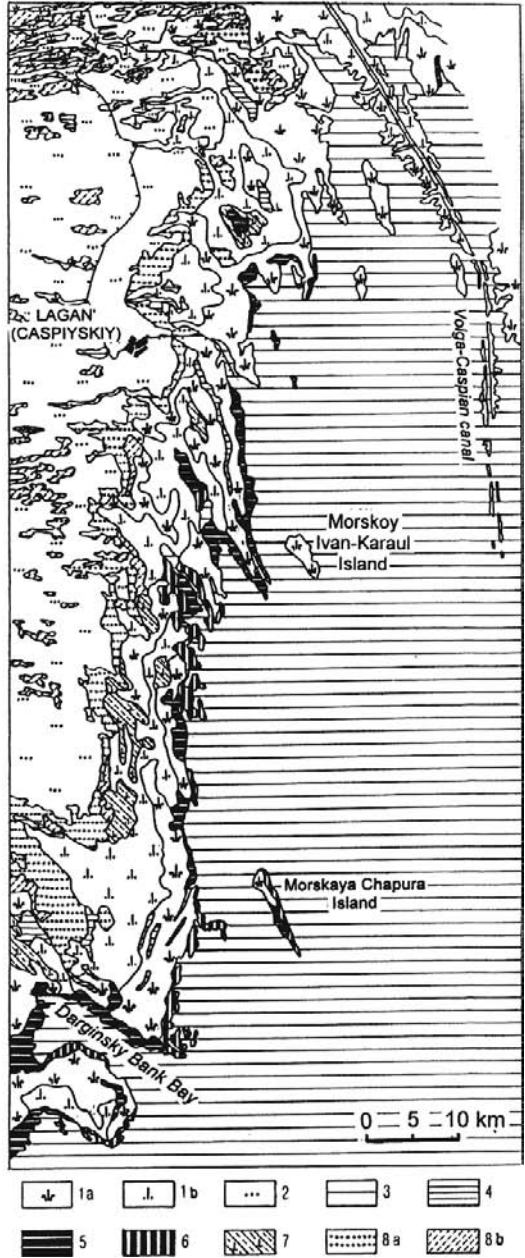
**Fig. 19.7** Dynamics of the Kalmykian coastal zone in 1991–1997: 1 – shoreline: 1a – in 1991, 1b – in 1997; 2 – submerged reed mudflat (zone of the coast retreat); 3 – reed mudflat retained; 4 – reed mudflat newly formed (zone of the landward shift of the reed mudflat) in place of: 4a – lagoon behind the reed mudflat, 4b – waterlogged area along the lagoon, 4c – semi-desert plain; 5 – retained segments of the lagoon behind of the reed mudflat; 6 – narrow strips of water appeared along beach ridges within the reed mudflat; 7 – waterlogged area along the reed mudflat: 7a – retained, 7b – newly formed at the semi-desert plain; 8 – solonchak meadows in the troughs between Baer’s mounds and in erosional basins: 8a – retained, 8b – newly formed; 9 – semi-desert plain; 10 – inner water bodies: 10a – retained, 10b – newly formed; 11 – canals; 12 – urban area; 13 – sea; 14 – boundaries of objects which: 14a – retained and newly formed, 14b – disappeared



### 19.3.2 Radar Images Analysis

We used SAR and ASAR images from ERS-1, 2 and Envisat satellites for 1995, 1999, 2004 to analyze the coastal zone change. All images were acquired in June so that the vegetation phenological condition should be approximately identical.

**Fig. 19.8** Dynamics of the Kalmykian coastal zone in 1997–2001: A. Ecosystems without significant changes: 1 – reed mudflat: 1a – with dense vegetation cover, 1b – with sparse vegetation cover; 2 – steppe and semi-desert vegetation of shore plains; 3 – sea; 4 – lakes B. Ecosystems with significant changes: 5 – submerged reed mudflats (zone of shoreline retreat); 6 – reed mudflats, new formed within sea zone (zone of coast accretion); 7 – reed mudflats with deteriorated vegetation; 8 – steppe and semi-desert vegetation, formed in place of: 8a – reed mudflat with deteriorated vegetation, 8b – reed mudflat and troughs with healthy vegetation



The images covered 1995 when the sea-level rise culminated and then began to decline. The main features in the Kalmykian coastal zone can be clearly defined in the SAR images: smooth water surfaces are in dark, almost black; the reed zone is in light gray and nearly white colors; and the inland dry steppe plains are in

gray. We created a color composite of the three-date radar images by using digital image processing, which were used as a complementary approach to the optical images interpretation discussed in Sect. 19.3.1. We specifically designed an interpretation key that allowed us to identify the nature of changes by using different colors (Kravtsova and Baldina 2006). The technical details for creating the color composite and designing the interpretation key are discussed in Sects. 19.3.2.1 and 19.3.2.2.

### 19.3.2.1 Color Compositing of the Multi-Date Images

Image color compositing was used to combine three images by displaying the first image in the red gun, the second in the green gun and the third in the blue gun. By combining three images of different dates we can obtain a color composite of the multi-date images, which can be further used to analyze the change of interest objects.

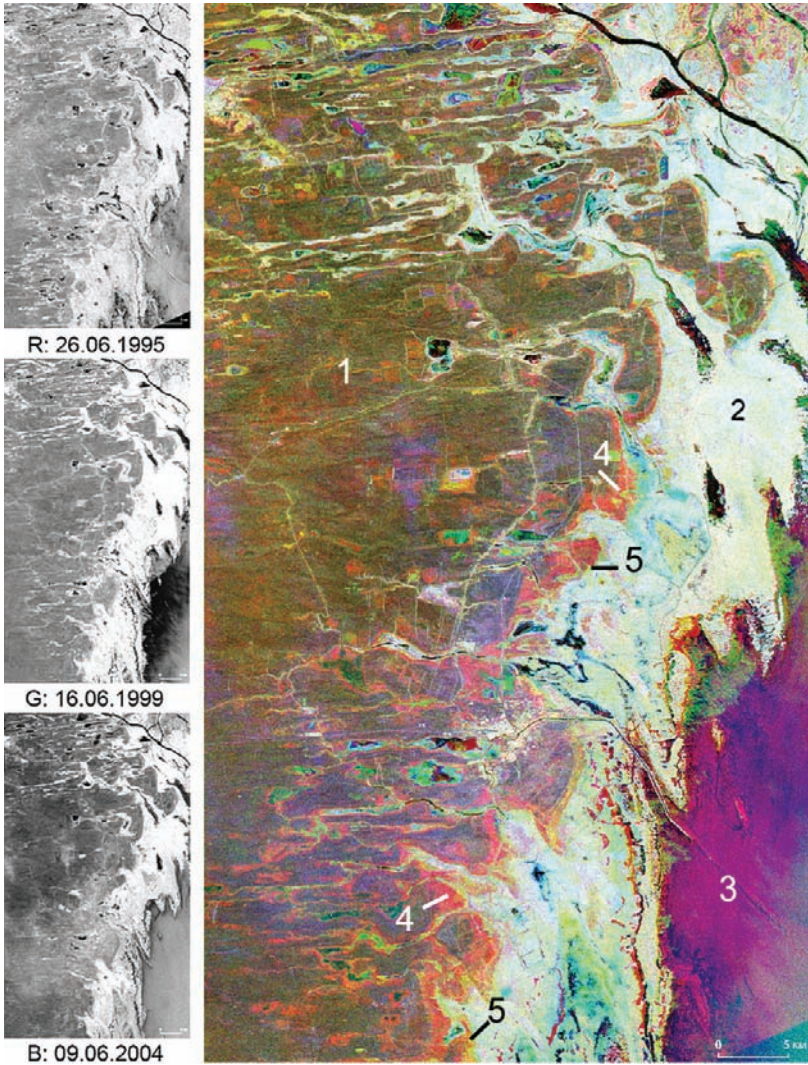
Success in applying this technique depends on how sharply the changing objects stand out against the image background. Thus, it is more desirable to use images with maximum contrast. For example, near infrared images are the most suitable for studying changes within the coastal zone since they have the highest contrast between water and bare land or vegetation. Obviously, images acquired at different times should be precisely co-registered prior to the color compositing. Moreover, the grey levels of each image should be balanced by their histograms prior to color compositing. Finally, color compositing allows using any order of multi-date images. But we prefer to apply Red – Green – Blue colors in order from an earlier survey date to a later one since this way can help interpret the resultant color composite.

Given the above considerations, we produced a color composite by synthesizing the three-date radar images, with the red band for 1995, green band for 1999, and blue band for 2004 (Fig. 19.9). To understand this color composite, we specifically constructed an interpretation key that will be explained in the next section.

### 19.3.2.2 Interpretation Key

Through visual analysis of the color composite image (see Fig. 19.9), we noticed that the features with little change are achromatic and the areas with much changes are in bright colors. Each color of changing areas corresponds to a specific combination of brightness from the multi-date images, and such combinations can be used to compile the interpretation key (Table 19.4).

Table 19.4 was constructed by analyzing the three radar images and through visible image interpretation (see Sect. 19.3.1). It shows specific combinations of brightness in the multi-date images that correspond to different colors. This is actually a way of color coding using the additive color theory. This key can help define the nature of changes within the coastal zone for each color from the multi-date color



**Fig. 19.9** Multi-temporal color composite image for the Kalmykian coastal zone of the Caspian Sea, composed of multi-date SAR (ASAR) images: 1 – dry steppe and semi-desert plain of Caspian terraces; 2 – reed mudflat; 3 – sea; 4 – zone of reed mudflat retreat in 1995–1999 (pink color); 4 – zone of reed mudflat retreat at 1999–2004 (yellow color)

composite. For example, red color results from a combination of the maximum brightness (i.e. reeds) in 1995, and the minimum brightness (i.e. water) in 1999 and 2004; orange from a combination of reeds in 1995, dry land in 1999 and water in 2004. The multi-date changes of brightness are shown in the last column with charts.

**Table 19.4** Colors in the color composite multi-temporal image resulting from different tones of the initial images

Color on Multi-Temporal Composite Image	Tone (Object) on Initial Images for Different Years, Being Color With Different Filters			Temporal Signature of Objects
	1995 Red	1999 Green	2004 Blue	
Red	Reed	Water	Water	
Orange	Reed	Land	Water	
Yellow	Reed	Reed	Water	
Yellow-green	Land	Reed	Water	
Green	Water	Reed	Water	
Green-blue	Water	Reed	Land	
Light-blue	Water	Land	Reed	
Blue	Water	Water	Reed	
Blue-violet	Land	Water	Reed	
Violet	Reed	Water	Reed	
Rose-violet	Reed	Water	Land	

Note that white color corresponds to reed, gray to dry land, and black tone to water. Letters at the vertical axes of the temporal mean signature graphs: w – white, g - gray, and b – black. Numbers at the horizontal axes are for years (1995, 1999, 2004).

**19.3.2.3 Results**

The coastal zone response to sea-level fluctuations can be examined by using the interpretation key. We found that the front reed belt had the minimum change during 1995–2004, while the rear reed mudflat generally retreated seawards. This pattern is understandable since even a small sea-level decline would cause groundwater level to fall down. As a result, wet swamps would turn to dry land, and reeds would not grow in such a dry condition.

Reeds are found to have disappeared in the depressions between Baer’s mounds. The areas previously occupied by reeds are in yellow and pink strips in the color composite image (Fig. 19.9). Areas in pink are the reed retreat during 1995–1999 when the sea-level declined by 0.34 m; the retreat strip adjacent to dry land was 1–2 km in width. Areas in yellow are the reed retreat during 1999–2004 when the sea-level first declined by 0.18 m in 2002 and then rose by 0.14 m in 2004; the retreat strip adjacent to the sea was quite narrow, ranging from 200–300 m to completely unobservable. Please note that such a pattern is not seen everywhere. It is caused by the sea-level changes in various directions. Reeds are also found to have disappeared around the troughs between Baer’s mounds, where reeds flourished before. The reed retreat areas are in pink and yellow in the color composite image. Moreover, some lakes are found to have disappeared, and are in blue and violet.

Our radar image analysis further confirms some observations obtained by using optical image interpretation discussed in Sect. 19.3.1. For example, the multi-date radar image analysis reveals the rear reed mudflat retreated when the sea-level declined; such an observation was also obtained by using the optical images. Intensity and rate of the reed mudflat retrogression are very sensitive to sea-level fluctuations. The method of multi-date image interpretation identified in this case study certainly has a more general meaning and can be applied to other similar coastal areas.

## **19.4 Coastal Dynamics and Sea Level Fluctuations: The Ural River Delta**

River deltas are among the most dynamic ecosystems on Earth. Their evolution depends on the interaction between river and sea. Natural and anthropogenic factors could accelerate process of delta progradation or erosion. The Caspian Sea level fluctuations are considered to strongly impact not only on the coastal zone but also on the river mouth. The deltas along the Caspian coasts have undergone large-scale changes, which were caused by the significant sea-level decline during 1930th–1970th, the rapid rise during 1977–1995, and the slow decline and somewhat stabilization in 1995–2004, as well as the sediment discharge reduction. The Caspian deltas dynamics was investigated by the author and her colleagues, including virtually all the large deltas except the Volga delta (Mikhailov et al. 2003, 2004). Among these deltas, the Ural River delta has a broad reed belt at its periphery, which is changing in response to sea-level fluctuations. This reed belt is very important given the subject of this study.

Like other Caspian deltas, the Ural River delta in the eastern part of the Northern Caspian coast changed its position and dimension over a long period of sea regression. The formation of the modern delta began from 18th century. The growth of this delta was caused by the sea-level decline and a large amount of the sediment discharges. The rapid delta progradation in the 1940s–1960s was caused by the construction of the Ural-Caspian Sea channel. In 1977, when the sea-level was the lowest, the Ural River delta was 32 km in length, with a total area of 522 km<sup>2</sup>; it even included the Peshnoy Peninsula, which used to be an island (Kravtsova and Mikhailov 2007). Mapping of the delta with satellite images taken in 1977, 1992, 1996, and 2000 shows significant changes (Kravtsova and Shumatiev 2005) (Fig. 19.10).

In 1977–1995 the sea-level rise caused to flood the delta's periphery, and fuelled the reed growth, forming a broad reed belt along the shoreline (Fig. 19.11-I). By 1992 this reed belt was 15–30 km in width. Some lagoons were also formed along the rear reed belt, with 3–5 km in width. As a result, the dry delta became more humid, and finally turned into wet marshes. If we use the sea-reed bound as the shoreline, then the latter's position did not change much during the early stage of 1977–1995 despite the rapid sea-level rise; the shoreline even moved seaward a little due to the reed expansion. After 1992, when the sea-level rise exceeded 1.92 m,



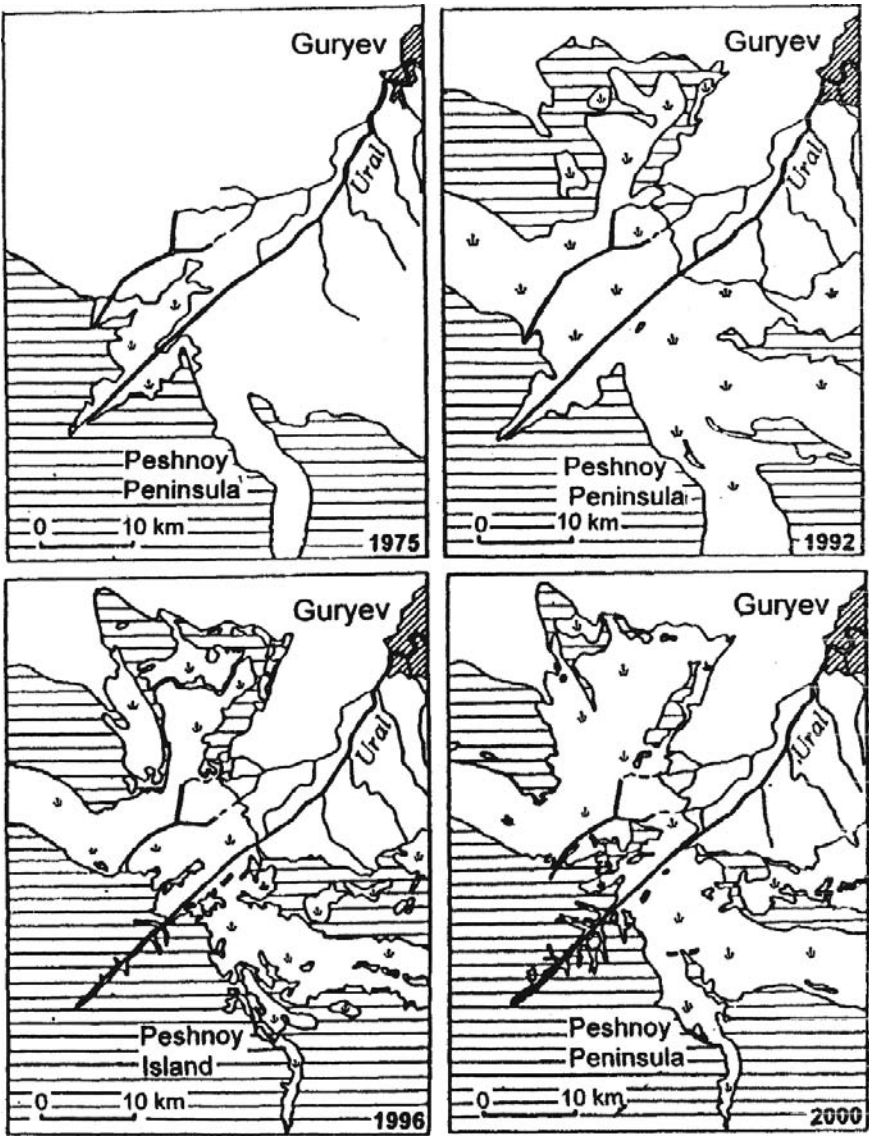
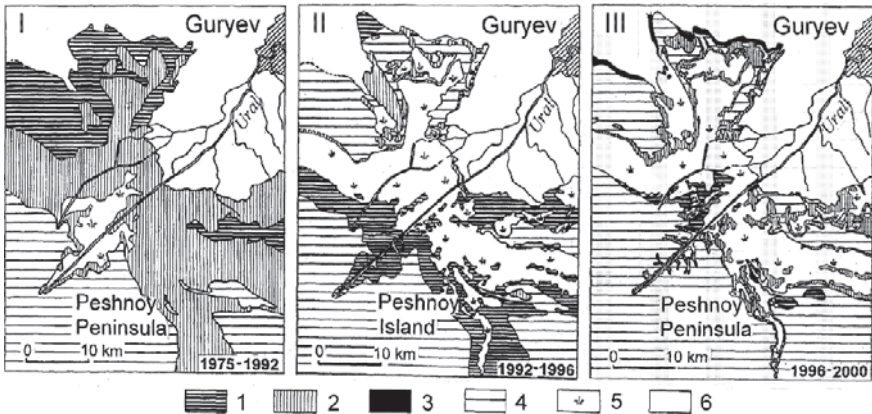


Fig. 19.10 The Ural River delta statuses in different years

the reed belt began to wither along the seaside so the shoreline began to move landward (Fig. 19.11-II). This change was caused by wave activities and ice breaking. In 1992–1996 the shoreline retreated 3–5 km, and some lagoons as wide as 7 km developed. Dry river channel was then filled with waters.

In 1996–2000, the sea-level began to decline gradually, and the reed belt regained. The reed belt’s front side moved seaward by 1 km (Fig. 19.11-III), while its



**Fig. 19.11** Changes of the Ural River delta in 1977–1992 (I), 1992–1996 (II), 1996–2000 (III): 1 – water instead of land and reed; 2 – reed instead of land and water; 3 – land instead of water and reed; 4 – water; 5 – reed; 6 – land

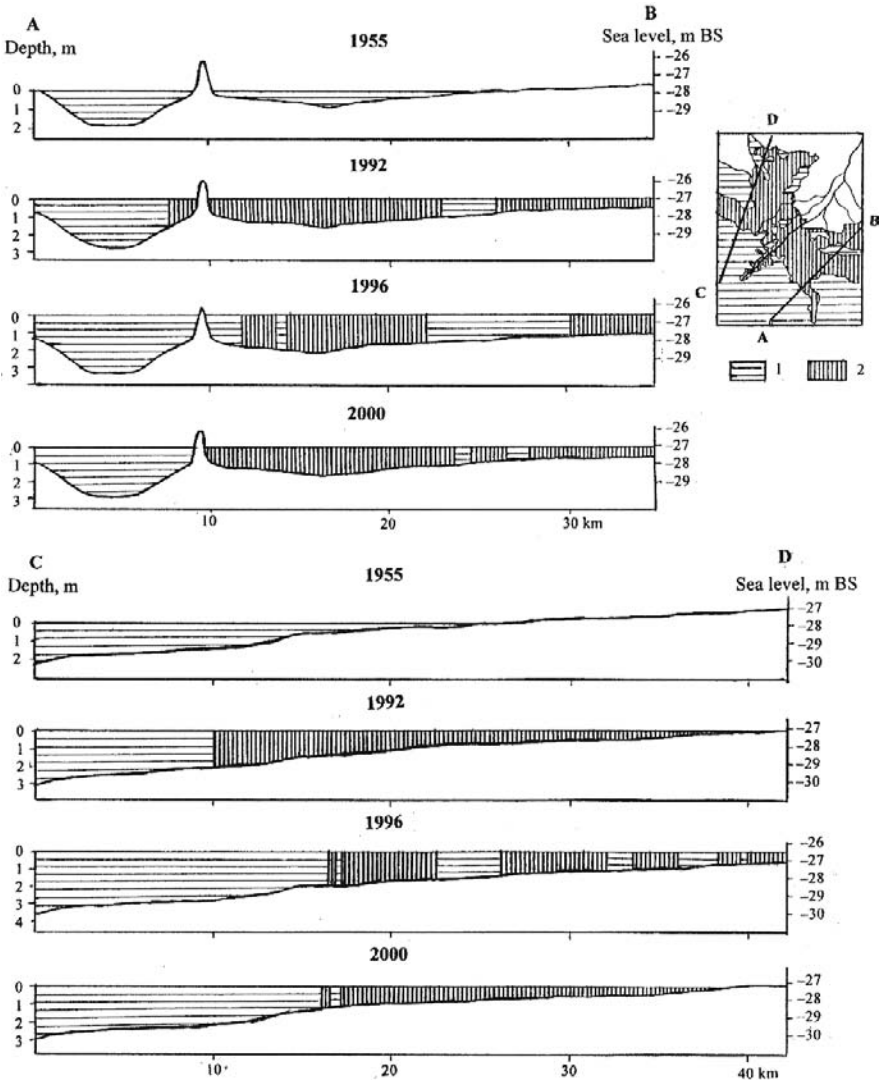
rear side expanded landward and even flourished over some lagoons. River channels ran dry again.

In summary, the Ural River delta response to the sea-level fluctuations was characterized by the formation of a reed belt along the shoreline when the sea-level rise exceeded 1.9 m. The expansion or withering of the reed belt was dependent upon the sea-level fluctuations and water depth.

## 19.5 Ecological Niche of the Reed Thickets

The changes revealed by satellite mapping of the Kalmykian coastal zone and the Ural River delta depended on the reed thickets in relation to the changing water level and hence the water depth. It is evident that reeds should have a specific ecological niche, probably around 1.9–2 m in depth, where reeds were quite sensitive to the bathymetry and water-level changes. When the sea-level rose to 2.35 m, the reed belt began to wither in area and width, its landscape structure became more fragmented, and the reed-open sea bound retreated, as indicated at the two test sites. When the sea-level declined moderately after 1995 (0.52 m by 2002), the reed thickets began to regain around the Ural River delta.

It is important to investigate the reed ecological niche and the influence of the water depth on the reed thickets. Such an investigation could help understand the past and predict the future of the coastal zone dynamics in the context of global sea-level rise. For this purpose, we constructed some profiles of the bathymetry and topography in the Ural delta region (Kravtsova and Shumatiev 2005). In these profiles, we also noted the sea-level heights for the dates our satellite data spanned over, and thus we created the water-depth profiles. The reed thicket bounds were



**Fig. 19.12** Profiles across the Ural River delta and surrounding sea which show bottom relief and reed thickets distribution: 1 – water, 2 – reed bushes

overlaid on these profiles (Fig. 19.12). This allowed us to analyze the relationship between reed distribution and water-depth fluctuations.

These profiles show that the reeds distributed at the sea with depth up to 1.7–2 m; these water areas were actually land during the previous sea regressive period. Reeds grew and widened until 1992 when the sea-level rise reached 1.92 m. More aggressive sea-level rise had not only caused the reeds to wither but also their landscape structure to be more fragmented; this trend was well observable, particularly

in 1992–1996 when water depth increased from 2 m to 2.3 m. Reeds stopped retreating when the sea-level rise was marginal and even negative; the reed-belt bounds were not only stable but also had begun to intrude into the sea and lagoons. Based on these observations, we determine the reed ecological niche in relation to water depth in the northern Caspian Sea; the growth of reeds reversed when the water depth was more than 1.9–2.0 m. Similar findings were noted when studying the Volga delta region during the Caspian Sea level rise period (e.g. Baldina et al. 1999); they reported that the reeds around the Chistaya Banka Island withered when water depth was between 1.5 and 2.0 m. Weisner (1991) noted that the maximum water depth reeds could tolerate should be between 1.6 and 1.7 m.

Of course, many other factors than water depth could affect reed distribution, including wind regime, sea ice, water chemistry, bottom sediments, among others. The reed distribution at the rear mudflat had something to do with groundwater level. Therefore, it may be important to know the height of groundwater level at which reeds could regain or wither. To answer this question, ground observations are necessary. Assessing the influence of these factors will help us to better understand the coastal zone dynamics based on the use of satellite imagery. New methods of heights measurements include the use of different spectral bands and through LiDAR surveys; the latter have been successfully applied in marsh investigations (Yang 2007). These new methods may help understand the relationship between groundwater level and reed distribution.

## 19.6 Conclusions

The response of the low-lying Kalmykian coasts to sea-level rise as examined by using satellite imagery included the formation of a lagoon complex and the growth of the reed mudflat zone; the reed mudflat shifted landward and further withered when water depth exceeded 2 m. A small sea-level decline led to the mudflat bounds moving seaward but the reed-land bound was more mobile. A similar pattern took place in the Ural River delta, where a broad reed belt formed as a result of the sea-level rise; the reed belt withered after the sea-level rise exceeded 1.9 m and the water depth reached 2 m and beyond.

The above observations suggest that the coastal ecosystem status depended upon the response of the reeds to water regime changes. This has been confirmed by our two case studies along the Kalmykian coastal zone and around the Ural River delta. Analysis of the reed thicket distribution change in relation to water depth shows that in the Caspian Sea reeds grew favourable where the water depth was less than 2 m. Beyond this limit, reeds withered, reed thickets became more fragmented, large water windows formed, and reed thicket bounds retreated.

Our research focus was on the local Caspian Sea level fluctuations rather than the global sea level change. But the reaction of the Kalmykian coastal zone and deltas to the Caspian Sea level rise can be interpreted as a benchmark to forecast the processes which can take place in the world coastal zones and river deltas in the context of global sea-level rise.

The two important conclusions are summarized:

- The reed belt survives a sea-level rise up to 2 m in water depth, and beyond this limit the reed belt will wither; and
- The reed-land bound is more sensitive to the sea-level fluctuations than the reed-sea bound. Therefore, it is necessary to reinforce the monitoring effort along this more mobile bound.

**Acknowledgement** The research reported here was supported by Russian Foundation of Basic Research through two grants (07-05-00187, 08-05-00305). The author expresses her special thanks to S. Lukyanova for geomorphological assistance in compiling the Kalmykian coastal zone maps, E. Baldina for multi-date color composition of the radar images and O. Tutubalina for proofreading the earlier version of the manuscript.

## References

- Baldina EA, De Leeuw J, Gorbunov AK, Labutina IA, Zhivogliad AF, Kooistra JF (1999) Vegetation change in the Astrachanskiy Biosphere Reserve (Lower Volga Delta, Russia) in relation to Caspian Sea level fluctuation. *Environ Conserv* 26:169–178
- Beetfink WG (1987) Vegetations responses to changes in tidal inundation of salt marshes. In: van Andel J, Bakker JP, Snaydon RW (eds) *Disturbance in Grasslands*, Dordrecht, Junk, pp 97–117
- De Leeuw J, Apon LP, Herman PMJ, De Munk W, Beetfink WG (1994) The response of salt marsh vegetation to tidal reduction caused by Oosterschelde storm-surge barrier. *Hydrobiologia* 282/283:335–353
- Goodbred SL, Hine AC (1995) Coastal storm deposition: salt-marsh response to a severe extratropical storm, March 1993, West-Central Florida. *Geology* 23:679–682
- Halls JN, Kraatz LM (2006) A spatio-temporal assessment of back-barrier salt marsh change: a comparison of multirate aerial photography and spatial landscape indices. Proc ISPRS midterm symposium 2006 “Remote Sensing: from Pixels to Processes”. Enschede, the Netherlands, 8–11 May 2006, pp 53–58
- Ignatov YeI, Kaplin PA, Lukyanova SA, Solovieva GD (1993) Evolution of the Caspian Sea coasts under conditions of sea-level rise: model for coastal change under increasing “green-house effect”. *J Coastal Res* 9:104–111
- Kravtsova VI, Baldina EA (2006) Study of natural and economical objects dynamics by color composition of multi-temporal images. Proc ISPRS midterm symposium 2006 “Remote Sensing: from Pixels to Processes”. Enschede, the Netherlands, 8–11 May 2006, pp 534–538
- Kravtsova VI, Lukyanova SA (1999) Dynamics of low-lying Kalmykian coast under the Caspian Sea level rise conditions; 1990’s. Proc 19 International Cartographic Conference. Ottawa, CD-ROM
- Kravtsova VI, Lukyanova SA (2000) Studies of recent changes in the Caspian coastal zone of Russia based on aerial and space imagery. *J Coastal Res* 16:196–206
- Kravtsova VI, Mikhailov VN (2006) Caspian coastal zone environment and river deltas dynamics: investigations by multi-temporal space images. Proc ISPRS midterm symposium 2006 “Remote Sensing: from Pixels to Processes”. Enschede, the Netherlands, 8–11 May 2006, pp 539–544
- Kravtsova VI, Mikhailov VN (2007) Response of some Caspian river deltas to changes in the sediment yield and sea level: investigations using multi-temporal space images. Proc 10th international symposium on river sedimentation, vol 4. pp 124–132

- Kravtsova VI, Shumatiev VV (2005) Reed mudflats of Caspian coasts under multiyears sea level fluctuations. In: Earth from space: the most effective solutions. Materials of the second International conference, 30 November–2 December 2005, pp 101–103 (in Russian and English)
- Mikhailov VN (1997) The Caspian Sea level. *Geoecologiya Pricaspiya* 2:36–43 (in Russian)
- Mikhailov VN, Kravtsova VI, Magritskii DV (2003) Hydrological and Morphological Processes in the Kura River Delta. *Water Resour* 30:495–508
- Mikhailov VN, Kravtsova VI, Magritskii DV (2004) Specific Features of Development of the Modern Sulak River delta. *Water Resour* 31:117–131
- Weisner SEB (1991) Within-lake patterns in depth penetration of emergent vegetation. *Freshwater Biol* 26:133–142
- Yang X (2007) Integrating lidar and high resolution imagery data for topographic and hydrological mapping over a coastal marsh area. In: XXIII International Cartographic Conference, 4–10 August 2007, Moscow, Russia. Abstracts of papers, p 225

## Chapter 20

# Integrating Satellite Imagery and Geospatial Technologies for Coastal Landscape Pattern Characterization

Xiaojun Yang

This chapter discusses the utilities of integrating remote sensing and related geospatial technologies for coastal landscape pattern characterization. The case study site is in the Pensacola estuarine drainage area, well known as one of the few exemplary large river-driven estuarine systems across the northern Gulf of Mexico, USA. Central to this study are the two Landsat images that have been used to extract land use/cover information with hierarchic classification and spatial reclassification techniques. The resultant land use/cover maps are then used to compute a large number of the initial landscape metrics for different spatial units. To suppress the information redundancy and improve the manageability, landscape ecology principles and multivariate statistical techniques are further used to help select a small set of core metrics on which the final interpretation and analysis are based. Throughout the entire watershed, the landscape structure exhibited a pronounced pattern of fragmentation, particularly around the city centers and along the coastlines; over time, the landscape mosaics became more heterogeneous while the classes of patches were more fragmented. These observed changes in landscape structure and pattern have been largely driven by vigorous urban and economic growth in the Pensacola metropolitan area during the 1990s. The findings reported here should be useful not only to those who study coastal watershed dynamics but also to those who must manage and provide services in such a sensitive environment. The analytical framework identified can be applicable easily to other coastal drainage basins. This can improve understanding of socio-ecological dynamics of landscape, thus facilitating a sophisticated approach to coastal conservation and protection.

## 20.1 Introduction

Because of large population and intensive development, global coastal ecosystems are under strain as never before, and there is a strong need for environmental monitoring and assessment in order to manage and protect these highly sensitive

---

X. Yang (✉)

Department of Geography, Florida State University, Tallahassee, FL 32306, USA  
e-mail: xyang@fsu.edu

ecosystems more effectively (EPA 1999, NRC 2000, Hobbie 2000, Shi and Singh 2003, Martinez et al. 2007, Richmond et al. 2007, Halpern et al. 2008). To assess environmental conditions in coastal ecosystems, a suite of indicators spanning the full spectrum of biological organization from generic markers to entire ecosystems are needed (Niemi et al. 2004, Yang 2005). Assessment of landscape patterns at the ecosystem level can help identify some important changes emerging from lower-level disturbances due to complex interactions between social and environmental processes (Turner et al. 2001).

The combination of landscape ecology principles and geospatial information technologies offers a workable framework supporting the quantitative assessment of spatio-temporal pattern of landscape composition and structure (Turner 1990, McGarigal and Marks 1995). Landscape ecology as the forefront of ecology and land management emphasizes the interaction between spatial pattern and ecological process (Turner et al. 2001). Interest in measuring landscape pattern is driven by the promise that there are essential links between ecological pattern and ecological function and process (Gustafson 1998). Landscape metrics as quantitative indices to describe structure and pattern of a landscape can be extracted from categorical land use/cover maps that are normally derived by remote sensing. They are increasingly being used to assess ecosystem health or as inputs for running various ecological models supporting numerous environmental assessment and planning efforts (e.g. Cain et al. 1997, Griffith et al. 2000, Fuller 2001, Leitao and Ahern 2002, Liu et al. 2003, Renofalt et al. 2005, Munroe et al. 2007, Hollister et al. 2008).

With the development of software engineering in geographic information systems, measurement of landscape metrics seems to be unlimited. However, there are several fundamental issues that need to be addressed before these quantitative indices can be meaningfully interpreted for landscape pattern analysis. Firstly, accurate land use/cover data are a prerequisite to measuring landscape metrics. Mapping land use/cover in the coastal environment is challenged by erratic climate conditions and complex landscape structure. The high humidity in coastal areas makes difficult to obtain cloud-free image scenes; the presence of complex urban impervious materials and agricultural lands, along with a variety of wetlands and vegetation covers, causes substantial inter-pixel and intra-pixel changes in the coastal environment. These factors collectively challenge the applicability and robustness of remote sensing technologies for coastal landscape change mapping.

Secondly, the choice of landscape metrics seems to be quite rich, but some may be partially or perfectly correlated with each other because they are basically derived from a few primary measurements that can be made from patches (McGarigal and Marks 1995); this results in information redundancy. Moreover, a large number of metrics would be difficult to interpret and analyze. Practically, a small set of metrics that are not redundant but capture the major properties of a landscape are more desirable. Selection of core landscape metrics can be accomplished by using landscape ecology principles as described by McGarigal (2002), and many applications were based on this approach of metrics selection for landscape pattern analysis (e.g. Zhang et al. 1997, Fuller 2001, Li et al. 2001, Baskent and Kadiogullari 2007).



However, this approach generally works well to reduce inherent redundancy but not empirical redundancy. Statistical methods (e.g. principal component analysis) can be used to reduce data redundancy and select a parsimonious suite of independent metrics for landscape pattern analysis (e.g. Riitters et al. 1995, Cain et al. 1997, Griffith et al. 2000, Herzog and Lausch 2001, Yang and Liu 2005a). Although recent studies indicate that landscape pattern can be characterized by using a small number of core indicators, consensus has not been reached on the choice of individual metrics (McGarigal 2002).

Lastly, the choice of an appropriate spatial unit is another critical issue because landscape metrics are sensitive to the extent over which they are calculated (Hunsaker et al. 1994). Thus, spatial units can affect the measurement of landscape metrics and hence the pattern-process relationship. On the other hand, landscape metrics are normally computed and aggregated by specific spatial units. The current landscape ecology literature, however, does not provide much guidance on how to choose spatial units, and therefore, further effort is needed to design spatial units which could explicitly reflect some hypotheses related to major processes acting upon a landscape under investigation.

The objective of this study was to evaluate the utilities of integrating remote sensing and relevant geospatial technologies for coastal landscape pattern characterization. This has been done through a case study focusing on the Pensacola estuarine drainage area, well known as one of the few exemplary, large river-driven estuarine systems across the northern Gulf of Mexico, USA. The study area has historically supported a rich and diverse ecosystem, productive fisheries, and considerable recreational opportunities in north-western Florida (EPA 1999). Since the beginning of 1990s, this area has witnessed significant population and economic growth, resulting in point and non-point source pollution, hydrologic alterations, and direct habitat destruction throughout the watershed (NFWMD 1997). These changes have provoked concerns over the degradation of ecosystem health in Pensacola Bay. Since 2000, the author has been involved in various research projects aiming to develop environmental indicators for integrated estuarine ecosystem assessment in the Gulf of Mexico; Pensacola Bay and its watershed have been targeted for coordinated research. This chapter examines the spatio-temporal pattern of landscape composition and structure in the Pensacola estuarine drainage area through the integration of geospatial information technologies, part of the above research effort. This should add useful insights into the emerging coastal environmental indicator research in which the development of broad-scale indicators is considered to be critical for coastal researchers and managers (Levinson 2005).

The following sections document the research framework that comprised several major components: choice of the study site, primary and secondary data acquisition, land use/cover classification from satellite imagery, design of spatial observational units, computation of initial landscape metrics, selection of core metrics, and interpretation and analysis (Fig. 20.1).

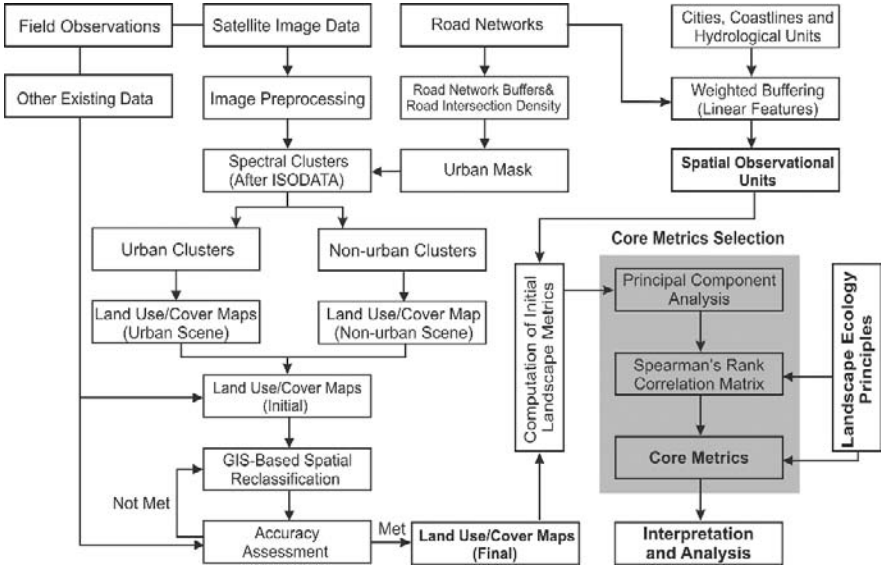


Fig. 20.1 Flowchart of the working procedural route

### 20.2 Case Study Site: Pensacola Estuarine Drainage Area

The geographical coverage of the Pensacola estuarine drainage area (PEDA) includes the majority of Escambia, Santa Rosa and Okaloosa counties, the northwestern part of Walton County in Florida, as well as portions of Conecuh, Covington, Escambia, and Monroe counties in Alabama (Fig. 20.2). The PEDA is defined according to National Oceanic and Atmospheric Administration (NOAA)'s Coastal Assessment Framework (CAF). CAF is a GIS-based digital spatial framework designed for managers and analysts to organize information on the nation's coastal, near-ocean, and Great Lakes' resources (NOAA 1999). The PEDA is the estuarine portion of the Pensacola Bay drainage basin, approximately 50% of the total watershed (NFWMD 1997). The entire basin discharges into the Gulf of Mexico through a narrow pass at the mouth of Pensacola Bay. The PEDA has a total area of 9,119km<sup>2</sup>, which includes 8,643km<sup>2</sup> of the upstream watershed and 476km<sup>2</sup> of bays, fitting well within a whole scene (180 × 180km<sup>2</sup>) of Landsat imagery.

Physiographically, the PEDA lies within the Coastal Plain province, which is underlain mainly by beds of sand, silt, and clay that dip gently seaward (Marsh 1966). The estuarine embayments are within the Gulf Coastal Lowlands subdivision and contain a series of parallel terraces rising from the coast in successively higher levels. Much of the area is less than 30 m above sea level. PEDA includes three major river systems, namely, Escambia, Blackwater and Yellow rivers. The climate is humid subtropical with generally warm temperatures.

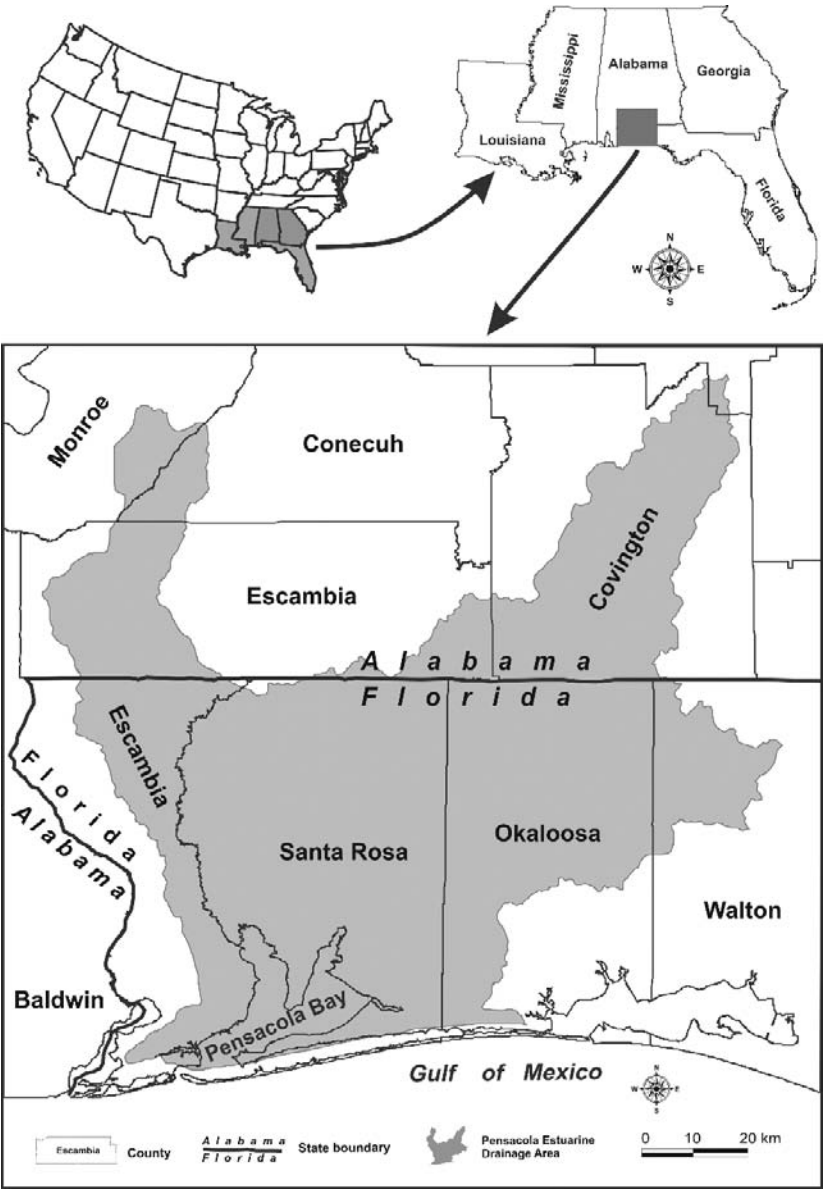


Fig. 20.2 Location of the study site

## 20.3 Land Use/Cover Classification

### 20.3.1 Data Acquisition and Preprocessing

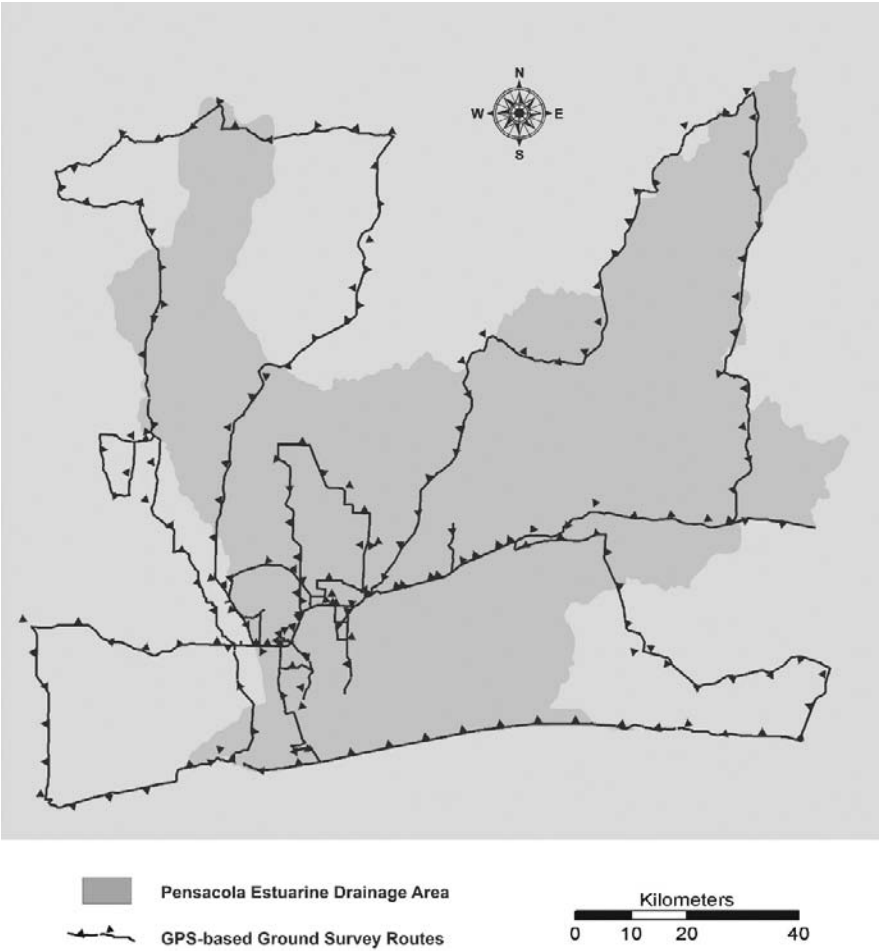
In order to compute landscape metrics, two different dates of land use/cover maps are produced. For this purpose, a predominantly cloud-free scene of Landsat Thematic Mapper (TM)/Enhanced Thematic Mapper (ETM+) image was acquired from USGS EROS Data Center for 1989 (6 April) and 2002 (20 May), respectively. To facilitate land use/cover mapping, a variety of ancillary data were collected, which include Digital Ortho Quarter Quads (DOQQs), topographical maps, hydrological and political boundaries, existing land use/cover maps, wetland datasets produced by National Wetland Inventory, and road networks. GPS guided field surveys were also conducted to acquire ground truth for classification scheme design and accuracy assessment (Fig. 20.3).

Both geometric rectification and radiometric normalization were conducted in the phase of image preprocessing. With USGS topographical maps, the 2002 image was georeferenced to the UTM map projection (Zone 16), NAD 1983 horizontal datum, and GRS 1984 ellipsoid. Then, this image was used as the reference to rectify the 1989 image. The radiometric normalization method of using radiometric control sets that was developed by Hall et al. (1991) was also applied to the image data.

### 20.3.2 Classification Scheme

Based on the research objectives, image spatial resolution and field surveys, a modified version of the Anderson scheme (Anderson et al. 1976) was developed (Yang and Liu 2005a):

- *High density urban* (HDU) is characterized by approximately 70–100% (impervious) construction materials, typically commercial and industrial buildings with large open roofs as well as large open transportation facilities; it also includes military bases, tourism and recreational facilities, and a low percentage of residential development residing in the city cores.
- *Low density urban* (LDU) consists of approximately 40–70% (impervious) construction materials, typically residential development including single/multiple family houses and public rental housing estate, as well as local roads and small transitional space as can be always found in a residential area; it also contains a various amount of vegetation cover.
- *Agricultural land* (AGL) is characterized by crops, pastures, and other herbaceous vegetation, including lands that are regularly mowed for hay or grazed by livestock and regularly tilled and planted cropland; it may contain small parks and golf courses.
- *Evergreen forest* (EGF) includes coniferous forests.



**Fig. 20.3** GPS-based field survey routes. The boundary of the Pensacola estuarine drainage area is shown. The total length of these routes is more than 1,500 km (from Yang and Liu 2005b)

- *Mixed forest* (MXF) consists of evergreen and deciduous species mixed with a various amount of shrubs, brushes and young trees.
- *Woody wetlands* (WWL) include hardwood, mixed forest, and shrubs, which are distributed along rivers and bays.
- *Emergent herbaceous wetlands* (EHW) is characterized by tall grasses such as black needle rush; it is also called swamp, salt marsh, and brackish marsh.
- *Barren land* (BRL) consists of the areas of sparse vegetation cover (less than 20%), including beaches, clearcuts, and transactional lands that are likely to change or be converted to other uses in the near future.
- *Water* (WTR) consists of all areas of open water, generally with greater than 95% cover of water, including streams, rivers, lakes, reservoirs, and bays.

### **20.3.3 Hierarchical Classification**

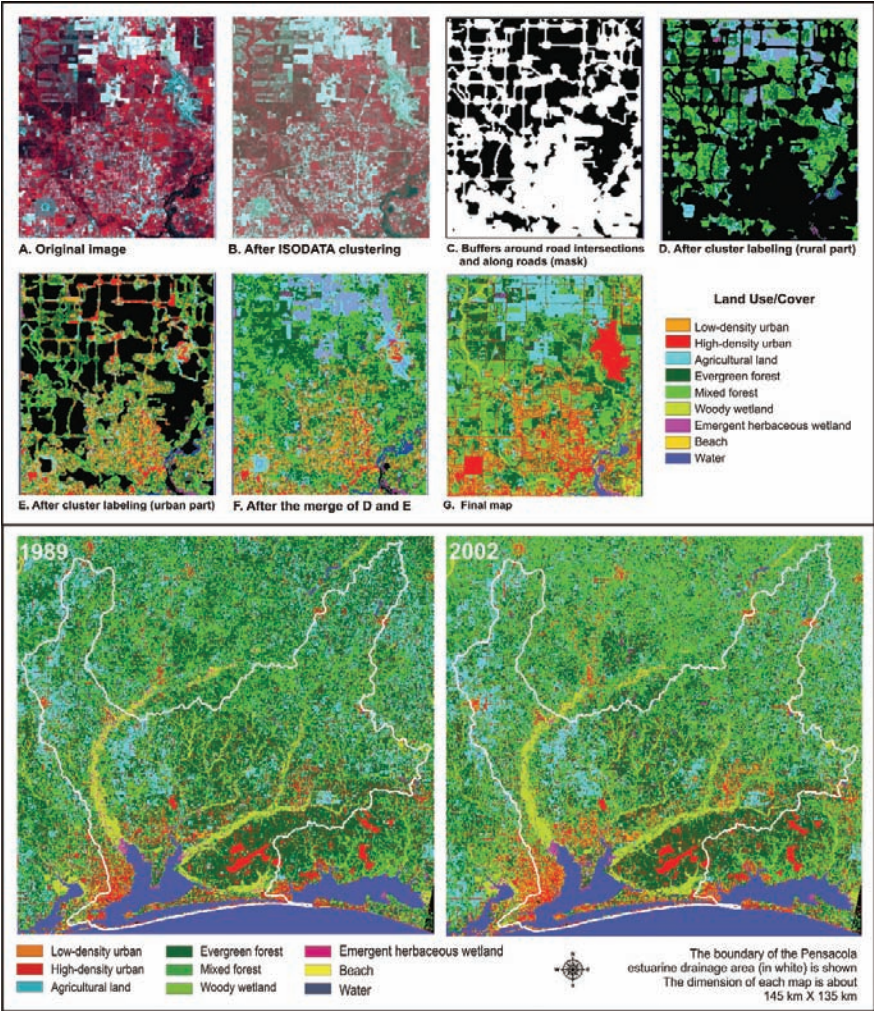
The adoption of hierarchical classification strategy was based on the observation that some types of land use/cover tend to be spectrally similar. For example, urban built-up land shows similar spectral reflectance to barren land and several types of agricultural land. This is actually a form of the spectral confusion problem being regarded as the major barrier to achieving adequate accuracy with a per-pixel based classification method from remotely sensed imagery with middle-size spatial resolutions and broad spectral bands (Yang 2002). To resolve spectral confusion, hierarchic classification and spatial reclassification procedures were developed in consideration of the imaging sensor and the scenic characteristics. This section describes the procedures of hierarchic classification, and Sect. 20.3.4 discusses the spatial reclassification. Hierarchic classification emphasizes the use of image subsets being organized hierarchically, rather than whole scenes, in a series of independent classification procedures. The purpose of using image subsets is to isolate the problematic categories so that the most effective classification decision can be developed for each subset. Hierarchic classification allows each form of information to be used in its most effective context, and its procedure is discussed in the following sections (see Fig. 20.4-above).

#### **20.3.3.1 ISODATA Clustering**

The ISODATA (Interactive Self-organizing Data Analysis) algorithm was used to identify spectral clusters from the image scenes excluding the thermal band. To avoid the impacts of sampling characteristics, the ISODATA algorithm was implemented without assigning predefined signature sets as starting clusters. Each scene was grouped into 60 spectral clusters when the convergence value reached at least 0.990.

#### **20.3.3.2 Landscape Segmentation**

The output of ISODATA clustering was separated into urban and rural subsets through the use of an image 'mask' that defines the urban area with road intersection density and road buffers through a three-step procedure. Firstly, road intersections were extracted from the Environmental System Research Institute (ESRI) 2002 and 2003 road networks, and their density was further computed; note that the road data for 1989 were derived from the ESRI 2002 data that were adjusted by using the 1989 TM imagery. Secondly, a threshold density value was determined interactively to include as much urban area as possible. With this threshold value, the density map was sliced into the urban and rural subsets. Lastly, the urban subset was unionized with 100-m road buffers to define the final urban subset, and other part was defined as the rural subset.



**Fig. 20.4** (Upper): Sequential procedures identified for land use and land cover classification: **A.** The original image in false color display; **B.** The cluster image in false color after ISODATA clustering; **C.** The mask image consisting of road intersection density slices and road buffers; **D.** The map for rural part after cluster labeling; **E.** The map for urban part after cluster labeling; **F.** The map after the merge of D and E; and **G.** The final map after conducting spatial reclassification. Detailed discussion on these procedures can be found from relevant text. (Lower): Land use and land cover maps derived from Landsat TM/ETM+ data

### 20.3.3.3 Interactive Classification

Each spectral cluster in either the urban or the rural subset was assigned into one of the nine land use/cover classes using visual inspection of the original images, the reference data, and the familiarity of the study area. This class labeling was

based on the examination of a targeted cluster at two different levels of details: at the large scale, the individual image color was mainly used in decision making while at the small scale such image elements as association and site were utilized to improve classification accuracy. The land use/cover classifications of both the urban and rural subsets were further combined to form a whole map. This was the initial land use/cover classification.

### ***20.3.4 Spatial Reclassification***

The initial land/cover maps after hierarchic classification came with the accuracies of approximately 65–75%. For this study, however, higher accuracy was needed. Therefore, a spatial reclassification procedure was developed to reduce image classification errors and improve accuracy. It was implemented by using image interpretation, ancillary data and a variety of GIS functions.

#### **20.3.4.1 Raster Modal Filtering**

A  $3 \times 3$  modal filter was used to reduce boundary errors at class boundaries due to the occurrences of intra-pixel spectral mixing and signal noises. Pixels identified as boundary errors are generally in the form of salt and pepper and they can be replaced with classes of their surroundings through a modal filter.

#### **20.3.4.2 Interactive Image Interpretation**

Although the spectral confusion described in Sect. 20.3.3 has been substantially suppressed after hierarchic classification, a varying degree of spectral confusion was still observable in some areas. These areas were further identified using an image interpretation procedure through which spectral and spatial contextual contents as well as human wisdom and experience were synthesized. Image interpretation can be implemented digitally using on-screen digitizing, multiple zooming, AOI (area of interest) functionality, and other relevant GIS tools such as overlaying and recoding. In addition, several image processing programs offer advanced tools of spatial modeling through which some ‘manual’ operations can be implemented automatically.

With the above methods, four major types of spectral confusion were identified: (i) low density urban (mostly residential)/mixed forest (sparse trees), (ii) low density urban (scattered residential)/agricultural land (sparse crops or grasses), (iii) mixed forest (sparse forest and shrubs)/agricultural land (cropland or grassland), and (iv) high density urban (large open roof buildings, air fields, and multilane highways)/barren land (large barren landmass, beaches, clearouts, and fallowed land). These pairs of land use/cover types are spectrally similar to varying degrees.



Whenever any spectrally confused cluster was identified, an AOI layer was immediately created through on-screen digitizing to define a 'mask' by which the problematic cluster was split and then recoded into a correct land use/cover class. This process was iterative until an acceptable accuracy was reached.

#### **20.3.4.3 GIS Data Overlay Enforcement**

Several GIS data layers were further overlaid with the classification product after the above procedures were completed, which include (i) weighted buffers of road networks for 1989 and 2002, respectively. Road data were derived from the ESRI 2002 road network adjusted with the reference of the two image scenes; (ii) airports, military fields, tourism and recreational facilities for the above two years. They were initially extracted from the 1995 Florida Department of Environmental Protection land use/cover map and were then modified by using the image scenes; and (iii) two types of wetlands which were extracted from National Wetland Inventory data sets for 1992 and then modified by using the above images.

#### **20.3.5 Accuracy Assessment**

A standard procedure described by Jensen (2005) was used for accuracy assessment using at least 50 test points per class that were selected with a stratified random sampling scheme. The reference data used for accuracy assessment were described in Sect. 20.3.1. Producer accuracy, user accuracy, and Kappa statistics were computed, and detailed reports are shown in Table 20.1. Overall, the two final maps (Fig. 20.4-below) met the minimum 85% accuracy stipulated by the Anderson classification scheme (Anderson et al. 1976), indicating that the image processing procedure developed has been quite effective.

### **20.4 Spatial Units and Landscape Metrics Computation**

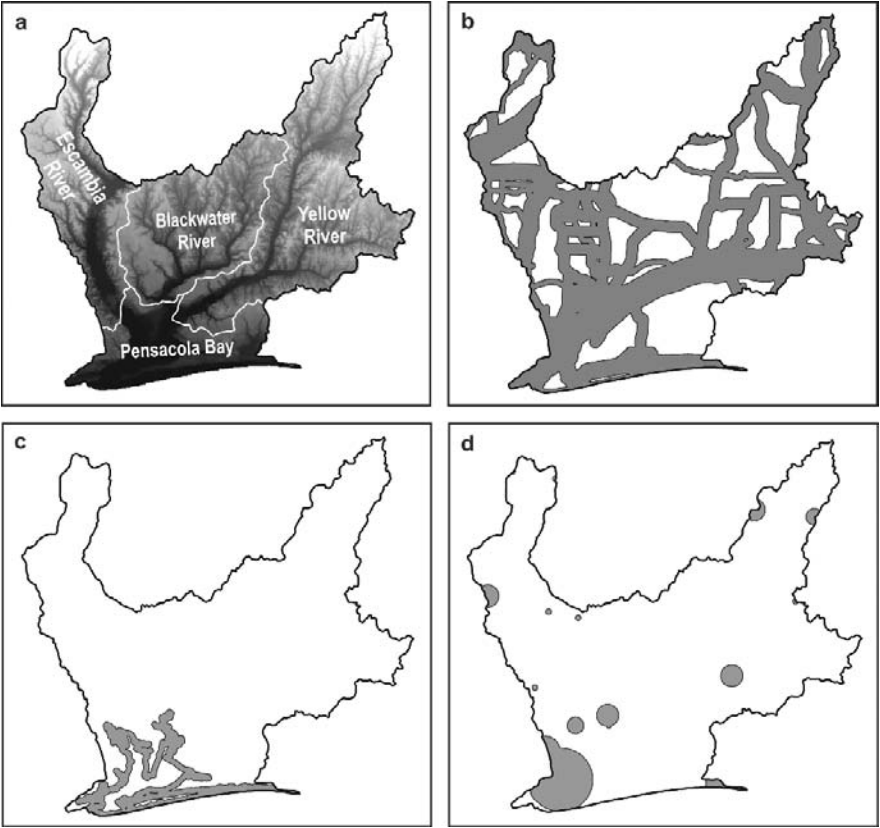
#### **20.4.1 Spatial Units**

Choosing an appropriate spatial unit is critical for landscape pattern analysis. Previous research reported the use of hexagons to sample a landscape (e.g. Hunsaker et al. 1994, Griffith et al. 2000), but also noted the significant discrepancy of pattern metrics between the hexagon sampling landscape and the complete landscape (Hunsaker et al. 1994). In this study, a different strategy was adopted. The spatial units used here are related to either a hydrological unit or a predefined buffer zone. They are associated with different levels or types of biophysical or human-dimension stressors, which are likely to impact landscape pattern.

**Table 20.1** Summary of the accuracy assessment reports for the 1989 and 2002 maps

Land Use/Cover*	1989			2002		
	Producer's Accuracy (%)	User's Accuracy (%)	Conditional <i>K</i> Coefficient of Agreement	Producer's Accuracy (%)	User's Accuracy (%)	Conditional <i>K</i> Coefficient of Agreement
Low Density Urban (LDU)	72.00	72.00	0.70	84.78	78.00	0.77
High Density Urban (HDU)	97.45	91.60	0.88	98.35	95.60	0.93
Agricultural Land (AGL)	88.07	96.00	0.95	89.72	96.00	0.95
Evergreen Forest (EGF)	88.89	96.00	0.96	84.91	90.00	0.89
Mixed Forest (MXF)	85.71	96.00	0.96	84.75	100.00	1.00
Woody Wetlands (WWL)	90.38	94.00	0.94	100.00	96.00	0.96
Emergent Herbaceous Wetlands (EHW)	97.62	82.00	0.81	94.12	96.00	0.96
Barren Land (BRL)	97.96	96.00	0.96	97.83	90.00	0.89
Water (WTR)	97.09	100.00	1.00	98.97	96.00	0.95
Overall	92.40		0.91	94.13		0.93

\*A total of 750 sample points were used with at least 50 points for each class.



**Fig. 20.5** Spatial observational units used in the study: (a) The entire Pensacola estuarine drainage area (PEDA) and its four sub-watersheds: Blackwater River(BLWR), Escambia River (ESCR), Pensacola Bay (PNSB), and Yellow River (YLWR); (b) Weighted highway buffers (HWYB); (c) One-kilometer coastline buffers (CSTB); (d) Weighted city buffers (CTYB) according to population size (from Yang and Liu 2005a)

The spatial units considered include the entire PEDA, four major sub-watersheds, and three predefined buffer areas (Fig. 20.5). PEDA was used as a background for comparison; the four sub-watersheds were used to examine the variation of landscape patterns across the watershed. The other three units considered are highway buffers, city buffers, and coastline buffers. The highway buffers were derived from the ESRI 2002 highway data, and their size was weighted according to highway types. Highway buffers occupy 5,402 km<sup>2</sup> or 59.21% of the total PEDA. The size of city buffers was weighted with a city's 2002 population size, and they occupy a total area of 611 km<sup>2</sup>. Coastline buffers consist of the area within 1 km from the coastline, representing 661 km<sup>2</sup> of the PEDA.

**Table 20.2** List of initial and final landscape metrics at the class and landscape levels, respectively

Structural Feature	Index (Acronym)	Full Name (Unit)*	Class Level		Landscape Level	
			Initial	Final	Initial	Final
<b>Area</b>	CA	Class Area (ha)	Yes			
	LPI	Largest Patch Index (%)	Yes	Yes	Yes	Yes
	PLAND	Percent of Landscape (%)	Yes	Yes		
	TA	Total Area (ha)			Yes	
<b>Patch</b>	MPS	Mean Patch Size (ha)	Yes	Yes	Yes	Yes
	NP	Number of Patches (none)	Yes	Yes	Yes	Yes
	PD	Patch Density (#/100 ha)	Yes		Yes	
	PSCV	Patch Size Coefficient of Variation (%)	Yes		Yes	
	PSSD	Patch Size Standard Deviation (ha)	Yes		Yes	
<b>Shape</b>	AWMPFD	Area Weighted Mean Patch Fractal Dimension (none)	Yes		Yes	Yes
	AWMSI	Area Weighted Mean Shape Index (none)	Yes	Yes	Yes	
	MPFD	Mean Patch Fractal Dimension (none)	Yes		Yes	
	MSI	Mean Shape Index (none)	Yes		Yes	
<b>Core Area</b>	CACV1	Core Area Coefficient of Variation (%)	Yes	Yes	Yes	Yes
	CACV2	Disjunct Core Area Coefficient of Variation (%)	Yes		Yes	
	CAD	Core Area Density (#/100 ha)	Yes		Yes	
	CASD1	Core Area Standard Deviation (ha)	Yes		Yes	
	CASD2	Disjunct Core Area Standard Deviation (ha)	Yes		Yes	
	CPLAND	Core Area Percent of Landscape (%)	Yes		Yes	
	LCAS	Landscape Core Area Similarity (%)			Yes	
	MCA1	Mean Area per Core (ha)	Yes		Yes	
	MCA2	Mean Core Area 2 (ha)	Yes		Yes	

**Table 20.2** (continued)

Structural Feature	Index (Acronym)	Full Name (Unit)*	Class Level		Landscape Level	
			Initial	Final	Initial	Final
<b>Diversity</b>	MCAI	Mean Core Area Index (%)	Yes		Yes	
	NCA	Number of Core Areas (none)	Yes		Yes	
	TCA	Total Core Area (ha)	Yes	Yes	Yes	Yes
	TCAI	Total Core Area Index (%)	Yes		Yes	
	MSIDI	Modified Simpsons Diversity Index (none)			Yes	Yes
	MSIEI	Modified Simpsons Evenness Index (none)			Yes	
	SHDI	Shannons Diversity Index (none)			Yes	
	SHEI	Shannons Evenness Index (none)			Yes	
	SIDI	Simpsons Diversity Index (none)			Yes	
SIEI	Simpsons Evenness Index (none)			Yes		
<b>Configuration</b>	IJI	Interspersion and Juxtaposition (%)	Yes	Yes	Yes	Yes

\*Detailed definitions on these landscape metrics can be found from McGarigal and Marks (1995).

### **20.4.2 Computation of Landscape Metrics**

Before the actual computation of landscape metrics, a  $5 \times 5$  modal filter was applied to the two raster maps to remove isolated pixels resulting from boundary errors (Yang 2002). This should help improve the speed in the computation of landscape metrics. Then, the two raster maps were converted into vectors, and landscape metrics were computed with Fragstats\* ARC (McGarigal and Marks 1995). A total of 56 metrics were considered in the context of our research objective and the landscape ecology principles (e.g. Turner 1990, Forman RRT 1995, McGarigal 2002). These metrics are related to either landscape composition (e.g. proportional abundance of each class) or configuration (e.g. patch size distribution and density, patch shape complexity, and interspersion). They are grouped into six major structural categories: area, patch, shape, core area, diversity, and configuration (Table 20.2). At the class level, there are a total of 25 metrics, falling within five of the six major structural groups. At the landscape level, there are a total of 31 metrics. These metrics were computed for each spatial unit using the 1989 and 2002 land use/cover data.

### **20.5 Selection of Core Metrics**

Principal component analysis (PCA) and Spearman's rank correlation analysis (SRCA) were used to help identify a set of metrics that best described characteristics of the landscape units. PCA is a multivariate method that linearly combines the original variables into several uncorrelated and independent variables known as principal components. Most of the variability in the original variables is captured in the first few principal components. PCA was used here to identify a smaller set of metrics from the initial list which are highly correlated with the first few components. Variables that were not strongly correlated with the first few principal components were excluded from further analysis. Spearman's rank correlation analysis (SRCA) was conducted after PCA. As a non-parametric method, SRCA uses the ranks of the data, rather than the actual data, to compute a correlation coefficient. With SRCA, a correlation coefficient matrix was created at the landscape and class levels, respectively. Additionally, several core metrics which are ecologically critical were included given the research objective and landscape ecology principles (e.g. McGarigal and Marks 1995, Turner et al. 2001). While any number of metrics could be eliminated after PCA and SRCA, it was decided to include at least one core metric for each structural group (see Table 20.2). This was to ensure that each structural group could be addressed in the further analysis. If no metrics were left for any structural group after PCA and SRCA, at least one critical metric for that group would have to be added back into the list. In this way, a final list of the core metrics was created at the landscape and class levels, respectively.

Table 20.3 summarizes the outcome of the PCA at the landscape level. In this computation, all 31 metrics at the landscape level were considered for eight spatial units at two different years. Thus, there were 16 'samples' used in the PCA. To

**Table 20.3** Results of principal component analysis (PCA) and varimax rotation of the first four components at the landscape level

	Component Number				
	1	2	3	4	
	<i>Eigenvalues and cumulative proportion of variance explained by principal component analysis</i>				
<b>Eigenvalue*</b>	15.926	7.954	4.209	1.637	
<b>Cumulative Variance</b>	51.375	77.034	90.610	95.891	
	<i>Component pattern after varimax rotation</i>				<i>Communality**</i>
<b>LPI</b>	<b>0.887</b>	0.121	-0.395	0.198	1.00
<b>TA</b>	-0.280	0.228	<b>0.905</b>	-0.157	0.97
<b>MPS</b>	0.188	-0.348	0.232	<b>-0.878</b>	0.98
<b>NP</b>	-0.323	0.317	<b>0.874</b>	-0.107	0.98
<b>PD</b>	-0.073	0.277	-0.235	<b>0.922</b>	0.99
<b>PSCV</b>	<b>0.907</b>	0.230	-0.149	0.308	0.99
<b>PSSD</b>	<b>0.970</b>	0.188	-0.068	-0.069	0.98
<b>AWMPFD</b>	0.629	-0.249	-0.717	0.093	0.98
<b>AWMSI</b>	0.681	0.043	-0.335	0.584	0.92
<b>MPFD</b>	0.640	0.072	-0.334	0.662	0.96
<b>MSI</b>	<b>-0.787</b>	-0.259	0.363	-0.268	0.89
<b>CACV1</b>	<b>0.804</b>	0.342	0.063	0.465	0.98
<b>CACV2</b>	0.743	0.455	0.330	0.319	0.97
<b>CAD</b>	<b>-0.893</b>	0.094	0.383	-0.069	0.96
<b>CASD1</b>	<b>0.964</b>	0.191	-0.013	-0.094	0.97
<b>CASD2</b>	<b>0.967</b>	0.144	-0.099	-0.001	0.97
<b>CPLAND</b>	<b>0.960</b>	0.061	-0.236	-0.113	0.99
<b>LCAS</b>	<b>0.960</b>	0.061	-0.236	-0.113	0.99
<b>MCA1</b>	<b>0.835</b>	-0.077	-0.071	-0.534	0.99
<b>MCA2</b>	<b>0.933</b>	0.019	-0.274	-0.107	0.96
<b>MCAI</b>	-0.735	-0.210	0.369	-0.457	0.93
<b>NCA</b>	-0.345	0.251	<b>0.879</b>	-0.131	0.97
<b>TCA</b>	-0.134	0.216	<b>0.933</b>	-0.188	0.97
<b>TCAI</b>	<b>0.960</b>	0.061	-0.236	-0.113	0.99
<b>MSIDI</b>	0.051	<b>0.946</b>	0.207	0.151	0.96
<b>MSIEI</b>	0.050	<b>0.945</b>	0.209	0.153	0.96
<b>SHDI</b>	0.283	<b>0.919</b>	0.151	0.111	0.96
<b>SHEI</b>	0.281	<b>0.920</b>	0.150	0.113	0.96
<b>SIDI</b>	0.083	<b>0.944</b>	0.198	0.158	0.96
<b>SIEI</b>	0.084	<b>0.945</b>	0.194	0.158	0.96
<b>IJI</b>	0.148	0.598	-0.285	-0.431	0.65
			<i>sum</i>		29.73
	<i>Variance explained by each component after rotation</i>				
	13.734	6.769	5.331	3.892	

\* The computation considers all spatial units at two different years. Descriptions of the metrics are given in Table 20.2. Entries (correlation coefficients) in bold are considered to be strongly associated with one or more principal components. The metrics which were excluded for further considerations are shaded.

\*\* Communality is the proportion of variance that each variable has in common with other variables.

increase interpretability, an orthogonal varimax rotation, which perceives the relative orientation, was used on the resulting component scores. Note that the first four components explain approximately 96% of the variability in the entire data set. Metrics that were weakly correlated with the first four principal components were excluded from further analysis. This resulted in the elimination of six metrics: AWMPFD, AWMSI, MPFD, CAV2, MCAI, and IJI (see Table 20.2 for the description of the metrics). Spearman’s rank correlation coefficients were computed for all the remaining 25 metrics and the results are summarized in Table 20.4. LPI, MPS, and NP were selected as the first three core metrics because they are critical to quantify landscape fragmentation (McGarigal and Marks 1995). Nine metrics whose correlations with any of the first three core metrics reached at least 0.85 were considered to be redundant and were eliminated from further consideration; they are PSCV, PSSD, MSI, CASD1, CASD2, PD, TA, NCA, and TCA. Then, CACV1 was selected as a critical metric representing the core area structural group (see Table 20.2). MSIDI, a Simpson index, was selected as a core diversity metric. Five metrics, namely MSIEI, SHDI, SHEI, SIDI, and SIEI, were eliminated because they were highly correlated with MSIDI. Six other metrics were eliminated because they were highly correlated with one or more of the metrics which were eliminated earlier. Finally, three ecologically critical metrics, namely AWMPFD, TCA, and IJI, which were eliminated earlier, were added back to represent three structural groups (see Table 20.2). Thus, the final list consists of eight metrics: LPI, MPS, NP, AWMPFD, CACV1, TCA, MSIDI, and IJI. Similar procedures were adopted at the class level, and the final list has eight metrics: LPI, PLAND, MPS, NP, AWMSI, CACV1, TCA, and IJI (see Table 20.2).

**Table 20.4** Spearman’s rank correlation coefficient matrix for 25 metrics at the landscape level

	LPI	TA	MPS	NP	PD	PSCV	PSSD	MSI	CACV1	CAD	CASD1	CASD2	CACV2	LCAS	MCA1	MCA2	NCA	TCA	TCAI	MSIDI	MSIEI	SHDI	SHEI	SIDI	SIEI		
LPI	1.00																										
TA	-0.68	1.00																									
MPS	-0.16	0.33	1.00																								
NP	-0.61	<b>0.94</b>	0.12	1.00																							
PD	0.16	-0.33	<b>-1.00</b>	-0.12	1.00																						
PSCV	<b>0.90</b>	-0.53	-0.21	-0.46	0.21	1.00																					
PSSD	<b>0.93</b>	-0.52	-0.06	-0.50	0.06	<b>0.97</b>	1.00																				
MSI	<b>-0.87</b>	0.59	0.25	0.56	-0.25	<b>-0.91</b>	<b>-0.93</b>	1.00																			
CACV1	0.84	-0.46	-0.30	-0.33	0.30	<b>0.96</b>	<b>0.91</b>	-0.84	1.00																		
CAD	-0.65	0.72	-0.24	0.77	0.24	-0.58	-0.61	0.54	-0.48	1.00																	
CASD1	<b>0.91</b>	-0.50	-0.07	-0.48	0.07	<b>0.98</b>	<b>0.99</b>	<b>-0.94</b>	<b>0.92</b>	-0.61	1.00																
CASD2	<b>0.91</b>	-0.52	-0.14	-0.46	0.14	<b>0.98</b>	<b>0.98</b>	<b>-0.91</b>	<b>0.95</b>	-0.61	<b>0.98</b>	1.00															
PLAND	0.74	-0.47	0.24	-0.55	-0.24	0.84	<b>0.86</b>	-0.77	0.74	-0.81	<b>0.87</b>	<b>0.85</b>	1.00														
LCAS	0.74	-0.47	0.24	-0.55	-0.24	0.84	<b>0.86</b>	-0.77	0.74	-0.81	<b>0.87</b>	<b>0.85</b>	<b>1.00</b>	1.00													
MCA1	0.41	-0.20	0.66	-0.40	-0.66	0.45	0.56	-0.39	0.29	-0.70	0.54	0.49	0.80	0.80	1.00												
MCA2	0.73	-0.55	0.26	-0.61	-0.26	0.77	0.79	-0.67	0.68	<b>-0.91</b>	0.79	0.78	<b>0.96</b>	<b>0.96</b>	0.81	1.00											
NCA	-0.66	<b>0.98</b>	0.27	<b>0.96</b>	-0.27	-0.51	-0.51	0.58	-0.41	0.77	-0.49	-0.51	-0.51	-0.51	-0.27	-0.59	1.00										
TCA	-0.45	<b>0.93</b>	0.47	<b>0.87</b>	-0.47	-0.26	-0.24	0.36	-0.21	0.49	-0.21	-0.24	-0.17	-0.17	0.06	-0.27	<b>0.90</b>	1.00									
TCAI	0.74	-0.47	0.24	-0.55	-0.24	0.84	<b>0.86</b>	-0.77	0.74	-0.81	<b>0.87</b>	<b>0.85</b>	<b>1.00</b>	<b>1.00</b>	0.80	<b>0.96</b>	-0.51	-0.17	1.00								
MSIDI	0.29	0.20	-0.43	0.36	0.43	0.43	0.34	-0.34	0.46	0.37	0.36	0.35	-0.01	-0.01	-0.26	-0.15	0.28	0.29	-0.01	1.00							
MSIEI	0.29	0.20	-0.43	0.36	0.43	0.43	0.34	-0.34	0.46	0.37	0.36	0.35	-0.01	-0.01	-0.26	-0.15	0.28	0.29	-0.01	<b>1.00</b>	1.00						
SHDI	0.36	0.08	-0.35	0.12	0.35	0.61	0.53	-0.54	0.57	0.13	0.56	0.52	0.31	0.31	0.08	0.15	0.10	0.22	0.31	<b>0.85</b>	<b>0.85</b>	1.00					
SHEI	0.36	0.08	-0.35	0.12	0.35	0.61	0.53	-0.54	0.57	0.13	0.56	0.52	0.31	0.31	0.08	0.15	0.10	0.22	0.31	<b>0.85</b>	<b>0.85</b>	<b>1.00</b>	1.00				
SIDI	0.29	0.20	-0.43	0.36	0.43	0.43	0.34	-0.34	0.46	0.37	0.36	0.35	-0.01	-0.01	-0.26	-0.15	0.28	0.29	-0.01	<b>1.00</b>	<b>1.00</b>	<b>0.85</b>	<b>0.85</b>	1.00			
SIEI	0.29	0.20	-0.43	0.36	0.43	0.43	0.34	-0.34	0.46	0.37	0.36	0.35	-0.01	-0.01	-0.26	-0.15	0.28	0.29	-0.01	<b>1.00</b>	<b>1.00</b>	<b>0.85</b>	<b>0.85</b>	<b>0.85</b>	1.00		

Note that only the coefficients in the lower diagonal part are presented above. The computation considers all spatial units at the two different years. Descriptions of the metrics are given in Table 20.2.



## 20.6 Interpretation and Analysis

### 20.6.1 Landscape Level

Based on Figs. 20.6 and 20.7, the spatio-temporal pattern of landscape composition and structure can be characterized at the landscape level for different spatial units. The mean patch size (MPS) is a critical metric and can serve as a habitat fragmentation index (McGarigal and Marks 1995). In 1989, among all eight units, the Pensacola Bay watershed and the city buffer area had the largest and smallest MPS, respectively. The MPS of the Pensacola Bay watershed was 6.91 ha, approximately 14.01% larger than the PEDAs mean patch size which was 6.06 ha; while the MPS of the city buffer area was 4.07 ha, approximately 33% smaller. This indicates that the landscape mosaic in the city buffer area was the most fragmented, while the Pensacola Bay watershed was the least. The two other buffer areas also had smaller MPS than the PEDAs in 1989. Among the four sub-watersheds, the Pensacola Bay had the largest MPS in 1989, followed by the Blackwater River (6.20 ha), the Yellow River (6.13 ha), and the Escambia River (5.22 ha), implying that the landscape mosaic in the Escambia was the most fragmented. In 2002, the mean patch size decreased consistently in each unit when compared with 1989, implying that the

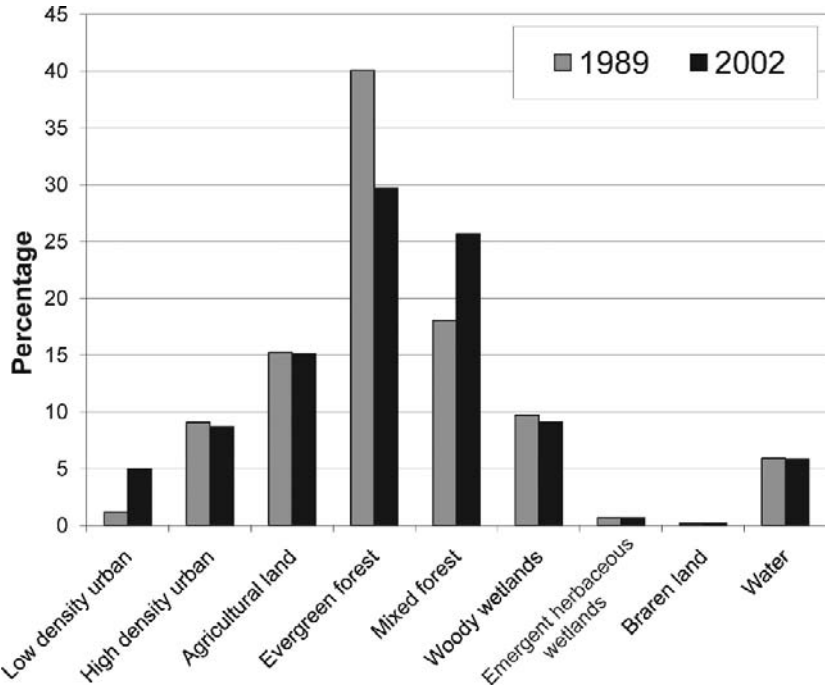


Fig. 20.6 Land use/cover changes for the Pensacola estuarine drainage area during the period of 1989 to 2002

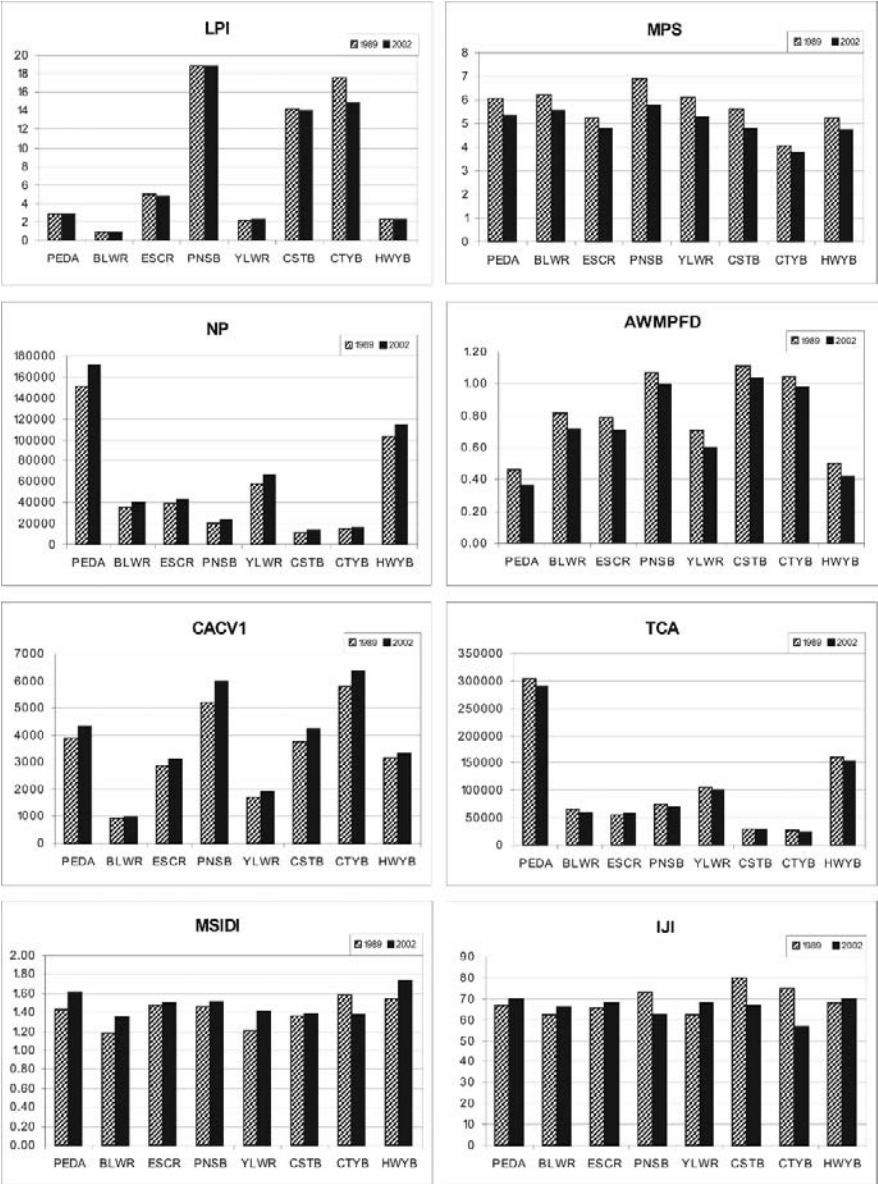


Fig. 20.7 Change in landscape composition and structure for different spatial units at the landscape level. Descriptions of the metrics and the spatial units are given in Table 20.1 and Fig. 20.4, respectively (from Yang and Liu 2005a)

landscape mosaic became more fragmented. In 2002, the Pensacola Bay watershed and the city buffer area were still the two opposite extremes in mean patch size. Among the eight units, the Pensacola Bay watershed had the highest rate of drop in mean patch size (16.32%), followed by the coastline buffers (15.23%), the Yellow River watershed (14.05%), the PEDAs (12.19%), the Blackwater River watershed (10.62%), the highway buffers (9.85%), the Escambia River watershed (8.10%), and the city buffers (7.37%).

In addition to MPS, seven other metrics were used to examine landscape composition or configuration for the entire mosaic at different units. Largest patch index (LPI) quantifies the percentage of total landscape area comprised by the largest patch, which can be used to examine how landscape configuration varies. In both 1989 and 2002, there were three units whose largest patches comprised more than 14% of the landscape: the Pensacola Bay watershed, the city buffer area, and the coastline buffer area. The largest patch in the Blackwater River watershed comprised less than 1% of the landscape. The LPI scores were quite stable between 1989 and 2002 for each unit except the city buffer area, where a decrease of 15.36% occurred.

Number of patches (NP) can be used to quantify spatial heterogeneity of the entire landscape mosaic (McGarigal and Marks 1995). In 1989, the Yellow River watershed had the largest number of patches (57,312) among the four sub-watersheds, followed by the Escambia River (38,763), the Blackwater River (35,566), and the Pensacola Bay (19,976). In 2002, the numbers of patches increased consistently for each unit, with the Pensacola Bay watershed increasing the most (19.50%). This indicates that the landscape mosaic for each unit became more heterogeneous.

Area weighted mean patch fractal dimension (AWMPFD) is an index quantifying the complexity of patch shape, with higher scores indicate greater complexity in patch shape. Among the four sub-watersheds, the Pensacola Bay received the highest AWMPFD scores in both years. The coastline buffer area and city buffer area received much higher scores than the PEDAs. Between 1989 and 2002, the AWMPFD scores for all units decreased, indicating less complexity in patch shape. This further confirms the earlier findings (e.g. Lam and de Cola 1993) that the patch shape of a landscape under intensive human influence tends to be more regular.

Two metrics characterizing core area were examined. Total core area (TCA) reflects both landscape composition and configuration, and can be used to quantify habitat quality (McGarigal and Marks 1995). Among the four sub-hydrological units, the Yellow River watershed had the largest TCA for both years. Between 1989 and 2002, the TCA for each unit shrank consistently. Patch core area coefficient of variation (CACV1) represents the relative variation in core area per patch, and conveys more useful information than TCA (McGarigal and Marks 1995). Among the four watersheds, the Pensacola Bay watershed showed the largest CACV1 scores in both years. In both 1989 and 2002, the city buffer area had larger CACV1 scores than the PEDAs. Between 1989 and 2002, the CACV1 scores increased consistently for all units, implying that the patch core areas became more variable.

The modified Simpson's diversity index (MSIDI) is used to measure diversity at the landscape level. For both 1989 and 2002, the MSIDI scores did not vary much

across units. Between 1989 and 2002, the MSIDI scores for all units except the highway buffer area shrank.

The last index used is IJI (interspersion and juxtaposition index), which measures the extent to which patch types are interspersed. In 1989, the Pensacola Bay watershed had the highest IJI score among four sub-hydrological units, but had the lowest score in 2002. This indicates that the landscape mosaic in Pensacola Bay watershed became less interspersed with similar adjacent patch types. Like the Pensacola Bay watershed, two buffer areas (city and coastline) also showed a decline in their IJI scores. All other units increased somewhat in IJI scores.

### ***20.6.2 Class Level***

The proportion of land use/cover classes for each spatial unit is important information about the composition of landscape mosaic. How this proportion changes can help understand the driving forces behind the observed changes in landscape pattern over space and time. The proportions of land use/cover for each unit are presented in Table 20.5. For the entire PEDA, the largest proportion of land class in 1989 was forest land, occupying 58.01% of the total area; this shrank to 55.48% in 2002. The two urban classes occupied 10.16% of the total area in 1989 and increased to 13.65% in 2002, representing an increase of 34.35%. Both woody wetland and agricultural land shrank slightly between 1989 and 2002.

When compared to the PEDA, the three predefined buffer areas had much higher proportions of urban land in both years. The city buffer area had the largest proportion of urban land among all units, which was 37.44% and 47.54% in 1989 and 2002, respectively, representing an increase of 26.98%. At the same time, forest land and agricultural land shrank by 36.56% and 59.85%, respectively. Between 1989 and 2002, the proportion of urban land in the coastline buffer area increased by 29.30%, while forest land and agricultural land decreased by 28.75% and 37.21%, respectively. Within the highway buffer area, agricultural land declined by 32.13% between 1989 and 2002.

Among the four sub-watersheds, the Pensacola Bay had the largest proportion of urban land in both 1989 (35.94%) and 2002 (45.07%), representing an increase of 25.04%. The proportion of forest land in the Pensacola Bay was the smallest among the four watersheds in both years. Between 1989 and 2002, agricultural land declined by 45.98% in the Pensacola Bay watershed. When compared with the Pensacola Bay watershed, the other three watersheds had a higher proportion of forest land; whereas urban land, although relatively smaller in the percentage, had increased at a much higher rate. Finally, during the period of 1989 to 2002, woody wetland declined consistently for all units with the highest drop rate occurred in the city buffer area.

Further analysis at the class level focuses on eight metrics for three classes: low-density urban, evergreen forest, and woody wetlands. These classes were chosen because they were quite dynamic, as can be seen from Table 20.5. The amount

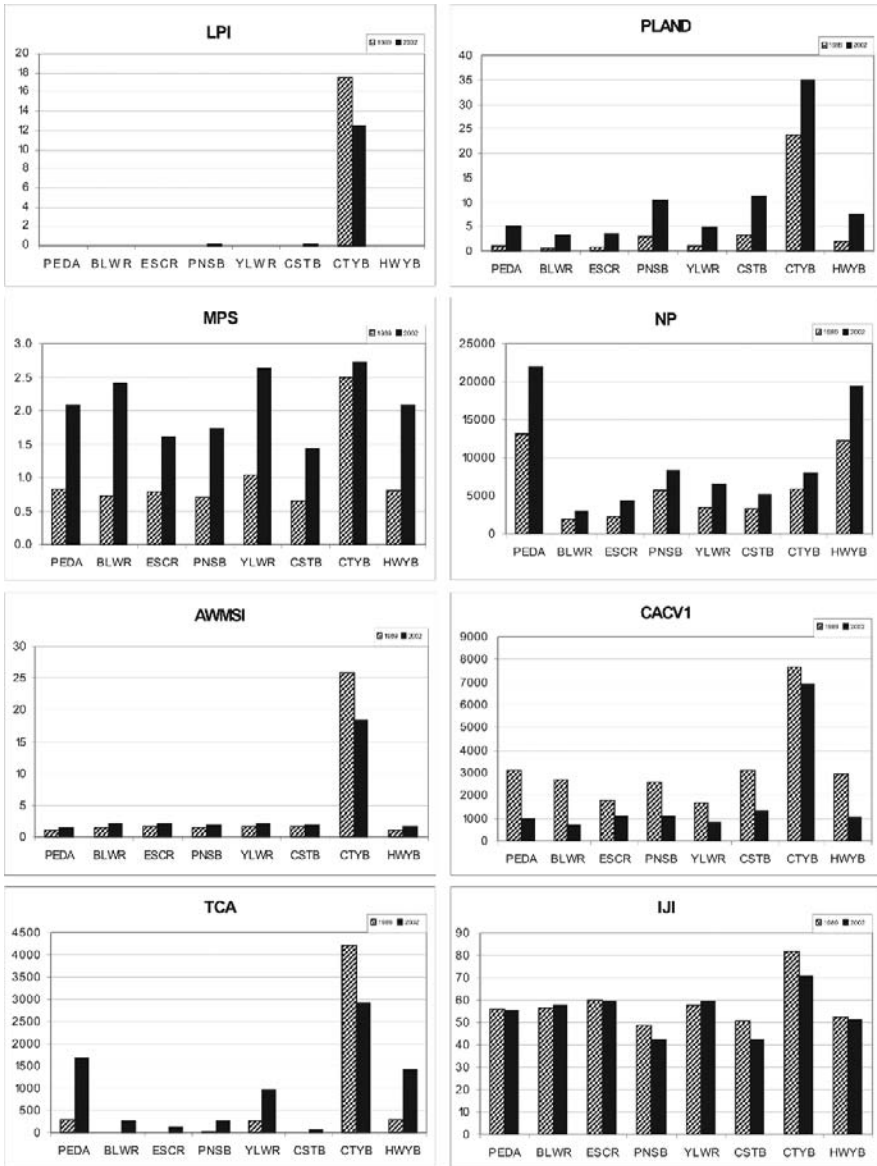
**Table 20.5** Land use/cover proportions for each spatial units

Land Use/Cover*		Spatial Units*							
		PEDA	BLWR	ESCR	PNSB	YLWR	CSTB	CTYB	HWYB
HDU	1989	8.99	6.38	6.74	31.39	7.58	19.70	13.65	11.04
	2002	8.64	6.23	7.08	29.11	7.15	18.59	12.55	10.27
	Change	-3.92	-2.45	5.10	-7.25	-5.59	-5.64	-8.05	-7.04
LDU	1989	1.17	0.62	0.84	4.55	1.00	3.27	23.79	1.83
	2002	5.01	3.26	3.40	15.96	4.90	11.11	34.99	7.39
	Change	326.81	423.67	304.42	250.50	389.65	239.69	47.07	303.26
AGL	1989	15.24	12.97	25.51	3.24	15.84	1.48	4.91	18.70
	2002	15.14	13.89	26.46	1.75	14.81	0.68	4.02	18.52
	Change	-0.69	7.04	3.74	-45.98	-6.51	-54.36	-18.08	-0.94
EGF	1989	40.15	48.36	29.10	34.97	47.96	11.28	13.49	35.89
	2002	29.74	38.82	19.69	29.44	33.81	7.08	5.41	24.36
	Change	-25.93	-19.73	-32.32	-15.83	-29.50	-37.21	-59.85	-32.13
MXF	1989	18.06	21.01	24.58	7.13	17.61	5.91	8.23	16.19
	2002	25.74	27.60	31.00	5.80	30.02	5.16	8.37	23.85
	Change	42.52	31.35	26.10	-18.60	70.42	-12.67	1.69	47.36
WWL	1989	9.73	9.83	11.56	13.13	9.02	8.75	2.42	8.38
	2002	9.14	9.12	11.05	12.41	8.41	7.90	1.87	7.78
	Change	-6.08	-7.21	-4.41	-5.54	-6.76	-9.78	-22.84	-7.22
EHW	1989	0.65	0.34	0.94	2.13	0.37	3.60	0.39	0.73
	2002	0.65	0.63	0.69	2.44	0.27	4.03	0.36	0.69
	Change	0.92	81.99	-27.22	14.64	-25.91	12.05	-7.74	-5.17
BRL	1989	0.10	0.00	0.01	1.72	0.00	2.28	0.99	0.28
	2002	0.10	0.00	0.02	1.70	0.01	2.26	0.28	0.29
	Change	-0.81	-22.95	89.64	-1.25	465.82	-0.97	-72.00	2.64
WTR	1989	5.91	0.47	0.60	1.72	0.62	43.72	32.13	6.96
	2002	5.84	0.45	0.49	1.70	0.61	43.18	32.14	6.86
	Change	-1.12	-3.67	-18.47	-1.25	-1.18	-1.23	0.02	-1.46

\*Descriptions of the abbreviated land use/cover units and the spatial units are given in Table 20.1 and Fig. 20.5.

of low-density urban increased substantially, while evergreen forest and woody wetlands declined consistently in each unit. Substantial change from forest and woody wetland to low-density urban may be an important change in landscape pattern that affects landscape function. Woody wetlands, although relatively small, are ecologically important for wildlife habitat, flood protection, water purification and recreation.

The mean low-density urban patch size (MPS) increased substantially in each unit during the period of 1989–2002 (Fig. 20.8). Among the eight units, the city buffer area had the largest MPS in both years. At the same time, both the number of low-density urban patches (NP) and class proportion (PLAND) increased in each unit. This represents a process of pervasive suburbanization by which numerous residential urban clusters emerged and agglomerated to form larger masses in each



**Fig. 20.8** Change in landscape composition and structure of the low-density urban land class for different spatial units. Descriptions of the metrics and the spatial units are given in Table 20.1 and Fig. 20.4, respectively (from Yang and Liu 2005a)

unit. The largest patch index (LPI) scores were quite small for each unit except the city buffer area. The shape of low-density urban patches was fairly regular, as indicated by relatively low AWMSI (Area-Weighted Mean Shape Index) scores in each unit except the city buffer area, where the AWMSI was quite large in 1989 but shrank substantially in 2002. In both years, the total low-density urban core area (TCA) was quite small for each unit except the city buffer area, where large, well-developed residential areas existed. The city buffer area also had the largest core area coefficients of variation (CACV1) among all units in both years. The IJI scores of low-density urban patches were greater than 40 in each unit for both years. The IJI scores showed little change between 1989 and 2002 except for the Pensacola Bay watershed, the city buffer area, and the coastline buffer area, where residential urban patches became less interspersed with similar adjacent patch types.

Between 1989 and 2002, the mean evergreen forest patch size (MPS) for the PEDAs declined, indicating that the evergreen forest landscape became more fragmented (Fig. 20.9). Among the four watersheds, the Escambia River had the smallest mean evergreen forest patch size in both years. The MPS of evergreen forest patches was relatively large in the Blackwater River and Yellow River watersheds in 1989, but declined substantially in 2002. In both years, the MPS of evergreen forest patches was relatively small for the coastline buffer and city buffer areas. The Pensacola Bay watershed was the only unit where the MPS of evergreen forest patches increased between 1989 and 2002, indicating that many small patches were removed as a result of intensified suburbanization. Between 1989 and 2002, the number of evergreen forest patches (NP) increased in the PEDAs and the watersheds of Blackwater River and Yellow River but declined in other units. The largest evergreen forest patch index (LPI) shrank in each unit. The evergreen forest patch shape tended to be less complex in each unit, as indicated by the decrease in AWMSI (Area-Weighted Mean Shape Index) scores between 1989 and 2002. Among all units, the city buffers and the coastline buffers had the smallest total evergreen forest core area (TCA) but their core area coefficients of variation (CACV1) score was the largest in both years. The TCA scores declined substantially in each unit during the period of 1989 and 2002; this decline in core evergreen forest area can adversely affect many area-sensitive species. The evergreen forest patches were fairly well interspersed in both years.

The Escambia River watershed had the largest mean woody wetland patch size (MPS) in both years (Fig. 20.10). Between 1989 and 2002, the MPS shrank in each unit except the Pensacola Bay watershed and the coastline buffer area where many small-size woody wetland patches were removed due to Pensacola's increased suburbanization. The number of woody wetland patches (NP) declined in each unit except the Blackwater River watershed where a small increase occurred. Among all units, the Escambia River watershed had the largest scores for largest woody wetland patch index (LPI) in both years while the city buffer area had the smallest scores. During the period of 1989 to 2002, the AWMSI (Area-Weighted Mean Shape Index) scores decreased in each unit except the coastline buffer area where a small increase occurred. The city buffer area had the smallest total woody wetland core area (TCA). The Escambia River watershed had the largest total woody

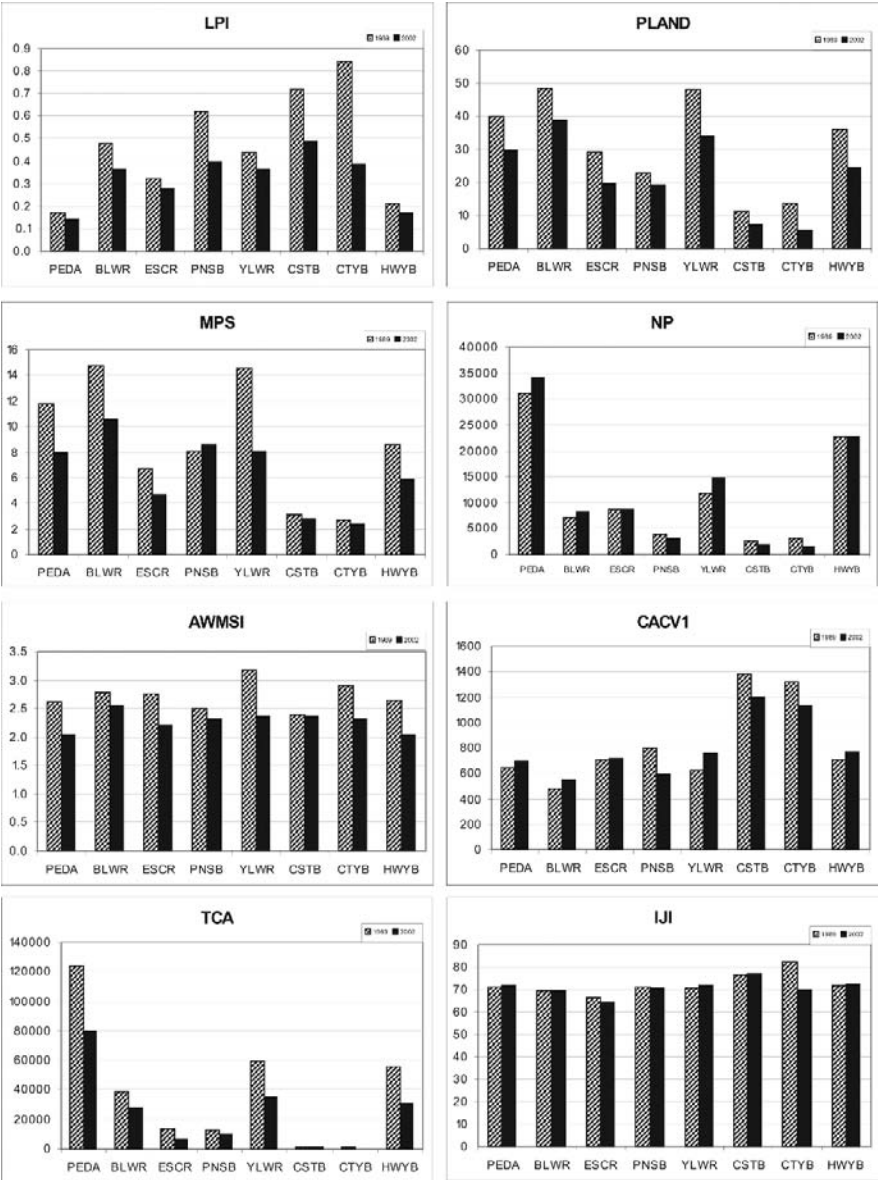
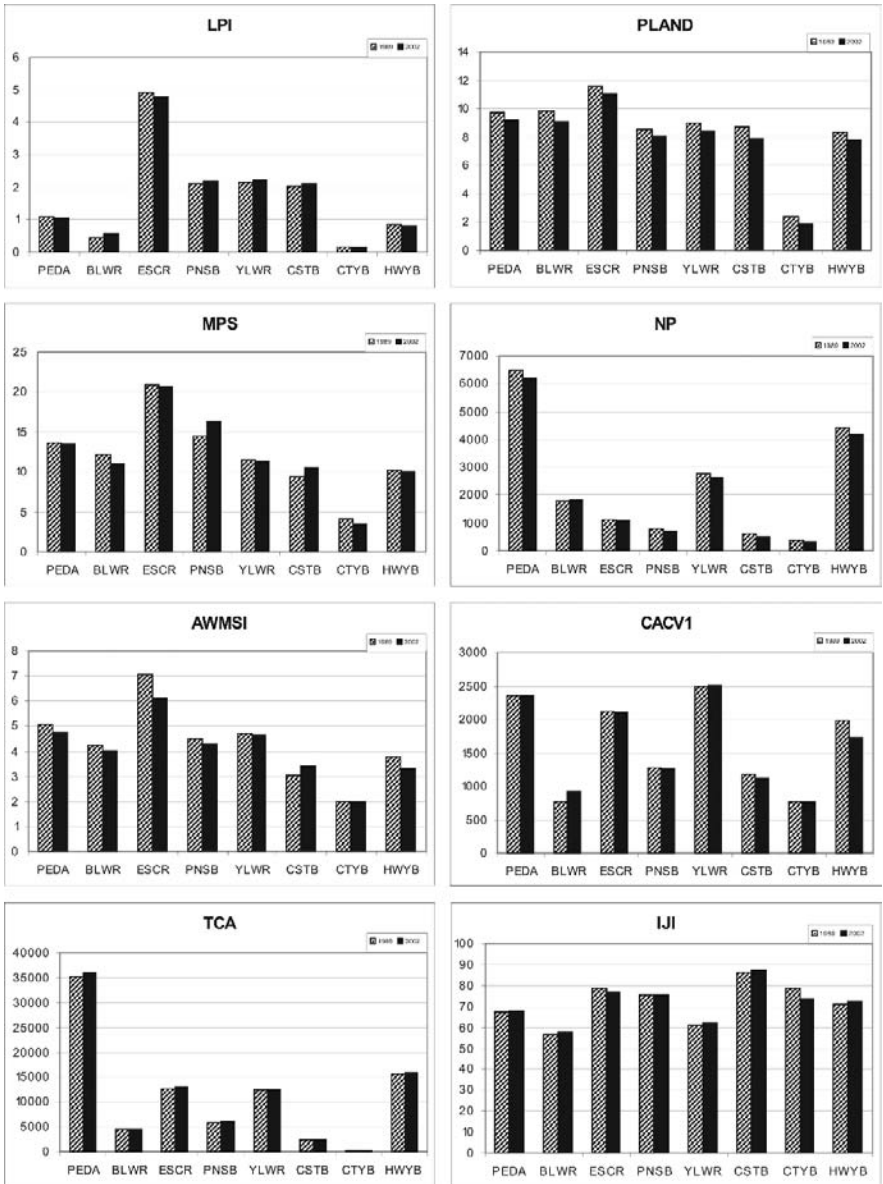


Fig. 20.9 Change in landscape composition and structure of the evergreen forest class for different spatial units. Descriptions of the metrics and the spatial units are given in Table 20.1 and Fig. 20.4, respectively (from Yang and Liu 2005a)





**Fig. 20.10** Change in landscape composition and structure of the woody wetland class for different spatial units. Descriptions of the metrics and the spatial units are given in Table 20.1 and Fig. 20.4, respectively (from Yang and Liu 2005a)

wetland core area among all the four watersheds in both years. The Yellow River watershed has the largest woody wetland core area coefficient of variation (CACV1) among all units in both years. Based on the IJI scores, woody wetland patches were fairly well interspersed in both years.

## 20.7 Summary and Conclusion

Large populations and intensified human economic activities threaten global coastal ecosystem health. Therefore, there is an urgent need to find efficient ways to manage and plan these highly sensitive environments. Analyzing landscape patterns can help understand some important changes emerging from lower-level disturbances due to complex interactions between social and environmental processes. Remote sensing allows a retrospective, synoptic viewing of large regions, thus providing useful data sources for computing landscape metrics that support landscape monitoring and assessment.

This study demonstrates the usefulness of integrating remote sensing and relevant geospatial technologies for coastal landscape pattern characterization. The methods identified here are based on an understanding of landscape features, the nature of landscape metrics, the characteristics of satellite imagery, and information extraction and reduction techniques. The entire research has gone through several major stages from the beginning of data acquisition and collection. The primary data were two Landsat images; ancillary data included ground truth data acquired through GPS-guided field surveys, DOQQs, existing land use/cover datasets, hydrological and political boundaries, road networks, cities, coastlines, among others. This was followed by hierarchic classification and spatial reclassification to produce two land use/cover maps from remotely sensed imagery. The maps were then used as the primary data for computing landscape metrics that quantify ecologically important landscape characteristics. The spatial units used were related to either a hydrological unit or a predefined buffer zone so that the variation of landscape pattern can be characterized. This should help understand the driving forces behind observed changes over space and time. A large set of landscape metrics were computed for different spatial units at the landscape and class levels. Landscape ecology principles, principal component analysis, and Spearman's rank correlation analysis were applied to help identify a small group of core metrics that capture the major properties of a landscape. With the use of these core metrics, the spatio-temporal patterns of landscape composition and structure were quantified for different spatial units at the landscape and class levels. Based on this research, it is found that the integration of remote sensing with other relevant geospatial technologies such as geographic information systems (GIS) and spatial modeling (e.g. landscape metrics and multivariate statistical modeling) has mutually reinforced the utility of these techniques. The integration has provided insights that would not otherwise be available if spatial data were not organized in a GIS environment and GIS were not integrated with remote sensing and spatial modeling. Only through this integration can geospatial technologies be effective for coastal landscape pattern characterization.

At the application level, this study provides a regional case study focusing on the Pensacola estuarine drainage area, one of few exemplary large-scale river-driven estuarine systems across the northern Gulf of Mexico. This study reveals that the overall landscape mosaics became more heterogeneous and the classes of patches tended to be more fragmented, which are largely driven by Pensacola's fast urban and economic growth since the beginning of 1990s. It is found that landscape composition and structure varied greatly across different spatial units. Landscape fragmentation was more intensive in the Pensacola Bay watershed, along the coastlines, and around the city centers, where urbanization and human economic activities were more concentrated. These findings should be useful not only to those who study coastal watershed dynamics but also to those who must manage and provide services in such a sensitive ecosystem. Coastal managers in the Pensacola estuarine drainage area should target the highly fragmented areas where restoration, management, or changes in policies are needed to slow, stop, or reverse declining environmental trends. Given that many world-wide coastal watersheds face the growing problems caused by urban and economic development, the landscape pattern characterization technical framework developed in this study focusing on Pensacola bay can be easily applicable to other coastal drainage basins. This method can improve our understanding of socio-ecological dynamics of landscape, thus facilitating a sophisticated approach to coastal conservation and protection.

**Acknowledgement** This project was partially funded through several summer research grants given by the Florida State University and the University of West Florida and a major research grant from the US Environmental Protection Agency's Science to Achieve Results (STAR) Estuarine and Great Lakes (EaGLe) program through funding to the CEER-GOM, US EPA Agreement R829458. The author wishes to thank Zhi Liu for his research assistance.

## References

- Anderson JR, Hardy EE, Roach JT, Witmer RE (1976) A land use and land cover classification system for use with remote sensor data. USGS Professional Paper 964, Sioux Falls, S. D., USA
- Baskent E-Z, Kadiogullari A-I (2007) Spatial and temporal dynamics of land use pattern in Turkey: A case study in Inegol. *Landscape Urban Plan*, 81:316–327
- Cain D, Riitters K, Orvis K (1997) A multi-scale analysis of landscape statistics. *Landscape Ecol* 12:199–212
- EPA (1999) The ecological condition of estuaries in the Gulf of Mexico. EPA 620-R-98-004
- Forman RRT (1995) *Land mosaic: the ecology of landscapes and regions*, 2nd edn. Cambridge University Press, England
- Fuller DO (2001) Forest fragmentation in Loudoun County, Virginia, USA evaluated with multi-temporal Landsat imagery. *Landscape Ecol* 16:627–642
- Griffith JA, Martinko EA, Price KP (2000) Landscape structure analysis of Kansas at three scales. *Landscape Urban Plan* 52:45–61
- Gustafson EJ (1998) Quantifying landscape spatial pattern: what is the state of the art? *Ecosystems* 1:143–156
- Hall FG, Strebel DE, Nickeson JE, Goetz SJ (1991) Radiometric rectification: toward a common radiometric response among multitemporal, multisensor images. *Remote Sens Environ* 35:11–27

- Halpern BS, Walbridge S, Selkoe KA, Kappel CV, Micheli F, D'Agrosa C, Bruno JF, Casey KS, Ebert C, Fox HE, Fujita R, Heinemann D, Lenihan HS, Madin EMP, Perry MT, Selig ER, Spalding M, Steneck R, Watson R (2008) A global map of human impact on marine ecosystems. *Science* 319:948–952
- Herzog F, Lausch A (2001) Supplementing land-use statistics with landscape metrics: some methodological considerations. *Environ Monit Assess* 72:37–50
- Hobbie JE (ed) (2000) *Estuarine science: a synthetic approach to research and practice*. Island Press, Washington, DC, USA
- Hollister JW, August PV, Paul JF (2008) Effects of spatial extent on landscape structure and sediment metal concentration relationships in small estuarine systems of the United States' Mid-Atlantic Coast. *Landscape Ecol* 23:91–106
- Hunsaker C, O'neill R, Jackson B, Timmins S, Levine D, Norton D (1994) Sampling to characterize landscape pattern. *Landscape Ecol* 9:207–226
- Jensen JR (2005) *Introductory digital image processing: a remote sensing perspective*, 2edn. Prentice-Hall, New Jersey
- Lam NSN, de Cola L (eds) (1993) *Fractals in geography*. Prentice Hall, New Jersey
- Leitao AB, Ahern J (2002) Applying landscape ecological concepts and metrics in sustainable landscape planning. *Landscape Urban Plan* 59:65–93
- Levinson B (2005) Remote sensing and the EPA Estuarine and Great Lakes Research Program. *Int J Remote Sens* 26:5343–5346
- Li X, Lu L, Cheng G, Xiao H (2001) Quantifying landscape structure of the Heihe River Basin, north-west China using FRAGSTATS. *J Arid Environ* 48:521–535
- Liu YB, Nishiyama S, Kusaka T (2003) Examining landscape dynamics at a watershed scale using landsat TM imagery for detection of wintering hooded crane decline in Yashiro, Japan. *Environ Manage* 31:365–376
- Martinez ML, Intralawan A, Vazquez G, Perez-Maqueo O, Sutton P, Landgrave R (2007) The coasts of our world: Ecological, economic and social importance. *Ecolog Econ* 63:254–272
- Marsh OT (1966) *Geology of Escambia and Santa Rosa counties, western Florida panhandle*. Florida Geological Survey Bulletin 46
- McGarigal K (2002) Landscape Pattern Metrics. In: El-Shaarawi AH, Piegorisch WW (eds) *Encyclopedia of environmetrics*, vol 2. Wiley & Sons, England, pp 1135–1142
- McGarigal K, Marks BJ (1995) FRAGSTATS: Spatial pattern analysis program for quantifying landscape structure. USDA forest service technical report PNW-GTR-351
- NFWMD (1997) *The Pensacola bay system surface water improvement and management plan*, Program development series 97–92
- Niemi G, Wardrop D, Brooks R, Anderson S, Brady V, Paerl H, Rakocinski C, Brouwer M, Levinson B, Mcdonal DM (2004) Rationale for a new generation of ecological indicators for coastal waters. *Environ Health Persp* 112:979–986
- NOAA (1999) ORCA's coastal assessment framework (CAF). Available online: <http://spo.nos.noaa.gov/projects/cads/description.html#caf> (Last access on 24 July 2007)
- NRC (2000) *Clean coastal waters: understanding and reducing the effects of nutrient pollution*. National Academy Press, Washington, DC, USA
- Munroe DK, Nagendra H, Southworth J (2007) Monitoring landscape fragmentation in an inaccessible mountain area: Celaque National Park, Western Honduras. *Landscape Urban Plan* 83:154–167
- Renofalt BM, Nilsson C, Jansson R (2005) Spatial and temporal patterns of species richness in a riparian landscape. *J Biogeography* 32:2025–2037
- Richmond RH, Rongo T, Golbuu Y, Victor S, Idechong N, Davis G, Kostka W, Neth L, Hamnett M, Wolanski E (2007) *Watersheds and coral reefs: Conservation science, policy, and implementation*. *Biosci* 57:598–607
- Riitters KH, O'neill RV, Hunsaker CT, Wickham JD, Yankee DH, Timmins SP, Jones KB, Jackson BL (1995) A factor analysis of landscape pattern and structure metrics. *Landscape Ecol* 10:23–39

- Shi H, Singh A (2003) Status and interconnections of selected environmental issues in the global coastal zones. *Ambio* 32:145–152
- Turner MG (1990) Spatial and temporal analysis of landscape patterns. *Landscape Ecol* 4:21–30
- Turner MG, Gardner RH, O'neill RV (2001) *Landscape ecology in theory and practice*. Springer-Verlag, New York
- Yang X (2002) Satellite monitoring of urban spatial growth in the Atlanta metropolitan area. *Photogramm Eng Rem S* 68:725–734
- Yang X (2005) Remote sensing and GIS applications for estuarine ecosystem analysis: an overview. *Int J Remote Sens* 26:5347–5356
- Yang X, Liu Z (2005a) Quantifying landscape pattern and its change in an estuarine watershed using satellite imagery and landscape metrics. *Int J Remote Sens* 26:5297–5323
- Yang X, Liu Z (2005b) Using satellite imagery and GIS to characterize land use and land cover changes for integrated estuarine watershed assessment. *Int J Remote Sens* 26:5275–5296
- Zhang D, Wallin DO, Hao Z (1997) Rates and patterns of landscape change between 1972 and 1988 in the Changbai Mountain area of China and North Korea. *Landscape Ecol* 12:241–254

**Part V**  
**Integrated Coastal Ecosystem Assessment**

## Chapter 21

# Remote Sensing and Spatial Analysis of Watershed and Estuarine Processes for Conservation Planning in Elkhorn Slough, Monterey County, California

Kristin B. Byrd

The Elkhorn Slough watershed, located on the coast of Monterey Bay in Central California, is a significant Pacific Coast estuarine system. It has become a nexus of remote sensing research due to partnerships with multiple nearby institutions, and innovative approaches in the research area have addressed several management issues in the watershed. Historical ecological research with archival aerial photographs identified significant trends in marshland conversion to other habitat types, mainly from hydrological modifications but also from off-farm sedimentation. Research addressing nutrient and sediment runoff demonstrate the potential to correlate estuarine disturbance and response to watershed inputs or properties. Spectral indices from HyMap hyperspectral imaging of salt marsh vegetation were correlated with water nutrient enrichment. Also the current extent of sedimentation in the salt marsh was linked to historical land cover and physical watershed variables. Repeat multibeam bathymetry surveys identify regions of the slough with high erosion rates from tidal scour and point to causes of salt marsh conversion. Despite challenges associated with these applications, remote sensing and GIS analyses, especially salt marsh vegetation change detection and bathymetric change detection, inform current restoration planning efforts described in the Elkhorn Slough Tidal Wetland Strategic Plan. Multiple committees and working groups have formed a consensus on the need to address the problem of tidal scour partly due to the availability of high quality, high resolution spatial data. In addition GIS-based watershed management continues to improve estuarine conditions, as agencies, land trusts and private landowners have reduced nutrient and sediment inputs through restoration and erosion control.

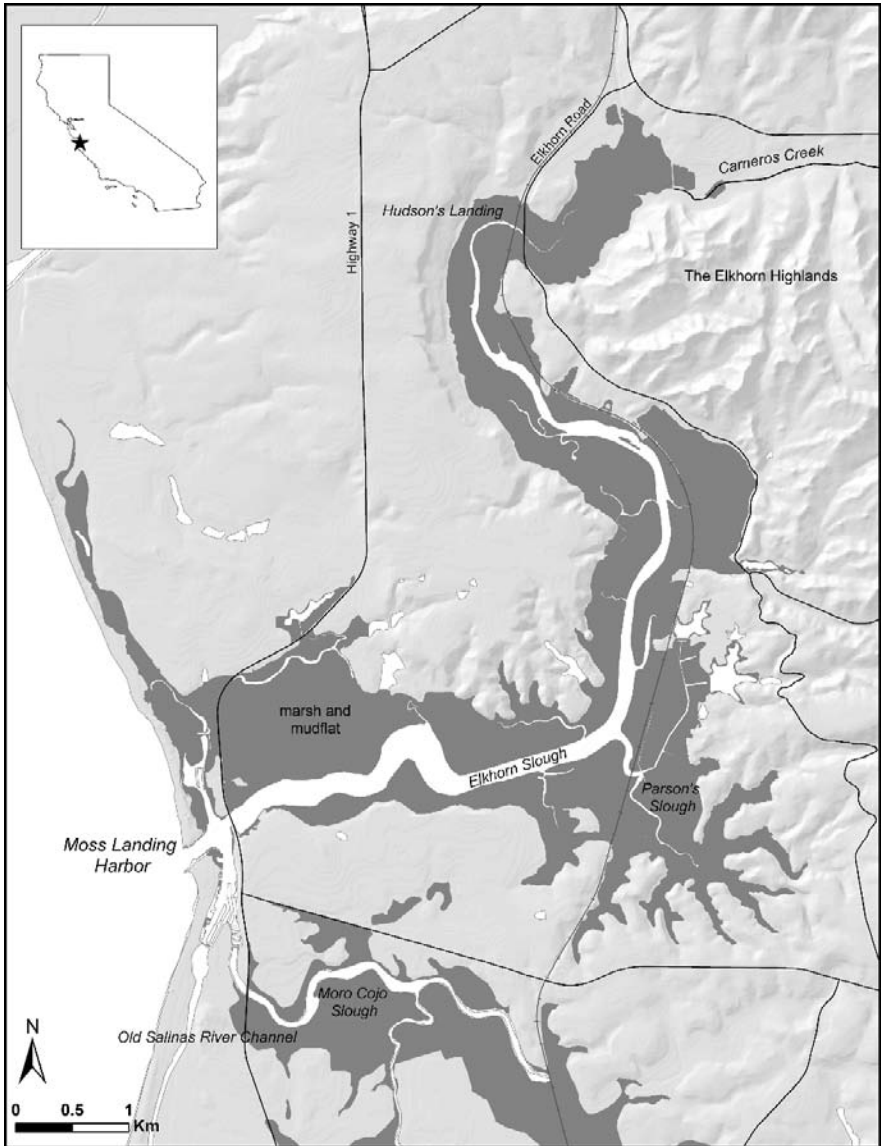
### 21.1 Overview of the Elkhorn Slough Watershed

The Elkhorn Slough watershed, located on the coast of Monterey Bay in Central California, is a significant estuarine system in California, with its tidal marshland

---

K.B. Byrd (✉)

California Academy of Sciences, San Francisco, CA 94118, USA  
e-mail: kbyrd@calacademy.org



**Fig. 21.1** The Elkhorn Slough watershed and Moss Landing Harbor, located on the coast of Monterey Bay in Central California

extent only second to that of San Francisco Bay (Fig. 21.1). The slough is a seasonal estuary extending inland for 11.4 km from Monterey Bay and contains approximately 1,090 ha of estuarine habitat types including subtidal channels, tidal creeks, mudflats, salt marshes, and tidal brackish marshes (Elkhorn Slough Tidal Wetland Project Team 2007). As only about 3% of conterminous United States salt marsh



acreage occurs along the Pacific Coast (Field et al. 1991), this represents a significant resource for wildlife, fisheries, research and education, and recreation. Despite its proximity to the urbanized Silicon Valley (about 90 km), Elkhorn Slough and its surrounding watershed have retained high biodiversity, attractive viewsheds, and open space. Elkhorn Slough estuarine habitats support over 340 birds (135 aquatic species), 550 marine invertebrates, and 102 fish species including 24 rare, threatened or endangered species (Caffrey et al. 2002). The watershed is drained by many small seasonal streams and one main channel, Carneros Creek. Steep hills rise 30 to 100 m from the marsh; while many hills are cultivated, the uplands contain a rich matrix of oak woodland, grassland and ridges covered with rare central maritime chaparral plant communities, including several endemic plant species. This diverse, interdependent complex of upland and wetland habitat types supports a diversity of species that may be the highest in California for a watershed of its size, 182 km<sup>2</sup> (Elkhorn Slough Foundation and Tom Scharffenberger Land Planning and Design 2002).

Over a century of human activity has affected Elkhorn Slough's natural environments in ways that have altered ecosystem processes required to sustain the rich complex of habitats and species diversity both within the estuary and its watershed. In 1872 a raised embankment for the Southern Pacific Railroad was constructed through the marshlands, and during the early to mid 1900s tidal wetlands were converted to pastureland for dairy operations, salt evaporation ponds, and waterfowl habitat (Van Dyke and Wasson 2005). In 1947 the U.S. Army Corps of Engineers modified the Elkhorn Slough main channel and created a new opening to Monterey Bay to accommodate vessel traffic in the newly created Moss Landing Harbor. Prior to this point, Elkhorn Slough joined the Salinas River, which meandered north along the shoreline and entered the bay approximately 1 km from the present-day harbor (Fig. 21.2). In less than 50 years the slough changed from a largely freshwater regime dominated by deposition from the Salinas River and surrounding watershed to a highly saline system characterized by stronger tidal flow and greater tidal reach (Schwartz et al. 1986, Crampton 1994). Within the watershed, farming on the plateau west and north of Elkhorn Slough began in the late 1880s with establishment of potatoes and sugar beets (ABA Consultants 1989) and intensified in the 1970s with the expansion of strawberry farms in response to growing markets (Dickert and Tuttle 1980, Caffrey et al. 2002). Between 1981 and 1993, crop area in the watershed increased 29%, with strawberry acreage increasing 53% (USDA-SCS 1994). Currently 24% of the Elkhorn Slough watershed is intensively farmed (Caffrey et al. 2002).

The ridge tops and south facing slopes of the eastern portion of the upper watershed, the Elkhorn Highlands, are highly desirable for farmers and residential buyers, which threatens large areas of undisturbed central maritime chaparral. A majority of the soils in the watershed uplands are derived from the Aromas sands formation, an aeolian sandy parent material producing soils with high sand content that are highly erodible when disturbed (Fig. 21.3). As the hills are highly susceptible to erosion, the health of aquatic habitats is intertwined with preservation of central maritime chaparral. With vegetation clearing, the sandy soils underneath can be washed away

**Fig. 21.2** Aerial photographs comparing the mouth of Elkhorn Slough in 1931 (prior to the 1947 construction of Moss Landing Harbor) and 1949. *Circles* represent where the Elkhorn Slough estuary enters Monterey Bay. Source: Elkhorn Slough Tidal Wetland Project Team (2007)





**Fig. 21.3** A mosaic of habitat types, including pickleweed-dominated diked salt marsh in the foreground, agricultural fields on the hillside, and coast live oak woodland and central maritime chaparral on the hilltops. Source: Tuxen (2003)

by winter runoff and greatly impact downstream wetlands (Elkhorn Slough Foundation and Tom Scharffenberger Land Planning and Design 2002).

The Elkhorn Slough watershed spans a complex patchwork of public and privately-owned lands. The southeastern portion of the estuary contains a NOAA National Estuarine Research Reserve (ESNERR), designated in 1979. The California Department of Fish and Game manages the 631 ha Research Reserve along with 583 ha of other wetlands including the Moss Landing Wildlife Management Area. The Elkhorn Slough Foundation, a land trust, and the Nature Conservancy have acquired through fee or easement 194 ha of wetland and 1227 ha of upland for conservation purposes. Together these land acquisitions and state designations account for a quarter of the estuary's habitats (Elkhorn Slough Tidal Wetland Project Team 2007). Cooperation among public and private owners, state and local agencies, and academic institutions have facilitated a conservation and restoration planning process targeting protection of important biological resources.

Likewise through the involvement of multiple institutions, Elkhorn Slough has become a nexus of remote sensing research. The ESNERR brings an inflow of GIS and remote sensing resources from the NOAA Coastal Services Center. Proximity to Silicon Valley, the home of NASA Ames Research Center, and the high concentration of research institutions in Monterey Bay, including the U.S. Naval

Postgraduate School, the Monterey Bay Aquarium Research Institute, the University of California, Santa Cruz and California State University, Monterey Bay also provide significant resources.

This chapter describes the influence of a conservation planning process in Elkhorn Slough on research applying GIS and remote sensing technologies. The chapter features innovations in geospatial research that address impacts to this estuarine system. It further highlights how results from these studies have informed recent planning strategies. Three areas of research relevant to Elkhorn Slough conservation and restoration are covered: historical ecology, connections between watershed land use and estuarine response, and change detection of tidal marsh and slough bathymetry.

## 21.2 Early Planning Initiatives

By 1999 State and federal land designations as well as several conservation programs were in place, and several individuals representing non-profit, local and state government, and academic institutions came together to develop a Watershed Conservation Plan that would guide future conservation activities. Central to this planning process was the development of a GIS, which was used to assess spatial distribution of biological resources and land use patterns in order to prioritize lands for acquisition, management and restoration. The plan identified critical resources, most significant threats to these resources, and strategies to protect these resources over time (Scharffenberger et al. 1999). Critical resources, or conservation targets, were defined as natural wetland and upland habitats and the rare and endangered species they support, and productive agricultural areas vital to the local and county economy. The report identified the most significant threats to Elkhorn Slough to be: (1) sedimentation and contamination of marshes mostly due to uncontrolled runoff from steep cultivated fields, (2) destruction and fragmentation of maritime chaparral habitat from residential development, (3) depletion of groundwater and accompanying seawater intrusion from excess pumping of wells for irrigation and (4) loss of marsh habitat by tidal erosion and conversion from human manipulation of marsh hydrology. These threats remain a high priority for resource managers, and threats (1) and (4) have been the focus of remote sensing-based research over the past eight years.

The location, area and distribution of conservation targets were mapped from aerial photography, and a planning strategy was built around five conservation zones delineated to represent major regions of the watershed that contained the most intact remaining conservation targets in the area. Generally, overarching conservation strategies applied to each zone were to acquire unprotected parcels through fee title or conservation easement, create vegetated buffers between cultivated fields and wetlands, and restore natural habitat where possible.

These conservation strategies were further refined in a follow-up planning document in 2002, called "Elkhorn Slough at the Crossroads" (Elkhorn Slough Foundation and Tom Scharffenberger Land Planning and Design 2002). One of its

major contributions was a more complete understanding of the watershed's sensitive habitats through detailed vegetation mapping. Authors of the report identified a high diversity of unusual interdependent habitats and reinforced the need to properly manage land uses since aquatic resources were so heavily impacted by runoff from cultivation and development. Upon completion of the report, the director of the Elkhorn Slough Foundation, Mark Silberstein stated, "The process of developing the GIS and the layers of information behind the maps has brought a new appreciation for the importance, beauty and fragility of the slough. Accurate mapping provides the basis for sound land use decisions and we supply this information in the spirit of informed dialogue as the community works toward a vision of the future of this part of the coast and toward a new General Plan for the County."

The keystone of the report was a vegetation map created through hand digitizing aerial photography in order to update the 1999 Watershed Conservation Plan's biological and agricultural resource inventories. The map contained 18 classes including dominant vegetation types and land uses such as agriculture, greenhouses, and developed areas. From these maps and coordinated efforts a vision was developed to create an intact and interconnected network of natural communities including over 1616 ha of coastal marsh within Elkhorn Slough and Moro Cojo Slough to the south, enhanced freshwater wetlands of McClusky Slough to the north, restored riparian forest along the lower Carneros Creek floodplain, and a series of upland ridges with unfragmented maritime chaparral in the Elkhorn Highlands. These natural communities were to be surrounded by productive, habitat-compatible farmland, scenic vistas and residences.

### 21.3 A Remote Sensing Approach to Historical Ecology

The implementation of conservation and restoration strategies in Elkhorn Slough required information about the area's environmental baseline conditions prior to major human modification of the watershed. Historical information has become increasingly important in setting sustainable management goals and has become central to the field of restoration ecology (Swetnam et al. 1999). Historical ecology is characterized by the use of a long time sequence of measurements or observations to gain information about changes in populations, ecosystem structures, disturbance frequencies, process rates, trends, and periodicities (Swetnam et al. 1999). Applied historical ecology involves the use of historical knowledge in ecosystem management and planning.

Recognizing the importance of historical information for informing conservation decisions, an historical ecology research program was developed at ESNERR. This program was made feasible by the rich archive of historical maps and aerial photographs of the region, due to the coastal location of the watershed and its proximity to the historical city of Monterey (Van Dyke and Wasson 2005). The direction of historical ecology research at ESNERR and elsewhere were influenced by two anthropogenic impacts discussed in the early planning documents: long-term

human modification of marsh hydrology and sedimentation into the slough from eroding upland cultivated areas. As research progressed, innovative remote sensing techniques were developed to discern historical environmental conditions from the archival materials and to assess historical ecological changes. The use of historical geographical data, like aerial photographs, for map-making is a key component of historical ecology research, as maps most clearly illustrate the relationship between physical processes and habitats, habitats and species, and habitats of different kinds (Grossinger 2001). Maps also can help identify significant historical habitat types and current habitat remnants that are an important source of regional species diversity (Grossinger 2001).

Aerial photography, which began early in the 20th century, is an especially important tool for monitoring long-term ecological changes. Not only can aerial photographs be used to quantify ecosystem changes, but they can help explore explicit linkages between ecosystem change and human resource uses that drive those changes. While several remote sensing data sources are available to map coastal areas and wetlands [e.g. Light Detection and Ranging (LiDAR) data, Landsat satellite imagery, Airborne Data Acquisition and Registration (ADAR) imagery], only color or color infrared (IR) aerial photography provides the combination of spatial and spectral resolution and temporal scale required to conduct long-term historical time series analysis of wetland change at fine spatial scales such as the plant community level.

Despite the advantageous spatial resolution provided by most aerial photography, the method of image capture creates several challenges when using the data. Problems with color balance and geometric distortion exist due to camera tilt, relief displacement, lens distortion, and atmospheric refraction, which can cause scale variation and horizontal error (Dickert and Tuttle 1980, Bolstad 1992, Barrette et al. 2000) and must be rectified. Contact printing and scanning introduce more distortion (Moore 2000), and the process of matching ground control points during rectification is another source of error (Van Dyke and Wasson 2005). Ideally, the problem being studied would determine the time between image dates chosen for historical studies or the frequency of change detection. Ultimately however, the availability of imagery influences the choice of image dates and what historical processes can be identified (Klema 2001).

At ESNERR a project was initiated to track trends in tidal wetland habitat changes due to human modification of the Elkhorn Slough system. Developing an efficient method for georeferencing and mosaicking multiple color and color IR contact prints was a key step to extracting information from historical aerial photographs. Van Dyke and Wasson (2005) scanned, georectified and mosaicked 26 historical maps and charts dating from 1853 to 1925 and 13 aerial photograph flights taken between 1931 and 2003, which together comprised more than 300 photos. This combination of black and white, true color and color IR aerial photos were scanned to produce a resolution of 0.6 m/pixel after rectification. Ground control features were identified in 0.6 m/pixel digital orthophotographs. Because image distortion increases with increasing distance from the image center, the team constructed the mosaic using the central portion of each overlapping image. This

central “effective area” was identified with a script that applied a proximity function and created a honeycomb polygon shapefile that served as a mask for assembling the mosaic. Control points were located at well spaced locations near the perimeter of the effective areas. Because camera tilt was likely the greatest source of distortion, the images were resampled with a four-point plane projective model.

Van Dyke and Wasson (2005) conducted a marsh and tidal creek time series analysis on 196 fixed 100 m<sup>2</sup> quadrats and 196 tidal creek cross sections in undiked areas from 12 dates ranging between 1931 and 2003. Within each quadrat and date they determined the percentages of vegetated salt marsh and unvegetated areas. Typical of Northern California salt marshes, the dominant vegetation at Elkhorn Slough is pickleweed (*Sarcocornia pacifica*), a low-growing succulent plant that forms dense monospecific stands across the marsh plain.

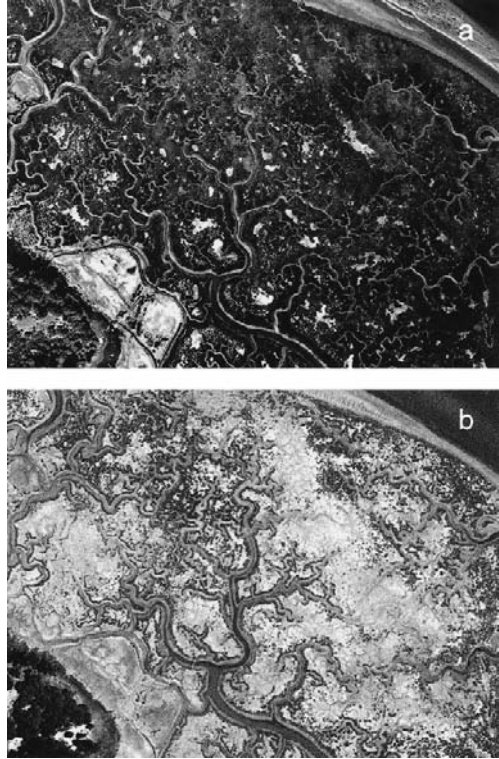
Black and white historical aerial photographs provide limited capacity to differentiate plant community types, especially through automated classification methods. To address this issue image classification was accomplished using a custom interactive application to perform semi-automated image interpretation. Starting with the first quadrat, the user selects a threshold grayscale value that defines the iso-line boundaries between vegetated and bare portions, then the tool automatically produces the corresponding set of polygons (vegetated and unvegetated) within a shapefile. Moving across the aerial photo, the initial grayscale selection seeds the selection for the following quadrat, and the tool allows the user to adjust the grayscale value to account for contrast variations among quadrats. All analysis was performed on grayscale imagery; for color IR photos the researchers converted red-green-blue to hue-saturation-intensity then interpreted the intensity component.

Interpretation of these aerial photos demonstrated that major changes to Elkhorn Slough’s wetland habitats occurred over 150 years. Since 1870 more than two thirds of the slough’s salt marsh has either degraded or been converted to other habitat types. From 1870 to 1956 the construction of more than 60 km of levees and embankments reduced the range of unobstructed tidal influence by 59%. During this same period of extensive diking, the extent of intact salt marsh (veg cover >75%) decreased by 66%. By 2000 the extent of high-quality marsh was 23% of its coverage 100 years before (Fig. 21.4) (Van Dyke and Wasson 2005).

From the quadrat analysis it became clear that much of the upper slough that was once densely vegetated is now mudflat and open water. The mean percentage of salt marsh vegetation cover in undiked areas decreased from 89.6% to 46.4% in 2003. Tidal creeks have also become wider in undiked areas, from an average of 2.5 m in 1931 to 12.4 m in 2003. The extent of marsh loss and changes in creek channel width increased with increasing distance from Monterey Bay (Fig. 21.5).

The changes to Elkhorn Slough’s marshlands over 100 years were attributed to two major alterations in the slough’s hydrology: restrictions to the range of tidal flow occurring earlier in the study period and expansion of tidal range, amplitude, and velocity that occurred since the opening of Moss Landing Harbor in 1947 (Van Dyke and Wasson 2005). The newly created, deeper, wider channel entrance to Monterey Bay increased the velocity and amplitude of tidal exchange within the slough, transforming it into a highly erosional system. The marsh quadrat and tidal creek analysis

**Fig. 21.4** An example of evolution of salt marsh to mud flat. Dark areas are salt marsh, light areas are unvegetated. (a) Tidal creek network and growing interior panes, 1980 aerial photo. (b) Deteriorated marsh largely converted to open mud flat, 2001 aerial photo. Source: Van Dyke and Wasson (2005), Fig. 8, p. 185; © 2005 Estuarine Research Federation, with kind permission of Springer Science and Business Media

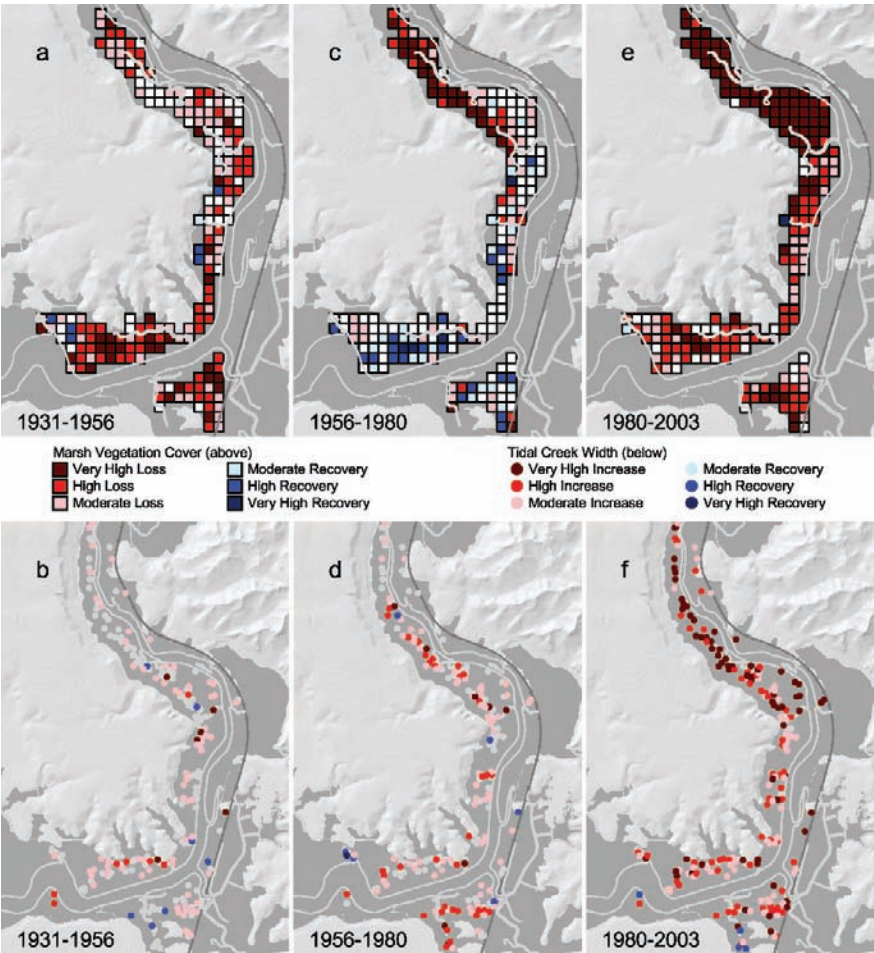


showed that conversion of salt marsh habitat to mudflat and widening of tidal creeks accelerated only after 1949, timing that coincides with artificial channel opening (Van Dyke and Wasson 2005).

Moving up into the watershed, an earlier study (Dickert and Tuttle 1980) examined historical land use change between 1931 and 1980 and calculated erosion rates associated with different land uses, soil types, and slopes. The authors identified sediment fans resulting from this erosion that had formed in the marsh at the base of slopes draining into the slough. Between 1931 and 1980 there was a 5-fold increase in the number of sediment fans and a doubling of their acreage in the pickleweed marsh as agriculture in the watershed increased by 282%. By 1980 at least 30 sediment fans had formed in the salt marsh, ponds, and freshwater marsh of Elkhorn Slough.

Another historical ecology project based out of the University of California, Berkeley, addressed this problem of watershed erosion and examined how sedimentation from eroding cultivated areas buried salt marsh vegetation at the upland margin of the slough. Byrd et al. (2004) analyzed the same archive of historical aerial photos used by Van Dyke and Wasson to produce a time series of vegetation change on sediment fans over four decades. A combination of black and white and color IR aerial photographs and orthophotos from May 1971, April 1980, May 1992,





**Fig. 21.5** Annualized change, vegetation cover and tidal creek width. 1931–1956: (a) High to very high marsh loss at lower slough; moderate loss at mid and upper slough. (b) Low to moderate overall tidal creek width increase. 1956–1980: (c) Little change or marsh recovery at lower and mid slough; very high loss at upper slough. (d) High to very high creek width increase at upper slough and southern part of lower slough; low to moderate increase elsewhere. 1980–2003: (e) Moderate to high marsh loss at lower and mid slough; very high loss at upper slough. (f) Moderate to very high creek width increase at lower and mid slough; very high increase at upper slough. Source: Van Dyke and Wasson (2005), Fig. 6, p. 183; © 2005 Estuarine Research Federation, with kind permission of Springer Science and Business Media

and May and June 2001 were chosen for analysis, and May 1931 aerial photographs provided reference conditions. Again all photos were scanned to generate digital images with a resolution of approximately 0.6 m/pixel. This sub-meter resolution was required to differentiate vegetation types in the salt marsh. Fifteen sediment fans present in salt marsh, both diked and undiked, were chosen as study areas.

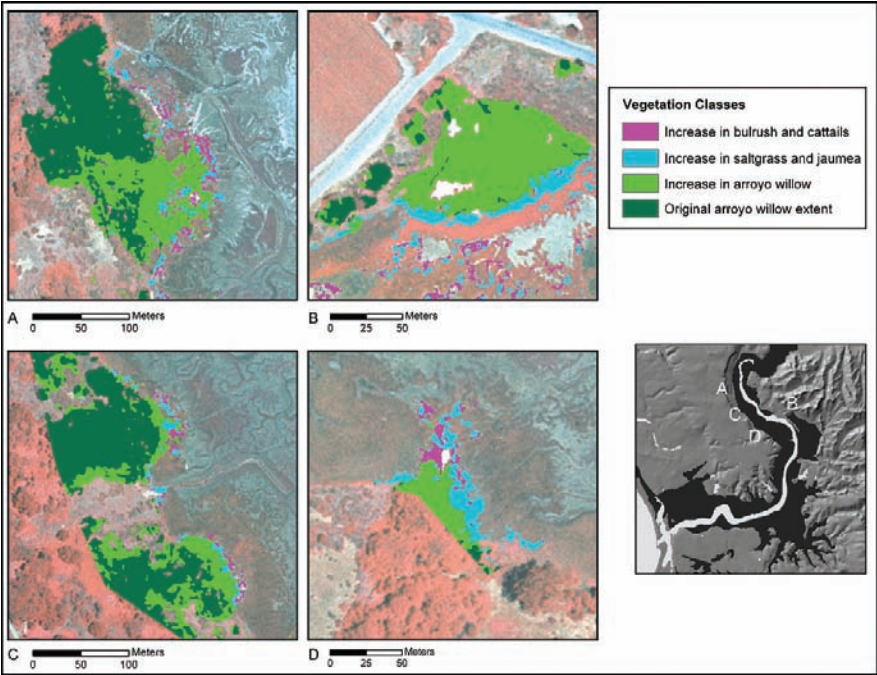
The color IR images (1980, 1992, and 2001) were classified based on a plant community level scheme derived from "A Manual of California Vegetation" (Sawyer and Keeler-Wolf 1995), and classes included bare soil (including mudflat), pickleweed, saltgrass/jaumea (*Distichlis spicata/Jaumea carnosa*), bulrush/cattail (*Schoenoplectus* spp./*Typha* spp.), arroyo willow/coast live oak (*Salix lasiolepis/Quercus agrifolia*), coyote brush scrubland (*Baccharis pilularis*), and California annual grassland. In the black and white images (1931 and 1971), only pickleweed and mudflat areas were classified.

Overall, a hierarchical supervised classification of color IR aerial photographs was successful in discriminating several plant communities. The study area had little heterogeneity within plant communities that were for the most part monotypic, which lent to a greater success rate. The high spatial resolution (0.6 m/pixel) enhanced separability among classes and likely reduced the number of spectrally mixed pixels. This resolution allowed for the analysis of vegetation change in relatively small areas. Together, all 15 study sites comprised 37 ha. Additional bands generated from the original IR, red and green bands also proved necessary for a successful classification. Use of NDVI was instrumental in separating vegetation from bare soil, and the IR and green variance texture bands contributed to the separation of forest from grasses and shrubs.

A time series analysis from 1980 to 2001 identified the relative change in area among pickleweed, bare soil, saltgrass/jaumea, and willows. The results demonstrated a process of succession that was typical on five sediment fans, all located on the western side of the slough where tidal action was still present. Between 1980 and 1992 as sedimentation occurred, pickleweed and mudflat were replaced by saltgrass and jaumea on fans below upland drainages. Between 1992 and 2001 sedimentation likely continued, especially during the strong El Niño winter of 1997–1998, and arroyo willow took the place of saltgrass and jaumea and continued to extend into the marsh plain. On the eastern side of the slough the pattern of successional change lacked the intermediate stage of saltgrass and jaumea, but the final outcome was still an expansion of willow cover and movement of willows into the salt marsh. Overall willow expansion occurred on 11 of 15 sediment fans encompassing an area of 4.75 ha (Fig. 21.6). Of this expansion 57% occurred as willows moved into grassland and 43% as willows extended into the marsh.

Though not a main objective of this project, it became evident that the post-classification change detection methods applied here separated effects of tidal erosion and sedimentation, the two contrasting processes of salt marsh loss both occurring within the study areas. A from-to matrix generated by the change detection from 1980 to 2001 revealed that pickleweed within the study area declined by 3.64 ha. Eighteen percent of the pickleweed was converted to mudflat, which can be interpreted as an impact of tidal erosion, the likely cause of pickleweed loss to mudflat (Van Dyke and Wasson 2005). Fourteen percent of pickleweed was converted to another vegetation class, primarily arroyo willow, and represents the establishment of new species where sedimentation occurred.

Despite the challenges associated with historical aerial photographs, such as image quality, scale, and image dates, they enable the study of historical ecological



**Fig. 21.6** Arroyo willow expansion on sediment fans from 1980 to 2001. Source: Byrd et al. (2004), Fig. 5, p. 361; © 2004 Bellwether Publishing Ltd

processes that help explain present-day land cover. Analyzing several dates of aerial photographs also provides information about transitional stages of ecological processes and sequential pressures acting upon habitat loss or gain. Documentation of historical patterns of change has supported conservation planning at other West Coast estuaries (Zedler 1996, Goals Project 1999, Borde et al. 2003) and has proven equally essential to planning efforts in Elkhorn Slough. As stated in Van Dyke and Wasson (2005), “Historical ecology may not supply easy answers to Elkhorn Slough’s complex habitat conservation questions, but a thoughtful analysis of the historical record can help guide development of feasible and sustainable restoration goals.”

### 21.4 Identifying Connections Between Watershed Land Use and Estuarine Response

Again returning to the initial planning documents, one of the greatest anthropogenic disturbances to Elkhorn Slough tidal wetlands is runoff of sediment and nutrients from cultivated fields. Agricultural fertilizers add 50–200 kg of nitrogen per ha per

year to the watershed and an estimated 50% remains unassimilated (Caffrey et al. 2002). Fertilizer runoff contributes significant excess nitrogen to the slough and is the primary source of water quality degradation and eutrophication (Caffrey et al. 2002).

As one of 27 National Estuarine Research Reserves, ESNERR is mandated to conduct monitoring programs to track key ecosystem, habitat, and community parameters over time. The monitoring provides long-term baseline data for researchers and students. Equally important, monitoring enables early detection of major changes, which would allow for adaptive management in the case of an anthropogenic disturbance. The ESNERR monitoring program has monitored water quality at 24 stations surrounding the slough monthly since 1988. Four additional stations along the main channel are sampled every 30 min (see <http://www.elkhornslough.org/esnerr.htm>).

As an alternative to water sampling, vegetation can be a bioindicator of salt marsh nutrient inputs. The nutrient content in plant tissues reflects the integration of the nutrient regime over a period of time that is related to the duration of retention and delayed use of nutrients, and this includes the effects of nutrient pulses that could be missed by periodic water sampling (Siciliano et al. 2008). The spectral response of wetland vegetation to variable nutrient uptake and storage can be potentially mapped and correlated with airborne hyperspectral sensors. As such a hyperspectral image could provide a synoptic view of a region, revealing spatial patterns of vegetation's integrated response to nutrients over time. To successfully detect a correlation between spectral response and water nutrient enrichment, vegetation must be nutrient limited, the vegetation's uptake of water column nutrients must produce a spectral response, and the spectral and spatial resolution of the imagery must be sufficient to detect spectral differences within and between vegetation patches (Siciliano et al. 2008).

A novel study in Elkhorn Slough tested the validity of using of pickleweed spectral responses derived from hyperspectral imagery to detect variations in estuarine nutrient enrichment. This was the first time salt marsh plants have been used as bioindicators of eutrophication potential in a "real" system, as opposed to an experimental setting under controlled conditions. It was also the first time that two spectral indices were tested at the landscape level with hyperspectral imagery, as opposed to tests with spectroradiometer readings (Siciliano et al. 2008).

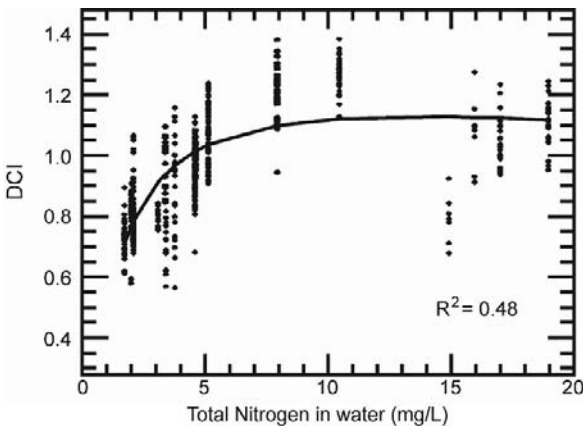
Researchers investigated two spectral indices for their potential to signal nutrient enrichment of salt marsh vegetation: the Derivative Chlorophyll Index (DCI) (Zarco-Tejada et al. 2002) and the Photochemical Reflective Index (PRI) (Gamon et al. 1997). DCI, the ratio of the derivative values at 705 and 725 nm, is correlated with increases in chlorophyll fluorescence and concentrations. As plant stress increases, such as with reduced nutrient levels, the magnitude of the 725 peak declines and the magnitude of the 700 peak increases consistently (Lamb et al. 2002, Smith et al. 2004). PRI is the ratio of narrow band reflectance at 531 and 570 nm  $(531-570)/(531+570)$  and indicates the efficiency of photosynthetic radiation use across nutrient levels and plant species. Nutrient deficient leaves with lower photosynthetic

rates have lower PRI values than fertilized plants, and this reduction is consistent among annual, perennial deciduous, and perennial evergreen plants (Gamon et al. 1997).

After confirming that pickleweed was nitrogen-limited from fertilization experiments, the researchers compared two spectral indices of fertilized and unfertilized pickleweed plots from spectroradiometer readings at leaf and canopy levels. Secondly the researchers tested correlations between the same spectral indices derived from hyperspectral imaging of pickleweed plots and water nutrient levels. HyMap hyperspectral imagery [126 bands, 2.5–3.0 m spatial resolution; (Cocks et al. 1998)] was acquired over Elkhorn Slough on May 3, 2000 by HyVista Corp. (Sydney, Australia). Eighteen regions of interest in the HyMap imagery, corresponding to monospecific pickleweed stands adjacent to 18 water quality stations, were analyzed by extracting every pixel and calculating the mean and variance of DCI and PRI within each region of interest. The researchers used regression analysis to test correlations between spectral indices and mean water-nitrogen levels for productive months (March through September) for five years preceding image acquisition.

Spectral signatures derived from spectroradiometer measurements at leaf and canopy scales were distinctly different between fertilized and unfertilized pickleweed plants. Results indicated that the spectral signature of pickleweed exposed to nutrient enrichment had a greater absorption between 555 nm and 680 nm, steeper red-edge slope, and higher PRI and DCI values.

Spectral indices from the hyperspectral imagery had significant but low correlations with average growing season nutrient levels. DCI values increased with increasing water nitrogen content ( $R^2 = 0.260$ ;  $P < 0.01$ ;  $N = 18$  stations). Nitrogen levels at two stations were an order of magnitude higher than at other stations; when these two stations were removed,  $R^2$  doubled to 0.485 (Fig. 21.7). PRI also increased



**Fig. 21.7** Regression (logarithmic fit) of Derivative Chlorophyll Index (DCI) from HyMap image spectra against mean total water Nitrogen (mean of productive seasons of 1996–2000) at each monitoring station ( $N = 16$ ), excluding 2 stations (Potrero Rd. North and Potrero Rd. South). DCI values are for each image-extracted spectrum of a  $2.5 \times 2.5$  meter pixel containing *Sarcocornia pacifica*. Source: Siciliano et al. 2008, Fig. 10, p. 4029; © 2008 Elsevier Inc

significantly with increasing water nitrogen content ( $R^2 = 0.258$ ) when 2 stations were removed for excess nitrogen and one was removed because of high phosphate concentrations, which are known to influence spectral response. Overall, nitrogen inputs could be differentiated spatially across the slough with spectral readings from the HyMap imagery (Siciliano et al. 2008).

In this study there was little or no DCI response to water nitrogen higher than 12 mg/L. From these results it was determined that the useful range of the DCI/water nitrogen relationship is limited from about 2 mg/l to 10 mg/l nitrogen. This is the range most commonly experienced by pickleweed marshes in Elkhorn Slough and spans unenriched to eutrophic conditions (Siciliano et al. 2008). Overall, the two spectral indices, DCI and PRI, have the potential to serve as proxies for nutrient input at least for qualitative mapping of relative nutrient variation and gradients. However the researchers suggest that more research is needed to determine how well spectral data and plant nitrogen content are related. Provided this relationship is found to be consistent and strong, the cost of airborne hyperspectral imagery may still limit this approach as a monitoring tool. However, hyperspectral satellite imagery would be a much more cost effective tool in the near future, when high resolution, high signal to noise ratio (SNR) hyperspectral satellites become operational (D. Siciliano, personal communication, September 17, 2007).

Nutrient runoff from cultivated fields has often been associated with off-farm sedimentation into Elkhorn Slough's salt marshes. The extent of sedimentation in salt marshes in relation to current and former watershed properties has also been identified through remote sensing applications (Byrd et al. 2007). Researchers explored the relationships between present-day sediment fan size with current (2001) and past (1980) land cover and watershed variables. Watershed variables were those that represented physical properties of the watershed, such as slope or area, while land cover included riparian forest, cultivated fields, and grazing land. The influence of sub-watershed size on the ability to identify these relationships was also investigated.

Land cover and watershed variables were derived from the 1980 color IR aerial photographs and the 2001 orthophotos applied to the study of vegetation change on sediment fans (Byrd et al. 2004). It was not possible to distinguish riparian forest cover from other types of forest cover using spectral-based automated classification of color IR aerial photographs; therefore, Byrd et al. (2007) developed a method using topographical data to model the likely distribution of riparian forest. This was accomplished with the program FLOW 95 (Schäuble 1999), which predicts areas of high sediment accumulation. FLOW 95 uses a multiple flow algorithm to calculate cumulative flow accumulation in watersheds from a DEM, and is based on the logic of Desmet and Govers' algorithm (Desmet and Govers 1996), which calculates overland flow. In contrast to the usual flow accumulation model, which is useful for delineating linear flow paths and stream channels, this model estimates flow accumulation over an areal extent, which is more suitable for estimating sediment flow and deposition. The FLOW 95 algorithm produced a flow accumulation grid with higher cell values corresponding to higher levels of sediment accumulation.

Overlaying a general forest cover map with the flow accumulation grid, forest cover meeting a flow accumulation value of 65 or higher was selected and labeled as riparian forest. This value was experimentally chosen based on the intersection between flow accumulation values and the presence of riparian forest cover (mostly arroyo willow), which was identified through photointerpretation and ground-truthing. The 1980 image had an overall classification accuracy of 88% and the 2001 image had an overall classification accuracy of 90%.

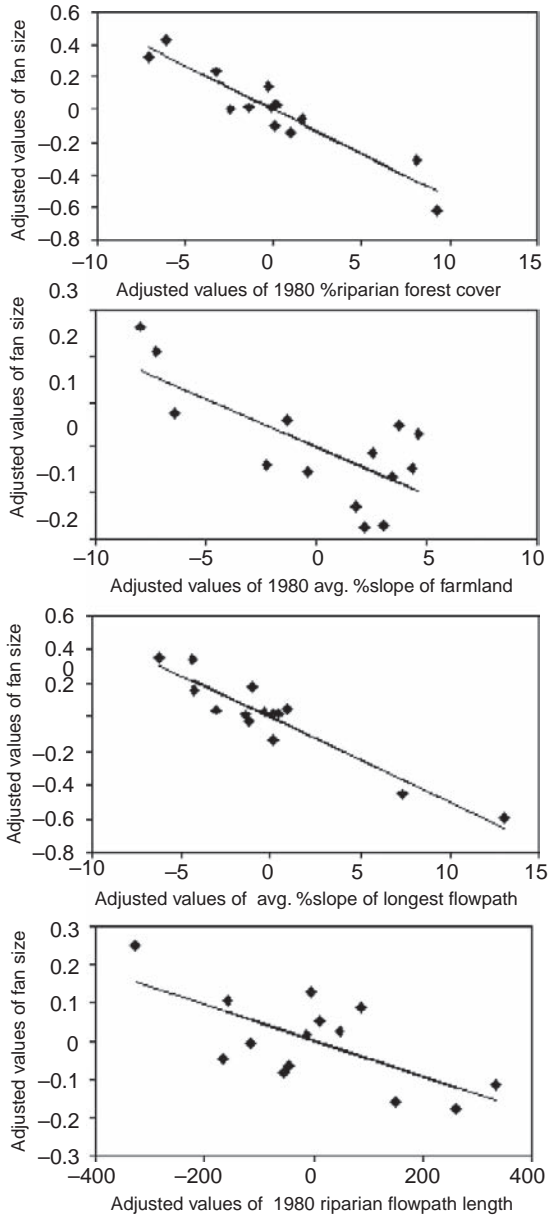
According to regression analysis the power to explain sediment fan size increased among large sub-watersheds (adjusted  $R^2 = 0.94$  vs. 0.75), and three historical watershed variables were significant. Sediment fan size increased with less riparian forest in 1980, less steep agricultural slopes in 1980, less steep sub-watershed flowpath slopes, and shorter riparian flowpath lengths in 1980 (water flowpaths within riparian forest located between farmland and marsh) (Fig. 21.8). Variables most correlated with fan size were 1980 %riparian forest cover ( $r = -0.94$ ) and longest flowpath slope ( $r = -0.94$ ).

Strong relationships between wetland conditions and watershed land cover may exist in large watersheds, while in smaller watersheds, the spatial arrangement of landscape patches or land use management may be more critical than the dominant land cover in explaining downstream impacts (Strayer et al. 2003). For example sediment flux may be highly variable in smaller watersheds, but less variable in large watersheds because they integrate random pulses of sediment occurring over their smaller sub-catchments (Benda and Dunne 1997). Because of this integration, in large watersheds the overall effect of land use on downstream impacts would be stronger, as soil erosion rates would vary according to land cover (Opperman et al. 2005).

Historical variables likely explained sediment fan size because there was a time lag between watershed land conversion and sedimentation in the marsh; intense storms stochastically drive sedimentation events that occur after land conversion (Benda and Dunne 1997). Subsequently once sediment deposits, several years pass before arroyo willow dominates the sediment fans. While many sediment fans formed during the 1980s, arroyo willow expansion on fans occurred most during the 1990s (Byrd et al. 2004). Historical riparian flowpath was related to sediment fan size, with short flowpaths leading to larger fans. Riparian flowpath length increased 70 m on average from 1980 to 2001, generally from the mid 1990s onward when most restoration activities began. If riparian flowpaths continue to lengthen then the amount of sediment transported to the marsh will possibly be reduced.

These studies addressing nutrient and sediment runoff have demonstrated the potential to correlate estuarine response to watershed inputs or properties through remote sensing applications. In one case salt marsh vegetation spectral response was related to spatial variation in water nitrogen concentration, and in the other the extent of sedimentation in salt marsh was related to land cover and physical watershed variables. These studies also emphasize the temporal component of watershed-estuarine connections. In the highly variable Mediterranean climate of coastal California, land use combined with stochastic winter rainstorm events drive nutrient and sediment inputs. Storms during the El Niño winter of 1997/1998 produced significant levels

**Fig. 21.8** Partial regression plots of significant independent variables against sediment fan size (square root transformed) for large sub-watersheds ( $n = 14$ ). Source: Byrd et al. (2007), Fig. 2, p. 107; © 2007 Springer Science and Business Media



of sedimentation and high nutrient pulses. In Elkhorn Slough spectral indices from hyperspectral imagery integrated vegetation response to the previous five years of nutrient uptake, including high nutrient concentrations from the El Niño winter. Finally, the current extent of sedimentation was linked to historical watershed properties, and represented a legacy of past land management and land use activities.



## 21.5 Change Detection of Salt Marsh Vegetation and Channel Bathymetry

The water quality and weather and biological monitoring programs at ESNERR are well established. However the rapid rate of marsh loss presented by Van Dyke and Wasson (2005) emphasizes the need for continued landscape-scale monitoring of tidal wetland coverage. With the expansion of the GIS program at ESNERR, the increasing frequency of digital aerial photo acquisition, and increasing availability of satellite imagery, LiDAR, and digital aerial photography, a geographical monitoring program became available to address this need. The goals of this program are to map and quantify changes in the extent of all emergent tidal wetlands over the entire estuarine system and emergent tidal wetland plant communities at selected locations every two to five years. Currently mapping will be conducted according to methods described in Van Dyke and Wasson (2005). But efforts are underway to develop a faster, more consistent protocol. A wealth of imagery from a variety of sources was made available to develop an efficient mapping program. These included true-color digital aerial photography yielding 0.45 m/pixels, Ikonos multispectral satellite imagery (4.0 m/pixel for multispectral and 1.0 m/pixel for pan), Quick-Bird multispectral satellite imagery (2.8 m/pixels for multispectral and 0.7 m/pixel for pan), HyMap hyperspectral imagery (126 bands, approximately 3 m/pixels), NASA AVIRIS hyperspectral imagery (224 bands, approximately 20 m/pixels), and PHILLS II hyperspectral imagery (124 bands, 3 m/pixels). Through experimentation, landscape-scale emergent tidal wetland mapping was found to be most effective with 1 m/pixel pan-sharpened multispectral satellite imagery.

In addition a new tidal wetland classification system is being developed at Elkhorn Slough for the NOAA Coastal Change Analysis Program (C-CAP) to be used for the entire NERR system. Instead of 30 m resolution Landsat imagery used in past C-CAP mapping, a high resolution (1 m) digital elevation model (DEM) derived from LiDAR data and 1 m pan-sharpened multispectral satellite data are being applied to develop a habitat classification system based on tidal datums and the Cowardin wetland classification system. This method is expected to create much more accurate estuarine habitat maps, as habitat types are inherently related to the extent of tidal inundation (Eric Van Dyke, personal communication, August 21, 2007).

Mapping and frequent monitoring of sub-tidal areas of the Elkhorn Slough estuary and beyond the mouth of the slough into Monterey Canyon have been facilitated by California State University's Seafloor Mapping Lab. Sequential bathymetric surveys of the slough channel have produced a time series of erosional and depositional patterns that can partially explain patterns of marsh loss and tidal creek widening. Data capture and analysis have been part of undergraduate student training, and were the subject of a number of senior thesis, or "capstone" projects, that provided information essential to restoration planning in the slough. Bathymetry data is collected with a Reson 8101 SeaBat multibeam sonar system that measures discrete depths, enabling complex underwater features to be mapped with precision. Differential GPS vessel positioning for multibeam surveys is provided by a GPS with

differential corrections. When higher accuracy x,y,z positioning is required, Real-Time Kinematic (RTK) mode is applied. (see <http://seafloor.csUMB.edu/descriptions/multibeamdescrip.html>).

Multibeam bathymetry imagery of the Elkhorn Slough channel was collected to study in detail the effect of hydrological changes caused by the development of the Moss Landing Harbor in 1947. When the harbor opened, Elkhorn Slough's main channel was exposed to direct tidal flow and flushing. As a result the tidal prism of the slough increased and the system became characterized by tidally mediated erosion, or tidal scour (Crampton 1994). Tidal scour has been attributed to the widening and deepening of the main channel and tidal creeks, and loss of pickleweed marsh, all of which expand the tidal prism. This process of expanding the tidal prism creates a positive feedback loop as tidal velocities increase, accelerating the erosion rate of channels and creeks. Determining the rate and distribution of tidal scour is of critical necessity for developing appropriate remediation plans. As a result resource managers would like to determine when or if the slough will reach equilibrium, whereby the net sediment flux approximates zero.

A student researcher collected multibeam bathymetry data of Elkhorn Slough in 2001 and compared results to bathymetry data collected in the same area by Malzone and Kvitek in 1993 (Dean 2003). In 1993 Malzone and Kvitek collected data along 67 cross-sections of the main channel and 6 across the mouth of Parson's Slough with a single beam sonar fathometer and a differential GPS with an accuracy of 2 m. Malzone calculated that the erosion rate for the total slough system was  $8.0 \times 10^4 \text{ m}^3/\text{year}$  (Malzone 1999). Later Dean's multibeam survey produced a grid of points at a resolution of 1 m or better. The results were to provide the basis for a hydrological model that would help planners predict changes in the slough.

By comparing survey points, Dean determined changes in cross-section area, thalweg depth, and channel volume, and identified areas of net erosion and deposition. Results showed that the mean cross-section area of the main channel increased by 16% between 1993 and 2001, and slough volume increased by 21% or an average of  $5.6 \times 10^4 \text{ m}^3$  per year. Portions of the main channel just upstream of Parson's Slough experienced relatively small changes in maximum depth and significant deposition occurred at the head of the slough, while the downstream portion of the slough grew much deeper, steepening the depth gradient. Since most of the erosion occurred downstream of the mouth of Parson's Slough, there is evidence that an increasing tidal prism within Parson's Slough had become a dominant influence on tidal scour downstream.

Sampey followed up with another multibeam bathymetry survey in 2003 (Sampey 2006). He produced a map of Elkhorn Slough's tidal prism and compared his survey results to those from Dean's 2001 survey to assess changes in erosion rates. A GPS receiver capable of RTK correction was used for primary navigation and in situ tide height data collection during all surveys, enabling the construction of tide models on the fly. Depth values were referenced to the North American Vertical Datum (NAVD) 1988. The use of RTK GPS tide data greatly increased the accuracy of the data over past surveys that used predicted tides from tidal stations. A high resolution 1-m DEM was produced from bathymetric data collected with multibeam and

single beam sonar systems at high tide, and topographical LiDAR data collected at low tide. While the bathymetry data covered subtidal areas, the topographical LiDAR provided coverage for marshes and mudflats. The tidal prism calculated from the 2003 DEM was  $6.22 \times 106 \text{ m}^3 \pm 1.00 \times 106$ . This represented a 12.71% increase in tidal prism since Malzone's calculation in 1999. Parson's Slough accounted for 30% of the tidal prism with a volume of  $1.39 \times 106 \text{ m}^3$ .

Comparison with the 2001 bathymetry data indicated that the thalweg continued to deepen along the length of the main channel. Between 2001 and 2003,  $2.4 \times 105 \text{ m}^3$  of sediment was lost. The net sediment volume change in the main channel was  $-1.23\%$  suggesting an erosion dominated system. Seventy percent of the total sediment volume eroded downstream of Parson's Slough. These data suggest that erosion rates are increasing, and the slough system has not reached a point of equilibrium. The upper slough remained a depositional dominated system as was seen in 1993 and 2001. The depositional pattern especially in these upper reaches corresponds with bank failure of tidal creeks, demonstrating the risk of further marsh habitat erosion.

While the multibeam bathymetry data has proven invaluable for resource managers working toward a solution for tidal scour, challenges exist with using the multibeam sonar equipment in a shallow estuarine environment. The twisting channels strained software designed to survey wide straight swaths of coast and open ocean. Erosion had compromised the reliability of navigational charts and tide models. Thick patches of eel grass tangled propellers, cluttered sonar returns with noise, and trapped sediment. Huge shoals of baitfish also interfered with sonar returns. Furthermore many areas were too shallow to survey (Dean 2003).

## 21.6 The Contribution of Remote Sensing Data to Modern Restoration Planning Strategies

The extensive marsh loss and estuarine habitat erosion documented in the remote sensing studies described here are receiving attention through a large, collaborative restoration planning process documented in the Elkhorn Slough Tidal Wetland Strategic Plan, published in March 2007. Over one hundred coastal resource managers, representatives from key regulatory and jurisdictional entities, leaders of conservation organizations, scientific experts and community members have come together to develop and implement strategies to conserve and restore estuarine habitats in the Elkhorn Slough watershed through the Elkhorn Slough Tidal Wetland Project (Elkhorn Slough Tidal Wetland Project Team 2007).

After reviewing an extensive scientific literature on Elkhorn Slough, major impacts were identified and addressed in the Strategic Plan, many of which were previously identified in former planning documents. Acknowledging multiple stressors to the Elkhorn Slough watershed, the Strategic Team prioritized the need to address interior marsh dieback and estuarine habitat erosion. Studies discussed here (Dean 2003, Van Dyke and Wasson 2005, Sampey 2006) calculated a rapid rate of change

in marsh environments and the existence of a non-equilibrium state in the estuarine system, emphasizing the need to identify solutions in order to slow habitat loss. It was determined that without action, salt marsh will continue to erode, the extent and cross-sectional area of tidal creeks will increase, sediment in soft-bottom areas exposed to strong tidal currents will erode leaving harder substrates, bank erosion will continue, cross sectional area of the main channel of the slough will increase, and the extent of mudflat will increase.

Overall the Tidal Wetlands Project identified three goals: (1) to conserve existing high quality estuarine habitats by reducing the rate of salt marsh and tidal creek conversion to other habitat types, reducing subtidal channel erosion, and reducing the loss of soft sediment from mudflat and subtidal channels, (2) to restore and enhance degraded estuarine habitats by increasing the extent of salt marsh, tidal brackish marsh, and high quality soft sediment in mudflat and subtidal channels, and (3) to restore the physical processes that support and sustain estuarine habitats by reducing the tidal prism in undiked areas, restoring tidal exchange to diked marshes, and increasing elevations to subsided marshes by re-establishing or augmenting the supply of suitable sediments (Elkhorn Slough Tidal Wetland Project Team 2007).

Establishment of these goals were informed by the availability of high quality data from multiple studies covering a wide spectrum of topics. The high resolution, both temporal and spatial, of the remote sensing data described in this chapter, especially from Dean (2003), Van Dyke and Wasson (2005), and Sampey (2006), were a valuable source of information that guided priority setting (Barb Peichel, personal communication, August 21, 2007). Aerial photos were also instrumental in communicating facts about estuarine change to community members, as long as they were accompanied with reference materials, such as site photos. Multiple committees and working groups that addressed several aspects of the slough system had access to this information that provided a common knowledge base from which each group operated. This data helped to establish a common consensus among the groups. On May 5, 2005, the strategic planning team made a consensus statement that the 50-year habitat trends in Elkhorn Slough are not acceptable and a no-action alternative is not an acceptable course of action.

One proposed restoration alternative is to restore or replicate the historical location, mouth size, and sinuosity of the Elkhorn Slough channel opening to Monterey Bay and block the current opening to Moss Landing with a structure. Another less extreme alternative is to more closely approximate the historical entrance of the estuary by decreasing the opening size under or near the Highway 1 bridge crossing the mouth of the slough using a structure such as an underwater sill. Further it was determined that an addition of thin layers of sediment may be needed to encourage plant growth, and there is potential need to re-establish riverine sediment supplies such as from the Salinas River, which was diverted in 1909.

The second strategy calls to restore and enhance degraded estuarine habitats through tidal exchange and creek modifications, sediment additions, upland best management practices, and freshwater augmentation. This strategy would involve a smaller scale restoration project at Parson's Slough where tidal influence would be reduced and sediment would be added to restore marsh habitat. This area was

targeted because, as mentioned earlier, Parson's Slough accounts for approximately 30% of the total Elkhorn Slough volume, and its increasing tidal prism is influencing tidal scour downstream in the main channel. Restoration here could potentially also slow marsh loss and habitat erosion in the rest of the estuary.

The Tidal Wetlands Plan identifies research needed to decide on a future course of action; a decision regarding the direction for restoration activities is set to be made in early 2009. Among multiple topics to be investigated, the Plan proposes research on ongoing changes to Elkhorn Slough bathymetry. There are plans to quantify rates of tidal erosion and deepening and widening of main Elkhorn Slough channel to build support for possible restoration actions and help predict future changes under different restoration scenarios. The spatial pattern of erosion in tidal channels and creeks will also be analyzed to create a five year projection of bathymetric changes and/or a 50-year range of projections. With the capability to quickly detect the rate and location of fine changes, change detection from bathymetric data will be important for assessing management decisions and monitoring the effects of restoration actions such as muting tidal flows (Rikk Kvitek, personal communication, September 14, 2007).

## 21.7 Conclusions

Upon inspection the chronologies of Elkhorn Slough conservation and restoration planning efforts and the progression of remote-sensing based research have run in parallel. Management problems identified in planning documents influenced the direction of research on watershed and estuarine processes applying remote sensing technologies. A rich archive of historical maps and aerial photos plus partnerships with multiple institutions that provided high quality imagery made this type of research possible. Taking advantage of rapidly advancing new technologies that provided imagery with better horizontal and vertical spatial resolution, researchers developed innovative methods for information extraction. The resulting datasets in turn informed further efforts to refine conservation and restoration strategies.

While information on watershed and estuarine processes described in this chapter has been useful to resource managers, application of geospatial technologies still pose challenges. With historical aerial photography one can discern past ecological conditions and changes but distortion and color imbalance of contact prints produce errors. Hyperspectral imagery has the potential to provide a spatially-explicit synoptic view of vegetation response to nutrient enrichment, but more research is needed on correlations between spectral data and plant nitrogen content. Conducting multibeam bathymetry surveys in a shallow estuarine system can be difficult, but the development of tide models on the fly with RTK GPS has reduced much of the error associated with this application. As research programs progress, they will further guide restoration decisions made by the Tidal Wetland Project Team.

Watershed management applying spatial data should also improve estuarine conditions. The Elkhorn Slough Foundation, in its 25th year, has acquired 90% of the

808 ha identified for conservation in the 1999 Watershed Conservation Plan. Since 1980 considerable management efforts have been made to reduce soil erosion in the Elkhorn Slough watershed. The Elkhorn Slough Foundation has implemented erosion control practices on their managed properties, including construction of sediment basins, native grass and willow plantings, soil stabilization, and reduction of annual crops. The Natural Resources Conservation Service and the Resource Conservation District of Monterey County, through the Elkhorn Slough Watershed Project, have worked with farmers to implement conservation practices on 3260 acres and prevent approximately 79,463 tons of soil loss between 1994 and 2001 (USDA-NRCS 2002). These projects have reduced the amount of sediment and nutrient runoff into the estuary, and these efforts are expected to continue in the future.

**Acknowledgement** I thank Eric Van Dyke, Kerstin Wasson and Barb Peichel, ESNERR, Rikk Kvitek, Joshua Sampey, and Edwin Dean, California State University Monterey Bay, Daria Siciliano, U.S. Naval Postgraduate School, and Maggi Kelly, University of California, Berkeley, for their contributions to this chapter and comments on the text.

## References

- ABA Consultants (1989) Elkhorn Slough wetland management plan. Prepared for California State Coastal Conservancy and Monterey County Planning Department, Capitola, CA, USA
- Barrette J, August P, Golet F (2000) Accuracy assessment of wetland boundary delineation using aerial photography and digital orthophotography. *Photogramm Eng Rem S* 66:409–416
- Benda L, Dunne T (1997) Stochastic forcing of sediment supply to channel networks from landsliding and debris flow. *Water Resour Res* 33:2849–2863
- Bolstad PV (1992) Geometric errors in natural-resource GIS data – tilt and terrain effects in aerial photographs. *Forest Sci* 38:367–380
- Borde AB, Thom RM, Rumrill SR, Miller LM (2003) Geospatial habitat change analysis in Pacific Northwest coastal estuaries. *Estuaries* 26:1104–1116
- Byrd KB, Kelly NM, Merenlender AM (2007) Temporal and spatial relationships between watershed land use and salt marsh disturbance in a Pacific estuary. *Environ Manage* 39:98–112
- Byrd KB, Kelly NM, Van Dyke E (2004) Decadal changes in a Pacific estuary: a multi-source remote sensing approach for historical ecology. *GISci Remote Sens* 41:347–370
- Caffrey J, Brown M, Tyler WB, Silberstein M (eds) (2002) Changes in a California estuary: a profile of Elkhorn Slough. Elkhorn Slough Foundation, Moss Landing, CA, USA
- Cocks T, Jossen R, Stewart A, Wilson I, Shields T (1998) The Hymap Airborne Hyperspectral Sensor: the system, calibration and performance. Proceedings of the first EARSEL workshop on imaging spectroscopy, Zurich, Switzerland
- Crampton TA (1994) Long term effects of Moss Landing Harbor on the wetlands of Elkhorn Slough. University of California, Santa Cruz, Santa Cruz, CA, USA
- Dean EW (2003) Tidal scour in Elkhorn Slough, California: a bathymetric analysis, Capstone Project. California State University, Monterey Bay, Seaside, CA, USA
- Desmet PJJ, Govers G (1996) A GIS procedure for automatically calculating the USLE LS factor on topographically complex landscape units. *J Soil Water Conserv* 51:427–433
- Dickert TG, Tuttle AE (1980) Elkhorn Slough Watershed: linking the cumulative impacts of watershed development to coastal wetlands. Institute of Urban and Regional Development, University of California, Berkeley, CA, USA

- Elkhorn Slough Foundation and Tom Scharffenberger Land Planning and Design (2002) Elkhorn Slough at the Crossroads: natural resources and conservation strategies for the Elkhorn Slough Watershed
- Elkhorn Slough Tidal Wetland Project Team (2007) Elkhorn Slough tidal wetland strategic plan. A report describing Elkhorn Slough's estuarine habitats, main impacts, and broad conservation and restoration recommendations
- Field DW, Reyer AJ, Genovesse PV, Shearer BD (1991) Coastal wetlands of the United States: an accounting of a valuable national resource. Office of Oceanography and Marine Assessment, National Ocean Service, National Oceanic and Atmospheric Administration, Rockville, MD, USA
- Gamon JA, Serrano L, Surfus JS (1997) The photochemical reflectance index: an optical indicator of photosynthetic radiation use efficiency across species, functional types, and nutrient levels. *Oecologia* 112:492–501
- Goals Project (1999) Baylands ecosystem habitat goals. U.S. Environmental Protection Agency, San Francisco and San Francisco Bay Regional Water Quality Control Board, Oakland, CA, USA
- Grossinger R (2001) Documenting local landscape change: the San Francisco Bay Area Historical Ecology Project. Island Press, Washington, DC, USA, pp 425–442
- Klemas VV (2001) Remote sensing of landscape-level coastal environmental indicators. *Environ Manage* 27:47–57
- Lamb DW, Steyn-Ross M, Schaars P, Hanna MM, Silvester W, Steyn-Ross A (2002) Estimating leaf nitrogen concentrations in ryegrass pasture using the chlorophyll red-edge: modelling and experimental observations. *Int J Remote Sens* 23:3619–3648
- Malzone CM (1999) Tidal scour and its relation to erosion and sediment transport in Elkhorn Slough. San Jose State University, San Jose
- Moore LJ (2000) Shoreline mapping techniques. *J Coastal Res* 16:111–124
- Opperman JJ, Lohse KA, Brooks C, Kelly NM, Merenlender AM (2005) Influence of land use on fine sediment in salmonid spawning gravels within the Russian River Basin, California. *Can J Fish Aquat Sci* 62:2740–2751
- Sampey J (2006) A bathymetric analysis of equilibrium potential within Elkhorn Slough, California, Capstone Project. California State University, Monterey Bay, Seaside, CA, USA
- Sawyer J, Keeler-Wolf T (1995) A manual of California vegetation. California Native Plant Society Press, Sacramento, CA, USA
- Scharffenberger T, Silberstein M, Cox R, Kelly C, Lozier L, Gear K (1999) Elkhorn Slough Watershed Conservation Plan. Scharffenberger Land Planning and Design
- Schäuble H (1999) Bodenerosionsprognosen mit GIS und EDV. Ein Vergleich verschiedener Bewertungskonzepte am Beispiel einer Gäulandschaft. Diploma at the Faculty of Geography, University of Tübingen, Germany
- Schwartz DL, Mullins HT, Belknap DF (1986) Holocene geologic history of a transform margin estuary: Elkhorn Slough, California. *Estuar Coast Shelf S* 22:285–302
- Siciliano D, Wasson K, Potts D, Olsen R (2008) Evaluating hyperspectral imaging of wetland vegetation as a tool for detecting estuarine nutrient enrichment. *Remote Sens Environ* 112:4020–4033
- Smith KL, Steven MD, Colls JJ (2004) Use of hyperspectral derivative ratios in the red-edge region to identify plant stress response to gas leaks. *Remote Sens Environ* 92:207–217
- Strayer DL, Beighley RE, Thompson LC, Brooks S, Nilsson C, Pinay G, Naiman RJ (2003) Effects of land cover on stream ecosystems: roles of empirical models and scaling issues. *Ecosystems* 6:407–423
- Swetnam TW, Allen CD, Betancourt JL (1999) Applied historical ecology: using the past to manage for the future. *Ecol Appl* 9:1189–1206
- USDA-NRCS (2002) The Elkhorn Slough watershed project 2000–2001 report. Natural Resources Conservation Service, Salinas, CA, USA
- USDA-SCS (1994) The Elkhorn Slough watershed project: watershed plan and environmental assessment. Davis, CA, USA

- Van Dyke E, Wasson K (2005) Historical ecology of a central California estuary: 150 years of habitat change. *Estuaries* 28:173–189
- Zarco-Tejada PJ, Miller JR, Mohammed GH, Noland TL, Sampson PH (2002) Vegetation stress detection through chlorophyll a + b estimation and fluorescence effects on hyperspectral imagery. *J Environ Qual* 31:1433–1441
- Zedler J (1996) Coastal mitigation in southern California: the need for a regional restoration strategy. *Ecol Appl* 6:84–93



## Chapter 22

# Runoff Water Quality, Landuse and Environmental Impacts on the Bellairs Fringing Reef, Barbados

Marko Tasic, Robert B. Bonnell, Pierre Dutilleul and Hazel A. Oxenford

In this study, the contributions of runoff to seawater quality degradation off Holetown, Barbados were documented with a watershed diagnostic of surface water quality and landuse, and an analysis of seawater quality following flow events. The following parameters were monitored during the rainy season of 2006: turbidity, total suspended solids (TSS), nitrate-nitrite nitrogen, soluble reactive phosphorus, nearshore sedimentation, salinity, and terrestrial discharge. Data from the watershed outlet reveal a first flush phenomenon for TSS. High mean nutrient concentrations despite the watershed's high proportion of natural land imply overfertilization of agricultural lands and enrichment from urban sources. This is supported by poorer water quality found in the subbasin which had the highest proportion of developed land. Marine data reveal a significant northward dispersion trend directing plumes towards the Bellairs Reef. All 4 documented events produced detrimental levels of turbidity, or TSS, or both above the reef. Seawater quality varied significantly among events in correspondence to total TSS loads and discharges from the outlet, though temporal variation above the nearby reef also depended on wind stress. Reef sedimentation rates were well above guidelines for 30% of the season. Estimated dissolved nutrient loads are expected to induce coastal eutrophication, especially with respect to phosphorus.

### 22.1 Introduction

“A high incidence of sunshine, unbroken warm temperatures, brilliantly clear seas and white coral sand beaches provide the natural attractions which bring a quarter million tourists to the West Indian Island of Barbados every year” (Bird et al. 1979). Little has changed since 1979 with respect to the described natural attractions though they currently bring four times as many tourists (Ministry of Tourism 2003). In addition to the quarter million local Barbadians (Ministry of Labour 2002),

---

M. Tasic (✉)

Department of Bioresource Engineering, McGill University, Macdonald Campus,  
QC, H9X 3V9, Canada  
e-mail: marko.tasic@mail.mcgill.ca

tourism has prompted extensive development of the coastal area (Nurse 1986). In the west coast catchment area of Holetown, urban areas have doubled between 1964 and 1996 causing higher proportions of rainfall to be transported as surface runoff to the coast (Leitch and Harbor 1999). Runoff events in the coastal area can leave the seawater somewhat less than “brilliantly clear” impacting another natural attraction not described above: the coral reefs.

A series of fringing coral reefs extends along the western, leeward coast of Barbados (Lewis 1960; Lewis and Oxenford 1996). These ecosystems have undergone considerable changes over the past 25 years as the fringing reefs have degraded both structurally (Lewis 2002) and biologically (Bell and Tomascik 1993; Delcan Consulting 1993). While these systems have been affected by acute disturbances such as Hurricane Allen (Mah and Stearn 1986), the mass mortality of the grazer *Diadema antillarum* (Hunte et al. 1986), and a recent bleaching event (Oxenford et al. 2008), an underlying cause of the demise has been eutrophication, and associated suspended particulate matter (SPM, or total suspended solids, TSS) and sedimentation (Bell and Tomascik 1993). This chronic stress has been documented along the west coast as a gradient of water quality deteriorating towards the southern more developed part of the island (Tomascik and Sander 1985).

If high levels of eutrophication and sedimentation are sustained, they act as chronic disturbances which may be more detrimental to coral communities than acute disturbances (Connell 1997; Bell et al. 2007). Coastal eutrophication has been shown to harm corals, which naturally live in clear, nutrient-poor environments. Nutrient enrichment can disrupt coral-zooxanthellae symbioses, but will more commonly be rapidly utilized by phytoplankton and macroalgae. The increased biomass of the former decreases water clarity, inhibiting growth of the light-dependent coral, and the latter competes with coral for substrate (Fabricius 2005). Sedimentation on reefs often results in reduced biodiversity as smothering can cause mortality. Certain morphologies, such as that of large branching corals, or the ability to remove settled particles make some corals more tolerant of sedimentation, however particle removal comes at a metabolic cost thus inhibiting growth (Rogers 1990).

Land-based sources have been linked to the eutrophication (Lapointe et al. 2004) and sedimentation (Bothner et al. 2006) of coral reef environments. Land-based anthropogenic impacts on nearshore marine life in Barbados have been clearly demonstrated through the use of sewage pollution indicators (Bellairs Research Institute 1997, Cabana 1997, Risk et al. 2007). Urban wastewater is widely known to cause nutrient enrichment in receiving waters (Peierls et al. 1991; Howarth et al. 1996). Other activities known to enhance nutrient and sediment concentrations via runoff include landuses such as agriculture, high-density grazing, industries, construction sites, and land-clearing (Kayhanian et al. 2001; Brodie and Mitchell 2005). Natural areas, on the other hand, do not commonly degrade water quality (Meybeck 1982) but can act as buffers in trapping nutrients and sediments.

Inputs to the nearshore zone of Barbados affecting water quality include runoff, groundwater, coastal point-sources, and oceanic currents. Periodic runoff events during the rainy season (June–December) create plumes of nutrient-rich, sediment-laden freshwater which can extend over 1 km offshore to the island’s bank reefs

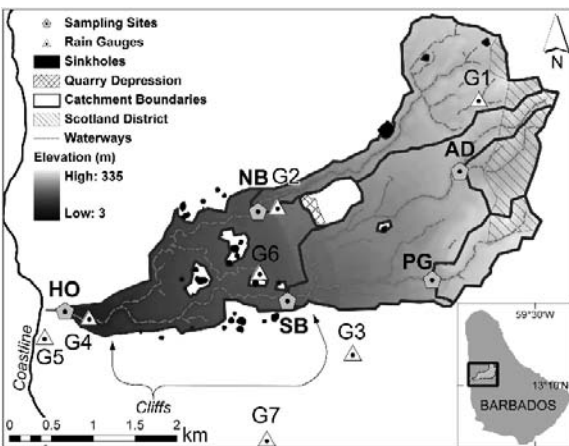
(Delcan Consulting 1994). Groundwater seepage along the west coast has been shown to make significant nutrient contributions (Lewis 1985, 1987), as have point source discharges such as rum refineries (Runnalls 1994). Ocean currents have the potential to bring productive waters from South America to Barbados, though such occurrences are somewhat unpredictable (Fratantoni and Glickson 2002).

This study aims to assess the specific contributions of runoff to the nearshore area of Holetown, Barbados, as well as to identify landuses degrading surface water quality. By monitoring stormwater runoff, flood plumes, and nearshore sedimentation from May–December 2006, an event-based assessment of water quality processes is presented. Mapping and GIS-based analyses of the watershed’s landuses further allowed for a watershed diagnostic.

## 22.2 Methodology

### 22.2.1 Study Area

The studied watershed is situated on the central west coast of Barbados and drains into the Holetown Lagoon, a body of surface water (approximately  $3 \times 10^6$  L) separated from the sea by a narrow, 9 m length of beach (Fig. 22.1). The occurrence of ephemeral runoff events quickly washes away this beach, flushing runoff and lagoon water out to sea. About 600 m north-west of this outlet lies the Bellairs Reef, a fringing coral reef which is separated into a northern and southern lobe. This study site was chosen due to its proximity to the Bellairs Research Institute and the wealth of past research focusing on this watershed and the Bellairs Reef.



**Fig. 22.1** Watershed sampling scheme and physical characteristics. Inset: location of study area on the island of Barbados. Labels identify sampling sites (HO, SB, NB, AD, PG) and rain gauges (G1–G7). Sampling site abbreviations: HO – Holetown Outlet; SB – South Branch; NB – North Branch; AD – Ape’s Hill Dam; PG – Porey Spring Gully

The watershed's karstic aquifer is mostly composed of coral limestone (89%) while the remainder lies within the Scotland District (Fig. 22.1), an area of impermeable and impervious soils and Tertiary oceanics (Vernon and Carroll 1965). A set of cliffs run parallel to the coastline and separate the watershed into three distinct terraces, the middle of which is highly karstified (Huang 2006). With an average porosity of 45% (Jones and Banner 2003), the watershed's limestone exhibits many karstic features such as sinkholes in the interfluvial zone, caves and fissures in the gullies, as well as intermittent springs.

The watershed drains an area of 9.9 km<sup>2</sup>, although removing areas draining to sinkholes and a quarry, the watershed's effective contributing area is 9.2 km<sup>2</sup>. Elevations range from 3 to 335 m with an overall slope of 4.0% over a longest flow length of 8314 m. Surface water flows ephemerally through a system of deep and extremely eroded gullies bordered by steep banks covered in dense forest (Stantec Consulting 2003). The watershed's time of concentration, the time needed for water to travel from the watershed's furthest point to the outlet, has been estimated at 145.8 minutes (Cumming Cockburn Ltd 1996).

Barbados has a sub-humid to humid maritime, tropical climate where large rainfall events are typically modulated by tropical waves moving westward across the Atlantic (Riehl 1954, Avila et al. 2000). The rainy season lasts from June–December, peaks during the months of August–October, and accounts for 60% of the total annual rainfall. Average annual precipitation spatially varies from 1300 to 2000 mm with values increasing towards higher elevations. However, spatial precipitation patterns vary seasonally as well, with totals increasing towards the western leeward side of the island during the rainy season (Jones and Banner 2003).

Extensive development in the watershed has altered its landuse greatly over the past 40 years. From 1964 to 1996, urban areas doubled resulting in a predicted 5.5% increase in runoff depth (Leitch and Harbor 1999). This intensification of hydrological response has been somewhat counterbalanced by the demise of the sugar cane industry. Sugar cane plantations covered 50% of the area in 1964, a proportion that was halved by 1996 (Leitch and Harbor 1999), and reduced to 1% by 2006 as many plantations have been converted into pasture or left idle and overgrown with brush (this study). This idle brushland is expected to lower hydrologic peaks and lengthen hydrologic event periods.

Figures 22.2 and 22.3 show the proportions and spatial distributions, respectively, of each of the major landuse categories found in the watershed and its upstream sub-basins. With all agricultural areas combining for only 6% (HO, Fig. 22.2), landuse is now dominated by natural lands (69%) including the forested gullies, grasslands, and brush. Animal husbandry accounts for 12% of the land, nearly all of which is in pasture grazed by moderate densities of horses or tethered cattle (about 25/km<sup>2</sup>). Urban areas and industries are utilizing 10% and 3% of the land, respectively. The watershed's industries include a sugar factory, a cement factory, a small catering service, construction of a golf course and reservoir, and a quarry. By-products of the sugar factory include fly ash, bagasse, and filter press mud (Dunfield 1991) which are left as big, loose, exposed piles in large plots on the property.

Urban areas in Barbados are distinctive in their wastewater disposal methods and their widespread utilization of garden plots. Most houses are equipped with

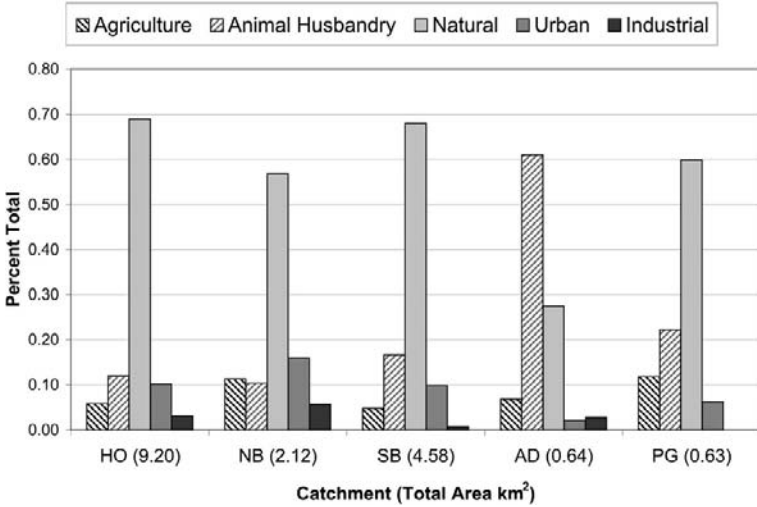


Fig. 22.2 Proportions of 2006 landuse in the entire watershed (HO) and in upstream subbasins (SB, NB, AD, PG). Distribution of landuses and locations of subbasins can be seen in Fig. 22.3

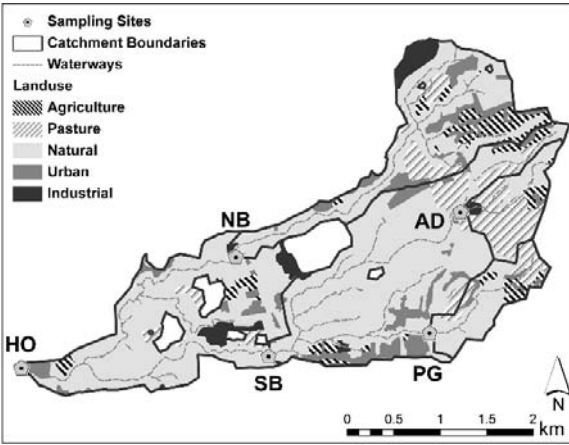


Fig. 22.3 Landuse distribution in the watershed in 2006. Labels identify sampling sites and the catchments draining to them

suckwells, or soakaways, for sewage disposal (73%), which connect a house’s water closet to the underground limestone aquifer (Stanley International Group Inc. 1998). However, overflows and resurfacing groundwater present a potential risk of these areas contributing nutrients to the runoff during flooding events. Garden plots of food crops or fruit trees are quite common to residential areas, and so the effects of agriculture on surface water quality may also be expected from residential areas to some extent. Lastly, much of the island lacks a proper waste collection system which has resulted in some of the gullies near urban areas being used as clandestine dumpsites (Stantec Consulting 2003).

### 22.2.2 Assembling Environmental Databases

Landuse, soil, and waterway information was obtained from McGill University's Geographic Information Center, Montreal, and verified in the field. Waterways required minor updates but landuse had changed considerably, requiring the digitization of a new layer. Sinkholes, landuses, and waterways were mapped using a Thales ProMark 3 GPS unit. GPS data were post-processed with data from the Continuously Operated Reference Station at the Barbados Coastal Zone Management Unit (CZMU). A digital elevation model was interpolated using ArcGIS 9.1 from 3.05 m contours digitized by Baird & Associates Ltd. ArcHydro was used to delineate the watershed with the utilization of stream-burning (Maidment 2002). Sinkholes, as well as a large quarry, represent areas of internal drainage which do not contribute to runoff at the watershed's outlet and so their catchment areas were delineated and removed from the total watershed area to define an effective contributing area (Fig. 22.1) (Wallace Evans and Partners 1973; Leitch and Harbor 1999).

Rain data recorded by 7 gauges, G1-G7 (Fig. 22.1), were contributed by various sources (Table 22.1). Additional historical data were also provided by the Caribbean Institute for Meteorology and Hydrology. Theissen polygons were computed from available rain gauges for each event and used to calculate average and total rainfall depths within the watershed. Hourly wind data were obtained from a weather station operated by the Barbados CZMU, and averaged over the time between the onset of flow and seawater sampling. The weather station was located on the roof of a building on the coastline 300m south of the terrestrial outlet (Fig. 22.4). Significant wave heights used to identify periods of higher wave action were obtained from a sensor stationed approximately 1km south of the seawater sampling area also operated by the Barbados CZMU.

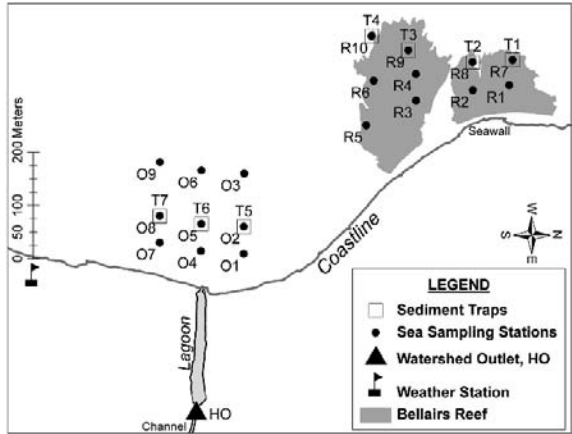
**Table 22.1** Sources of 2006 rain data. Gauge locations are shown in Fig. 22.1

Gauge ID	Recording interval	Operated by
G1-G4	1mm	Baird & Associates Ltd.
G5	1h	Coastal Zone Management Unit, Barbados
G6	0.2mm	Drainage Unit, Barbados
G7	1h	Sandy Lane Golf Course

### 22.2.3 Field Sampling and Measurement

Weather patterns were tracked and flow events were monitored from May–December 2006. Samples (300 ml) were taken from the runoff's surface water and analyzed for TSS, turbidity, soluble reactive phosphorus (SRP), and nitrate-nitrite-nitrogen ( $\text{NO}_x\text{-N}$ ). These variables are known indicators of eutrophication and sedimentation for which guidelines for the protection of marine health have been set by the Barbados Government's Marine Pollution Control Act (Government of Barbados

**Fig. 22.4** Marine sampling scheme. Labels identify sea sampling stations (Outlet Area: O1–O9, Reef Area: R1–R10) and sediment traps (T1–T7)



1998) as well as other organizations globally. Descriptions of all methodologies, laboratory analyses, rating curve data, and loading calculations are available online in Tomic (2007).

At the coastal outlet of the Hometown watershed, site HO (Fig. 22.1), single samples were taken every 5 minutes for at least the first 3 hours of each of 4 flow events (Oct. 16, Oct. 27, Nov. 14, Nov. 24). A high frequency of sampling is important due to rapid changes in concentrations during events (Brodie and Mitchell 2005). Triplicate samples were taken every 30 minutes to verify the precision of measurement. In addition, a set of 7 grab samples were taken at HO 2 hours after the initial flow of an event on Aug.24. These 5 flow events represent the first 5 of 9 events which occurred in 2006. TSS and turbidity were analyzed for all 5 events, SRP was analyzed for the events of Oct. 16, Oct. 27, Nov. 14, Nov. 24, and  $\text{NO}_x - \text{N}$  was analyzed for the events of Nov. 14 and Nov. 24.

Upstream sites for water quality sampling were selected based on accessibility (Fig. 22.1). For two events (Nov. 14, Nov. 24), triplicate sets of grab samples were taken from upstream sites in the following order: SB, NB, AD, and PG. Upstream sampling on Nov.14 and Nov.24 began 50 and 40 minutes after the initial flow at HO, respectively, and was complete within 55 and 45 minutes, respectively. The catchments draining to these sampling sites (Fig. 22.1) will hereafter be referred to by the names of their outlets.

A rating curve was established at site HO (Fig. 22.1) in the rectangular concrete channel (2.5 m width, 0.6 m depth) 25 m upstream of the Hometown lagoon. Velocity was measured at 6 tenths of the total depth below the surface at five points equally spaced across the channel's width using a model 1210 Price Type AA Current Meter (Herschy 1995). A pressure transducer in the channel operated by Baird & Associates Ltd. for the Barbados CZMU recorded continuous measurements of stage which were later converted to discharge using the rating curve. For above bank conditions, Manning's equation was used to calculate flow according to Arcement and Schneider (1989).

Seawater surface samples were collected at depths of 0.5 m (Devlin and Brodie 2005) from a sea kayak. Tidal level can affect seawater nutrient concentrations (Sander 1981; Lewis 1987), and so sampling was always done at the same tidal level for consistency. Sampling began immediately following low-tide such that tidal currents did not change during sampling. For each of 4 events (Aug. 24, Oct. 16, Oct. 27, Nov. 14), seawater sampling was done following the conclusion of flow in the channel, and one tidal cycle, such that the rising tide had rebuilt the beach. This corresponded to a period of 17 hours following the onset of flow which coincidentally always occurred within 1 hour of the same time of day (16:00 local time). A second set of samples was collected for the events of Aug. 24, Oct. 16, and Nov. 14 following periods of 67, 41, and 67 hours, respectively, after the onset of each flow event. Baseline data were collected on 4 occasions between Sept. 30–Oct. 14, at which point no flow event had occurred for at least 1 month. Seawater samples were taken at 19 stations (Fig. 22.4): 10 stations in the area of the Bellairs Reef (R1-R10) and 9 stations in the area of the terrestrial outlet (O1-O9). However, for 1 event (Aug. 24) only the reef area was sampled. In each area, sampling was done along onshore-offshore transects (Devlin and Brodie 2005) with 80 m between each transect and stations located at approximately 50, 100, and 200 m offshore. These offshore distances were selected in order to sample both the crest zone and the spur and groove zone of both North and South Bellairs. Stations R7-R10 were located in the spur and groove zone of the Bellairs Reef (depth = 5 m), while stations R1-R6 were located in the reef's crest zone (depth = 2 m). At each station, triplicate 1L samples were taken and analyzed for turbidity and TSS. Salinity was also measured in samples taken 17 hours after the onset of 2 flow events (Oct. 16, Oct. 27) and on 1 baseline sampling occasion using a YSI model 33 S-C-T meter.

Seven sediment traps were monitored from July 31 to Dec. 5 (Fig. 22.4). Traps were retrieved periodically, with sampling periods ranging between 3 and 30 days. Four traps were placed in the spur and groove zone of the Bellairs Reef (T1-T4) and three were placed directly offshore of the terrestrial outlet (T5-T7). Traps were placed 100 m offshore with the exception of two traps on South Bellairs, traps T3 and T4, for which offshore distances were adjusted to 175 and 225m, respectively, such that all traps on the reef were at equal depths of 5.4 m. The opening of each trap was positioned at a height of 60 cm off the seabed (Delcan Consulting 1994). Each trap comprised three PVC tubes (3.8 cm diameter, 25 cm length) spaced 20 cm apart on a single cement block. These dimensions yield an aspect ratio (height:mouth diameter) of 6.6, characteristic of an efficient sediment trap (Hargrave and Burns 1979).

#### **22.2.4 Data Analysis**

The statistical analyses of runoff water quality data were performed spatially using 5 sites and temporally using 2 events. In the case of seawater quality, statistical analyses were performed after subtraction of baseline levels. Spatial trends were analyzed for the 9 sampling stations in the outlet area as well as for the 10 sampling



stations in the reef area. Temporal trends were analyzed across 3 flow events in the outlet area and 4 flow events in the reef area. Changes in runoff water quality and seawater quality in the nearshore area following a flow event were first analyzed using classical unmodified ANOVA. The basic ANOVA model was a fixed two-way factorial model with replicates, the sampling station and flow event being the two crossed factors.

However, the spatio-temporal data of runoff and seawater exhibited signs of autocorrelation and heteroscedasticity in violation of the circularity condition required for unmodified ANOVA *F*-tests (Huynh and Feldt 1970; Rouanet and Lepine 1970). Thus, a modified univariate testing procedure was performed, using estimates of Box’s epsilon (Box 1954a,b) to correct the numbers of degrees of freedom in a given *F*-test statistic and adjust the probability of significance. A doubly multivariate model, called the matrix normal model, was used to compute estimates of Box’s epsilon and adjust probabilities of significance of the modified ANOVA *F*-tests for space, time, and space-time effects (Dutilleul and Pinel-Alloul 1996). When main effects of sampling station or flow event were declared significant ( $P < 0.05$ ) by the modified ANOVA *F*-test, multiple comparisons of means were performed with a modified Student-Newman-Keuls procedure. In this procedure, the error number of degrees of freedom was multiplied by the corresponding Box’s estimate.

## 22.3 Results

### 22.3.1 Runoff Water Quantity and Quality

The flow regime of the watershed’s gully system is dominated by the characteristics of flash floods (Gaume et al. 2004). Discharges at the watershed’s outlet, site HO, rise from zero to peak flow within the first 15 minutes of flow and then gradually decrease (Fig. 22.5). A second peak discharge was visible for 5 of the events

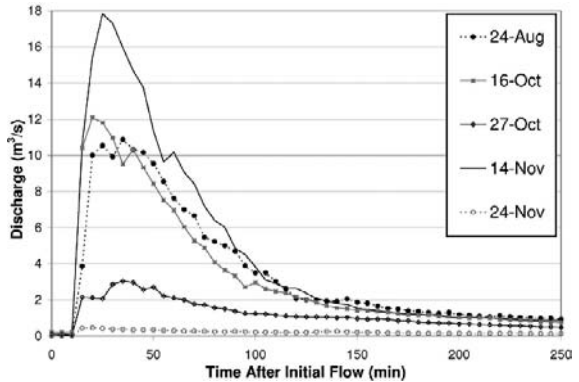


Fig. 22.5 Discharge at the Hometown watershed outlet (HO) for the first 5 of 9 flow events that occurred in 2006

10–20 minutes after the first peak, indicating the arrival of another tributary’s runoff. Most flow events resulted from rainfall intensities between 30 and 45 mm/h, though values of 94 and 78 mm/h were recorded on Oct. 16 and Nov. 28, respectively, at the gauge furthest upstream, G1. The period of time between peak rainfall at G1 and peak discharge at HO varied between 1–1.5 hours for high-flow events and 2.5–3 hours for low-flow events. During the study period 9 flow events occurred at HO, all of which breached the beach and flowed directly to sea.

Total annual rainfall was average in the watershed’s upper terrace, G1, and below average near the coast, G4, compared to the past 25 years (unpublished data, Caribbean Institute for Meteorology and Hydrology). During this rainy season’s peak, Aug.–Nov., all monthly totals were below average at all stations except G1 where monthly rainfall was below average only in September and above average in November. September was an unusually dry month yielding no flow events and creating public concern over the upcoming year’s groundwater reserve (Price 2006).

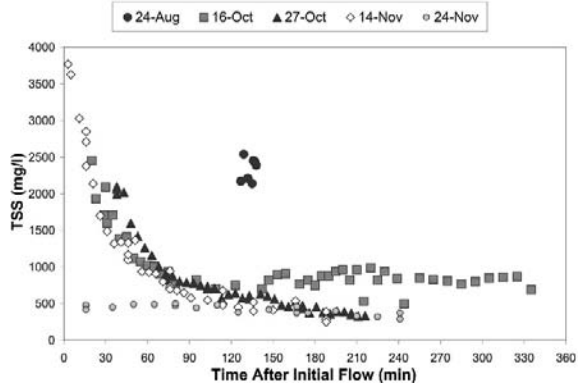
The spatial distribution of rainfall within the watershed showed high heterogeneity (Table 22.2). During some storms, parts of the watershed received almost no rain while the vast majority of rainfall was localized in the upper terrace (e.g. Oct. 16). For most flow events rainfall was highest at gauge G1, though later in the season the proportion of event rainfall near the coastal area increased, typical of distribution patterns in the rainy season (Jones and Banner 2003). The common discrepancy between rainfall at G5 and nearby gauge G4 is a good example of how sharply contrasting these distributions can be. The data show that rainfall from a single station cannot be used as an indicator of runoff from this watershed, as has been used in some past research (Sander 1981), especially considering the hydrological complexities involved in karstic drainage in addition to those of tropical rainfall. More detailed analyses of the watershed’s hydrology can be found in Tosic (2007).

Nutrient concentrations at HO revealed event mean concentrations of 0.34 + / – 0.06 mg SRP/l and 0.7 + / – 0.3 mg NO<sub>x</sub>-N/l but no discernable temporal patterns. Concentration curves for TSS and turbidity during the events monitored at HO are displayed in Figs. 22.6 and 22.7, respectively. The temporal variation of TSS during the high-flow events (Oct. 16, Oct. 27, Nov. 14) exhibits the characteristics of the first flush phenomenon: a disproportionately high delivery of a substance’s mass during the initial portions of a flow event (Sansalone and Cristina 2004). On Oct. 16,

**Table 22.2** Event rainfall totals (mm) for 2006. Hyphens (–) indicate a lack of data

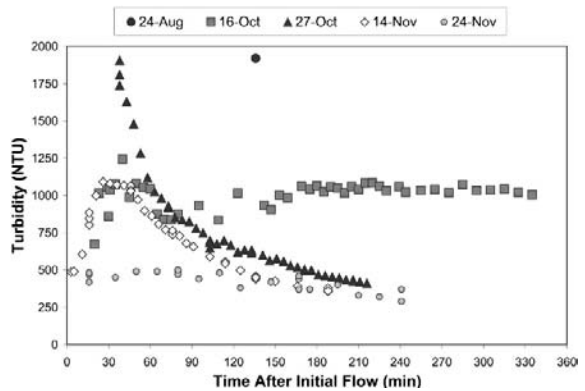
ID	Aug. 24	Oct. 16	Oct. 27	Nov. 14	Nov. 24	Nov. 25	Nov. 28	Dec. 6	Dec. 10	Dec. 19
G1	97	58	40	54	18	11	37	4	12	12
G2	–	–	–	55	–	0	53	–	–	–
G3	–	3	22	14	3	0	9	32	19	2
G4	–	7	31	32	4	7	11	36	15	1
G5	69.4	1.8	24.6	0	0	0	0.2	33.4	10.6	0.2
G6	55.7	18	16.8	39	3.7	6.3	9.5	–	–	–
G7	46.7	1.8	6.3	25	4.1	6.6	2	25	8.6	–

**Fig. 22.6** TSS concentrations at the Hometown watershed outlet, HO



Oct. 27, and Nov. 14, 80% of the total TSS load was delivered within the first 59%, 38%, and 46% of total runoff volume, respectively. TSS concentrations 2 hours into the year’s first flow event, Aug.24, were much higher than those 2 hours into any other event (Fig. 22.6), and so it appears that there may also be a seasonal first flush phenomenon (Lee et al. 2004). Correspondingly, TSS in the residual discharge of the year’s second event, Oct. 16, was higher than that of the events to follow. Such a phenomenon can naturally be expected as a result of sediment accumulation during the year’s 8 month dry season proceeded by sediment exhaustion by the season’s first flow.

Similarly, turbidity values in the events’ residual discharge decreased with each successive event (Fig. 22.7). Temporal variation of turbidity within a given event was different from TSS. The 2 high-flow events during which samples were taken within the first 30 minutes (Oct. 16, Nov. 14) showed that turbidity gradually increased during the initial period of flow. The observed differences between turbidity and TSS in the first 30 minutes could conceivably be due to the presence of sizable organic matter flushed out of the gullies (where illicit dumping is common)



**Fig. 22.7** Turbidity at the Hometown watershed outlet, HO

which would add to TSS mass but not be accounted for in the turbidity measurement. Higher turbidity may be related to discharge with a short lag or, alternatively, originate from a further location.

Means of water quality results from various sites in the watershed during the events of Nov. 14 (high-flow) and Nov. 24 (low-flow) are displayed in Figs. 22.8 and 22.9. Values at HO used for comparison are values obtained 30 minutes after sampling at sites NB and SB, to allow for travel time between the two terraces. Overall, turbidity and TSS were significantly higher among all sites for the high-flow event ( $P < 0.001$ ), which is expected as a result of higher water velocities capable of eroding and transporting more sediments. Differences in nutrient concentrations between the events were insignificant, showing the potential for nutrient transport even by low-flow events.

The results of the modified ANOVA showed that the upstream site NB had significantly higher turbidity ( $P < 0.001$ ), TSS ( $P < 0.001$ ), and SRP ( $P = 0.001$ ) than all other sites, with the exception of there being no significant difference between TSS at NB and HO. However, the ranking of sampling sites for these parameters was not the same for both events (Figs. 22.8 and 22.9), which reflected a significant station\*time interaction for turbidity ( $P < 0.001$ ), TSS ( $P < 0.001$ ), and SRP ( $P = 0.014$ ). Urban, agricultural, and industrial landuses combine for 33% of sub-basin NB's area, a much higher proportion than in catchments HO (19%), SB (15%),

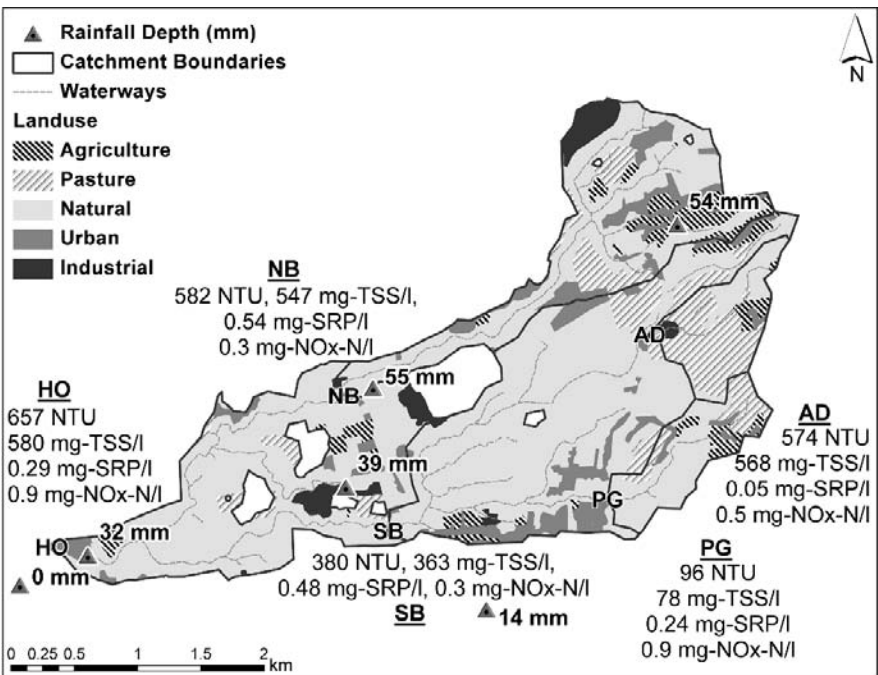


Fig. 22.8 Upstream water quality sampling Nov. 14. Values given at each site are event means

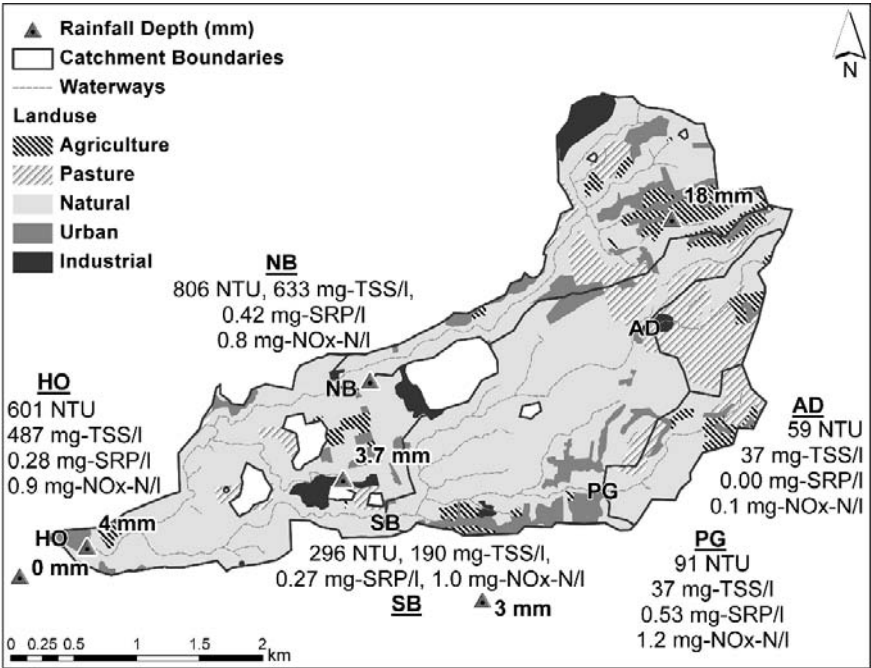


Fig. 22.9 Upstream water quality sampling Nov. 24. Values given at each site are event means

AD (12%), and PG (18%) (Fig. 22.3). This suggests that the landuses in subbasin NB are contributing much higher turbidity, TSS, and SRP per unit area of land than the landuses in the other subbasins. The impact of these upstream tributaries on downstream water quality would best be assessed by their total loads but these cannot be calculated accurately as the shapes of their hydrographs are unknown and may be different.

Subbasin NB was further examined with samples taken at locations further upstream (Fig. 22.10). These samples were taken during the late stages of a low-flow event in which runoff did not arrive downstream to NB, presumably due to internal drainage (Tosic 2007). Water levels were low enough that the 2 tributaries sampled (MS & MN which flow to M) were the only ones flowing. Low water levels and the fact that the tributary running from the nearby construction site (“Industrial” Fig. 22.10) wasn’t flowing are the likely reasons turbidity and TSS were low compared to levels at NB during other events. However, it is clear that the tributary draining the urban and agricultural areas of Hillaby, MS, is contributing much higher levels of all the tested parameters than the tributary draining the less developed area to the north, MN.

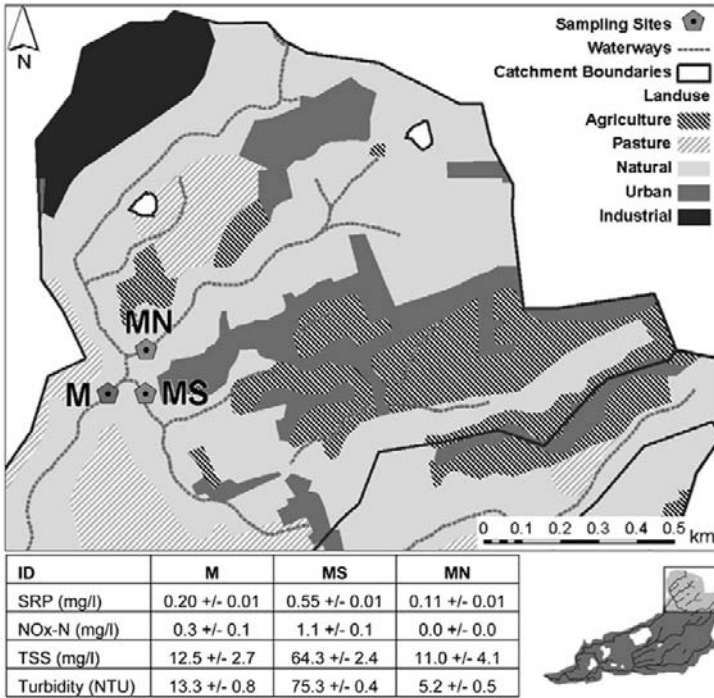


Fig. 22.10 Upstream water quality in subbasin NB, Nov. 23

### 22.3.2 Environmental Impacts of Runoff on the Reef Area

Effluents from the entire watershed and wind data for each event are summarized in Table 22.3. Total discharge, peak discharge, and TSS load were positively related. The single exception is the TSS load of Aug. 24, estimated to be much higher than the load of Nov. 14 which had a higher total discharge and peak discharge. As previously discussed, the Aug. 24 event was the year’s first flow which can contain much higher concentrations (Lee et al. 2004). Wind speed showed strong variation and although wind direction varied, it was consistently offshore with a northward component.

While the nutrient loads presented in Table 22.3 would be expected to enrich the nearshore seawater it is difficult to assess the impact these loads would have on ambient nearshore concentrations without concurrent measurements of seawater nutrients during the events. Loads can be used to predict the potential for eutrophication, however, this would require knowledge of the nearshore flushing rate (Valiela et al. 2004).

Seawater analyses showed no difference in salinity between baseline values and post-event values (34.6 +/- 0.4 ppt) meaning that surface waters were well-mixed by the time of sampling, 17 hours after the onset of flow. Baseline TSS values

**Table 22.3** Summary of flow event data. Hyphens (–) indicate a lack of data necessary for making estimates. Estimates of potential error are presented in parentheses. Wind direction is given in degrees where zero represents north and angles are measured clockwise

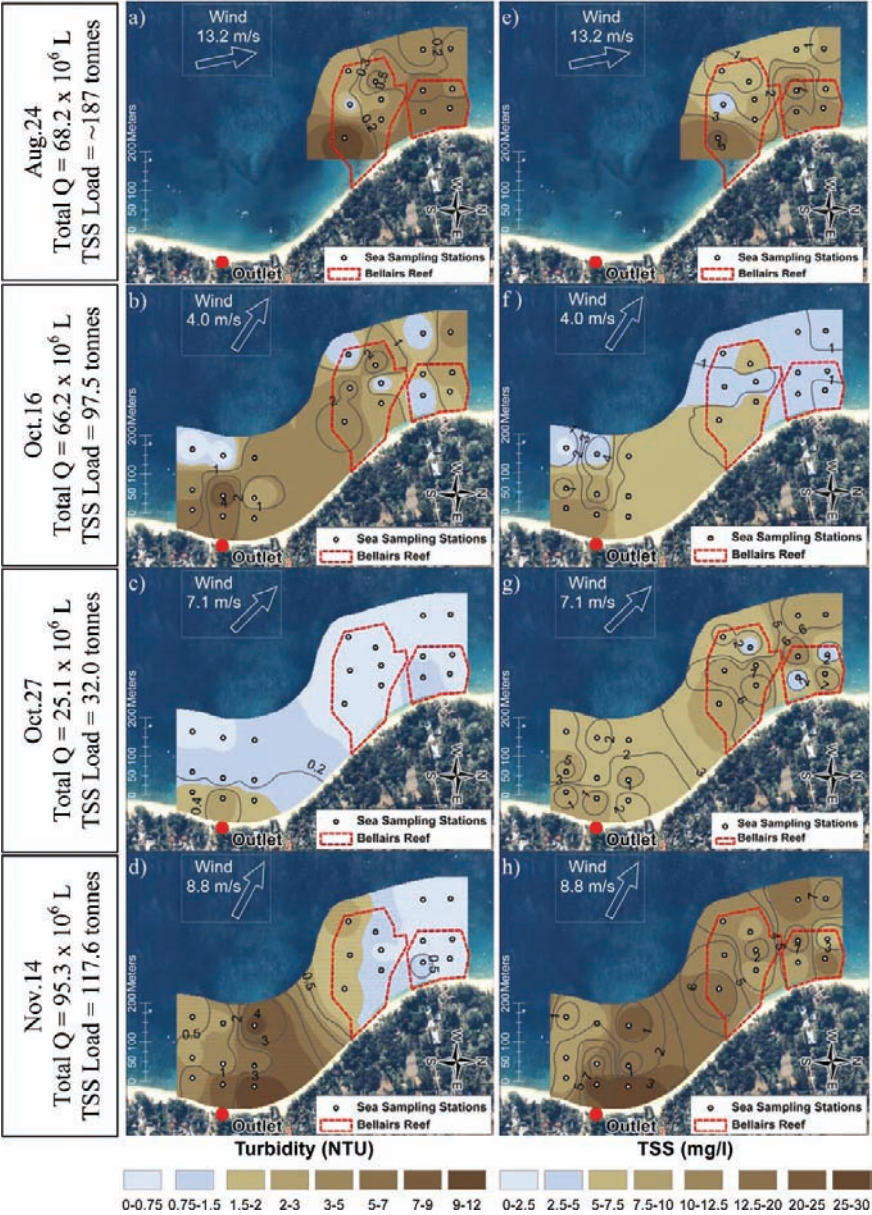
Event date	Total discharge (10 <sup>6</sup> L)	Peak rate of discharge (m <sup>3</sup> /s)	TSS Load (tonnes)	SRP Load (kg)	NO <sub>x</sub> -N Load (kg)	Wind speed (m/s)	Wind direction (degrees)
Aug. 24	68.2 (9.2)	10.9 (0.4)	~187 (25)	–	–	13.2	168.2
Oct. 16	66.2 (6.5)	12.1 (0.5)	97.5 (13.2)	22.5 (6.2)	46.4 (24.6)	4.0	123.2
Oct. 27	25.1 (6.5)	3.0 (0.3)	32.0 (4.1)	8.6 (4.0)	17.6 (13.7)	7.1	135.0
Nov. 14	95.3 (13.6)	17.8 (0.6)	117.6 (20.4)	32.4 (10.4)	66.7 (38.5)	8.8	118.1

averaged  $2.24 + / - 0.26$  mg/l and baseline turbidity averaged  $0.47 + / - 0.07$  NTU. The results of post-event seawater turbidity and TSS analyses are shown in Fig. 22.11 for the 4 events documented in this study. Turbidity and TSS values from each sampling station were used for interpolation using the IDW method to the power of 3. Standard deviations at sampling stations were similarly interpolated and are displayed as contours (Antonic et al. 2001). Guidelines for the protection of marine health have been set by the Barbados Government's Marine Pollution Control Act (MPCA) for turbidity and TSS at 1.5 NTU and 5.0 mg/l, respectively (Government of Barbados 1998). On all occasions, the Bellairs Reef was affected by excessive levels of turbidity, or TSS, or both, with respect to these guidelines.

Second sets of seawater samples taken 41 and 67 hours after the onset of flow showed that above-guideline turbidity levels did not remain in the surface water for long (Fig. 22.12a). On the other hand, TSS levels did not recede showing little, if any change (Fig. 22.12b). As a result, this study shows that when plumes reach the reef, it is subject to harmful TSS conditions due to runoff for a minimum of 3 days following an event.

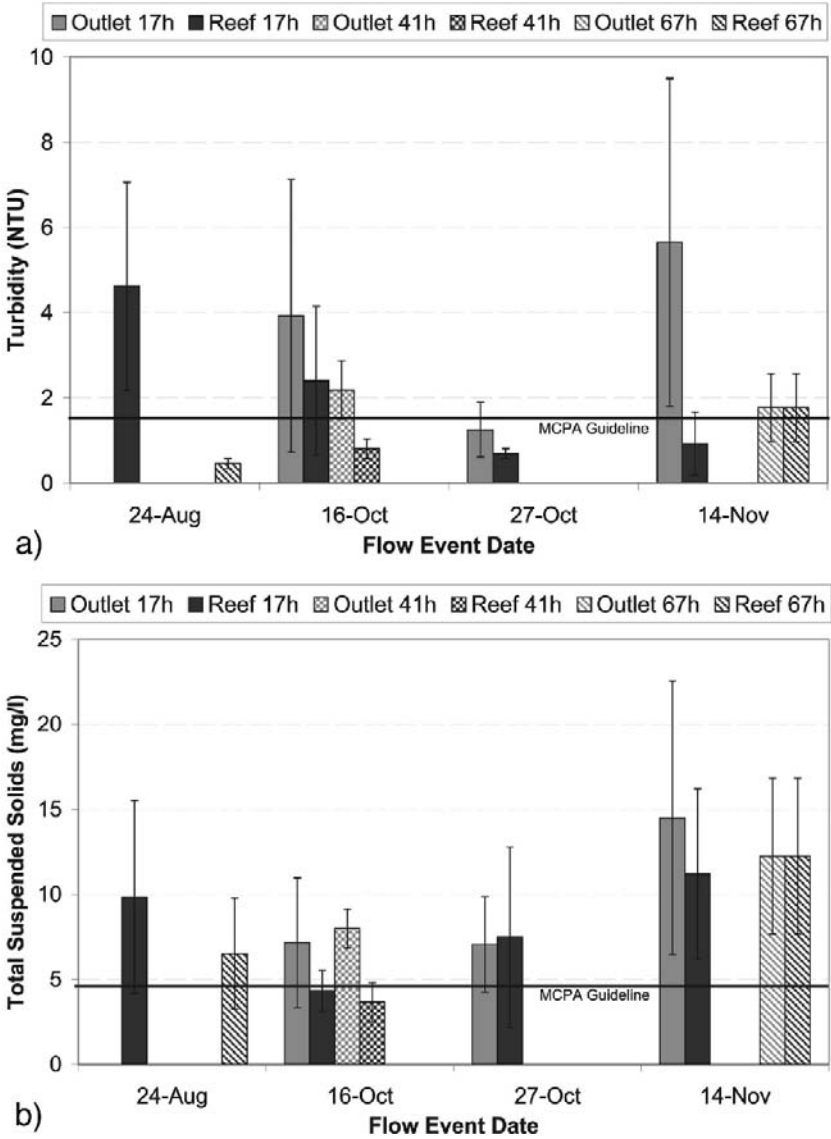
Statistical analyses of spatio-temporal variance in seawater quality showed that all effects exhibited a departure from the circularity condition with exception to TSS in the outlet area which was close to satisfying the condition on the temporal scale (Table 22.4). Adjustments to *P*-values had a slight effect with exception to TSS in the reef area, where station effects were highly significant before correction ( $P = 0.0080$ ) and no longer significant at the 5% level after correction ( $P = 0.0773$ ). The station\*time interaction effects for TSS in the reef area were neither significant before nor after adjustment. All other effects were found to be significant after correction, while time effects were highly significant in all cases.

The significant station effects in the outlet area show high spatial variation of water quality (Fig. 22.13). In terms of both turbidity and TSS, the station directly in front of the outlet, O4, had the poorest water quality overall, followed by the station O1 to the north. Station O9, 200 m offshore and to the south, was least affected by the flow events, followed by station O6, 200 m directly offshore of the outlet. This indicates a northward trend for the fate of runoff as the stations to the north yielded significantly higher values than those to the south for turbidity at 50 m and 200 m offshore, and for TSS at 50 m offshore.



**Fig. 22.11** Seawater turbidity (a–d) and TSS (e–h) following flow events on Aug. 24 (a, e), Oct. 16 (b, f), Oct. 27 (c, g), and Nov. 14 (d, h). Contours indicate standard deviations. Indicated on the left are each event’s total discharge of water (Total Q) and TSS





**Fig. 22.12** Overall averages of (a) turbidity and (b) TSS of post-event seawater samples. Error bars show standard deviations. Samples were taken 17, 41, and 67 hours after the onset of flow

On the reef, the lack of statistically significant station effects for TSS following correction indicates that there is no consistent spatial variation in the area (Fig. 22.14a). Therefore, most of the variation observed among stations before correction was due to the data’s autocorrelation and heteroscedasticity. Spatial trends for turbidity on the reef were limited to the station closest to the outlet, R5, having

**Table 22.4** Results of the repeated measures ANOVA *F*-tests in terms of probabilities of significance (*P*) and the estimates of Box's epsilon used to calculate the adjusted probabilities

Parameter	Main effects and interactions	Outlet			Reef		
		Unadjusted <i>P</i>	Adjusted <i>P</i>	Epsilon	Unadjusted <i>P</i>	Adjusted <i>P</i>	Epsilon
Turbidity (NTU)	station	<0.0001	0.0038	0.313	<0.0001	0.0251	0.149
	time	<0.0001	<0.0001	0.630	<0.0001	0.0003	0.413
	station*time	<0.0001	0.0118	0.185	<0.0001	0.0304	0.047
TSS (mg/l)	station	<0.0001	0.0025	0.314	0.0080	0.0773	0.384
	time	<0.0001	<0.0001	0.927	<0.0001	0.0004	0.770
	station*time	<0.0001	0.0016	0.278	0.2790	0.3656	0.179

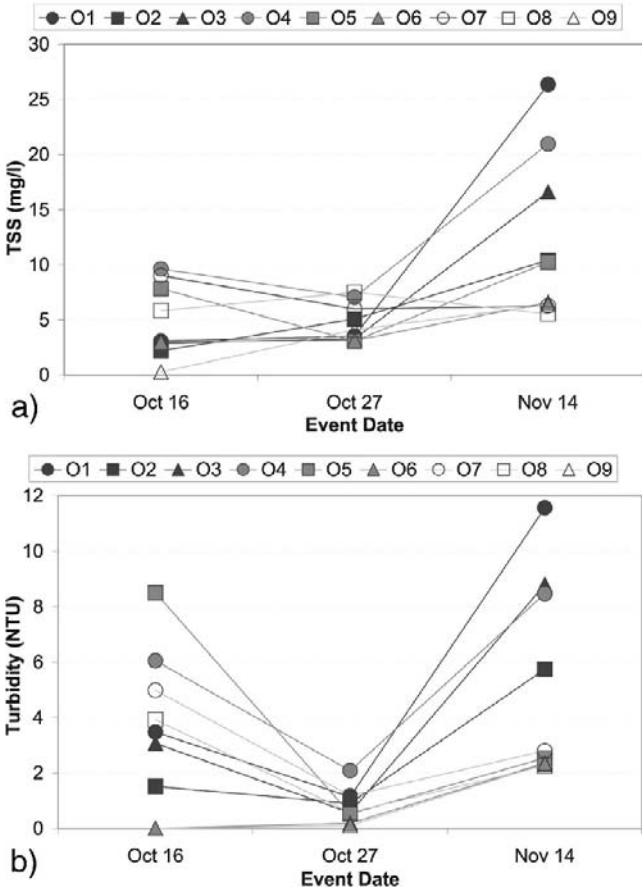


Fig. 22.13 (a) TSS and (b) turbidity at sea sampling stations (O1–O9) in the outlet area

significantly higher values than the rest (Fig. 22.14b). There were no differences in turbidity or TSS between the reef’s spur and groove zone and crest zone nor between the north and south lobes of the reef.

Considering all sampling stations in the reef and outlet areas together, negative relationships were observed between turbidity and distance from the outlet and between TSS and distance from the outlet (Fig. 22.15). The single exception is TSS on Oct. 27 in which stations at further distances are no lower than those directly in front of the outlet.

Significant station\*time interactions indicate that differences between stations were not constant from one event to the next, as was the case for turbidity and TSS in the outlet area and turbidity in the reef area. In particular, the station with the highest turbidity or TSS value in each area varied among the events. These interaction effects are evident in the differing slopes of the straight lines fitted for each event in Fig. 22.15. For example, both turbidity and TSS decreased rapidly

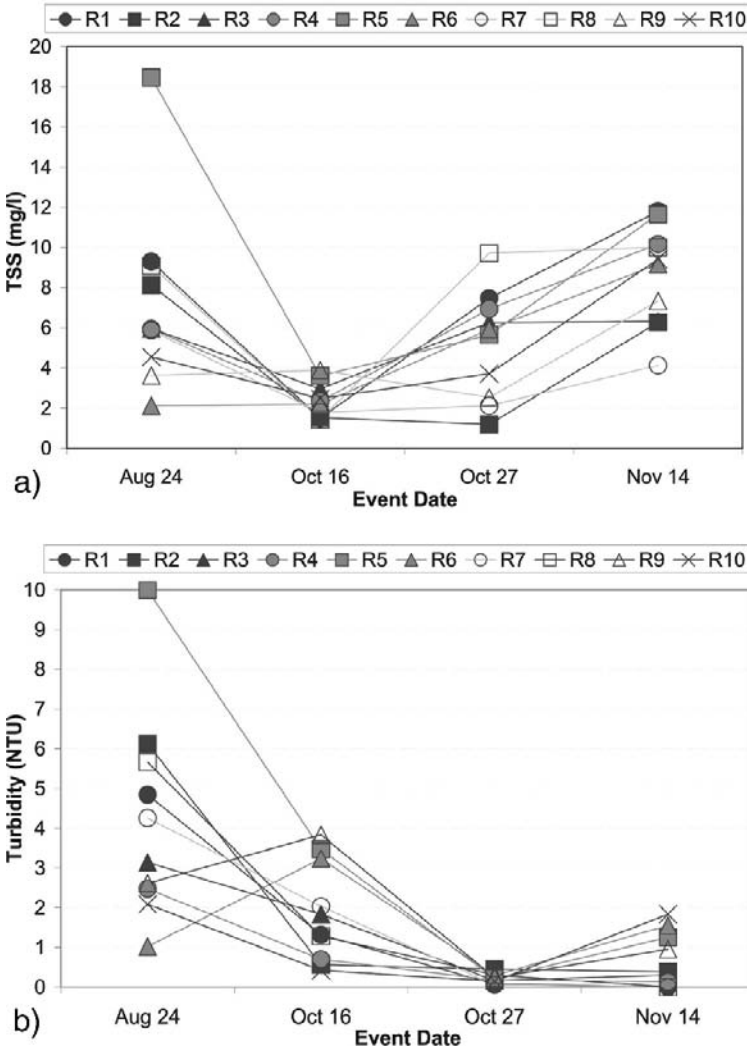


Fig. 22.14 (a) TSS and (b) turbidity at sea sampling stations (R1–R10) in the reef area

with distance from the outlet on Nov. 14 while the event of Oct. 27 produced lines with much flatter slopes.

The most important effects were those due to temporal variation which were highly statistically significant in all cases. This variation may be associated with the differences between the individual events (Table 22.3, Fig. 22.11). In the outlet area, all three events produced significantly different turbidity levels. The event of Nov. 14 produced the highest turbidity values followed by the events of Oct. 16, and then Oct. 27. This ranking is in accordance to differences in the total discharge, peak discharge, and TSS load of the three events sampled. TSS levels yielded the same

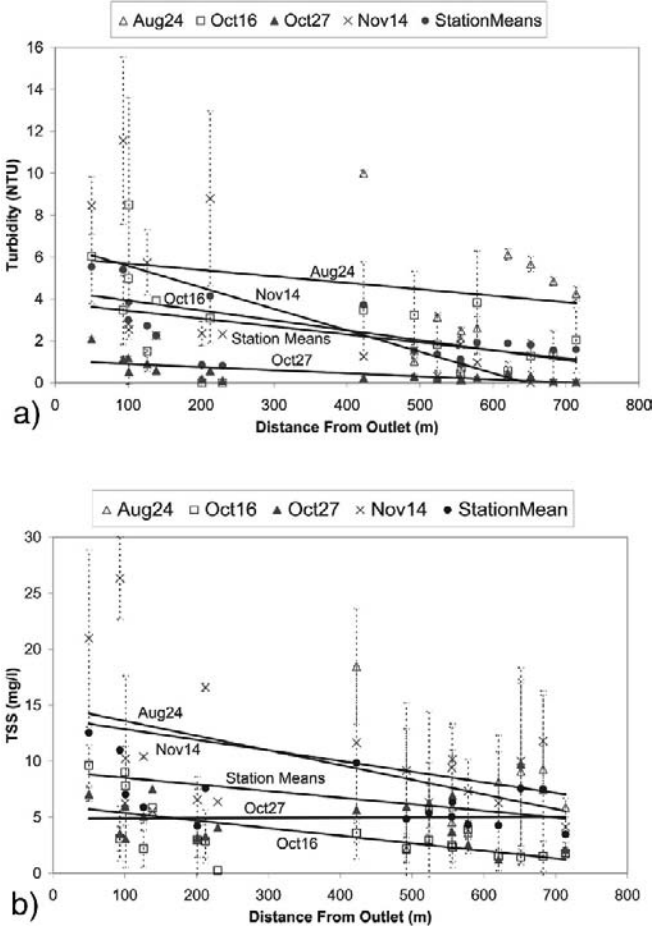


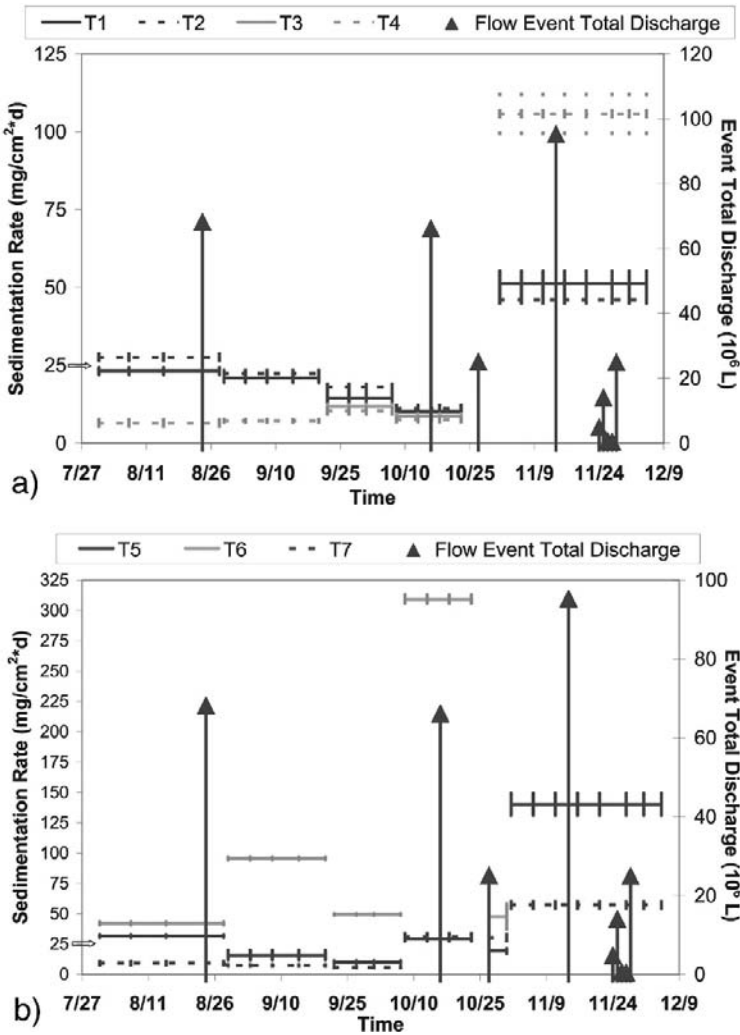
Fig. 22.15 Water quality vs. distance to outlet. (a) Turbidity and (b) TSS at all stations displayed with error bars of standard deviations and trend lines labeled by event date

ranking; however, there was no significant difference between the events of Oct. 16 and Oct. 27.

In the reef area, changes in turbidity due to the four events sampled showed significant differences. The events of Aug. 24 and Oct. 27 respectively produced the highest and lowest seawater turbidity values as well as TSS loads in the runoff (Table 22.3, Fig. 22.11). However, the event of Nov. 14 had less of an effect on turbidity in the reef area than the event of Oct. 16 which yielded a lower discharge and TSS load, and had much weaker wind speeds. A possible explanation could be that the strong winds of Nov. 14 directed more offshore caused the plume to disperse offshore fast enough to avoid a high turbidity impact to the nearby reef to the north. Seawater TSS levels in the reef area were significantly higher for the two events with the greatest discharges and loads, Aug. 24 and Nov. 14. The event with the

lowest discharge and load, Oct. 27, created greater changes in the reef's seawater TSS levels than that of the Oct. 16 event. Again, this could be explained by wind direction, as the winds on Oct. 27 were much stronger and pushed surface water more northward than those of Oct. 16.

Time-averaged sedimentation rates are displayed in Fig. 22.16, though on occasion some traps were not set or found knocked over, resulting in missing data. Sedimentation rates were above the MPCA guidelines ( $25 \text{ mg/cm}^2 \cdot \text{d}$ ) for the last 35 days of sampling on both lobes of the reef (Fig. 22.16a). On North Bellairs, traps T1 and T2, sedimentation rates were above or near the guidelines for the first



**Fig. 22.16** Time-averaged sedimentation rates ( $\text{mg/cm}^2 \times \text{d}$ ) in the (a) reef area and the (b) outlet area, and flow event total discharge volumes ( $10^6 \text{ L}$ ). Vertical error bars show standard deviations. MPCA guidelines ( $25 \text{ mg/cm}^2 \times \text{d}$ ) are indicated on the left vertical axes with an arrow

52 days of sampling. However, it is most likely that the average rate of the first sampling set was elevated by the first flow event (Aug. 24) occurring at the end of the sampling period, and that the period during which rates were near MCPA guidelines was approximately 26 days.

In the outlet area, temporal variation of sedimentation rates appears to be regulated by inputs of terrigenous sediment. For example, rates increased following the event of Aug. 24 and then gradually decreased until the next event (Fig. 22.16b). Sedimentation rates at trap T6, directly in front of the outlet, are extremely high following the event of Oct. 16. While this event was not the largest in magnitude, its resulting plume did not disperse widely due to the low wind speeds, as seen in the TSS values (Fig. 22.11f), which may have resulted in the considerably large mass of accumulated sediment at T6. Spatial variation was similar to that of the surface water with the trap to the north of the outlet, trap T5, collecting larger quantities than the trap to the south, trap T7.

In the reef area, it appears that temporal variation was also regulated by the input of terrigenous sediment. However, in this case the input is not only dependent on the occurrence of flow events but on the presence of substantial wind speeds capable of transporting plumes to the reef; wind speeds were weak during the event of Oct. 16 resulting in a lack of input to the reef area, as was the result for surface water TSS. Waves, which also have the potential to resuspend both terrigenous and marine source sediments in the reef increasing recorded sedimentation rates (Bothner et al. 2006), gradually increased in height during the survey period. However, the sedimentation rates gradually decreased for the first 3 months of sampling, thus weakening hypotheses of temporal variation depending on wave heights. Though wave data were not recorded over the spatial scale of the sediment traps, observations of sea conditions were made daily. During times of low wave action, significant resuspension may still occur in the spur and groove zone of North Bellairs due to its close proximity to the coastline. This coastline is bordered by a seawall (Fig. 22.4) against which waves are regularly crashing. This may be the reason sedimentation rates were higher on the reef's northern lobe, traps T1 and T2, for the first 3 months of sampling. At the end of the study period, wave heights increased and substantially greater surf took place upon South Bellairs, traps T3 and T4. This likely caused increases in resuspension and sedimentation rates on South Bellairs to be higher than on North Bellairs. Taking averages over the entire sampling season, overall sedimentation rates on the two lobes of the reef were equal.

## 22.4 Discussion

### 22.4.1 Runoff Water Quality and Landuse

A previous study sampling just 300 m upstream of HO on multiple occasions during the wet season reported similar nitrogen concentrations (0.610 mg NO<sub>3</sub>-N/l) though lower phosphorus concentrations (0.096 mg PO<sub>4</sub>-P/l) (data converted from original, Hunte 1989). A reduction in agriculture and expansion of urban areas

over the time period between these two studies suggests SRP increases could be the result of greater amounts of urban wastewater, though increased fertilizer availability and use are also possibilities. The nutrient concentrations reported in this study are similar to those in some of the world's large contaminated rivers (Meybeck 1982). Brodie and Mitchell (2005) report dissolved inorganic nitrogen ( $\text{DIN} = \text{NH}_4\text{-N} + \text{NO}_x\text{-N}$ ) concentrations of 0.14–1.40 mg/l in northern Australian catchments dominated by agriculture. High nutrient concentrations in agricultural watersheds are expected due to widespread fertilizer use, however, with only 6% of the present watershed's land devoted to agriculture (HO, Fig. 22.2) these values are quite high. Whereas natural areas in this watershed account for 69% of the land, natural catchments around the world typically have nitrate-nitrogen and phosphate-phosphorus concentrations of 0.1 mg/l and 0.01 mg/l, respectively (Meybeck 1982).

On Nov. 14, the surface water's turbidity, TSS, and  $\text{NO}_x\text{-N}$  increased as it traveled from sites NB and SB to site HO (Fig. 22.8), indicating sources in the area between the sites. These increases could very possibly be caused by the sugar factory which has large fields of loose piles of the factory's particulate by-products. An accumulation of fine sediments was also observed at the base of a clearing through the bank of the gully adjacent to the factory's property. Hunte (1989) sampled this gully directly downstream of the factory and reported high nitrate levels (0.843 mg  $\text{NO}_3\text{-N/l}$ ) which were much higher than concurrent samples taken downstream, near HO, on 3 of 4 occasions. The first flush phenomenon is commonly seen in runoff from urban areas, highways, and construction zones (Sansalone and Buchberger 1997; Deletic 1998; Lee et al. 2002; Kayhanian and Stenstrom 2005), supporting the identification of these landuses as sources of sediment in this watershed. Unfortunately, these findings cannot be corroborated by the data from Nov. 24, as the lower terrace received very low amounts of rainfall during this event (Fig. 22.9), suggesting that surface runoff was not generated in the area, and that values at HO simply resulted from mixing of the upstream tributaries.

Subbasin PG had the 2<sup>nd</sup> highest SRP concentrations and the highest  $\text{NO}_x\text{-N}$  concentrations among sites, though the lowest levels of turbidity and TSS. This subbasin is similar to NB in its high nutrient concentrations and high proportion of agricultural landuse (12%) relative to SB, AD, and HO. However, PG and NB differ in that PG has no industries and a smaller amount of urban area (5%) than NB (16%). The low levels of TSS and turbidity at PG support the notion that sources of sediment and turbidity are, at least in this watershed, more likely to be industrial and urban rather than agricultural areas. Meanwhile the high nutrient concentrations support the identification of agriculture as a source of nutrients in the runoff.

A pasture covers much of the area draining to site AD (61%). Nutrient concentrations at this site were the lowest among all sites showing how little pastures contribute to nutrients in this watershed's runoff. The higher TSS and turbidity levels seen on Nov. 14 are surely flushed from the large-scale construction site immediately upstream, yet they were very low on Nov. 24, as a part of the station\*time interaction effects. These inconsistent results may be due to differences in flow levels between the two events, or may also be specific to the state of the construction site during the events.



### 22.4.2 Nearshore impacts

Estimates of nutrient loads can be compared to other primary nutrient inputs to the nearshore area of Hometown such as the water of the Hometown Lagoon and groundwater seeping through the beach. Sampling the Hometown lagoon over space and time, Braithwaite (2004) reported nutrient concentrations averaging  $0.7 + / - 0.3 \text{ mg/l NO}_3\text{-N}$  (converted from original) and  $24.0 + / - 13.9 \text{ mg/l PO}_4\text{-P}$ . A hotel acts as a point-source input to this water body discharging its laundry effluent directly (Braithwaite 2004) and treated wastewater (secondary treatment) (Stanley International Group Inc. 1998). The reported nitrogen concentrations in the lagoon are similar to that of wastewater which typically has nutrient concentrations of about  $0.7 \text{ mg/l NO}_3\text{-N}$  and  $5.0 \text{ mg/l PO}_4\text{-P}$  (Stanley International Group Inc. 1998). The higher concentrations of phosphorus in the lagoon indicate another source which could likely be the laundry effluent as detergents are typically rich in phosphates. Another plausible source of phosphorus could be sediment from previous runoff events settled in the lagoon slowly releasing dissolved phosphorus by the process of desorption (Froelich 1988). With an approximate volume of  $3 \times 10^6 \text{ L}$ , lagoon water represents estimated nutrient loads of  $2.1 + / - 1.3 \text{ kg-NO}_3\text{-N}$  and  $72 + / - 54 \text{ kg-PO}_4\text{-P}$ . While this nitrate load is less than even the smallest estimate of that for runoff (Oct. 27 =  $17.6 + / - 13.7 \text{ kg-NO}_x\text{-N}$ ), the load of reactive phosphorus in the lagoon is more than twice the estimate of that due to runoff during the year's largest flow event (Nov. 14 =  $32.4 + / - 10.4 \text{ kg-SRP}$ ).

This combined load of dissolved phosphorus is of great importance as phosphorus may be the nutrient limiting algal growth in the nearshore area. The molar ratio of dissolved inorganic nitrogen to dissolved inorganic phosphorus has been reported as 28.1:1 (Sander and Moore 1979), greater than the average cellular ratio of 16:1 (Hecky and Kilham 1988). Current research shows that estimates of this ratio are more accurately described by total nutrient levels (Downing 1997). Wellington (1999) measured total nutrients in the coastal waters of Hometown in both the wet and dry season, and reported values yielding N:P molar ratios of no less than 69:1. However, others have reported a much lower average TN:TP molar ratio of 14:1 (Bellairs Research Institute 1997), and so further research is needed.

Based on groundwater and offshore sources, Wellington (1999) estimated nutrient loading rates of approximately  $1 \text{ kg NO}_3\text{-N/day}$  and  $0.009 \text{ kg PO}_4\text{-P/day}$  entering a  $1200 \text{ m}^2$  area along 100 m of Hometown's coast. Though such quantifications are subject to large error, the magnitudes of these estimates suggest that runoff makes substantial dissolved nutrient contributions to the coastal system, especially with respect to phosphorus. Extending Wellington's estimates over the entire 2 km coastline of Hometown (i.e. multiplying by 20), dissolved nitrogen loading due to runoff is apparently comparable to that which naturally enters the coastal water daily. However, the combined dissolved phosphorus load of runoff and the lagoon is still 2 orders of magnitude greater than that due to natural daily loading. Under these assumptions, a single runoff event contributes a dissolved phosphorus load equal to the annual load estimated by Wellington (1999). Of course, the nutrient loads due

to runoff compared here are only minimum estimates of the total nutrient loads, as only reactive nutrients were measured.

A trend of northward flow from the outlet for turbidity was confirmed by stations to the north yielding significantly higher values than those to the south at 50 m and 200 m offshore. The fact that this trend was not observed at 100m offshore may be explained by the irregular bathymetry of the northern transect. The three stations O1, O2, and O3 located 50 m, 100 m, and 200 m along this transect have depths of 4.4, 6.1, and 4.2 m, respectively. According to Fick's Law, the concentration at any location will be inversely proportional to the location's depth during dispersion of a given flux. Thus, the greater depth of station O2 could explain its turbidity levels being lower than that of the further station, O3.

The use of an appropriate statistical model, in this case the matrix normal model and the corresponding modified ANOVA  $F$ -tests (Dutilleul and Pinel-Alloul 1996), proved to be essential to a sound comprehension of our results. Station effects of TSS in the reef area were finally declared non-significant at the 5% level, although had the ANOVA  $F$ -test not been modified the effects would have been found to be significant. Thus, the use of the matrix normal model avoided the generation of artifact effects, which were in fact due to the spatial autocorrelation and heteroscedasticity of the data.

The lack of spatial effects in the distribution of plume waters over the reef indicated that if an event's plume reaches the reef, it will affect the entire reef similarly. While this suggests that different zones of the reef will be affected equally by poor surface water quality, the implications may be greater for the reef crest. This zone takes the brunt of the wave action and has far poorer coral species diversity than that of the spur and groove zone (Lewis and Oxenford 1996). Wave action may be considered a chronic stress upon coastal ecosystems (Grigg 1998; Tewfik et al. 2007). Perhaps the added stresses of eutrophication and sedimentation restricting coral growth in the crest zone are thus inhibiting the coral's resistance to the zone's naturally turbulent environment.

In addition to the potential effects caused by the estimated nutrient loads, event-water plumes with detrimental levels of turbidity and TSS could be termed a chronic stress to the Bellairs Reef as flow events occur every year and all of the events sampled produced detrimental water quality levels above the reef making this a predictable seasonal disturbance. Of the 3 events for which second sets of seawater samples were taken, the two largest events both caused initially high TSS levels that did not recede within 67 hours from the onset of flow. It thus appears that large events can cause poor water quality to linger above the reef but further sampling is needed to confirm this and establish the full duration of influence. Few flow events occurred this year until late November when more frequent flows from the outlet restricted reformation of the beach separating the lagoon from the sea. Residents of Holetown state that this flow regime usually dominates much more of the rainy season, and rainfall in the watershed was below average for the year (unpublished data, Caribbean Institute for Meteorology and Hydrology), suggesting that more than the observed 9 flow events would normally occur. In fact, adjacent watersheds to the north and south atypically did not generate runoff at all in 2006,

minimizing stress incurred by the Bellairs Reef due to additional sources of runoff. During the final stages of the study period, when the lagoon flowed continuously and wave heights were highest, sedimentation rates on the reef were far above the recommended guidelines. Such heavy surf continues for months into the dry season potentially sustaining high sediment resuspension rates. While the complexities of coastal sediment transport exceed the scope of this study, the documented terrestrial sediment loads represent a significant contribution to the nearshore zone and thus the excessive levels of sedimentation observed on the reef.

Excessive sedimentation commonly decreases coral diversity as few species are resilient to such conditions (Cortes and Risk 1985). Large branching corals can typically survive the stress of sedimentation as their morphology limits the accumulation of sediment on their surfaces (Rogers 1990). However, the proliferation of such corals may impede the resilience of a reef's coral community as their tolerance to sedimentation is counterbalanced by their susceptibility to large waves (Blanchon and Jones 1997). For example, the southern part of South Bellairs was once densely covered by the branching coral *Porites porites* (James et al. 1977) until the passing of Hurricane Allen in 1981 destroyed 96% of this species (Mah and Stearn 1986).

### 22.4.3 Recommendations

The first flush phenomenon observed in TSS at the watershed's outlet shows that if any efforts were made to reduce sediment fluxes to the sea, this could efficiently be done by retarding as much of the initial discharge as possible to allow for settling, and protecting the accumulated sediment from erosive action during future events. In this regard, it has been suggested to divert the tributary upstream of site NB into the nearby quarry (Cumming Cockburn Ltd 1996). The present study supports that this venture would not only be a viable solution for reducing runoff peak flows but turbidity, TSS, and SRP loads as well. Capturing only half of the runoff would capture 80% of the TSS, and the tributary to the north has been shown to be contributing the highest concentrations per unit area of land.

Given the low proportions of agricultural and urban landuses, it appears that excessive application of fertilizers is occurring. A recent survey of farmers in a nearby watershed revealed that none were aware of the fertilizer quantities being applied (Denis and Hughes 2003). Though not an immediate solution, it is likely that agricultural practices will eventually require improvement and control as ongoing farming development and population growth will only expand agricultural landuse.

Increases in the island's local and tourist populations will also enhance the potential for wastewater contamination of runoff. Remediation of this problem has been addressed and awaits the progress of the West Coast Sewerage Project (Stanley International Group Inc. 1998). An additional solution would be to phase out the use, or importation, of soaps and detergents containing phosphates. This last solution would be beneficial to conservation of the nearshore marine environment considering the large SRP load shown in this study and that phosphorus has been

suggested to be the nutrient limiting algal growth (Sander and Moore 1979; Wellington 1999). However, it appears that water from the coastal lagoon flushed by runoff events presents a greater dissolved phosphorus load than that delivered by the runoff itself. This lagoon has a volume equal to 10% of an average flow event's total discharge, meaning that regardless of all the upstream nutrient sources, the most efficient means for reducing phosphorus loading would be to control this lagoon's point-sources. These sources are known to have been discharging large quantities of phosphorus for a long time (Brewster 1990; Braithwaite 2004).

## 22.5 Conclusions

Water quality in the watershed is much poorer than it ought to be with such a high proportion of natural land. While high-flow events have a much higher potential for transporting solids, similar nutrient concentrations were observed in high- and low-flow events alike. The high levels of TSS, turbidity, and SRP in the most developed subbasin support the hypothesis of sources being agricultural, urban, and industrial areas.

The first-flush phenomenon observed for TSS and turbidity shows that most of the runoff's sediment content is transported rapidly. Sources are most likely those where solids are abundant and unstable such as the various construction sites and the fields of by-product storage at the sugar factory. This hypothesis is supported firstly by elevated TSS and turbidity levels drained from the areas with large industries, and secondly by lower levels coming from a subbasin containing no industries, a small urban area, and greater agricultural landcover relative to the rest of the watershed.

The reported nutrient concentrations are quite high considering what little agricultural land remains. Expected reductions in nutrient contamination due to the demise of agriculture in the watershed's recent history may have been offset by increased fertilizer application in the remaining areas and urban growth. Identification of agricultural areas as sources of nutrients is supported by high nutrient concentrations found draining from a subbasin with relatively larger agricultural and smaller urban landcover. Pastures, on the other hand, yielded much smaller concentrations of nutrients.

Runoff into the nearshore zone of Holetown causes plumes in excess of the MPCA guidelines for turbidity (1.5 NTU) and TSS (5 mg/l), and delivers large loads of sediments and nutrients contributing to the chronic effects of eutrophication and sedimentation. Including water from the Holetown lagoon, surface water flushed by runoff events appears to be the chief source of SRP to the nearshore area, doubtlessly enhancing coastal eutrophication as phosphorus has been cited in the literature as the limiting nutrient for algae growth (Sander and Moore 1979; Wellington 1999). Plumes around the outlet revealed a trend of northward flow towards the Bellairs Reef. This study's data show that the magnitude of post-discharge changes in the seawater depends on a flow event's TSS load and total discharge, which were proportional for the three events monitored in the outlet area. In the reef area, factors

controlling seawater quality changes included TSS load and total discharge, as well as the strength and direction of prevailing winds. Turbidity levels were above the MPCA guidelines for less than 2–3 days following events but TSS levels showed the potential to remain high for at least three days following the sampled events. Sedimentation represents a definite chronic disturbance as accumulation rates on the reef were far above the recommended guidelines for 35 of the 118 days monitored, and were near the threshold on North Bellairs for an additional 26 days.

The fringing reefs of Barbados are still recovering from the acute disturbances which occurred over 20 years ago as their recovery is impeded by the chronic disturbances of eutrophication and sedimentation resulting from land-based sources (Bell and Tomascik 1993). Remediation of the degrading seawater is critical to the health of the reefs (Bellairs Research Institute 1997). If measures are taken to improve water quality, there is potential for the reef's subsequent improvement. A recent study on the island's south coast revealed ecosystem recovery following local improvements in seawater quality due to enhanced flushing rates in a coastal lagoon (Risk et al. 2007).

**Acknowledgement** We wish to thank Baird & Associates Ltd. and the Barbados Coastal Zone Management Unit for contributing a wealth of essential data and allowing the use of their past reports. The authors also thank the Caribbean Institute for Meteorology and Hydrology for providing equipment and rain data used in this study. Additional rain data were generously contributed by the Barbados Drainage Unit and Sandy Lane Golf Course. We owe a large thanks to John B. Lewis for suggestions on the project's design and helpful comments on an earlier draft of the manuscript. We are very grateful to Renata Goodridge and Ramon Roach for helpful advice throughout the course of this project. We thank the staff of the Bellairs Research Institute for all of their support, especially Victor Small for his assistance constructing field equipment. This work was partially supported by a grant from the National Science and Engineering Research Council of Canada to the second author. This study could not have been completed without the dedicated field and lab assistance of Olivia Drescher, Matthew Martin, and the students of the 2006 McGill Barbados Field Study Semester.

## References

- Antonic O, Krizan J, Marki A, Bukovec D (2001) Spatio-temporal interpolation of climatic variables over large region of complex terrain using neural networks. *Ecol Model* 138(1–3): 255–263
- Arcement GJ Jr, Schneider VR (1989) Guide for selecting Manning's roughness coefficients for natural channels and floodplains. U.S. Geol Surv Water Supply Pap 2339
- Avila LA, Pasch RJ, Jiing JG (2000) Atlantic tropical systems of 1996 and 1997: Years of contrasts. *Mon Weather Rev* 128(10):3695–3706
- Bell PRF, Tomascik T (1993) The demise of the fringing coral reefs of Barbados and of regions in the Great Barrier Reef (GBR) lagoon - impacts of eutrophication. In: Ginsburg RN (ed) *Proceedings of the Colloquium on global aspects of coral reefs – health, hazards and history*. University of Miami, pp 319–325
- Bell PRF, Lapointe BE, Elmetri I (2007) Reevaluation of ENCORE: support for the Eutrophication Threshold Model for coral reefs. *Ambio* 36(5): 416–424

- Bellairs Research Institute (1997) Environmental deterioration and water quality at fringing reefs on the west coast of Barbados. Report prepared for Stanley International and the Government of Barbados
- Bird BJ, Richards A, Wong PP (1979) Coastal subsystems of western Barbados, West Indies. *Geogr Ann A* 61(3/4):221–236
- Blanchon P, Jones B (1997) Hurricane control on shelf-edge-reef architecture around Grand Cayman. *Sedimentology* 44(3):479–506
- Bothner MH, Reynolds RL, Casso MA, Storlazzi CD, Field ME (2006) Quantity, composition, and source of sediment collected in sediment traps along the fringing coral reef off Molokai, Hawaii. *Mar Pollut Bull* 52(9):1034–1047
- Box GEP (1954a) Some theorems on quadratic forms applied in the study of analysis of variance problems. 2. Effects of inequality of variance and of correlation between errors in the 2-way classification. *Ann Math Stat* 25(3):484–498
- Box GEP (1954b) Some theorems on quadratic forms applied in the study of analysis of variance problems. 1. Effects of inequality of variance in the one-way classification. *Ann Math Stat* 25(2):290–302
- Brathwaite RJ (2004) Pollution effects and remediation strategy for the Holetown Lagoon. MSc Thesis, University of the West Indies
- Brewster L (1990) Pollution and beach erosion control on the west coast of Barbados: a case study of pollution at the Hole. Tech. Rep. for the Coastal Conservation Project Unit, Barbados Ministry of Labour and Community Development
- Brodie JE, Mitchell AW (2005) Nutrients in Australian tropical rivers: changes with agricultural development and implications for receiving environments. *Mar Freshwater Res* 56(3):279–302
- Cabana G (1997) A comparative study of food-web processes in aquatic systems using stable isotopes. PhD Thesis, McGill University
- Connell JH (1997) Disturbance and recovery of coral assemblages. *Coral Reefs* 16:S101–S113
- Cortes J, Risk MJ (1985) A reef under siltation stress - Cahuita, Costa Rica. *B Mar Sci* 36(2):339–356
- Cumming Cockburn Ltd (1996) Barbados stormwater drainage study. Report prepared in association with Errol Clarke & Associates Ltd., Franklin and Franklin Ltd., and Charlesworth & Associates Ltd., for the Government of Barbados
- Delcan Consulting (1993) Feasibility studies on coastal conservation. Nearshore benthic marine communities of the west and south-west coasts of Barbados: importance, impacts, present status and management recommendations. Report prepared for the Barbados Ministry of Environment, Housing and Lands, Coastal Conservation Project Unit
- Delcan Consulting (1994) Feasibility studies on coastal conservation. Nearshore marine water quality of the west and southwest coasts of Barbados: present status and management recommendations. Report prepared for the Barbados Ministry of Environment, Housing and Lands, Coastal Conservation Project Unit
- Deletic A (1998) The first flush load of urban surface runoff. *Water Res* 32(8):2462–2470
- Denis P, Hughes M (2003) Nitrate contamination in Ashton Hall catchment, Barbados. Final report for McGill University's Barbados Field Study Semester. Bellairs Research Institute Library, Holetown, Barbados
- Devlin MJ, Brodie J (2005) Terrestrial discharge into the Great Barrier Reef Lagoon: nutrient behavior in coastal waters. *Mar Pollut Bull* 51(1–4):9–22
- Downing JA (1997) Marine nitrogen: Phosphorus stoichiometry and the global N:P cycle. *Biogeochemistry* 37(3):237–252
- Dunfield PF (1991) Effects of a sugar-factory byproduct compost on root growth and mycorrhizal infection of sugarcane in Barbados. MSc Thesis, McGill University
- Dutilleul P, Pinel-Alloul B (1996) A doubly multivariate model for statistical analysis of spatio-temporal environmental data. *Environmetrics* 7(6):551–565
- Fabricius KE (2005) Effects of terrestrial runoff on the ecology of corals and coral reefs: Review and synthesis. *Mar Pollut Bull* 50(2):125–146

- Fratantoni DM, Glickson DA (2002) North Brazil current ring generation and evolution observed with SeaWiFS. *J Phys Oceanogr* 32(3):1058–1074
- Froelich PN (1988) Kinetic control of dissolved phosphate in natural rivers and estuaries: A primer on the phosphate buffer mechanism. *Limnol and Oceanogr* 33(4):649–668
- Gaume E, Livet M, Desbordes M, Villeneuve JP (2004) Hydrological analysis of the river Aude, France, flash flood on 12 and 13 November 1999. *J Hydrol* 286(1–4):135–154
- Government of Barbados (1998) Marine Pollution Control Act: List of Prohibited Concentrations. 1998-40-4
- Grigg RW (1998) Holocene coral reef accretion in Hawaii: A function of wave exposure and sea level history. *Coral Reefs* 17(3):263–272
- Hargrave BT, Burns NM (1979) Assessment of sediment trap collection efficiency. *Limnol Oceanogr* 24(6):1124–1136
- Hecky RE, Kilham P (1988) Nutrient limitation of phytoplankton in fresh-water and marine environments – a review of recent-evidence on the effects of enrichment. *Limnol Oceanogr* 33(4):796–822
- Herschey RW (1995) Streamflow measurement. E & FN Spon an imprint of Chapman & Hall, London, New York
- Howarth RW, Billen G, Swaney D, Townsend A, Jaworski N, Lajtha K, Downing JA, Elmgren R, Caraco N, Jordan T, Berendse F, Freney J, Kudeyarov V, Murdoch P, Zhu ZL (1996) Regional nitrogen budgets and riverine N&P fluxes for the drainages to the North Atlantic Ocean: Natural and human influences. *Biogeochemistry* 35(1):75–139
- Huang H-H (2006) Geomorphologic investigations on karst terrain: A gis-assisted case study on the island of Barbados. MSc Thesis, McGill University
- Hunte W (1989) Water quality in the Holetown catchment area. Report prepared for the Barbados Ministry of Employment, Labour Relations and Community Development, Coastal Conservation Project Unit
- Hunte W, Cote I, Tomascik T (1986) On the dynamics of the mass mortality of *Diadema antillarum* in Barbados. *Coral Reefs* 4(3):135–139
- Huynh H, Feldt S (1970) Conditions under which mean square ratios in repeated measurements designs have exact *F*-distributions. *J Am Stat Assoc* 65:1582–1589
- James NP, Stearn CW, Harrison RS (1977) Field guide book to modern and Pleistocene reef carbonates, Barbados, W.I. Proceedings of the Third International Symposium on Coral Reefs. University of Miami, Miami, Florida, p 30
- Jones IC, Banner JL (2003) Hydrogeologic and climatic influences on spatial and interannual variation of recharge to a tropical karst island aquifer. *Water Resour Res* 39(9)
- Kayhanian M, Stenstrom MK (2005) Mass loading of first flush pollutants with treatment strategy simulations. *Transport Res Rec* 1904:133–143
- Kayhanian M, Murphy K, Regemortier L, Haller R (2001) Characteristics of storm-water runoff from highway construction sites in California. *Transport Res Rec* 1743:33–40
- Lapointe BE, Barile PJ, Matzie WR (2004) Anthropogenic nutrient enrichment of seagrass and coral reef communities in the Lower Florida Keys: discrimination of local versus regional nitrogen sources. *J Exp Mar Biol Ecol* 308(1):23–58
- Lee H, Lau SL, Kayhanian M, Stenstrom MK (2004) Seasonal first flush phenomenon of urban stormwater discharges. *Water Res* 38(19):4153–4163
- Lee JH, Bang KW, Ketchum LH, Choe JS, Yu MJ (2002) First flush analysis of urban storm runoff. *Sci Total Environ* 293(1–3):163–175
- Leitch C, Harbor J (1999) Impacts of land use change on freshwater runoff into the near-coastal zone, Holetown Watershed, Barbados: Comparisons of long-term to single-storm effects. *J Soil Water Conserv* 54(3):584
- Lewis JB (1960) The coral reefs and coral communities of Barbados, West Indies. *Can J Zool* 38:1133–1145
- Lewis JB (1985) Groundwater discharge onto coral reefs, Barbados (West Indies). In: Gabrie C, Harmelin M (eds) Proceedings of the Fifth International Coral Reef Congress. Tahiti, pp 477–481

- Lewis JB (1987) Measurements of groundwater seepage flux onto a coral-reef - Spatial and temporal variations. *Limnol Oceanogr* 32(5):1165–1169
- Lewis JB (2002) Evidence from aerial photography of structural loss of coral reefs at Barbados, West Indies. *Coral Reefs* 21(1):49–56
- Lewis JB, Oxenford HA (1996) A field guide to the coral reefs of Barbados. Department of Biology, McGill University, Montreal
- Mah AJ, Stearn CW (1986) The effect of Hurricane Allen on the Bellairs fringing-reef, Barbados. *Coral Reefs* 4(3):169–176
- Maidment DR (2002) Arc hydro: GIS for water resources. ESRI Press, Redlands, CA, USA
- Meybeck M (1982) Carbon, nitrogen, and phosphorus transport by world rivers. *Am J Sci* 282(4):401–450
- Ministry of Labour (2002) Barbados labour market information system: population and vital statistics. Government of Barbados
- Ministry of Tourism (2003) Annual Tourism Statistical Digest 2003. Government of Barbados
- Nurse LA (1986) Development and change on the Barbados leeward coast: a study of human impact on the littoral environment. PhD Thesis, McGill University
- Oxenford HA, Roach R, Brathwaite A, Nurse LA, Goodridge R, Hinds F, Baldwin K, Finney C (2008) Quantitative observations of a major coral bleaching event in Barbados, Southeastern Caribbean. *Climatic Change* 87:435–449
- Peierls BL, Caraco NF, Pace ML, Cole JJ (1991) Human influence on river nitrogen. *Nature* 350(6317):386–387
- Price S (2006) “Too hot to handle”. Sunday Sun, September 24, 2006(19A), Barbados
- Riehl H (1954) Tropical meteorology. McGraw-Hill, New York
- Risk MJ, Nairn R, Hunte W, Sherwood O, Sammarco P, Brathwaite A, Weatherhead L, Goodridge R (2007) Better water quality brings back corals: Worthing, Barbados. Conference Presentation at the 30th Congress of the International Association of Theoretical and Applied Limnology. Montreal, Quebec
- Rogers CS (1990) Responses of coral reefs and reef organisms to sedimentation. *Mar Ecol-Prog Ser* 62(1–2):185–202
- Rouanet H, Lepine D (1970) Comparison between treatments in a repeated-measurement design – ANOVA and multivariate methods. *Brit J Math Stat Psy* 23:147–163
- Runnalls LA (1994) Effects of rum refinery effluent on reef growth and on inorganic constituents (major/trace) in reef carbonate sediments, Barbados, West Indies. MSc Thesis, University of Reading
- Sander F (1981) A preliminary assessment of the main causative mechanisms of the “island mass” effect of Barbados. *Mar Biol* 64(2):199–205
- Sander F, Moore E (1979) Significance of ammonia in determining the N-P ratio of the seawater off Barbados, West Indies. *Mar Biol* 55(1):17–21
- Sansalone JJ, Buchberger SG (1997) Partitioning and first flush of metals in urban roadway storm water. *J Environ Eng* 123(2):134–143
- Sansalone JJ, Cristina CM (2004) First flush concepts for suspended and dissolved solids in small impervious watersheds. *J Environ Eng* 130(11):1301–1314
- Stanley International Group Inc. (1998) West Coast Sewerage Project Master Plan Report. Report prepared for the Barbados Ministry of Public Works, Transport and Housing
- Stantec Consulting (2003) Gully ecosystem management study: Stormwater management and groundwater augmentation. Report prepared for Barbados Ministry of Physical Development and Environment
- Tewfik A, Guichard F, McCann KS (2007) Influence of acute and chronic disturbance on macrophyte landscape zonation. *Mar Ecol-Prog Ser* 335:111–121
- Tomascik T, Sander F (1985) Effects of eutrophication on reef-building corals. 1. Growth-rate of the reef-building coral *Montastrea annularis*. *Mar Biol* 87(2):143–155
- Tosic M (2007) Impacts of landuse and runoff water quality on coral reef environments in Barbados. MSc Thesis, McGill University <http://www.agrenv.mcgill.ca/agreng/theses/theses/360MarkoTosic2007/360MarkoTosic2007.pdf> (Last accessed June 1, 2008)



- Valiela I, Mazzilli S, Bowen JL, Kroeger KD, Cole ML, Tomasky G, Isaji T (2004) ELM, an estuarine nitrogen loading model: Formulation and verification of predicted concentrations of dissolved inorganic nitrogen. *Water Air Soil Poll* 157(1–4):365–391
- Vernon KC, Carroll DM (1965) Soil and land-use surveys No.18 Barbados. University of West Indies, Imperial College of Tropical Agriculture: Trinidad
- Wallace Evans and Partners (1973) Stormwater Drainage Study Barbados. Government of Barbados and Overseas Development Administration, Foreign and Commonwealth Office
- Wellington C (1999) A nutrient mass balance for nitrogen and phosphorous for the nearshore water of the west coast of Barbados, W.I., July 1996 to May 1997. MSc Thesis, McGill University

# Index

## A

Accuracy assessment, 198, 203, 226, 227, 391, 396, 471, 472  
Advanced Microwave Scanning Radiometer (AMSR), 26  
Aerial photography, 9, 11, 18–20, 23, 48, 211, 212–213, 215–216, 220, 226, 228, 233, 235, 236, 238, 239–240, 242, 243, 245, 247, 252, 253, 254, 263, 264, 298, 301, 302, 312, 348, 351–352, 353, 356, 391, 393, 394, 395, 396, 399, 403, 500, 501, 502, 513  
Agent-based models, 46, 47, 60, 61  
Airborne Data Acquisition and Registration (ADAR), 502  
Air-photo interpretation, 264  
AISA Eagle hyperspectral imager, 177  
Algae, 10, 34, 105, 181, 185, 186, 196, 198, 199, 200, 205, 206, 207–208, 214, 221, 237, 279, 280, 282, 283, 284, 285, 286, 287, 288, 289, 291, 548  
    brown algae, 279  
Altimeter, 8, 17, 20, 35, 40, 236, 366, 375  
Ameland, 8, 67, 68, 69, 74, 77–78  
Ancillary data, 13, 18, 30, 466, 470  
Anderson land cover classification, 26–29, 471  
ANOVA *F*-test, 529, 538, 546  
Apparent Optical Properties (AOPs), 139, 142, 147, 154, 181–182  
Area Weighted Mean Patch Fractal Dimension (AWMSI), 474, 481  
ASTER, 10, 27, 279, 283–284, 285, 287, 289  
Atmospheric correction, 19, 33, 132, 141, 157, 178–179, 187, 188, 189, 196, 207

AVHRR, 24, 34, 40, 56  
AVIRIS, 181, 513

## B

Backscattering properties, 148–151  
Barbados, 2, 12, 521–524, 526, 527, 535, 549  
Barrier island marshes, 7, 391–411  
Bathymetry, 8, 20, 27, 28, 33, 36, 40, 59, 120, 174, 179–181, 211, 213, 216, 221, 223, 224, 226, 227, 228, 233, 245, 246, 251, 254, 273, 305, 320, 383, 456, 495, 500, 513–515, 517, 546  
Beach erosion, 18, 30, 300, 313  
Bellairs Fringing Reef, 521, 523, 528, 535, 546–547, 548  
Benthic habitats, 2, 4, 6, 9, 171–208, 211, 213, 215, 220, 222, 228  
Bidirectional Reflectance Distribution Function (BRDF), 38  
Bioindicators, 508  
Bio-optical algorithms, 9, 141, 142, 146, 156, 171, 182  
Bio-optical characteristics, 9, 139–162  
Bio-optical models, 139, 142, 147  
Buffering, 46, 47, 50–51, 62  
Burnt marshes, 11, 415, 421, 429, 431, 433

## C

Canopy  
    height, 11, 365, 367, 369, 373, 374, 375–377, 380, 382, 386  
    structure, 11, 366, 373, 380–383, 384, 415, 417, 419, 424, 429, 432, 433  
Caribbean sea, 172  
Caspian sea, 12, 439–440, 443, 452, 454, 458

- Cellular automata models, 46, 47, 60–61
- Change detection, 10, 11, 12, 27, 28, 31, 45, 88, 305, 345, 377, 391, 396–406, 407, 408–409, 410, 495, 500, 502, 506, 513, 517
- Channel bathymetry, 513–515
- Chesapeake Bay, 5, 7, 9–10, 26, 35, 37, 115–136, 139–162, 233–255
- Chesapeake Bay Remote Sensing Program (CBRSP), 115, 117–118
- Chlorophyll concentrations, 18, 32
- Chlorophyll-*a* (or *Chl-a*), 9, 32, 35, 38, 39, 40, 115, 116, 117, 118, 119, 120, 121, 122, 123, 124, 125, 126, 127, 128, 129, 130, 131–132, 141, 156, 161
- Clustering analysis, 46, 47, 56, 57–58, 62
- Clustering-Based Neural Network (CBNN), 10–11, 232, 323, 327, 328, 329, 330, 331, 338
- Coastal Assessment Framework (CAF), 464
- Coastal change, 10, 297–321, 345, 513
- Coastal geomorphology, 47, 365
- Coastal hazards, 46
- Coastal Louisiana, 417, 426–427, 433–434
- Coastal waters, 2, 3, 6, 8, 12, 17, 20, 26, 34, 36, 39–40, 58, 116–117, 125, 134–135, 141, 147, 150, 151–152, 153, 157, 158, 160, 161, 216, 320, 324, 343, 383, 461, 489, 545
- Coastal watershed, 12, 26, 34, 50, 58, 343, 461, 489
- Coastal wetland, 2, 4, 6, 18, 29, 48, 352, 417
- Coastal Zone Color Scanner (CZCS), 32, 141, 178
- Colored Dissolved Organic Matter (CDOM), 132, 144, 145–146, 147, 153, 154, 157, 161
- Color scanner, 35
- Conifer forests, 375
- Conservation and restoration planning, 499
- Coral reefs, 4, 7, 30–31, 40, 51, 52, 171–207, 211, 212, 215–216, 522
- Core Area Coefficient of Variation (CACVI), 474, 481, 488
- Crisp object model, 78, 84, 88
- Cross-tabulation matrices, 398, 399, 400, 403, 404, 405
- Cross-track, 384
- D
- Data dimension reduction, 334
- Data models
  - arc marine data model, 46
  - Event-based Spatio-Temporal Data Model (ESTDM), 49
  - geodatabase data model, 49
  - object-oriented data model, 48–49
  - spatio-temporal data models, 49–50
- Data portal, 8, 91, 93, 94, 99, 105–107
- Deciduous forests, 375, 380
- Delaware Bay, 34, 35, 37
- Delta
  - Caspian delta, 439, 440, 454
  - Ural river delta, 12, 441, 442, 454–456, 457
- Derivative Chlorophyll Index (DCI), 508–510
- Descriptive statistics, 46, 56
- Diffuse attenuation coefficient, 33, 172
- Digital aerial camera, 18
- Digital Elevation Model (DEM), 10, 20, 48, 55, 69, 94, 239, 297, 299, 306, 307, 308, 309, 310, 311, 316, 366, 513, 514, 526
- Digital libraries, 91, 100–101
- Digital Orthophotos Quadrant (DOQQ), 239, 243, 304, 316, 318, 319, 466, 488
- Digital Terrain Model (DTM), 367, 375, 378–379
- Digitizing, 11, 220, 243, 264, 285, 299, 302, 306, 313, 353–354, 372, 386, 391, 396, 410, 470–471, 501
- Dissolved organic matter, 140, 142, 161, 194
- Dissolved substances, 17
- Distance modeling, 46, 50, 52
- Diver visibility, 33
- Doppler radar systems, 36
- Drought-flood cycle, 115
- Dune field evolution, 46
- 3-D visualization, 227
- E
- Earth Observing System (EOS), 26
- Earth science enterprise, 26
- Ecological niche, 12, 439, 456, 458
- Eigenvalues, 185, 203, 205, 477
- Electromagnetic spectrum, 5, 21, 351, 366
- Elkhorn slough watershed, 495–497, 499, 515, 518
- El Niño Southern Oscillation (ENSO), 171
- Emergent Herbaceous Wetlands (EHW), 467, 472, 483
- Enhanced Thematic Mapper Plus (ETM+), 282
- ENVI, 285
- ERDAS imagine, 239, 243
- Euclidean distance, 52, 58
- Eutrophication, 12, 35
- Event-scale perturbations, 115

## F

- Farming practice, 12
- Feature-based models, 62
- Fertilization, 509
- Field data collection, 8, 17, 22, 39, 345
- Field techniques, 17–18, 376
- Fire management, 417, 418
- Fire scars, 415–435
- Fluorescence, 147–148, 153, 154, 156, 157, 197, 508
- Fournier Forand (FF), 149, 150, 154
- Fractal dimension index, 406–408
- Fragmentation, 18, 29, 398, 461, 478, 479, 489, 500
- Fuzziness test, 11, 391
- Fuzzy landscape classification, 73–74
- Fuzzy logic, 46, 47, 56, 59, 61–62
- Fuzzy object model, 77–78, 88
- Fuzzy spatial representation, 74–77

## G

- Galeta marine laboratory, 325–326, 332
- Gaussian filter, 302
- Geary's index (C), 53
- General G-statistics, 53
- Geographical entities, 49, 72, 88
- Geographic Information Systems (GIS), 2, 6, 7, 8, 9, 10, 11, 12, 18, 30, 39, 45–62, 91, 93–94, 97, 99, 103, 106, 211, 212, 215, 219–220, 233, 239, 241, 244, 245, 246, 261, 265, 275, 297, 299, 305, 348, 356, 391, 394, 395–396, 462, 464, 470, 471, 488, 495, 499, 500, 501, 513, 523
- Georeferencing, 177, 302, 314, 320, 502
- Geospatial technologies, 1–4, 5–13, 348–349, 461–489
- Geostationary satellites, 23
- Global change, 12, 439
- Global Positioning System (GPS), 217, 367
- Global Spatial data Infrastructure (GSDI), 92, 93, 109
- Gulf of Mexico, 146, 417, 427, 440, 463, 464, 489

## H

- Habitat changes, 391–411
- Hierarchical classification, 468–470
- Historical ecology, 500, 501–507
- Holetown Lagoon, 12, 523, 527, 545, 548
- Hudson river estuary, 10, 259, 260, 261

## Hurricane

- Isabel, 123, 125, 133
- Katrina, 37, 440
- HyMap, 495, 509–510, 513
- Hyperion EO-1, 28
- Hyperspectral remote sensing, 331–337

## I

- IKONOS, 10, 24, 25, 27, 30, 32, 37, 40, 171, 173, 175, 179, 180, 181, 183, 184, 185, 187, 188, 189, 190, 191, 192, 194, 195, 197, 198, 199, 200, 202, 203, 205, 256, 323, 325, 326, 330, 352, 513
- Image classification, 29–30, 38, 40, 73, 75, 185, 206–207, 346, 353–354, 470, 503
- Image segmentation, 29, 303, 354–355
- Inbocht Bay, 270–271, 274
- Inertial Navigation System (INS), 305, 367
- Inherent Optical Properties (IOPs), 142, 146, 147, 148, 151, 154, 155, 157
- Integrated Coastal Zone Management (ICZM), 7, 8, 67–87, 106
- Interactive classification, 469–470
- Interactive image interpretation, 470–471
- Interferometric Synthetic Aperture Radar (IFSAR), 383–384
- International marine metadata interoperability initiative, 101–102
- Interspersion and Juxtaposition (IJ), 417, 475, 477, 478, 482, 485, 488
- Intertidal zone, 10, 279, 323
- Invasive species, 18, 29, 61, 212, 343, 379, 382
- Inverse distance weighting, 55
- ISODATA, 185, 186, 197, 203, 205, 303, 327, 354, 468–469

## K

- Kalmykian Coast, 12, 439, 440, 441, 442, 443, 444, 445, 446, 447, 448, 449, 450, 452, 456
- Kaloko-Honokohau National Historic Park, 9, 211
- Kappa statistics, 471
- Kriging, 55

## L

- Land cover, 8, 11–12, 17–18, 19, 25, 26, 29, 30, 38, 39–40, 51–52, 59, 60–61, 70, 303, 313, 319, 324, 329, 330, 344–345, 346, 354, 355, 377, 378–379, 386, 391,

- 394, 396, 398, 403, 404, 405, 409–410, 469, 470, 495, 507, 510, 511, 513
  - Land cover change, 19, 26, 30, 61, 394, 398
  - Landscape
    - composition, 55, 462–463, 476, 479, 480, 481, 484, 486, 487, 488–489
    - configuration, 55, 481
    - ecology, 12, 355, 461–463, 476, 488
    - level indicator, 18
    - metrics, 12, 46, 47, 52, 55, 58, 62, 406, 461, 462–463, 466, 471–476
    - mosaics, 461, 489
    - pattern, 8, 12, 55, 347, 461–463, 471, 473, 482, 483, 488–489
    - segmentation, 468–469
  - Land use, 3, 8, 12, 18, 26, 27, 28, 45–46, 47, 51, 57, 88, 96, 244, 245, 343, 348, 354, 394, 461, 462, 463, 466, 468, 469–470, 471, 472, 476, 479, 482, 483, 488, 500–501, 504, 507–512
  - change, 27, 28, 410, 504
  - Largest Patch Index (LPI), 474, 477, 478, 481, 485
  - Laser penetration depth, 33
  - Light Detection and Ranging (LIDAR), 20, 365–366, 502
  - Linear Discriminate Analysis (LDA), 323, 333–334, 335
  - Linear regression, 57, 60, 130, 146, 161
  - Local Geary's Index (C), 53
  - Local Moran's Index (I), 53
  - Logistic regression, 60
  - Low-density urban, 482–483, 484, 485
- M**
- Macrophytes, 4, 10, 260, 272–273, 279–280, 282, 284, 285
  - Mangroves, 3, 4, 10, 48, 323–326, 330, 332, 337, 347, 379, 382
  - Manhattan distance, 52
  - Map overlay, 47, 50, 51–52, 62
  - Marsh burn recovery, 418, 419–420, 421–423, 424–426, 433–435
  - Marsh productivity, 18
  - Maximum Likelihood Classifier (MLC), 11, 323, 325, 328, 329, 330–331, 338, 354
  - Mean Patch Size (MPS), 474, 479, 481
  - MEDium Resolution Imaging Spectrometer (MERIS), 28, 32, 141, 157
  - Microwave radiometer, 17, 20, 21, 35, 36
  - Minimum Mapping Unit (MMU), 21, 215, 221, 264, 352, 396
  - Minimum Noise Fraction (MNF), 185–186, 203, 204, 205
  - Modal Filtering, 470, 476
  - MODerate resolution Imaging Spectroradiometer (MODIS), 26, 117, 141
  - Modified Simpsons Diversity Index (MSIDI), 475, 477, 478, 481–482
  - Modified Soil Adjusted/Vegetation Index (MSAVI), 32
  - Monterey Bay, 101, 102, 146, 495–500, 503, 516
  - Moran's index (I), 53
  - Morphologic operation, 309
  - Mudflats, 4, 12, 439–458, 496, 515
  - Multi-date color composite, 441
  - Multi-layer perceptron (MLP), 59
  - Multispectral imagers, 30, 32
  - Multispectral Scanner (MSS), 19, 21, 25, 40, 282, 324, 352, 394
  - Multivariate regression, 57, 58
- N**
- NASA Ocean Data Acquisition System (ODAS), 117, 119–120, 123, 132–133
  - National Estuarine Research Reserve (NERR), 499, 508, 513
  - Nearest-neighbor analysis, 46, 47, 52, 54, 62
  - Nearshore sedimentation, 521, 523
  - Neighborhood functions, 46, 50, 51
  - Neural networks, 34, 38, 46, 47, 56, 58–59, 62, 208, 323, 410
  - Nitrate-nitrite nitrogen, 521, 526
  - Nitrogen, 39, 116, 133, 507–508, 509–510, 511, 521, 526, 545
  - NOAA
    - Coastal Change Analysis Program (C-CAP), 29, 345, 513
    - coastal remote sensing program, 18
    - coastal services center, 92, 97, 108, 305, 499
  - Non-Algal Particles (NAP), 142, 144, 151–152, 154, 156–161, 162
  - Non-point Source Pollution, 463
  - Non-seasonal Marsh, 11
  - Normalized Difference vegetation Index (NDVI), 32, 345, 348, 420–421
  - Number of Patches (NP), 474, 477, 478, 481, 483, 485
- O**
- Object-Based Image Analysis (OBIA), 354, 355, 356, 357–358

## Ocean

- color, 27, 32, 33, 34, 35, 38, 117, 118, 119, 123, 131–132, 139–143, 147, 156, 157, 161, 171–208
- waves, 17
- winds, 17

Off nadir pointing, 25

Oil spills, 4, 34, 36

Ontology, 99–100, 101–102, 107

Orbital altitude, 25

Orbview–2, 24

Orbview–3, 25, 27, 352

Oregon coastal atlas, 95–96, 97–99, 100–102, 103–104, 107

Organic suspended particles, 17

Orthophotos, 39, 48, 318–319, 504–505, 510

Orthorectification, 239, 302, 316, 318

Overfertilization, 12, 521

## P

Particulate Organic Carbon (POC), 158

Pensacola Bay, 463–464, 473, 479, 481, 482, 485, 489

Pensacola Estuarine Drainage Area (PEDA), 461, 463, 464–465, 467, 473, 479, 481, 482, 483, 485, 489

Percent of Landscape (PLAND), 474, 478, 483

Phosphorus, 39, 116, 521, 526, 545, 547–548

Photochemical Reflective Index (PRI), 508–510

Photogrammetry, 2, 383–384

Photo Interpretation, 10, 12, 233, 235, 236, 239–240, 241, 243, 264, 353, 354

Photosynthetic carbon assimilation, 116

Phytoplankton, 5, 9, 33, 115–116, 117, 118, 119, 120, 121, 122, 123–124, 125, 128, 129, 142, 143, 145–146, 153, 158–159, 160, 172, 181, 189, 193–194, 197, 240, 282, 522

biomass, 115–116, 117, 120, 122, 123–125, 128, 129, 142, 143

Point source pollution, 522–523, 545, 548

Polarization, 415, 417–418, 422–423, 425, 432–433

Polynomial Regression, 55

Population growth, 343, 391, 392–393

Post-classification comparison, 31, 40, 398

Primary productivity, 5, 9, 115–116, 120–121, 129–131, 143, 153, 259, 260, 273, 342, 343

Principal component analysis, 46, 47, 56, 58, 62, 333, 463, 476–478, 488

Probabilities, 31, 529, 538

Profilers, 20

Proximity analysis, 50, 52

Punta Galeta, 325–326

## Q

Quadrat analysis, 46, 47, 52, 53–54, 62, 503

Quality assurance, 236, 264, 266

QuickBird, 10, 25, 30, 37, 48, 171, 176, 179, 181, 183, 184, 185, 186, 187, 188, 189, 190, 192, 194, 195, 197, 198, 201, 202, 203, 205, 206, 279, 284, 287, 288, 289, 290, 291, 325, 352, 356, 357

## R

Radar, 8, 12, 17, 19, 20, 21, 35, 36, 37, 40, 101, 280, 284, 287, 289, 291, 325, 346, 418, 419, 424, 425, 426, 432–433, 434, 439, 441, 442, 449, 451, 454

Radarsat, 10, 20, 28, 279, 284, 287, 290

Radial basis function, 55

Radiative transfer model, 9, 139, 140, 147, 149, 150, 151, 153, 154–156

Radiometers, 17, 20, 21, 36, 40, 117, 119, 175, 419

Radiometric resolution, 19, 23, 283–284

Rectification, 11, 31, 177, 239, 302, 316, 318, 391, 466, 502

Reeds, 442, 443, 445, 447, 448, 452, 453, 456, 457, 458

Reef sedimentation, 521

Region grouping, 303

Registration, 100, 243, 326

Repeat cycles, 25, 37

Resampling, 285, 326

Riparian buffers, 18

River

Blackwater river, 473, 479, 481, 485

Escambia river, 473, 479, 481, 485

Lower York river, 248, 251, 252

Petaluma river, 348, 349

RMS, 189, 191, 243, 285, 326, 379, 391

Roatan Island, 9, 171, 172, 173, 176, 179, 190, 193, 202

Runoff water quality, 521–549

## S

SAC-C, 10, 279, 282, 283, 285, 286, 288

St. Marks National Wildlife Refuge, 418, 420

Salinity, 3, 4, 10, 17, 19, 20, 33, 35, 36, 39, 120, 238, 241, 246, 259, 262, 272, 273,

- 300, 331, 337, 342, 343, 345, 347, 365, 427, 521, 528, 534
- Salt marshes, 3, 45, 61, 342, 346, 355, 356, 366, 392, 394, 395, 440, 496, 503, 510
- San Francisco Bay, 11, 341, 342, 344, 346, 347, 348, 349, 350, 352, 357, 496
- Scatterometers, 8, 17, 20, 35, 36
- Seagrasses, 4, 30, 54, 172, 173, 194, 196, 206, 234, 290, 410
- Sea-level change, 4, 300, 439, 440, 447, 453
- Sea level fluctuation, 12, 439–459
- Seasonal marsh, 433–435
- Sea surface height, 17, 19, 20, 35
- Sea surface roughness, 19, 284
- Sea surface temperature, 17, 19, 33, 35, 100, 117
- Sea-viewing wide field-of-view sensor (SeaWiFS), 24, 27, 32, 33, 112, 117, 131, 132, 141, 142, 156, 157, 160, 178
- SeaWiFs Aircraft Simulator (SAS), 117, 119, 120, 133
- Sediment plume, 289
- Semivariogram, 53
- Sensitivity analysis, 135
- Sewage treatment, 140
- Shoreline erosion, 4, 46, 146, 301, 313, 324
- Shoreline mapping, 7, 297–321
- Sidelooking Airborne Radar (SLAR), 19, 20
- Side-scanning sonar, 20
- Small-Footprint, Discrete-Return LIDAR, 369–370, 372, 374, 376, 377, 380, 381, 385
- Small-Footprint, Waveform-Resolving LIDAR, 365, 370–374, 376, 377, 386
- Soil moisture, 17, 19, 20, 35, 36, 377
- Solar illumination angle, 23
- Space-Time Composite Model (STCM), 49
- Spatial analysis, 5, 6, 7, 8, 11, 12, 45–62, 95, 96, 396, 495–518
- Spatial autocorrelation, 46, 47, 52–53, 546
- Spatial data infrastructures, 91–109
- Spatial interpolation, 46, 47, 52, 55–56, 301, 306, 307, 312
- Spatial modeling, 8, 46, 47, 60–61, 62, 470, 488
- Spatial observational units, 463, 473
- Spatial pattern analysis, 8, 46, 47, 52–56
- Spatial reclassification, 12, 461, 468, 469, 470
- Spatial resolution, 9, 23, 25, 26, 33, 34, 36, 48, 117, 120, 123, 132, 133, 140, 141, 171, 172, 177, 206, 207, 282, 283, 284, 291, 305, 311, 314, 315, 316, 324, 325, 326–328, 346, 348, 351, 352, 354, 355, 356, 357, 366, 379, 394, 396, 418, 441, 466, 468, 502, 506, 508, 509
- Spatio-Temporal Object Model (STOM), 49
- Spearman's rank correlation, 476, 478
- Spectral absorption coefficient, 33
- Spectral backscattering, 33
- Spectral library, 208
- Spectral resolution, 23, 48, 150, 177, 181, 206, 207, 324, 325, 341, 345, 346, 351, 352, 366, 502
- Spectroradiometer, 26, 117, 141, 508, 509
- SPOT, 24, 25, 27, 205, 324, 394
- Statistical models, 46, 47, 60
- Submersed Aquatic Vegetation (SAV), 233–255
- Supervised classification, 29, 30, 38, 73, 202, 319, 506
- Synthetic Aperture Radar (SAR), 11, 20, 28, 35, 36, 37, 40, 284, 346, 383, 415, 418, 422, 426, 432, 433, 442, 449, 450, 452
- T
- Temporal dimension, 49, 62
- Temporal resolution, 6, 8, 17, 21, 22, 36, 39, 117, 132, 134, 135, 282, 345, 352, 358, 373
- Terra, 26, 27, 283, 382
- Thematic Mapper (TM), 26, 282, 324, 352, 394, 415, 418, 420, 427, 466
- Thermal Emission and Reflection Radiometer (ASTER), 27, 283–284, 285, 287, 289
- Thermal infrared scanners, 8, 17, 36
- Thiessen polygons, 55
- Tidal datums, 298, 300, 301, 311, 513
- Tidal wetland, 7, 11, 48, 275, 341, 343, 344–345, 347–348, 349, 351, 354, 495, 496, 497, 499, 502, 507, 513, 515, 516 change, 347–348
- Tierra Del Fuego, 279–292
- Topographic maps, 39, 266, 298
- Topography, 19, 20, 35, 48, 281, 284, 301, 305, 306, 307, 343, 346, 365, 366, 367, 372–373, 374, 375, 377–379, 382, 383, 384, 385, 386, 456
- Topsail Island, 11, 391, 393, 394, 395, 396, 397, 406, 410
- Total Core Area (TCA), 475, 477, 478, 481, 485
- Total Suspended Sediments (TSS), 35, 39, 160, 521, 522, 526, 527, 528, 530, 531, 532, 533, 534–535, 536, 537, 538, 539–540, 541, 542, 543, 544, 546, 547
- Triangular Irregular Networks (TIN), 48, 216

Triangulation, 55, 383–384

Turbidity, 10, 12, 18, 27, 30, 35, 134, 233, 234, 235, 237, 240, 246, 252, 259, 261, 272, 273, 274, 421, 521, 526, 527, 528, 530, 531, 532, 533, 535, 536, 537, 538, 539, 540, 541, 544, 546, 547

## U

Uncertainties, 8, 67, 68, 71, 72, 74, 83, 85, 86, 139, 142, 147, 148, 151, 155, 160

Undersea photography, 174

Unsupervised classification, 30, 202

Upper Texas Gulf Coast, 10, 299, 309, 312, 313–320

## V

Vegetation

indices, 25, 32, 345, 351  
metrics, 375

Virginia Water Quality Standards, 248

Vocabulary Integrated Environment (VINE), 102

Volume Scattering Function (VSF), 148, 149, 150, 151

Volunteer monitoring, 261, 265, 266–267, 273

## W

Water

quality, 3, 4, 6, 8, 9, 12, 18, 33, 34, 35, 38, 57, 103, 117, 135, 140, 142, 156, 207, 242, 243, 248, 252, 260, 508, 509, 513, 521–549

turbidity, 18, 30, 233, 235, 252, 535, 536, 541

Waveform-Resolving Large-Footprint LIDAR, 374–375

Whisk-broom, 21

Woody wetlands, 467, 472, 482, 483